

**Hydrothermal Upgrading of
Lignocellulosic Biomass:
Kinetic Analysis of Model Dimers**

Artur José Rolo de Andrade

May 2023

Supervisor: Dr. Christopher J. Tighe

Department of Chemical Engineering

Imperial College London

Submitted in fulfilment of the requirements for the degree of
Doctor of Philosophy in Chemical Engineering of Imperial College London
and the Diploma of Imperial College London

Abstract

The transport sector is responsible for a significant fraction of the world's total greenhouse gas (GHG) emissions. When derived from relatively abundant non-food renewable sources, such as lignocellulosic biomass, biofuels are a viable option to reduce GHG net-emissions. Hydrothermal liquefaction (HTL) is a process that transforms biomass into a wide range of products, including bio-oil; this in turn can be converted into direct replacements for fossil fuel-derived gasoline and diesel, being considered “drop-in” biofuel. The HTL process, which has already been demonstrated at pilot scale, is facilitated by the marked variation in the properties of water as it nears its critical point, allowing the fine-tuning of, *e.g.*, density, acidity, and solubility of organics.

HTL of lignocellulosic biomass is a complex process due to the variability in the composition of the naturally occurring feedstocks, intricate reactional network, and strong dependence on operating conditions. This objective of the work presented in this thesis was to close the gap in knowledge between the kinetic mechanisms for the HTL of complex lignocellulosic biomass, and relatively simple model compounds. A methodology was developed to achieve this objective and tested using feedstocks of dimers that represent structures found in woody biomass: dibenzyl ether (DBE), representative of lignin, and sucrose, representative of cellulose.

Experiments were conducted in a configuration expected to be scalable for industrial applications, consisting of a continuous process, with operating pressure controlled independently from temperature. A confined jet mixer generated rapid mixing at the reactor's inlet. Reactions occurred in a tubular section, being halted by quenching with water, followed by heat exchange with chilled water. For experiments using DBE as feed, HTL products were distributed between gas and liquid phases, with the latter clearly divided in organic and aqueous fractions. When sucrose was fed to the reactor, solid particles were also produced alongside compounds in gas and liquid phases. Separation and analytical methods were used to measure the amount of each phase and quantify selected products.

The mixing patterns around the confined jet mixer were analysed using computational fluid dynamics (CFD) simulations, which were representative of the performed experiments. All simulations with water fed under supercritical conditions achieved 99.9% of average outlet composition 16 mm after the jet's outlet, confirming a very fast mixing. The conversion and yields of each simulation were compared against equivalent CFD models which did not consider feed mixing. No significant variations were observed between the outputs of the two types of models. Therefore, modelling the confined jet mixer in detail was not required to analyse the experimental results. Instead, each experiment could be simulated as a plug flow reactor with a single inlet consisting of the hot mixture of water and organic feed. The mathematical model developed included the calculation of: reaction rates, heat losses through the tube wall, thermodynamic and transport properties, and dispersive transport.

Those simulations were used to estimate kinetic parameters by minimising the difference between measured and estimated reaction yields, accounting for the respective experimental uncertainty. The hydrothermal cleavage of the ether bond in dibenzyl ether was studied at temperatures in the range 287 – 369 °C, pressures from 245 to 254 bar, and residence times between 5 and 7 seconds. Simulations accounted for hydrolysis and degradation reactions. Detailed hydrolysis rates including two observed kinetic constants provided a better fitting between experimental data and calculated values. However, the estimated parameters exhibited a large uncertainty. Based on simplified reaction rates, DBE hydrolysis most likely occurred through an S_N2 mechanism with OH⁻ as the substitution nucleophile, being affected by the concentration of this ion, as well as H⁺. For this reaction, the apparent activation energy was estimated as 180 ± 2 kJ/mol.

The degradation of sucrose in the hydrothermal medium was investigated at temperatures, pressures and residence times in the ranges 282 – 372 °C, 246 – 254 bar, and 3 – 7 seconds, respectively. The system was modelled as a homogeneous liquid, with organic compounds divided in three groups: soluble organics, volatiles, and solids. The first group included glucose, fructose, 5-(Hydroxymethyl)furfural (5-HMF), pyruvaldehyde, and 1,6-anhydro-β-D-glucose, resulting in a total of 16 possible reactions. A stepwise approach was developed to obtain kinetic parameters under increasing levels of model complexity and considering the effect of water's self-ionisation product in subcritical conditions when relevant. Analysing the standard deviation of the obtained kinetic parameters identified the ones that overparameterized the estimation, resulting in the simplification of the 16 reactions to 9. Those reactions included: (1) isomerisation between glucose and fructose, which was driven towards the latter (activation energy of 73 ± 2 kJ/mol); (2) 1,6-anhydro-β-D-glucose formation from glucose and (3) degradation (activation energies of 45 ± 7 and 45 ± 10 kJ/mol, respectively); (4) formation of pyruvaldehyde from fructose (activation energy of 71 ± 5 kJ/mol); (5) 5-HMF production from fructose and (6) degradation (activation energies of 52 ± 9 and 220 ± 60 kJ/mol, respectively). From those, only the rates of (3) and (5) were expected to be significantly affected by [OH⁻] or [H⁺].

Declaration of originality

I hereby certify that the work presented in this thesis is the result of my own investigations during the PhD project undertaken at the Department of Chemical Engineering at Imperial College London between November 2018 and July 2022. All else is referenced and properly acknowledged.

Artur José Rolo de Andrade

May 2023

Copyright declaration

The copyright of this thesis rests with the author. Unless otherwise indicated, its contents are licensed under a Creative Commons Attribution – Non Commercial 4.0 International Licence (CC BY-NC). Under this licence, you may copy and redistribute the material in any medium or format. You may also create and distribute modified versions of the work. This is on the condition that: you credit the author and do not use it, or any derivative works, for a commercial purpose. When reusing or sharing this work, ensure you make the licence terms clear to others by naming the licence and linking to the licence text. Where a work has been adapted, you should indicate that the work has been changed and describe those changes. Please seek permission from the copyright holder for uses of this work that are not included in this licence or permitted under UK Copyright Law.

I won't stop being a blacksmith. If I can be something more, why not attempt it?

– translated from Eduardo Duarte Ferreira

Acknowledgements

First and foremost, I would like to acknowledge my supervisor Dr. Chris Tighe. I am extremely grateful to Chris for granting me the opportunity to expand my horizons beyond process modelling, towards experimental chemical engineering and academic research. His trust, guidance, and dedication were key. I would also like to thank UK Research and Innovation for offering me a PhD scholarship.

Thank you, Mário Calado, for introducing me to hydrothermal liquefaction of biomass. Mário, being the first in our group to study this phenomenon, laid the groundwork for this topic, and I will be forever grateful for his guidance and availability. I will always remember our enthusiastic and long discussions (frequently to the displeasure of those around us). I hope I was a worthy successor.

I would also like to thank Parth Shah, who along with Mário and Chris, designed the primary structure of the HTL rig and helped me get reacquainted with working in a lab. I would like to acknowledge my other lab partners who made these four years a significantly better experience: Tianyi, Nathan, Janet, Sirong, and Louis. For this same reason, I would like to thank my PhD colleagues Tanuj and Mariana.

For their expertise and patience, I would like to thank Patricia Carry and Kaho Cheung. The analytical part of this work was conducted under guidance at Imperial's Analytical Services. I would also like to extend my gratitude to Susie Underwood for her support in dealing with academic bureaucracy, and Ben Kistnah for always finding the right equipment and for the countless refills of liquid nitrogen.

To Umang Shah, James Campbell, and Claire Adjiman, thank you for making this PhD a richer experience by offering me tutoring positions in Knowledge Labs and Advanced Process Optimisation. The former was particularly challenging as it involved transitioning from experimental to model-based activities during the COVID-19 pandemic. I am grateful Umang and James believed I would rise to the occasion.

I am thankful for the support of my "UK family": the flatmates I had over the years and particularly the WhatsApp group *PT Refugees*. I certainly owe the latter my mental stability over the last four years. I am extremely grateful for their patience and company in the endless pub nights, boardgame evenings, all-day BBQ's, impromptu coffees, and afternoons in the park.

Additionally, I would like to thank my long-distance friend groups *Maniar de falar* and *Teremos sempre o Tramagal*, who always welcomed me back with open arms when I needed a break.

I would like to thank my family for raising me to be person I am today. I appreciate the effort of my brother and sister-in-law, Adriano and Alexandra, to understand my work while I chattered about it for the last four years; and for giving me the most adorable niece and nephew. It is impossible to express how grateful I am to my mother, Almerinda. Her unconditional trust and support kept me going, as well as the countless hours of listening and nodding to my theories, complaints, and other stories.

Lastly, I would like to acknowledge my first math teacher, my father, Ernesto. His unexpected passing was the catalyst that led me to this PhD. I wish you were here to see the result. This thesis is dedicated to you.

Contents

Abstract.....	i
Acknowledgements.....	vi
Contents	viii
List of figures.....	xvi
List of tables.....	xxiv
Nomenclature.....	xxvii
List of abbreviations	xxvii
List of symbols.....	xxix
Roman letters	xxix
Greek letters	xxxii
Chapter 1 Introduction	1
1.1 Towards carbon-neutrality	1
1.2 Second-generation biofuels.....	3
1.2.1 Why hydrothermal liquefaction?.....	6
1.3 Project motivation	7
1.4 Objectives and scope.....	8
1.5 Structure of this thesis.....	9
Chapter 2 Literature review	10
2.1 Introduction.....	10
2.2 HTL of lignocellulosic biomass.....	10
2.2.1 Properties of water	13
2.2.2 Cellulose	15
2.2.3 Hemicellulose.....	16
2.2.4 Lignin.....	17
2.3 Continuous HTL	19
2.3.1 Particle size	21

2.3.2	Feed concentration	22
2.3.3	Temperature	22
2.3.4	Residence time and heating/cooling rates	23
2.3.5	Solvents and co-solvents	23
2.3.6	Homogeneous catalysis and pH	25
2.3.7	Heterogenous catalysis	25
2.4	Downstream processing	26
2.5	Concluding remarks	28
Chapter 3 Experimental		30
3.1	Introduction	30
3.2	Materials	31
3.3	Design of HTL apparatus	31
3.3.1	Process description	32
3.3.2	Safety considerations	35
3.3.3	Confined jet mixer and reactor	36
3.3.4	Supercritical water heater	38
3.3.5	Double pipe heat exchanger and cooling water chiller	39
3.4	Operation of HTL apparatus	39
3.4.1	Start-up	40
3.4.2	Steady state operation and sampling	41
3.4.3	Shutdown	41
3.5	Separation methods	42
3.5.1	Filtration	42
3.5.2	Gas sweep	42
3.5.3	Centrifuging and syringe extraction	43
3.5.4	Solvent extraction and evaporation	43
3.6	Analytical methods	44
3.6.1	High-performance liquid chromatography	44
3.6.2	Ultraviolet and visible spectrometry	46

3.6.3	Refractive index spectrometry	47
3.6.4	Gas chromatography	48
3.6.5	Mass spectrometry	48
3.6.6	Flame ionisation detection	49
3.6.7	Fourier-transform infrared spectrometry.....	49
3.7	Errors and Uncertainties.....	50
Chapter 4 Hydrothermal reactor model		52
4.1	Introduction.....	52
4.1.1	Software for mathematical modelling.....	52
4.1.2	Equations of state	52
4.1.3	Parameter estimation, optimisation, and sensitivity analysis.....	53
4.2	Modelling supercritical water	54
4.2.1	Supercritical transition temperature	55
4.2.2	Pseudo-vapour fraction	57
4.2.3	Density and specific enthalpy	58
4.2.4	Viscosity and thermal conductivity.....	60
4.3	Top-level model: reactor.....	61
4.4	Sub-model: reaction rate	63
4.5	Sub-model: heat transfer	64
4.5.1	Detailed heat balance	64
4.5.2	Simplified heat balance	66
4.6	Sub-model: thermophysical properties	67
4.7	Sub-model: dispersion coefficient	70
Chapter 5 Preliminary analysis of the HTL rig.....		72
5.1	Introduction.....	72
5.2	Actual pump flowrate.....	72
5.3	Cooling capacity	74
5.4	Supercritical water and reactor temperature	76
5.4.1	Tests using only water.....	78

5.4.2	Tests using DBE/water mixtures.....	81
5.5	Reactor's heat transfer coefficients.....	81
5.6	Concluding remarks.....	82
Chapter 6 CFD analysis of the confined jet mixer.....		84
6.1	Introduction.....	84
6.1.1	Computational fluid dynamics.....	84
6.1.2	Background.....	85
6.2	Model configuration.....	85
6.2.1	Geometry.....	86
6.2.2	Material properties.....	89
6.2.3	Turbulent flow model.....	89
6.2.4	Heat transfer.....	90
6.2.5	Chemistry.....	91
6.2.6	Transport of concentrated species.....	92
6.2.7	Multiphysics interface.....	93
6.2.8	Simplified model.....	93
6.3	Description of simulation cases.....	94
6.3.1	Dynamic simulation.....	95
6.3.2	Mass and energy conservation.....	96
6.3.3	Discretisation mesh.....	97
6.4	Results and discussion.....	98
6.4.1	Mass and energy conservation.....	99
6.4.2	Recirculation zones.....	100
6.4.3	Distance to achieve full mixing.....	106
6.5	Comparison between detailed and simplified CFD models.....	110
6.6	Concluding remarks.....	112
Chapter 7 Kinetics of the hydrothermal processing of dibenzyl ether.....		114
7.1	Introduction.....	114
7.1.1	Background.....	114

7.1.2	Objectives	116
7.2	Experimental setup.....	116
7.2.1	Progress summary	117
7.2.2	Operating conditions.....	119
7.3	Product analysis	120
7.3.1	Gas phase	120
7.3.2	Liquid phase.....	123
7.3.3	Hydrolysis products	126
7.3.4	Pyrolysis products.....	127
7.4	Kinetic modelling.....	129
7.4.1	Rate equation for the hydrolysis of dibenzyl ether	129
7.5	Kinetic parameters estimation.....	131
7.5.1	Estimated parameters	133
7.5.2	Fitting quality	133
7.5.3	Range of applicability	138
7.6	Model sensitivity analysis.....	138
7.6.1	Property corrections and real composition.....	138
7.6.2	Heat loss and enthalpy of reaction	140
7.6.3	Dispersion and coefficient calculation method	141
7.6.4	Comparison with literature.....	142
7.7	Concluding remarks	143
Chapter 8 Kinetics of the hydrothermal processing of sucrose.....		146
8.1	Introduction.....	146
8.1.1	Background	146
8.1.2	Objectives	150
8.2	Experimental setup.....	150
8.2.1	Operating conditions	151
8.2.2	Progress summary	152
8.3	Product analysis	155

8.3.1	Phase distribution.....	157
8.3.2	Gases.....	159
8.3.3	Soluble organics.....	162
8.4	Mathematical model description.....	171
8.4.1	Component list and reaction network.....	171
8.5	Kinetic parameters estimation.....	172
8.5.1	Systematic workflow.....	173
8.5.2	Estimated parameters.....	176
8.5.3	Fitting quality.....	179
8.5.4	Range of applicability.....	184
8.5.5	Comparison with literature.....	186
8.6	Concluding remarks.....	188
Chapter 9 Conclusions.....		191
9.1	Summary of estimated reaction pathways.....	193
9.1.1	Hydrolysis of dibenzyl ether.....	193
9.1.2	Hydrothermal processing of sucrose.....	193
9.2	Future Work.....	195
9.2.1	Improving current case studies.....	195
9.2.2	Further model validation.....	196
9.2.3	Expanding case studies.....	197
Appendix A Hydrothermal liquefaction apparatus.....		200
A.1	Operating procedure.....	200
A.1.1	Start-up.....	200
A.1.2	Steady state operation.....	202
A.1.3	Shut-down.....	202
A.2	Process and instrumentation diagram (P&ID).....	204
Appendix B Instrument calibration.....		205
B.1	Rotameter calibration.....	205
B.2	HPLC with UV-vis detection.....	205

B.2.1	Chromatographic method.....	206
B.2.2	Composition calibration.....	206
B.3	HPLC with RID	208
B.4	GC with FID	210
Appendix C	Detailed calculations and results: Preliminary analysis.....	212
C.1	Additional mass and energy balances	212
C.1.1	Feed mixing	212
C.1.2	Downstream cooling	212
C.2	Detailed results.....	213
Appendix D	Detailed calculations and results: CFD analysis	216
D.1	Discretisation mesh selection.....	216
D.1.1	Radial axis.....	216
D.1.2	Vertical axis	218
D.1.3	Auto-refinement in jet and mixing sections	219
D.1.4	Combined effect.....	221
D.2	Complete geometry profiles.....	223
Appendix E	Detailed calculations and results: Dibenzyl ether	228
E.1	Calculation summary	228
E.2	Detailed results.....	230
E.3	Averaged results.....	236
E.4	Rate equations for the hydrolysis of dibenzyl ether.....	237
E.4.1	Mechanism: S_N1 / S_N2	237
E.4.2	Mechanism: S_N1	237
E.4.3	Mechanism: S_N2	239
E.5	Proton concentration	240
Appendix F	Detailed calculations and results: Sucrose	242
F.1	Calculation summary	242
F.2	Detailed results.....	244
F.3	Averaged results.....	255

F.4	Progression of the parameter estimation workflow	257
	Bibliography	263

List of figures

Figure 1.1: UK’s annual GHG (full lines) and CO ₂ (dashed lines) net emissions between 1990 and 2020 [11]. Left axis referred to total emissions (black lines), and right axis to emissions specific to the transport sector (green lines).....	2
Figure 1.2: UK’s distribution of CO ₂ emissions within the transport sector [11]. Values referred to the year 2020, with CO ₂ emissions in this sector of 113 Mt.....	2
Figure 2.1: Representative molecular structure and relative distribution of the polymers found in lignocellulosic biomass [2,3,47].	11
Figure 2.2: HTL overall reaction steps from biomass feed to bio-oil and other biproducts.	12
Figure 2.3: Water density (a), specific enthalpy (b), and viscosity (c) near the critical point (374 °C and 221 bar). Calculated using IAPWS-95 [55].	14
Figure 2.4: (a) Water self-ionisation product (K_w) and (b) dielectric constant (ϵ_r) near the critical point (374 °C and 221 bar). Calculated using density-based correlations [56,57].	15
Figure 2.5: Molecular structure of hemicellulose’s typical monomers.....	16
Figure 2.6: Molecular structure of lignin’s monomers.	18
Figure 2.7: Yong et al.’s reactional pathway for lignin hydrolysis. Adapted from [84].	19
Figure 2.8: Generic block diagram of a complete HTL process.	20
Figure 3.1: HTL process flow diagram (a) and simplified P&ID for the assembled rig (b).	32
Figure 3.2: Initial (top) and final (bottom) implementations of the confined jet mixer. Adapted from [124] with permission from the author.	37
Figure 3.3: Initial (left) and final (right) reactor sections, with 80 and 354 mm, respectively.	38
Figure 3.4: Flow arrangement around valve V-7 during pressurisation/heating (left) and normal operation (right).	40
Figure 4.1: Variation of water density with temperature at different pressures, including inflexion points.....	55
Figure 4.2: Saturation temperature, critical point, supercritical transition temperature, and associated 2 nd order polynomial regression.	56
Figure 4.3: Water SCTT estimated using linear, quadratic, and logarithmic regressions.....	57
Figure 4.4: Variation of pseudo-vapour fraction (z_{SCT}) with temperature and parameters in equation (4.5). $SCT = 381$ °C.	57
Figure 4.5: Water density (a) and specific enthalpy (b) estimated using IAPWS and SAFT- γ Mie.....	59
Figure 4.6: Water density (a) and specific enthalpy (b) estimated using IAPWS and SAFT- γ Mie correction model after optimisation.	59
Figure 4.7: Water viscosity (a) and thermal conductivity (b) estimated using IAPWS and the CALS method.	60

Figure 4.8: Water viscosity (a) and thermal conductivity (b) estimated using IAPWS and the CALS method with correction model after optimisation.	60
Figure 4.9: Structure of the hydrothermal reactor model.	61
Figure 4.10: Reactor temperature profiles estimated using the detailed heat transfer sub-model. Cases selected from water-only (a) and water-DBE (b) in Appendix C.2.	66
Figure 4.11: Reactor temperature profiles estimated using the simplified heat transfer sub-model. Cases selected from water-only (a) and water-DBE (b) in Appendix C.2.	67
Figure 4.12: Reactor density profiles estimated using the detailed property calculation sub-model. Cases selected from Chapter 7 (a), and from Chapter 8 (b), applying kinetics from scenario 5 and scenario 2, respectively.	68
Figure 4.13: Reactor viscosity profiles estimated using the detailed property calculation sub-model. Cases selected from Chapter 7 (a), and from Chapter 8 (b), applying kinetics from scenario 5 and scenario 2, respectively.	69
Figure 4.14: Reactor proton concentration profiles estimated using the detailed property calculation sub-model. Cases selected from Chapter 7 (a), and from Chapter 8 (b), applying kinetics from scenario 5 and scenario 2, respectively.	69
Figure 5.1: K-type thermocouple inserted in respective well.	76
Figure 5.2: Thermocouple location and configuration changes between the supercritical heater to the reactor's outlet.	77
Figure 5.3: Temperatures measured in the SCW line during preliminary tests using water only. H-1 setpoint divided in three ranges: 360 – 400 °C (a), 410 – 450 °C (b), and 460 – 500 °C (c).	79
Figure 5.4: Temperatures measured in the reactor during water-only preliminary tests with SCW-to-organic feed ratio fixed at 2 (a) and 3 (b).	79
Figure 5.5: Variation of water's heat capacity at constant pressure (C_p) with temperature for selected pressures.	80
Figure 5.6: Temperatures measured during preliminary tests using DBE/water mixtures (heater setpoint fixed at 460 °C).	81
Figure 6.1: Geometrical representation of the HTL reactor and surrounding tubing implemented in COMSOL: complete geometry (a), and jet area (b). Dimensions are given in Table 6.1...	87
Figure 6.2: Inlets and outlets of mass and energy in the geometrical representation of the HTL reactor.	90
Figure 6.3: Best fitted simplified pathway for sucrose's hydrothermal reactions (Section 8.5.2). Reactions numbered according to the network described in Section 8.4.1.	92
Figure 6.4: Simplified geometrical representation of the HTL reactor and surrounding tubing implemented in COMSOL. Sizes in Table 6.1.	94

Figure 6.5: Variation of average outlet temperature (a) and organic mass fraction (b) in the dynamic simulation of cases S1 to S5.	95
Figure 6.6: Variation of average outlet temperature (a) and organic mass fraction (b) in the dynamic simulation of cases D1 to D5.	96
Figure 6.7: Temperature profile surrounding the SCW jet for sucrose simulations (scenarios S1 to S5). Velocity field is indicated by non-scaled arrows.	101
Figure 6.8: Total organic mass fraction profile surrounding the SCW jet for sucrose simulations (scenarios S1 to S5). Velocity field is indicated by non-scaled arrows.	102
Figure 6.9: Temperature profile surrounding the SCW jet for DBE simulations (scenarios D1 to D5). Velocity field is indicated by non-scaled arrows.	103
Figure 6.10: Total organic mass fraction profile surrounding the SCW jet for DBE simulations (scenarios D1 to D5). Velocity field is indicated by non-scaled arrows.	104
Figure 6.11: Temperature (a) and total organic mass fraction profiles (b) for case S3 neglecting gravitational effects.	105
Figure 6.12: Temperature (a) and total organic mass fraction profiles (b) for case D1 neglecting gravitational effects.	105
Figure 6.13: Discretised profiles showing fraction of total mixture surrounding the SCW jet for sucrose simulations (S1 to S5).	108
Figure 6.14: Discretised profiles showing fraction of total mixture surrounding the SCW jet for DBE simulations (D1 to D5).	109
Figure 7.1: Molecular representations of diphenyl ether (DPE), benzyl phenyl ether (BPE) and dibenzyl ether (DBE).	114
Figure 7.2: Compositions of CO (a), toluene (b), and benzene (c) measured in the FTIR analyser during experiments 1, 2, and 3. Each experiment is represented sequentially by two vertical bars. First vertical bar (long dashed) signals the minute when the organic feed was initiated. Second vertical bar (short dashed) signals the minute when the first liquid sample was collected.	122
Figure 7.3: Compositions of CO (a), toluene (b), and benzene (c) measured in the FTIR analyser during experiments 7, 8, and 10. Each experiment is represented sequentially by two vertical bars. First vertical bar (long dashed) signals the minute when the organic feed was initiated. Second vertical bar (short dashed) signals the minute when the first liquid sample was collected.	122
Figure 7.4: Compositions of CO (a), toluene (b), and benzene (c) measured in the FTIR analyser during experiments 12, 13, and 15. Each experiment is represented sequentially by two vertical bars. First vertical bar (long dashed) signals the minute when the organic feed was initiated. Second vertical bar (short dashed) signals the minute when the first liquid sample was collected.	122

Figure 7.5: Compositions of CO (a), toluene (b), and benzene (c) measured in the FTIR analyser during experiments 4, 11, and 5. Each experiment is represented sequentially by two vertical bars. First vertical bar (long dashed) signals the minute when the organic feed was initiated. Second vertical bar (short dashed) signals the minute when the first liquid sample was collected.	123
Figure 7.6: Phase separation in a DBE degradation liquid sample after centrifuging. On the left, before the first extraction of aqueous phase, and on the right, before the second extraction.	123
Figure 7.7: Variation of organic phase mass fraction with measured temperature, residence time (RT), and inlet composition.	124
Figure 7.8: Organic (a) and aqueous (b) phases chromatograms from HPLC with UV-vis detection (Experiment 8).	124
Figure 7.9: Variation of dibenzyl ether conversion (a) and benzyl alcohol yield (b) with measured temperature, residence time (RT), and inlet composition.	125
Figure 7.10: Variation of benzaldehyde (a) and toluene (b) yields with measured temperature, residence time (RT), and inlet composition.	126
Figure 7.11: Proton (a) and water (b) concentrations estimated for performed experiments.	127
Figure 7.12: Yield comparison between benzaldehyde, toluene and reacted dibenzyl ether except benzyl alcohol.	128
Figure 7.13: Vapour pressures of DBE, BAL, BZA, TOL, benzene, and water vs. temperature [107].	128
Figure 7.14: Step 1.1 of the reaction mechanism for the hydrolysis of DBE (reaction 1) via S_N1 and S_N2 mechanisms.	130
Figure 7.15: Step 1.2 of the reaction mechanism for the hydrolysis of DBE (reaction 1) via S_N1 mechanism.	130
Figure 7.16: Step 1.3 of the reaction mechanism for the hydrolysis of DBE (reaction 1) via S_N1 mechanism.	130
Figure 7.17: Step 1.2 of the reaction mechanism for the hydrolysis of DBE (reaction 1) via S_N2 mechanism.	131
Figure 7.18: Parity plot for DBE conversion (a) and BAL yield (b) for scenarios 1, 2 and 3. Diagonal passing through the origin represents equality between measured and predicted yields. .	134
Figure 7.19: Parity plot for DBE conversion (a) and BAL yield (b) for scenarios 3, 4 and 5. Diagonal passing through the origin represents equality between measured and predicted yields. .	134
Figure 7.20: Parity plot for DBE conversion (a) and BAL yield (b) for scenarios 6 to 9. Diagonal passing through the origin represents equality between measured and predicted yields.	135
Figure 7.21: Parity plot for DBE conversion (a) and BAL yield (b) for scenarios 5 and 8.	136
Figure 7.22: SSD ratio to DBE conversion (a) and BAL yield (b) in scenarios 5 and 8.	137

Figure 7.23: Ratio between deviation and uncertainty for DBE conversion (a) and BAL yield (b), considering scenario 5.....	138
Figure 8.1: Expected reactional pathway for sucrose in hydrothermal medium. Dashed arrows represent non-preferential reactions.	149
Figure 8.2: Chemical structures of cellulose (a) and sucrose (b).....	150
Figure 8.3: Examples of the effluent obtained at different concentrations and temperatures. Samples in order of increasing concentration and identified by the experiment numbers in Table 8.2.	155
Figure 8.4: From left to right, examples of phase separation during solvent extraction, and evaporated samples of solids, WSO, and DSO.	157
Figure 8.5: Distribution of products in total soluble organics (TSO), solids, and volatiles for increasing reactor temperature.	158
Figure 8.6: TSO (a), solids (b), and volatiles (c) yield variation with temperature, residence time (RT), and inlet composition. Larger error bars after 360 °C	159
Figure 8.7: Compositions of CO ₂ (a), CO (b), methane (c), and ethylene (d) measured in the FTIR analyser during experiments 13, 14, and 15. Each experiment is represented sequentially by two vertical bars. First vertical bar (long dashed) signals the minute when the organic feed was initiated. Second vertical bar (short dashed) signals the minute when the first liquid sample was collected. All compositions are in mass basis referred to the total flowrate of gas at the rig's outlet.	160
Figure 8.8: CO ₂ (a), CO (b), methane (c), and ethylene (d) yield variation with temperature, residence time (RT), and inlet mass fraction (w(Suc) ₀). All yields were calculated in mass basis referred to the inlet mass of sucrose.....	161
Figure 8.9: Gases relative distribution within volatiles for increasing reactor temperature.	162
Figure 8.10: DSO (a) and WSO (b) yield variation with temperature, residence time (RT), and inlet mass fraction (w(Suc) ₀).....	163
Figure 8.11: 5-HMF yield variation with temperature, residence time (RT), and inlet mass fraction (w(Suc) ₀). Includes only experiments 11 to 20.....	166
Figure 8.12: HPLC-RID chromatograms obtained for WSO samples representative of different feed concentrations. Sucrose mass fraction at the inlet of the reactor was 4.9, 2.38, and 7.3 % for samples 13.1 (a), 5.1 (b), and 20.3 (c), respectively.	168
Figure 8.13: Glucose (a), fructose (b), 1,6-Anhydro-β-D-glucose (c), and pyruvaldehyde (d) yield variation with temperature, residence time (RT), and inlet mass fraction (w(Suc) ₀).....	169
Figure 8.14: Soluble organic distribution for increasing reactor temperature. Absence of 5-HMF indicates it was not measured, thus being included as other WSO.....	170
Figure 8.15: Modelled reactional pathway for glucose and fructose in hydrothermal medium.	171

Figure 8.16: Workflow developed for the systematic estimation of kinetic parameters. Reaction number referred to the network in Figure 8.15.	174
Figure 8.17: Sub-workflow applied in each individual parameter estimation.	175
Figure 8.18: Steps followed during the estimation of kinetic parameters related to sucrose's hydrothermal degradation.	177
Figure 8.19: Parity plots for TSO (a) and solids (b) yields, considering the estimated kinetic parameters in Table 8.8. Diagonal passing through the origin represents equality between measured and predicted yields.	180
Figure 8.20: Parity plots for glucose (a) and fructose yields, considering the estimated kinetic parameters in Table 8.8. Diagonal passing through the origin represents equality between measured and predicted yields.	180
Figure 8.21: Parity plots for 1,6-anhydro- β -D-glucose (a) and pyruvaldehyde (b) yields, considering the estimated kinetic parameters in Table 8.8. Diagonal passing through the origin represents equality between measured and predicted yields.	181
Figure 8.22: Parity plots for 5-HMF yields, considering the estimated kinetic parameters in Table 8.8. Diagonal passing through the origin represents equality between measured and predicted yields.	181
Figure 8.23: SSD ratio for TSO (a) and solids (b) yields, considering random variations of the estimated kinetic parameters in Table 8.8.	182
Figure 8.24: SSD ratio for glucose (a) and fructose (b) yields, considering random variations of the estimated kinetic parameters in Table 8.8.	182
Figure 8.25: SSD ratio for 1,6-anhydro- β -D-glucose (a) and pyruvaldehyde (b) yields, considering random variations of the estimated kinetic parameters in Table 8.8.	183
Figure 8.26: SSD ratio for 5-HMF yields, considering random variations of the estimated kinetic parameters in Table 8.8.	183
Figure 8.27: Ratio between deviation and uncertainty for TSO (a) and solids (b) yields, considering parameters from estimation 1.	184
Figure 8.28: Ratio between deviation and uncertainty for glucose (a) and fructose (b) yields, considering parameters from estimation 1.	185
Figure 8.29: Ratio between deviation and uncertainty for 1,6-anhydro- β -D-glucose (a) and pyruvaldehyde (b) yields, considering parameters from estimation 1.	185
Figure 8.30: Ratio between deviation and uncertainty for 5-HMF, considering parameters from estimation 1.	185
Figure 8.31: Comparison between kinetic constants calculated using estimated parameters and equivalent ones in literature, for reactions 1 and 11 to 15 in Figure 8.15 [64,104,159]. Ratio (on the left axis) defined as the literature values divided by the one estimated in this study.	187

Figure A.1: Process and instrumentation diagram of the hydrothermal liquefaction rig described in Chapter 3.....	204
Figure B.1: Rotameter calibration plots for different feed pressures, and respective calibration parameters.....	205
Figure B.2: HPLC with UV-vis detection: calibration plots for BAL at low (a) and high (b) composition ranges.....	207
Figure B.3: HPLC with UV-vis detection: calibration plots for BZA at low (a) and high (b) composition ranges.....	207
Figure B.4: HPLC with UV-vis detection: calibration plot for TOL.....	207
Figure B.5: HPLC with UV-vis detection: calibration plots for DBE at low (a) and high (b) composition ranges.....	208
Figure B.6: HPLC with RID: calibration plot for sucrose.....	209
Figure B.7: HPLC with RID: calibration plot for glucose (a) and fructose (b).....	209
Figure B.8: HPLC with RID: calibration plot for 1,6-anhydro- β -D-glucose (a) and pyruvaldehyde (b).....	209
Figure B.9: GC with FID: calibration plot for 5-HMF.....	210
Figure D.1: Total organic mass fraction profiles for varying number of nodes in the radial axis ($I = 1, 25, 50, 100, \text{ and } 150$).....	217
Figure D.2: Total organic mass fraction profiles for varying number of nodes in the vertical axis ($MS = 25.7, 3.74, \text{ and } 0.374 \text{ mm}$).....	219
Figure D.3: Total organic mass fraction profiles for different auto-refinement levels in jet and mixing sections (No auto-refinement, and ARL from 1 to 4).....	220
Figure D.4: Total organic mass fraction profiles for different mesh sizes, combining the effects of different I , MS , and ARL.....	222
Figure D.5: Temperature profile in the complete reactor geometry for sucrose simulations (Scenarios S1 to S5). Velocity field indicated by non-scaled arrows.....	224
Figure D.6: Total organic mass fraction profile in the complete reactor geometry for sucrose simulations (Scenario S1 and S2). Velocity field indicated by non-scaled arrows.....	225
Figure D.7: Temperature profile in the complete reactor geometry for DBE simulations (Scenarios D1 to D5). Velocity field indicated by non-scaled arrows.....	226
Figure D.8: Total organic mass fraction profile in the complete reactor geometry for DBE simulations (Scenarios D1 to D5). Velocity field indicated by non-scaled arrows.....	227
Figure E.1: Step 1.1 of the reaction mechanism for the hydrolysis of DBE (reaction 1) via S_{N1} and S_{N2} mechanisms.....	237
Figure E.2: Step 1.2 of the reaction mechanism for the hydrolysis of DBE (reaction 1) via S_{N1} mechanism.....	237

Figure E.3: Step 1.3 of the reaction mechanism for the hydrolysis of DBE (reaction 1) via S_N1 mechanism.237

Figure E.4: Step 1.2 of the reaction mechanism for the hydrolysis of DBE (reaction 1) via S_N2 mechanism.239

List of tables

Table 1.1: Main processes for synthesis of second-generation biofuels.	4
Table 2.1: Typical results of proximity and ultimate analysis for different biomass sources. Adapted from [21], considering a dry and ash free basis.	11
Table 2.2: Comparison between batch and continuous operation [4,21,47,88].	20
Table 2.3: Critical properties of solvents tested for biomass liquefaction, adapted from [49,106,107].	24
Table 2.4: Comparison between the elemental composition and HHV of conventional crude with bio-oil before and after HDO.	27
Table 3.1: Summary of the substances required during this research project.	31
Table 3.2 - List of equipment existing in the HTL rig.	33
Table 3.3: Summary of equipment uncertainty.	51
Table 4.1: Variation in selected results and simulation time for all tested cases due to increasing the number of discretisation elements. Kinetic models based on DBE's scenario 5 (Section 7.5.1) and sucrose's scenario 2 (Section 8.5.2).	63
Table 5.1: Pump flowrate analysis: nominal ($Q_v^{NOM}/Q_{nominal}$) flowrate; measured flowrate ($Q_{measured}$) calculated from mass accumulated (m_s) over known time (t_c), and respective variation. Sum of squared absolute variation of 375.	73
Table 5.2: Pump flowrate analysis: correction factors.	73
Table 5.3: Pump flowrate analysis: corrected mass flowrates and variation against measured values. Sum of squared absolute variation of 1.	74
Table 5.4: Cooling capacity analysis: case summary.	75
Table 5.5: Cooling capacity analysis.	76
Table 6.1: Sizes used in the geometrical representation of the HTL reactor and surrounding tubing (Figure 6.1).	88
Table 6.2: Sections in the geometrical representation of the HTL reactor and surrounding tubing (Figure 6.1).	88
Table 6.3: Inputs for CFD representative simulations: organic feed composition ($w_{FO,i}$); feed flowrates (Q_i); composition expected after mixing (w_i^{in}); temperatures measured at different sections and calculated after feed mixing (T_{mix}); and applied heat transfer coefficient with the environment (htc).	94
Table 6.4: CFD simulation analysis: time required to completion and conservation ratios for total mass (R_{tot}), mass of organic compounds (R_{org}), and energy (R_{heat}).	99
Table 6.5: CFD simulation outputs for case S3 considering and omitting the effect of gravity in the turbulent flow model.	106

Table 6.6: CFD simulation outputs for case D1 considering and omitting the effect of gravity in the turbulent flow model.....	106
Table 6.7: Distance required to achieve R_{mix} from 90 to 99.9% and related parameters for all cases.....	110
Table 6.8: Temperatures and yields obtained from sucrose-based CFD simulations (Table 6.3), using detailed and simplified models.	111
Table 6.9: Temperatures, conversion, and yield obtained from DBE-based CFD simulations (Table 6.3), using detailed and simplified models.....	111
Table 7.1: Summary of recent work on dibenzyl ether's hydrothermal degradation.....	115
Table 7.2: Progress summary during the study of dibenzyl ether's hydrothermal degradation.....	118
Table 7.3: Experimental conditions for DBE hydrothermal degradation: feed nominal flowrate, DBE mass fraction at the reactor's inlet ($w^{\text{in}}_{\text{DBE}}$), pressure, and temperature.....	119
Table 7.4: Flowrates, temperature boundaries, and residence time for each DBE hydrothermal degradation experiment.....	120
Table 7.5: Flowrate distribution between inlets and products for each DBE hydrothermal degradation experiment.....	121
Table 7.6: Range of observed mass fraction in each phase and overall.....	125
Table 7.7: Activation energy (E_a) and kinetic constant (k_{ref}) at reference temperature (T_{ref}) estimated for different hydrolysis rate equations, and respective objective function (OF).....	132
Table 7.8: Variation (Δ) of calculated DBE conversion (C_v) and BAL yield (Y_{BAL}) for different property calculation methods.	139
Table 7.9: Variation (Δ) of calculated DBE conversion (C_v) and BAL yield (Y_{BAL}) for different heat transfer assumptions.....	140
Table 7.10: Variation (Δ) of calculated DBE conversion (C_v) and BAL yield (Y_{BAL}) for different dispersion assumptions.	142
Table 7.11: Comparison between kinetic constants for DBE hydrolysis estimated in this study and existing in literature [149] in the range of tested conditions (287 – 368 °C).....	142
Table 8.1: Summary of recent work on hydrothermal degradation of sucrose related products.....	147
Table 8.2: Flowrates and sucrose mass fractions for sucrose hydrothermal degradation experiments.	152
Table 8.3: Measured pressure and temperature, estimated temperature boundaries and average residence time for sucrose hydrothermal degradation experiments.....	153
Table 8.4: Average mass of solids accumulated per minute through the different filtration processes.	154
Table 8.5: Variation of WSO mass for equivalent samples evaporated using a rotary evaporator or atmospherically.....	154
Table 8.6: HTL rig's flowrates: total inlet, suspension sample, and estimated gaseous product.....	156
Table 8.7: Compounds identified through GC-MS.....	164

Table 8.8: Activation energy (E_a) and kinetic constant (k_{ref}) at reference temperature (T_{ref}) estimated for the three considered solutions, and respective objective function (OF).....	178
Table 8.9: Parameters used to calculate the kinetic constants in Figure 8.31, to compare the current study with literature values.	186
Table B.1: Maximum UV absorption wavelength [154–157], and elution time at different mobile phase concentrations for each analyte.....	206
Table B.2: HPLC with UV-vis calibration: calibration parameters.....	208
Table B.3: HPLC with RID: calibration parameters.....	210
Table B.4: GC with FID: calibration parameters.....	211
Table C.1: Preliminary tests using DBE/water mixtures: operating conditions and measured temperatures.....	213
Table C.2: Preliminary tests using DBE/water mixtures: calculated temperatures using estimated heat transfer coefficients.....	213
Table C.3: Preliminary tests using only water: operating conditions and measured temperatures.....	214
Table C.4: Preliminary tests using only water: calculated temperatures using estimated heat transfer coefficients.....	215
Table D.1: Conservation ratios, average temperatures, and yields for different number of nodes in the radial axis ($I = 1, 25, 50, 100, \text{ and } 150$).....	218
Table D.2: Conservation ratios, average temperatures, and yields for different number of nodes in the vertical axis ($MS = 25.7, 3.74, \text{ and } 0.374 \text{ mm}$).....	218
Table D.3: Conservation ratios, average temperatures, and yields for different auto-refinement levels in jet and mixing sections (No auto-refinement, and ARL from 1 to 4).....	221
Table D.4: Conservation ratios, average temperatures, and yields for different mesh sizes, combining the effects of different I , MS , and ARL.....	221
Table E.1: Detailed results for dibenzyl ether hydrothermal degradation.....	230
Table E.2: Averaged results for dibenzyl ether hydrothermal degradation.....	236
Table F.1: Detailed results for sucrose hydrothermal degradation – Inlet data.....	244
Table F.2: Detailed results for sucrose hydrothermal degradation – FTIR data.....	245
Table F.3: Detailed results for sucrose hydrothermal degradation – Experiments 1 to 10.....	246
Table F.4: Detailed results for sucrose hydrothermal degradation – Experiments 11 to 20.....	250
Table F.5: Averaged yields for sucrose hydrothermal processing.....	255
Table F.6: Averaged fractional values for sucrose hydrothermal processing.....	256
Table F.7: Reactions included, objective function, and progression comments for each parameter estimation.....	258

Nomenclature

List of abbreviations

Abbreviation	Description
5-HDF	5-(hydroxymethyl)-2-(dimethoxy methyl)furan
5-HMF	5-(Hydroxymethyl)furfural
ACN	Acetonitrile
AGluc	1,6-Anhydro- β -D-glucose
ARL	Auto-refinement level
BAL	Benzyl alcohol
BPE	Benzyl phenyl ether
BZA	Benzaldehyde
BTO	1,2,4-Benzenetriol
BTX	Benzene, toluene, and xylene
CFD	Computational fluid dynamic
DBE	Dibenzyl ether
DCM	Dichloromethane
DHA	Dihydroxyacetone
DI	De-ionised
DPE	Diphenyl ether
DSO	Dichloromethane-soluble organics
EoS	Equation of state
Ery	Erythrose
ETBE	Ethyl tert-butyl ether
Exp	Experiment
FAME	Fatty acid methyl esters
FDM	Finite difference method
FEM	Finite element method
FID	Flame ionisation detection
FO	Organic feed
Fruc	D-Fructose
FTIR	Fourier-transform infrared

Abbreviation	Description
GC	Gas chromatography
GHG	Greenhouse gases
Gluc	Glucose
Glyce	Glyceraldehyde
Glyco	Glycolaldehyde
HDO	Hydrodeoxygenation
HHV	Gross heating value
HPLC	High-performance liquid chromatography
HTC	Hydrothermal carbonisation
HTL	Hydrothermal liquefaction
HVO	Hydrotreated vegetable oil
IAPWS	International association for the properties of water and steam
LPG	Liquefied petroleum gas
MetOH	Methanol
MS	Mass spectrometry
MTBE	Methyl tert-butyl ether
MtCO _{2e}	Million tonnes of CO ₂ equivalent
NIST	National Institute of Standards and Technology
OD	Outer diameter
OF	Objective function
PSV	Pressure safety valve
Pyr	Pyruvaldehyde
P&ID	Process and instrumentation diagram
RAC	Retro-aldol condensation
RANS	Reynolds-averaged Navier-Stokes

Abbreviation	Description
RID	Refraction index detection
RT	Average residence time
SAFT- γ Mie	Statistical association theory for variable range Mie potentials
SCTT	Supercritical transition temperature
SCW	Supercritical water
SCWG	Supercritical water gasification
S _N 1	Unimolecular nucleophilic substitution
S _N 2	Bimolecular nucleophilic substitution
SO	Soluble organics
SS-316L	Stainless steel 316 L
SSD	Simulated standard deviation
Suc	Sucrose
TOL	Toluene
TSO	Total soluble organics
UK	United Kingdom
UV-vis	Ultraviolet and visible
VLE	Vapour-liquid equilibrium
WSO	Water-soluble organics
WT	Wall thickness

List of symbols

Roman letters

Symbol	Description	Dimensions	Units
$A_{i,p}$	Area under signal measurement	$[i, p]$	(variable)
Ab_i	Absorbance	$[i]$	-
A_{CS}	Reactor's cross-sectional area	-	m ²
A_L	Reactor's lateral area	-	m ²
$A_{SCT} / B_{SCT} / C_{SCT}$	Coefficients for SCTT approximation	-	°C.bar ⁻² / °C.bar ⁻¹ / °C
$C_{i,z} / [i]_z$	Concentration	$[i, z]$	mol.m ⁻³
C_p	Heat capacity	-	J.kg ⁻¹ .K ⁻¹
C_v	Conversion	-	(%)
$D_{i,z}$	Diffusion coefficient	$[i, z]$	m ² .h ⁻¹
$E_{i,z}$	Dispersion coefficient	$[i, z]$	m ² .h ⁻¹
$E_{a,r}$	Activation energy	$[r]$	kJ.mol ⁻¹
$F_i / F_{i,z}$	Molar flowrate	$[i, z]$	mol.h ⁻¹
$F_{i,z}^{convective}$	Convective molar flowrate	$[i, z]$	mol.h ⁻¹
$F_{i,z}^{dispersive}$	Dispersive molar flowrate	$[i, z]$	mol.h ⁻¹
$F_{i,p}^{out}$	Outlet molar flowrate	$[i, p]$	mol.h ⁻¹
f	Feed	$[f]$	-
f_p	Mass phase fraction	$[p]$	(wt%)
f_p^{ACN}	Mass fraction in the acetonitrile diluted sample	$[p]$	(wt%)
f_p^R	Mass phase fraction at the reactor's outlet	$[p]$	(wt%)
h_z	Specific enthalpy	$[z]$	kJ.kg ⁻¹
h_{in}	Specific enthalpy at the reactor's inlet	-	kJ.kg ⁻¹
h_m	Specific enthalpy at the reactor's thermocouple	-	kJ.kg ⁻¹
h_{mix}	Mixture		
h_{out}	Specific enthalpy at the reactor's outlet	-	kJ.kg ⁻¹
h_w	Heat transfer coefficient	-	W.m ⁻² .K ⁻¹
i	Component from a mixture	$[i]$	-
I	Integer number	-	-
$ID / ID_{reactor}$	Reactor's internal diameter	-	m
ID_{jet}	Jet's internal diameter	-	m
K_a^i	Acid dissociation constant	$[i]$	mol/m ³
$k_{0,r}$	Arrhenius pre-exponential factor	$[r]$	(variable).h ⁻¹
k_b	Stefan-Boltzmann constant	-	W.m ⁻² .K ⁻⁴
k_r	Reaction rate coefficient	$[r]$	(variable).h ⁻¹
$k_{ref,r}$	Reaction rate coefficient at reference temperature	$[r]$	(variable).h ⁻¹
k_t	Thermal conductivity	-	W.m ⁻¹ .K ⁻¹
K_w	Water self-ionisation product	-	mol ² .kg ⁻²
$K_{SCT} / K_{SCT,2} / K_{SCT,1} / K_{SCT,0}$	Supercritical transition coefficients	-	- / bar ² / bar / -
l	Optical path length	-	m

Symbol	Description	Dimensions	Units
$L_{additional} / L'_{additional} / L''_{additional} / L^{total}_{additional}$	Additional lengths in the CFD model geometry	-	m
L_{jet}	Jet's length	-	m
L_{MS}	Mixing section's length	-	m
$L_R / L_{reactor}$	Reactor's length	-	m
L_{TC}	Thermocouple location from the outlet	-	m
mc_i	Calibration slope	$[i]$	(variable)
$m_s / m_p^s / m_p^{s2} / m_p^{ACN} / m_p^{MetOH}$	Sample mass	$[p]$	g
MS	Maximum length between nodes	-	m
MW_i	Molecular weight	$[i]$	$g.mol^{-1}$
N	Number of measurements	-	-
n	Integer number	$[n]$	-
$n_{i,r}$	Reaction order	$[i,r]$	-
n_p	Number of points between inlet and outlet for property calculations	-	-
n_{SCT}	Supercritical transition exponent	-	-
p_z	Pressure	$[z]$	bar
p	Phase	$[p]$	-
p_{crit}	Critical pressure	-	bar
$P_z / P_{liq} / P_{vap}$	Generic overall/liquid/vapour property	$[z]$	(variable)
$p^{H^+}_{r,z}$	Proton concentration contribution	$[r, z]$	$mol.m^{-3}$
$Pe_{i,z}$	Péclet number	$[i, z]$	-
$Pe^0_{i,z}$	Péclet number at laminar-turbulent transition	$[i, z]$	-
Pe_{∞}	Péclet number at high Reynolds numbers (0.2)	-	-
q	Heat flow	-	W
q_{wall}	Heat flow through the tube's wall	-	W
q_{loss}	Total heat losses	-	W
Q / Q_z	Mass flowrate	$[z]$	$kg.h^{-1}$
Q_f	Feed mass flowrate	$[f]$	$kg.h^{-1}$
Q_p / Q_p^{out}	Outlet mass flowrate	$[p]$	$kg.h^{-1}$
Q_{in}	Inlet mass flowrate	-	$kg.h^{-1}$
Q_i^p	Component mass flowrate	$[i,p]$	$kg.h^{-1}$
Q_i^{out}	Outlet component mass flowrate	$[i]$	$kg.h^{-1}$
Q_{org}	Total organic flowrate	-	$kg.h^{-1}$
$Q_R / Q_{reactor}$	Mass flowrate at reactor inlet	-	$kg.h^{-1}$
$Q_{v,z}$	Volumetric flowrate	$[z]$	$m^3.h^{-1}$
$Q_{v,f}^{NOM}$	Feed nominal volumetric flowrate	$[f]$	$m^3.h^{-1}$
r	Reaction	$[r]$	-
r	Radius	-	m
R	Ideal gas constant	-	$J.K^{-1}.mol^{-1}$
R^2	Coefficient of determination	-	-
$R_{0,i}$	Solute radius	$[i]$	m

Symbol	Description	Dimensions	Units
$r_{r,z}$	Reaction rate	$[r, z]$	$\text{mol.h}^{-1}.\text{m}^{-3}$
Re_z	Reynolds number	$[z]$	-
Re_0	Reynolds number at laminar-turbulent transition	-	-
R_{heat}	Relative variation of total energy flow	-	%
R_{mix}	Full mixture ratio	-	%
R_{org}	Relative variation of total organic mass flowrate	-	%
R_{tot}	Relative variation of total mass flowrate	-	%
s	Geometry section	s	-
s_C	Measurement uncertainty	-	(variable)
$Sc_{i,z}$	Schmidt number	$[i, z]$	-
$SCTT$	Supercritical transition temperature	-	$^{\circ}\text{C}$
s_r	Standard deviation about the regression	-	(variable)
S_{xx}	Squared calibration concentrations	-	(variable)
T_z	Reaction temperature	$[z]$	$^{\circ}\text{C}$
T_{amb}	Ambient temperature ($20\text{ }^{\circ}\text{C}$)	-	$^{\circ}\text{C}$
T_{bubble}	Bubble point at constant pressure	-	$^{\circ}\text{C}$
t_c	Collection time	-	s
T_{crit}	Critical temperature	-	$^{\circ}\text{C}$
T_f	Feed temperature	$[f]$	$^{\circ}\text{C}$
T_{in} / T_{mix}	Temperature at the reactor's inlet	-	$^{\circ}\text{C}$
T_m	Temperature at the reactor's thermocouple	-	$^{\circ}\text{C}$
T_{out}	Temperature at the reactor's outlet	-	$^{\circ}\text{C}$
$T_{ref,r}$	Reference temperature	$[r]$	$^{\circ}\text{C}$
T_{sat}/T_{sat}^n	Saturation temperature	$[n]$	$^{\circ}\text{C}$
u_z	Velocity	$[z]$	m.h^{-1}
U_{ht}	Overall heat transfer coefficient	-	$\text{W.m}^{-2}.\text{K}^{-1}$
$w_{i,z}$	Mass fraction	$[i, z]$	wt%
$w(i)_0 / w_{i,i}^{in}$	Mass fraction at reactor inlet	$[i]$	wt%
$w_{i,p}^{ACN} / w_{i,p}^{MeOH} / w_{i,p}^{Water}$	Mass fraction in a sample diluted in ACN, MeOH or water.	$[i, p]$	wt%
$w_i^f / w_{i,f}$	Feed mass fraction	$[i, f]$	wt%
w_{org}	Total organic mass fraction	-	wt%
wt	Wall thickness	-	m
wt_{jet}	Jet's wall thickness	-	m
$x_{i,z}$	Molar fraction	$[i, z]$	mol%
x_i^{Gs}	Molar fraction in the gas sample	$[i]$	mol%
Y_i	Yield	$[i]$	%
y_c	Measured value	-	(variable)
$y_r^{H^+}$	Proton concentration activator (0 or 1)	-	-
z	Dimensionless axial position (from 0 to 1)	$[z]$	-
z_n	Position of property calculation point	$[n]$	-
z_{SCT}	Pseudo-vapour fraction for supercritical transition	-	-

Greek letters

Symbol	Description	Dimensions	Units
β_f	Pump correction factor	$[f]$	-
ε_i	Molar absorptivity	$[i]$	$\text{mol}^{-1}.\text{m}^2$
ε_r	Dielectric constant / Relative permittivity	-	-
$\gamma_{i,r}$	Stoichiometric coefficient	$[i, r]$	-
$\Delta_{absolute}$	Absolute variation	-	(variable)
$\Delta_{relative}$	Relative variation	-	%
Δp_{SCTT}	Pressure spacing used in SCTT estimation	$[-]$	bar
ρ_{crit}	Critical density	-	$\text{kg}.\text{m}^{-3}$
$\rho_f^{T_{amb,p}}$	Feed's density at ambient temperature and operating pressure	$[f]$	$\text{kg}.\text{m}^{-3}$
$\rho_{i,z}$	Component specific density	$[i,z]$	$\text{kg}.\text{m}^{-3}$
ρ_w	Water's density	-	$\text{kg}.\text{m}^{-3}$
ρ_z	Density	$[z]$	$\text{kg}.\text{m}^{-3}$
φ	Angular position	-	rad
μ_z	Viscosity	$[z]$	Pa.s

Chapter 1

Introduction

The importance of developing carbon-neutral alternatives to transportation fuels is addressed in the following sections. Afterwards, the role lignocellulosic biomass plays in this carbon-neutral transition is presented as this project's motivation, from which specific scientific and engineering objectives are derived. This chapter concludes with a summary of the structure of this thesis.

1.1 Towards carbon-neutrality

Between 1990 and 2020, the world's population increased by 47%, particularly in urban areas, which saw a rise of 92% in the same period [1]. This is linked with an increased energy and fuel consumption, which, when based on fuel sources like oil, coal, or natural gas, leads to the release of significant amounts of greenhouse gases (GHG). These gases include CO₂, CH₄, and N₂O, which are related to global warming and the associated climate change [2–7].

As part of the *Paris Agreement* [8], the United Kingdom (UK) is committed to minimise climate change through sustainable development. The international accord aims to limit the global average temperature to only 1.5 °C above pre-industrial levels. To achieve this goal, the country is committed to, by 2030, reduce net GHG emissions by at least 68% compared to 1990 levels [9]. The amended *Climate Change Act* [10] further expands this target to net zero GHG emissions by 2050.

The total net GHG emissions in the UK between 1990 and 2020 are plotted in Figure 1.1 [11]. In the most recent year, the UK emitted 406 MtCO₂e¹, representing a decrease of 9% compared to the previous year, and 50% compared to 1990. From these emissions, CO₂ represents a large and relatively constant fraction (74 – 83%). Figure 1.1. also shows the emissions relative only to the transport sector, which, in 2020, represented 28% of the total value, being its largest contributor and mainly composed of CO₂ (98%). This sector observed a 19% drop in emissions in 2020, caused by the traffic reduction during country-wide lockdowns due to the COVID-19 pandemic [11]. However, this will undoubtedly be a short-lived decrease, as transportation emissions were considerably steady between 1990 and 2019, showing a decrease of only 8%.

¹ Million tonnes of CO₂ equivalent. Unit that normalises the emissions of each gas according to their global warming potential compared to CO₂.

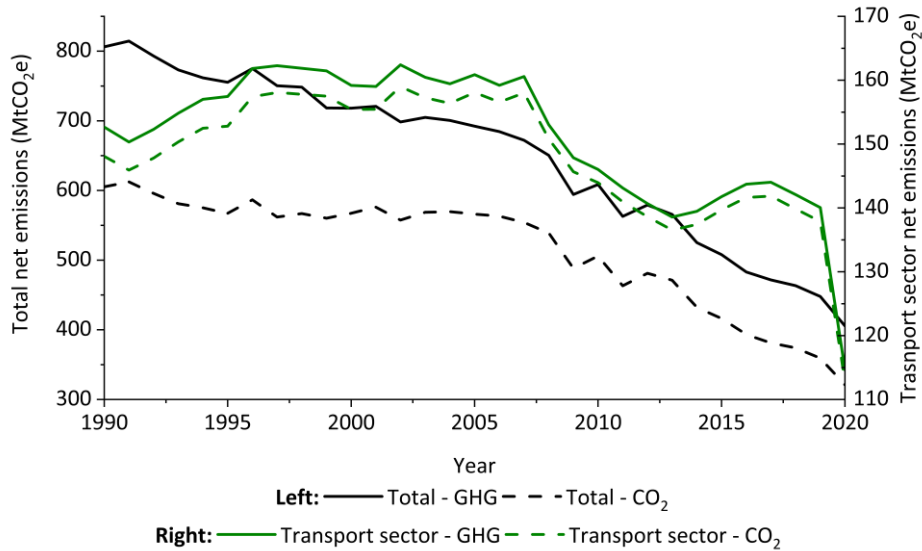


Figure 1.1: UK's annual GHG (full lines) and CO₂ (dashed lines) net emissions between 1990 and 2020 [11]. Left axis referred to total emissions (black lines), and right axis to emissions specific to the transport sector (green lines).

Figure 1.2 presents the distribution of CO₂ emissions within the transport sector in the UK, during 2020. It is observable that most of the transportation sector's emissions result from road transport, particularly domestic cars. Therefore, this type of transportation is a clear target on the objective towards net-zero emissions. For this reason, UK's government has implemented the *Renewable Transport Fuel Act* [12,13], establishing that, by 2032, 12.4% of transport fuel results from renewable sources, which is a substantial increase from the 5.9% in 2020 [14]. These renewable fuels are defined as the ones fully derived from biological sources, *i.e.*, biofuels, such as biodiesel, bioethanol, biogas, and bio-LPG, or blends with fossil fuels in quantities above 25%, like hydrotreated vegetable oil (HVO), fatty acid methyl esters (FAME), bio-ethyl tert-butyl ether (ETBE), and bio-methyl tert-butyl ether (MTBE) [12]. Hydrogen and derived synthetic fuels are also part of this category, if they are produced using renewable energy sources, like solar, or wind.

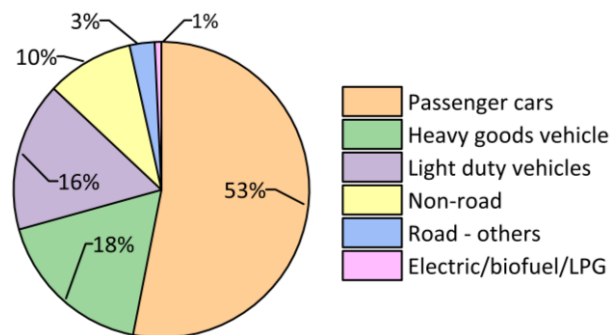


Figure 1.2: UK's distribution of CO₂ emissions within the transport sector [11]. Values referred to the year 2020, with CO₂ emissions in this sector of 113 Mt.

Fuels derived from biomass sources, like plants or organic wastes, present a viable alternative for the reduction of GHG emissions, particularly as it can be directly applied on existing diesel or gasoline engines (drop-in fuel). Besides being globally available and renewed within a period of months to years, plants remove CO₂ from the atmosphere by photosynthesis. Considering that, when a biofuel is burnt, the same amount of CO₂ is released, it creates a cycle with net-zero emissions [2–4,15,16].

1.2 Second-generation biofuels

Even though producing fuel from plants is a viable option to reduce GHG emission, the effects of planting biofuel-dedicated crops must also be accounted for, particularly if these interfere with existing crops that produce food for humans or animals. This is defined as land-use change and can be classified as direct, when crops are planted on previously non-utilised areas, or indirect, when the repurposing of an existing crop for biofuel production leads to the change or creation of other agricultural areas [17]. Both may result in feedstock price increase, as well as the expansion of agricultural areas, leading to the loss of natural CO₂ sinks, such as forests and grasslands [17,18]. Consequently, without a detailed study, intensifying biofuel-dedicated crops has the potential to result in net positive GHG emissions [16]. For this reason, the *Renewable Transport Fuel Act* [12,13], in addition to benefiting waste-based fuels, introduced a cap of 2% by 2032 on the volume of biofuels obtained from dedicated crops.

To avoid the negative effects of land-use change, a distinction was created between first- and second-generation biofuels. As mentioned above, the first relates to fuels produced from food crops, such as vegetable oils and sugars. Current applications of these include biodiesel or FAME produced from palm, rapeseed, soybean, or sunflower oils, and bioethanol obtained from sugar or corn [7,15].

On the other hand, second-generation biofuels are obtained from non-food sources, such as lignocellulosic biomass. This is an abundant source that can be obtained from the waste of several industries like paper, forestry, agriculture, and food production. Therefore, it minimises the accumulation of CO₂ in the atmosphere, when compared to first-generation biofuels. Nonetheless, the economic viability of producing and upgrading these fuels is yet to be demonstrated [7,15].

Table 1.1: Main processes for synthesis of second-generation biofuels.

Process	Operating conditions	Main products	Brief description	Advantages	Challenges	Ref.
Hydrothermal liquefaction (HTL)	250 – 400 °C 200 – 300 bar	Bio-oil Biogas Char	Chemical transformation of biomass in presence of subcritical/supercritical water.	Does not require drying, handling both dry and wet biomass. Biofuel with relatively high gross heating value (HHV, 30 – 40 MJ/kg). Lower oxygen content than pyrolysis. Keeps aromatic structure of lignin. Considerable thermal stability. Reduced NO _x and SO _x emissions Feed pathogens are eliminated. Potential for co-processing with conventional crude.	Severe conditions, potentially resulting in a process with high energy demand. Complex and un-explored reaction mechanism. Pumping a concentrated slurry to high pressure and temperature. High bio-oil viscosity. Requires bio-oil upgrading. Recycling/recovering aqueous phase.	[19–25]
Hydrothermal / supercritical water gasification (SCWG)	> 374 °C 250 – 350 bar	CH ₄ rich gas (< 500 °C) H ₂ rich gas (> 500 °C) Tar		Gas product upgradable via Fischer-Tropsch or water-gas shift reactions. Option to upgrading organics in the HTL aqueous phase.	Salt precipitation and corrosion. Low overall efficiency, requiring a catalyst, particularly at lower temperature.	[3,24–27]
Hydrothermal carbonization (HTC)	180 – 250 °C 20 – 60 bar	Biochar equivalent to low rank coal		Higher HHV and carbon content compared to feedstock. Directly usable as a solid fuel. Increased grindability compared to raw biomass, being a possible pre-treatment for further processing.	Typically, a batch process not yet scaled up.	[20,21,28,29]

Continuation of Table 1.1.						
Process	Operating conditions	Main products	Brief description	Advantages	Challenges	Ref.
Fast pyrolysis	500 – 600 °C < 50 bar	Bio-oil Biogas Char	Chemical transformation in a gaseous medium without oxygen followed by quick recombination.	Short residence time (seconds). Higher bio-oil yields/less char formed compared to HTL. Less viscous bio-oil.	Requires drying. Severe conditions. Higher oxygen content than HTL. Bio-oil is more unstable, corrosive bio-oil with lower HHV (16 – 18 MJ/kg). Requires bio-oil upgrading.	[3,20,30–34]
Hydrogenolysis / hydrocracking	90 – 200 °C 10 – 40 bar	Bio-oil rich in monomeric phenols	Catalytic cleavage of the polymer structure via substitution with hydrogen atoms.	Expected high yields. Applicable as bio-oil deoxygenation process. Alike implemented processes.	Requires hydrogen and a heterogeneous catalyst. Catalyst susceptible to deactivation.	[20,35,36]
Fermentation	35 – 45 °C	Bioethanol Biobutanol	Conversion of sugars using micro-organisms.	Existing technology allows use as a drop-in gasoline substitute or additive.	Requires pre-treatment to remove lignin and hydrolyse cellulose. Large residence times (> 48 h). Limited by yeast's survivability conditions.	[7,27,34,37,38]
Anaerobic digestion	< 55 °C	CH ₄ rich biogas	Organic matter digested by anaerobic bacteria.	Both solid and aqueous waste may be used as fertilizers.	Requires pre-treatment to remove lignin and hydrolyse cellulose. Retention time of 20 – 30 days. Limited by bacteria's survivability conditions. Only partially degrades biomass.	[27,31,34,39]
Transesterification	< 65 °C	FAME/ Biodiesel	Conversion of fatty acids by reaction with an alcohol and a catalyst.	Existing technology allows use as a drop-in diesel substitute if blended with conventional fuel. Use less pollutant than conventional diesel. Glycerine produced as a by-product.	Feedstock limited to non-edible vegetable oils, animal fats, and algae. Requires corrosive acid or alkaline catalyst.	[7,31,40]

1.2.1 Why hydrothermal liquefaction?

Table 1.1 summarises the main processes to synthesise second-generation biofuels. Depending on the operating conditions, from similar feedstocks, different products may be obtained with a wide range of applications. Regarding drop-in transportation fuels, fermentation and transesterification are the most well-known technologies, being applied worldwide [27,31].

Bioethanol is produced through enzymatic hydrolysis of cellulose and hemicellulose. It can be used in existing gasoline engines if blended up to 15% in volume. For higher concentrations of biofuel, engine modifications are required (*e.g.*, to some seals, which are incompatible with components of biofuel). However, its production requires pre-treatments to allow the penetration of enzymes in lignocellulose's rigid structure (see Section 2.2.2), such as reducing cellulose's crystallinity, or removing lignin, which is not consumed and acts as a physical barrier [31,41]. Biodiesel is produced via transesterification of organic oils and typically contains smaller amounts of aromatic and organosulfur compounds than conventional diesel. However, depending on its source, biodiesel may form a gel at temperatures up to 16 °C, which is significantly above atmospheric conditions in colder regions. Consequently, biodiesel must be blended with conventional fuel in a volume fraction that depends on the vehicle and the country's legislation [31,42].

While fermentation and transesterification address alternative transportation fuels with reduced GHG emissions, their range of applications is limited to this single application. On the other hand, bio-oil that results from the thermal depolymerisation of all lignocellulosic biomass components (see Section 2.2) provides a wide distribution of chemical products besides drop-in transportation fuels, such as carboxylic acids, alcohols, phenols, and aldehydes, thus improving the process economic viability [20,43,44].

As shown in the Table 1.1, bio-oil can be produced via hydrogenolysis, fast pyrolysis, and hydrothermal liquefaction (HTL); these processes are based on the fast reaction of biomass at high temperature and pressure in different environments: hydrogen-rich atmosphere over a catalyst, inert gas, and aqueous, respectively [20].

Comparing fast pyrolysis and HTL, the former process typically provides higher bio-oil yields, reaching 60 – 75% compared to 40 – 60% in the latter [3,27,31]. On the other hand, fast pyrolysis requires higher temperature (over 500 °C compared to under 400 °C for HTL) and a dry feedstock. Since HTL is conducted at high pressure in aqueous medium, no vaporisation occurs, which reduces energy demand and operating costs [45]. Bio-oil from fast pyrolysis is also associated with higher oxygen content, which consequently increases its viscosity and decreases its energy density [3,20,25,45].

Hydrotreatment via hydrogenolysis reduces the oxygen content of biomass or products derived from biomass upgrading, by reaction with hydrogen to form water. It employs milder temperatures [35], and

is typically conducted over a metal catalyst [20]. The information available on direct applications to a biomass feedstock is limited, and mostly applied directly on lignin [20,35,44]. Nonetheless, it is a process commonly associated to HTL or pyrolysis bio-oil upgrading, in which cases it is usually designated hydrodeoxygenation (HDO) [3,45,46].

Given the variety of obtainable products, the milder operating conditions, when compared to pyrolysis, and the possibility of processing a wide range of feedstock without drying requirements, HTL presents a viable option to synthesise second-generation biofuels.

1.3 Project motivation

The work presented in this thesis is motivated by the need to achieve net-zero carbon emissions, particularly in the transport sector, and the relevance of hydrothermal liquefaction of lignocellulosic biomass in providing drop-in fuels. A secondary economic motivation is also considered: the process produces a wide range of chemical substances apart from biofuels. A capability to optimise the product mix according to current market demand may make the process more economically viable and resilient.

These motivations are aimed at moving HTL from technical demonstration to commercial implementation. This requires a holistic approach to HTL, analysing it from the perspective of: (1) the process flowsheet, which requires an empirical knowledge of the process yields at different operating conditions, and how it interacts with surrounding operations, like upstream pre-treatment, and downstream upgrading; (2) reaction engineering, ensuring it is achievable at the required conditions, and scale; and (3) chemical mechanisms and kinetics, such as thermodynamic properties, reaction kinetics, and transport limitations, allowing the creation of models that represent hydrothermal reactions more accurately. This project focused on developing and demonstrating a methodology to sequentially obtain data for (3), whilst utilising a new confined-jet reactor design for (2), culminating in data that enable (1) with higher fidelity.

As discussed in Chapter 2, lignocellulosic biomass is a mixture of complex biopolymers. Consequently, creating an accurate kinetic model is an effortful task both mathematically and experimentally. Existing literature either focus on analysing bio-oil yields at different conditions, or on the underlying mechanism of monomers [27]. This thesis aims to develop a methodology that would eventually close this gap, by applying it to two organic dimers: dibenzyl ether (DBE) and sucrose, as models of lignin and cellulose's molecular structures, respectively.

Despite the relatively simple molecular structure of the tested compounds, two scientific contributions are proposed: strengthen the knowledge regarding the reactional mechanisms of those specific substances in hydrothermal medium; provide confidence in applying the developed methodology to sequentially more complex molecules, eventually reaching lignocellulosic biomass.

1.4 Objectives and scope

The overall aim of this project is to close the gap in knowledge between the kinetic mechanisms for the HTL of complex lignocellulosic biomass, and relatively simple model compounds. This goal is to be achieved through a methodology that relies on: hydrothermal experiments at clearly defined operating conditions; quantitative analysis of selected compounds; mathematical modelling of adequate complexity; estimation of relevant kinetic parameters with adequate accuracy.

The following more specific scientific and engineering objectives contribute to meeting this overall aim:

- Analyse the performance of a laboratorial-scale continuous hydrothermal reactor using a confined jet mixer configuration to achieve nearly instantaneous feed mixing.
- Evaluate the efficiency of the new confined jet mixer design, through a computational fluid dynamics (CFD) model.
- Perform hydrothermal experiments on different organic feeds, representative of chemical bonds in lignocellulosic biopolymers: dibenzyl ether and sucrose, applying pre-defined operating conditions like inlet compositions, temperature, pressure, and residence time.
- Define analytical methods capable of characterising the different HTL effluents and quantify selected components.
- Develop a generic mathematical model of the HTL reactor that accounts for: medium's near-critical properties; complex kinetic networks and/or rate equations; heat and mass transfer phenomena.
- Create a systematic methodology capable of estimating kinetic parameters of hydrothermal reactions with adequate accuracy, accounting for the influence of subcritical water's self-ionisation product. Apply this methodology in the context of the performed experiments, using obtained experimental results and the mathematical model representative of the HTL reactor.
- Characterise the mechanism of hydrothermal reactions based on estimated kinetic parameters.

1.5 Structure of this thesis

This thesis is divided in nine chapters (including this introductory chapter), with the remaining eight structured as follows:

Chapter 2 reviews existing literature on hydrothermal liquefaction of lignocellulosic biomass. It analyses the components involved and highlights the benefits of continuous processing, as well as its drawbacks.

Chapter 3 describes the materials, equipment, and methods used in each experiment.

Chapter 4 presents the mathematical model developed to simulate the hydrothermal reactor.

Chapter 5 summarises the results of tests conducted on the HTL rig to characterise its performance, prior to obtaining reaction data. These tests focused on comparing nominal and actual feed flowrates, cooling capacities, and heat losses.

Chapter 6 comprises an analysis on the mixing patterns surrounding the confined jet mixer at HTL reactor's inlet. For that CFD simulations were used, which basis and configurations are described.

Chapter 7 presents the study on the hydrolysis of dibenzyl ether in subcritical water. It comprises a qualitative and quantitative analysis of the reactor's effluents. The obtained data is used to estimate kinetic parameters, from which conclusions are drawn regarding hydrolysis mechanisms.

Chapter 8 presents the study on the hydrothermal fragmentation of sucrose. It includes a qualitative and quantitative analysis of the reaction products; and a methodology to sequentially estimate kinetic parameters for a relatively complex reaction network, with focus on the effect of water's self-ionisation product.

Chapter 9 summarises key conclusions, while providing future work recommendations.

Chapter 2

Literature review

2.1 Introduction

This chapter presents and critically analyses the current knowledge regarding hydrothermal liquefaction (HTL) of lignocellulosic biomass. It starts with a description of the compounds involved, reacting medium, and chemical transformations. This is followed by a review on the advantages of continuous processing, and the effect of different operating parameters. Finally, it concludes with a summary of required downstream processes to obtain drop-in biofuels.

In this process, several articles published over the past decades were analysed. From those, the reviews by Peterson *et al.* [24], Elliott *et al.* [21], Cocero *et al.* [47], Gollakota *et al.* [48], Castello *et al.* [4], Baloch *et al.* [3], and Mishra *et al.* [6], were of significant importance.

In addition to this review, Chapters 3 to 8 of this thesis contain a more detailed review on the subject of each chapter.

2.2 HTL of lignocellulosic biomass

Biomass consists of the different materials obtained from recent biological sources, contrasting with fossil fuels, which result from very long decomposition processes. Those materials are derived from plants, such as trees and crops (lignocellulosic), or animals, like manure or sewage (which also contain proteins). For thousands of years, woody biomass has been used as an energy source [7,27,31], usually from direct combustion. The ultimate analysis of biomass samples allows the quantification of specific elements, such as carbon, hydrogen, oxygen, nitrogen, and sulphur. The gross, or higher, heating value (HHV) of the biomass energetic potential (assuming liquid water as the product), can be approximated by correlating the fractions obtained from the ultimate analysis [21]. A high ratio of H/C and low ratio of O/C tend to increase the mixture's HHV, and, consequently, the fuel's quality. The amounts of N and S should be minimal, thus reducing NO_x and SO_x emissions during combustion [3,34]. Table 2.1 shows representative values of these parameters for different biomass sources. Compared to other feedstocks, lignocellulosic biomass presents a HHV similar to macro- and microalgae, which is due to similar H/C and O/C ratios. On the other hand, manure, and sewage sludge present higher variability in composition, which results in larger HHV intervals.

Table 2.1: Typical results of proximate and ultimate analysis for different biomass sources. Adapted from [21], considering a dry and ash free basis.

Feedstock	Lignocellulosic	Macroalgae	Microalgae	Manure	Sewage Sludge
Ash (wt%)	5 – 11	11 – 39	7 – 27	37 – 38	22 – 52
C (wt%)	48 – 53	38 – 47	51 – 58	49 – 72	23 – 40
H (wt%)	5 – 6	5 – 7	6 – 8	6 – 10	3 – 6
O (wt%)	41 – 45	44 – 50	25 – 34	15 – 40	18 – 24
N (wt%)	0.4 – 1.3	1 – 4	8 – 12	3 – 4	2 – 8
S (wt%)	0.1 – 0.3	1 – 4	0.5 – 0.8	0.1 – 1.1	0.8 – 1
H/C (mol/mol)	1.6 – 1.7	1.4 – 1.9	2.6 – 3.8	1.9 – 7.4	2.4 – 3.1
O/C (mol/mol)	0.5 – 0.7	0.7 – 1	0.3 – 0.5	0.1 – 0.7	0.4 – 0.7
HHV (MJ/kg)	17 – 21	18 – 24	14 – 24	21 – 35	8 – 23

Lignocellulosic biomass includes the material derived from living plants, which can be used as an energy source. It comprises both organic and inorganic compounds, as well as up to 50% of water. The main organic compounds are the polymers found in the cellular wall: cellulose, hemicellulose, and lignin. Their representative molecular structures and distribution are presented in Figure 2.1 [2,3,47]. Other molecules, such as proteins, fats, aromatics, and resins are also present, but in quantities below 2% [2,47], being a source of nitrogen and sulphur. Inorganics compounds form the non-combustible matter, which is usually measured as ash content [34].

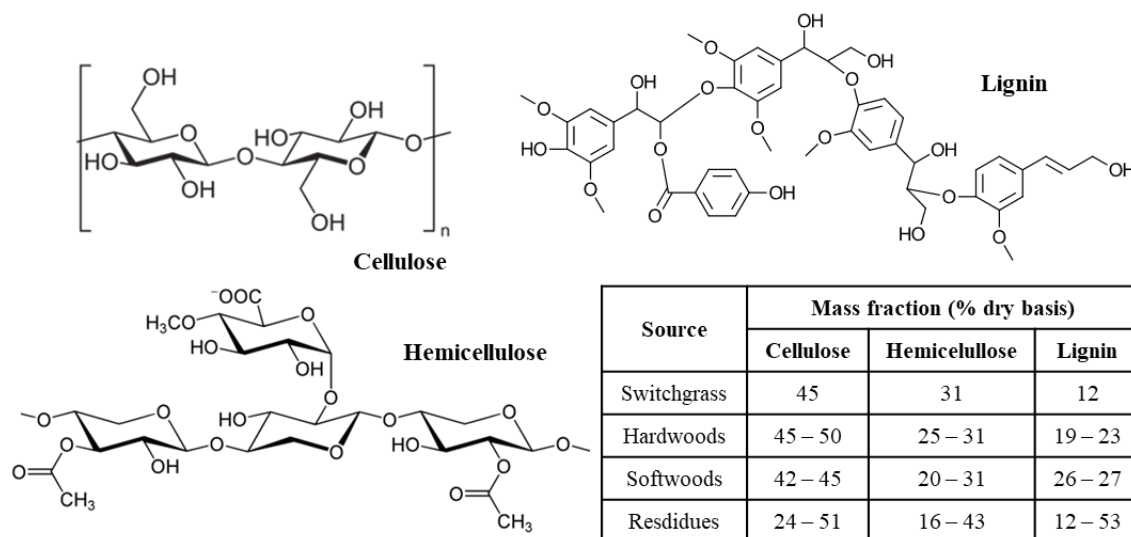


Figure 2.1: Representative molecular structure and relative distribution of the polymers found in lignocellulosic biomass [2,3,47].

When organic compounds, such as the biopolymers in lignocellulosic biomass, are exposed to a temperature in range of 250 – 400 °C in an aqueous medium, at a pressure between 200 and 300 bar,

they undergo a complex set of reactions [3,4]. Those reactions are the core of the hydrothermal liquefaction. They can be divided in the three steps depicted in Figure 2.2 [2,4,6,48–50]:

- Depolymerisation: the biopolymers are sequentially hydrolysed to smaller oligomers and monomers. Water is a reactant in this stage and its capacity of penetrating the polymers' rigid structure is highly influenced by the subcritical environment.
- Degradation: the smaller fragments are further degraded, undergoing reactions such as dehydration, dehydrogenation, deoxygenation, and decarboxylation. The resulting degradation products are mainly polar organic molecules like furfurals, aldehydes, phenols, and organic acids. They are reasonably soluble in water and highly reactive.
- Recombination: The reactive fragments regroup through condensation, cyclisation, or polymerisation. Larger molecules are formed and segregated from the aqueous phase, thus forming bio-oil and eventually solid biochar.

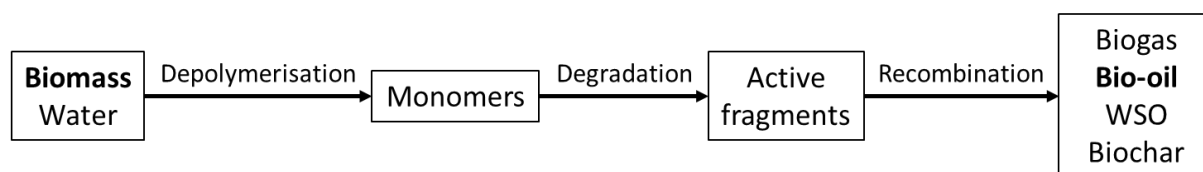


Figure 2.2: HTL overall reaction steps from biomass feed to bio-oil and other byproducts.

As shown in Figure 2.2, HTL products are obtained in four phases:

- Organic phase or bio-oil: viscous, dark coloured, and water insoluble liquid. Its composition may include over 300 organic compounds, such as aldehydes, furans, carboxylic acids, ketones, sugars, guaiacols, esters, and phenols [5,27,48].
- Aqueous phase: contains smaller water-soluble organics (WSO), such as alcohols, ketones, carboxylic acids, and phenols. Organic content in non-recycled fraction requires treatment or upgrading before disposing [4,21].
- Biogas phase: comprises mostly CO₂, with smaller amounts of H₂, CH₄ and CO [4].
- Solids: high molecular weight components resulting from repolymerization reactions or unreacted feedstock [4,48]. Usable in soil amendment, contributing to carbon sequestration, as a fertiliser, or as a carbon-based catalyst [51].

Table 2.4 in Section 2.4 presents typical compositions and HHV of conventional crude oil and bio-oils obtained from different sources. Compared to conventional crude oil, whose oxygen fraction is typically below 1 wt%, bio-oil can contain up to 25 wt% (under dry ash free basis) [3,19,52,53]. As mentioned, this is associated to a low HHV, as well as high viscosity, and poor thermal stability. Furthermore, the significant fraction of carboxylic acids in the bio-oil lowers the mixture's pH, making it corrosive, thus

requiring additional precautions during transportation [3]. Consequently, the obtained bio-oil is expected to require further upgrading like hydrodeoxygenation (HDO) before being used as a fuel [19,52], which is further analysed in Section 2.4. Nonetheless, the bio-oil directly obtained from HTL represents an energetic valorisation, with an HHV in the order of 30 MJ/kg, compared to the typical values of lignocellulosic biomass and pyrolysis bio-oil of 10 – 20 MJ/kg [19,21,52].

The undesirable solid formation occurs in the third step, tending to be favoured by high temperatures and long residence times. The heating value of the produced biochar also increases to 20 – 30 MJ/kg, being at least more valuable as a combustion material than its feed [50,54]. It is commonly agreed in literature that the presence of a hydrogen donor solvent, like ethanol, a homogenous catalyst, such as an alkali carbonate, or a nickel-based solid catalyst inhibit the reactivity of the active fragments, contributing to higher bio-oil yields [48,49].

The next sections describe the benefits (and drawbacks) of using water as a reaction medium and the current knowledge on each biopolymer hydrothermal degradation.

2.2.1 Properties of water

A key aspect of the HTL reactional process is water's physical state [2,4,5,24,47]. At pressures and temperatures near its critical point (374 °C and 221 bar), its properties change considerably. The density, specific enthalpy, and viscosity of water are plotted against temperature, in Figure 2.3 (a) to (c), respectively [55]. Unlike the step change in a phase transition, a smooth progression is observed, allowing the tuning of the properties of water to intermediate values otherwise unattainable in the liquid or gaseous state [4].

In this study, the region with pressure above the critical value and temperature low enough for water to remain under liquid-like properties is designated subcritical. The centre of the transition zone for a given pressure was called supercritical transition temperature (SCTT). In literature, this point is also called pseudo-critical point and can be identified as the maximum heat capacity at a fixed pressure [5].

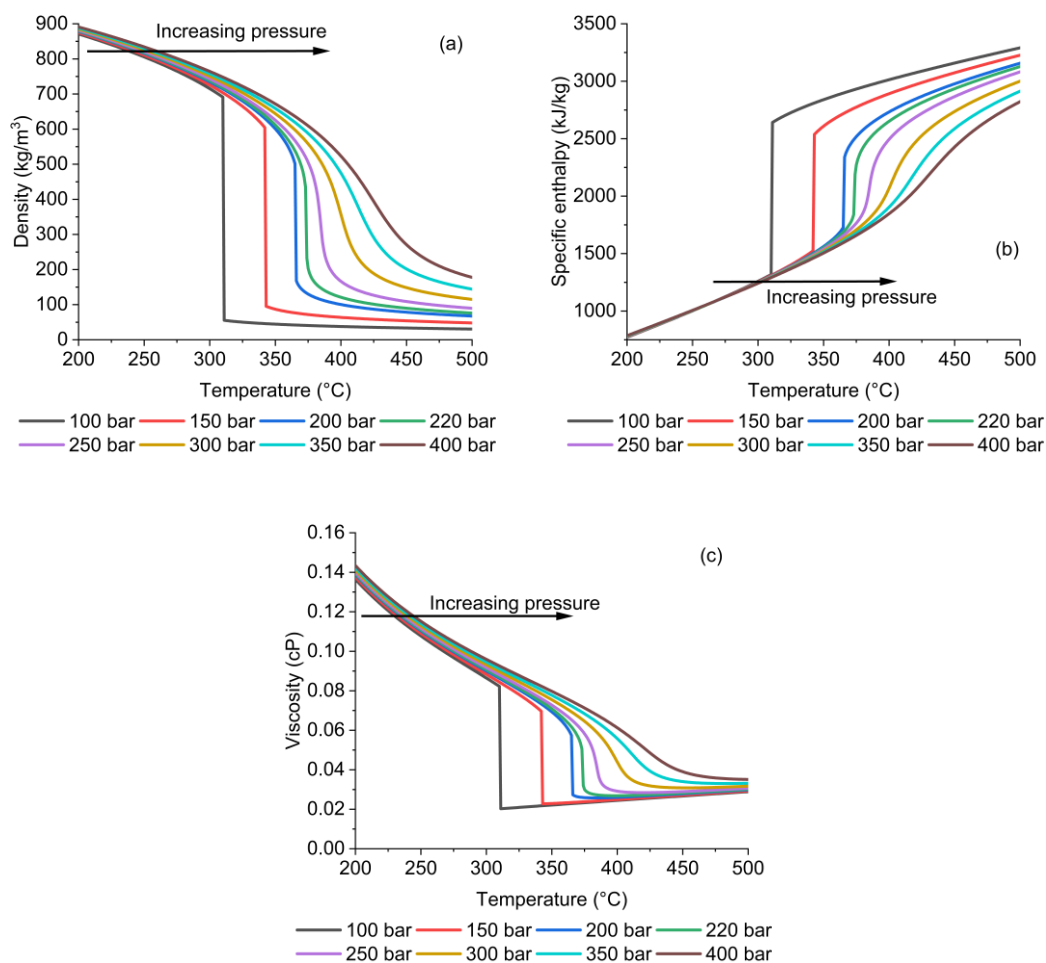


Figure 2.3: Water density (a), specific enthalpy (b), and viscosity (c) near the critical point (374 °C and 221 bar). Calculated using IAPWS-95 [55].

The increased compressibility of water as it approaches the SCTT influences other properties, which are directly correlated with density [5,24]. Figure 2.4 (a) and (b) show the variation of water's self-ionisation product (K_w), and dielectric constant (ϵ_r), respectively, in this region [56,57]. Water's self-ionisation product shows a maximum in the subcritical region, resulting in a variation of the medium's acidity, given the higher product between H^+ and OH^- . These conditions are particularly favourable to acid- or base-catalysed reactions, such as hydrolysis [4,5,58].

The dielectric constant and degree of hydrogen bonding decrease significantly as temperature approaches the SCTT, which in turn increases the solubility of non-polar compounds [5,58]. Though not plotted here, diffusivity increases in the same region [2,59]. The combination of these two improvements reduces mass transfer limitations, helping water to penetrate the rigid structure of lignocellulosic biomass [47].

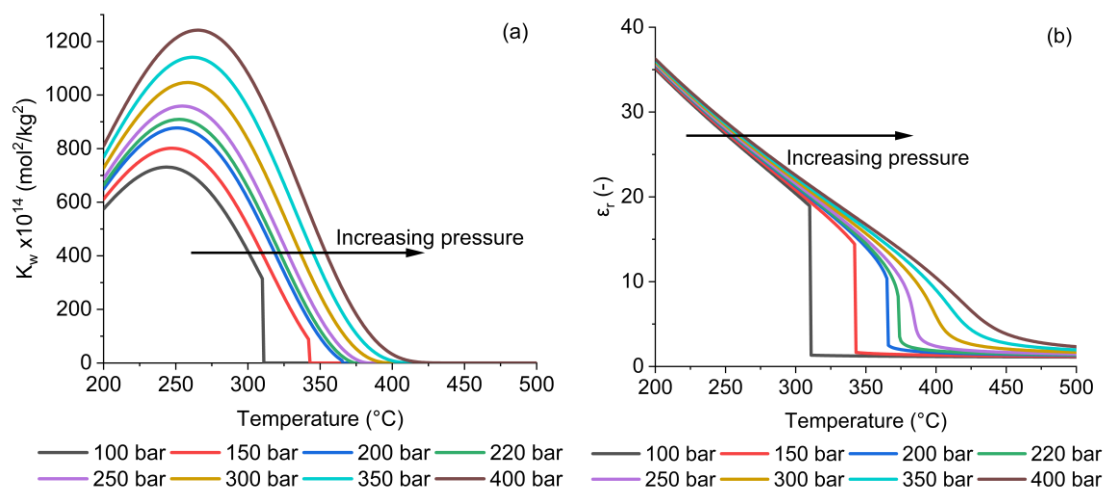


Figure 2.4: (a) Water self-ionisation product (K_w) and (b) dielectric constant (ϵ_r) near the critical point (374 °C and 221 bar). Calculated using density-based correlations [56,57].

Overall, the possibility of tuning the acidity and polarity of water through the manipulation of pressure and temperature, makes subcritical water a favourable medium to transform biomass into bio-oil [2,47]. Furthermore, flattening the transition between liquid- and gas-like enthalpy, means the disappearance of latent heat requirement and a heat capacity reduction. Together with the fluids increased compressibility, these effects have the potential to minimise HTL's overall energy requirement [4].

Apart from water, other solvents have been tested in biomass liquefaction. Given the lower critical points of organic solvents like methanol, ethanol or acetone, milder conditions may be applied, and higher yields obtained [49,60,61]. Nonetheless, water still poses as a viable option given that it is cheaper, easier to obtain, and environmentally friendlier when compared to an organic solvent.

2.2.2 Cellulose

Cellulose is the most abundant biopolymer in the world [31]. It is a linear polymer of glucose monomers (represented in Figure 2.5) connected via β -1,4 glycosidic ether bonds, as depicted in Figure 2.1, with a molecular weight between 10 and 1000 kDa² [3,24,31,47]. The linear structure combined with intermolecular hydrogen bonds create fibrils arranged in a crystalline matrix. This is a rigid structure that prevents water penetration, resulting in it being insoluble at ambient conditions, and only allowing hydrolysis above 200 °C [5,24,47,62]. Due to its high oxygen content, cellulose's HHV is approximately 17 MJ/kg, being close to that of hemicellulose, but considerably lower than lignin's [34,63].

² 1 Dalton defined as 1/12 of the mass of atomic carbon-12, being approximately 1.66×10^{-27} kg [232].

Despite its rigidity and water insolubility, cellulose's structure can be partially degraded, either by physical processes, such as milling, or by chemical dissolution, creating amorphous sections which facilitate hydrolysis [34,47]. Apart from this rigid structure, other polymers like lignin further inhibit access of water access to cellulose. Owing to this structural limitation, slower kinetics are expected for lignocellulosic biomass when compared to pure cellulose, as heterogeneous mass transfer limitations become more significant [31,47,64].

Cellulose hydrolysis breaks the glycosidic bonds between its monomers, producing oligosaccharides, and eventually glucose. This monomer can be further degraded into several valuable compounds [65] which include: 5-(hydroxymethyl)furfural (5-HMF), a platform chemical with applications in fuels or polymer production [66,67]; levulinic acid, a building block in fuel additives and pharmaceuticals [68,69]; lactic acid, used in food, chemical, and cosmetic industries [67]; glycolaldehyde, an intermediate in the production of fine chemicals, and food colourants [70]; and 1,6-anhydro- β -D-glucose, which can be applied in the production of biodegradable surfactants [71]. A more complete review of the reactions of glucose in a hydrothermal medium is provided in Chapter 8.

Manipulating the residence time, in the order of milliseconds, and adjusting temperature and pressure near the critical point, allows the product to be richer in glucose or in its degradation products [24,47,72,73].

2.2.3 Hemicellulose

Hemicellulose covalently bonds cellulose fibres to the lignin's hard structure [34,47]. It is composed by different monomers like the ones in Figure 2.5, combining pentoses with hexoses in a biopolymer with a maximum molecular weight of 70 kDa [5,6,47]. Unlike cellulose, the monomers form a branched configuration, as exemplified in Figure 2.1, which hinders inter-molecular bonding, creating an amorphous structure. Consequently, compared to cellulose, hemicellulose is soluble in water and more reactive, being hydrolysed from 150 °C [2,34,47,74].

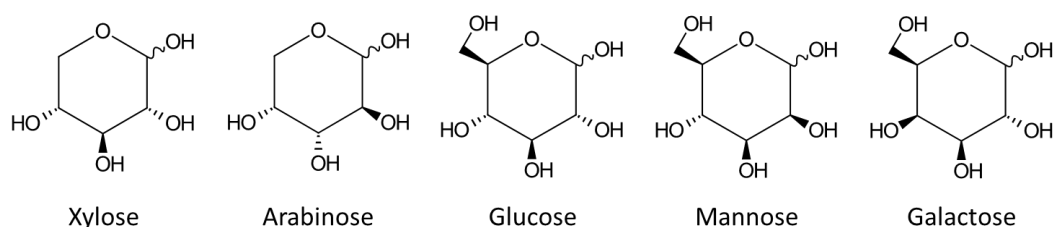


Figure 2.5: Molecular structure of hemicellulose's typical monomers.

The structure of hemicellulose and the composition of its monomers is highly varied, depending on factors like the plant's species or cellular location [34]. Typically, mannose is the most frequent monomer in hemicellulose obtained from softwoods, while xylose prevails in hardwoods and agricultural residues [24,75]. Therefore, the last is frequently considered a model compound of hemicellulose [76]. Depolymerisation starts by cleaving the polymer into different sized oligomers, which, when short enough, are released from the solid main structure and solubilized. Given enough temperature and residence time, all hemicellulose is converted into oligomers, and these to monomeric sugars, which can also be further degraded [47].

Mittal *et al.* [77] developed a comprehensive model which accounts for the polymer's hydrolysis into oligomers and xylose, and the monomer's degradation into furfural. The model considered pore formation in wood chips, reactions inside and outside those pores, and associated mass transfer between the two media. This model was validated against data from a batch reactor at relatively low temperature (less than 175 °C).

Hosseini *et al.* [78,79] developed a kinetic model accounting for the polymer degradation into successively smaller oligomers and eventually xylose, considering not only the process kinetics, but also particle diffusion. It was also only validated at a relatively low temperature (160 °C) and does not account for the monomer's degradation.

On the other hand, Paksung *et al.* [76] formulated a comprehensive model for xylose's hydrothermal decomposition from experiments at 250 bar, with temperatures between 300 and 450 °C, and residence times from 0.5 to 7 seconds. Under those conditions the degradation products of xylose are analogous to those of glucose, showing a reaction pathway like the one in Figure 8.1 in Section 8.1.1. This includes the equilibrium with a more reactive isomer, xylulose; retro-aldol condensation to glycolaldehyde, glyceraldehyde, and dihydroxyacetone; and dehydration to furfural (instead of 5-HMF). The last was the most abundant product at subcritical conditions. Paksung *et al.* [76] expected all the products would further degrade to carboxylic acids.

2.2.4 Lignin

Lignin is an aromatic polymer, of which the monomers are the phenolic alcohols shown in Figure 2.6: p-coumaryl, coniferyl and synapyl. As in hemicellulose, their relative abundance in the polymer varies with the type of lignocellulosic biomass [5]. These are linked via condensed (C-C) and ether (C-O-C) bonds, with a natural frequency of approximately 30% and 70%, respectively [5,20]. The large variety of possible combinations between the three alcohols creates a complex and unpredictable structure, which is amorphous like hemicellulose, but water-insoluble like cellulose [48].

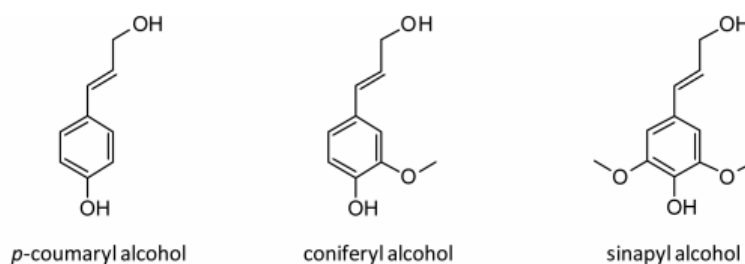


Figure 2.6: Molecular structure of lignin's monomers.

Current industrial applications are different for the three biopolymers that compose woody biomass. While cellulose and hemi-cellulose are mainly utilised in the paper industry, lignin is a by-product with few current applications. Nonetheless, from the three biopolymers, it is the one with lowest oxygen content, and consequently, highest HHV (25 – 30 MJ/kg) [4,59,63,80]. However, from all lignin produced annually, only 2% are valorised, with the remainder being burnt as fuel [20]. Given its aromatic structure, lignin has the potential to be used as a chemical additive in resins, as well as a raw material to produce a wide range of relevant chemicals, such as phenol, benzene, toluene, and xylene (BTX), vanillin, guaiacol, and biofuel [20,74].

The isolation of lignin from lignocellulosic biomass is achievable via physical, biological, and chemical processes. The first employs steam explosion, or grinding at extreme conditions, thus leading to high energy costs [20,36,81]. The second uses enzymes to break intermolecular bonds, through long and inefficient processes [20,36,82]. On the other hand, chemical processes allow higher efficiencies at milder conditions (up to 190 °C), being widely applied in the pulp and paper industry [20,74]. From these processes result the isolated polymer, usually called technical lignin, with variable properties.

A review by Rinaldi *et al.* on lignin processing [74] highlighted the Kraft and Organosolv pulping methods. The first is a well-established process, producing approximately 130 million tons of pulp per year, with a substantial part of the lignin by-product being used as fuel. It removes lignin from wood through its exposure to a Na₂S aqueous solution in alkaline conditions. In this process, native lignin is partly degraded and repolymerised, resulting in a technical lignin with a substantially smaller fraction of ether bonds (approximately one seventh). It also results in the emission of organosulfur compounds.

On the other hand, the Organosolv-type processes apply aqueous solutions of organic solvents, such as alcohols, cyclic ethers, or ketones, with the common addition of an acid catalyst. The extracted technical lignin is expected to maintain a larger fraction of the native ether bonds than Kraft's. Nonetheless, Organosolv-type processes never passed the demonstration stage [74].

Compared to condensed C-C bonds, ether bonds exhibit a significantly lower dissociation energy (54 – 76 instead of 75 – 1180 kcal/mol [74]). Consequently, a technical lignin becomes less reactive, requiring

more energy to depolymerise. Therefore, compared to Kraft lignin, Organosolv lignin is a more suitable feedstock for hydrolysis.

Given its complex and variable nature, information fully describing lignin's hydrolysis mechanism is rare and relies on model compounds, such as vanillic acid, syringol, coniferyl or synapyl alcohols, to better understand the overall mechanism [47].

Zhang *et al.* [83] compared the hydrothermal degradation of different lignin sources under subcritical conditions, through a series of batch experiments; these demonstrated that the yield of liquid products was affected by lignin's pre-treatment, from which a simplified kinetic model was derived.

Yong *et al.* [84,85] performed several experiments in continuous reactors under sub- and supercritical conditions and residence times shorter than 10 seconds, using Kraft lignin as feed. They observed complete degradation in less than 5 seconds. Based on the measured products, a reaction pathway like the one in Figure 2.7 was proposed. Char formation through repolymerisation was observed even at very short residence times (under 1 second), with the amount of char produced increasing at supercritical conditions. The overall rate of decomposition of lignin increased with temperature in accordance with Arrhenius' law. However, this was not the case for all reactions, suggesting those could be affected by the decrease in the ionic product of water with increasing temperature. Forchheim *et al.* [80] developed a similar kinetic model based on batch experiments using enzyme hydrolysed lignin.

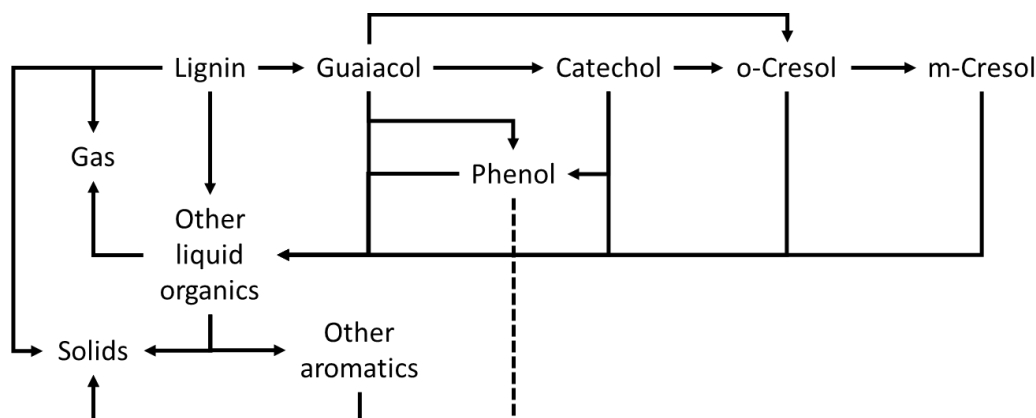


Figure 2.7: Yong *et al.*'s reactional pathway for lignin hydrolysis. Adapted from [84].

2.3 Continuous HTL

Converting lignocellulosic material to bio-oil dates to the 1920's. Noting the high carbon content in plants, Berl proposed their liquefaction in aqueous medium and subsequent hydrogenation to obtain liquid fuel as an alternative to natural oil [86,87]. Major research projects started in the 1970's and have evolved from batch to continuous operation, testing different feedstocks, solvents, and catalysts. Nonetheless, most of the liquefaction studies found in the literature are still based on experiments under

batch conditions [21]. Batch reactors are simple to operate and typically consist of an autoclave loaded with biomass and water, which is heated to the required temperature. After a certain time, the reactor is cooled and the products recovered, frequently employing solvent extraction [4,19,24].

On the other hand, continuous operation requires additional equipment, like pumps, backpressure regulators, and filters, as shown in Figure 2.8. Nonetheless, it is considered more economical for the industrial production of large volumes, as would be required for alternative drop-in transportation fuels [4,6,48].

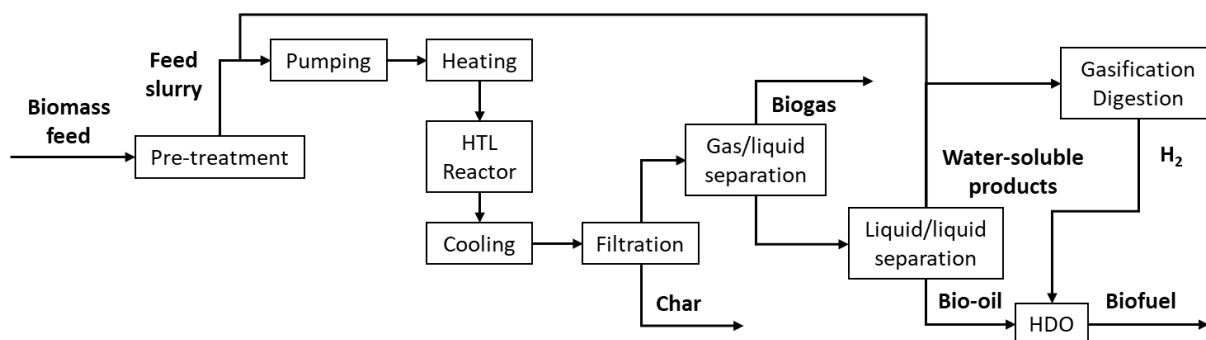


Figure 2.8: Generic block diagram of a complete HTL process.

The main differences between the two operation modes are summarised in Table 2.2. Pressure and temperature affect the solvent's properties when operating near the critical point, thus changing the reaction pathway, and overall bio-oil yield [4]. For batch reactors, pressure is defined by the mixture's saturation at operating temperature, not being controllable. In continuous operation, pressure control is independent from temperature, being possible through devices like backpressure regulators or parallel hydraulic release systems [19,21].

Table 2.2: Comparison between batch and continuous operation [4,21,47,88].

Operation	Batch	Continuous
Heating/cooling rates	Slow	Fast
Residence time	Minutes to hours	Milliseconds to minutes
Pressure control	Autogenic pressure, resulting from vapour pressure of liquid	Backpressure regulator, independent of temperature
Feedstock dry matter concentration	No direct limitations	Limited by pipe plugging and feedstock pumpability
Heat integration / energy recovery	Not possible	Possible
Industrial feasibility	Only for limited amounts of high value products	Adequate to the high throughput required by fuel production

As referred in Section 2.2, HTL is defined by a reactional sequence that terminates in a repolymerisation step. Given the inherent dynamics of batch reactors, heating and cooling are slow processes, requiring transient periods to achieve operating conditions. Continuous operation is based on steady state

processing with constant output. As reviewed in Section 2.3.4, a flow configuration allows high heating and cooling rates, thus minimising residence time at intermediate conditions, and reducing the formation of unwanted products [4,88].

Despite all the advantages presented, continuous processing is limited by the possibility of creating a stable biomass slurry and transporting it across the system. When pressurised, biomass fibrous structures tend to agglomerate through bridging, entangling, and self-adhering, which results in its segregation from the liquid phase. This effect causes accumulation and eventually blockages in constrictions such as valves and pumps and is directly related to particle size and biomass concentration [4,21,89]. Consequently, customised positive displacement pumps are recommended to reach HTL's high operating pressure [89].

Castello *et al.* [4] compiled a list of continuous HTL processes implemented or announced from 1982 until 2018. It shows an evolution in scale from pilot to commercial demonstration, with most projects being implemented during the 2010's, possibly related to increasing oil prices. Selected feedstocks have also moved from specially grown wood to waste and algae. Regarding operating conditions, since 2011, pressures above the critical value have been preferred, while keeping temperatures below the supercritical transition. The importance of operating near the critical point is recognised, but there are also benefits in maintaining dense, liquid-like properties. The typical residence times have decreased over the years, from hours to less than 30 minutes. Limited information on catalyst selection shows that alkali-carbonates are preferred, *i.e.*, a base-catalysed mechanism.

The following sections review recent research on the different factors that affect the HTL reactions system, including operating conditions, and introduction of solvents and/or catalysts.

2.3.1 Particle size

The simplified flow diagram shown in Figure 2.8 includes a pre-treatment unit responsible for transforming the biomass source into a pumpable slurry. This involves processes like removing contaminants, chemical treatment, and particle size reduction [4,19,48]. When harvested, woody biomass is chipped to a size in the range of 10 – 50 mm, ensuring it can be transported and stored in reasonable amounts [90,91]. Further size reduction improves pumpability and increases the overall surface area, thus reducing heat and mass transfer limitations [92,93].

However, technologies for particle size reduction, like milling and comminution, are energy intensive processes, associated to high operational costs, which increase exponentially and vary with the wood source, moisture, and equipment [6,93–95]. Regarding pumpability, the maximum particle size varies with the process scale. Laboratorial experiments require smaller particles (up to 30 micron), while pilot and production scale allow larger sizes (up to 6 mm) [89]. Overall, there is a trade-off between

minimising mass and heat transfer limitations, preventing excessive pre-treatment costs, and producing a pumpable slurry.

2.3.2 Feed concentration

The use of high solid concentration allows operation with smaller volumetric flows; consequently, both equipment size and heat demand are lowered, thus reducing capital and utility costs [4]. Its effect on the bio-oil yield has been studied with different results observed [4,6]. Given the water's purpose not only as a solvent, but also as reactant and catalyst [6], lowering its fraction during the liquefaction of lignocellulosic biomass reduces the bio-oil yield, while promoting char formation [3,54,90,96,97]. Furthermore, increasing the feed's solid fraction reduces the capacity of the water to fully solubilise the biomass particles, thus increasing the mass transfer limitations in the overall kinetic process, and therefore slowing hydrothermal reactions [47]. On the other hand, Castello *et al.* [4] pointed out that reducing the amount of water available during phase separation forces organic molecules to remain in the bio-oil phase, thus increasing its yield.

Regardless of its effect on bio-oil yield, increasing the feed dry content increases the probability of segregation, *i.e.*, accumulation of solids and plugging. Pump providers agree with the use of typical values around 15 wt%, but also consider that 45 wt% is possible using customised equipment [4,89]. To counter pumpability limitations, Dărăban *et al.* [98,99] proposed pre-treating the feed with sodium hydroxide (NaOH) at 180 °C for 120 min. This medium partially degrades the lignocellulosic particles, making them more soluble, and allowing the processing of a slurry with 25% solids.

Therefore, optimising the fraction of solids at the reactor's inlet requires not only a good understanding of its effect on the reaction mechanism, but also of additional operating costs and technical limitations.

2.3.3 Temperature

Mishra *et al.* [6] and Baloch *et al.* [3] summarised the results of recent studies regarding the temperature effect on the HTL of different biomass sources. Both concluded that, despite not being possible to define an ideal temperature, which is universal to all the feedstocks, most studies indicate an optimum value for each specific source. This maximum is frequently associated with an increased yield of solids and gases at higher temperatures, suggesting bio-oil degradation and repolymerisation overcome its formation [65]. Nonetheless, it should also be considered that maximum yield, does not necessarily mean optimum bio-oil properties, such as HHV [100].

In Section 2.2.1, it was mentioned that under subcritical conditions, pressure and temperature can be used to fine-tune the properties of water [2,47], such as density and viscosity, particularly at higher

pressures. In a simplified approach, pressure could be manipulated to ensure suitable medium properties at optimum yield temperature. However, with reaction rates and mass transfer being affected by density, viscosity, and related properties like ionic product and diffusivity, such a crude approach is not viable. Therefore, a complete understanding of biomass' reactional mechanism at different pressures and temperatures is fundamental to select optimal operating conditions [48].

2.3.4 Residence time and heating/cooling rates

As hydrolysis cleaves polymers into smaller fragments, repolymerisation recombines them into more recalcitrant structures, producing char at short residence times [48,65,85,88]. Therefore, it is beneficial to limit the reaction to residence times in the order of seconds, thus minimising recombination reactions.

Based on batch HTL of actual biomass, Brand *et al.* [101] verified that short residence times contributed to higher bio-oil yield if associated with fast heating and cooling rates, before and after the process, respectively.

Since hydrothermal carbonization starts at 180 °C [2], several reactions occur while the mixture reaches liquefaction temperatures, between 250 and 400 °C, or cools down through this range. Therefore, controlling the residence time for liquefaction would benefit significantly from instantaneous heating and cooling at the reactor's inlet and outlet. Tran [102] pointed out that high heating rates are not achievable in industrial batch reactors or even in continuously stirred reactors with upstream heating. Aida *et al.*, in 2007 [103], Chuntanapum, *et al.*, in 2008 [104], and Cantero *et al.* in 2013 [72], all proposed a tubular configuration where "ultra-fast" heating is achieved by mixing a supercritical water (SCW) stream with a cold biomass slurry in a tee section at the reactor's inlet. Nonetheless, Tran [102] also mentioned that this type of configuration might result in tee plugging when operated with real biomass slurries at commercial scale.

Cooling of the effluent is also required to be fast, though this can be more easily achieved through quenching, particularly if a hydrogen donor is added [101,102].

2.3.5 Solvents and co-solvents

During biomass liquefaction, the solvent must penetrate the rigid polymer matrix and promote depolymerisation reactions. Subcritical water is an attractive option due to increased dissociation and reduced dielectric constant near the critical point. It also has the advantage of being cheap, easily accessible, and environmentally innocuous. Furthermore, it allows the processing of biomass without upstream drying [4,5,24,47,49,100].

Nonetheless, other solvents have been tested with the objective of increasing bio-oil yield. Those tests considered solvents of different categories, such as polar protic, like methanol, ethanol, ethylene glycol, propanol, or butanol; polar aprotic, such as acetone or 1,4-dioxane; and non-polar, *e.g.*, toluene or tetralin [49,105,106]. Table 2.3 presents the critical properties of some of these solvents [49,106]. The organic compounds have critical pressures and temperatures lower than water, suggesting that liquefaction may be conducted at milder conditions. Nonetheless, their use also requires an efficient recovery process to keep the process economically feasible, particularly for more complex solvents [100].

Table 2.3: Critical properties of solvents tested for biomass liquefaction, adapted from [49,106,107].

Type	Solvent	T_c (°C)	p_c (bar)	ρ_c (kg/m ³)	ϵ_r at 20 °C
Polar protic	Water	374	221	332	79.7
	Methanol	240	79.6	272	32.6
	Ethanol	243	63.9	276	22.4
Polar aprotic	Acetone	235	48.0	278	20.4
	1,4-dioxane	315	52.1	370	2.21
Non-polar	Tetralin	447	36.5	324	2.77
	Toluene	319	41.1	292	2.38

Different solvents result in distinct bio-oil compositions, suggesting that they actively influence the reaction pathway [6,100,106]. Not only protic polar solvents, but also non-polar hydrogen donor solvents such as tetralin, tend to improve bio-oil yield and HHV [49,65,100]. Though the mechanism of this solvent effect is not well known, most authors agree that by acting as a hydrogen donor, the organic solvent stabilises liquefaction intermediaries, thus reducing repolymerisation [61,96,101,105].

To take advantage of the different solvents' properties, combinations of water and an organic co-solvent have been tested [6,100,105]. Typically, ethanol is the selected co-solvent since it is moderately polar with H-donor capabilities and requires operating conditions less aggressive than water. Furthermore, it can be obtained from biomass fermentation [49].

Feng *et al.* [105] observed a significant increase in bio-oil yield, associated to a decrease in solid yield, when ethanol was used as a solvent in the liquefaction of lignin and cellulose. The process was further optimised when a water/ethanol mixture (50:50 in volume) was applied, particularly to a pure lignin feedstock. Belkheiri *et al.* [59,108] tested the effect of including phenol and methanol alongside water in Kraft lignin depolymerisation, as these are also expected to be produced during the process. It was observed that phenol increased bio-oil yield, while adding methanol suppressed char formation.

Nonetheless, there is a considerable knowledge gap on the actual effect on the reactional pathway when co-solvents are used, particularly a systematized approach to continuous processes.

2.3.6 Homogeneous catalysis and pH

Nine of the continuous processes listed by Castello *et al.* [4] use alkali carbonates, Na_2CO_3 or K_2CO_3 , as homogenous catalysts for HTL. The former is commonly found in literature at a concentration of 5 wt% [4,109]. Besides these, other alkali hydroxides like KOH, and organic acids, such as acetic and formic acids, have been tested for catalytic activity in HTL [3,6,19,109]. Cocero *et al.*'s review on lignin's depolymerisation [47] concluded that the process is preferably base-catalysed, due to the polymer's deprotonation reducing hydrogen bonding, thus weakening its rigid structure, and facilitating hydrolysis.

Several authors demonstrated a gain in bio-oil yield caused by including an alkali salt in batch reactors at optimal concentrations and temperatures [50,54,110,111]. Based on a larger pH variation for a reaction in the presence of K_2CO_3 (12 to 6 compared to 7 to 4 without catalyst), Zhu *et al.* [111] proposed that alkaline solutions not only promote hydrolysis, but also stabilise reactive acidic intermediaries. Consequently, the solid yield was reduced, while the both bio-oil yield and HHV increased.

Belkheiri *et al.* [112] tested the effect of increasing the feed's pH on a continuous reactor for Kraft lignin's depolymerisation using KOH. They observed a changing product composition, with minimised solid formation, higher concentration of organics in the aqueous phase, and lower oxygen content in the bio-oil. Nazari *et al.* and Malins [50,54] compared not only the effect of homogeneous catalysts (Na_2CO_3 and NaOH), but also heterogeneous ones, concluding that the former provided higher bio-oil yields and HHV.

However, despite improving the quantity and quality of biocrude, including an alkali salt means increasing the mixture's pH and consequently corrosivity, thus requiring more resistant and expensive equipment. Furthermore, it is complex and costly to recover a homogeneous catalyst, thus limiting their recyclability and process economy, since they effectively become a consumable instead of a catalyst [109].

2.3.7 Heterogenous catalysis

Malins [54] compared the effect of different metal catalysts and homogenous catalysts in wood liquefaction. It was observed that, nickel-based catalysts gave marginally smaller bio-oil yields (less than 10%) than the sodium salts described in Section 2.3.6. Nonetheless, heterogenous catalysts have a significant advantage as they do not increase the mixture's corrosivity and are easily recovered [109,113].

Castello *et al.* [4] identified several continuous processes using zirconia (ZrO_2) as catalyst. Little information is available about this catalyst's performance, either due to proprietary processes *e.g.*, CatLiq[®] [114] or lack of dedicated research [59]. Hammerschmidt *et al.* [115] also used zirconia as a catalyst to successfully produce bio-oil through liquefaction of different biomass sources, based on earlier lignin gasification experiments by Watanabe *et al.* [116]. It was observed that using this catalyst, the amounts of residues was reduced, while the aqueous phase was more easily separated due to the presence of components with higher polarity [115].

Duan and Savage [117] tested the effect of solid catalysts used in conventional refineries during the batch liquefaction of algae. Those included carbon-supported noble metals (Pd/C, Pt/C and Ru/C), and aluminosilicates (Ni/SiO₂-Al₂O₃, CoMo/Al₂O₃, and aluminium silicate zeolite). All experiments increased the bio-oil yield, with the largest variation produced by Pd/C.

Ma *et al.* [113] compared different metal catalysts supported on cerium oxide (CeO₂) as an alternative to expensive noble metals in the batch liquefaction of lignocellulosic biomass. The maximum increase in the bio-oil yield was observed for the nickel catalyst (Ni/CeO₂).

Li *et al.* [118] observed that the amount of nickel over an aluminium matrix affected the yield of liquid products from lignin liquefaction, which had already increased even in the absence of nickel particles. This confirmed the existence of synergetic effects between aluminium and nickel. The first acts as a Lewis acid, promoting hydrolysis, while the second as hydrogen binding site, thus stabilising reactive intermediaries. The same effect had been reported regarding iron-based catalysts [3].

All the examples above show the positive effects of metal catalysts used in conventional refineries in increasing bio-oil yield at typical HTL temperature and pressure, not requiring milder conditions. Despite the significant amount of studies using these catalysts, it is typically highlight how little is known about the mechanism of the interactions between metal catalysts and lignocellulosic biomass.

2.4 Downstream processing

As generically represented in Figure 2.8, the hydrothermal liquefaction of lignocellulosic biomass yields organic products in four phases: gas, bio-oil, aqueous liquid, and char. The first can be separated via flash depressurisation or in a hydro-cyclone. Solids can be collected by inline filtration. The feasibility of performing the filtration under hot pressurised conditions is a subject of current research [4,19,119], as avoiding cooling the mixture allows significant energy savings.

The separation of the two liquid phases should happen spontaneously, in which case an oil/water separation drum is sufficient. Solvents like dichloromethane, tetrahydrofuran, or acetone are typically used to extract the remaining organics from the aqueous phase at laboratory-scale. However, it is

difficult to scale-up, as it would increase both capital and operating costs, due to the recovery of solvent required to meet environmental limits on emissions [109,120].

Nonetheless, regardless of being extracted, the organic content in the aqueous phase prevents a direct discharge. Therefore, it must be recycled and/or further transformed. Recycling water can improve feed pumpability and increase bio-oil yield. Further treatment of the wastewater, via gasification or anaerobic digestion, provides a wider range of useful products such as methane [4,98,121].

Table 2.4 contains the elemental composition of bio-oils from different sources, as well as literature values for common crude oil [52,53,87,122,123]. A major difference is observed in the amount of oxygen, which is considerably higher in bio-oils. As mentioned in Section 2.2, this lowers the oil's HHV (also in Table 2.4), and increases density, viscosity, and acidity, leading to high corrosivity, and poor thermal stability. Compared to pyrolysis, bio-oil produced via HTL presents a smaller oxygen concentration, which can be attributed to different reaction pathways, as well as polar molecules containing oxygen (as described in Section 2.2) being retained in the aqueous phase [22,24,53]. Nonetheless, in those conditions, HTL bio-oil may not be directly used as a drop-in transport fuel, instead requiring an oxygen removal process [109]. This is achievable by HDO, which removes oxygen atoms and reduces the fraction of aromatic molecules [3,122]. It applies technologies like hydrodesulphurisation, hydrodenitrogenation, and hydrocracking, commonly applied in fossil crude processing [4,21,24]. HDO is conducted in the presence of hydrogen over a metal catalyst (nickel, cobalt, molybdenum, or platinum based), typically in the same temperature range as HTL, but at lower pressure, *e.g.*, 100 – 180 bar [24,87].

Table 2.4: Comparison between the elemental composition and HHV of conventional crude with bio-oil before and after HDO.

Feed	Conventional crude	Pyrolysis bio-oil	Crude HTL bio-oil			Upgraded HTL bio-oil			
			Microalgae	Hardwood	Rice stalk	N/A	Microalgae	Hardwood	Rice stalk
C (wt%)	85	45	73	76	65	> 83	84	84	80
H (wt%)	13	8	10	8	8	> 1	12	12	9
S (wt%)	2	2	0.8	0	0	N/A	0	N/A	2
N (wt%)	0.1	0.1	6	0	1	N/A	3	N/A	2
O (wt%)	0.1	47	16	15	26	< 2	1	5	7
HHV (MJ/kg)	45	20	35	35	30	~ 44	45	43	39
Ref	[52]		[122]	[123]	[53]	[87]	[122]	[123]	[53]

Table 2.4 also includes examples of the composition of upgraded bio-oils, demonstrating the decrease in oxygen composition and increase in HHV, which approach those of a conventional crude oil. Yang *et al.* [5] observed that density, viscosity, and acidity were also decreased through HDO. Overall, as a technology, HDO remains in earlier stage of development compared to HTL [4].

2.5 Concluding remarks

A literature review has been conducted on hydrothermal liquefaction of lignocellulosic biomass. It focused on understanding the aqueous reaction medium and the reactions with the main components of biomass; why and how it can be implemented as a continuous process; how different operating parameters affect bio-oil yields; and what downstream processing is required. The following conclusions can be drawn from this analysis:

The smooth variation of water's properties in the subcritical region, particularly ionic product, and dielectric constant, results in an aqueous medium of tuneable acidity and solubility, suitable for the conversion of biomass into bio-oil.

Lignocellulosic biomass is composed of three biopolymers of distinct compositions and properties: cellulose, hemicellulose, and lignin. Their hydrothermal reactions can be summarised as: depolymerisation via the biopolymer hydrolysis into oligomers and monomers; degradation into active fragments; and recombination into larger molecules. Changing operating conditions, and consequently the medium's properties, allows the process to focus on the products of a specific step.

Existing HTL kinetic models describe different aspects of the process:

- Mass transfer between biomass solid particles and water.
- Polymer hydrolysis into smaller oligomers, eventually reaching monomers.
- Monomer degradation into active fragments.

Implementing biomass HTL as a continuous process ensures the processes economic viability at large throughputs. Furthermore, HTL continuous processing allows better reaction control through independent pressure and temperature manipulation, fast heating and cooling rates, and shorter residence times. Particle size, concentration, and operating conditions allow the optimisation of bio-oil yields and composition. However, a major technical limitation lies on the viability of pumping a concentrated biomass slurry through the process.

Other processes, which have been shown to improve bio-oil yield, include adding to the reactional mixture an alkali salt, such as Na_2CO_3 , or a hydrogen donor organic co-solvent, like ethanol, or conducting reactions over a metal-supported catalyst.

Compared to conventional crude, the high oxygen content in HTL bio-oil lowers its HHV, and increases acidity and viscosity, thus requiring downstream upgrading before being used as a drop-in transport fuel. This is achievable via hydrodeoxygenation, similar to existing hydrotreatment processes ones in conventional oil refining.

It is possible to improve the output of an HTL process by manipulating its operating conditions, and consequently the properties of the water. Understanding and quantifying the underlying kinetic mechanisms allows the development of mathematical models capable of predicting and optimising the type and range of products obtained from lignocellulosic biomass. To achieve this goal, fundamental and reliable measurements are required, particularly using fast heating rates at small residence times. This is possible through continuous HTL, which also allows independent manipulation of temperature and pressure.

Therefore, the objective of the present study is to use an existing lab scale continuous hydrothermal system to investigate the reactions of model compounds representative of components of lignocellulosic feedstocks. These measurements will be used in the development and reduction of reaction mechanisms, and estimation of kinetic parameters.

Chapter 3

Experimental

3.1 Introduction

The hydrothermal upgrading of lignocellulosic biomass was investigated by studying the reaction behaviour of model compounds in contact with hot compressed water. Those studies were based on bench scale experiments performed in a continuous rig, which at its core contained a confined jet mixer followed by tubular reactor. The bulk of the experimental apparatus was the same as that used in a previous study [124], with additional modifications and calibrations conducted during this project.

This chapter describes the hydrothermal liquefaction rig, with additional details on custom equipment. This is followed by an analysis of the operating procedure. Next, the methods for separating and analysing the HTL rig's effluent are described. Finally, potential sources of errors and uncertainties are summarised.

As referred in Section 2.3, as early as the 1970's there have been attempts at liquefying woody biomass in continuous reactors [4,102,125]. The continuous reactor used in this study aims to provide a systematic approach to obtain reliable kinetic data related to biomass liquefaction. To fulfil this objective, the following aspects were considered in the design of the experiments [102]:

- Temperature and residence time control, through very quick heating at the reactor inlet and immediate cooling and quenching at its outlet.
- Independent pressure control without gas addition, possible with back pressure regulation.
- Suitability for scale-up, by implementing the process in a larger continuous tubular reactor and, or multiple reactors in parallel.

The rig setup was based on existing designs for continuous processes in hydrothermal media [64,102–104,126,127], using a patented confined jet mixer originally developed for the synthesis of nanoparticles [128–130].

Unlike processes with feed pre-mixing and heating upstream of the reactor [125,126], this configuration allowed very fast heating immediately at the inlet of the reactor [128–130]. Therefore, it was ensured that reactions were avoided during the heating process, only starting in the well-defined reactor section.

Compared to processes where SCW and organic feeds are mixed in a common tee junction [64,102,103], the turbulence generated by the high velocity at the outlet of the confined mixer (see

Section 6.4) promotes an active mixing between the two feeds, even when the downstream flow is under a laminar regime.

3.2 Materials

Table 3.1 provides information on the materials used in the experiments.

Table 3.1: Summary of the substances required during this research project.

Compound	Supplier	Purity	Application
De-ionised water (DI water)	Purified using a CENTRA [®] system by ELGA – Veolia [™]	18.2 MΩ.cm	Process feed and quench. Sample dilution. Mobile phase for HPLC.
Dibenzyl ether (DBE)	Acros Organics	99%	Organic feed. Standard for HPLC calibration.
Benzyl alcohol (BAL)	Sigma-Aldrich	99%	Standard for HPLC calibration.
Benzaldehyde (BZA)	Sigma-Aldrich	99.5%	
Toluene (TOL)	Fisher	99%	
Acetonitrile (ACN)	Sigma-Aldrich	99.9%	Sample dilution. Mobile phase for HPLC with UV-vis detection.
Sucrose (Suc)	Alfa Aesar	99%	Organic feed. Standard for HPLC calibration.
D-Glucose (Gluc)	Sigma	99.5%	Standard for HPLC calibration.
D-Fructose (Fruc)	Alfa Aesar	99%	
Pyruvaldehyde (Pyr)	Alfa Aesar	35-45%	
1,6-Anhydro-β-D-glucose (Agluc)	Acros Organics	99%	
5-(hydroxymethyl)furfural (5-HMF)	Acros Organics	98%	Standard for GC-FID calibration.
Dichloromethane (DCM)	Acros Organics	99.8%	Extraction solvent.
Methanol (MetOH)	Fisher	99.9%	Sample dilution.
Sulfuric acid (H ₂ SO ₄)	Acros Organics	25%	Mobile phase for HPLC with RID.

3.3 Design of HTL apparatus

The HTL process flow diagram is presented in Figure 3.1 a), with its basis being described in the following sections. A detailed process and instrumentation diagram (P&ID) of the hydrothermal liquefaction (HTL) rig is included in Appendix A.2, while a simplified version is presented in Figure

3.1 b). This schematic contains all key equipment (apart from water tank, T-1 and nitrogen cylinders, C-1 and C-2), which is summarised in Table 3.2.

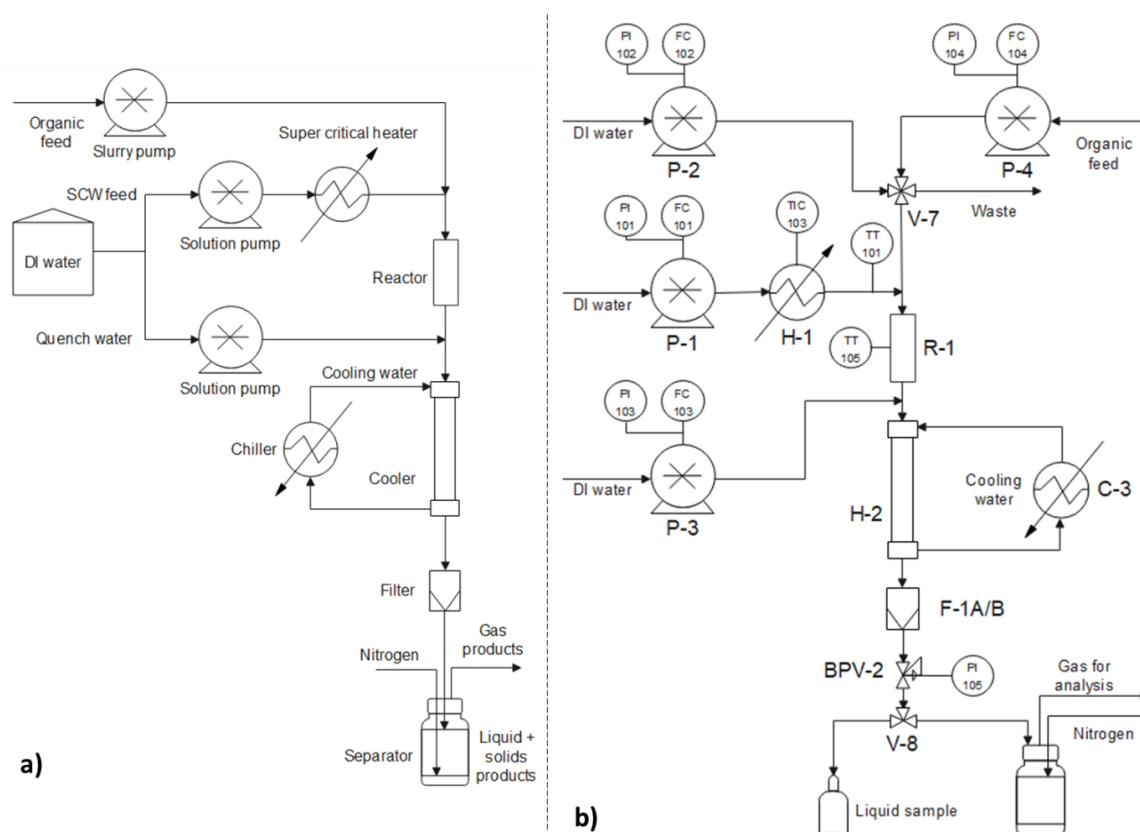


Figure 3.1: HTL process flow diagram (a) and simplified P&ID for the assembled rig (b).

3.3.1 Process description

The hydrothermal liquefaction process comprised two main feeds: supercritical water (SCW) and organic, supplied by positive displacement pumps P-1 and P-4, respectively. Two additional water feeds were included: the one supplied by P-2 replaced the organic feed during pressurisation and warm-up, and the one fed by P-3 downstream of the reactor, which quenched the mixture. DI water was continuously supplied to high-performance liquid chromatography (HPLC) pumps P-1, P-2, and P-3, which were operated at specified volumetric flowrates. The SCW feed was heated by an electrical heater (H-1), with the heat input being controlled by TIC-103 to maintain the desired setpoint temperature. The heater, as well as all downstream tubing and fittings up to the reactor's outlet, was insulated with three layers of glass fibre ribbon surrounded by aluminium foil.

The organic feeding process was designed considering that it could be a liquid containing suspended solid particles. Since HPLC pumps are not suited to such mixtures, a syringe pump from Teledyne Isco (P-4) was preferred, for its suitability for pumping solid suspension [131]. The pre-prepared organic

mixture was loaded into the pump's cylinder, which was then pushed into the pressurised reactor at a specified flowrate.

Table 3.2 - List of equipment existing in the HTL rig.

Tag	Description	Model / Supplier	Specifications
R-1	Hydrothermal reactor	Custom / Swagelok®	Length: 354 mm. OD: ¼". WT: 0.049".
T-1	Water reservoir	LA612 / ELGA - Veolia™	Maximum capacity of 40 L.
P-1	Dual piston pump (HPLC): Supercritical feed	PR100SFT2A / Teledyne SSI	Flowrate: 0.1-100 mL/min (± 3%). Pressure: up to 275 bar (± 3 bar). Adjustable trip: 270 bar.
P-2	Dual piston pump (HPLC): Replacement organic feed		
P-3	Dual piston pump (HPLC): Quench feed		
P-4	Syringe pump (Isco): Organic feed	260D / Teledyne Isco	Cylinder capacity: 266 mL. Flowrate: 0.001-107 mL/min (± 0.5%). Pressure: up to 517 bar (± 3 bar).
H-1	Electrical heater	Custom / Swagelok®	Length: 5.5 m. OD: ¼". WT: 0.049".
H-2	Double pipe heat exchanger	Custom / Swagelok®	Length: 800 mm. Inner tube: OD: ¼"; WT: 0.049". Outer tube: OD: ¾"; WT: 0.109". Cooling water from C-2.
C-1	High pressure N ₂ cylinder	Genie® / Linde	Maximum pressure: 300 bar @ 15 °C.
C-2	Low pressure N ₂ cylinder		
C-3	Water chiller	ThermoFlex™ 10 000 / Thermo Fisher Scientific	Temperature setpoint: 5 – 40 °C Maximum cooling capacity: 10 kW.
F-1A	Left solids filter	4400 series / Norman Filter Company	Mesh size: 100 µm. Length: 7". OD: 2.¼". WT: 0.345".
F-1B	Right solids filter		Mesh size: 100 µm. Length: 4.12". OD: 1.¼". WT: 0.267".
FIC-104	Isco controller	D-series / Teledyne Isco	Action on on/off pneumatic valves. Controls P-4 suction and discharge. Selects between F-1 A and B. Adjustable trip: 265 bar.
TIC-103	Heater controller	Custom	Controls H-1 power supply. Maximum power: 3 kW. Adjustable trip: 510 °C.

The mixing between SCW and organic feeds occurred at the reactor's inlet in a confined jet arrangement. The section in which the reaction occurred (R-1) consisted of a ¼" tube insulated with glass fibre ribbon and aluminium foil. A length of 80 mm was used in the first set of experiments, subsequently replaced by a larger 354 mm section, which also facilitated the inclusion of a thermocouple in this reactor (TI-105).

Downstream of the reactor, the mixture was quenched using a third DI water stream supplied by P-3 (typical flowrate of 60 mL/min), stopping any reactions at that point. The mixture was further cooled in a tube-in-tube heat exchanger (H-2), which used water refrigerated to 11 °C in a chiller (C-3).

After being cooled, the product mixture was filtered in either F-1A or F-1B. The supplier and mesh size were the same for both filters, which differed only in volume. Besides allowing solid collection, this configuration protected the diaphragm in the downstream backpressure regulator.

The system's pressure was controlled by an Equilibar[®] backpressure regulator (BPV-2), with a PEEK diaphragm. The process fluid circulated on one side of the polymer sheet, while on the other side a pilot pressure of nitrogen resulted in an equal backpressure in the system, due to mechanical equilibrium [124]. This high-pressure (HP) nitrogen is supplied via a self-venting pressure-reducing pilot regulator (BPV-1) supplied by Swagelok[®]. Given the insignificant pressure difference (~1 bar) between the pressures measured by P-1, P-2/P-4, P-3 and the pilot pressure on BPV-1, it was reasonable to assume that the system operated at constant pressure.

Downstream of the regulator, the product mixture was at atmospheric pressure and close to ambient temperature, therefore could be collected in a glass container. A three-way valve (V-8) allowed switching between accumulation of product and liquid sample collection in different containers. The first position accumulated the rig's effluent in a 2 L bottle (C-4) where gas-liquid separation occurred, and the gases were routed for online analysis (Sections 3.5.2 and 3.6.7). The second position permitted the collection of samples for further analysis (sections 3.6.1 to 3.6.4), as well as a periodic quantification of the total flowrate using a container of known mass and a stopwatch (± 1 second).

Organic feed composition

As mentioned in Section 3.3.1, the organic feed pump was selected to allow the processing mixtures of liquids with suspended solids. This mixture would be pre-prepared and loaded into the cylinder in the syringe pump, inside which it would remain during the entire experiment (up to 35 minutes). However, this compartment had no stirring, nor other methods of keeping a suspension in a pseudo-homogeneous state. Therefore, it was not possible to ensure that a concentration of a multiphase mixture of two liquids or of a solid and a liquid would remain with a constant concentration, throughout the entire experiment.

Consequently, the application of the described process to the hydrothermal liquefaction of organic feeds containing suspended solids will require equipment modifications that allow a continuous stirring of the suspension, thus keeping a constant feed composition.

The above was not a setback for the experiments described in Chapter 8 since the solubility of sucrose is 179 g per 100 g of water [132]. Therefore, mixtures of sucrose and water in a wide range of

concentrations would remain a homogeneous mixture during the entire experiment. On the other hand, the organic feed selected for the experiments described in Chapter 7 was dibenzyl ether (DBE), which is practically insoluble in water [133]. Due to this insolubility, suspensions of DBE in water were attempted in initial experiments (see Table 7.2 in Section 7.2.1). However, it was not guaranteed that those suspensions would keep a constant concentration in single experiment. Therefore, all experiments in Chapter 7 were conducted with a pure DBE feed.

Due to the lower polarity of subcritical water (see Section 2.2.1) and turbulence around the supercritical jet (see Section 3.3.3), it is not expected that the insolubility of DBE in water had a significant effect in the reaction section of the HTL rig.

Quenching downstream of the reactor

The method selected to ensure all reactions downstream of the reactor were stopped was quenching by direct contact with an additional feed of DI water at ambient temperature. The addition of a large flowrate of water compared to the reactor outlet (60 ml/min compared to a maximum of 40 mL/min) aimed at quickly reducing both temperature and concentration of organic compound. This was expected to lower reaction rates to minimal values, thus stopping the reaction section to the reactor.

On the other hand, applying this quench greatly increases the fluid flowrate in the process, thus requiring larger equipment and the adequate disposal of larger amounts of contaminated water. Both aspects may turn the process economically unfeasible at industrial scale, thus requiring alternatives.

Fast cooling and dilution of the reaction mixture would not be possible by only using the double-pipe heat exchanger downstream of the quench (H-2), as the overall organic concentration would not have changed, and the cooling process would have depended on residence time. Although not part of the current study, if the kinetic analysis is expanded to lower temperatures, it could be included in the design of H-2 and the overall process, possibly avoiding the need of quench at industrial scale.

3.3.2 Safety considerations

The HTL rig was operated at pressures around 250 bar and process temperatures of up to 450 °C. Therefore, ensuring safety and system integrity was of the utmost importance, with the following measurement being taken:

- All pressurised streams circulated in stainless steel 316 L (SS-316L) tubing, connected by double-ferruled compression fittings from Swagelok [134]. Typically, these tubes had an outer diameter (OD) of ¼", and a wall thickness (WT) of 0.049".

- All chemical pumps (P-1, P-2, and P-3) had internal shutdown trips, which were set at 270 bar. Pressure safety valves (PSV's) were included in each pump's discharge line, being calibrated to relieve at 260 bar.
- The Isco pump (P-4) was shut off by its controller when the pressure reached 265 bar.
- The high-pressure nitrogen line that supplies BPV-2 had a PSV, which is set to open at 275 bar.
- The supercritical heater (H-1) is protected by an independent trip system based on the temperature measured in the heating block (TS-104), which stops the power input when a set value is reached. Since the highest setpoint used during this study was 500 °C, the heater trip temperature was kept just above this value (~ 510 °C).

3.3.3 Confined jet mixer and reactor

The two main feeds of the HTL process, SCW and organic, were mixed immediately upstream of the reactor section (R-1) in a confined jet mixer configuration. This is a patented configuration developed by Darr *et al.* [128–130]. It was applied to the production of nanoparticles, given its demonstrated suitability for rapid mixing of cold aqueous solutions of metal salts with hot pressured water of much lower density [135–138].

The configurations in Figure 3.2 describe the confined jet mixer in the HTL rig. A pre-heated supercritical water stream circulated in a tube which inner diameter is reduced from 3.86 mm (OD: 1/4") to 0.88 mm (OD: 0.00625"). Consequently, the fluid's velocity increases approximately 20 times, typically from 0.5 – 2 to 10 – 40 cm/s. This smaller tube was inserted in a 1/4" tee through a bored-through reducer, where it contacted with the cold fluid [124]. The sudden size increase at high velocity created a jet that promoted a fast mixing between the two streams.

This type of mixer has been applied under different configurations, which included downwards co-current [136,137], upwards co-current [135,139], and counter-current [137–140]. In 2012, Ma *et al.* demonstrated that mixing is more efficient in co-current systems compared to counter-current [137]. Given the eventual use of the HTL rig to process biomass slurries, a downwards configuration was preferred, thus using gravity to reduce any particle accumulation and blockages. Therefore, the initial downwards co-current configuration in Figure 3.2 was implemented.

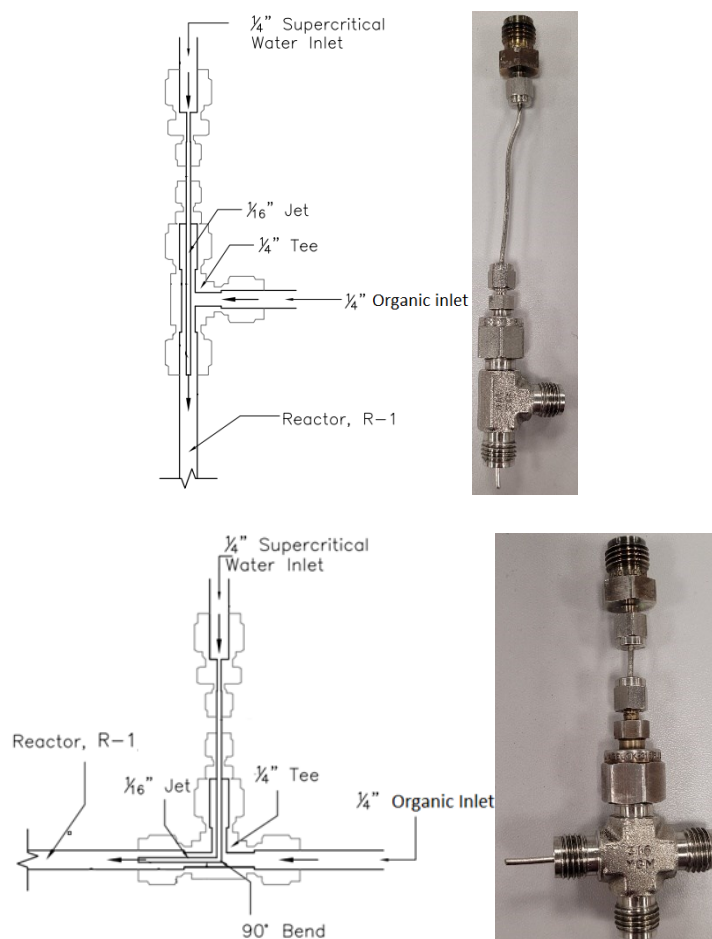


Figure 3.2: Initial (top) and final (bottom) implementations of the confined jet mixer. Adapted from [124] with permission from the author.

Figure 3.3 shows photos of the reactor sections used in the present study. The initial configuration consisted of a linear $\frac{1}{4}$ " tube (wall thickness: 0.049") with 80 mm. Under typical operating conditions, this allowed residence times between 1 and 2 seconds, which for the reactions described in Chapter 7, resulted in conversions of DBE between 11 and 17%. In order to extend the range of conversions, which could be studied, the reactor residence time was increased by replacing the existing section with a longer one (354 mm) of the same diameter and wall thickness. All reported cases in this thesis use the last configuration. The reactor section on the right side of Figure 3.3 was further modified by including a tee with a thermocouple well on the middle part (Section 5.4), while keeping its total length.

Due to space restrictions, the longer reactor section required a modification in the confined jet mixer. This resulted in the change from the configuration on the top of Figure 3.2, to the one on the bottom. The co-current pattern was kept, and even though the jet entrance in the outer tube is sideways, the overall reactor configuration is still downwards. Therefore, no appreciable differences are expected in the mixing behaviour at the jet outlet.



Figure 3.3: Initial (left) and final (right) reactor sections, with 80 and 354 mm, respectively.

According to the computational fluid dynamic (CFD) analysis of confined jet mixers by Ma *et al.* [137], the length required to achieve complete mixing after the jet outlet is equal to 7 times the inner tube diameter. For the present study this is equivalent to 6 mm, which represents less than 2% of the reactor total length. The effect of poor mixing in such a small section effect was expected to be negligible. Nonetheless, this assumption of rapid mixing is investigated in Chapter 6, using a CFD model adapted to the operating conditions used in this work.

3.3.4 Supercritical water heater

The high temperatures required for the supercritical water feed are achieved in the heater H-1, which was designed and built in-house in a previous project [124]. At its centre was an electric heating rod supplied by Watlow[®], with a maximum capacity of 3 kW. The rod was inserted in an aluminium block in which a coiled tube was cast. The water feed circulated inside this coiled tube.

Two thermocouples, TIC-103 and TS-104, were inserted in the aluminium block at a depth of 50 mm and a radial distance of 5 mm from the heating rod. The temperature measured in TIC-103 defined the heat input into the rod, through a control loop. TS-104 is connected to an independent temperature trip, which stops the rod's power supply when the set point value was reached (usually 20 °C above SCW temperature objective).

The heater was designed to warm up 46.5 mL/min of water at 250 bar from ambient conditions to 450 °C, assuming a heating block at 460 °C. The design coil length was oversized to 5.5 m, which would allow water flowrates as high as 155 mL/min. Nonetheless, from early experiments it was observed that the fluid temperature in the heater outlet line was far from 450 °C [124].

This discrepancy was also observed during this study's preliminary experiments study in Section 5.4. For flowrates no higher than 24 mL/min and block temperatures up to 500 °C, the maximum temperature measured in the supercritical water line was 414 °C (TT-101). Two factors may have resulted in these lower temperatures, when compared to design: heat losses between H-1 and TT-101, and lower than expected heat transfer coefficient due the properties of supercritical water, *e.g.*, relatively low thermal conductivity.

3.3.5 Double pipe heat exchanger and cooling water chiller

The double pipe heat exchanger (H-2) is located downstream of the reactor and subsequent quench. It cooled the process fluid to a temperature that was safe to be manually handled, *i.e.*, below 60 °C. Like the supercritical heater, this was designed and built before the current project [124].

The reactor effluent flowed through H-2's inner tube, while chilled water circulated through the outer copper tube. The exchanger's length was defined by ~ 0.8 m height available inside the HTL enclosure. Assuming an increase of 6 °C between the supply and return of the cooling water, it was expected that this heat exchanger should be able to cool 46.5 mL/min of reactional mixture from 350 to 60 °C [124].

The cooling water required in the double pipe heat exchanger was provided by a recirculating chiller (C-2). It operates in a closed loop, with the cooling water temperature defined by a setpoint. Over the present study, this setpoint was kept as 11 °C, which, according to the equipment specification, provides a maximum cooling capacity of approximately 6 kW [141].

The adequacy of the quench, double pipe heat exchanger, and chiller to reduce the process fluid to 60 °C is further analysed and discussed in Section 5.3.

3.4 Operation of HTL apparatus

The major limitation when operating the HTL rig was the finite volume available in the syringe pump responsible for discharging the organic feed (P-4). This volume was approximately 266 mL, and, for a selected flowrate, it defined the maximum duration of an experiment, as it was not possible to re-fill this pump without interrupting the organic feed for several minutes. Furthermore, as demonstrated in Section 7.3, it took at least 13 minutes from the start of the organic feed to reach a steady state of concentration in rig's effluent. Consequently, less time was available for sample collection during each experiment. As an example, for an organic feed flowrate of 10 mL/min, the total available time was approximately 26 minutes. From these, less than 14 minutes are expected to occur under steady state. It is during this time that liquid samples can be retrieved, with typical collection times of approximately 90 seconds.

The following sections provide an analysis of the rig's start-up, operation, and shutdown, with reference to Figure 3.1. A detailed operating procedure is included in Appendix A.1.

3.4.1 Start-up

The start-up procedure of the HTL rig was established upon its construction and may be divided in three stages: pressurisation, heating, and time to reach steady state. Given P-4's volume limitation, the first two stages are conducted with a DI water feed, supplied by P-2, instead of the organic feed.

The pressurisation step was initiated by starting the DI water flow in all three HPLC pumps at selected operating flowrates. The system's backpressure was generated by allowing increasingly higher pressures of nitrogen in BPV-2, through the manipulation of BPV-1. To maintain the integrity of the HPLC pumps and BPV-2's diaphragm, pressurisation was performed in steps of approximately 10 bar, allowing time for each increase to be observed in each pump's pressure gauge. Furthermore, during the first steps air was purged from the system, by opening relief valves V-10 and V-11.

Once the final pressure was reached, the heat input from H-1 was started, by specifying TIC-103's setpoint. As observed in previous studies, the heater's power draw is approximately 15 A, considering a maximum capacity of 3 kW, an electrical efficiency of 85%, and Ohm's law [124]. This was marginally below the circuit break limit of 16 A. Consequently, the heating of the SCW feed was conducted by increasing the temperature set-point over several steps of decreasing magnitude, with intervals of five minutes. Once the final temperature setpoint was reached, the system reached thermal steady state after ~ 1 hour.

When a stable temperature was observed in all thermocouples (*i.e.*, TT-101, TT-102, and TT-105), the organic feed was initiated by rotating the four-way valve V-7. This valve changed the flow configuration as shown in Figure 3.4, where the organic feed from P-4, which was pressurised against a closed valve in a waste stream, was re-routed to the reactor, while the water stream from P-2 was discarded.

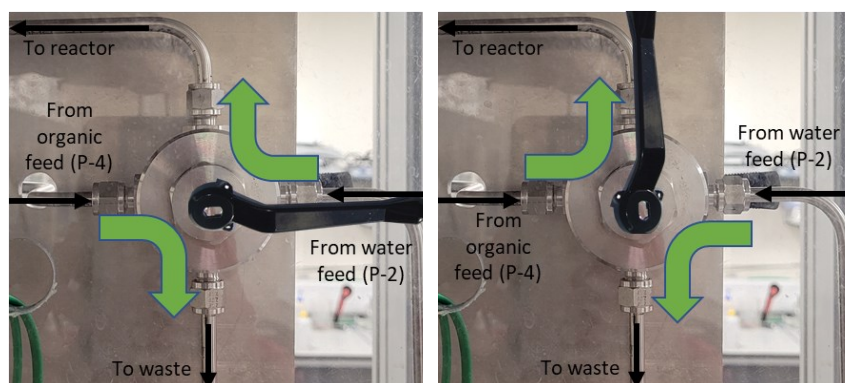


Figure 3.4: Flow arrangement around valve V-7 during pressurisation/heating (left) and normal operation (right).

For experiments using a diluted organic feed (Chapter 8), the flow through P-2 the same as the actual organic feed (accounting for the different pump calibration corrections in Section 5.2), thus minimising temperature differences when changing V-8's position. However, the same did not happen when using a concentrated/pure organic feed (Chapter 7), given the fluid's different thermal properties. Consequently, to minimise temperature variations when the position of V-7 is switched, an equivalent flowrate must set for P-2 during pressurisation and heating. This equivalence is established by comparing the different sets of temperature measurements in the preliminary analysis described in Section 5.4.2.

3.4.2 Steady state operation and sampling

When the organic feed was initiated, the three-way valve V-8 was in accumulation mode, thus routing the rig's effluent to a 2L collection bottle (C-3). As during the heating stage, thermal steady state was directly evaluated by the temperature measurements in the reactor's thermocouple (TT-105). Meanwhile, composition steady state was evaluated through the continuous analysis of gaseous products using an online FTIR spectrometer (Section 3.6.7).

Once a stable gas composition was observed, the system was considered in steady state operation. At this point, the filters downstream of H-3, F-1A or F-1B, were switched by rotating pneumatic operated valves XV-103A/B. This way, the newly selected filter collects solids only formed during steady state. The filter configuration was switched back before shutdown, thus ensuring the solids eventually accumulated were only obtained during a timed period of steady state.

Liquid products and solids that were not retained in F-1A/B were not analysed in-line as was done with the gaseous products. Therefore, individual samples were collected by rotating V-8 to collection mode for a measured period (typically 90 seconds). During each collection, the gas flow to the FTIR was disrupted, thus gas measurements were disregarded after the first liquid sample was initiated.

3.4.3 Shutdown

After the last liquid sample was retrieved, the shutdown procedure was initiated by switching V-7 to replace the organic feed with DI water and stopping the heat supply to H-1. Once the supercritical water temperature was below its boiling point at atmospheric conditions (*i.e.*, 100 °C), the system was depressurised.

3.5 Separation methods

The products obtained during the experiments carried out using the HTL rig were distributed between solid, gas, and liquid phases. Furthermore, when water-insoluble organics were present in the liquid samples, a separation of organic and aqueous phases was observed (Section 7.3). The methodology followed to isolate each of these four phases is described in following sections.

3.5.1 Filtration

Two parallel filters of different volumes were included in the liquefaction rig (F-1A/B in Figure 3.1). Both contained a mesh of 100 μm , and were positioned in the process after cooling, but still at high pressure. As mentioned in Section 3.4.2, the valves that select the operating filter can be manipulated in order to one of them only operating during steady state. After the rig's cooling and depressurisation, the filters were removed and opened for the collection of accumulated solids.

A second filtration was applied to the liquid samples collected at the rig's outlet alongside solvent extraction. After each individual extraction, but before settling in the separation funnel, the sample is filtrated under vacuum³, using Whatman™ filter paper for particle retention over 11 μm (GE Healthcare, diameter: 70 mm). The sample filtration is repeated three times, being followed by the washing of the accumulated solids with water and the extraction solvent (DCM).

The filter paper containing the washed solids is deposited in petri dish and kept in a fume hood for drying at ambient conditions. The sample is considered dry when its weight remains constant overnight.

It should be noted that no solids were found in filters F-1A or B after the experiments with dibenzyl ether (Chapter 7). For the processing of sucrose (Chapter 8), the amount of solids accumulated in the filters was found to be negligible compared to the mass accumulated during the second filtration process (Section 8.3.1).

3.5.2 Gas sweep

While operating in accumulation mode, the products from the rig were accumulated in a 2 L bottle (C-4). To release the gases dissolved and entrained in the liquid phase, and push them into the FTIR spectrometer, the accumulation bottle was continuously swept with low-pressure nitrogen from C-2.

The flowrate of sweeping gas was relevant for the quantification of gas products (equation (3.2)). Therefore, a rotameter (F-105 in Appendix A.2) was included in the low-pressure nitrogen line. The

³ Using a vacuum micro pump NMS 030.1.2 from KNF.

gas flowrate was regulated by a needle valve downstream of the rotameter, depending on its position, as well as the pressure at C-3's regulator (usually 2 barg). The required equipment calibration is presented in Appendix B.1.

3.5.3 Centrifuging and syringe extraction

The method described in this section was selected to separate liquid samples with visibly distinct phases, such as the ones collected during DBE's hydrothermal degradation (Chapter 7).

In addition to the spontaneous separation in the collection bottle, further phase separation was promoted by centrifuging the sample in its collection bottle for 30 minutes at 4500 rpm in a bench top centrifuge (Mega Star 1.6, supplied by VWR®). The top phase (the most abundant) was extracted using a syringe, leaving a small amount behind to avoid dragging out any of the bottom phase.

This extraction was further refined by repeating the process of phase separation, by pouring the bottom phase into a smaller tube, then centrifuging the mixture for a second time, at the same conditions. Since a smaller container was used, more of the top phase could be extracted; this was mixed with the top phase collected previously.

After this process of phase separation, each of the samples were diluted in neat or aqueous acetonitrile, as described in Section 3.6.2, before being injected into the HPLC analyser (described in Section 3.6.1).

3.5.4 Solvent extraction and evaporation

This method was based on the work of He *et al.* [142,143], and aimed at extracting organic components from a liquid sample without clear aqueous/organic phases, such as the samples collected from the hydrothermal degradation of sucrose (see Chapter 8). It is based on the solute's higher affinity towards an organic solvent when compared to water. A typical solvent used for this process in literature is dichloromethane (DCM) [53,109,144,145], as its high volatility facilitates its easy removal by evaporation after extraction.

The liquid sample was mixed in the collection bottle with an approximately equal volume of DCM. After vigorous shaking, the mixture was filtered under vacuum, as described earlier. The top layer (aqueous phase) was poured back into the collection bottle, while the bottom layer went to a separation funnel. This process was repeated a total of three times. After the last filtration, the entire sample was poured into the separation funnel, as well as the solvents used for solid washing.

When the two phases in the funnel were clearly divided, they were separated into individual beakers, which were kept in a fume hood at room conditions for solvent evaporation. Given that water takes

significantly more time to evaporate than DCM, the total aqueous sample was weighted, but only a known fraction of it was evaporated in the fume hood. Both DCM- and water-soluble samples were considered dry when their weights remained constant overnight.

3.6 Analytical methods

The following of analytical methods were employed during this study:

1. High performance liquid chromatography with ultraviolet and visible (HPLC with UV-vis) detection.
2. High performance liquid chromatography with refractive index detection (HPLC with RID).
3. Gas chromatography with mass spectroscopy and flame ionisation detection (GC-MS with FID).
4. Fourier transform infrared (FTIR) spectrometry.

The first and second methods were used to analyse water-containing liquid samples, with the detection method depending on analysed molecules. The third was used to detect and quantify additional organic molecules, using previously dehydrated samples. The fourth technique was used to continuously analyse the composition of rig's gaseous effluent (see Section 3.4.2). The following sections contain a description of the equipment used in each method, operating principles, calibration methods, and sample preparation.

3.6.1 High-performance liquid chromatography

HPLC was used to analyse samples obtained from the experiments described in both Chapters 7 and 8, being conducted in a Prominence Modular system, supplied by Shimadzu UK [146]. This separation technique was based on the elution of a known volume of sample by a solvent (mobile phase) through a column containing a specific substrate (stationary phase). Due to the different affinities towards the mobile and stationary phases, each species in the sample (analytes) spent a specific time in the column (elution time). Consequently, each analyte was eluted at different times, thus promoting the sample separation [147,148]. The column's effluent was routed to an UV-Vis spectrometer (described in Section 3.6.2) or an RID (see Section 3.6.3), which were installed in the same module, providing a continuous measurement over time registered in a chromatogram.

Since the analyte's affinity towards the mobile phase affects its elution time, this solution's composition may be constant throughout the analysis (isocratic elution) or varied through mixing of different solvents (gradient elution). Besides composition and flowrate, temperature also affects elution, thus the column was inserted in an oven, which was heated to a specified temperature. All measurements in the

present work were conducted under isocratic elution. Typical values for eluent flowrate (0.5 mL/min), column temperature (30 °C), and injection volume (10 µL) were tested with satisfactory results, and therefore kept throughout the study.

Products from dibenzyl ether hydrothermal degradation

Both organic and aqueous samples produced in the experiments described in Chapter 7 were analysed by HPLC. Those samples included dibenzyl ether, benzyl alcohol, benzaldehyde, and toluene, *i.e.*, aromatic species of variable affinity towards water.

Based on the separation procedure described by González and Montané [149] for a similar process, an aqueous acetonitrile solution was selected as both sample solvent and mobile phase. For non-ionic analytes with molecular mass under 2000, bonded-phase chromatography is recommended [147]. Since a polar solvent was selected as mobile phase, this is designated reverse phase chromatography and the selected column should be non-polar. For that purpose, a C8 Kromasil column produced by Phenomenex (L: 125 mm; OD: 4.60 mm; particle size: 100 Å) was chosen for the studies in Chapter 7.

The column conditions required to analyse the composition of the mobile phase were determined by trial-and-error to obtain satisfactory resolution and elution time [147]. This process is described in Appendix B.2, resulting in an acetonitrile mass fraction of 42%, which ensured an elution time of 45 minutes.

Products from sucrose hydrothermal degradation

For the cases studied in Chapter 8, HPLC was applied in the quantification of specific organics in the aqueous phase. Ionic-exchange columns have been widely used for the separation of sugar derivatives, using water or a diluted acid as mobile phase [71,80,103,150–152]. An ion-exclusion principle applies, *i.e.*, the different hydronium groups in each analyte bond with the column's cationic matrix [147], leading to different elution times for each sugar derivative.

A cationic column SUPELCOGEL™ C610H (L: 30 cm; OD: 7.8 mm; particle size: 9 µm) with an upstream guard section was selected for the analysis of those samples. The mobile phase was diluted sulfuric acid (0.1%), and the analysis of standard solutions shown that an elution time of 20 minutes would be sufficient for the expected sucrose degradation products. However, initial analysis of the actual samples lead to this time being extended to 70 minutes, thus ensuring all components in the injected sample were eluted from the column.

3.6.2 Ultraviolet and visible spectrometry

UV-vis spectrometry was one of the analytical methods applicable to the chromatography eluate, using the SPD-20A detector in the HPLC module [146]. This analytical method is based on the amount of radiation absorbed by a sample at a given wavelength in the ultraviolet-visible region, *i.e.*, 200 to 700 nm [147]. In the selected equipment, the light beam is produced in a deuterium lamp and goes through a wavelength selector with an accuracy of 1 nm. Afterwards, it crosses the sample cell (quartz, length: 10 mm, volume: 12 μ L), with the transmitted light being received in a signal processor.

The measured signal quantifies the samples absorbance (Ab_i), defined as the logarithm of the intensity ratio between incident (I_0) and transmitted light (I) [148,153]. At low concentrations (< 0.01 M) Beer's law applies [147,148], and absorbance is proportional to a species molar concentration (C_i) as expressed in equation (3.1), which accounts for the optical path length (l) and specific molar absorptivity (ϵ_i).

$$Ab_i = \log\left(\frac{I_0}{I}\right) = l \times \epsilon_i \times C_i \quad (3.1)$$

Continuous measurement of HPLC's eluate generates an absorbance chromatogram, where each absorbing species produces a usually gaussian peak. Each point of the peak corresponds to the concentration passing through the detector at that moment. Consequently, the absorbance integral, *i.e.*, the area under the absorbance peak, will be proportional to total amount injected in the HPLC system. For fixed injection volumes and eluent flowrate, this means the peak area is proportional to the concentration in the injected sample. Furthermore, if density is approximately the same between analysed samples, the peak area (A_i) is also proportional to the mass fraction in the analysed sample (w_i), as depicted in equation (3.2).

$$A_i = \int Ab_i \approx mc_i \times w_i \quad (3.2)$$

UV-vis detection was applied to the quantitative analysis of dibenzyl ether's degradation products (Chapter 7), which included the reactant, as well as benzyl alcohol, benzaldehyde, and toluene. All those species were expected to absorb radiation at a wavelength close to 260 nm [148,154–157], so this was selected for all measurements.

The concentration of each molecule in the sample being analysed defined the shape and size of the obtained peak in the chromatogram [147]. This is reflected in resolution, *i.e.*, distance between peaks, and height, which might surpass the equipment's limit of detection. For the case of DBE's degradation products, a dilution was required for both organic and aqueous phase samples. Given the full miscibility of acetonitrile in water [158], and its presence in the mobile phase, this was the selected solvent. To minimise solvent waste, analytical samples of approximately 10 g were prepared from each separated phase. Assuming a small concentration of organics in the aqueous phase, 1.5 g of it were diluted in pure acetonitrile. On the other hand, the organic phase was considered to contain a negligible amount of

water, so 0.1 g were diluted in an acetonitrile aqueous solution at 85 wt%. Therefore, it was ensured a consistent overall composition between phase samples, where solutes represent less than 1%.

The proportionality constant (mc_i) for the four analytes was determined by integrating the signal produced by standard solutions of known concentrations. Those solutions were prepared by diluting the pure components in the same acetonitrile aqueous solution used for the dilution of organic samples. The results of the individual calibrations are detailed in Appendix B.2.

3.6.3 Refractive index spectrometry

Besides UV-vis detection, the Prominence Modular system also includes refractive index analysis in a RID-10A [146]. This method is typically associated to HPLC when analysing sucrose's degradation products [71,80,103,150,159,160], thus was selected for the analysis of the aqueous samples obtained during the experiments described in Chapter 8.

The refractive index of a transparent medium is defined as ratio between the radiation's speed in vacuum and in sample being analysed [147], and is affected by the amount of analytes in solution. In the selected spectrometer, an amplified light beam from a tungsten lamp crosses a sample cell, which is divided in two sections. Those two sections are separated by a glass plate with the eluted sample circulating on one side, and the other previously filled with a reference, *i.e.*, the mobile phase. When crossing between sections there is a variation in the beams refractive index, which is captured by the equipment's photodiode [147,153].

Compared to UV-vis detection, RID is considered less sensitive, but more versatile, since it is not limited to the solute's absorbing properties [147,153]. Like the remaining quantitative methods, for each eluted analyte a peak appears in the chromatogram, whose area is considered proportional to its mass fraction in the injected sample (equation (3.2)).

During the experiments described in Chapter 8, RID was used to quantify the analytes in the aqueous samples obtained after extraction with dichloromethane. Those analytes included: sucrose, glucose, fructose, pyruvaldehyde, and 1,6-anhydro- β -D-glucose. The respective proportionality constants were determined using standard solutions, as detailed in Appendix B.3.

Unlike with UV-vis detection, the concentration of analytes in the aqueous samples was adequate for the refractive index detector, thus no additional dilution was required. Each sample was directly collected after solvent extraction and before evaporation, only having to pass through a syringe filter (VWR[®], 0.2 μ m) before being analysed.

3.6.4 Gas chromatography

During this study Gas Chromatography (GC) was performed in a Nexis GC-2030 module supplied by Shimadzu UK, which combines column chromatography with mass spectrometry and flame ionisation detection [161]. This method was applied during the experiments described in Chapter 8 to both dichloromethane- and water-soluble samples obtained after solvent evaporation. As in HPLC, separation occurs in a column, promoted by the different affinities of analytes carried in a mobile phase towards a stationary phase. However, GC is performed at higher temperatures, vaporising the sample. The mobile phase consists of an inert gas, which carries the sample across a longer and thinner column. In this column the stationary phase is an immobilised inert liquid spread as very thin layer [147,162].

A generic method, based on typical operating conditions, was applied during the GC runs performed over this study. The separation occurred in a fused silica capillary column supplied by Shimadzu (SH-Rxi-5ms, L: 30 m; ID: 0.25 mm; film thickness: 0.25 μm), with a stationary phase suited for low polarity hydrocarbons (5% diphenyl / 95% dimethyl polysiloxane). The sample was inserted at 280 °C, through split injection (split ratio: 10). Helium was the carrier gas, with final flowrate inside the column of 1 mL/min.

Chromatography occurred in the column, inside an oven, which allowed for temperature ramping, thus improving the chromatogram resolution, while minimising elution time [147]. For this analysis, a single ramp was applied from 40 to 320 °C, with a rate of 10 °C/min. Considering initial and final holding times of 3 and 5 minutes, respectively, the total elution time was 36 minutes.

As mentioned, the samples analysed using GC were obtained after dichloromethane extraction and solvent evaporation. Consequently, a re-dilution was required, preferably using a solvent suitable for both DCM- and water-soluble samples. For this reason, methanol was selected. After dilution, the evaporated sample represented less than 1% of the diluted sample mass.

3.6.5 Mass spectrometry

MS was one of the methods used to analyse the gas chromatography's effluent, being included in the same equipment module (GCMS-QP2020 NX [161]). It was used for qualitative purposes, *i.e.*, in the identification of the various organic molecules in each sample.

The analytical technique starts by ionising the gas molecules leaving the GC column. In the current study, an electron-impact source (EI) was selected, which means the analytes collided with a beam of energetic electrons circulating from a filament at 200 °C to an anode [147,148]. The resulting molecular cations are highly unstable and split in several charged fragments, which are routed to the mass analyser.

GCMS-QP2020 NX contains a quadrupole spectrometer, which separates and analyses the different ionic fragments. It produces a mass spectrum every 0.20 seconds, registering the relative abundances of each fragment according to their m/z ratio in a range between 10 and 300. By comparing each spectrum to the ones in an existing library, it is possible to identify the molecule that originated it [147,148]. For this analysis, the comparison library was the one published in 2017 by the National Institute of Standards and Technology (NIST) [163]. The spectrometer also registers the variations in the ion current over time, creating a chromatogram, where each point containing a mass spectrum. Therefore, it is possible to associate a specific compound to each peak of both MS and FID chromatograms.

3.6.6 Flame ionisation detection

FID is also included in the GC module [161], allowing the quantification of the effluent's composition. This is a widely used detection method, being suited for general hydrocarbons, with high sensitivity [147]. Part of the GC's effluent is directed to an air-hydrogen flame (200:32 mL/min), where it is burned, and consequently ionised. The variation of current in the burning mixture is measured, producing the FID chromatogram.

The current registered in the FID is commonly considered to be directly proportional to the number of carbon atoms in the sample being burned [147], and consequently to the mass of the analyte being eluted at that time. For this reason, for similar samples and fixed injection volume, the area under each current peak is approximately proportional to the analyte's mass fraction, as described by equation (3.2).

Given the wide distribution of species detected in samples obtained from the experiments in Chapter 8, only the most abundant species, 5-(hydroxymethyl)-2-(dimethoxy methyl)furan, was quantified. This compound wasn't commercially available, so calibration was performed with a similar but more common species, 5-(hydroxymethyl)furfural. This calibration is detailed in Appendix B.4.

3.6.7 Fourier-transform infrared spectrometry

A MultiGasTM Analyzer 2030 CEM-Cert, supplied by MKS Instruments, Inc. [164] was used to quantify the concentration of IR-active gases such as CO₂ and CO. Infrared spectroscopy results from the comparison of a sample's absorption spectra in the frequency range of 5000-400 cm⁻¹ against known standards. Particularly, FTIR is characterised by generating the absorption spectrum from a transformed interference pattern, which is produced by two identical light beams which cross the sample from varying paths [147,148]. Advantages of this method include an automatic and quick covering of the

entire infrared spectra with high-resolution. For the selected equipment each scan took 60 seconds, and a spectral resolution of 0.5 cm^{-1} is offered.

The sample entered the spectrometer through a coated tube, which pre-heats the stream to the measurement's temperature, thus preventing any water condensation. The infrared source was a silicon carbide element heated to $1200 \text{ }^\circ\text{C}$, while a He-Ne laser was used as reference. The modulated beam was reflected through several mirrors, entering the nickel/aluminium gas cell, through a zinc selenide window. The cell path was 5.11 m long, and its window was water insoluble. After passing the sample, the beam reaches the detector, which was cooled using liquid nitrogen. Both sides of the sample cell were continuously purged with low pressure nitrogen at 0.2 LPM , routed from the same cylinder as the sweeping gas (C-2).

An interference spectrum was generated at fixed periods, which the equipment's software converted into absorption, and ultimately into concentration (as described in equations (3.1) and (3.2)) using calibration curves provided by MKS (the capability to use calibration curves measured on another spectrometer is a unique feature of this instrument). The supplier's software included a library of absorption spectra for a wide range of molecules, all measured at $191 \text{ }^\circ\text{C}$ and atmospheric pressure. In the present study, the following gases were selected for detection and quantification: water, carbon dioxide, carbon monoxide, methane, ethylene, propane, propylene, formaldehyde, toluene, and benzene. This selection was adapted for each case study, removing the gases that were not detected. Since the standards library was referred to $191 \text{ }^\circ\text{C}$, this was defined as the equipment's operating temperature.

The molar fraction of each species during steady state (x_i^{Gs}) was the average of the values measured between the time a stable reading (95% of steady state value) was first observed and the time when the first liquid sample was collected. The quantification of each species' molar flowrate at the rig's outlet ($F_{i,G}^{out}$) is derived from the low-pressure nitrogen molar flowrate (F_{N_2}), given by FI-105 calibration (detailed in Appendix B.1), as represented by equation (3.3). This flowrate was corrected for the composition of all measured species, from which only water was expected to be relevant, and multiplied by the molar fraction obtained during steady state operation.

$$F_{i,G}^{out} = x_i^{Gs} \frac{F_{N_2}}{1 - \sum x_i^{Gs}} \quad (3.3)$$

3.7 Errors and Uncertainties

The errors associated to the values reported in the present thesis have three distinct origins: equipment uncertainty, method calibration, and statistical variation. The following table summarises the first type of error, associated with the equipment specifications and direct measurements reported in this thesis.

Table 3.3: Summary of equipment uncertainty.

Equipment	Model / supplier	Variable(s)	Units	Uncertainty (\pm)
Balance	LA 254i / VWR [®]	Mass up to 250 g	g	0.001
	FX-3000i / A&D Company limited	Mass up to 3.2 kg	g	0.01
Timer	Brannan [™]	Sample collection time	sec	1
Pump	PR100SFT2A / Teledyne SSI	Volumetric flowrate	mL/min	3%
		Pressure	bar	3
	260D / Teledyne Isco	Volumetric flowrate	mL/min	0.5%
		Pressure	bar	3
Thermocouple	K-type / TC Ltd.	Temperature	°C	1.5

The second type of error is associated to the calibration of the different analytical methods, which are detailed in Appendix B. When considering the error associated with an analytical measurement, two types of uncertainty were considered for each sample: standard preparation, and calibration. The first is calculated via error propagation of the measurements performed while preparing the standard solutions used during calibration [165]. The last results from extracting a value from a calibration line, accounting for its non-linearity. For each measurement, the uncertainty (s_c) is calculated according to equation (3.4), based on the measured value (y_c), calibration slope (mc), number of calibration measurements (N), sum of squared calibration concentrations (S_{xx}), and standard deviation about the regression (s_r) [147].

$$s_c = \frac{s_r}{mc} \left(1 + \frac{1}{N} + \frac{y_c^2}{m_c^2 \times S_{xx}} \right)^{\frac{1}{2}} \quad (3.4)$$

It was considered that a concentration obtained via a calibration line could not be more accurate than the standards used to obtain this line. Therefore, the error associated with calibration lines is the maximum of these two errors.

The third type of error is associated with results derived from the measurements mentioned in this chapter and was estimated through error propagation [165]. Nonetheless, the yields reported in Chapters 7 and 8 were obtained by averaging the ones calculated from the composition of at least two samples. Once more, two types of uncertainties were considered: the sample-specific variances derived through error propagation, and the standard deviation between averaged values. The maximum between those types was considered the error in the yield.

Chapter 4

Hydrothermal reactor model

4.1 Introduction

This chapter describes the mathematical models developed to simulate the reactions in the hydrothermal reactor described earlier. After a brief description of the software used, a section is dedicated to its application in the estimation of parameters such as the kinetic variables. This is followed by the methodology applied when modelling water near its critical point (374 °C and 221 bar). The last sections present a detailed characterisation of the reactor model, including all sub-models within it.

4.1.1 Software for mathematical modelling

The mathematical models used in this work were developed in the gPROMS[®] modelling platform, more specifically gPROMS Process (Academic) 2.2.2. This was the selected software as it allows the following [166,167]:

- Integration of complex thermodynamic models based on different equations of state.
- Custom modelling in an equation-oriented environment, thus permitting the use of both first principle and empirical models.
- Hierarchical combination of models.
- Parameter fitting to experimental data and model validation, based on detailed statistical analysis.
- Sensitivity analysis by quasi-random variation of selected inputs and direct observation of its impact on selected outputs.
- Optimisation of process variables to maximise yields or net revenue.

4.1.2 Equations of state

A key aspect of hydrothermal liquefaction are the properties of water at near-critical conditions. Since most experiments were conducted in a large excess of water, it was relevant to predict its physical properties in this region. Two implementations were considered in this study: 1) water-only and 2) detailed.

The first assumed that the system is diluted enough to be sufficiently described by the properties of pure water. Therefore, density, enthalpy, viscosity, and thermal conductivity were externally calculated using "The IAPWS Formulation 1995 for the Thermodynamic Properties of Ordinary Water Substance for General and Scientific Use" defined by the International Association for the Properties of Water and Steam (IAPWS) [55], through a Microsoft Excel add-in. The values for a wide range of temperature and pressure were copied as a table into gPROMS, which quickly read and interpolated them in each simulation.

The detailed method considered that, even though water is in excess, the overall properties are significantly affected by other species in the mixture. Therefore, a more refined equation of state is required to properly model the reactional mixture under different temperatures, pressures, and compositions. It should be noted that this methodology was based on using existing models, which were validated for different compounds and different conditions. No validation was conducted in this study. Nonetheless, a comparison of reaction parameters between the two implementations (water-only and detailed) is presented in Section 7.6.1.

In gPROMS, thermodynamic properties, such as vapour-liquid equilibrium (VLE), density and enthalpy, are estimated through built-in physical property packages; these include the statistical association theory for variable range Mie potentials (SAFT- γ Mie), an equation of state (EoS) that represents the behaviour of real fluids through the association of different reference segments (building blocks) that compose the actual molecule. This is particularly useful when modelling complex and long organic molecules. The current implementation is based on the work developed at the Sargent Centre for Process Systems Engineering in Imperial College London, which reports improvements in the description of critical systems, particularly in organic binary mixtures, thus it is useful for bio-oil components [168,169].

Besides the properties mentioned above, the models developed in this study also required viscosity, diffusivity, and thermal conductivity, which were not predictable using the selected EoS. Viscosities and thermal conductivities were calculated using the Chung-Ajilan-Lee-Starling method. This a simple and straightforward procedure, which was validated in a wide range of conditions against polar and non-polar fluids including water and aromatic organics [170]. Diffusivities were estimated through the Hayduk and Minhas correlations for predicting Maxwell-Stephan diffusion coefficients in liquid-phase [171].

4.1.3 Parameter estimation, optimisation, and sensitivity analysis

The model developed during the present study aimed to represent reactions in hydrothermal medium. An important step to achieve this objective is selecting kinetic parameters that give an acceptable

agreement with the experiments over a relevant range of conditions. Therefore, these parameters were estimated using data directly extracted from experiments performed in the hydrothermal rig, using the “model validation” tool available in the gPROMS platform [166].

In this software, performing a parameter estimation consisted of solving a maximum likelihood problem, though an optimisation procedure. Given a set of unknown parameters included in a mathematical model, these were estimated by maximising the likelihood of that model predicting measured data within a given uncertainty [166,172,173]. For fixed uncertainties, the overall optimisation revolved around minimising the sum of square difference between predicted and measure values divided by the respective variance [174].

The experimental data was provided in independent experiments, according to their specific inputs, *i.e.*, operating conditions. These contained information on the different measured values and respective variances. The parameters being estimated were the decision variables of the optimisation process, being constrained by lower and upper bounds. The optimisation was solved through sequential quadratic programming applied to nonlinear problems [166,175].

Besides the estimated values, the output of a parameter estimation also included the respective standard deviation and confidence intervals. Furthermore, it provides a t-test, where the ratio between estimated parameter and the 95% confidence interval (95% t-value) was tested against a critical value⁴ [176]. A ratio below the critical value indicated the statistical insignificance of the estimated parameter within the range and number of experiments.

The adequacy of the estimated parameters was tested through sensitivity analysis, using the “global system analysis” tool in gPROMS. The kinetic parameters are defined as normal distributions centred around the estimated value and considering the calculated standard deviations. A number of points large enough (200 for example) was generated per parameter, through a pseudo-random Monte Carlo method [177]. Afterwards, the impact of the combined distributions was evaluated by the variance caused in the main outputs of this study.

4.2 Modelling supercritical water

As presented in Section 2.2.1, water properties at pressures and temperatures higher than the critical point behave differently than what is expected for a pure component. Figure 2.3 presents plots of density, specific enthalpy, and viscosity against temperature and pressure, which show that instead of a sharp transition between liquid and gas-like properties, a steep curve is observed. As pressure increases,

⁴ Critical value given by the inverted t-distribution for a probability of 5% and degrees of freedom equal to number of data points minus the number of estimated parameters.

this transition becomes smoother and occurs at higher temperatures. For a given pressure, the inflection-point around which the fluid changes from liquid to gas-like properties was designated supercritical transition temperature (SCTT) [178].

Within the gPROMS platform, density, viscosity, specific enthalpy, and thermal conductivity can be calculated through built-in EoS and other methods. The properties predicted in this way by gPROMS for pure water were compared to the ones estimated using IAPWS-95.

4.2.1 Supercritical transition temperature

Equations (4.5) and (4.7) require the SCTT, which, unlike dew or bubble temperatures, was not a direct calculation in gPROMS. Therefore, a specific model was created to determine it. Figure 4.1 shows how the density of water changes with temperature for different pressures after the critical point, as well as the inflexion point of each curve. These were determined by numerically finding the second derivative of each curve and identifying the temperature at which there is a signal change from positive to negative.

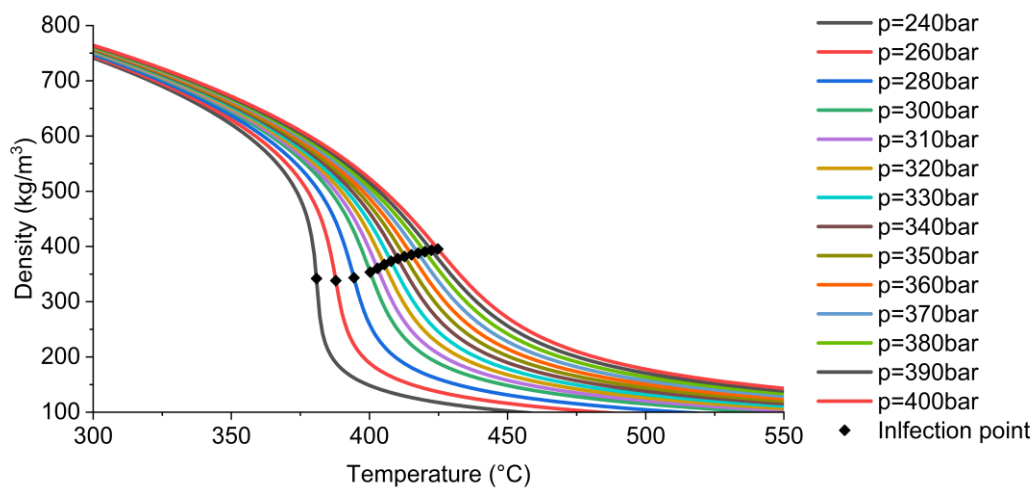


Figure 4.1: Variation of water density with temperature at different pressures, including inflexion points.

The obtained inflection points are plotted in Figure 4.2, which also contains water's saturation temperatures at subcritical pressures, calculated using IAPWS-95. The trajectory defined by all plotted points resembles a polynomial or logarithmic function, such as the second-order polynomial fit shown as the dashed curve in Figure 4.2. Furthermore, from these plots, water's SCTT tends to follow the trajectory defined by the saturation temperatures below the critical point.

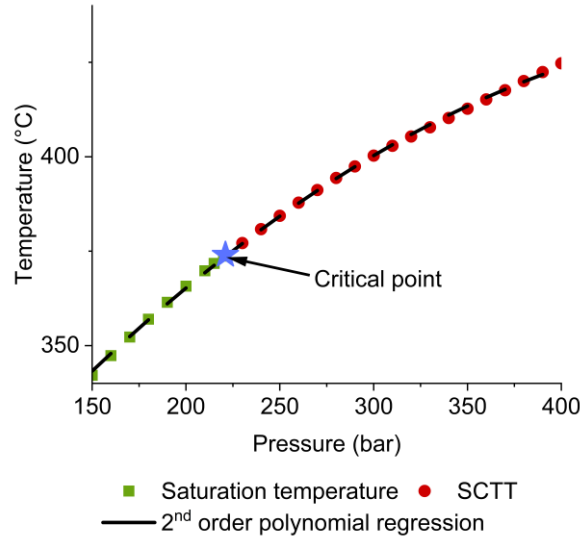


Figure 4.2: Saturation temperature, critical point, supercritical transition temperature, and associated 2nd order polynomial regression.

This hypothesis was implemented in a gPROMS model, considering three possible approximations: linear, polynomial, and logarithmic. The first and second were defined by equation (4.1), while the last used equation (4.2).

$$SCTT = A_{SCTT} \times p^2 + B_{SCTT} \times p + C_{SCTT} \quad (4.1)$$

$$SCTT = B_{SCTT} \times \ln(p) + C_{SCTT} \quad (4.2)$$

The coefficients A_{SCTT} , B_{SCTT} , and C_{SCTT} , were calculated by applying the same equations to enough sub-critical saturation temperatures (T_{sat}^n), *i.e.*, three for a second order polynomial approximation, and two for linear or logarithmic approximations. Those temperatures were simultaneously estimated at equally spaced pressures of 5 bar from a specified critical value (p_{crit}). This equivalence was expressed by equations (4.3) and (4.4), where a bubble temperature⁵ (T_{bubble}) was directly estimated using the built-in EoS for sub-critical pressures spaced by Δp_{SCTT} .

$$\begin{aligned} T_{sat}^n &= T_{bubble}(p_{crit} - (n - 1) \times \Delta p_{SCTT}) \\ &= A_{SCTT} \times (p_{crit} - (n - 1) \times \Delta p_{SCTT})^2 \\ &\quad + B_{SCTT} \times (p_{crit} - (n - 1) \times \Delta p_{SCTT}) + C_{SCTT} \end{aligned} \quad (4.3)$$

$$\begin{aligned} T_{sat}^n &= T_{bubble}(p_{crit} - (n - 1) \times \Delta p_{SCTT}) \\ &= B_{SCTT} \times \ln(p_{crit} - (n - 1) \times \Delta p_{SCTT}) + C_{SCTT} \end{aligned} \quad (4.4)$$

The SCTTs estimated using the described model were plotted in Figure 4.3 for pressures near water's critical point. While the linear regression noticeably deviated from the SCTT for pressures above 250 bar, the other two approximations given by equations (4.3) and (4.4) remained relatively close for most

⁵ For a pure component like water, it is irrelevant the use of dew or bubble point.

of the trajectory, only diverging at approximately 350 bar. Both quadratic and logarithmic approximations were adequate to model water's SCTT in the scope of this study (~ 240 -260 bar). Therefore, the first was used in all simulations.

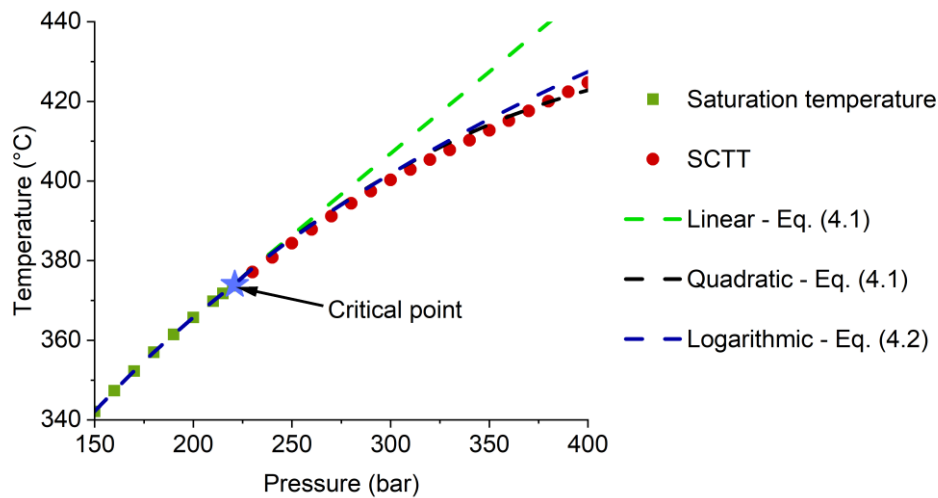


Figure 4.3: Water SCTT estimated using linear, quadratic, and logarithmic regressions.

4.2.2 Pseudo-vapour fraction

Generally, at a given pressure, the transition in properties calculated in gPROMS from a subcritical to a supercritical state is sharper than IAPWS-95. To more closely align gPROMS predictions to those of IAPWS-95, a correction model was developed for each calculation method. These started by defining a pseudo-vapour fraction (z_{SCT}) as a hyperbolic tangent that varies between 0 and 1, and centred around the SCTT, as represented in Figure 4.4.

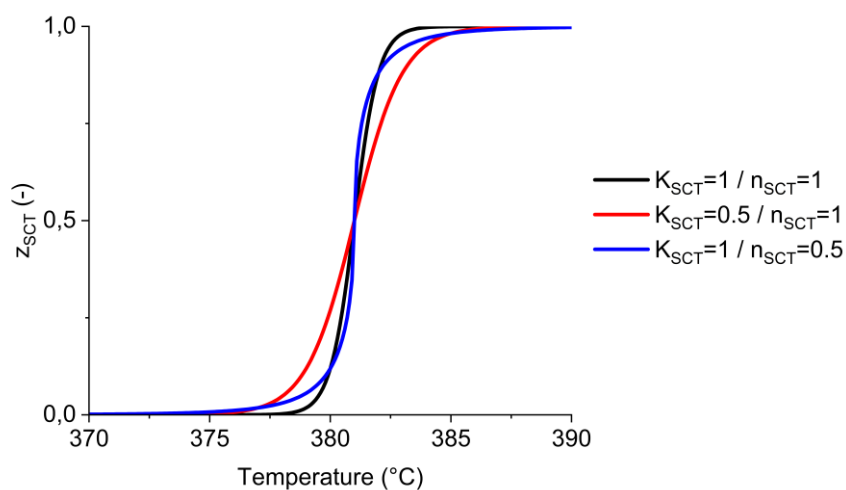


Figure 4.4: Variation of pseudo-vapour fraction (z_{SCT}) with temperature and parameters in equation (4.5). $SCT = 381$ °C.

The representation above resulted from applying equation (4.5). The coefficient K_{SCT} and the exponent n_{SCT} were included to adjust the size and smoothness of the transition, as represented in the additional plots.

$$z_{SCT} = \frac{1 + \tanh(K_{SCT}(T - SCTT)|T - SCTT|^{(n_{SCT}-1)})}{2} \quad (4.5)$$

Furthermore, K_{SCT} was defined as a second order polynomial in respect to inverse pressure:

$$K_{SCT} = \frac{K_{SCT,2}}{p^2} + \frac{K_{SCT,1}}{p} + K_{SCT,0} \quad (4.6)$$

The property correction model applied the estimated pseudo-vapour fraction to the properties calculated in gPROMS assuming a specific phase (P_{liq} and P_{vap}). Therefore, a corrected property (P) is calculated through:

$$P(T, p) = (1 - z_{SCT}) \times P_{liq}(\min(T, SCTT), p) + z_{SCT} \times P_{vap}(\max(T, SCTT), p) \quad (4.7)$$

The coefficients $K_{SCT,i}$ and exponent n_{SCT} were determined for each property calculation method by minimising the sum of squared differences between values calculated in gPROMS and predicted by IAPWS-95. The optimisation was conducted as described in Section 4.1.3, and the optimised corrections are presented in sections 4.2.3 and 4.2.4.

4.2.3 Density and specific enthalpy

Density and specific enthalpy are thermodynamic properties that can be directly calculated using SAFT- γ Mie. Figure 4.5 contains both properties predicted using this EoS and the scientific standard given by IAPWS-95 [55], for pressures of interest (225-300 bar) and temperatures around the supercritical transition zone.

To ensure a consistent comparison, the estimated specific enthalpies were subtracted from their value at 25 °C and 1 bar, thus moving their reference state to liquid water at those conditions.

For both properties, SAFT's estimation causes a sharper transition around the same inflexion point. As mentioned in the beginning of this section, the correction model described by equations (4.5) to (4.7), was applied, using optimised parameters. The optimisation was conducted in gPROMS (Section 4.1.3) by including in the same model densities estimated using the correction model and IAPWS (as described in Section 4.1.2) at the pressures and temperatures in Figure 4.5. The squared difference between the two predictions was minimised, with the coefficients and exponent in equations (4.5) and (4.6) as decision variables. The optimised values for $K_{SCT,2}$, $K_{SCT,1}$, $K_{SCT,0}$, and n_{SCT} were 75672, -450, 0.902, and 0.475, respectively. The densities estimated using the optimised correction model are shown in Figure 4.6. Though not perfectly fitted, when compared with Figure 4.5, the new predictions are significantly closer to IAPWS values, particularly at lower pressures.

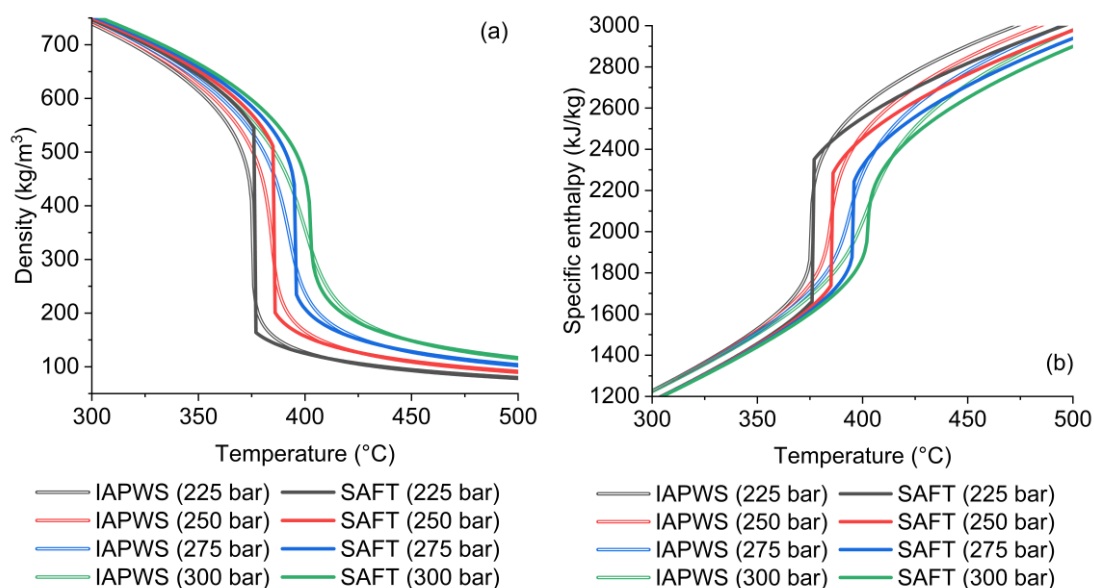


Figure 4.5: Water density (a) and specific enthalpy (b) estimated using IAPWS and SAFT- γ Mie.

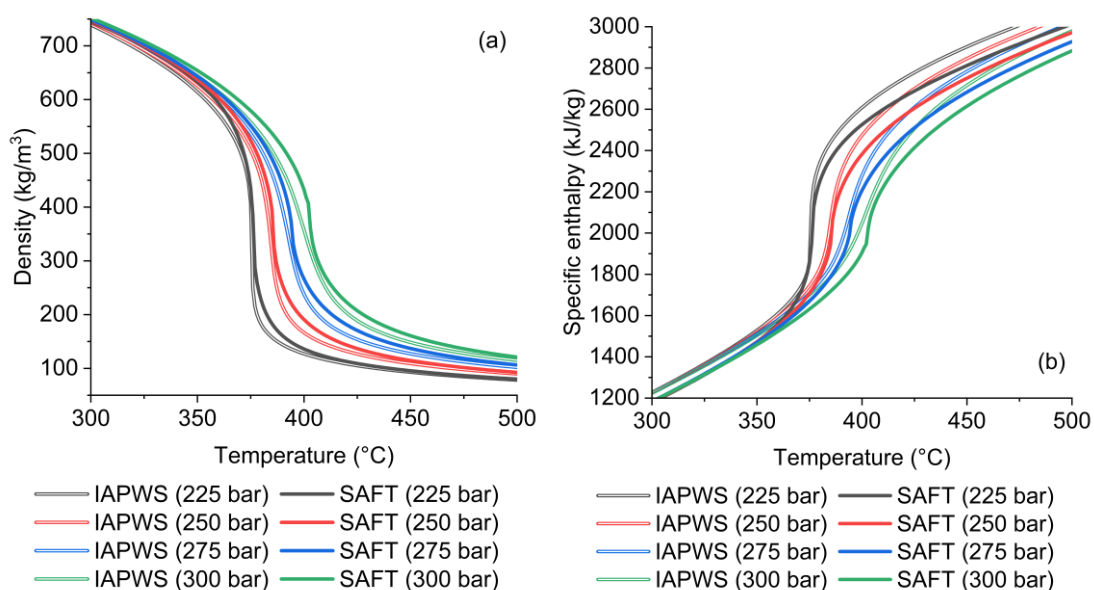


Figure 4.6: Water density (a) and specific enthalpy (b) estimated using IAPWS and SAFT- γ Mie correction model after optimisation.

The same optimisation procedure was applied to specific enthalpy. A negligible variation was observed in the optimised correction parameters ($K_{SCT,2}$, $K_{SCT,1}$, $K_{SCT,0}$, and n_{SCT} were 75464, -447, 0.952, and 0.559, respectively), which was expected since density and enthalpy are based on the same thermodynamic model. Therefore, the same parameters were used for predicting both properties, generating the values plotted on the right side of Figure 4.6.

4.2.4 Viscosity and thermal conductivity

Unlike density and enthalpy, viscosity and thermal conductivity were not estimated using SAFT- γ Mie. The Chung-Ajilan-Lee-Starling (CALs) method was selected for these two properties and the predicted values were compared against IAPWS, as plotted in Figure 4.7. A sharper transition at higher temperatures was observed. Therefore, this method was also corrected according to equations (4.5) to (4.7). The minimisation procedure was applied to viscosity, and generated the optimal correction parameters $K_{SCT,2}$, $K_{SCT,1}$, $K_{SCT,0}$, and n_{SCT} with values of 76301, -407, 0.645, and 0.989, respectively. The plots in Figure 4.8 resulted from applying those parameters to both viscosity as well as thermal conductivity.

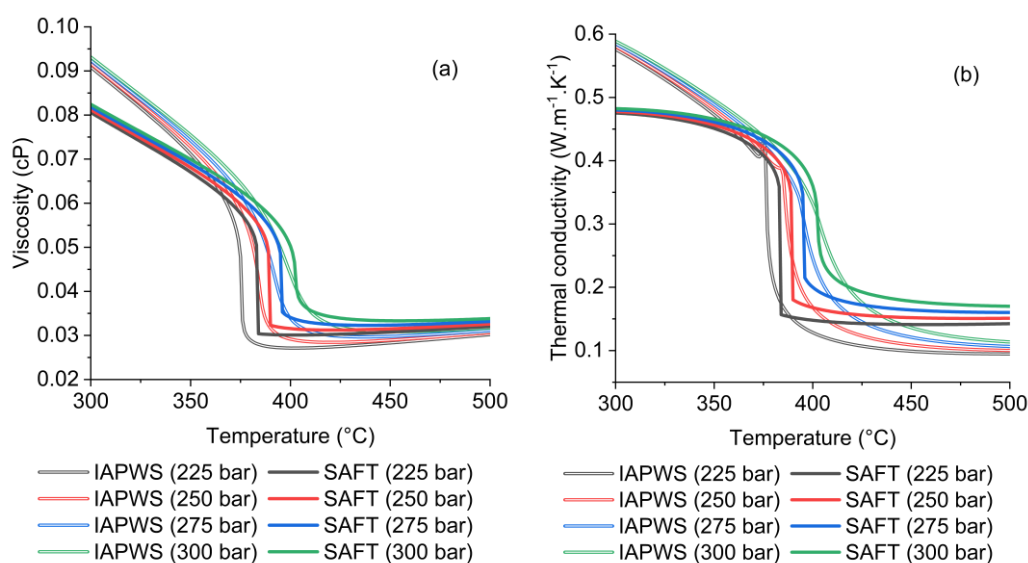


Figure 4.7: Water viscosity (a) and thermal conductivity (b) estimated using IAPWS and the CALs method.

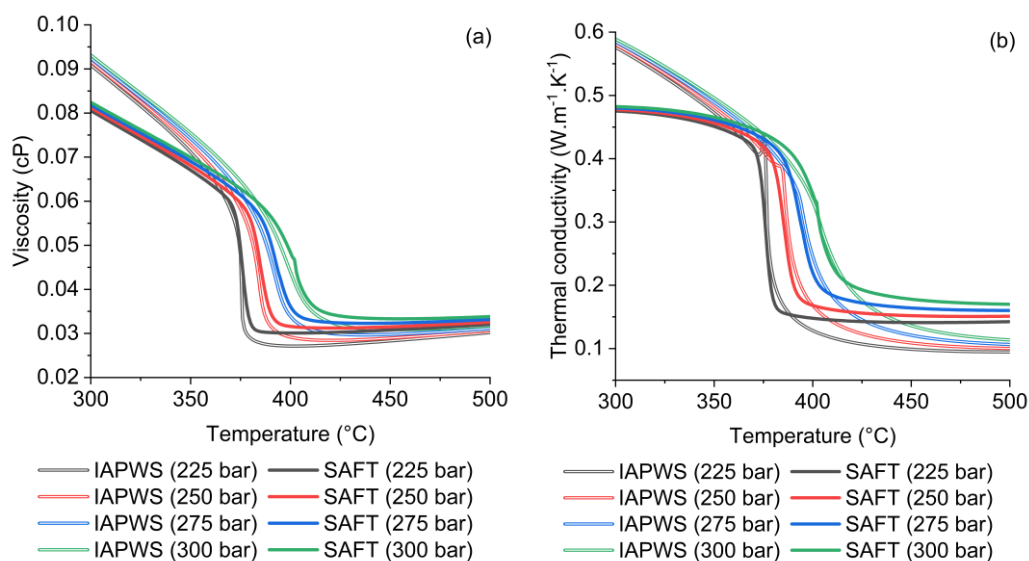


Figure 4.8: Water viscosity (a) and thermal conductivity (b) estimated using IAPWS and the CALs method with correction model after optimisation.

The fitting of both properties was improved around the supercritical transition zone. Nonetheless, it must be considered that both viscosity and thermal conductivity are underpredicted before the supercritical transition zone temperatures, and overpredicted after. Therefore, care is advised when applying this methodology outside the supercritical transition region.

4.3 Top-level model: reactor

The hydrothermal reactor was modelled using the following assumptions:

- Perfect mixing of supercritical and organic feeds within a length that was small compared to the total reactor length.
- The length of the supercritical water jet inside the reactor was negligible, compared to the total reactor length.
- Negligible radial gradients of concentration, temperature, and velocity.

These approximations are prevalent in other work [135,149,179]; nevertheless, their validity was evaluated in Chapter 6, using a more detailed computational fluid dynamics model.

From the assumptions above, the HTL system was modelled as a steady state plug flow reactor with axial dispersion [179,180]. Figure 4.9 shows the modular approach followed when developing this model. The top-level model comprised the mass balance for each molecule, generically describing the reactor. It required the calculation of reaction rates, heat losses, thermodynamic properties, and dispersion coefficients, which were performed in individual sub-models. All of these were connected in the top-level model, which retrieved information from them, but also allowed the propagation of common variables like pressure, temperature, mass fractions, or concentrations.

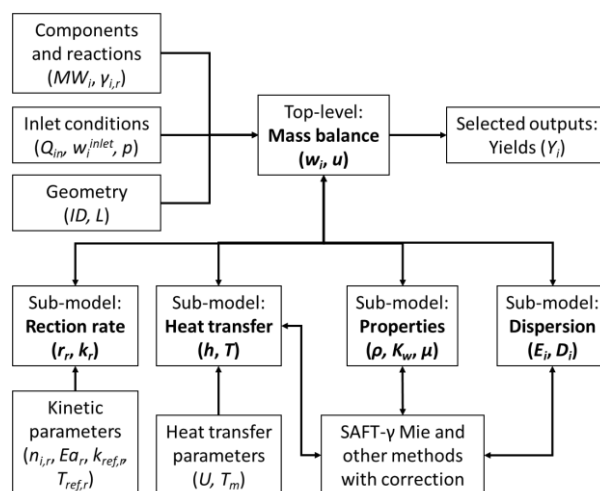


Figure 4.9: Structure of the hydrothermal reactor model.

The top-level model was described by the following molar balance [179]:

$$\frac{\partial F_{i,z}}{\partial z} = \sum_r (\gamma_{i,r} \times r_{r,z}) \times A_{CS} \times L_R \quad (4.8)$$

It calculated the variation of each component's (i) molar flowrate ($F_{i,z}$) in a dimensionless axial point, defined between 0 and 1 (z), caused by the different reaction's rate ($r_{r,z}$), considering the respective stoichiometry ($\gamma_{i,r}$) and the reactor's cross sectional area (A_{CS}) and length (L_R)⁶. The required the boundary condition was given by equation (4.9), specifying the inlet composition (w_i^{in}) and mass flowrate (Q_m):

$$F_{i,z=0} = \frac{Q_{in} \times w_i^{in}}{MW_i} \quad (4.9)$$

The molar flowrate of each species was divided into convective and dispersive flows, according to [179]:

$$F_{i,z} = F_{i,z}^{convective} + F_{i,z}^{dispersive} \quad (4.10)$$

The convective fraction was given by:

$$F_{i,z}^{convective} = C_{i,z} \times Q_{v,z} = C_{i,z} \times u_z \times A_{CS} = C_{i,z} \times \frac{Q_z}{\rho_z} \quad (4.11)$$

It reflects the relationship between concentration ($C_{i,z}$) and volumetric flowrate (Q_v), which was in turn related to the average velocity (u_z) and the total mass flowrate (Q_z).

In literature [179], dispersion is attributed to the non-uniformity of velocity in the radial direction, which creates a concentration gradient in the flow direction (axial). Unlike diffusion, dispersion is a macroscopic phenomenon, though both can be mathematically represent using Fick's first law, resulting in equation (4.12) [179–181], which applied a dispersion coefficient ($E_{i,z}$):

$$F_{i,z}^{dispersive} = -E_{i,z} \times \frac{A_{CS}}{L_R} \times \frac{\partial C_{i,z}}{\partial z} \quad (4.12)$$

The additional partial equation requires a new boundary condition, for which the Danckwerts outlet condition in equation (4.13) is typically used [182].

$$\frac{\partial C_{i,z=1}}{\partial z} = 0 \quad (4.13)$$

The equations in the reactor model were defined over three sets: components (i), normalised axial domain (z), and reaction (r). The first was defined by a list of the species found in the reactional mixture,

⁶ The reactor length is included in equation (4.8) since the axial discretisation axis is normalised between 0 and 1.

each associated with a molecular weight (MW_i). From this list, one component must be identified as solvent (typically water) and another as lumping component. The latter was used when the list contains species, such as pseudo-components, that were not included in the software's thermodynamic database. Therefore, when performing a physical properties calculation, the mass fraction of all components outside of the database was summed to the lumped component.

The reaction set was defined by the total number of reactions being modelled. Each was characterised by the component-specific stoichiometric coefficients.

The axial domain was the discretisation space across which the partial differential equations in the model are solved. It was characterised by its boundaries, discretisation method, and number of elements. Since the model is defined across a non-dimensional length, boundaries are 0 and 1. The discretisation method affects the numerical stability and accuracy of the problem. For a system of second-order partial derivatives, it is recommended the use of a centred finite difference method [183]. The number of elements impacts the accuracy of the results, with a significant effect on the simulation time. Table 4.1 presents the maximum variation caused by increasing the number of elements on the main results from the case studies in Chapters 7 and 8. These variations were below 1% in all cases, while simulation time increased significantly, thus illustrating the trade-off between time and accuracy.

Table 4.1: Variation in selected results and simulation time for all tested cases due to increasing the number of discretisation elements. Kinetic models based on DBE's scenario 5 (Section 7.5.1) and sucrose's scenario 2 (Section 8.5.2).

Variation in the number of elements	Maximum relative variation			
	Organic feed: DBE		Organic feed: Sucrose	
	Conversion	Simulation time	Pyruvaldehyde yield	Simulation time
10 → 50	+ 0.9%	+ 57%	+ 0.8%	+ 210%
50 → 100	+ 0.02%	+ 63%	+ 0.05%	+ 160%
100 → 200	+ 0.006%	+ 95%	+ 0.01%	+ 161%

The model defined by the equations in this chapter required as direct inputs the mixed feed conditions (Q_{in} , $w_{i,i}^{in}$, and p) and the reactor's geometry (ID and L_R). On the other hand, variables like reaction rate, dispersion coefficient, and density were calculated in the sub-models, which are presented in the following sections.

4.4 Sub-model: reaction rate

This model calculates the rate of each reaction in all points of the discretised z axis. Each rate ($r_{r,z}$) was defined by a power law function generically represented by [132]:

$$r_{r,z} = k_{r,z} \times \prod_i (C_{i,z}^{n_{i,r}}) \times P_{r,z}^{H^+} \quad (4.14)$$

This equation is characterised by a kinetic constant ($k_{r,z}$), the orders in relation to each molecule ($n_{i,r}$), and the variable $P_{r,z}^{H^+}$, which accounted for the proton concentration. Several kinetic mechanisms in Chapter 7 and Chapter 8 included this property in the rate equations; this additional variable was defined by:

$$P_{r,z}^{H^+} = (1 - y_r^{H^+}) + y_r^{H^+} [H^+]_z \quad (4.15)$$

In equation (4.15), the actual proton concentration ($[H^+]$) was multiplied by a reaction specific binary variable ($y_r^{H^+}$). A reaction which includes the proton concentration in its rate equation required the specification of $y_r^{H^+}$ as 1, thus making $P_{r,z}^{H^+}$ equal to $[H^+]$. On the other hand, if the reaction is independent from the proton concentration, $y_r^{H^+}$ was 0, resulting in $P_{r,z}^{H^+}$ of $1 - y_r^{H^+}$, i.e., 1.

The kinetic constant was defined as a function of temperature (T_z) according to [184]:

$$k_{r,z} = k_{ref,r} \times \exp \left[-\frac{E_{a,r}}{R} \left(\frac{1}{T_z} - \frac{1}{T_{ref,r}} \right) \right] \quad (4.16)$$

Unlike the common Arrhenius equation [132], which was solely based on activation energy (E_a) and pre-exponential factor ($k_{0,r}$), the implemented function replaced the last with a kinetic constant at a specified reference temperature ($k_{ref,r}$ at $T_{ref,r}$). For each reaction, the reference temperature was selected to minimise the correlation between estimated parameters, an output of each parameter estimation, thus facilitating optimisations and minimising standard deviations [184].

The sub-model described in this section required as inputs for each reaction: $n_{i,r}$ (which was 0 if a component is absent from a reaction), $y_r^{H^+}$, $E_{a,r}$, $T_{ref,r}$, and $k_{ref,r}$. Temperature, stoichiometry, and concentrations of listed species as well as protons were also required; these were obtained from the top-level reactor model, which in turn receives a rate for each reaction at each discretisation point.

4.5 Sub-model: heat transfer

The hydrothermal reactor was initially assumed to be isothermal. As shown in Section 5.4, temperature measurements at different points of the reactor (middle and outlet) proved that this assumption was incorrect. Therefore, the heat transfer sub-model was created to account for heat losses through the outer tube's wall, establishing a temperature profile that is used in the remaining models. Different approaches were considered to minimise the required computational time.

4.5.1 Detailed heat balance

Initially, the temperature distribution (T_z) was calculated using a conventional energy balance [185]:

$$Q_z \times \frac{\partial h_z}{\partial z} = -h_w \times A_L \times (T_z - T_{amb}) \quad (4.17)$$

This was based on the driving force between the fluid's temperature and its surroundings (at $T_{amb} = 20$ °C), using a wall heat transfer coefficient (h_w) and the reactor's lateral surface area (A_L). The specific enthalpy (h_z) was calculated through the corrected model described in Section 4.2.3, being a function of temperature, pressure, and composition:

$$h_z = f(T_z, p, w_{i,z}) \quad (4.18)$$

The appropriate boundary condition for this partial differential equation was the temperature (T_m), measured by the thermocouple at $z_{TC} = 47\%$ (measured from the reactor's inlet), *i.e.*, just before the mid-point of the reactor. Consequently, equation (4.17) was divided in two: from 0 to z_{TC} , and from z_{TC} to 1, both subject to the boundary condition:

$$T_{z=z_{TC}} = T_m \quad (4.19)$$

The mass flowrate (Q), composition (w_i), pressure (p), and geometry were variables provided by the top-level model, which retrieved from this sub-model the temperature in each discretised element of the axial grid. Therefore, the only inputs specific to this sub-model were the temperature measured at the reactor's thermocouple and its relative location, as well as the heat transfer coefficient.

Before being used in the simulation of the hydrothermal reactor, the heat transfer sub-model was used to estimate the required heat transfer coefficient based on preliminary experiments in the HTL rig, as described in Section 4.1.3. Section 5.4 details how the experimental data was obtained, while Section 5.5 summarises the estimation procedure. The conditions of these preliminary experiments were relevant to the case studies presented in Chapter 7 and 8, as dibenzyl ether has thermal properties significantly different from water [107]. Therefore, different heat transfer coefficients were estimated for each case. For the water-only system, the estimated heat transfer coefficient was $51 \pm 1 \text{ W.m}^{-2}.\text{K}^{-1}$, while for the water-DBE system, it was $46 \pm 3 \text{ W.m}^{-2}.\text{K}^{-1}$.

Figure 4.10 shows the temperature profiles across the reactor, calculated using the estimated heat transfer coefficients, for selected preliminary cases from Appendix C.2. In all cases, the temperature profile is highly linear, thus a simplification of the heat transfer sub-model was considered.

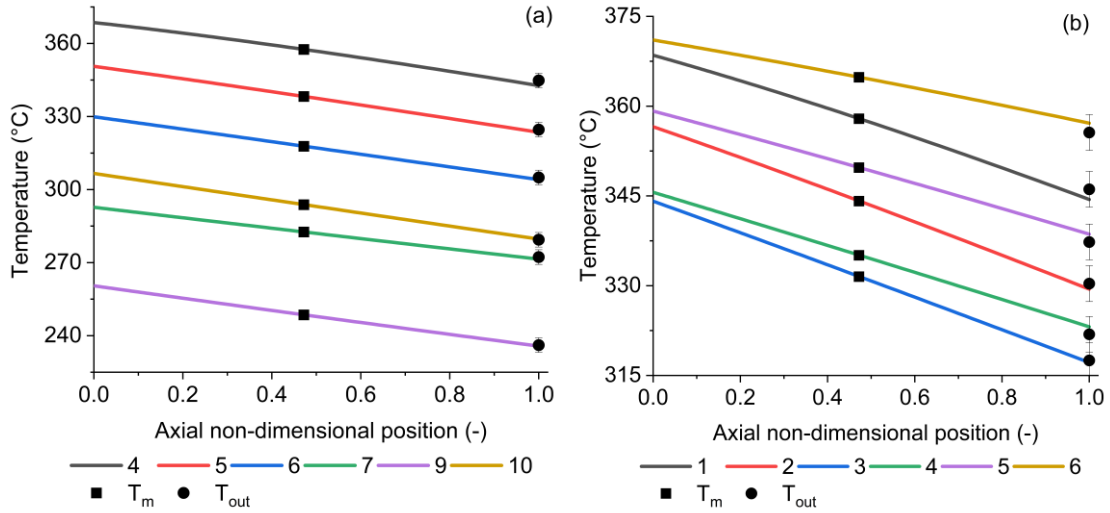


Figure 4.10: Reactor temperature profiles estimated using the detailed heat transfer sub-model. Cases selected from water-only (a) and water-DBE (b) in Appendix C.2.

4.5.2 Simplified heat balance

The simplified heat transfer sub-model aimed to reduce the number of specific enthalpy calculations, thus shortening the simulation time. The detailed energy balance in equation (4.17) was replaced by the two-section overall balance in equations (4.20) and (4.21), which apply an overall heat transfer coefficient (U_{htc}) [185]:

$$Q(h_{in} - h_{T_m}) = U_{ht} \times A_L \times z_{TC} \frac{(T_{in} - T_m)}{\ln\left(\frac{T_{in} - T_{amb}}{T_m - T_{amb}}\right)} \quad (4.20)$$

$$Q(h_{T_m} - h_{out}) = U_{ht} \times A_L (1 - z_{TC}) \frac{(T_m - T_{out})}{\ln\left(\frac{T_m - T_{amb}}{T_{out} - T_{amb}}\right)} \quad (4.21)$$

Since both inlet and outlet specific enthalpies (h_{in} and h_{out}) were functions of the respective temperatures (T_{in} and T_{out}), these temperatures were the only unknown variables in the equations above. Finally, the temperature profile was calculated assuming a linear variation between inlet and outlet, which was defined by equation (4.22) and boundary condition (4.23):

$$\frac{\partial T_z}{\partial z} = T_{in} - T_{out} \quad (4.22)$$

$$T_{z=0} = T_{in} \quad (4.23)$$

The simplified model required the same inputs as the detailed one, with the overall transfer coefficient replacing the local. This variable was also estimated as described in Section 5.5. For water-only cases, the estimated value was $50 \pm 1 \text{ W.m}^{-2}.\text{K}^{-1}$, while for water-DBE cases, it was $46 \pm 3 \text{ W.m}^{-2}.\text{K}^{-1}$. These values were virtually the same that were estimated before, thus demonstrating good agreement between

simplified and detailed methods. This agreement is demonstrated by the temperature profiles plotted in Figure 4.11, which are almost identical to the equivalent profiles in Figure 4.10.

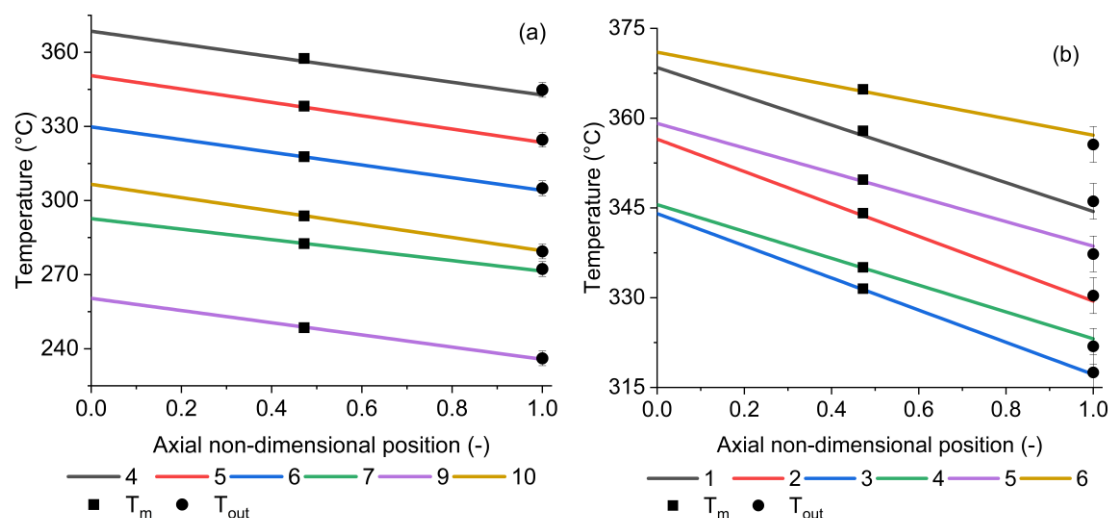


Figure 4.11: Reactor temperature profiles estimated using the simplified heat transfer sub-model. Cases selected from water-only (a) and water-DBE (b) in Appendix C.2.

For the water-only system, simulating the 41 cases in Appendix C.2 took 3 times longer using the detailed heat transfer model, compared to the simplified one. For DBE-water, the increase was 54 times for simulating 6 cases. The observed variations in simulation time can be attributed to the number of required enthalpy calculations. For the detailed model, these are equal to the number of discretised elements, plus one (101 in this case), while the simplified model only requires 3. Consequently, the simplified model was used for all the heat transfer calculations in this work.

4.6 Sub-model: thermophysical properties

This sub-model calculated the thermophysical properties required as inputs by the other models, by applying the methods in Section 4.1.2 and the corrections in Section 4.2. These properties consisted of: SCTT, required to correct SAFT predictions; density, used for example in the top-level to calculate the volumetric flowrate; viscosity, required in the dispersion sub-model; and proton concentration, included in the reaction rate sub-model.

As presented in Section 2.2.1, the ionic product of water (K_w) changes considerably near the supercritical transition from liquid to gas-like. In literature it has been empirically correlated with density [56]:

$$\begin{aligned} \text{Log}(K_w(\text{mol}^2/\text{kg}^2)) &= -4.098 - \frac{3245.2}{T(K)} + \frac{2.2362 \times 10^5}{T(K)^2} - \frac{3.984 \times 10^7}{T(K)^3} \\ &+ \log(\rho_w(\text{g}/\text{cm}^3)) \left(13.957 - \frac{1262.3}{T(K)} + \frac{8.5461 \times 10^5}{T(K)^2} \right) \end{aligned} \quad (4.24)$$

If water is assumed to be the only species in the reacting mixture to dissociate into H^+ and OH^- , the concentration of those ions is the same and given by [149,186]:

$$K_w(\text{mol}^2/\text{kg}^2) \times \rho_w^2 = [\text{H}^+][\text{OH}^-] = [\text{H}^+]^2 \quad (4.25)$$

The first version of the property estimation model performed calculations in all points of the axial grid. It was tested on selected cases from Chapter 7, which accounted for the composition of the reaction mixture in each point, and from Chapter 8, which assumed water properties. As shown in Figure 4.14 to Figure 4.14, for all cases the profiles for density, viscosity, and proton concentration were nearly linear.

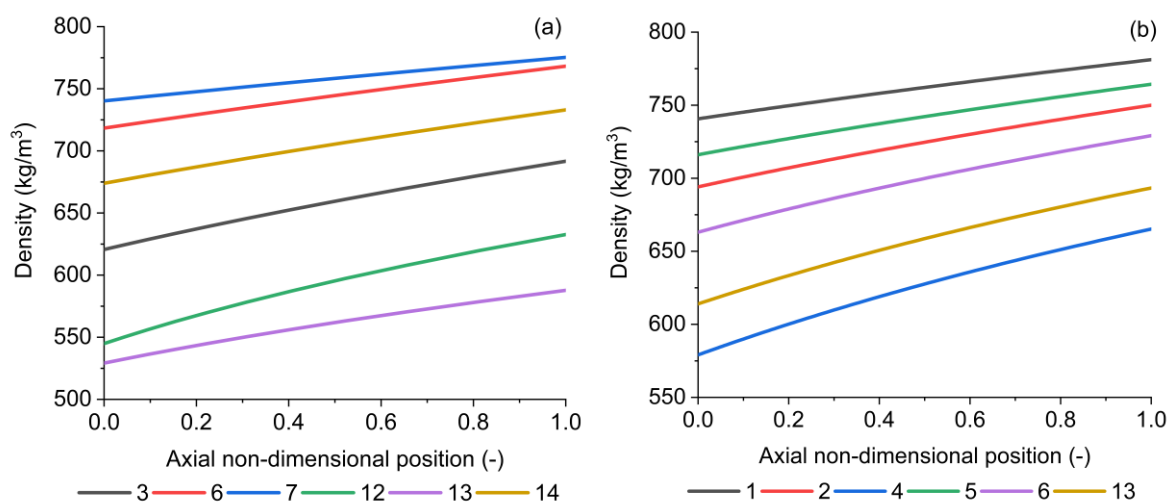


Figure 4.12: Reactor density profiles estimated using the detailed property calculation sub-model. Cases selected from Chapter 7 (a), and from Chapter 8 (b), applying kinetics from scenario 5 and scenario 2, respectively.

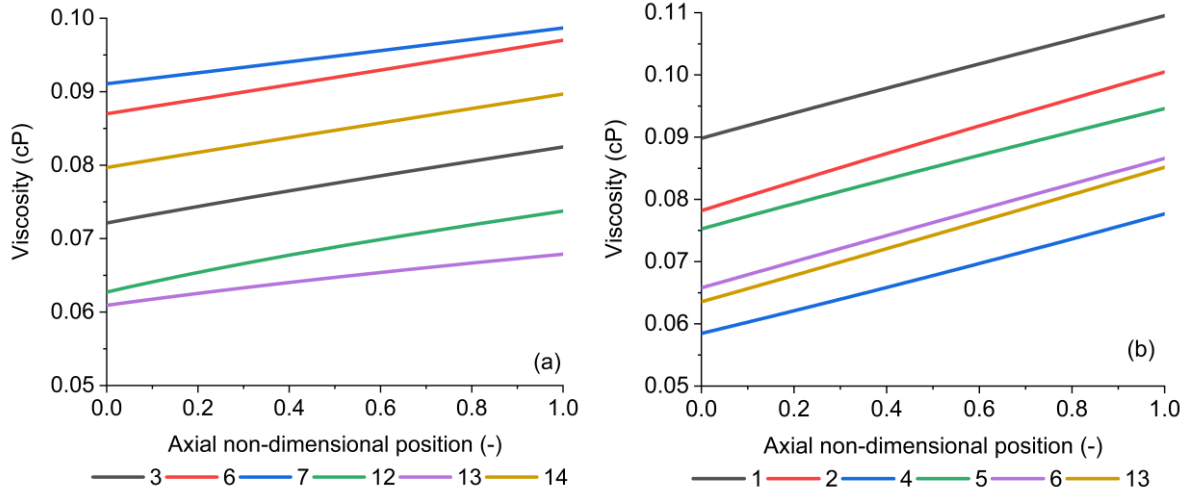


Figure 4.13: Reactor viscosity profiles estimated using the detailed property calculation sub-model. Cases selected from Chapter 7 (a), and from Chapter 8 (b), applying kinetics from scenario 5 and scenario 2, respectively.

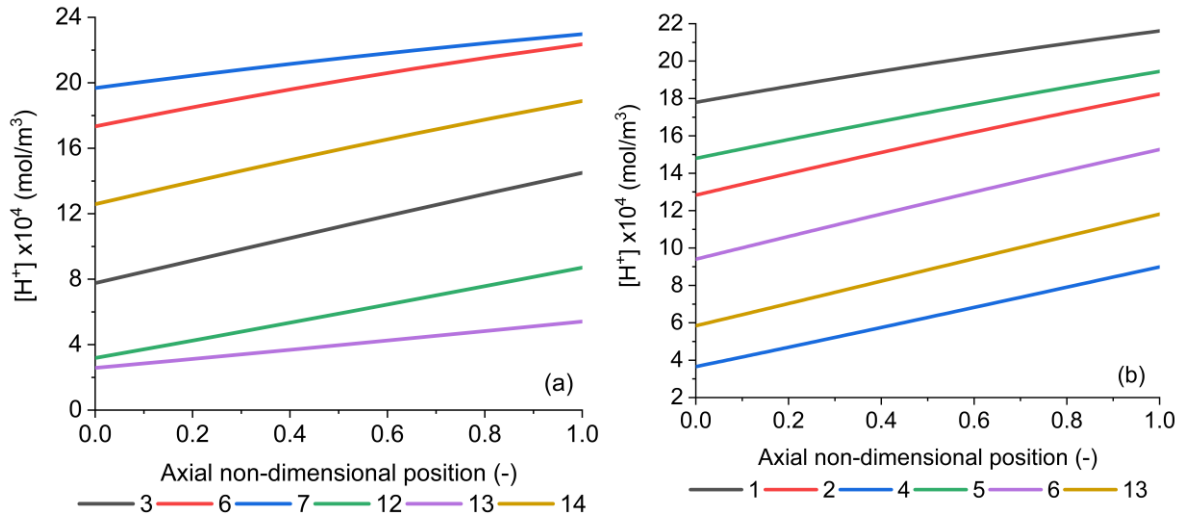


Figure 4.14: Reactor proton concentration profiles estimated using the detailed property calculation sub-model. Cases selected from Chapter 7 (a), and from Chapter 8 (b), applying kinetics from scenario 5 and scenario 2, respectively.

The thermophysical properties model, like the heat transfer model, was also simplified by assuming a linear profile. Calculations at the reactor boundaries were always performed, with a specified number of points (n_p) between them. The position of those points in the axial grid (z_n) was given by:

$$z_n = \frac{n-1}{n_p+1}, \quad 1 \leq n \leq (n_p+2) \quad (4.26)$$

The properties calculated in those specific points ($P_{z,n}$) acted as boundary conditions for equation (4.27), which creates the linear profile between them.

$$\frac{\partial P_z}{\partial z} = \frac{P_{z_{n+1}} - P_{z_n}}{z_{n+1} - z_n}, \quad z_n < z < z_{n+1}, \quad 1 \leq n \leq (n_p + 1) \quad (4.27)$$

The impact of this simplification on the accuracy of the predictions was tested on all case studies from Chapter 7 and Chapter 8, considering 2 points between inlet and outlet (four calculations in total), and evaluating the relative variation of selected results against simulation time. For DBE simulations, conversion was affected in less than 0.1% (relative), while the simulation time decreased 60%. For sucrose simulations, the highest relative variation in pyruvaldehyde yield was only 0.2%, while simulation time decreased 19%. Therefore, for the operating conditions in this study, the penalty of linearising density, viscosity, and proton concentration between inlet and outlet using two points between inlet and outlet was negligible, while simulation time was significantly reduced.

4.7 Sub-model: dispersion coefficient

Dispersion results from the velocity profile across the radial direction, thus the physical mechanism differs significantly from laminar to turbulent flow regimes [179–181]. For the first, when radial gradients are negligible the Taylor-Aris theory is applicable, and the dispersion coefficient is given by [179–181]:

$$\frac{1}{Pe_{i,z}} = \frac{1}{Re_z \times Sc_{i,z}} + \frac{Re_z \times Sc_{i,z}}{192} \quad (4.28)$$

It correlates the inverse Péclet number ($1/Pe$) with Reynolds and Schmidt numbers (Re and Sc), which are calculated from:

$$\frac{1}{Pe_{i,z}} = \frac{E_{i,z}}{u_z \times ID} \quad (4.29)$$

$$Re_z = \frac{\rho_z \times u_z \times ID}{\mu_z} \quad (4.30)$$

$$Sc_{i,z} = \frac{\mu_z}{\rho_z \times D_{i,z}} \quad (4.31)$$

Consequently, the dispersion coefficient is a function of each species diffusivity coefficient (D), which can be estimated using the correlations of Hayduk and Minhas [171], which uses thermophysical properties already calculated by the gPROMS model. Alternatively, the Stokes-Einstein equation [179], could also be applied, requiring the additional input of the solute radius ($R_{0,i}$):

$$D_{i,z} = \frac{k_B \times T_z}{6 \times \pi \times \mu_z \times R_{0,i}} \quad (4.32)$$

For turbulent flow, the radial velocity gradient is smaller than in laminar flow and so the effects of dispersion decrease significantly as the Reynolds number increases. This relation is plotted in literature for different Schmidt numbers [180,181], which can be described by:

$$\log\left(\frac{1}{Pe_{i,z}}\right) = \frac{Re_0}{Re_z} \times \log\left(\frac{1/Pe_{z,i}^0}{1/Pe_\infty}\right) + \log\left(\frac{1}{Pe_\infty}\right) \quad (4.33)$$

Equation (4.33) is parameterised by two inverse Peclet numbers: one at infinite Reynolds number ($1/Pe_\infty$), which in literature is approximately 0.2; and the other at the laminar-turbulent transition ($1/Pe_{z,i}^0$). The latter was calculated using equation (4.28) to the transition Reynolds number ($Re_0 = 2100-2300$), thus ensuring the two regimes overlapped at this point.

The dispersion sub-model implemented equations (4.28) to (4.33), which were calculated for every element of the axial grid, and to all components except the one defined as solvent. Given this component's high concentration throughout the reactor in all experiments (sections 7.3.3), its concentration gradient, and consequent dispersion, are negligible. Therefore, the solvent's dispersion coefficient was defined as 0.

Depending on the selected diffusion coefficient estimation method, this model sub-model requires no inputs (Hayduk and Minhas), or simply each non-solvent molecule solute radius (Stokes-Einstein).

The dispersion coefficient sub-model was only active during the simulations presented in Chapter 7, regarding dibenzyl ether's hydrothermal degradation. For those, the Reynolds number changed from 1300 to 2800, showing experiments were conducted under both laminar and turbulent conditions. A comparison between the two diffusivity calculation methods (Hayduk and Minhas, and Stokes-Einstein) is included in Section 7.6.3. The differences between the two methods were demonstrated to be negligible. For the experiments in Chapter 7, those coefficients were in the range $15 - 55 \times 10^{-5} \text{ cm}^2/\text{s}$, which resulted in dispersion coefficients between 15 and $150 \text{ cm}^2/\text{s}$. The associated inverse Péclet numbers were between 5 and 75.

Chapter 5

Preliminary analysis of the HTL rig

5.1 Introduction

Before conducting the experiments described in Chapters 7 and 8, the performance of the hydrothermal liquefaction rig was evaluated from an operational point of view, ensuring expected operating conditions were in effect. This preliminary analysis is presented in the following sections and focuses on actual flowrate delivered by feed/quench pumps; adequacy of the quench stream and downstream cooling; and temperature variation across the supercritical feed and reactor section. Finally, the heat transfer sub-model described in Chapter 4 was fitted to the temperature measurements obtained in this chapter, to estimate heat transfer coefficients used in later modelling.

5.2 Actual pump flowrate

Initial tests suggested that the flowrate delivered by the three pumps supplying SCW (P-1), the organic feed (P-4), and quenching fluid (P-3) during the rig's continuous operation were slightly different from their set points. To quantify this discrepancy, a series of tests were performed by running the HTL rig with water at high pressure and room temperature (~ 20 °C). Each test consisted of a different flowrate combination between P-1, P-4, and P-3 as presented in Table 5.1. The outlet flowrate ($Q_{measured}$) was quantified according to equation (5.1) by weighting the mass of water accumulated (m_s) over a known period (t_c):

$$Q_{measured} = \frac{m_s}{t_c} \quad (5.1)$$

The sum of specified volumetric flowrates (Qv_f^{NOM}) was converted to a mass basis ($Q_{nominal}$) applying equation (5.2) and considering water's density at 20 °C and operating pressure ($\rho_f^{T_{amb}, p}$, estimated as described in Section 4.1.2):

$$Q_{nominal} = \sum_f (Qv_f^{NOM} \times \rho_f^{T_{amb}, p}) \quad (5.2)$$

The calculated and measured values, as well as their variation obtained through equations (5.3) and (5.4) are also shown in Table 5.1. Variations for each pump were not included since individual flowrates were not measured, as that would not represent normal operation.

$$\Delta Q_{absolute} = Q_{measured} - Q_{nominal} \quad (5.3)$$

$$\Delta_{relative} = \frac{\Delta_{absolute}}{Q_{nominal}} \quad (5.4)$$

Table 5.1: Pump flowrate analysis: nominal ($Q_v^{NOM}/Q_{nominal}$) flowrate; measured flowrate ($Q_{measured}$) calculated from mass accumulated (m_s) over known time (t_c), and respective variation. Sum of squared absolute variation of 375.

Test	P (bar)	Q_v^{NOM} (mL.min ⁻¹)				$Q_{nominal}$ (g/min)	t_c (sec)	m_s (g)	$Q_{measured}$ (g/min)	Variation	
		P-1	P-4	P-3	Total					Relative	Absolute
A	248	30	5	80	115	116	70	144.732	124	6.9%	8
B	248	30	1	80	111	112	70	140.630	121	7.6%	9
C	247	30	5	40	75	76	90	121.746	81	7.2%	5
D	247	20	10	60	90	91	80	128.809	97	6.4%	6
E	247	20	20	60	100	101	80	142.484	107	5.9%	6
F	247	20	10	30	60	61	90	96.277	64	6.0%	4
G	247	30	10	30	70	71	186	233.656	75.4	6.7%	5
H	247	30	1	30	61	62	90	99.001	66	7.2%	4
I	243	30	1	60	91	92	90	147.565	98	7.1%	7
J	245	26	0	0	26	26.2	240	113.072	28.3	7.7%	2
K	243	15	1	60	76	77	80	110.435	83	8.0%	6

Consistently positive variations were observed, showing the pumps tend to discharge a flow larger than the specified value. Furthermore, the relative variations were significantly above the 3% and 0.5% uncertainties quoted by the HPLC [187] (P-1 and P-3) and Isco [188] (P-4) pump suppliers, respectively. Therefore, the observed discrepancy in the total flowrate was not a consequence of the inaccuracy of the flowrate from the individual pumps.

To account for this overshoot, a correction factor (β_f) was included when calculating the actual mass flowrate (Q_f) for each feed (f) according to:

$$Q_f = Qv_f^{NOM} \times (1 + \beta_f) \times \rho_f^{T_{amb},P} \quad (5.5)$$

The value for each pump was estimated by minimising the sum of square absolute variations using the Solver tool in Microsoft® Excel®. The estimated correction factors are shown in Table 5.2. The higher accuracy of the Isco pump was demonstrated by its negligible correction factor, while the HPLC pumps gave similar factors, which was expected given that the pumps were identical.

Table 5.2: Pump flowrate analysis: correction factors.

Feed	Correction factor (β_f)
P-1 (SCW)	8%
P-4 (Organic)	0%
P-3 (Quench)	7%

Using these correction factors, the sum of squared absolute deviations was minimised from 375 to 1, reflecting the proximity to the measured results, as displayed in Table 5.3. Therefore, all calculations in the present work applied the estimated factors.

Table 5.3: Pump flowrate analysis: corrected mass flowrates and variation against measured values. Sum of squared absolute variation of 1.

Test	Corrected flowrate (g/min)				Variation	
	P-1 (SCW)	P-4 (Organic)	P-3 (Quench)	Total	Relative	Absolute
A	33	5.0	87	124	-0.230%	0
B	33	1.01	87	120	0.195%	0
C	33	5.0	43	81	0.234%	0
D	21.7	10.1	65	97	-0.248%	0
E	21.7	20.2	65	107	-0.071%	0
F	21.7	10.1	33	64	-0.217%	0
G	33	10.1	33	75	0.257%	0
H	33	1.01	33	66	-0.145%	0
I	33	1.01	65	99	-0.229%	0
J	28.2	0	0	28	0.167%	0
K	16.3	1.01	65	82	0.613%	1

5.3 Cooling capacity

The mixture exiting the hydrothermal reactor was immediately diluted and cooled through direct quench with a DI water stream discharged by P-3. Downstream, the mixture was further cooled in double-pipe heat exchanger H-2, using chilled water at 11 °C. Besides slowing any reactions happening outside of the reactor, these cooling processes also ensured that the depressurised reactor effluent is collected at a safe to handle temperature, *i.e.*, lower than 60 °C [189].

The suitability of the quench stream and downstream cooler for this purpose was tested through a series of mass and enthalpy balances, which are detailed in Appendix C.1. Three preliminary cases were defined, considering the expected conditions at the reactor's outlet summarised in Table 5.4.

Case 1 is relevant to the experiments described in Chapter 8. The organic feed is a diluted aqueous solution containing sucrose, thus water-only properties were considered as defined in Section 4.1.2. Cases 2 and 3 represent the experiments in Chapter 7, including, besides water, the organic compounds dibenzyl ether and benzyl alcohol. The first assumes no reaction, while the last considers full conversion. For these calculations, densities and enthalpies were estimated as described in Section 4.2. The operating conditions were defined by approximations of maximum expected temperatures, flowrates, and compositions. A typical overall heat transfer coefficient of 800 W.m⁻².K⁻¹ for water-to-water exchange was used [190].

Table 5.4: Cooling capacity analysis: case summary.

Parameter		Case 1	Case 2	Case 3
Composition at reactor inlet (SCW + organic feed)		Sucrose: 8 wt%	Dibenzyl ether: 50 wt%	Benzyl alcohol: 50 wt%
Property calculation method		IAPWS-95	SAFT- γ Mie with correction	SAFT- γ Mie with correction
Reactor outlet	Flowrate (g/min)	45		
	Pressure (bar)	250		
	Temperature (°C)	370		
Quench	Flowrate (mL/min)	60		
	Temperature (°C)	20		
Cooler	Water temperature (°C)	11		
	Water temperature increase (°C)	10		
	Area (m ²)	0.016		
	Overall heat transfer coefficient (W.m ⁻² .K ⁻¹)	800		

The temperatures predicted at the quench mixing point and downstream of H-2 are summarised in Table 5.5, which also includes the outlet organic composition and required cooling duty. For each of the three cases defined earlier, different operating scenarios were considered. The first, refers to normal operating conditions, and shows outlet temperatures within requirements, *i.e.*, below 60 °C [189]. It also shows that the required cooler duty is well below the chiller's maximum cooling capacity of 6 kW [141].

Apart from the expected normal operation, three additional scenarios were considered. The “quench failure” shows that although the quench quickly reduced the temperature during normal operation, a lack of quench lead to lower outlet temperatures from the cooler, due to the reduced flowrate and higher driving force for heat transfer. Nonetheless, this is not a desirable situation, as the mixture would remain concentrated and warmer for a longer period, which potentiates additional reactions.

The “organic feed failure” scenario considers that the SCW feed is not mixed in the reactor, keeping the elevated temperature from the outlet of H-1. A maximum of 450 °C was assumed, and the mass flowrate was reduced to 2/3 of the other scenarios. Coincidentally, according to this calculation, the temperature downstream of the cooler would be expected to remain unchanged compared to Case 1 in normal operation.

The final scenario establishes the loss in cooling efficiency that would result in the outlet temperature exceeding ~60 °C. It was found that reducing the overall heat transfer coefficient by 20% (*i.e.*, 640 W.m⁻².K⁻¹) would have this effect for diluted feed experiments (Case 1). Since this is not a large margin, regular maintenance of the double pipe heat exchanger was recommended, as accumulation of fouling could lead to a high outlet temperature, potentially scalding the operator [190].

Table 5.5: Cooling capacity analysis.

Scenario	Parameter	Case 1	Case 2	Case 3	
Expected operation	Total flowrate after quench (g/min)	105	105	105	
	Organic mass fraction after quench (wt%)	3%	20%	20%	
	Temperature (°C)	After quench	185	161	163
		After H-2	46	37	35
	Cooler duty (kW)	1.07	0.86	0.85	
Quench failure	Total flowrate after quench (g/min)	45	45	45	
	Organic mass fraction after quench (wt%)	8%	50%	50%	
	Temperature (°C)	After quench	370	370	370
		After H-2	22	15	15
	Cooler duty (kW)	1.26	0.97	0.96	
Organic feed failure (2/3 flowrate and 450 °C)	Total flowrate after quench (g/min)	90	-	-	
	Organic mass fraction after quench (wt%)	0	-	-	
	Temperature (°C)	After quench	232	-	-
		After H-2	46	-	-
	Cooler duty (kW)	1.25	-	-	
Overall heat transfer coefficient reduction of 80%	Total flowrate after quench (g/min)	105	105	105	
	Organic mass fraction after quench (wt%)	3%	20%	20%	
	Temperature (°C)	After quench	185	161	163
		After H-2	59	48	46
	Cooler duty (kW)	0.97	0.80	0.78	

Overall, the analysis in this section demonstrates that both the quench and downstream cooler ensured that the HTL rig's effluent was obtained at a temperature below 60 °C, thus being safe to handle without additional protection.

5.4 Supercritical water and reactor temperature

The temperature measurements across the HTL rig were conducted using K-type thermocouples supplied by TC Ltd. [191], with an accuracy from ± 1.5 °C or $\pm 0.4\%$ of the measured value, whichever is higher. The thermocouple tip (OD: 1.5 mm) was inserted in a drilled stainless-steel rod, which was attached to a tee or cross piece, as shown in Figure 5.1. Temperatures were recorded using a TC-08 Data Logger, supplied by Pico Technology.

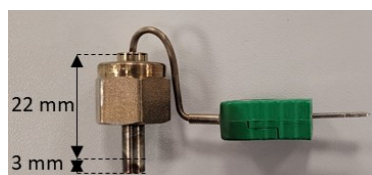


Figure 5.1: K-type thermocouple inserted in respective well.

As mentioned in Section 3.3.3, the reactors of increasing length were investigated in the early stages of this study, which allowed the insertion of a thermocouple in its mid-section. The schematics in Figure 5.2 depict those modifications, as well as the position of the different thermocouples included between the supercritical heater (H-1) and the reactor's outlet. To minimise heat losses, all the sections were wrapped in at least three layers of glass fibre ribbon and aluminium foil.

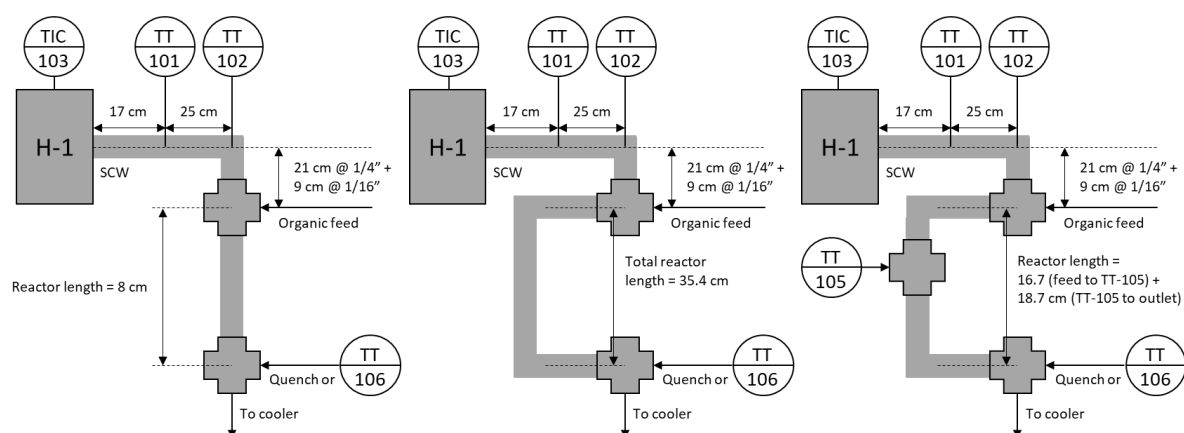


Figure 5.2: Thermocouple location and configuration changes between the supercritical heater to the reactor's outlet.

Given the applied insulation and the small size of the first reactor section, this was initially assumed and expected to be isothermal. Since no continuous temperature measurement was available, a preliminary run was conducted for each set of conditions, where the quench feed was replaced with thermocouple TT-106 and measurements taken. However, when the reactor size was increased from 8 to 35.4 cm, significantly different outlet temperatures disproved the isothermal reactor assumption. For this reason, the final configuration was implemented, with thermocouple TT-105 located at approximately 16.7 cm from the section's inlet, *i.e.*, 47% of its total length.

Measurements from TT-105 demonstrated that, unlike previous studies on confined jet mixers which measured negligible temperature variations [137,192], the experiments in this study were not conducted in an isothermal reaction section. Given the dependence of both reaction rates and subcritical water properties with temperature [56,132], it is important to account for this temperature variation across the reactor in further result analysis and reaction modelling. For that reason, preliminary tests were conducted to evaluate how temperature varies across the SCW inlet and reactor sections, *i.e.*, from TT-101 to TT-102, and from TT-105 to TT-106, respectively. Since TT-106 used the quench port, there was no quench flow into the system during those tests. This thermocouple was not used during the actual experiments, as the lack of quench would allow reactions to continue inside H-2 as temperature slowly decreases, thus invalidating any results. Therefore, no sucrose or other substances were added to the organic feed in these preliminary experiments, which were designated as water-only.

On the other hand, as indicated in Section 3.3.1 and detailed in Chapter 7, experiments using dibenzyl ether were conducted by mixing a pure organic feed (*i.e.*, DBE was not diluted in water) with supercritical water at the inlet of the reactor. Since the thermal conductivity and heat capacity of this organic liquid are significantly smaller than water's (at room conditions, 83% and 62%, respectively [107]), it is expected that significant concentrations of DBE in the reactor affect the amount of heat lost to environment. Consequently, the temperature profile in the reactor should be different when a pure organic feed is used instead of a diluted one. Therefore, a second set of preliminary experiments was performed, using an organic feed containing only DBE.

5.4.1 Tests using only water

Regardless of heat losses, the reactor's outlet temperature is a function of the ratio between the two feed flowrates. Therefore, the conducted tests were divided in two sets, with volumetric ratios fixed at 2 and 3. In each set, the supercritical heater setpoint (specified in TIC-103) and individual flowrates were varied. The detailed values measured during these tests are tabulated in Appendix C.2.

The temperatures measured in the SCW inlet section (*i.e.*, at TT-101 and TT-102) are plotted in Figure 5.3, being divided in three setpoint ranges.

The measured temperatures presented an increase nearly proportional to the heater setpoint across the three setpoint ranges. In the lowest (360 – 410°C, in Figure 5.3a) and highest (450 – 500°C, Figure 5.3c) ranges, the measurements from TT-101 clearly surpass the ones for TT-102 by up to 8°C. Heat losses to the environment were the intuitive explanation to this temperature decrease. No systematic behaviour in this trend was observed with respect to the flowrate of liquid, suggesting that its effect on heat losses was negligible in the range of 15 – 24 mL.min⁻¹.

In the midrange of set points (410 – 450 °C, Figure 5.3b), a reduction in the temperature difference between TT-101 and 102 was observed. Furthermore, for all tests with a setpoint between 420 and 450 °C TT-102 was in fact higher than TT-101 by up to 3 °C.

Since there was no heat input between TT-101 and TT-102, this surprising observation must be attributed to a radial gradient in temperature. Both measuring devices and thermowells were identical, but the radial position of the thermocouple is not precisely defined. Consequently, TT-102 may be in a radial position, which is slightly hotter than TT-101. To ensure that this effect is accounted for in the analysis of the experimental results, the uncertainty associated with all thermocouple measurements was increased to ± 3 °C.

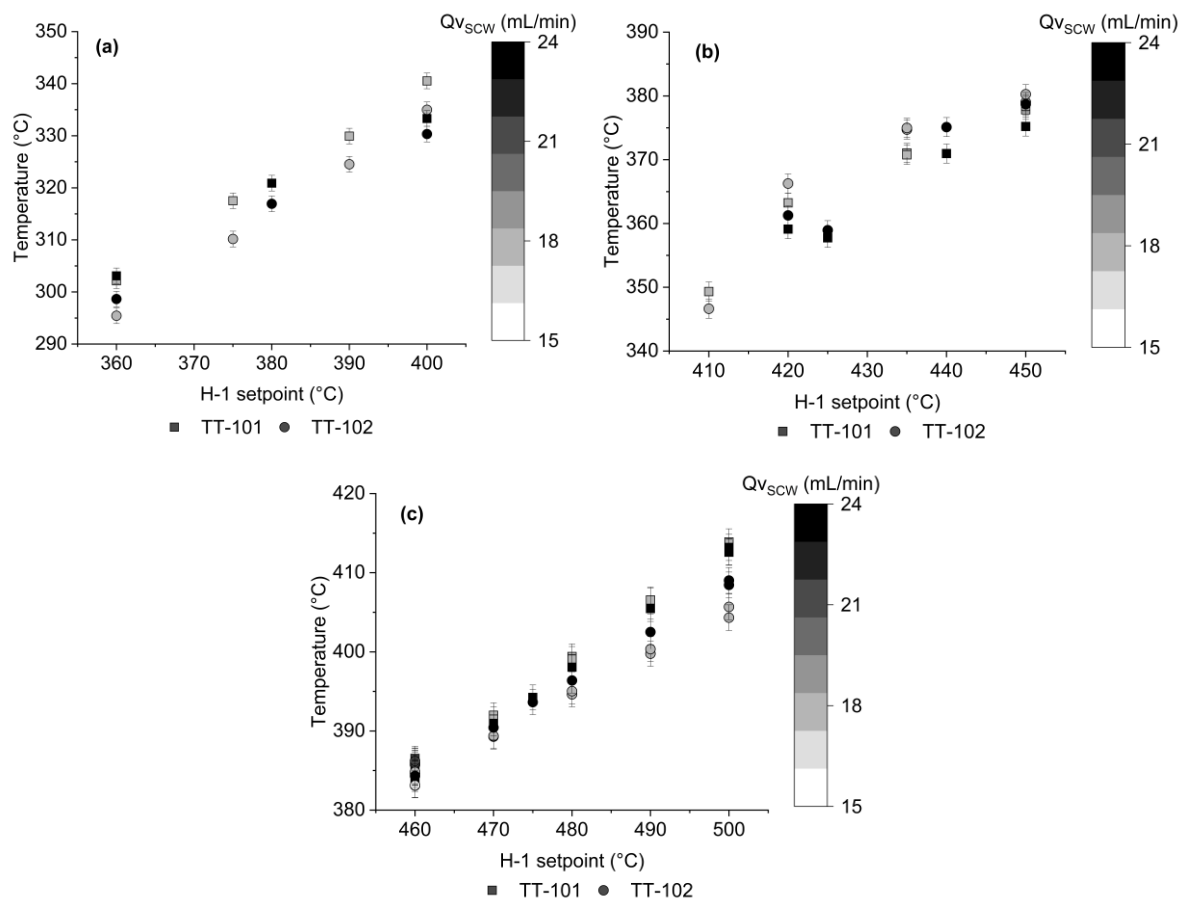


Figure 5.3: Temperatures measured in the SCW line during preliminary tests using water only. H-1 setpoint divided in three ranges: 360 – 400 °C (a), 410 – 450 °C (b), and 460 – 500 °C (c).

The temperatures measured in the reactor section (TT-105 and TT-106) are plotted in Figure 5.4. The temperature decrease is more significant in this section of the process, varying from 7 to 15 °C. Furthermore, instead of a linear increase with the heater setpoint, the measured temperatures plateaued at ~ 370 °C.

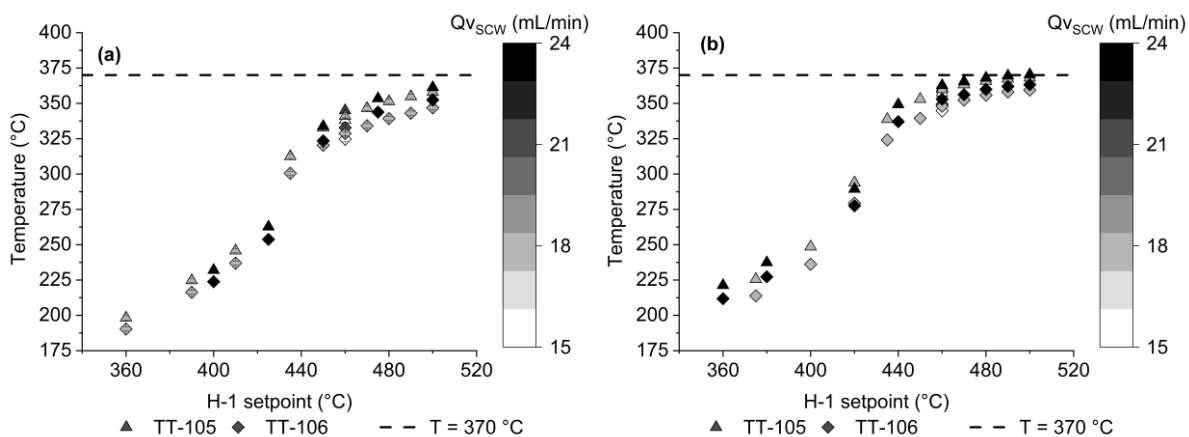


Figure 5.4: Temperatures measured in the reactor during water-only preliminary tests with SCW-to-organic feed ratio fixed at 2 (a) and 3 (b).

This plateau in temperature may be explained by the transition between liquid- and vapour-like properties close to the critical point (374 °C). As plotted in Figure 4.5 in Section 4.2.3, at constant pressure there is a sharp increase in specific enthalpy with increasing temperature. This sharp increase is reflected as a peak in the heat capacity (C_p) of water shown in Figure 5.5. In here the sharp increase in C_p starts at ~ 370 °C.

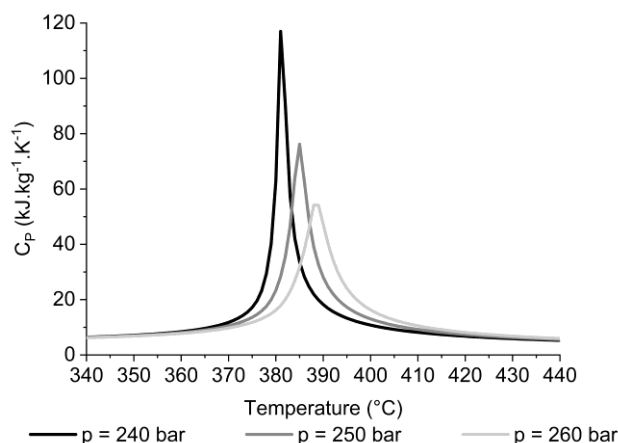


Figure 5.5: Variation of water's heat capacity at constant pressure (C_p) with temperature for selected pressures.

A high C_p means that more heat must be removed by either the organic feed or the surroundings to reduce the temperature of the SCW. In other words, the same magnitude of heat loss has a smaller impact on the fluid temperature when it is above 370 °C, which is the likely origin of the plateau in Figure 5.4. Consequently, if the temperature of the stream falls below 370 °C before reaching TT-105, or the temperature of the water from the heater is already less than 370 °C, then a smaller heat loss is needed to reduce the temperature by 1 °C, resulting in the change in slope in Figure 5.4.

The C_p variation was not relevant for the supercritical heater, since it has enough capacity to cross water's transition enthalpy, thus the measurements in TT-101 and TT-102 did not present a plateau.

Nonetheless, it was still responsible for the reduced temperature decrease between TT-101 and TT-102 when the measured values were between 370 and 400 °C.

Finally, it was also observed that for similar temperatures measured at TT-101 (in the SCW inlet) and at TT-105 (in the reactor section), the temperature drops in the reactor section were larger. As shown in Figure 5.2, the distance between thermocouples in the SCW inlet (TT-101 to TT-102 was 25 cm) was larger than the length between thermocouples in the reactor section (TT-105 to TT-106 was 18.7 cm). Furthermore, the flowrate increased between TT-102 and TT-105 due to the addition of the cold feed. Both differences point to a larger temperature decrease in the SCW line (higher heat losses), which was not observed. This unexpected behaviour can be explained by a more effective insulation in the

SCW line, reducing the temperature decrease, or poor mixing in the reactor section. The last explanation was refuted by the CFD analysis described in Chapter 6.

5.4.2 Tests using DBE/water mixtures

To account for this different temperature variation due to the higher concentration of organic compounds (*i.e.*, DBE and degradation products), six additional preliminary tests were conducted. This time, only the feed flowrates and respective ratios were varied, with the heater setpoint fixed at 460 °C. The obtained measurements are also included in Appendix C.2 and plotted in Figure 5.6.

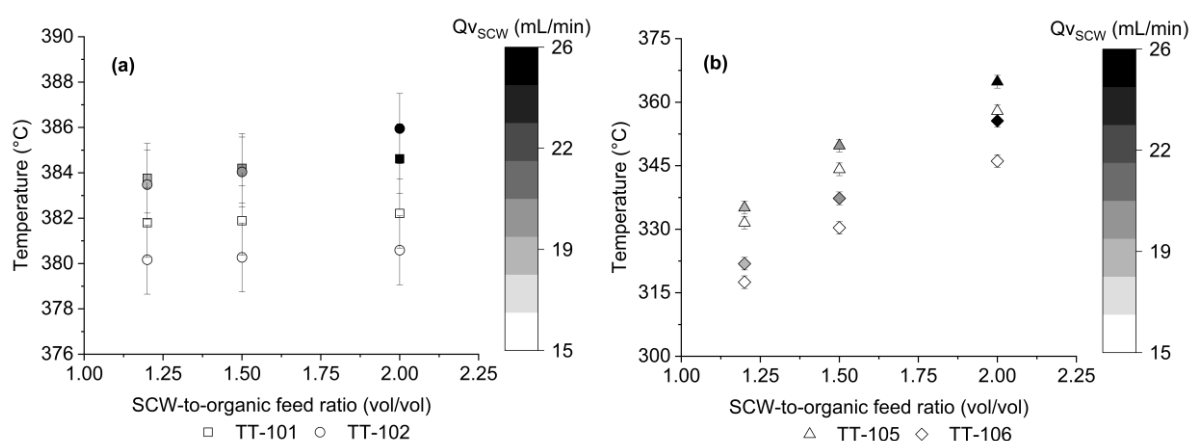


Figure 5.6: Temperatures measured during preliminary tests using DBE/water mixtures (heater setpoint fixed at 460 °C).

The temperatures measured in the reactor are higher than those obtained in the tests using only water at otherwise equivalent conditions. Given the lower heat capacity of DBE when compared to water this was to be expected. Regarding the SCW line, temperatures measured by TT-01 and TT-02 agreed within $\pm 3^\circ\text{C}$ (*i.e.*, the uncertainty assigned to all temperature measurements in this study).

5.5 Reactor's heat transfer coefficients

Both detailed and simplified heat transfer sub-models described in Section 4.5 use heat transfer coefficients (htc and U_{ht} , respectively) to model the heat loss across the reactor's wall. This heat loss was directly related to the temperature decrease between TT-105 and TT-106 discussed in the previous section. Therefore, the different preliminary cases in Appendix C.2 were simulated using the heat transfer sub-model (equation (4.17) to (4.23) in Section 4.5) to estimate the heat transfer coefficients required while simulating the HTL reactor. The respective operating conditions, *i.e.*, inlet flowrate and

composition, pressure, and temperatures measured in the reactor ($TT-105 = T_m$) and at its outlet ($TT-106 = T_{out}$) are detailed in Appendix C.2 (Table C.1 to Table C.2).

As DBE and water feeds result in different temperature variations across the reactor, specific heat transfer coefficients were estimated for Chapters 7 and 8. The parameter estimation was conducted in gPROMS as described in Section 4.1.3. The measured data was defined as the difference between measured and estimated outlet temperatures ($T_{out} - T^*_{out}$). For all experiments this difference was measured as 0, with an uncertainty of 3 °C, as defined in the previous section. Applying the detailed heat transfer sub-model, for water-only systems, the estimated heat transfer coefficient was $51 \pm 1 \text{ W.m}^{-2}.\text{K}^{-1}$, while for the water-DBE system it was $46 \pm 3 \text{ W.m}^{-2}.\text{K}^{-1}$, which was considerably close.

The temperatures predicted (T^*_{out}) using the estimated heat transfer coefficients for each preliminary case are included in Appendix C.2 (Table C.2 and C.4), with representative temperature profiles plotted in Figure 4.10 in Section 4.5. The differences between measured and predicted values are well within the measurements' uncertainty, thus demonstrating a good fit to experimental data.

Using the simplified version of the heat transfer sub-model, for water-only cases, the estimated value was $50 \pm 1 \text{ W.m}^{-2}.\text{K}^{-1}$, while for water-DBE cases, it was $46 \pm 3 \text{ W.m}^{-2}.\text{K}^{-1}$. These values are almost identical to those using the detailed model, demonstrating that the simplified method is sufficient. The close agreement between the detailed and simplified heat transfer models was also confirmed by the estimated temperatures in Appendix C.2, and temperature profiles plotted in Figure 4.10 and Figure 4.11 of Section 4.5.

5.6 Concluding remarks

This chapter described different analysis conducted before the actual experiments in chapters 7 and 8. From this analysis the following was concluded.

SCW and quenching pumps (P-1 and P-3) discharged a mass flowrate, which was slightly higher than their set points. Correction factors of approximately 8% were estimated to match calculated and measured values. The syringe pump (P-4) used to discharge the organic feed did not require any correction factor, thus reflecting its robustness compared to the HPLC pumps (P-1 and P-3).

Mass and energy balances indicated that the typical quench flowrate of 60 mL/min combined with double-pipe cooler supplied with chilled water at 11 °C should ensure a reactor effluent at temperature below 60°C, which was safe to handle without the risk of scalding. This was verified at typical operating conditions, as well as abnormal scenarios were quench and organic feed streams fail. Quenching the reactor effluent decreased the temperature at that point. However, the increased flowrate due to quenching resulted in a warmer stream at the outlet of the double-pipe cooler.

The duty of the cooler was always significantly below the capacity of the recirculating chiller. A decrease of 20% in the overall heat transfer coefficient of the double-pipe cooler would result in outlet temperatures above 60 °C, possibly scalding the operator. Consequently, monitoring of temperatures was recommended, as well as cleaning or replacement of the inner pipe in the cooler when this temperature starts increasing.

Temperatures measured at different points of the SCW feed and reactor sections indicated that there were heat losses, that could not be neglected, and therefore needed to be accounted for in the analysis of the experimental results.

Over 25 mm of the SCW feed (35% of its total length), the maximum temperature decrease was 8 °C. A slightly increasing temperature (higher downstream than upstream) was observed in the SCW feed line, for heater setpoints between 410 and 450 °C. This behaviour was attributed to different radial positioning of the thermocouples inside the tube. Due to this observation, the highest temperature difference of 3 °C, was taken as the uncertainty for all temperature measurements.

Over 18.7 cm of the reactor section (53% of its total length), measured temperatures shown a decrease between 7 and 15 °C. A temperature plateau was observed in the reactor as it approached the supercritical transition between liquid- and gas-like properties at operating pressure. This was attributed to the sharp increase of water's heat capacity in this section.

Tests using a pure dibenzyl ether organic feed showed higher reactor temperatures than equivalent water-only tests. This was expected, considering DBE's smaller heat capacity when compared to water.

Heat transfer coefficients were estimated, to account for the temperature decrease across the reactor. The estimation was performed by simulating the temperature profiling experiments using the heat transfer sub-model described in Section 4.5, whilst minimising the difference between measured and calculated outlet temperatures. The detailed and simplified heat transfer models gave almost identical results. For water-only conditions, the overall heat transfer coefficient was estimated as $50 \pm 1 \text{ W}\cdot\text{m}^{-2}\cdot\text{K}^{-1}$. The maximum difference between measured and predicted temperatures was 3 °C. For water-and-DBE cases, the overall heat transfer coefficient was estimated as $46 \pm 3 \text{ W}\cdot\text{m}^{-2}\cdot\text{K}^{-1}$. In this case the difference between measured and predicted temperatures reached 6 °C.

Chapter 6

CFD analysis of the confined jet mixer

6.1 Introduction

This chapter presents an analysis on the mixing patterns surrounding the jet formed when supercritical water contacts with the colder organic feed. Computational fluid dynamics (CFD) was applied to model in detail the hydrodynamics around this mixing point and downstream tubular section, considering momentum, heat, and mass transfer. The developed model was applied to case studies representative of the experiments described later in this thesis (Chapter 7 and Chapter 8).

The objectives of this hydrodynamic study were to:

- Determine the length required to reach complete mixing and compare it against similar studies in literature [137,139,192].
- Compare the detailed confined jet model with a simplified version where mixing is not explicitly modelled, by analysing selected outputs.
- Evaluate the loss of accuracy when the confined jet mixer is neglected, and the HTL reactor is simply modelled as a tubular section.

6.1.1 Computational fluid dynamics

CFD consists of numerically solving the partial differential equations related to the conservation of momentum, energy, and material, by discretising complex systems into smaller geometrical elements [132]. For chemical engineering, this allows the simulation of non-isothermal fluid flow in the presence of reactions, which is the case of the hydrothermal reactor in this study.

Steps for solving a CFD problem usually consist of [132]: (1) discretising the space being modelled as a mesh of nodes united by lines, in which values are calculated; (2) converting partial differential equations into algebraic ones using numerical methods; (3) solving the obtained equations.

Overall, the numerical methods for solving partial derivative equations are divided in finite difference method (FDM) and finite element method (FEM) [132,193]. The former consists of approximating differential terms by limited intervals, which can be estimated by first or higher order approximations, such as a Taylor expansion [193]. The latter is based on approximating the variation between nodes by a generic function, which is included in the model's equations, creating a residual function. The residual

function is multiplied by a weighting function and integrated over the control volume. By setting this integration to zero, algebraic variables are obtained [132,194]. Finite difference methods are considered simpler, thus less demanding computationally, while finite element methods present more complex formulations, but with improved results [193].

6.1.2 Background

In 2012, Ma *et al.* [137] implemented a CFD model for both counter-current reactor and downwards confined jet mixer, which was applied to the production of nanoparticles using supercritical water. Their configuration was the basis for the one used in the present thesis (see Section 3.3.3); thus, the outer and inner tubes are of the same diameter. The simulation applied the two-equation k - ε model for turbulent flow, and IAPWS-95 water properties under adiabatic conditions. The temperature of the SCW was between 350 and 450 °C, with flowrates varying between 10 and 25 mL/min, while the organic feeds were kept at 10 and 20 mL/min. The CFD simulation [137] showed that a recirculation zone occurred around the confined jet mixer, with a mixing distance up to 7 times the jet's exit diameter. The simulation's temperature profile across the reactor (up to 5 cm downstream of the jet tip) was compared against equivalent experiments, with predictions matching measurements. Overall, it was observed that higher SCW temperature's promote recirculation around the jet, thus reducing the length and time required for complete mixing.

In 2014, the same research group [139,192] published a similar study with the same confined jet mixer, but in an upwards configuration. The mixing zone was reduced to 5 times the jet's exit diameter, and again shown a good agreement between predicted and experimental temperatures. More recently [195], the same configuration and model were applied in the simulation of reactive crystallisation, also obtaining a good agreement with experiments.

The described cases shown that CFD can be applied to model the confined jet mixer with good accuracy. To verify if their conclusions hold under the present study's conditions, particularly when using a pure organic feed, a CFD model was developed, and several simulations were conducted.

6.2 Model configuration

The mixing of supercritical water with organic feeds in a confined jet were modelled through computational fluid dynamics using COMOSL Multiphysics 5.6. This software solves partial differential equations through FEM [196–199], and has been successfully implemented in problems involving jet flow [196,197,200,201], mass transfer [196], heat transfer [199,202,203], and chemical reactions [198,202].

The inner and outer tubes were modelled in a concentric configuration, with the geometries extending upstream and downstream of the mixing zone. Particularly, the entire length of the outer tube after the jet inlet was included in the model. As shown in Figure 3.3.3, the jet and section immediately downstream start with a horizontal tube, which is followed by a vertical section. Nonetheless, the CFD model was simplified to include only a vertical section.

Given the concentric and vertical configurations, it was possible to model the 3D system as 2D axisymmetric. The software's existing models were used in the present study, being divided in the following modules: turbulent flow, heat transfer in fluids, transport of concentrated species, and chemistry. Additionally, the turbulent flow module was individually coupled with the ones relative to heat transfer and species transport. The following sections present a description of the implemented geometry, properties, and individual modules.

6.2.1 Geometry

The geometry of the reactor is shown in Figure 3.2 and Figure 5.2, of Section 3.3.3 and Section 5.4, respectively. The HTL reactor is defined by the tubular section located between the tee where the SCW jet is inserted, and the tee connected to the quench feed, with a total length $L_{reactor} = 354$ mm. The CFD representation of the confined jet mixer extended this geometry, by considering the following:

- The SCW jet protruded 1 cm into the outer tube (L_{jet}). In this section, the hot fluid exchanged heat with the jet's metal wall, which propagated it to the cold feed.
- The jet was also extended 2 cm upstream of the reactor section ($L_{additional}$), representing the contact inside the feed tee.
- TT-105 was located at 18.7 cm from the reactor outlet.
- To investigate potential backflow of warmer organic feed, owing to buoyancy effects, its inlet section was extended by 8 cm ($L''_{additional}$). In this section, the fluid no longer contacted with the jet wall.
- All sections exchanged heat with the exterior. Insulated (SCW and reactor) and non-insulated (organic feed) sections were distinguished by different heat transfer coefficients.

In COMSOL, the axisymmetric 2D system's geometry can be defined by the aggregation of rectangular domains of specified dimensions in a radial plane ($r: z$) with symmetry axis at $r=0$. Figure 6.1 shows how the above considerations were implemented in this radial plane, resulting in the model's geometry. Table 6.1 details the dimensions shown in that figure. The discretisation mesh of the model was built by refining this geometry as described in Section 6.3.3.

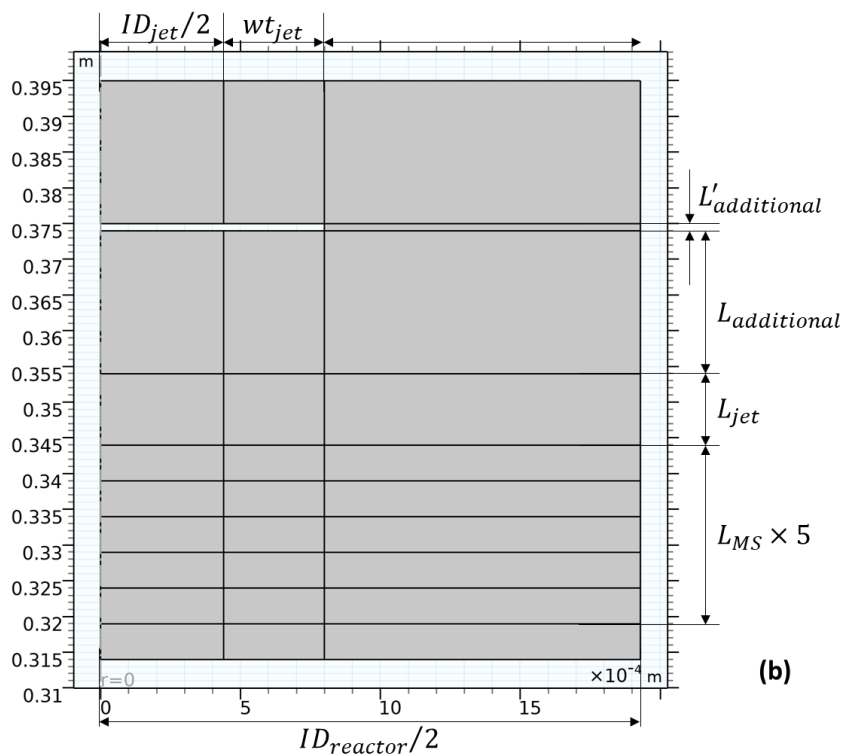
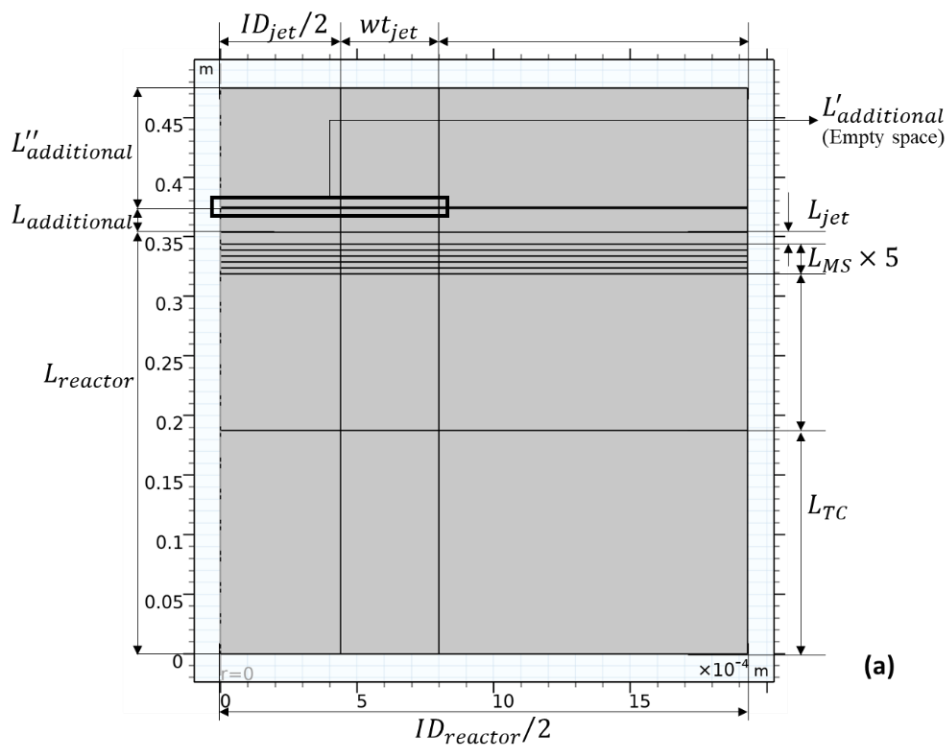


Figure 6.1: Geometrical representation of the HTL reactor and surrounding tubing implemented in COMSOL: complete geometry (a), and jet area (b). Dimensions are given in Table 6.1.

Table 6.1: Sizes used in the geometrical representation of the HTL reactor and surrounding tubing (Figure 6.1).

Parameter	Description	Size (mm)
$ID_{reactor}$	Outer tube inner diameter	3.86
$L_{reactor}$	Outer tube length	354
ID_{jet}	Jet inner diameter	0.88
w_{tjet}	Jet wall thickness	0.36
L_{jet}	Jet length inside the outer tube	10
$L_{additional}$	Length upstream the outer tube (with jet)	20
$L'_{additional}$	Transition between sections	1
$L''_{additional}$	Length upstream the outer tube (without jet)	80
$L^{total}_{additional}$	Total length considered upstream the reactor tube	101
L_{TC}	Thermocouple location from the outlet	187
L_{MS}	Mixing section length	5

The implemented geometry resulted in a flow in the inverse direction of the vertical axis, and the origin of the radial plane, $(r, z) = (0, 0)$, corresponded to the centre of the reactor's outlet. This representation can be divided in the radial and axial sections in Table 6.2. All these sections exchanged material and energy at their common boundaries, with two exceptions: (1) the intersection of the metal wall and jet sections corresponded to a physical barrier, only allowing the exchange of energy across it; (2) the intersection of the transition with the jet and metal wall sections, which was an empty space without mass or energy exchange. This empty space had no physical meaning and was only included to isolate the extension of the cool feed section from the SCW feed, being represented by a very small volume. Alternatively, a simpler boundary without mass and energy transfer could have been implemented. However, this would have required a more complex model approach.

Table 6.2: Sections in the geometrical representation of the HTL reactor and surrounding tubing (Figure 6.1).

Axis	Section	Lower limit	Upper limit
Radial	Inner tube/jet	0	$ID_{jet}/2$
	Metal wall	$ID_{jet}/2$	$ID_{jet}/2 + w_{tjet}$
	Outer tube	$ID_{jet}/2 + w_{tjet}$	$ID_{reactor}/2$
Vertical	d/S TT-105	0	L_{TC}
	u/S TT-105	L_{TC}	$L_{reactor} - L_{jet} - 5L_{MS}$
	Mixing	$L_{reactor} - L_{jet} - 5L_{MS}$	$L_{reactor} - L_{jet}$
	Jet	$L_{reactor} - L_{jet}$	$L_{reactor} + L_{additional}$
	Transition	$L_{reactor} + L_{additional}$	$L_{reactor} + L_{additional} + L'_{additional}$
	Cool feed	$L_{reactor} + L_{additional} + L'_{additional}$	$L_{reactor} + L^{total}_{additional}$

The mixing section was defined immediately after the jet and was given enough length for complete mixing of the jet and cold fluid. It was further divided in five smaller sections with 5 mm, to allow the calculation of average values along their boundaries. The remaining downstream sections were only divided to identify the location of the reactor's thermocouple (TT-105).

6.2.2 Material properties

The CFD model in this chapter was applied to cases that represent the experiments in Chapter 7 and Chapter 8. For the latter, the organic feed consisted of a diluted mixture, thus all fluid phases were assumed to have the properties of pure water. On the other hand, in Chapter 7, the organic feed consists of pure dibenzyl ether (DBE), with the main product being benzyl alcohol (BAL). Therefore, and accounting for the inner tube's metal wall, four types of materials were implemented in the CFD model: SCW, DBE, BAL, and steel.

The properties of fluid materials included: viscosity (μ), heat capacity (C_p), density (ρ), thermal conductivity (k_t), and specific enthalpy (h). For the three liquid species, these properties were interpolated from values estimated at 250 bar and different temperatures, using the methodology in Section 4.2. This meant that for water, properties were calculated using the IAPWS-95 equation of state [55], while for DBE and BAL, they were estimated using SAFT- γ Mie [169].

6.2.3 Turbulent flow model

This module calculates the velocity and pressure in each node of the discretisation grid described in Section 6.3.3. It solves the Reynolds-averaged Navier-Stokes (RANS) equations to calculate velocity in a turbulent flow regime [194,204], applying the two-equation model k - ω [205] to calculate turbulent kinetic energy and its dissipation rate. This model used an automatic wall treatment to account for the low Reynolds number in this section, which is considered suitable for jet flow [205]. The modified k - ω - SST model was also considered, given its higher accuracy [197,201]. However, this had to be abandoned due to the software's increased difficulty in converging to a solution. The turbulent model was further expanded to account for the fluid compressibility, swirl formation, and gravity. The last was defined downwards and resulted in buoyancy forces due to density differences in the fluid.

The specifications for this module included the location of inlet and outlet flows in accordance with Figure 6.2. Walls with no slip condition were defined around the outer tube boundary, the jet metal wall, and the empty space separating feed sections. The hot and cold inlets were characterised by the SCW and organic feeds mass flow rate (Q_{SCW} , Q_{FO}), respectively. The outlet specification required a boundary condition, which in all simulated cases was a pressure fixed at 250 bar.

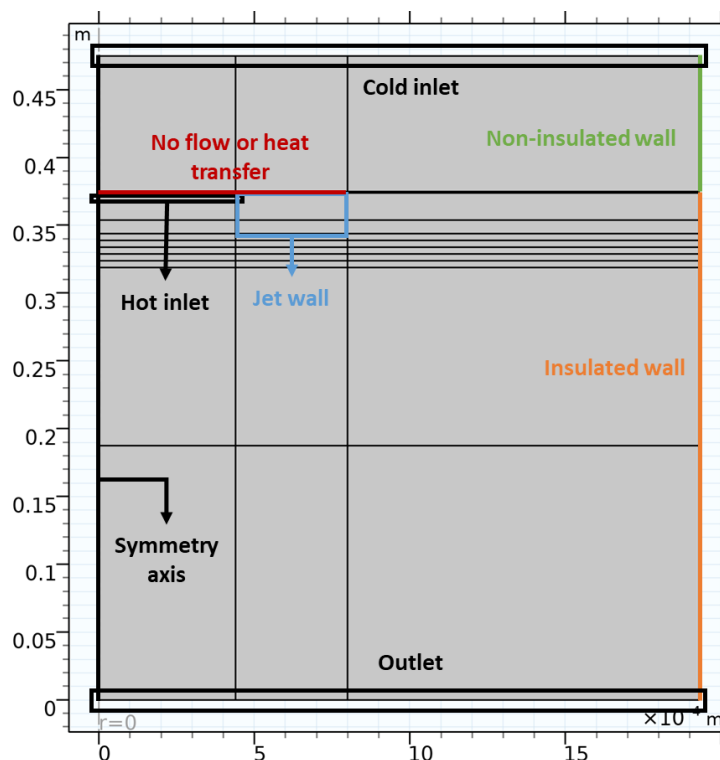


Figure 6.2: Inlets and outlets of mass and energy in the geometrical representation of the HTL reactor.

6.2.4 Heat transfer

This module estimated the temperature in each node, though an energy balance that accounted for sensible heat transfer, conduction, and heat flow to or from external sources. The latter accounted for losses to the environment through the outer tube's wall, as well as heat of reaction in the cases with a pure organic feed.

This was the only module that explicitly includes the inner tube's metal wall, establishing a conductive heat flow through it. As in the previous module inlets and outlets of energy were identified as shown in Figure 6.2. The inlets were characterised by temperature boundary conditions (T_{SCW} , T_{FO}), which for the cold inlet was always ambient ($T_{FO} = 20$ °C). The outlet boundary condition imposes a strictly convective flow.

Figure 6.2 also details which sections of the outer tube were insulated. As mentioned earlier, these include all geometry apart from the extension of the organic feed. In the context of this study, this means heat losses were minimised in this wall, but were still accounted for in the model. Therefore, a heat flow was implemented in the entire outer tube wall, based on the temperature difference between the fluid at the boundary and the exterior ($T_{amb} = 20$ °C), multiplied by a heat transfer coefficient. In Chapter 5, heat transfer coefficients were estimated for a similar basis, considering diluted and pure feeds (51 ± 1 and 46 ± 3 W.m⁻².K⁻¹, respectively). These estimated parameters were directly applied to the insulated

section, while for the non-insulated section a very high value (1000 times higher than the estimated) was used.

6.2.5 Chemistry

This module characterised the different molecules in the system, as well as the chemical reactions between them. It also implemented mixture calculations for density (ρ), heat capacity (C_p), thermal conductivity (kt), and viscosity (μ), according to the following equations:

$$\rho = \frac{1}{\sum \frac{w_i}{\rho_i}} \quad (6.1)$$

$$C_p = \sum w_i \cdot C_{p_i} \quad (6.2)$$

$$kt = \frac{1}{2} \left(\sum x_i \cdot kt_i + \frac{1}{\sum \frac{x_i}{kt_i}} \right) \quad (6.3)$$

$$\log(\mu) = \sum x_i \log(\mu_i) \quad (6.4)$$

Hydrothermal conversion of DBE

In Chapter 7, two reactions are considered for DBE's hydrothermal conversion: hydrolysis, and degradation (see Section 7.4). Nonetheless, given the considerable larger extent of the former, the CFD model was simplified by not including degradation reactions. Therefore, three species were identified: water, DBE, and BAL, taking account of their specific properties (Section 6.2.2).

The hydrolysis reaction was defined by equation (6.5). Its rate was based on scenario 5 defined in Section 7.5, which is given by equation (6.6). This equation includes the kinetic parameters, E_a and k_{ref} , estimated from experimental data in Section 7.3.3. The product $[H^+][OH^-]$ is equal to water's self-ionization, which is estimated by equation (4.24) in Section 4.6. The heat of reaction was automatically calculated from the specific enthalpies of the components.



$$r(\text{mol}/(\text{m}^3 \cdot \text{s})) = 139 \times 10^3 \exp \left[-\frac{180 \times 10^3}{R} \left(\frac{1}{T + 273.15} - \frac{1}{620.65} \right) \right] [DBE][H^+][OH^-] \quad (6.6)$$

Sucrose's hydrothermal degradation

As mentioned in Section 6.2.2, for the cases based on Chapter 8, the organic feed was considered dilute enough that mixture properties could be described using the equation of state for pure water. Therefore, equations (4.20) to (6.4) were replaced by a direct calculation of water properties.

From the different reaction pathways described in Section 8.5, the simplified pathway which best fitted the experimental data was selected, thus avoiding unnecessarily complex CFD simulations. This simplified pathway is shown in Figure 6.3, which considers four reactions, numbered according to the network described in Section 8.4.1, and involves four components: glucose (sub-feed A/gluc), fructose (sub-feed B/fruc), total soluble organics (TSO), solids, and volatiles.

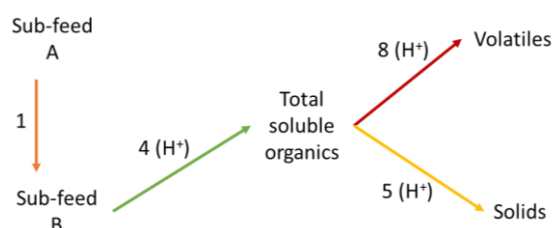


Figure 6.3: Best fitted simplified pathway for sucrose's hydrothermal reactions (Section 8.5.2). Reactions numbered according to the network described in Section 8.4.1.

Each component and reaction individually specified. The reaction rates were given by equations (6.7) to (6.10), using parameters estimated from experimental data (see Section 8.5). Since each component's enthalpy is approximated to that of water, the heat of reaction is neglected.

$$r_1 = 0.405 \times \exp \left[-\frac{67 \times 10^3}{R} \left(\frac{1}{T + 273.15} - \frac{1}{605.3} \right) \right] \times [\text{gluc}] \quad (6.7)$$

$$r_4 = 921 \times \exp \left[-\frac{92 \times 10^3}{R} \left(\frac{1}{T + 273.15} - \frac{1}{605.3} \right) \right] \times [\text{fruc}][H^+] \quad (6.8)$$

$$r_5 = 5.4 \times \exp \left[-\frac{80 \times 10^3}{R} \left(\frac{1}{T + 273.15} - \frac{1}{605.3} \right) \right] \times [TSO][H^+] \quad (6.9)$$

$$r_8 = 75 \times \exp \left[-\frac{240 \times 10^3}{R} \left(\frac{1}{T + 273.15} - \frac{1}{605.3} \right) \right] \times [TSO][H^+] \quad (6.10)$$

6.2.6 Transport of concentrated species

This module calculated the mass fraction of each component defined in the chemistry section. It applied individual molar balances that include convection, dispersion (using Fick's law), and reaction rates. Nonetheless, to improve the model's performance, dispersion was neglected, thus minimise solute

mixing, leading to conservative mixing patterns. A zero-flux boundary condition was used at all the tube walls.

The mass fraction was specified at each inlet boundary for each component except water, which is calculated by difference. The mass fractions of the components at those boundaries were set to 0, except for the species present in the organic feeds, *i.e.*, DBE or glucose and fructose⁷ ($w_{FO,i}$). The outlet boundary condition imposed a purely convective flow.

6.2.7 Multiphysics interface

The Multiphysics interface individually combined the heat transfer and transport of concentrated species modules with the turbulent flow one. For both, this meant adding a turbulent term to their respective mass and momentum balances, given by the Kays-Crawford model [196,203,206].

6.2.8 Simplified model

The performance of the detailed CFD model was compared against a simplified version, where the mixing zone was not explicitly modelled. The implemented geometry is presented in Figure 6.4, consisting of a rectangle with the entire reactor's section length ($L_{reactor}$) and a single feed. Therefore, any effect of the jet's wall was ignored.

Essentially, this simplified model consisted of a two-dimensional representation of the gPROMS model presented in Chapter 4, thus requiring similar inputs. The single feed was characterised by total inlet flowrate ($Q_{reactor} = Q_{SCW} + Q_{FO}$), mixture temperature (T_{mix}), and average inlet mass fraction (w_i^{in}). Remaining features, such as wall heat losses and chemical reactions, were the same as the detailed model.

⁷ As shown in Section 8.3.3, no sucrose was found in the reactor's outlet, thus it was assumed it degrades instantaneously in glucose and fructose.

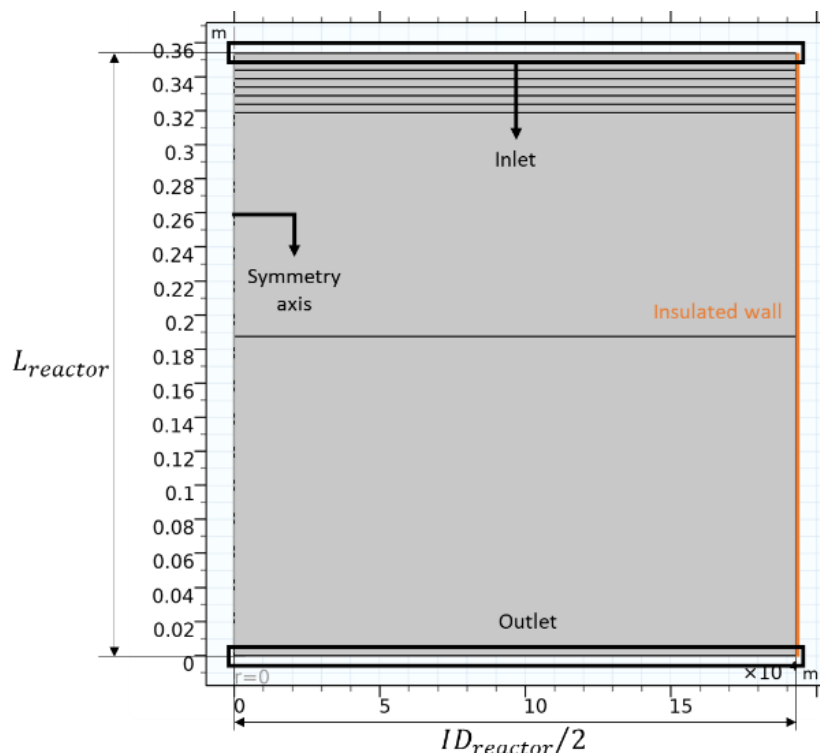


Figure 6.4: Simplified geometrical representation of the HTL reactor and surrounding tubing implemented in COMSOL. Sizes in Table 6.1.

6.3 Description of simulation cases

The detailed analysis of the hydrodynamics and heat transfer around the confined jet mixer was applied to 10 cases that represented experiments conducted in Chapter 7 and Chapter 8. These were selected from the preliminary tests presented in Appendix C.2, being described in Table 6.3.

Table 6.3: Inputs for CFD representative simulations: organic feed composition ($w_{FO,i}$); feed flowrates (Q_i); composition expected after mixing (w^{in}_i); temperatures measured at different sections and calculated after feed mixing (T_{mix}); and applied heat transfer coefficient with the environment (htc).

Organic feed	Case	Flowrate (g/min)			w^{in}_i	Temperature (°C)		
		Q_{FO}	Q_{SCW}	$Q_{reactor}$		At TT-105	T_{mix}	T_{SCW}
Sucrose ($w_{FO,gluc} = w_{FO,fruc} = 15\%$; $htc = 51 \text{ W.m}^{-2}.\text{K}^{-1}$)	S1	10	20	29	10%	198	207	291
	S2	13	26	39	10%	232	240	331
	S3	11	16	27	12%	318	330	391
	S4	7	20	26	8%	368	375	392
	S5	9	26	35	8%	370	376	392
DBE ($w_{FO,DBE} = 100\%$; $htc = 43 \text{ W.m}^{-2}.\text{K}^{-1}$)	D1	9	17	26	33%	358	367	387
	D2	11	16	27	39%	344	354	387
	D3	16	20	36	45%	335	343	388
	D4	14	21	35	39%	350	357	388
	D5	14	28	42	33%	365	370	387

The heat transfer model described in Section 4.5 was used to estimate the temperature at the reactor's inlet (T_{mix}), based on the measurements from TT-105. Using this value, the temperature of the SCW feed (T_{SCW}) was determined through an energy balance around the inlet mixing point, as detailed in Appendix C.1.

6.3.1 Dynamic simulation

The detailed model described in this chapter was challenging to initialise in steady state, which was attributed to large gradients on the mixing zone between SCW and cold fluid. Based on the real operation of the HTL rig, a dynamic simulation was implemented to guide the model from a simpler state to actual operating conditions.

Initial conditions for this time dependent simulation were 2 bar above operating pressure, ambient temperature throughout the system, and absence of organics ($w_i = 0$). Both SCW temperature and organic feed mass fraction started from those initial conditions and were increased in a smooth ramp to their final values.

The ramped increase in mass fraction was centred on a simulation time of 2 hours, with a duration of 30 minutes. This was followed by the temperature increase, which was centred at 6 hours, requiring a longer transition of 2 hours. The variations of average outlet temperatures (T_{out}) and total organic mass fractions (w_{org}^{out} defined in equation (6.15)) with time are plotted in Figure 6.5 and Figure 6.6, showing that a total simulation time of 10 hours was sufficient to reach the final steady state. Under these conditions, simulations took from 4 minutes to 9 hours depending on the selected mesh.

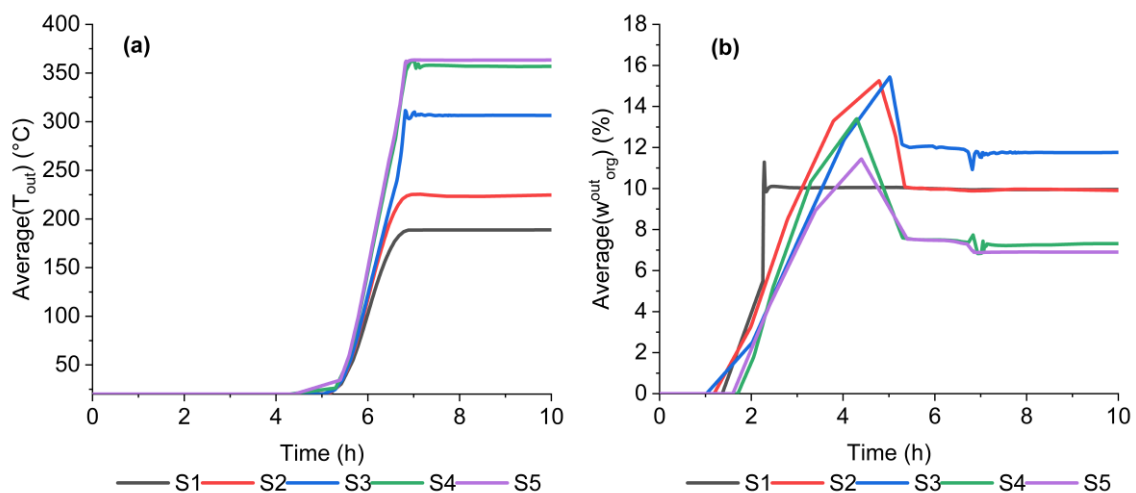


Figure 6.5: Variation of average outlet temperature (a) and organic mass fraction (b) in the dynamic simulation of cases S1 to S5.

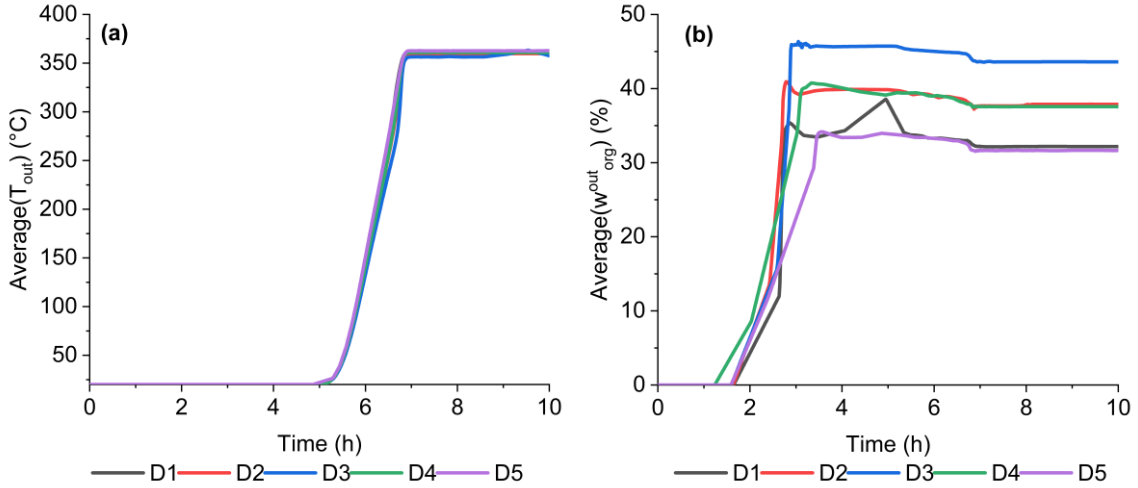


Figure 6.6: Variation of average outlet temperature (a) and organic mass fraction (b) in the dynamic simulation of cases D1 to D5.

6.3.2 Mass and energy conservation

The conservation of total mass in the model was evaluated using the total mass flowrate (Q) that crosses a radial section (r_0 to r_1) at a fixed axial position ($z=z_i$), as defined in equation (6.11), where u is the vertical component of the velocity vector.

$$Q|_{z=z_i}^{r_0 < r < r_1} = \oint \int_{r_0}^{r_1} -u \times \rho \, dr \, d\phi \Big|_{z=z_i} \quad (6.11)$$

Applying this equation to the boundaries in Table 6.2, allows the calculation of both inlets and outlet total flowrates. The relative variation of total flowrate (R_{tot}) between inlet and outlet, represented by equation (6.12), was the variable chosen to measure the deviation from a closed mass balance.

$$R_{tot} = 1 - \frac{Q|_{z=0}^{0 < r < ID_{reactor}/2}}{Q|_{z=L_{reactor}+L_{additional}}^{0 < r < ID_{reactor}/2} + Q|_{z=L_{reactor}+L_{additional}}^{0 < r < ID_{reactor}/2}} \quad (6.12)$$

The same concept was applied to the total flowrate of organic species (Q_{org}), according to:

$$Q_{org}|_{z=z_i}^{r_0 < r < r_1} = \oint \int_{r_0}^{r_1} -u \times \rho \times w_{org} \, dr \, d\phi \Big|_{z=z_i} \quad (6.13)$$

$$R_{org} = 1 - \frac{Q_{org}|_{z=0}^{0 < r < ID_{reactor}/2}}{Q_{org}|_{z=L_{reactor}+L_{additional}}^{0 < r < ID_{reactor}/2} + Q_{org}|_{z=L_{reactor}+L_{additional}}^{0 < r < ID_{reactor}/2}} \quad (6.14)$$

R_{org} was based on the mass fraction defined in (6.15), accounting for all organic compounds as if they were in their feed state. Therefore, R_{org} evaluates the mass balance relative to organic species.

$$w_{org} = \sum_{i \neq \text{water}} \left(w_i \frac{MW_{i=feed}}{MW_i} \frac{\gamma_{i=feed}}{\gamma_i} \right) \quad (6.15)$$

The energy balance was also verified by similar equations. The total enthalpic flow was calculated using equation (6.16):

$$q|_{z=z_i}^{r_0 < r < r_1} = \oint \int_{r_0}^{r_1} -u \times \rho \times h_{mix} dr d\varphi \Big|_{z=z_i} \quad (6.16)$$

Where the mixture's specific enthalpy results from the mass average of its components:

$$h = \sum_i (h_i \times w_i) \quad (6.17)$$

Since the above specific enthalpies were estimated considering an element reference state, the heat of reaction is implicitly accounted when this property was calculated. Therefore, it was not required to be explicitly included in the equations above.

Unlike the mass balances, the energy balance must account for the losses through the outer tube's wall (q_{wall}). These are calculated through equation (6.18), and must consider the different heat transfer coefficients, resulting in the sum in equation (6.19):

$$q_{wall}|_{z_0 < z < z_1} = htc|_{z_0 < z < z_1} \oint \int_{z_0}^{z_1} (T_{amb} - T) dz d\varphi \Big|_{r=ID_{reactor}/2} \quad (6.18)$$

$$q_{loss} = q_{wall}|_{0 < z < L_{reactor} + L_{additional}} + q_{wall}|_{L_{reactor} + L_{additional} < z < L_{reactor} + L_{additional}^{total}} \quad (6.19)$$

As with the other balances, the energy balance was evaluated by the relative variation between inlet and outlet (R_{heat}):

$$R_{heat} = 1 - \frac{q|_{z=0}^{0 < r < ID_{reactor}/2} + q_{loss}}{q|_{z=L_{reactor} + L_{additional}}^{0 < r < ID_{reactor}/2} + q|_{z=L_{reactor} + L_{additional}}^{0 < r < ID_{reactor}/2} + q|_{z=L_{reactor} + L_{additional}}^{total}} \quad (6.20)$$

6.3.3 Discretisation mesh

As mentioned earlier, the CFD solver discretises partial differential equations across a mesh of nodes that represents the system's geometry [132]. Increasing the number of nodes improves the model accuracy, but greatly increases the required computational time [193,194], and reduces the likelihood of convergency.

The geometry in Figure 6.1 was discretised using a rectangular grid. Across the vertical axis, a maximum length between nodes (MS) was defined based on the software's default values of 14.2 and 3.74 mm. The number of nodes across the radial direction was defined for each of the three sections (s)

of length L_s , considering a default distance of 3.74 mm, and multiplying it by an integer (I), as shown in equation (6.21).

$$N_s = \max\left(1, \text{round}\left(\frac{L_s}{0.00374}\right) \times I\right) \quad (6.21)$$

Since large gradients are expected around the SCW jet, the obtained mesh was further refined in the fluid sections of jet and mixing, using a 4-level algorithm in COMSOL (ARL from 1 to 4).

The choice of suitable mesh parameters is detailed in Appendix D.1. The quality of the assembled mesh was evaluated by comparing the model's performance while increasing the three parameters above. This evaluation was conducted on case S5 in Table 6.3, relying on the comparison of total organic mass fraction and velocity profiles, variations on mass and energy balances, required simulation time and main outputs (average temperatures and yields). In summary, it was observed that:

- Increasing the number of radial elements, *i.e.*, increasing I , affected the velocities profile. Nonetheless, this effect was less evident when auto-refinement was used.
- Increasing the number elements in the vertical axis had a minimal effect on the velocity or mass fraction profiles. However, it effectively reduced variations in the total organic and energy balances, bringing their variations to acceptable levels, that is, smaller than 10%.

The final combination shows all variations below 5%. However, this comes at the cost of increasing the simulation time by nearly four times. This was considered unjustified, compared to the profile and results shown by the previous simulation. This resulted in an auto-refinement level of 3, an integer multiplier on equation (6.21) of 25, and a maximum distance between nodes on the vertical direction of 3.74 mm.

6.4 Results and discussion

Velocity, temperature, and total organic mass fraction profiles were obtained from simulations of the ten cases listed in Table 6.3. Appendix D.2 contains plots of their profiles over the entire domain of the model as shown in Figure 6.1. A qualitative observation of the velocity profiles, depicted by the normalised arrows, shows that, for all cases, both inlets and outlet flows are mainly in the vertical direction. Therefore, this result confirms that those boundaries have been defined sufficiently far from the jet; thus, the boundary conditions did not influence the formation of the jet.

6.4.1 Mass and energy conservation

Table 6.4 shows the time necessary to complete each simulation and the resulting ratios describing the conservation of mass and energy, as defined in Section 6.3.2, using either the detailed or the simplified model. The cases relative to sucrose using the detailed model show an average simulation time of 2.5 hours, and acceptable conservation of mass and energy (<5%), which is in accordance with the mesh selected in Appendix D.1.

Table 6.4: CFD simulation analysis: time required to completion and conservation ratios for total mass (R_{tot}), mass of organic compounds (R_{org}), and energy (R_{heat}).

Organic feed	Case	Detailed model				Simplified model			
		Simulation time (sec)	Conservation ratio			Simulation time (sec)	Conservation ratio		
			R_{tot}	R_{org}	R_{heat}		R_{tot}	R_{org}	R_{heat}
Sucrose	S1	10043	0%	0%	0%	181	0%	0%	0%
	S2	2638	0%	1%	0%	181	0%	0%	0%
	S3	6989	0%	2%	-1%	241	0%	-1%	0%
	S4	15348	0%	2%	0%	307	0%	0%	1%
	S5	8446	-1%	7%	0%	283	0%	1%	0%
DBE	D1	6241	0%	3%	9%	165	0%	0%	1%
	D2	17859	0%	3%	11%	190	0%	0%	0%
	D3	9934	0%	3%	13%	185	0%	0%	0%
	D4	6108	0%	4%	11%	184	0%	0%	0%
	D5	19752	0%	5%	9%	249	0%	0%	0%

On average, detailed simulations for the DBE cases took 55 minutes longer than those performed for sucrose. Both total and organic mass balances gave variations that were within expectations of numerical errors. On the other hand, significant positive deviations were observed in the enthalpic balance, resulting from downstream temperatures that were lower than expected had all the energy been conserved.

As shown in Section 6.2.2, the major difference between the models used for sucrose and DBE was in the material properties. In the sucrose cases, properties of pure water were used throughout, whilst the model for DBE combined properties for each species. The resulting differences affected the accuracy of the model's heat transfer calculations, resulting in temperatures lower than expected from the energy balance. This explanation is further supported by the fact that R_{heat} follows the increase of the relative amount of the organic feed from 33% to 45% in the reaction mixture. Furthermore, since no significant deviations were observed when using the simplified models, the lack of satisfactory conservation in the enthalpy appears to be a consequence of the widely varying properties in the mixing section.

Overall, it was observed that combining different thermodynamic properties significantly increased the model's complexity, resulting in longer simulation times and an energy unbalance, which was less conservative than might have been expected.

6.4.2 Recirculation zones

Figure 6.7 to Figure 6.10 present the temperature and total organic mass fraction profiles surrounding the SCW jet (*i.e.*, the jet and mixing sections listed in Table 6.2). The five temperature profiles from cases S1 to S5, show the formation of at least two recirculation areas: one located immediately to the right of the jet's outlet, and another in the region of cold fluid adjacent to the jet's wall. Comparing the profiles in Figure 6.7 and in Figure 6.8, the top swirl results only in temperature propagation, not affecting the distribution of solute molecules. In cases S4 and S5, this recirculation reaches as far as the outer wall, due to the SCW's higher temperature and flowrate ratio to the organic feed.

On the other hand, the recirculation zone at the jet's outlet affected not only temperature, but also the total organic mass fraction. It was a consequence of the convection caused by the SCW jet, responsible for the efficient mixing in the confined jet.

The results of case S3 showed a recirculation zone between the two mentioned above, which also contributed to the dissipation of mass and energy, but to a smaller extent when compared to the other recirculation areas. Unlike S3, the SCW in S1 and S2 was fed at a temperature below the supercritical transition temperature (SCTT = 386 °C), thus having liquid-like properties. Furthermore, for case S3, the organic feed composed 40% of the reaction mixture, while for S4 and S5 it was only 25%.

Figure 6.9 and Figure 6.10 show the profiles obtained for cases D1 to D5, which are based on DBE's hydrothermal reactions. Unlike sucrose, these profiles show less recirculation of fluid next to the jet wall. This absence can be attributed to DBE's thermal conductivity being lower than water's [107], which results in a smaller conductive heat transfer through the DBE when compared to water.

The recirculation area of dibenzyl ether-based cases at the jet's outlet was similar to the sucrose-based cases, particularly the ones where SCW was fed at higher temperatures (S3 to S5). On the other hand, the intermediate swirl occurred in more cases, only being absent in D3, which is the case with highest fraction of organic feed in the reactional mixture.

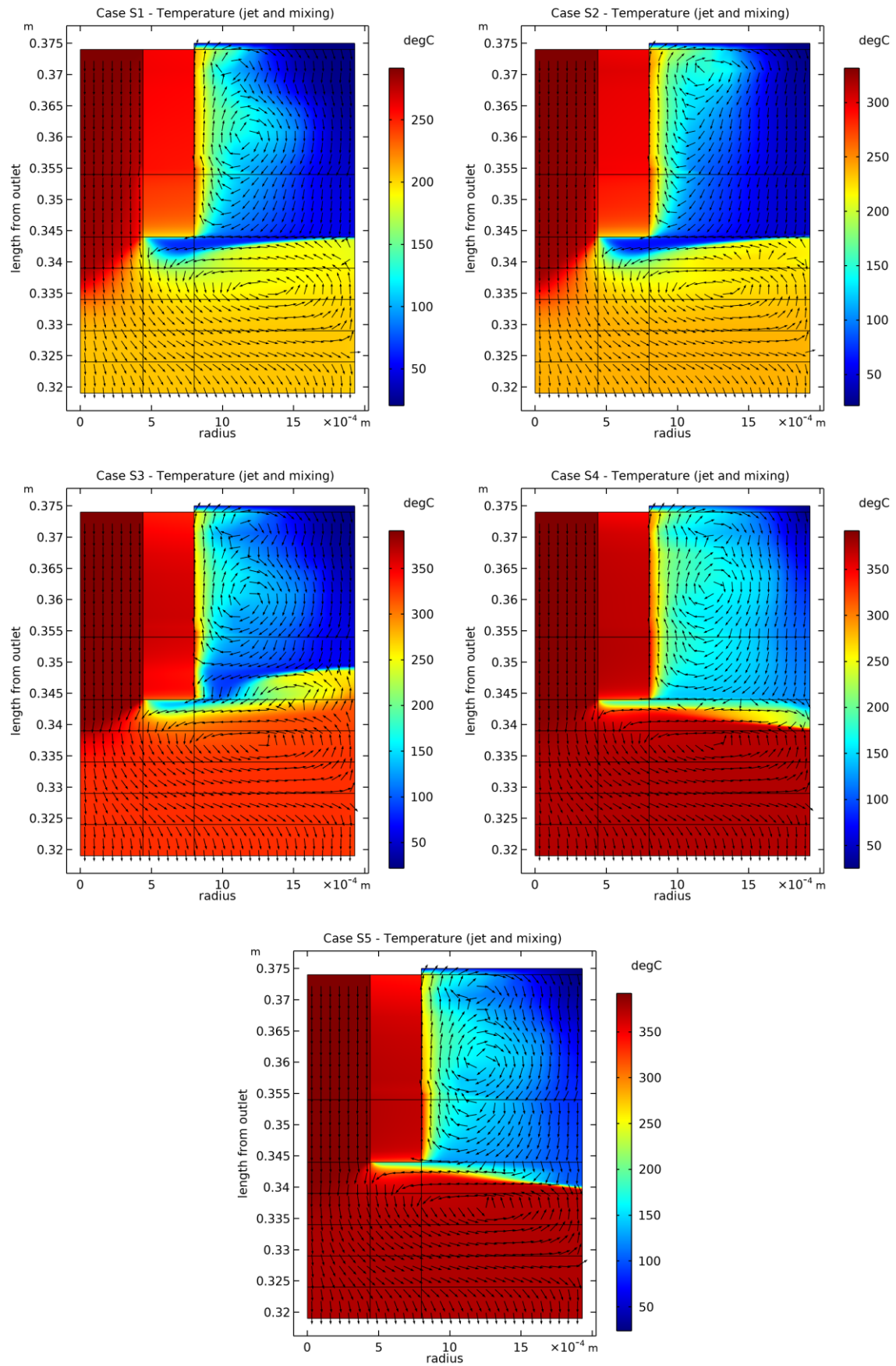


Figure 6.7: Temperature profile surrounding the SCW jet for sucrose simulations (scenarios S1 to S5). Velocity field is indicated by non-scaled arrows.

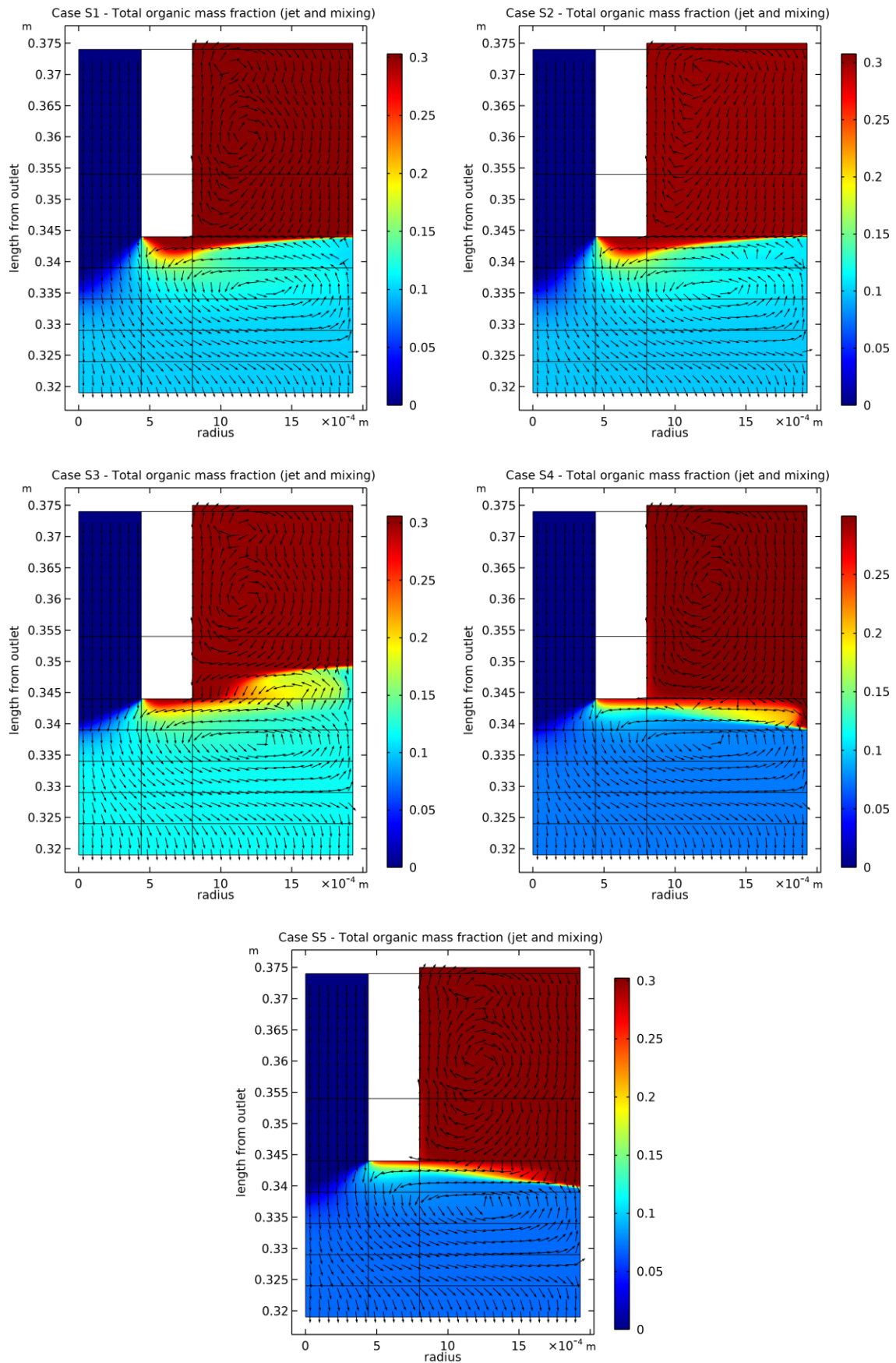


Figure 6.8: Total organic mass fraction profile surrounding the SCW jet for sucrose simulations (scenarios S1 to S5). Velocity field is indicated by non-scaled arrows.

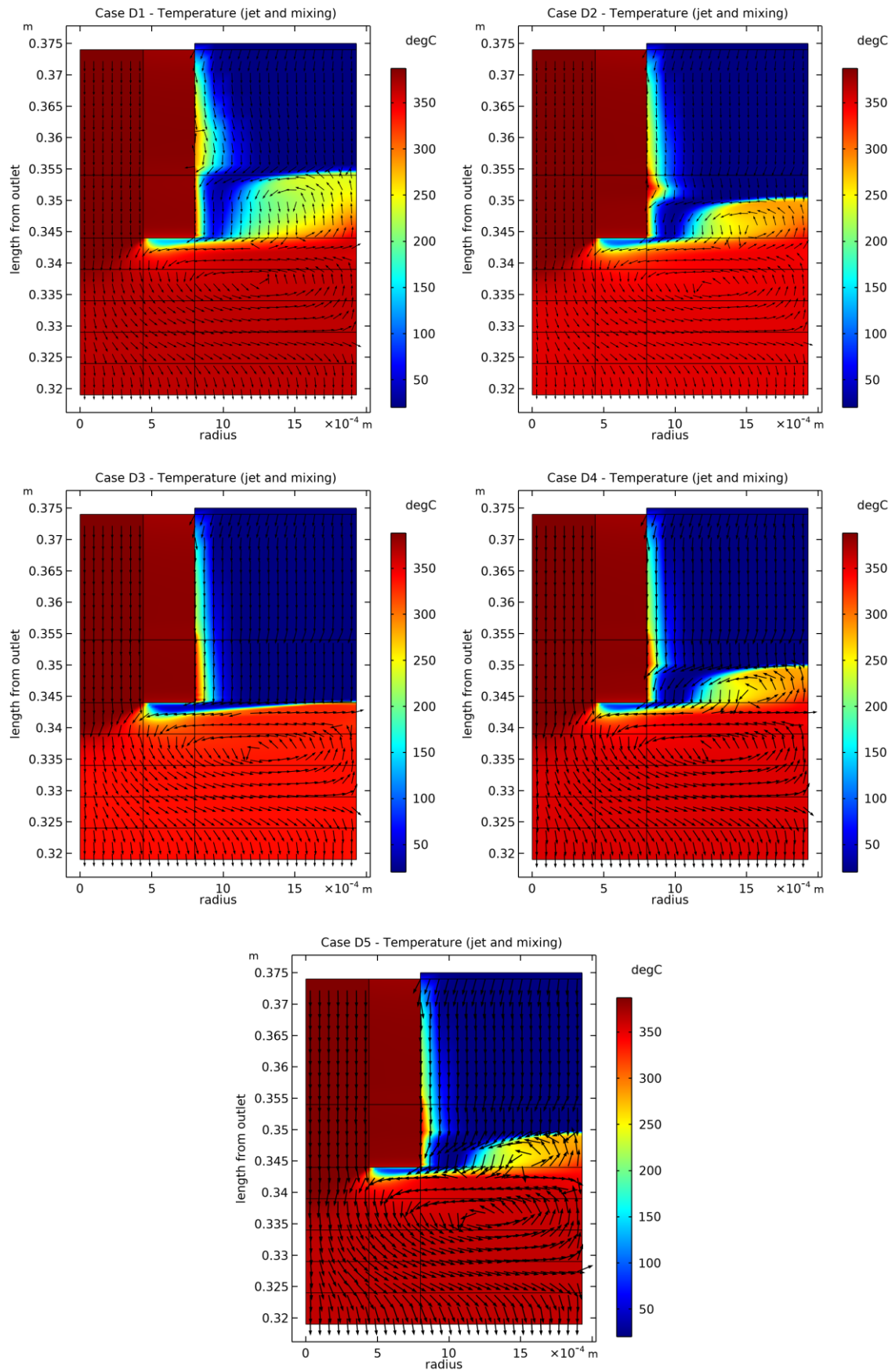


Figure 6.9: Temperature profile surrounding the SCW jet for DBE simulations (scenarios D1 to D5). Velocity field is indicated by non-scaled arrows.

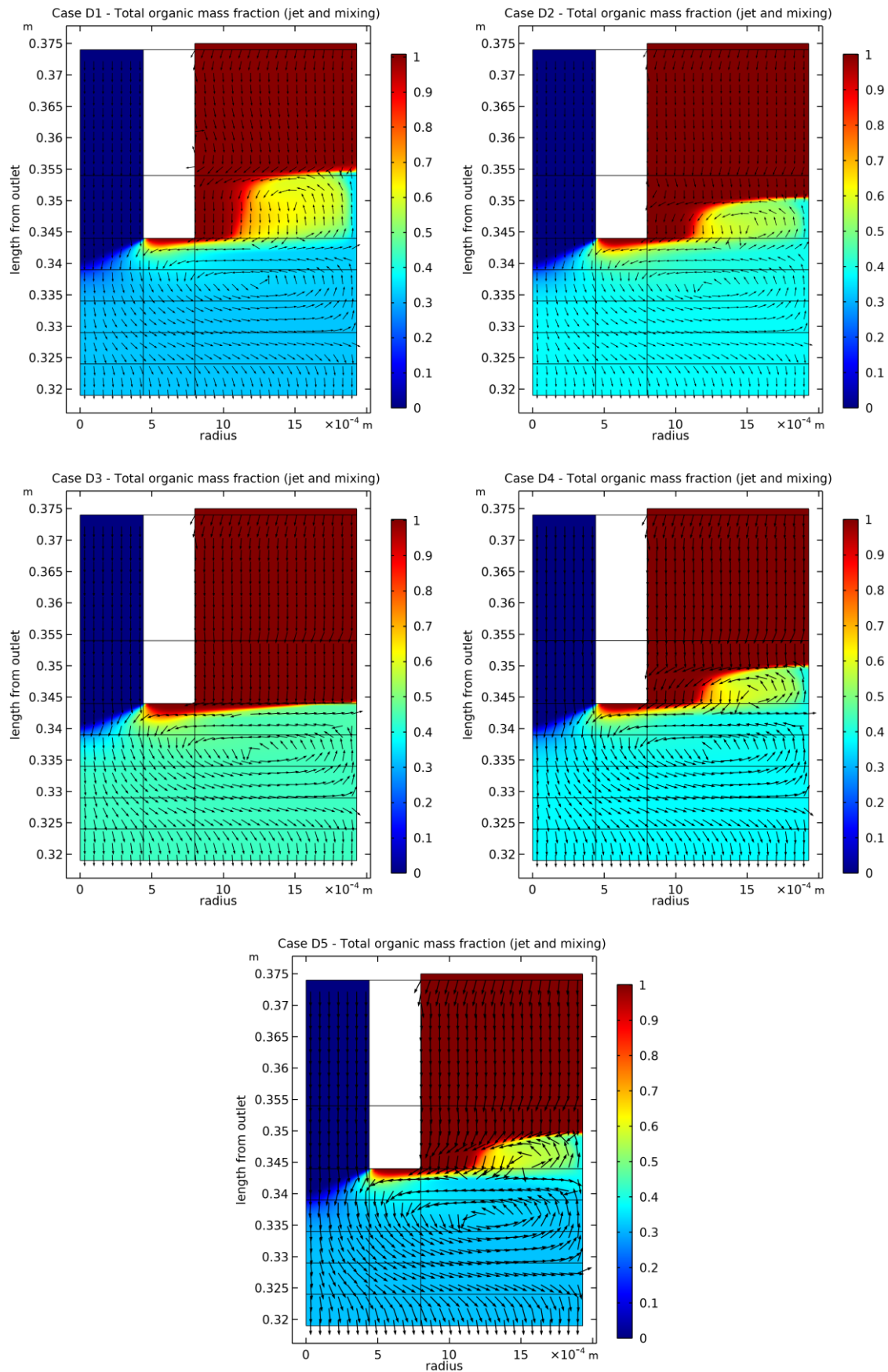


Figure 6.10: Total organic mass fraction profile surrounding the SCW jet for DBE simulations (scenarios D1 to D5). Velocity field is indicated by non-scaled arrows.

As mentioned in Section 6.2.3, the CFD turbulence model accounted for the effects of gravity and therefore buoyancy forces in the fluid. In reality, the confined jet mixer and downstream reactor were not strictly vertical as it was approximated in the CFD model. Therefore, gravity and buoyancy do not affect the system strictly as modelled. To test the consequences of the inaccurate consideration of gravity/buoyancy in the turbulent flow model, this was neglected in the simulation of two representative cases, S3 and D1. From those simulations resulted the profiles in Figure 6.11 and Figure 6.12, which show no recirculation zones around the jet's wall.

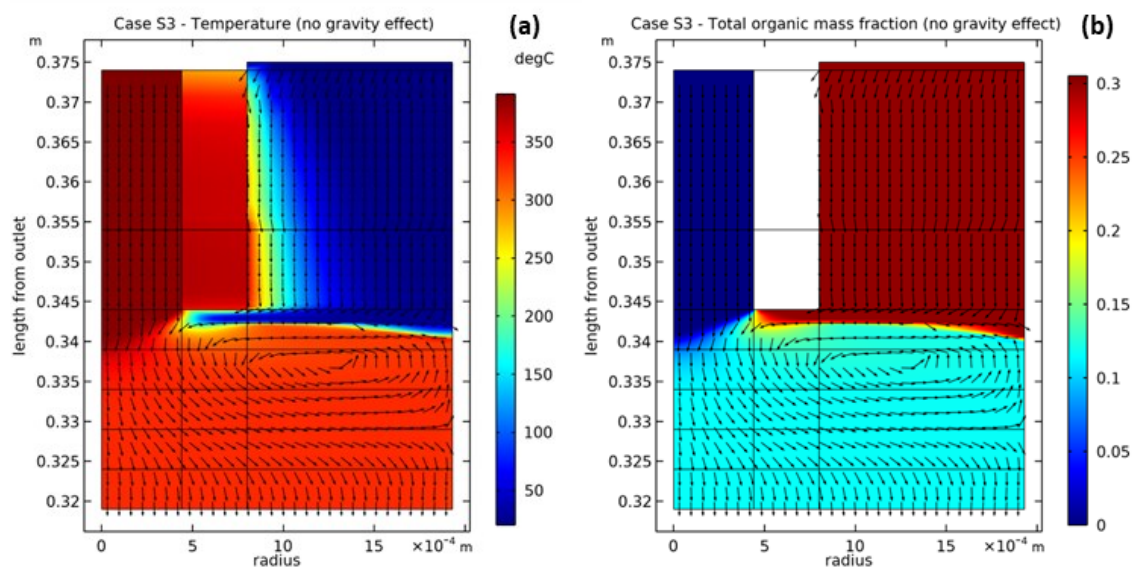


Figure 6.11: Temperature (a) and total organic mass fraction profiles (b) for case S3 neglecting gravitational effects.

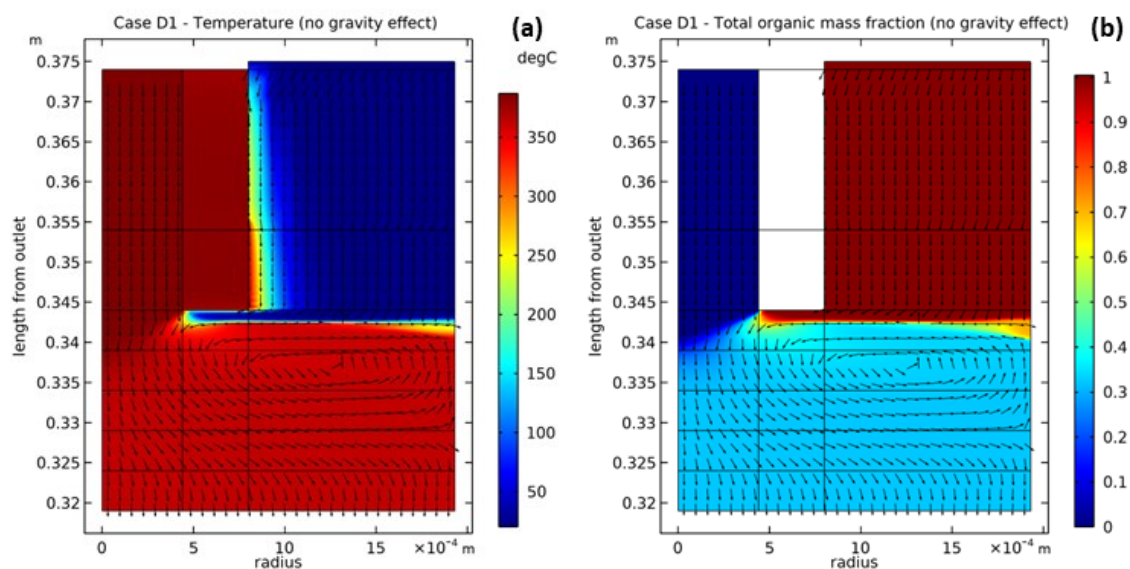


Figure 6.12: Temperature (a) and total organic mass fraction profiles (b) for case D1 neglecting gravitational effects.

This strongly suggests that those swirls were a consequence of the heat conducted across the jet wall, with the higher fluid temperature producing a buoyancy-driven recirculation. On the other hand, the recirculation zone at the jet's exit remained similar in all cases, being driven by the momentum of the jet. The effect of considering gravity on cases S3 and D1 was further evaluated using the model outputs presented in Table 6.5 and Table 6.6. Compared to the base cases, where gravity was considered, similar temperatures and yields are observed, thus showing the negligible effect of including gravitational effects in the model.

Table 6.5: CFD simulation outputs for case S3 considering and omitting the effect of gravity in the turbulent flow model.

Case	Model	Temperature (°C)		Yield (wt%)				
		TT-105	Outlet	Glucose	Fructose	TSO	Solids	Volatiles
S3	Considering gravity	320	306	8%	3%	73%	2%	14%
	Omitting gravity	320	307	8%	3%	73%	2%	14%

Table 6.6: CFD simulation outputs for case D1 considering and omitting the effect of gravity in the turbulent flow model.

Case	Model	Temperature (°C)		Conversion (%)	Y_{BAL} (mol%)
		TT-105	Outlet		
D1	Considering gravity	364	362	35%	65% ⁸
	Omitting gravity	363	361	35%	71%

6.4.3 Distance to achieve full mixing

The length required for the SCW jet to be fully mixed with the organic feed was evaluated using a mixing ratio (R_{mix}) as defined in equation (6.22). It consisted of the total organic mass fraction in each point divided by its average value at the reactor's outlet (*i.e.*, $z = 0$).

$$R_{mix}|_z = \frac{w_{org}|_z}{\left(\frac{\oint \int_0^{ID/2} w_{org} dr d\phi \Big|_{z=0}}{A_{CS}} \right)} \quad (6.22)$$

The mixture ratio profiles shown in Figure 6.13 and Figure 6.14 were discretised in sections, reflecting different degrees of mixing on each side of the jet. In those profiles the SCW feed is represented by the section with concentration below 90% (being in fact 0%). On the other hand, the organic feed is more concentrated than the outlet, being represented by the section above 100%.

⁸ BAL yield is smaller than twice the conversion due to mass balance inconsistency mentioned in Section 6.4.1.

It can be seen that, due to the recirculation mentioned above, from ~ 5 mm below the jet, there is only a small percentual difference in the mixing ratio of the liquid at the wall and that closer to the centre.

Table 6.7 summarises the distances required to achieve increasing degrees of mixing from 90 to 99.9% in each case. Two different reference points were considered: the outer tube inlet ($L_{reactor} = 0.354$ m from the outlet), and the jet's outlet ($L_{reactor} - L_{jet} = 0.344$ m from the outlet). The former was used for comparison with the simplified CFD and gPROMS models, showing that the space occupied by the jet in the outer tube represented up to 9% of what was defined as the reactor's total length. The latter criterion was equivalent to the criteria used in previous modelling work [137], indicating that 99.9% of the full mixture was achieved between 16 and 22 mm from the jet's outlet.

All the results from the DBE-based cases and sucrose cases S3 to S5 indicated that complete mixing was achieved within 16 mm of the jet's outlet. Comparing the case-specific parameters in Table 6.7, S1 and S2 have a noticeably lower T_{SCW} than the other cases. In fact, these are below water's SCTT at 250 bar, which is approximately 386 °C [55], suggesting that the water jet penetrates the organic feed at a low velocity, with liquid-like properties. Therefore, local density and resulting velocity are the key factors in defining the length required to disperse the organic phase in the water jet and thus achieving complete mixing.

This observation is in agreement with [137], which pointed that unlike the confined jet mixer, the counter-current reactor configuration resulted in a liquid-like jet, which led to a longer mixing distance; this mixing length was up to 7 times the jet's exit diameter (0.88 mm). For cases S3 to S5, and D1 to D5, the number of equivalent diameters was estimated to be 14 to 18, depending on whether complete mixing was defined as 99 or 99.9% of the outlet value. Nonetheless, the mixing length up to 7 times the jet's exit diameter stated in [137] was obtained at higher supercritical water temperatures (400 °C), which means smaller densities, and using the $k-\varepsilon$ turbulence model. The model developed in this study applies the $k-\omega$ turbulence model, which is more suited for modelling radial jets [205].

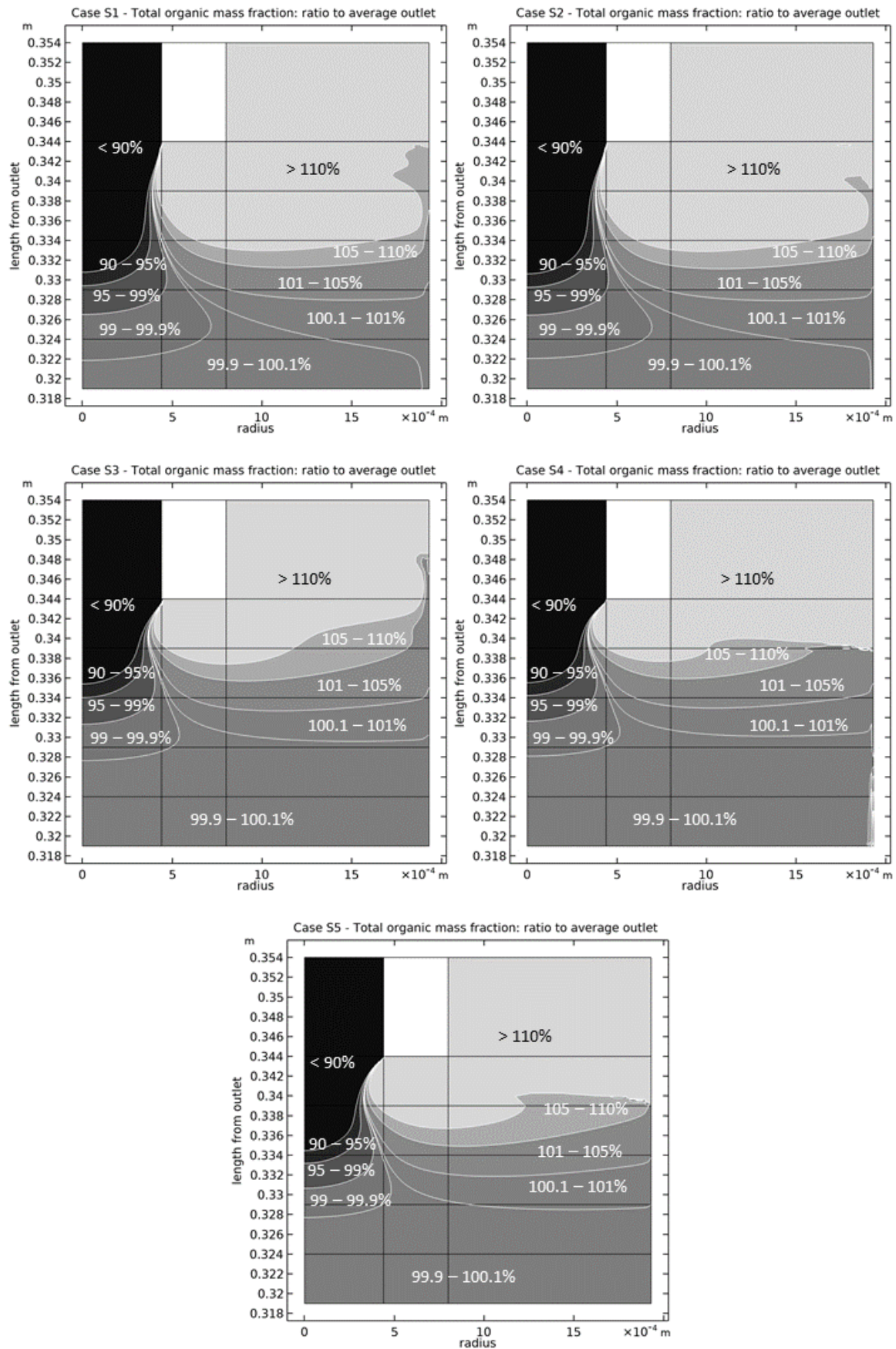


Figure 6.13: Discretised profiles showing fraction of total mixture surrounding the SCW jet for sucrose simulations (S1 to S5).

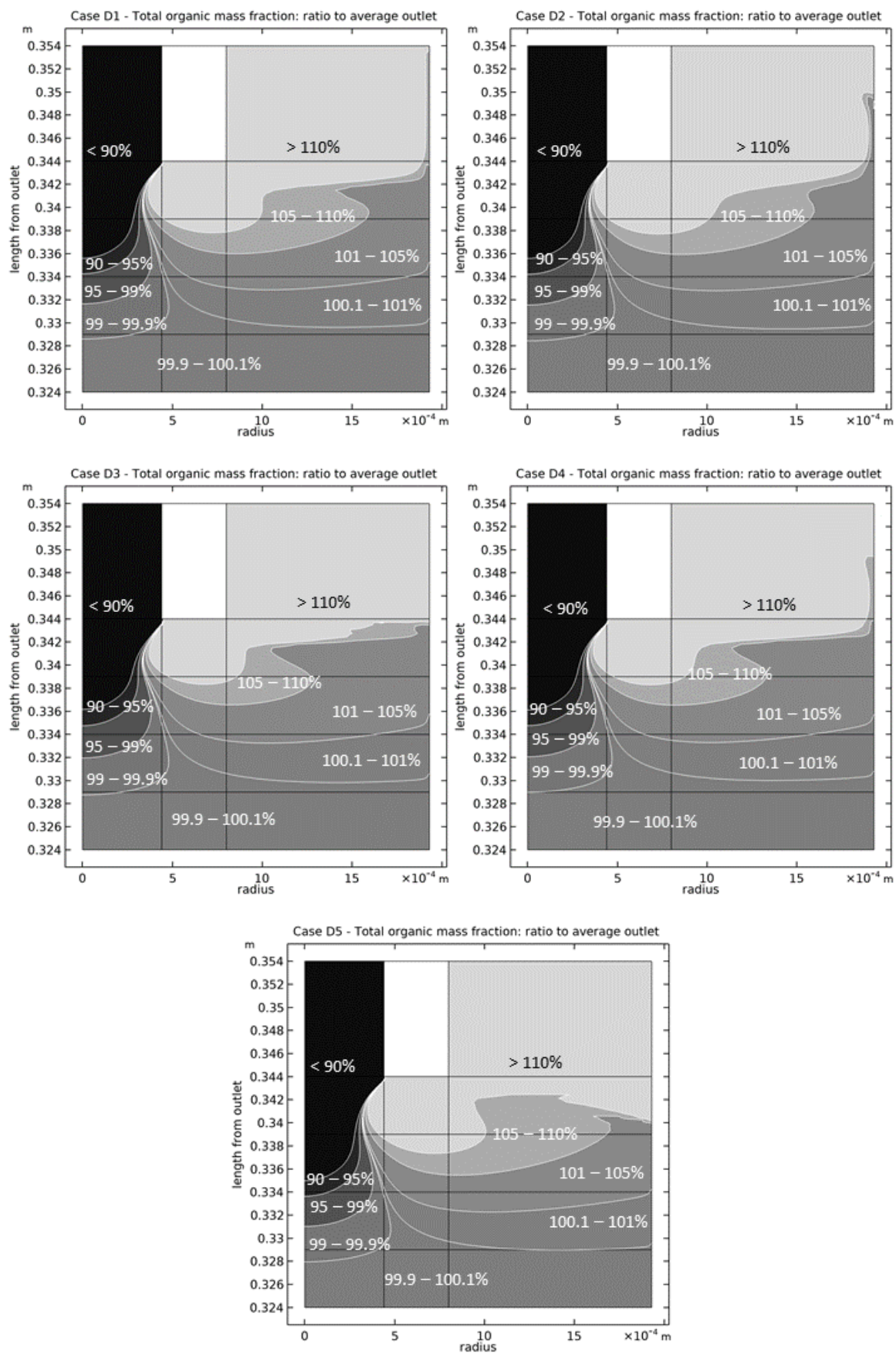


Figure 6.14: Discretised profiles showing fraction of total mixture surrounding the SCW jet for DBE simulations (D1 to D5).

Table 6.7: Distance required to achieve R_{mix} from 90 to 99.9% and related parameters for all cases.

Parameter	R_{mix}	Sucrose cases					DBE cases				
		S1	S2	S3	S4	S5	D1	D2	D3	D4	D5
Distance from outer tube inlet (mm)	90%	23	24	18	18	20	18	18	18	18	19
	95%	24	25	20	20	21	20	20	19	19	20
	99%	28	28	22	22	23	22	22	22	22	23
	99.9%	32	32	26	26	26	26	26	25	25	26
Distance from outer tube inlet (% of total length)	90%	6%	7%	5%	5%	6%	5%	5%	5%	5%	5%
	95%	7%	7%	6%	6%	6%	6%	6%	5%	5%	6%
	99%	8%	8%	6%	6%	6%	6%	6%	6%	6%	6%
	99.9%	9%	9%	7%	7%	7%	7%	7%	7%	7%	7%
Distance from jet outlet (mm)	90%	13	14	8	8	10	8	8	8	8	9
	95%	14	15	10	10	11	10	10	9	9	10
	99%	18	18	12	12	13	12	12	12	12	13
	99.9%	22	22	16	16	16	16	16	15	15	16
Distance from jet outlet (Number of jet ID's)	90%	15	16	9	9	11	9	9	9	9	10
	95%	16	17	11	11	13	11	11	10	10	11
	99%	20	20	14	14	15	14	14	14	14	15
	99.9%	25	25	18	18	18	18	18	17	17	18
Flowrate (g/min)	Q_{FO}	10	13	11	7	9	9	11	16	14	14
	Q_{SCW}	20	26	16	20	26	17	16	20	21	28
w^{in}_i (wt%)		10%	10%	12%	8%	8%	33%	39%	45%	39%	33%
Temperature (°C)	T_{SCW}	291	331	391	392	392	387	387	388	388	387
	T_{mix}	207	240	330	375	376	367	354	343	357	370

6.5 Comparison between detailed and simplified CFD models

The second objective of modelling the confined jet mixer through CFD was evaluating the effect of omitting the mixing zone. For that the simplified model described in Section 6.2.8 was applied to the same cases in Table 6.3, and the outputs compared with the detailed model.

The time required to complete each simulation in Table 6.4 shows that the simplified model was significantly less computationally demanding, with each simplified simulation taking less than 5 minutes instead of 2 to 3 hours for the detailed model. Furthermore, it was observed that mass and energy balances were always closed when the simplified model was used.

To investigate whether the simplified model could be used instead of the detailed one, the performance of the two models was compared using the average temperature at TT-105's location and at the reactor's

outlet, as well as each component's molar yields, as defined in Appendix E.1 and Appendix F.1, for DBE and sucrose, respectively. Those values are summarised Table 6.8 and Table 6.9.

Table 6.8: Temperatures and yields obtained from sucrose-based CFD simulations (Table 6.3), using detailed and simplified models.

Case	Model	Temperature (°C)		Yield (wt%)				
		TT-105	Outlet	Glucose	Fructose	TSO	Solids	Volatiles
S1	Detailed	198	189	47%	49%	4%	0%	0%
	Simplified	198	189	47%	49%	4%	0%	0%
S2	Detailed	232	225	43%	42%	15%	0%	0%
	Simplified	232	223	43%	42%	15%	0%	0%
S3	Detailed	320	306	8%	3%	73%	2%	14%
	Simplified	319	305	7%	3%	73%	2%	14%
S4	Detailed	368	357	1%	2%	30%	1%	66%
	Simplified	368	358	1%	2%	29%	1%	68%
S5	Detailed	371	363	2%	8%	41%	1%	49%
	Simplified	370	363	2%	7%	40%	1%	50%

Table 6.9: Temperatures, conversion, and yield obtained from DBE-based CFD simulations (Table 6.3), using detailed and simplified models.

Case	Model	Temperature (°C)		Conversion (mol%)	Y _{BAL} (mol%)
		TT-105	Outlet		
D1	Detailed	364	362	35%	65%
	Simplified	365	363	31%	63%
D2	Detailed	359	360	44%	80%
	Simplified	361	362	40%	79%
D3	Detailed	349	358	40%	74%
	Simplified	356	361	36%	73%
D4	Detailed	359	361	35%	63%
	Simplified	362	363	30%	61%
D5	Detailed	364	363	24%	44%
	Simplified	368	366	16%	32%

For sucrose-based simulations, nearly identical temperatures and yields were obtained from the detailed and simplified models. The maximum variations were ± 1 °C and $\pm 2\%$, which are well within the experimental uncertainty of this work (table F.5 in Appendix F.3).

The comparisons in Table 6.9 indicate larger differences when comparing the detailed and simplified models applied to dibenzyl ether instead of sucrose. A maximum absolute difference of 8% was obtained for conversion in case D5, which is higher than typical experimental error (Table E.2 in Appendix E.3). Given that only one reaction was implemented in those models, the yield of BAL should

be exactly twice the value of conversion, which is not observed in the detailed model, reflecting the relatively poor closing of the mass balance, previously described, and shown in Table 6.4.

The temperatures in Table 6.9 also differ significantly, by up to 7 °C in case D3, which was the case with largest discrepancies in the energy balance. In fact, the temperatures derived from the detailed model were always below the ones from the simplified version. This is consistent with the positive values of R_{heat} , which can be interpreted as the system's energy content decreasing more than expected, resulting in lower temperatures. For typical reactions, lower temperatures lead to a decrease in reaction rates [180]. However, as presented in Section 2.1.1, that may not be the case for acid- or base-catalysed reactions, due to water's self-ionisation product decreasing as it approaches the SCTT (Figure 2.4).

Therefore, the observed increase in DBE's conversion from the simplified to the detailed model may be attributed to the temperature decrease, due to mass and energy imbalances. Given the accurate performance of the simplified model for sucrose, and the similarities between their mixing profiles in Figure 6.13 and Figure 6.14, the variation in the conversion of DBE between the simplified and detailed models is not a consequence of omitting the mixing zone.

Based on the good agreement between the simplified and detailed models using sucrose as solute, it can be concluded that neglecting the mixing zone in the confined jet mixer did not significantly affected the model's results. Therefore, it is an acceptable approximation, further demonstrating that the confined jet mixer produces rapid and complete mixing of mass and energy between the SCW and organic streams, and significantly simplifying the analysis of the experiments.

6.6 Concluding remarks

This chapter focused on developing a detailed CFD model that reproduced the confined jet mixer with sufficient accuracy, in terms of hydrodynamics, as well as heat and mass transfer, to establish whether assumptions used in analysing the experimental measurements were valid. The model was applied to ten cases representative of the experiments conducted during this study. The conclusions were as follows:

The discretisation mesh for the mixer was defined through successive refinements. This aimed at accurately representing the system, ensuring conservation of mass and energy, whilst avoiding onerous computation times. For simulations relating to sucrose (cases S1 to S5), deviations in the calculated mass and energy balances only exceeded 5% in one case (S5). For dibenzyl-based cases (cases D1 to D5), significant deviations (ranging from 9 to 13%) were observed in the heat balance, which were attributed to the calculation of mixture properties and large variation in physical properties within the mixing zone.

A larger refinement of the discretisation mesh is expected to improve the model's energy balance, particularly in simulations considering different component properties. However, this would require more computational power than was available for this project.

The length of the SCW jet was established by comparing the local organic mass fraction with average outlet value. All cases with supercritical water feed (S3 to S5, and D1 to D5) reached over 99.9% of the outlet mass fraction within 16 mm of the jet's outlet. This represented 7% of the reactor's total length, and 18 times the jet's inner diameter. This value is higher than the 7 times quoted in literature [137], which was attributed to the different turbulence model.

The developed CFD model was based on the $k-\omega$ turbulence model [205], widely recommended for turbulent jets, component specific properties, and simplified, yet temperature-dependent, reaction kinetics. Nonetheless, this was not directly compared against experimental data. Validation against experimental measurements is recommended, similar to the ones in literature [137,139,192].

Cases with water feed in subcritical conditions (S1 and S2) required a larger length of 22 mm to reach the same degree of mixing. The jet's density and therefore velocity resulting from a specified mass flowrate was important, with lower densities and high velocities resulted in shorter mixing lengths.

The detailed model of the confined jet mixer was compared against a simplified modelled, which omitted the mixing zone. For simulations relating to sucrose, no significant difference was observed in temperature downstream of the mixing point, and in product yields.

For cases using dibenzyl ether, the detailed model showed significantly higher conversion and lower temperatures. This was attributed to the lack of closure of the energy balance, which always closed in the simplified model.

It can be concluded that omitting the mixing zone in the confined jet does not significantly affect the accuracy of a model representing the entire reactor. Furthermore, this justifies the assumption used in the analysis of experimental measurements, that mixing is very rapid when using the confined jet mixer, and consequently the region around the supercritical water jet does not need to be considered.

Chapter 7

Kinetics of the hydrothermal processing of dibenzyl ether

7.1 Introduction

The present chapter focuses on the reaction of dibenzyl ether (DBE), a model compound representative of the R-O-R bonds in lignin, in a hydrothermal environment. It characterises the performed experiments, followed by a critical analysis of the observed yields. Next, it presents the deduction of rate equations considering different hydrolysis mechanisms, and the respective kinetic parameters estimated based on the experimental results. Finally, the likelihood of each mechanism is discussed based on how well the associated parameters fit the measured data.

7.1.1 Background

Lignin is a complex biopolymer with a significantly variable nature. Information fully describing its hydrolysis mechanism is rare and relies on model compounds [47]. Even though, there is no guarantee that conclusions retrieved from model compounds are applicable to actual lignin, it helps to identify intermediaries and which operating conditions are not effective in breaking the polymer's most frequent structures [74]. The aromatic compounds shown in Figure 7.1 are considered to represent the ether bonds in the lignin polymer, and their behaviour in hydrothermal medium [149,207]. For this study, dibenzyl ether (DBE) was selected as a model compound of lignin, since it is a liquid at room conditions, unlike the other two ethers [208]. Therefore, the organic feed does not necessarily need to be diluted in water, which would be a problem, given the negligible solubility of these three ethers in water [133].

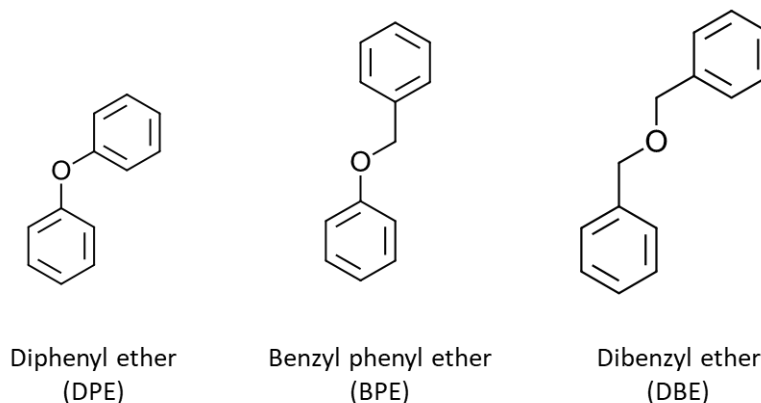
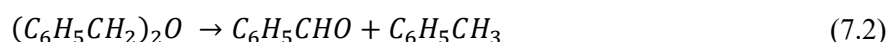
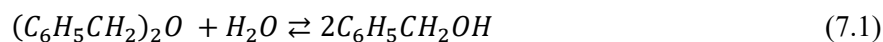


Figure 7.1: Molecular representations of diphenyl ether (DPE), benzyl phenyl ether (BPE) and dibenzyl ether (DBE).

Table 7.1: Summary of recent work on dibenzyl ether's hydrothermal degradation.

Year	Reactor type	Conditions	Kinetic model summary	Main conclusions	Ref.
1985	Micro (batch) reactor	374 - 412 °C 1 - 60 min	Pyrolysis and hydrolysis reactions. Products polymerise.	Hydrolysis and thermolysis reactions occur simultaneously. The first produces benzyl alcohol, while the last produces benzaldehyde and toluene. Hydrolysis is favoured in hydrothermal media and is up to two orders of magnitude quicker. For longer reaction times, polymer formation is observed.	[209]
1988				Solvent density affects the medium polarity and hydrolysis rate. Higher densities stabilise this reaction's polar intermediates.	[210]
1992	SS autoclave	374 - 380 °C ~270 bar 30 min	Hydrolysis is a function of the dielectric constant (ϵ).	Addition of NaCl increased the hydrolysis rate. Pyrolysis rate affected by using a new SS reactor. Hydrolysis rate in the order of 10^{-4} mol.L ⁻¹ .s ⁻¹ .	[211]
1997	Micro (batch) reactor	390 - 415 °C 275 - 365 bar 30 - 180 min	Reversible hydrolysis. Main products decomposition.	Product behaviour analysed at 400 °C. BAL yields DBE, suggesting its hydrolysis is reversible. BZA produces mainly benzene, associated to CO release (conversion: 20% at ~60 min). TOL tends to dimerise (Conversion: 50% at ~200 min). $Ea_{hydrolysis} = 112$ kJ/mol. $Ea_{pyrolysis} = 120$ kJ/mol.	[212]
2005	Continuous	325 - 390 °C 225 - 362 bar 3 - 50 sec	Reversible hydrolysis. BAL decomposition. Acid catalysis.	At subcritical temperatures, pressure increase promotes hydrolysis marginally. At supercritical temperatures, increasing pressures reduces reaction rates, but improves BAL selectivity. Only longer reactions (up to 50 sec) support reversible hydrolysis. BZA and TOL concentrations remain similar. Pyrolysis appears to be non-ionic, and the rate tends to decrease with increasing density. $Ea_{hydrolysis} = 160$ kJ/mol. $Ea_{degradation} = 170$ kJ/mol. $Ea_{pyrolysis} = 80$ kJ/mol.	[149]
2008	Micro (batch) reactor	250 °C 60 min	Hydrolysis rate considers an alternative pathway with water as catalyst.	Acid catalysis isn't enough to describe the hydrolysis pathway for different pH. A rate constant expression that accounts for both proton and water catalysis is proposed.	[213]

A review of the literature regarding dibenzyl ether's hydrothermal degradation is summarised in Table 7.1. Existing studies, based on both batch [210–213] and continuous experiments [149], divide the hydrothermal degradation of this molecule ($(C_6H_5CH_2)_2O$) in hydrolysis and pyrolysis, represented by equations (7.1) and (7.2), respectively:



The first reaction results from dibenzyl ether's interaction with water, producing two benzyl alcohol ($C_6H_5CH_2OH$, or BAL) molecules. The second is DBE's cleavage due to high temperature, producing equimolar amounts of benzaldehyde (C_6H_5CHO , or BZA) and toluene ($C_6H_5CH_3$, or TOL). The same studies also indicate a predominance of hydrolysis products over pyrolysis.

Besides dibenzyl ether, BAL, BZA and TOL are susceptible to further thermal degradation, which have also been individually analysed in literature [212]. It was demonstrated that in supercritical conditions, benzaldehyde is consumed more quickly, mainly producing benzene and carbon monoxide. The same study also refers to the reversibility of the hydrolysis reaction. Nonetheless, a more recent study, based on continuous experiments, proposes that reversibility is only relevant for residence times over 50 seconds [149] *i.e.*, much longer than the maximum of 7 seconds investigated in this study.

Apart from reversibility, studies [149,211,213] also indicate that the hydrolysis reaction tends to be influenced by water's changing properties around the critical point.

7.1.2 Objectives

This study was primarily aimed at demonstrating the suitability of the continuous confined jet reactor for hydrothermal upgrading of lignin, using a model compound, dibenzyl ether, under sub-critical conditions. Furthermore, the analysis of the reactor's effluent was used to estimate kinetic parameters using the mathematical model described in Chapter 4, and to elucidate the most likely mechanism of DBE's hydrolysis.

7.2 Experimental setup

The hydrolysis of dibenzyl ether was conducted in the hydrothermal liquefaction rig described in Section 3.3, following the procedure in Section 3.4, at high pressure (245-254 bar at the outlet) and temperature (295-360 °C at the reactor thermocouple, TT-105). The supercritical feed consisted of de-ionised water heated above its critical point. Since dibenzyl ether has negligible solubility in water [133], initial experiments aimed at producing emulsions of this organic, that could be used as feed. These resulted in procedure 1 in Table 7.2. The emulsions tested with 2 wt% of DBE in water (and no

additional emulsifiers) did not remain mixed for the required time, resulting in unreliable measurements. Therefore, the organic feed consisted of 100% DBE in all analysed experiments.

The experiments described in this chapter required some of the organics detailed in Table 3.1 of Section 3.2. As mentioned above, DI water and DBE were used as process feeds. The expected products, benzyl alcohol (BAL), benzaldehyde (BAL), and toluene (TOL), were required to calibrate the analytical methods. Finally, acetonitrile was used as the HPLC mobile phase, and to dilute the liquid samples.

The products of DBE's hydrothermal degradation were distributed between two liquid phases and a gas phase. The separation of the gas phase followed the procedure described in Section 3.5.2. The outlet mixture collected in a 2 L bottle was continuously bubbled with nitrogen, allowing an online measurement of vapour products. This analysis was conducted in the Fourier-transform infrared (FTIR) spectrometer described in Section 3.6.7. Measured species included small amounts of carbon monoxide, carbon dioxide, water, methane, ethane, formaldehyde, acetaldehyde, methanol, ethanol, benzene, and toluene. The moment steady state was reached in the reactor following introduction of the organic feed could be identified using these gas measurements. Ideally, liquid samples would be taken after a clear stabilisation of the measured gas composition. However, given the time constraint imposed by the limited volume in the syringe pump providing the organic feed, a complete steady state was not always achieved, as demonstrated by the plots in Section 7.3.1. Nonetheless, liquid samples were always collected typically around 13-15 minutes after the organic feed was started, which was significantly after the initial increase in gas concentration, when only small variations were observed in the gas phase composition. From this point, the collection outlet was switched from the glass bottle to liquid sampling, and at least two liquid samples were collected for analysis.

Separation of the two-phase liquid samples is described in Section 3.5.3, consisting of centrifuging the liquid sample, and two-step extraction with a syringe. Composition analysis was conducted through high-performance liquid chromatography (HPLC) with ultraviolet-visible (UV-vis) detection as detailed in Section 3.6.1 and Section 3.6.2.

7.2.1 Progress summary

Defining the correct operation of the hydrothermal rig when processing dibenzyl ether was a stepwise approach. The study progressed over three stages as more information was obtained regarding operating conditions and product analysis. Those stages are summarised in Table 7.2. The results reported in this chapter consisted predominantly of experiments in the last procedure (3.0), along with three experiments from the previous one (2.2).

Table 7.2: Progress summary during the study of dibenzyl ether's hydrothermal degradation.

Procedure	1	2.0	2.1	2.2	3.0
Feed	2 wt% DBE in water	100 wt% DBE			
Reactor length	80 mm			354 mm	
Quench	50 mL/min	60 mL/min			
Heater setpoint	Fixed (460 °C)				Variable (415 - 500 °C)
Temperature	Preliminary experiments	Estimated from equivalent experiments			Measured
Rig sample	~ 5 g	~ 125 g			
Liquid analysis	No phase separation. Sample diluted in acetonitrile up to 85wt%.	See Section 7.3.2.			
Gas analysis	Not applied.			See Section 7.3.1.	
Key findings	Inconsistent results. Poor knowledge of residence time. Back-calculated inlet composition different from initial dilution. Toluene not found in diluted cases. Small sample size may lead to non-significant results.	Required time for steady state ~13 min. Small conversions (10-13%). High variability in aqueous phase analysis. Difficulties in closing mass balance. Twice the amount of benzaldehyde compared to toluene.	Consistent aqueous phase measurements. BZA/TOL ratio remained similar (small yield increase). Difference is insignificant within standard deviation between experiments.	DBE conversion and BAL yield agree with residence time increase. BZA and toluene concentration remained similar. Difference to closed mass balance increased. TOL detected in gas products.	Non-isothermal behaviour observed in the reactor. Conversion and BAL yield general increase with temperature. Maximum observed as it approaches the SCTT. Small BZA and TOL yields with insignificant variations.
Following steps	Re-evaluate residence time. Increase sample size and include phase separation. Focus on pure feed.	Improve aqueous phase handling.	Achieve more significant conversions by increasing reactor length.	Include "Others" in the mass balance. Implement continuous temperature measurement. Study the temperature effect at constant inlet composition (only changing heater set point).	Estimate overall heat transfer coefficient estimated. Remove BZA and TOL from model. Estimate kinetic parameters.

7.2.2 Operating conditions

A total of 15 experiments were performed under the conditions displayed in Table 7.3. Three combinations of supercritical water and organic feed flowrates were considered. These resulted in flowrate ratios of 1.2, 1.5, and 2, corresponding to dibenzyl ether mass fractions at the reactor's inlet (w_{DBE}^0) between 33 and 45 wt%. For each combination, different supercritical heater setpoints were selected, leading to different temperatures profiles across the reactor. Those variations are shown in Table 7.3 by the temperature measured at the reactor thermocouple (TT-105). Finally, a quench of 60 mL/min was used in all cases, and pressure was maintained at 250 bar.

Table 7.3: Experimental conditions for DBE hydrothermal degradation: feed nominal flowrate, DBE mass fraction at the reactor's inlet (w_{DBE}^{in}), pressure, and temperature.

Exp	Nominal flowrate (mL/min)			w_{DBE}^{in} (wt%)	Pressure (bar)	Temperature (°C)		
	SCW	Organic	Quench			Setpoint	At TT-102	At TT-105
1	16	8	60	33 ± 1	250	415	369	301
2	16	8	60	33 ± 1	250	420	372	321
3	16	8	60	33 ± 1	250	430	375	342
4	16	8	60	33 ± 1	252	430	378	349
5	16	8	60	33 ± 1	252	430	378	349
6	16	8	60	33 ± 1	247	460	385	358
7	15	10	60	40 ± 1	251	425	374	314
8	15	10	60	40 ± 1	247	438	377	334
9	15	10	60	40 ± 1	248	460	385	344
10	15	10	60	40 ± 1	246	500	412	360
11	16	12.5	60	43 ± 2	254	438	381	333
12	15	12.5	60	45 ± 2	248	420	372	295
13	15	12.5	60	45 ± 2	250	438	376	318
14	15	12.5	60	45 ± 2	245	460	384	332
15	15	12.5	60	45 ± 2	250	500	412	350

Table 7.4 gives the actual mass flowrate in the reactor, accounting for the SCW pump calibration and densities at operating pressure and room temperature. The same table also shows the expected temperatures for the reactor's inlet and outlet, assuming a linear profile, the estimated overall heat transfer coefficient ($46 \text{ W}\cdot\text{m}^{-2}\cdot\text{K}^{-1}$), and the kinetic parameters from scenario 5 (derived in Section 7.5). Temperature drops over the reactor were estimated to be between 16 and 25 °C, with the maximum temperature never exceeding the SCTT at the inlet conditions, thus showing that the mixture had liquid-like properties. Table 7.4 also gives the average residence time, ranging from 5 to 7 seconds, which was calculated using density at measured temperature and pressure, and inlet composition.

Table 7.4: Flowrates, temperature boundaries, and residence time for each DBE hydrothermal degradation experiment.

Exp	Reactor feed flowrate (g/min)	Predicted temperature (°C)				Average Residence time (s)
		Inlet	Outlet	Difference	SCTT	
1	25.9 ± 0.6	311	290	21	386	7
2	25.9 ± 0.6	332	308	24	386	7
3	25.9 ± 0.6	353	329	24	386	6
4	25.9 ± 0.6	359	336	23	386	6
5	25.9 ± 0.6	359	336	23	386	6
6	25.9 ± 0.6	367	346	21	385	6
7	27.0 ± 0.6	324	303	22	388	7
8	27.0 ± 0.6	345	321	23	387	6
9	27.0 ± 0.6	354	331	23	387	6
10	27.0 ± 0.6	368	348	20	386	6
11	30.7 ± 0.7	343	322	21	391	7
12	29.6 ± 0.6	302	287	16	390	6
13	29.6 ± 0.6	328	307	20	390	6
14	29.6 ± 0.6	342	320	22	389	5
15	29.6 ± 0.6	359	338	21	390	6

7.3 Product analysis

Two or more samples were collected during each experiment at least 13 minutes after the organic feed was started. Their composition was evaluated as a molar yield (Y_i in mol_{*i*}/mol_{DBE}%), *i.e.*, the molar amount of each compound per mole of dibenzyl ether fed to the reactor. Appendix E contains a summary of these yields' calculations from experimental data.

The values presented for each experiment result from averaging the ones obtained for all related samples, with associated uncertainties estimated as described in Section 3.7. Both sample-specific and experiment-averaged values are also included in Appendix E.

The flowrate of liquid products was quantified by dividing the mass of each sample by the respective collection time (typically 90 seconds). The rate of gas production was defined as the difference between the inlet flowrate (both feeds) and the one of liquid products. These results, as well as each liquid phase flowrate, are included in Table 7.5.

7.3.1 Gas phase

As reported in Table 7.5, the calculated gas flowrate was negligible based on the uncertainty in measurements of liquid flowrate. Therefore, although some gaseous species were identified by the on-line FTIR measurements, they were only a negligible fraction of the products produced.

Table 7.5: Flowrate distribution between inlets and products for each DBE hydrothermal degradation experiment.

Experiment	Inlet flowrate (g/min)		Product flowrate (g/min)			
	Reactor	Reactor and quench	Liquid	Gas	Aqueous phase	Organic phase
1	25.9 ± 0.6	91 ± 2	91 ± 1	0 ± 2	82.8 ± 0.9	7.6 ± 0.1
2	25.9 ± 0.6	91 ± 2	91 ± 1	0 ± 2	83.4 ± 0.9	7.1 ± 0.1
3	25.9 ± 0.6	91 ± 2	91 ± 1	0 ± 2	83.5 ± 0.9	7.2 ± 0.1
4	25.9 ± 0.6	91 ± 2	91 ± 1	0 ± 2	84.0 ± 0.9	6.7 ± 0.1
5	25.9 ± 0.6	91 ± 2	91 ± 1	0 ± 2	84.2 ± 0.9	6.2 ± 0.1
6	25.9 ± 0.6	91 ± 2	90 ± 1	2 ± 2	82.5 ± 0.9	6.7 ± 0.1
7	27.0 ± 0.6	92 ± 2	92 ± 1	1 ± 2	82.1 ± 0.9	9.1 ± 0.1
8	27.0 ± 0.6	92 ± 2	92 ± 1	0 ± 2	82.5 ± 0.9	8.9 ± 0.1
9	27.0 ± 0.6	92 ± 2	91 ± 1	1 ± 2	82.0 ± 0.8	8.9 ± 0.1
10	27.0 ± 0.6	92 ± 2	92 ± 1	0 ± 2	83.0 ± 0.9	9.0 ± 0.1
11	30.7 ± 0.7	96 ± 2	95 ± 1	1 ± 2	84.0 ± 0.9	10.9 ± 0.1
12	29.6 ± 0.6	95 ± 2	95 ± 1	0 ± 2	82.3 ± 0.9	11.9 ± 0.1
13	29.6 ± 0.6	95 ± 2	95 ± 1	0 ± 2	83.9 ± 0.9	10.4 ± 0.1
14	29.6 ± 0.6	95 ± 2	95 ± 1	0 ± 2	82.6 ± 0.9	11.5 ± 0.1
15	29.6 ± 0.6	95 ± 2	95 ± 1	0 ± 2	82.8 ± 0.9	11.5 ± 0.1

The spectrometer continuously recorded the outlet gas composition during an experiment. From the measured species listed in Section 3.6.7, carbon monoxide, benzene, and toluene presented the largest concentrations. These measurements are plotted in Figure 7.2, Figure 7.3, Figure 7.4, and Figure 7.5 for twelve of the performed experiments (experiments 6, 9, and 14 were performed earlier, without this type of analysis).

In each plot, two vertical bars were included per experiment, with each experiment identified sequentially by a different colour (blue, red, and green). The first vertical bar of each experiment, with longer dashes, indicates the minute when the organic feed was initiated. The second vertical bar, with shorter dashes shows the minute when the first sample was collected.

In all cases, it was observed that the measured components track the reaction's progress, *i.e.*, their concentration increased when the organic feed was initiated. The presence of carbon monoxide and benzene is in line with previous studies, which refer them as benzaldehyde's main degradation products [212].

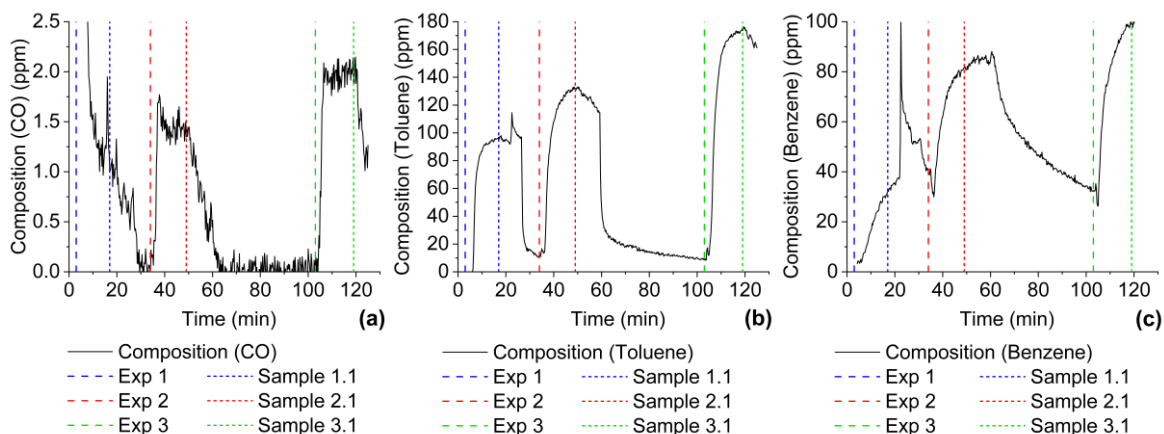


Figure 7.2: Compositions of CO (a), toluene (b), and benzene (c) measured in the FTIR analyser during experiments 1, 2, and 3. Each experiment is represented sequentially by two vertical bars. First vertical bar (long dashed) signals the minute when the organic feed was initiated. Second vertical bar (short dashed) signals the minute when the first liquid sample was collected.

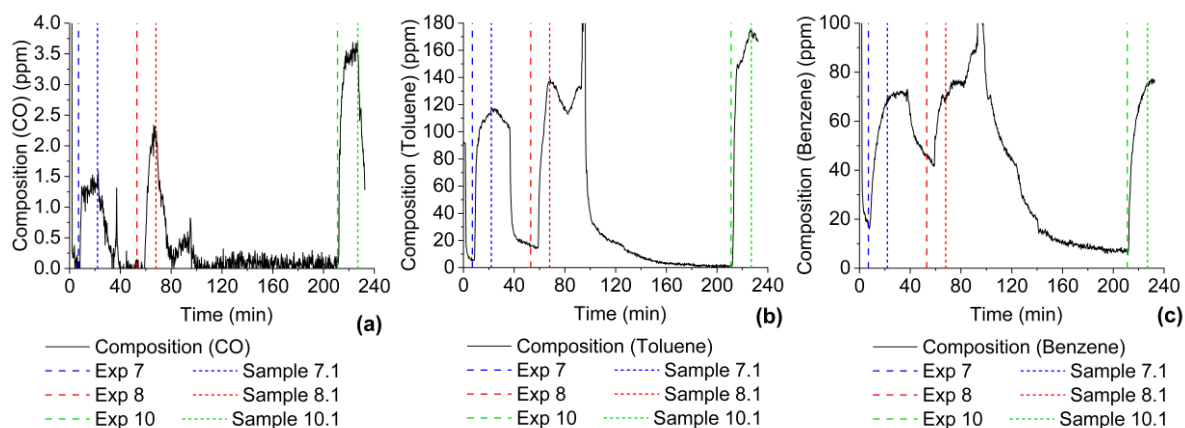


Figure 7.3: Compositions of CO (a), toluene (b), and benzene (c) measured in the FTIR analyser during experiments 7, 8, and 10. Each experiment is represented sequentially by two vertical bars. First vertical bar (long dashed) signals the minute when the organic feed was initiated. Second vertical bar (short dashed) signals the minute when the first liquid sample was collected.

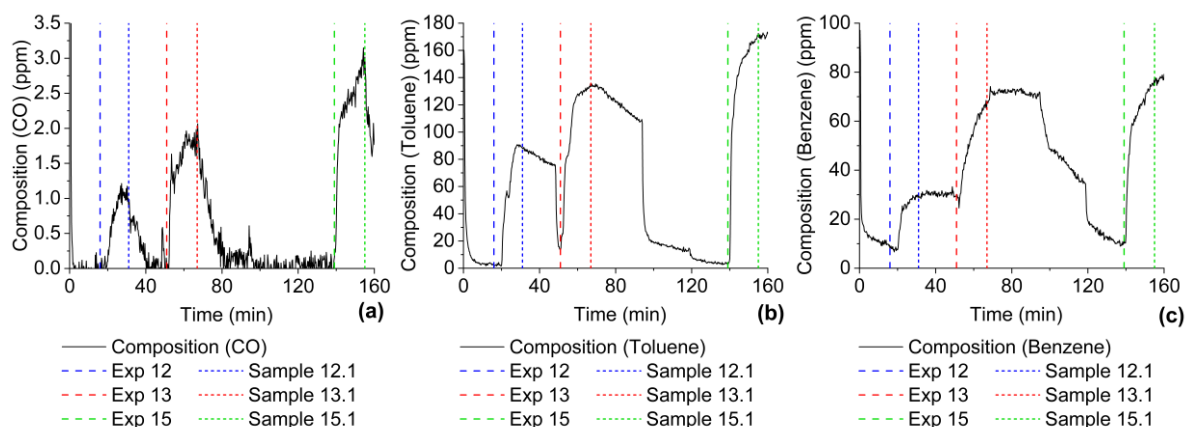


Figure 7.4: Compositions of CO (a), toluene (b), and benzene (c) measured in the FTIR analyser during experiments 12, 13, and 15. Each experiment is represented sequentially by two vertical bars. First vertical bar (long dashed) signals the minute when the organic feed was initiated. Second vertical bar (short dashed) signals the minute when the first liquid sample was collected.

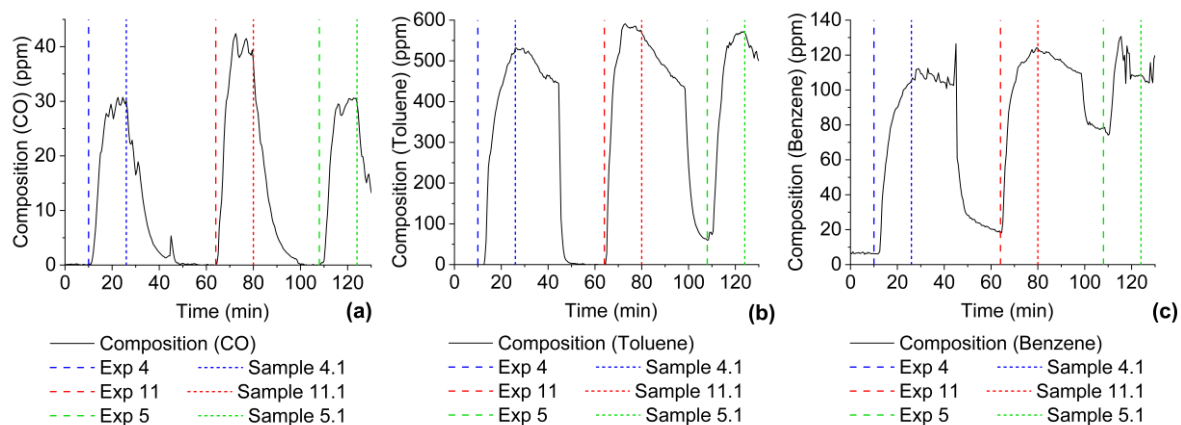


Figure 7.5: Compositions of CO (a), toluene (b), and benzene (c) measured in the FTIR analyser during experiments 4, 11, and 5. Each experiment is represented sequentially by two vertical bars. First vertical bar (long dashed) signals the minute when the organic feed was initiated. Second vertical bar (short dashed) signals the minute when the first liquid sample was collected.

7.3.2 Liquid phase

The liquid product consisted of a colourless liquid mixture divided in two distinct phases, exemplified in Figure 7.6. Given dibenzyl ether's higher density compared to water and negligible solubility in it [107], the bottom phase was the organic one.

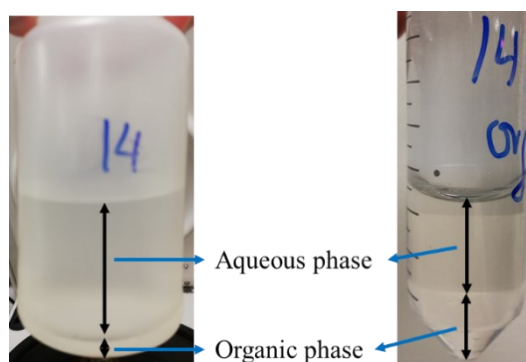


Figure 7.6: Phase separation in a DBE degradation liquid sample after centrifuging. On the left, before the first extraction of aqueous phase, and on the right, before the second extraction.

The relative amount of the organic phase remaining after the reaction was calculated by dividing the organic flowrate in Table 7.5 by the reactor's inlet flowrate in Table 7.4 (equations (E.7) and (E.8) in Appendix E.1); thus, not include water from the quench. Its variation with temperature, residence time, and feed mass fraction is plotted in Figure 7.7. All values are lower than the initial fraction, *i.e.*, the fraction of DBE at the reactor's inlet, thus indicating the formation of water-soluble products. Unfortunately, the high uncertainty associated with these values does not allow further conclusions

regarding the influence of temperature or residence time on the fraction of organic phase remaining after the reaction.

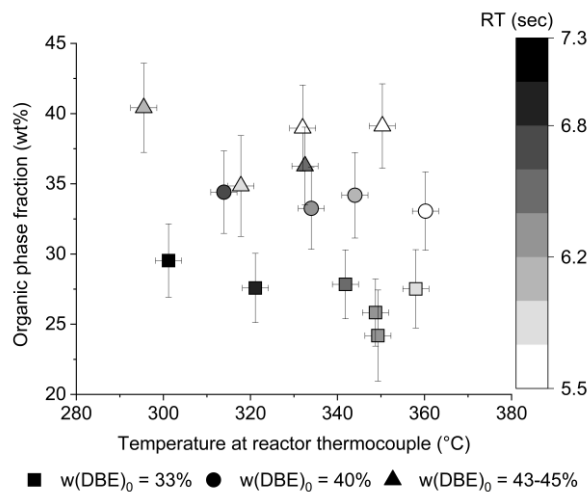


Figure 7.7: Variation of organic phase mass fraction with measured temperature, residence time (RT), and inlet composition.

Examples of the chromatograms obtained through HPLC with UV-vis detection for aqueous and organic phase samples are presented in Figure 7.8. Dibenzyl ether and toluene solely appear in the first chromatogram, which corresponds to the bottom phase, thus confirming it as the organic phase. The presence of DBE in this example, and all experiments indicates that it was not fully converted; thus, allowing the measurement of reaction kinetics. Benzyl alcohol and benzaldehyde were found in both phases, because of their partial solubility in water at room temperature [214]. Furthermore, the presence of additional peaks in the organic phase chromatogram demonstrates the existence of reactions in addition to (7.1) and (7.2), which mainly produced water-insoluble compounds.

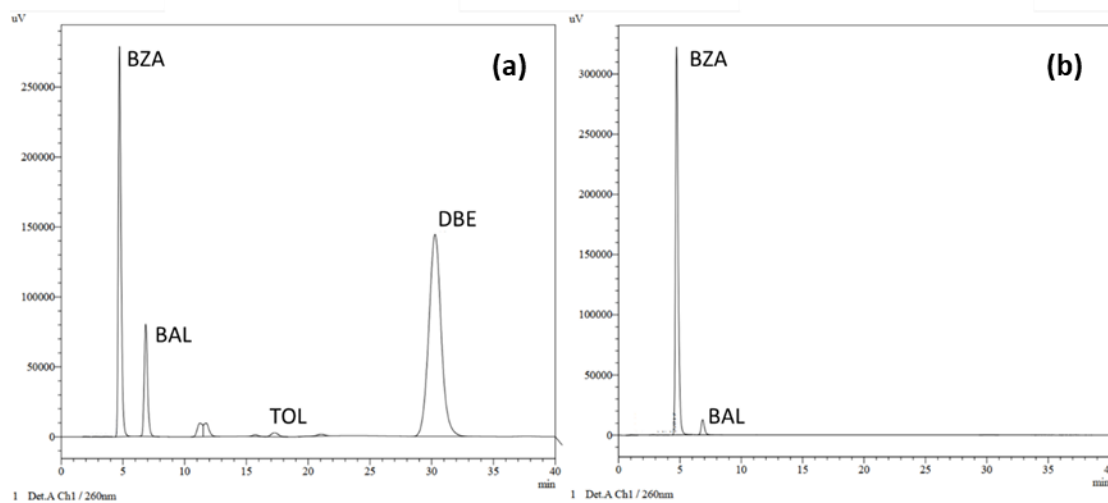


Figure 7.8: Organic (a) and aqueous (b) phases chromatograms from HPLC with UV-vis detection (Experiment 8).

The typical range of mass fractions observed for each component is summarised in Table 7.6. These show that unreacted dibenzyl ether accounts for most of the organic phase. As observed in existing literature [149,209,212], the product formed in the largest quantity was benzyl alcohol, while benzaldehyde and toluene were found in considerably smaller amounts.

Table 7.6: Range of observed mass fraction in each phase and overall.

Species	Mass fraction range (%)		
	Organic	Aqueous	Overall
Dibenzyl ether	54 – 94	-	4 – 12
Benzyl alcohol	5 – 40	1 – 3	1 – 6
Benzaldehyde	0.2 – 2	0.002 – 0.06	0.02 – 0.2
Toluene	0.1 – 0.8	-	0.01 – 0.08

The flowrate of the measured components at the reactor's outlet, was calculated using the compositions and relative amount of each phase. Since the feed concentration was varied between experiments, these flowrates were expressed as conversion and specific molar yields relative to the inlet molar amount of DBE ($\text{mol/mol}_{\text{DBE}}\%$); their variation with temperature, residence time (RT), and inlet composition ($w(\text{DBE})_0$) is plotted in Figure 7.9 and Figure 7.10.

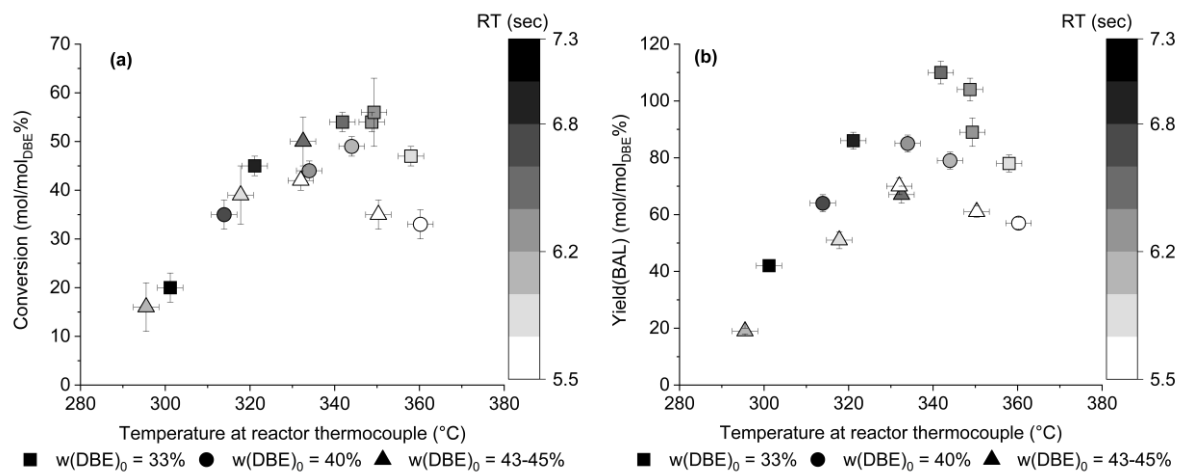


Figure 7.9: Variation of dibenzyl ether conversion (a) and benzyl alcohol yield (b) with measured temperature, residence time (RT), and inlet composition.

In Figure 7.9 b), the yield of BAL reached values above 100%, being higher than the conversion of DBE in Figure 7.9 a) for equivalent experiments. This was related to the stoichiometry of the hydrolysis reaction shown in equation (7.1), since a molecule produces twice the amount of BAL. Therefore, if all DBE reacted to produce BAL, conversion would be 100% and the yield of BAL would be 200%.

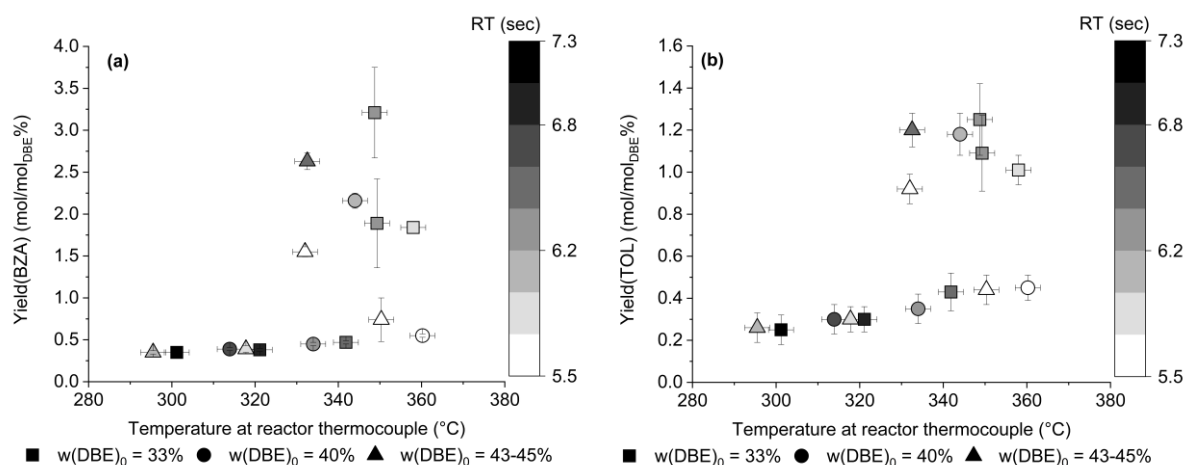


Figure 7.10: Variation of benzaldehyde (a) and toluene (b) yields with measured temperature, residence time (RT), and inlet composition.

7.3.3 Hydrolysis products

Figure 7.9 (a) and (B) show that below 330 °C, conversion and benzyl alcohol yield increased almost linearly with temperature, as expected for a single step first order reaction. Between 330 and 350 °C, both reach a maximum after which they decrease appreciably. A similar pattern was suggested by the increasing residence time. On the other hand, both measurements tend to decrease for higher inlet concentrations.

Benzyl alcohol's degradation to other products at high temperatures would explain the observed maximum in the respective yield. However, this would not cause the maximum in dibenzyl ether's conversion, unless less benzaldehyde and toluene were produced, which is not the case. Therefore, this is not a sufficient explanation. On the other hand, several literature sources indicate that the hydrolysis of dibenzyl ether is expected to be affected by the availability of free protons in the mixture [149,211,213]. Accordingly, the proton concentration was calculated for each experiment using equation (4.25) in Section 4.6, at the pressures and reactor temperatures in Table 7.3. The proton concentration is plotted in Figure 7.11 (a); this shows a nearly linear decrease with increasing temperature, with an almost four-fold reduction over the analysed range. Therefore, the decrease in protons available for reaction counteracts the expected rate increase due to temperature, which likely explains the observed maxima.

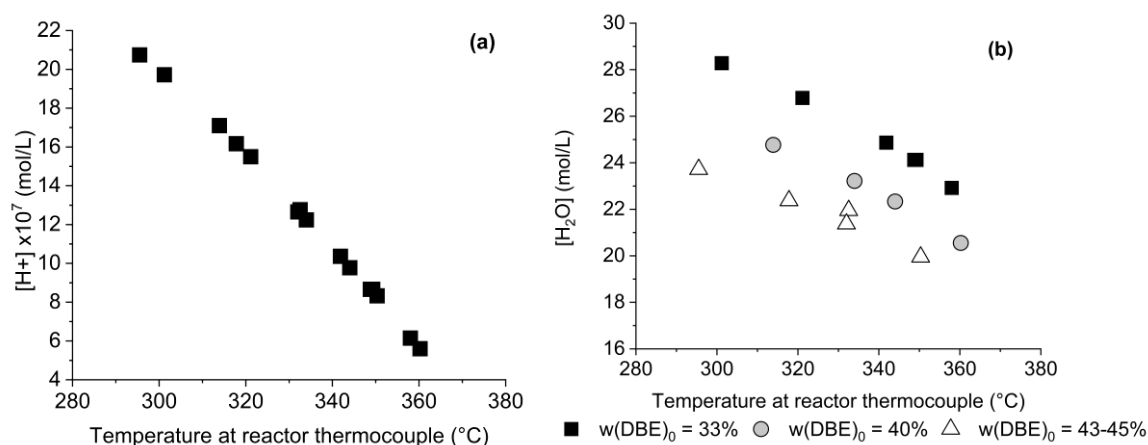


Figure 7.11: Proton (a) and water (b) concentrations estimated for performed experiments.

Water was in great excess in the reaction mixture (55% on a mass basis is equivalent to 93% on a molar basis), thus the effect of the concentration of water in the reaction kinetics within an experiment is expected to be negligible. On the other hand, increasing DBE's mass fraction between experiments was estimated to reduce water's concentration by 16 to 18%, as shown in Figure 7.11 (b). If water participates in the hydrolysis reaction, reducing its concentration could explain the reduction of conversion and alcohol yield between experiments at similar temperatures, as observed in Figure 7.9.

From this analysis, it is proposed that dibenzyl ether's hydrolysis rate is affected by the proton concentration, which decreases with increasing temperature, and by the concentration of water in each experiment. These effects were accounted for in a subsection of the rate equations proposed in Section 7.4.1, and tested using mathematical modelling in Section 7.5.

7.3.4 Pyrolysis products

The molar yields of benzaldehyde and toluene were less than 5% of the initial number of moles of dibenzyl ether. Such small values are in line with experiments found in literature using similar residence times and temperatures [149]. If only pyrolysis (reaction 7.2) and hydrolysis (7.1) occurred, the molar amounts of benzaldehyde and toluene would be the same and equal to the amount of DBE that reacted, less the amount that formed benzyl alcohol produced, *i.e.*, $DBE_0 - (DBE + BAL / 2)$. As plotted in Figure 7.12, the latter was consistently higher than the yields of BZA and TOL, even considering the large uncertainty. Further degradation of hydrolysis and pyrolysis products would explain the observed difference. Nonetheless, there was no evidence to indicate which of these species if any was degraded. Existing literature refers to benzaldehyde being more reactive than benzyl alcohol or toluene under hydrothermal conditions [212], thus it is likely that this molecule was the source of most of the undetected species. The presence of carbon monoxide and benzene among the gas products, indicates

that these were formed in the reactor. The latter would likely be found in the organic phase if identified. Since these are the main products of hydrothermal degradation of benzaldehyde, it also explains the extended degradation of this molecule.

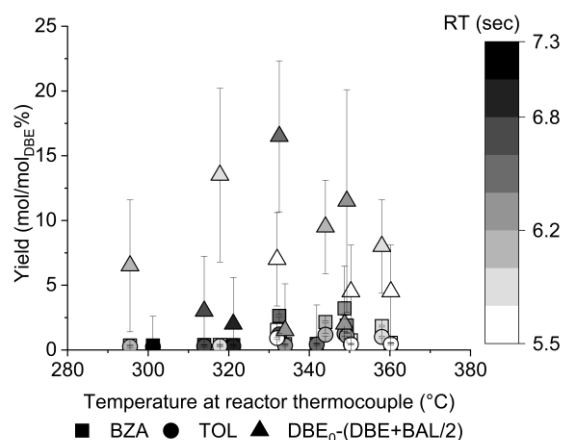


Figure 7.12: Yield comparison between benzaldehyde, toluene and reacted dibenzyl ether except benzyl alcohol.

Although this argument explains the lower-than-expected amount of benzaldehyde in the liquid samples, it does not explain why it still appeared to be higher than the amount of toluene. With reference to reaction (7.2), both components are expected to be produced in equimolar amounts [149,209,211,212]. However, comparing both yields in Figure 7.10, this was not observed, with the aldehyde showing up in larger amounts. The reason behind this difference may be the evaporation of the more volatile components. The vapour pressures for the different compounds at near ambient temperatures are shown in Figure 7.13. Toluene is considerably more volatile than DBE, BAL and BZA. Consequently, it is possible that the pyrolysis products were indeed formed in equimolar amounts, but a larger amount of toluene evaporated, compared to benzaldehyde, during collection, dilution, or sample preparation.

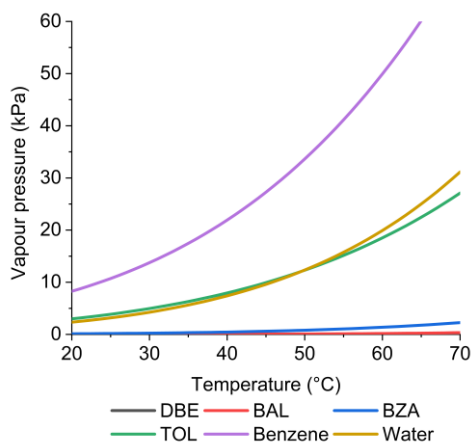


Figure 7.13: Vapour pressures of DBE, BAL, BZA, TOL, benzene, and water vs. temperature [107].

Figure 7.10 and Figure 7.12 show that benzaldehyde and toluene yields appear to increase slightly with temperature when below 330 °C and are independent of inlet concentration. However, a wider scatter of values was observed at higher temperatures, with no evident trend. All experiments were performed under equivalent conditions, but not all in the same campaign. The experiments which appeared to produce higher yields of BZA and TOL were performed several months before from the remaining experiments, which were all conducted within the same week. This raises the possibility that the variation in thermal degradation products at such a small yield (less than 5% of the initial amount of DBE) may be due to losses during the workup of the products for analysis, rather than an effect of the reaction conditions. These losses would be expected to be relatively smaller for species with higher yields, such as benzyl alcohol, but would affect species produced in smaller amounts, as the case of the pyrolysis products.

7.4 Kinetic modelling

The degradation of dibenzyl ether in subcritical water was simulated using the reactor model described in Chapter 4. Input specifications included the reactor's geometry and operating conditions. The modified properties calculation model was applied to a list of all known molecules, with benzyl alcohol serving as the lumping components for unknown species. Heat losses to the environment were accounted using the overall heat transfer coefficient estimated specifically for DBE. Dispersion was included through the correlations described in Section 4.7. The default kinetic model was modified to accommodate rate equations with more than one observable kinetic constant, as shown in Section 7.4.1.

7.4.1 Rate equation for the hydrolysis of dibenzyl ether

The hydrolysis reaction was modelled according to different reaction mechanisms and respective rate equations, as described in the following section. The reversibility of this reaction was not included, as similar studies demonstrated that it was irrelevant for residence times in the order of a few seconds or less [149]. Though generically described by equation (7.1), several authors have proposed that the hydrolysis of dibenzyl ether occurs through nucleophilic substitution, thus comprising more than one elementary step [149,211,213,215]. Earlier studies proposed a bimolecular mechanism (S_N2) [211,215], while recent ones proposed a unimolecular substitution (S_N1) step [149,213]. Both mechanisms were considered in this study and presented in this section. The detailed deduction of the respective reaction rates is included in Appendix E.4.

Regardless of the substitution type, those studies consider that both pathways are preceded by an initial step, where dibenzyl ether is protonated (Figure 7.14).

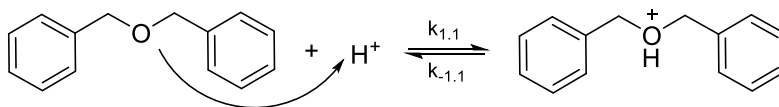


Figure 7.14: Step 1.1 of the reaction mechanism for the hydrolysis of DBE (reaction 1) via S_N1 and S_N2 mechanisms.

If this is assumed to be the rate limiting step, the hydrolysis rate (r_1) is given by equation (7.3), which is commonly found in literature [149,213].

$$r_1 \approx r_{1.1} = k_{obs,1}[DBE][H^+] \quad (7.3)$$

Unimolecular nucleophilic substitution (S_N1) is favoured when the ether group is sterically hindered. In literature, this was considered for diphenyl ether [216] and assumed to be applicable to the less hindered dibenzyl ether [149]. As represented in Figure 7.15 and Figure 7.16, the mechanism proceeds via two steps, 1.2 and 1.3. The first consists of the carbocation scission, being followed by the addition of a water molecule [217].

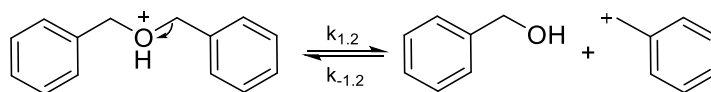


Figure 7.15: Step 1.2 of the reaction mechanism for the hydrolysis of DBE (reaction 1) via S_N1 mechanism.

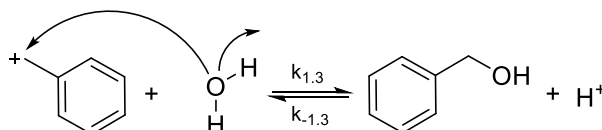


Figure 7.16: Step 1.3 of the reaction mechanism for the hydrolysis of DBE (reaction 1) via S_N1 mechanism.

Considering a steady-state approximation to the intermediate consumed in step 1.2, and that this step is irreversible and rate limiting [218], the obtained rate equation is equivalent to (7.3), *i.e.*, first order in $[DBE]$ and $[H^+]$ (derivation is in Appendix E.4.2).

On the other hand, if step 1.3 is considered rate limiting then equation (7.4) is obtained (derivation is in Appendix E.4.2), where $k_{obs,1.1}$ and $k_{obs,1.2}$ are the observed kinetic constants⁹.

$$r_1 \approx r_{1.3} \approx \frac{k_{obs,1.1}[DBE][H^+][H_2O]}{k_{obs,1.2}[BAL] + [H_2O]} \quad (7.4)$$

⁹ The designation $k_{obs,1.1}$ and $k_{obs,1.2}$ is not directly related to reaction steps 1.1 and 1.2. Instead, it indicates that both observed kinetic constants are related to reaction 1, *i.e.*, hydrolysis.

If bimolecular nucleophilic substitution (S_N2) is assumed [211,215], the scission occurs in a single step, as shown in Figure 7.17 [217,219].

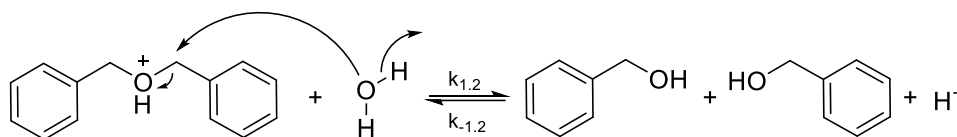


Figure 7.17: Step 1.2 of the reaction mechanism for the hydrolysis of DBE (reaction 1) via S_N2 mechanism.

Assuming step 1.2 is rate limiting and irreversible [218], the hydrolysis rate is defined by equation (7.5) (derivation is in Appendix E.4.3).

$$r_1 \approx r_{1.2} \approx \frac{k_{obs,1.1}[DBE][H^+][H_2O]}{k_{obs,1.2} + [H_2O]} \quad (7.5)$$

If the reverse reaction of step 1.1 is significantly quicker than step 1.2 (equations (E.26) to (E.28) in Appendix E.4.3), equation (7.5) can be simplified into equation (7.6), which involves a single observed kinetic constant.

$$r_1 \approx r_{1.2} \approx k_{obs,1}[DBE][H^+][H_2O] \quad (7.6)$$

The presented mechanisms assume water as the substitution nucleophile. However, earlier studies also considered OH^- in this role [215]. For those cases, in equations (7.3) to (7.6), water's concentration is replaced with the concentration of the hydroxide ion.

7.5 Kinetic parameters estimation

The models described in the previous section were applied to the estimation of the respective kinetic parameters, following the parameter estimation procedure described in Section 4.1.3. Initially, three reactions were considered: hydrolysis and pyrolysis, represented by equations (7.1) and (7.2), as well as the further degradation of the pyrolysis product benzaldehyde. However, as demonstrated by the experimental data in Section 7.3.4, for the considered residence time and temperature ranges, pyrolysis products were found in very small amounts and their variation (if any) with temperature and residence time could not be observed owing to uncertainty in the measurements. Therefore, there was no advantage in including separate reactions for pyrolysis and the further degradation of BZA. Consequently, the kinetic model was simplified by aggregating both pyrolysis and degradation in a single first order reaction, where DBE is decomposed into a lumped component called "Others" (equations (7.7) and (7.8)). The properties of this component were assumed to be the same as benzyl alcohol and its stoichiometric coefficient in the degradation reaction (γ) was adjusted to close the mass balance.

Table 7.7: Activation energy (E_a) and kinetic constant (k_{ref}) at reference temperature (T_{ref}) estimated for different hydrolysis rate equations, and respective objective function (OF).

Scenario	Basis (Limiting step)	Nucleophile	Hydrolysis rate equation	Observed kinetic constant ($k_{obs,i}$)	E_a (kJ/mol)	k_{ref} ($X.s^{-1}$)	T_{ref} ($^{\circ}C$)	OF
1	-	-	$k_{obs,1}[DBE]$	1	60 ± 2	$(92 \pm 1) \times 10^{-3}$	347.5	525
				2	-	$(27 \pm 2) \times 10^{-3}$		
2	-	-	$k_{obs,1}[DBE][H_2O]$	1	67 ± 2	$(420 \pm 7) \times 10^{-8}$	347.5	435
				2	-	$(25 \pm 2) \times 10^{-3}$		
3	Protonation / S_{N1} (Step 1)	-	$k_{obs,1}[DBE][H^+]$	1	120 ± 2	114 ± 2	347.5	340
				2	-	$(23 \pm 2) \times 10^{-3}$		
4	S_{N2} (Simplified)	H_2O	$k_{obs,1}[DBE][H^+][H_2O]$	1	128 ± 2	$(520 \pm 8) \times 10^{-5}$	347.5	258
5		OH^-		1	180 ± 2	$(139 \pm 2) \times 10^3$		
6	S_{N1} (Step 2)	H_2O	$\frac{k_{obs,1.1}[DBE][H^+][H_2O]}{k_{obs,1.2}[BAL] + [H_2O]}$	1.1	290 ± 25	$(14 \pm 6) \times 10^2$	347.5	149
				1.2	296 ± 16	$(4 \pm 2) \times 10^2$		
7	S_{N1} (Step 2)	OH^-	$\frac{k_{obs,1.1}[DBE][H^+][OH^-]}{k_{obs,1.2}[BAL] + [OH^-]}$	2	-	$(15 \pm 2) \times 10^{-3}$	277.5	170
				1.1	332 ± 40	$(9 \pm 3) \times 10^{-1}$		
				1.2	241 ± 29	$(9 \pm 2) \times 10^{-8}$		
8	S_{N2} (Complete)	H_2O	$\frac{k_{obs,1.1}[DBE][H^+][H_2O]}{k_{obs,1.2} + [H_2O]}$	1.1	378 ± 48	$(33 \pm 6) \times 10^{-1}$	287.5	140
				1.2	311 ± 41	$(15 \pm 2) \times 10^{-3}$		
				2	-	$(26 \pm 4) \times 10^2$		
9	S_{N2} (Complete)	OH^-	$\frac{k_{obs,1.1}[DBE][H^+][OH^-]}{k_{obs,1.2} + [OH^-]}$	1.1	541 ± 160	23 ± 4	297.5	197
				1.2	389 ± 155	$(22 \pm 6) \times 10^{-4}$		
				2	-	$(17 \pm 2) \times 10^{-3}$		



$$r_2 = k_2[DBE] \quad (7.8)$$

The 15 experiments listed in Table 7.3 and Table 7.4 were the basis of the estimation of kinetic parameters. The experiment specific inputs were inlet's flowrate, composition, and pressure, as well as the temperature measured in the reactor's thermocouple. The measured data used for these estimations consisted of the molar conversions and benzyl alcohol yields plotted in Figure 7.9 (Section 7.3.2), including the associated error bars. Since the yield of the pseudo-component "Others" resulted from closing the mass balance in the reactor, including it as "measured data" would be redundant.

7.5.1 Estimated parameters

A parameter estimation was conducted for each of the hydrolysis rate equations derived in Section 7.4.1. These equations are summarised in Table 7.7 alongside the respective estimated parameters and associated standard deviation, as well as reference temperature and minimised objective function (OF). The first two scenarios consider simplified rate equations based on the overall reaction. The remaining cases are based on mechanistic considerations and can be divided according to the number of observed kinetic constants: two ($k_{obs,1}$ and $k_{obs,2}$) or three ($k_{obs,1.1}$, $k_{obs,1.2}$ and $k_{obs,2}$).

Regarding the pyrolysis/degradation reaction, it was initially hypothesised that the rate would follow an Arrhenius relationship, *i.e.*, increase exponentially with temperature. However, it was found that the measurements did not show any variation with temperature (Section 7.3.4). Consequently, when included in the parameter estimation process, the confidence interval in the activation energy for reaction 2 was in fact larger than its actual value, thus rendering this parameter meaningless. For example, considering scenario 5, this parameter was estimated as 11 ± 16 kJ/mol, giving an objective function of 241. Given this lack of statistical significance, the Arrhenius expression was removed for the degradation reaction, *i.e.*, the activation energy was fixed at 0. Therefore, this reaction was no longer temperature dependant. and only the kinetic constant at reference temperature was estimated, as shown in Table 7.7.

7.5.2 Fitting quality

The objective function in Table 7.7 resulted from the parameter estimation process described in Section 4.1.3. It represents the sum of the squared error between model and experiment divided by the respective uncertainties. Therefore, it reflects the adequacy of the model to fit the experimental data and should be as low as possible. The parity plots in Figure 7.18, Figure 7.19, and Figure 7.20 show the difference

between measured and model predicted values for every experiment. The equality diagonal that passes through the origin of the graphs represents a perfect agreement between measures and predicted values. Consequently, the closest a point is to the equality diagonal, the better is this agreement.

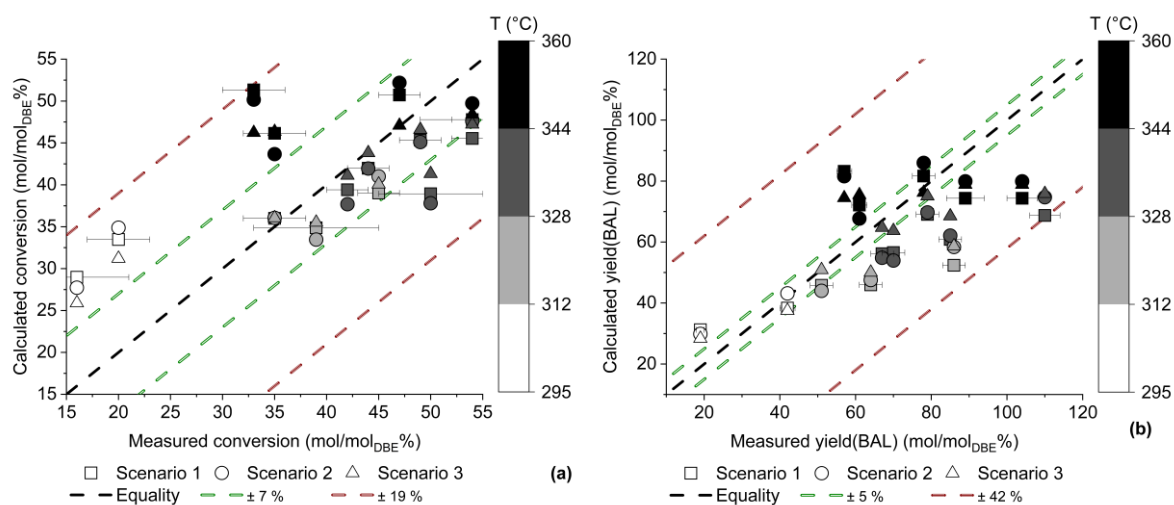


Figure 7.18: Parity plot for DBE conversion (a) and BAL yield (b) for scenarios 1, 2 and 3. Diagonal passing through the origin represents equality between measured and predicted yields.

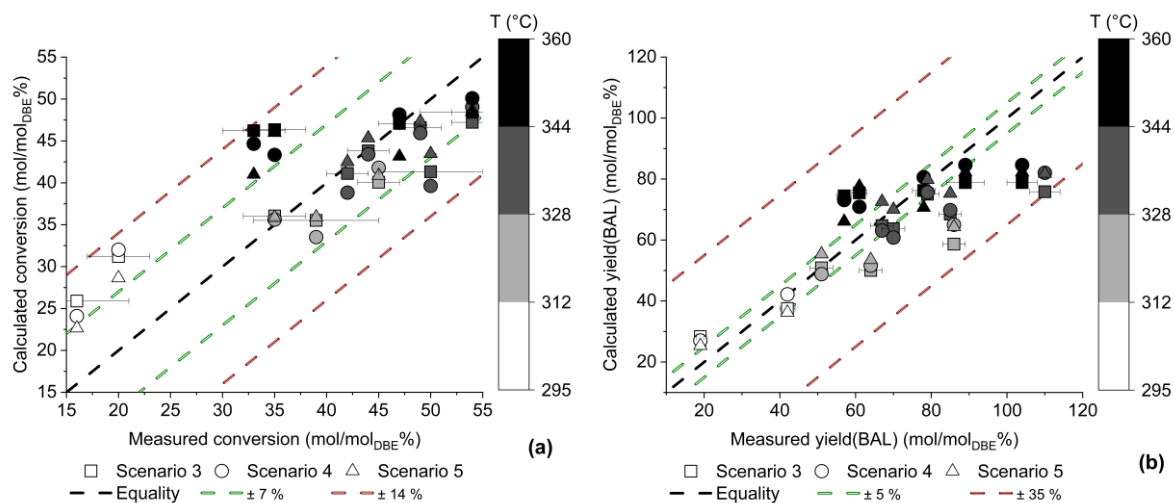


Figure 7.19: Parity plot for DBE conversion (a) and BAL yield (b) for scenarios 3, 4 and 5. Diagonal passing through the origin represents equality between measured and predicted yields.

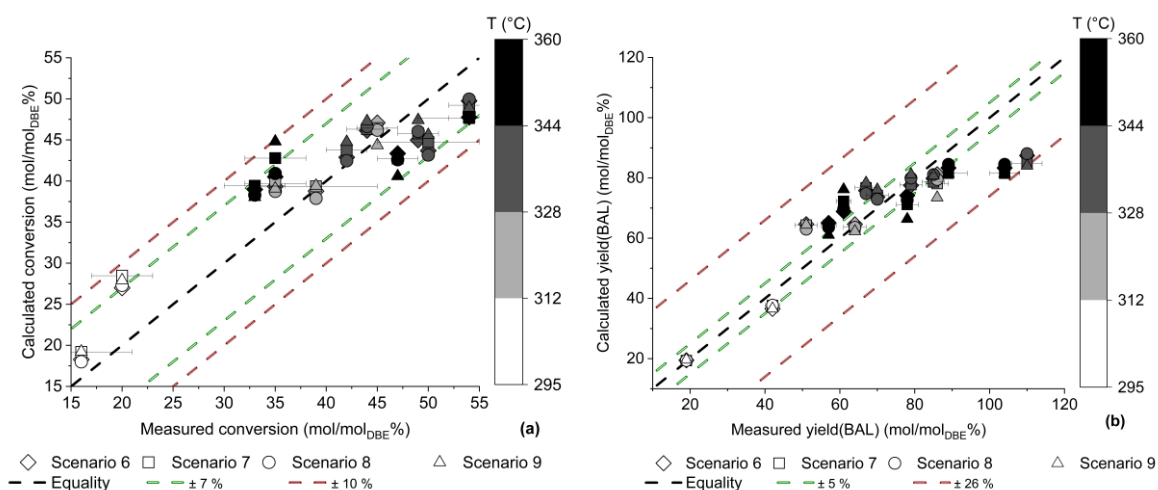


Figure 7.20: Parity plot for DBE conversion (a) and BAL yield (b) for scenarios 6 to 9. Diagonal passing through the origin represents equality between measured and predicted yields.

Compared to the mechanism-based scenarios, 1 and 2 showed considerably higher objective functions, thus proving the inadequacy of the simplified rate equations. The respective parity plots (Figure 7.18) further confirmed it, with scenario 3 being generally closer to the equality diagonal than 1 and 2. Within the mechanism-based scenarios based on a single observed kinetic constant for hydrolysis (*i.e.*, 3, 4 and 5), scenario 5 presented the lower objective function, being closer to equality in Figure 7.19. Such a result indicated that the protonation step is not rate limiting in the hydrolysis of DBE as typically assumed [149,211,213]. Furthermore, the reaction is more likely to occur through an S_N2 mechanism than S_N1 , with OH^- as the preferred substitution nucleophile. This was in line with earlier experimental observations which suggested the influence of proton concentration, based on the self-dissociation of water, as well as the concentration of water (Section 7.3.3).

The difference between substitution nucleophiles is defined by the products $[H^+][H_2O]$ and $[H^+][OH^-]$ in the rate equations. For both, the proton concentration was calculated assuming that water was the only source of protons, in which case the concentration of H^+ and OH^- would be the same. For higher conversion and consequent increase in the concentration of benzyl alcohol, it is possible that this species also affects the overall proton concentration, increasing the hydrolysis rate. This would mean replacing equation (4.25) with (7.9), as derived in Section E.5, which requires the alcohol's dissociation constant (K_a^{BAL}) at near critical conditions.

$$[H^+]^2 = K_w \rho_w^2 + K_{a_{BAL}} [BAL] \quad (7.9)$$

On the other hand, the product $[H^+][OH^-]$ is not directly dependent on the proton concentration, since it is related to water's self-dissociation constant, which is calculated from experimental data at subcritical conditions [56]. Therefore, the referred product and associated hydrolysis rate model

required fewer approximations, which may justify the better fitting of scenario 5 to experimental data when compared to scenario 4.

The scenarios with three estimated observed kinetic constants showed the lowest objective functions. As plotted in Figure 7.20, scenarios 6 and 8 provide the best fitting, pointing to water as the preferred nucleophile, unlike previous scenarios. On the other hand, the similarity in agreement between model and experiment for the two scenarios did not allow a distinction to be made between substitution mechanisms.

Compared to scenarios 1 to 5, the last four scenarios (6 to 9) required different reference temperatures (as presented in Table 7.7) to minimise the standard deviations associated to the estimated parameters, which were significantly higher. This lack of statistical significance may be associated to the increase in the number of estimated parameters, while the number of experiments remained. Therefore, a larger number of experiments in a wider range of conditions would be required to estimate more statistically significant parameters.

Compared to the other scenarios based on hydrolysis rates with two observed kinetic constants (*i.e.*, 6 to 9), scenario 8 provides a marginally better fitting; thus, the mechanism associated with this scenario is considered the likelier for DBE hydrolysis. A comparison between the two likeliest scenarios with two and three observed kinetic constants, *i.e.*, 5 and 8, is plotted in Figure 7.21. As expected from the lower objective function, the values predicted in scenario 8 are closer to the experimental measurements.

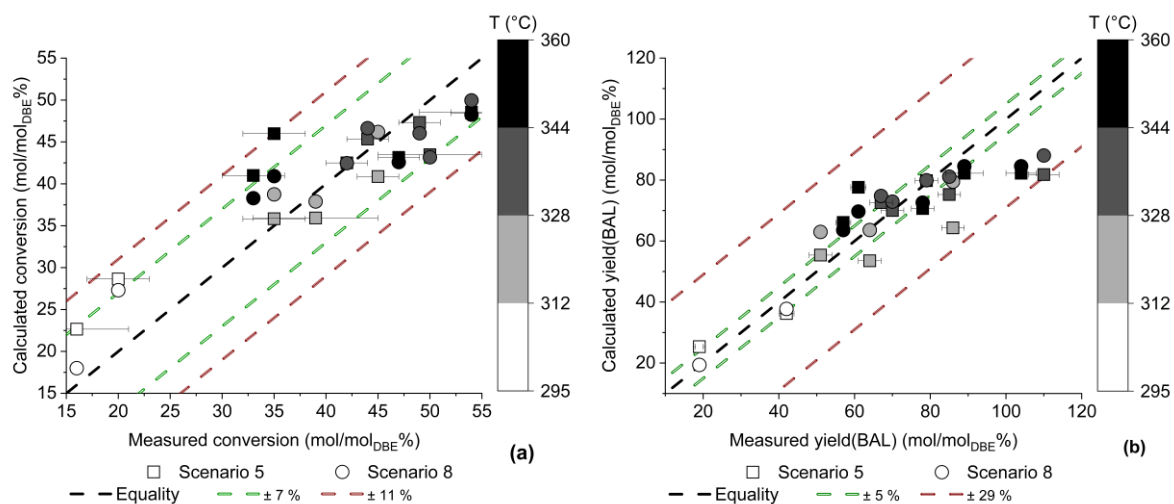


Figure 7.21: Parity plot for DBE conversion (a) and BAL yield (b) for scenarios 5 and 8.

When the second observed kinetic constant is included in the hydrolysis rate, the number of estimated kinetic parameters increased from 3 to 5. *i.e.*, one E_a and two k_{ref} , compared to two E_a and three k_{ref} , while the number of measurements remained 30 (one conversion and BAL yield for the 15

experiments). The flexibility to provide similar fittings to the experimental data regardless of the hydrolysis mechanism suggests that using 5 adjustable parameters is excessive for the number of experiments in the domain defined by temperature (295 – 360 °C), residence time (5 – 7 seconds), and feed concentration (33 – 45 wt%). Therefore, it appears that using the models with 3 observed kinetic constants, the problem has been overparameterized.

The standard deviations associated to the parameters estimated in scenarios 6 to 9 are considerably higher when compared with the remaining scenarios. To analyse its effect on eventually predicted values, a new set of simulations was conducted through a global system analysis (see Section 4.1.3), based on the parameters estimated in scenarios 5 and 8. In this process, each kinetic parameter was randomly varied 50 times according to a normal distribution centred in the estimated values and considering the calculated standard deviations. From those simulations, averages and standard deviations were calculated for DBA conversion and BAL yield. The latter were designated simulated standard deviations (SSD), being divided by the value originally calculated. The variation of this ratio with temperature measured at the reactor thermocouple and average residence time is plotted in Figure 7.22. The values associated to scenario 8 were considerably larger than the ones relative to scenario 5, thus reflecting the process overparameterization and its inaccuracy when describing DBE's hydrolysis. Expanding the operating domain would allow a clearer parameter estimation and a more accurate definition of the hydrolysis mechanism.

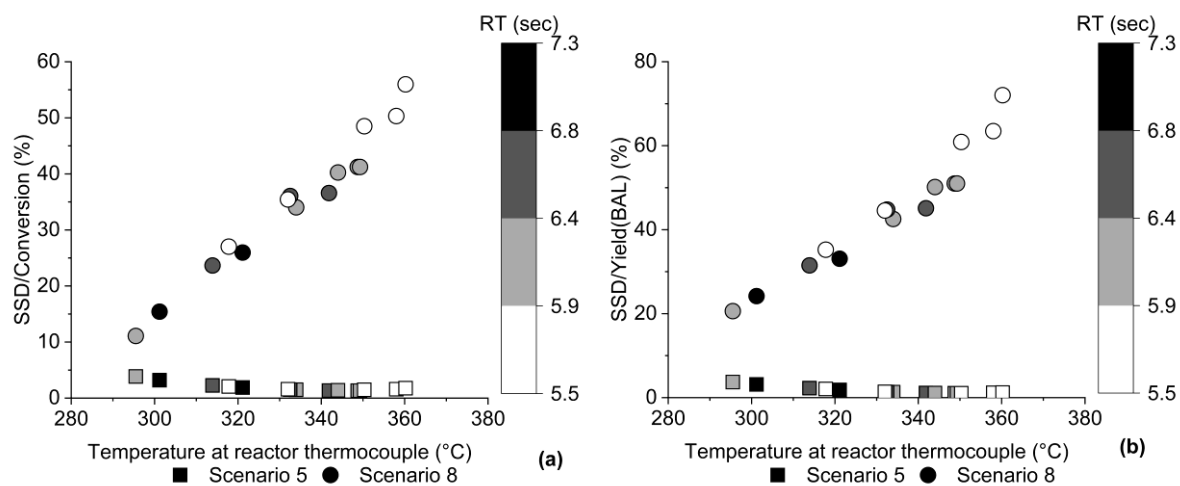


Figure 7.22: SSD ratio to DBE conversion (a) and BAL yield (b) in scenarios 5 and 8.

From all the scenarios evaluated, 5 is considered the one that most accurately represents dibenzyl ether's hydrolysis. Consequently, based on the experimental and modelling approach used in this study, the hydrolysis of DBE is more likely to occur via an S_N2 mechanism with hydroxide ions acting as the substitution nucleophile. This conclusion is similar to observations found in earlier literature [211,215], differing from the more recent ones, which only refer S_N1 mechanisms [149,213].

7.5.3 Range of applicability

To verify if the estimated parameters accurately reproduced the measured results across the entire range of conditions tested experimentally, the deviation between experimental and estimated values was divided by the associated uncertainty. This ratio was plotted against the tested operating conditions as shown in Figure 7.23, not showing any clear trend with temperature, residence time, or inlet concentration. Therefore, the accuracy of the model based on scenario 5 is not directly related to operating conditions in the tested range.

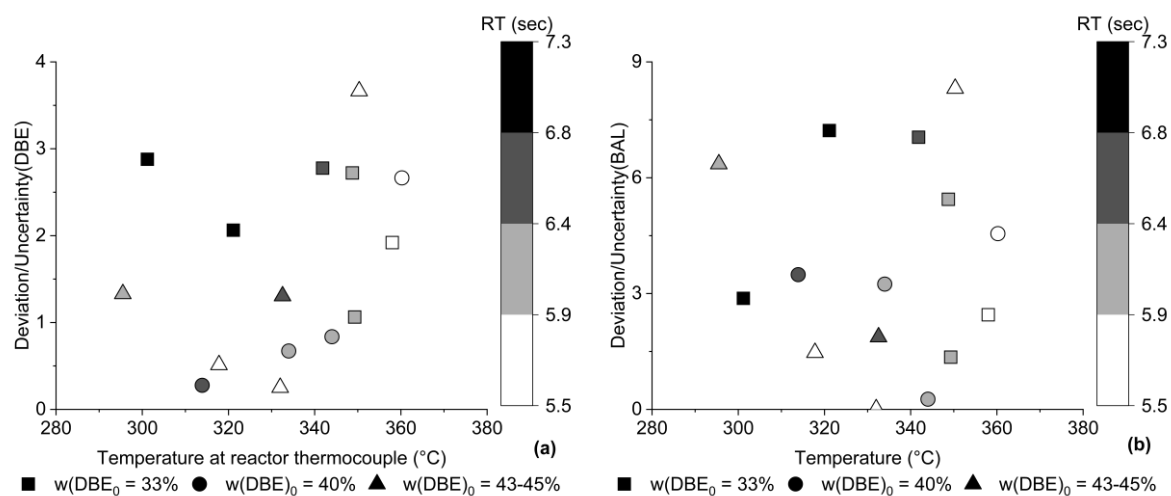


Figure 7.23: Ratio between deviation and uncertainty for DBE conversion (a) and BAL yield (b), considering scenario 5.

7.6 Model sensitivity analysis

As described in Chapter 4, the mathematical model used to simulate dibenzyl ether hydrothermal reactions relies on four sub-models that calculate: reaction rates, thermodynamic and transport properties, heat losses to the environment, and dispersion. These sub-models were based on different assumptions. Their effect was evaluated by changing the sub-model basis, with fixed kinetic parameters (scenario 5), and comparing the model outputs.

7.6.1 Property corrections and real composition

The properties sub-model accounts for the composition at fixed points of the reactor, applying the equation of state SAFT- γ Mie and the CALS method. Section 4.2 shows how both calculation types were optimised to better fit pure water properties near the critical point, which were calculated using

the IAPWS. In this chapter, it was assumed that those corrections were valid for mixtures containing water, DBE, and BAL.

Literature data to validate this assumption was lacking, so the effect of the corrections implemented was tested by comparing the calculated conversion of DBE and yield of BAL in simulations that considered or ignore them, *i.e.*, applied SAFT- γ Mie and the CALS original values. Table 7.8 contains the absolute variations (Δ) observed in DBE conversion (C_V) and BAL yield (Y_{BAL}), defined as the difference between the new and original values. This table also includes the variation caused by ignoring the mixture composition, and applying pure water properties, calculated using IAPWS-95 (see Section 4.2) which is a common approximation in the literature [149,209,212].

Table 7.8: Variation (Δ) of calculated DBE conversion (C_V) and BAL yield (Y_{BAL}) for different property calculation methods.

Scenario Exp.	Original		No property corrections		Water properties	
	C_V (%)	Y_{BAL} (mol/mol _{DBE} %)	$\Delta(C_V)$ (%)	$\Delta(Y_{BAL})$ (mol/mol _{DBE} %)	$\Delta(C_V)$ (%)	$\Delta(Y_{BAL})$ (mol/mol _{DBE} %)
1	28.6 ± 0.9	36 ± 1	0.6	1	-0.5	-0.6
2	40.9 ± 0.8	64 ± 1	0.6	1	-0.9	-1
3	48.4 ± 0.6	81.8 ± 0.9	0.1	0.2	-1	-2
4	48.5 ± 0.6	82.2 ± 0.9	0.1	0.2	-1	-2
5	48.5 ± 0.6	82.2 ± 0.9	0.1	0.2	-1	-2
6	43.1 ± 0.7	70.6 ± 0.8	0.2	0.3	-2	-3
7	35.8 ± 0.8	54 ± 1	0.7	2	-0.9	-1
8	45.3 ± 0.7	75.2 ± 1	0.1	0.2	-1	-2
9	47.4 ± 0.7	79.8 ± 0.9	0.1	0.1	-2	-3
10	41 ± 0.7	66.1 ± 0.8	0.2	0.3	-2	-4
11	43.5 ± 0.7	72.6 ± 1	0.1	0.2	-2	-3
12	22.6 ± 0.9	25.3 ± 0.9	0.5	0.9	-0.5	-0.5
13	35.9 ± 0.7	55 ± 1	0.8	2	-1	-2
14	42.5 ± 0.7	70 ± 1	0.08	0.1	-2	-3
15	46 ± 0.7	77.6 ± 0.8	0.1	0.2	-3	-5

Compared to the initial model setup, ignoring property corrections resulted in variations that, except for experiments 7 and 13, are within the standard deviations presented in Section 7.5.2. If these intervals are expanded to the experimental uncertainties in Figure 7.9 and Appendix E.3, the difference between the predictions of the corrected and uncorrected models are negligible.

As shown in Figure 4.5 (Section 4.2.3), the property corrections are only relevant around the supercritical transition between liquid- and gas-like properties. Looking at the temperatures estimated for the reactor's inlet in Table 7.4, these are at least 17 °C lower than the SCTT. Therefore, the corrections are negligible for the experimental conditions used.

On the other hand, when the properties of pure water were assumed, larger variations were observed, with absolute values considerably exceeding the associated standard deviations. Nonetheless, these

variations are typically of the same magnitude of the experimental uncertainty, except for experiments 10 and 15, which are slightly higher.

7.6.2 Heat loss and enthalpy of reaction

The heat-transfer sub-model quantified the temperature reduction along the reactor due to heat losses through the tube's wall, as well as exo- or endotherms due to each reaction. Table 7.9 shows the variations on DBE conversion and BAL yield caused by neglecting heat losses, increasing the heat transfer coefficient by $5 \text{ W.m}^{-2}.\text{K}^{-1}$, and ignoring the heats of reaction. All scenarios show relatively small variations, especially when compared to the experimental uncertainties in Figure 7.9 and Appendix E.3.

Table 7.9: Variation (Δ) of calculated DBE conversion (C_v) and BAL yield (Y_{BAL}) for different heat transfer assumptions.

Scenario Exp.	No heat loss		$U_{ht} = 46 + 5 \text{ W.m}^{-2}.\text{K}^{-1}$		No heat of reaction	
	$\Delta(C_v)$ (%)	$\Delta(Y_{BAL})$ (mol/mol _{DBE} %)	$\Delta(C_v)$ (%)	$\Delta(Y_{BAL})$ (mol/mol _{DBE} %)	$\Delta(C_v)$ (%)	$\Delta(Y_{BAL})$ (mol/mol _{DBE} %)
1	-0.4	-0.8	0.1	0.2	0.3	0.5
2	-0.1	-0.2	-0.01	-0.04	-0.004	-0.03
3	0.3	0.9	-0.2	-0.5	-0.2	-0.5
4	-0.002	0.5	-0.2	-0.4	-0.3	-0.7
5	-0.002	0.5	-0.2	-0.4	-0.3	-0.7
6	-1	-2	-0.0006	-0.09	-0.4	-1
7	-0.4	-0.7	0.06	0.1	0.09	0.2
8	0.1	0.5	-0.1	-0.3	-0.09	-0.3
9	-0.01	0.5	-0.2	-0.4	-0.3	-0.6
10	-1	-1	-0.02	-0.1	-0.6	-1
11	0.1	0.4	-0.09	-0.2	-0.09	-0.2
12	-0.3	-0.4	0.1	0.2	0.4	0.7
13	-0.4	-0.7	0.06	0.1	0.08	0.1
14	0.09	0.3	-0.07	-0.2	-0.1	-0.2
15	0.3	0.9	-0.2	-0.5	-0.5	-1

The effect of excluding heat losses, *i.e.*, assuming isothermal behaviour based on the temperature measured at TT-105, is only noticeable in experiments 6, 10 and 15, which were performed at the highest temperatures for a given flowrate. Considering the position of TT-105 at 47% of the reactor's length from its inlet, and the linear profiles estimated in Section 4.5.2, the measured temperatures represent a good estimate of the average temperature in the reactor section. Consequently, it has a limited effect on the model predictions.

The second scenario represents the impact, which turned out to be small, of increasing the overall heat transfer coefficient to a value higher than the standard deviation in the measurement ($\pm 3 \text{ W.m}^{-2}.\text{K}^{-1}$).

Since this is minimal, the estimated value is adequate. Furthermore, the higher heat transfer coefficient tested in the new scenario, was similar to that estimated from the experiments using only water ($50 \pm 1 \text{ W.m}^{-2}.\text{K}^{-1}$). Therefore, for the experimental conditions investigated in this work, using the same heat transfer coefficient when analysing experiments with both diluted and concentrated organic feeds gives essentially the same result.

Until this point, the heat of reaction has not been discussed. Particularly, it was neglected when estimating heat transfer coefficients in Section 4.5, since those calculations were performed without any reactions occurring. Nonetheless, given the element reference state considered by gPROMS[®] when calculating specific enthalpies of the mixtures, the heat released or consumed in each reaction is implicitly accounted for. This was irrelevant for the calculations in Chapter 8, as the properties of pure water (including enthalpy) were used.

Consequently, the third scenario in Table 7.9 calculated the enthalpy at the local temperature, but with constant composition equal to that at the inlet. As in the first scenario, but to a smaller extent, the variation was negligible except in the higher temperature scenarios (6, 10, and 15). Therefore, the inclusion of the heat of reaction had a negligible effect on the results.

7.6.3 Dispersion and coefficient calculation method

Table 7.10 shows the variation in model prediction when mass dispersion effects were excluded, and when using the Stokes-Einstein equation to calculate the diffusion coefficients, instead of estimating them using the gPROMS thermodynamic package, as described in Section 4.7.

Neglecting dispersive effects resulted in the prediction of higher conversions and alcohol yields. This can be attributed to higher local concentrations of DBE, which does not disperse over the concentration gradient, resulting in higher reactions rates. These variations were significant when compared to the experimental uncertainty.

Using the Stokes-Einstein equation kept the calculated values within the experimental uncertainty. Therefore, the two diffusivity calculation methods can be considered equivalent.

Table 7.10: Variation (Δ) of calculated DBE conversion (C_V) and BAL yield (Y_{BAL}) for different dispersion assumptions.

Scenario	No dispersion		D_i calculated using Stokes-Einstein equation	
	$\Delta(C_V)$ (%)	$\Delta(Y_{BAL})$ (mol/mol _{DBE} %)	$\Delta(C_V)$ (%)	$\Delta(Y_{BAL})$ (mol/mol _{DBE} %)
1	2	3	0.2	0.3
2	4	7	0.4	0.7
3	6	9	0.5	0.9
4	5	9	0.5	0.9
5	5	9	0.5	0.9
6	4	6	0.4	0.7
7	3	5	0.5	0.7
8	5	8	0.7	1
9	5	8	0.7	1
10	3	4	0.4	0.6
11	4	6	0.6	1
12	1	1	0.2	0.2
13	3	5	0.5	0.8
14	4	6	0.6	1
15	3	5	0.5	0.8

7.6.4 Comparison with literature

The kinetic parameters estimated in this chapter were compared with a similar study conducted by González *et al.* [149]. To ensure parameters were compared on an equivalent basis, this used kinetic constants reported at certain specific temperatures, as shown in Table 7.11. However, since the self-ionisation product of water was accounted for in different ways in each study, it has been included alongside the kinetic constants in Table 7.11.

Table 7.11: Comparison between kinetic constants for DBE hydrolysis estimated in this study and existing in literature [149] in the range of tested conditions (287 – 368 °C).

Temperature (°C)	$[H^+] = [OH^-]$ (mol/L $\times 10^6$)	This study: $\ln(k_{obs,i}/[H^+][OH^-])$ (s ⁻¹)	Literature: $\ln(k_{obs,i}/[H^+])$ (s ⁻¹)
325	1.5	-2.5	-3.9
350	0.81	-2.3	-3.0
375	0.18	-3.9	-2.2

The first order rate constants derived from this study were always higher than the ones found in literature, which were four times higher at the lower end of the temperature range. Apart from temperature, compared to the operating conditions in this work, the experiments conducted by González *et al.* [149] considered a lower DBE mass fraction at the reactor's inlet (10 wt%), and longer residence times (up to 40 seconds). Furthermore, their mathematical model assumed an isothermal reactor without presenting any evidence of this, properties of pure water, and that dispersion effects were negligible. From the sensitivity analysis conducted in the previous sections, the last two approximations had the

largest influence on the result of the analysis. Therefore, this work's mathematical model is inherently different from the one implemented by González *et al.*, thus a direct comparison between kinetic constants is inconclusive. A comparison of measured yields is also difficult given the different operating conditions, particularly inlet concentration.

7.7 Concluding remarks

This chapter described the experiments conducted in the hydrothermal rig with an organic feed consisting of pure dibenzyl ether. Based on the data retrieved from those experiments, kinetic parameters estimated and used to understand the reactional mechanism. The following outcomes were observed:

Dibenzyl ether was degraded in a confined jet reactor using supercritical water as hot feed. Therefore, it was successfully demonstrated that this configuration and tested conditions are suitable to break ether bonds between aromatic compounds, which are commonly observed in lignin.

For pressures around 250 bar, temperatures between 287 and 369 °C, and inlet concentrations from 33 to 45 wt%, the conversion of dibenzyl ether was in the range of 16 – 56%. Products were distributed between a two-phase liquid and gas phases (solids were not significantly found).

The flowrate of gaseous products was below the uncertainty associated with the feed flow. Qualitatively, toluene, benzene, and carbon monoxide were detected during the experiments. The two-phase liquid effluent was successfully separated without extractants and analysed through HPLC with UV-vis detection.

The main product was benzyl alcohol, found in both aqueous and organic phases, with molar yields between 19 and 110%. This reflects the prevalence of hydrolysis over pyrolysis, as stated in literature [149,211,213]. Other products included benzaldehyde and toluene with individual molar yields smaller than 5%. Overall, the detection of benzaldehyde and toluene in the liquid products confirmed that pyrolysis occurs in hydrothermal media. For residence times between 5 and 7 seconds and average temperature in the range of 295 – 360 °C, reduced amounts of these species were measured, with molar yields smaller than 5%. Uncontrolled aspects like extended degradation, evaporation and temperature fluctuations were shown to have affected these yields, thus suggesting that the described method is not accurate enough to capture a component's behaviour at such a small scale.

Hydrolysis rate equations were derived assuming either S_N1 or S_N2 reaction mechanisms. Kinetic parameters were estimated for both, considering different levels of complexity. Non-mechanism-based models fit significantly worse the measured data. Mechanism-based models with three observed kinetic constants provided the best fitting. However, the associated parameters were estimated with excessive

uncertainty, suggesting that the estimation was overparameterized for the amount and range of measured data. Mechanism-based models with two observed kinetic constants provided an acceptable and accurate fitting. From those, the lowest objective function was found when considering an S_N2 , suggesting this is the likeliest mechanism.

For this mechanism, H_2O and OH^- were considered as substitution nucleophiles, with the latter showing a marginally better fitting quality. The rate equations considering as nucleophiles H_2O and OH^- differ in the products $[H^+][H_2O]$ and $[H^+][OH^-]$, respectively. It was hypothesised that OH^- provided a better fitting because $[H^+][OH^-]$ results directly from water's self-ionisation product, thus requiring fewer approximations than $[H^+][H_2O]$.

A sensitivity analysis to the model assumptions demonstrated that:

- The corrections applied to the property calculation methods were not relevant given the distance from operating temperatures and SCTT.
- Since temperature measurements were taken from a position near the reactor's middle point, neglecting heat losses, or assuming an overall heat transfer coefficient estimated for diluted mixtures do not significantly affect the reaction yields.
- Considering pure water properties and neglecting dispersion significantly affect the model output. Consequently, a direct comparison with equivalent experiments in literature was not conclusive.

Future work

Since DBE hydrolysis is likely to be influenced by the self-dissociation product of water, the respective mechanism characterisation can be improved by expanding the domain of operating conditions. This should pass by manipulating the reaction pH and testing higher conversions. The first would allow a clearer distinction between preferred nucleophiles but would require the inclusion of additional species in the reactor, which could be subject to precipitation or hydrothermal degradation themselves. The last would reflect the true influence of benzyl alcohol in the hydrolysis rate, improving the distinction between the more detailed rate models.

A relevant difference between the experiments described in this chapter and the ones in literature for HTL of lignin is the absence of solid products, which are typically formed through repolymerisation [74]. Yong *et al.* refer that these reactions occur even at short residence times, and the produced char was mainly phenolic [84,85]. This indicates that repolymerisation is possibly initiated in phenolic groups like the ones in the monomers that form lignin, *i.e.*, p-coumaryl alcohol, coniferyl alcohol, and synapyl alcohol (see Figure 2.6). For this reason, the production of benzyl alcohol instead of phenol during the hydrolysis of dibenzyl ether may have been the reason solid formation was not observed

during the experiments in this chapter. Therefore, it would be of interest to repeat the experiments described in this chapter using phenolic ethers like the ones in Figure 7.1, *i.e.*, diphenyl ether or benzyl phenyl ether. Both molecules are expected to be hydrolysed in a phenol molecule, unlike dibenzyl ether [149,207].

Chapter 8

Kinetics of the hydrothermal processing of sucrose

8.1 Introduction

In common with the previous chapter, this chapter presents the measurement of the kinetics of the degradation of an organic dimer in contact with water at subcritical conditions, and their analysis to elucidate a reaction mechanism. In this case, the selected dimer was sucrose since it comprises a glycosidic bond similar to the ones found in cellulose. Therefore, it may be considered a model compound of this biopolymer. The chapter starts by reviewing existing studies on this subject, followed by a description of the experiments performed, and an analysis of observed yields. Subsequently, those measurements are used in the estimation of kinetic parameters, which are used to draw conclusions regarding the reaction pathways.

Given sucrose's more complex reaction network compared to dibenzyl ether's, the parameter estimation process started from an approximated pathway, composed by lumped compound groups, then gradually increasing complexity by including specific compounds. A systematic workflow was implemented to find the best solution, avoiding overparameterization and accounting for the effect of temperature on water's self-ionisation constant where relevant.

8.1.1 Background

Cellulose represents 40 to 50 wt% of lignocellulosic biomass [47]. It is a linear-chain polymer, formed by the aggregation of glucose monomers through a specific type of ether bond, named β -1,4 glucosidic. In hot pressurised water, cellulose is hydrolysed into smaller oligosaccharides, and eventually glucose [73]. This monomer can be further degraded into several compounds like 5-(hydroxymethyl)furfural (5-HMF) [66,67], levulinic acid [68,69], lactic acid [67]; glycolaldehyde (Glyco) [70], and 1,6-anhydro- β -D-glucose (Agluc) [71], all of which have a wide range of commercial uses as described in in Section 2.2.2.

Table 8.1 presents a summary of the studies conducted over the past decades on the reactional behaviour of glucose, 5-HMF, and cellulose in hydrothermal medium. The High Pressure Processes Group in the Department of Chemical Engineering and Environmental Technology of the University of Valladolid have previously demonstrated the hydrolysis of glucosidic bonds in a continuous hydrothermal microreactor [64,73].

Table 8.1: Summary of recent work on hydrothermal degradation of sucrose related products.

Year	Reactor type	Feed	Conditions	Kinetic model summary	Main conclusions	Ref.
1999	Continuous	Gluc / Fruc / AGluc / Ery (0.25 – 0.6 wt%)	FO+SCW: 6+14 mL/min 300 – 400 °C 250 – 400 bar < 2 sec	<u>Isomerisation:</u> Gluc ↔ Fruc / DHA ↔ Glyce <u>Dehydration:</u> Gluc → AGluc / Glyce → Pyr <u>RAC:</u> Gluc/Fruc → Ery/Glyco Gluc/Fruc → Glyce <u>Others:</u> pyr/AGluc → formic/acetic acids fruc → 5-HMF	Negligible gas formation. Glyce degrades preferably to Pyr than DHA. Isomerisation of Gluc and Fruc favours the last. 5-HMF production is not significant at short residence times. Changing from subcritical to supercritical did not affect Arrhenius relations.	[159]
2005	Micro (batch) reactor	Gluc (10 wt%)	200 – 500 °C 250 bar 30 – 90 sec	CO ₂ produced from acids' decarboxylation. CO produced from C-C bond breaking. H ₂ produced from water-gas shift reaction.	Yield of hydrocarbon gases (CH ₄ , C ₂ H ₄ , C ₂ H ₆ , C ₃ H ₆ , C ₃ H ₈) under 1 mol%. Char formed in small quantities. H ₂ yield and CO/CO ₂ ratio increased with temperature.	[160]
2007	Continuous	Gluc (0.15 M)	FO+SCW: 5 – 10+10 – 20 mL/min 350 – 400 °C 400 – 800 bar 0.2 – 2 sec	<u>Isomerisation:</u> Gluc ↔ Fruc / DHA ↔ Glyce <u>Dehydration:</u> Fruc → 5-HMF / 5-HMF → BTO Glyce → Pyr → Lactic acid <u>RAC:</u> Gluc → Ery/Glyco Gluc/Fruc → Glyce/DHA <u>Others:</u> 5-HMF → Furfural	Yields of 5-HMF, furfural, and BTO increase with water density. K _w variation near the SCTT considered as a reason for hydrolysis and dehydration rate increase with density. Longer residence times promote 5-HMF conversion.	[103]
2008	Continuous	5-HMF (0.1 M)	175 – 350 °C 400 – 450 °C 250 bar 80 – 400 sec	<u>Subcritical conditions:</u> 5-HMF → BTO 5-HMF → Levulinic/formic acids <u>Supercritical conditions:</u> 5-HMF → Other Furfurals	No reactions below 250 °C. Negligible solid formation. Hydrocarbon gases (CH ₄ , C ₂ H ₄) only found in traces. CO ₂ , CO, H ₂ more abundant. Kinetic parameters for 5-HMF degradation.	[104]
2008	Continuous	Gluc	300 – 400 °C 1 bar 0.2 – 0.4 sec	<u>Isomerisation:</u> Gluc → Fruc <u>Dehydration:</u> Gluc → AGluc / Gluc/Fruc → 5-HMF <u>RAC:</u> Gluc → Ery/Glyco <u>Others:</u> 5-HMF → Formic/Levulinic acids	AGluc yield shows optimum residence time. Yield of water-soluble organics reached 80%.	[71]

Continuation of Table 8.1.						
Year	Reactor type	Feed	Conditions	Kinetic model summary	Main conclusions	Ref.
2012	Micro (batch) reactor	Cellulose	pH: 3, 7, 14 280 – 320 °C Up to 30 min	<u>Hydrolysis:</u> Cellulose → Gluc <u>Isomerisation:</u> Gluc ↔ Fruc <u>Dehydration:</u> Glyce → Pyr → Lactic acid <u>RAC:</u> Gluc/Fruc → Ery/Glyco Gluc/Fruc → Glyce <u>Hydration:</u> 5-HMF → Formic/Levulinic acids <u>Others:</u> Fruc → 5-HMF 5-HMF → Solids / 5-HMF → BTO Glyco → Formic/Acetic acids	Medium acidity affected product distribution in both bio-oil and water-soluble fraction. 5-HMF was the main product under acid and neutral conditions. Under alkaline conditions the main products were carboxylic acids and DHA. Formation of gaseous and solid products observed at longer residence times.	[144]
2013	Continuous	Cellulose (7.5 wt%)	275 – 400 °C 250 bar 0.004 – 30 sec	<u>Hydrolysis:</u> Cellulose → Oligosaccharides → Gluc <u>Isomerisation:</u> Gluc → Fruc / DHA ↔ Glyce <u>Dehydration:</u> Fruc → 5-HMF <u>RAC:</u> Gluc → Glyco/Ery / Fruc → Glyce <u>Others:</u> Glyce → Pyr / Gluc → AGLuc Fruc/Pyr/Ery/AGluc → acids	Extensive review of kinetic parameters in existing literature. Parameters for Arrhenius equations depend on reactions occurring at sub- or supercritical conditions. Kinetic parameters for glucose isomerisation and 5-HMF formation,	[64]
2015				Reaction times higher than 0.1 seconds yielded mainly monosaccharides compared to oligosaccharides (70 vs. 30 wt%). Yields of 5-HMF and Glyco enhanced by higher residence time.	[73]	
2019	Batch reactor	Gluc	211 °C for 15 minutes 20 bar	<u>Isomerisation:</u> Gluc ↔ Fruc <u>Dehydration:</u> Fruc → 5-HMF <u>Hydration:</u> 5-HMF → Formic/Levulinic acids	Use of seawater improved 5-HMF yield.	[152]

Cellulose's hydrolysis into its monomer, and subsequent glucose degradation, produces a wide range of products, which have been shown to depend on the medium's acidity [144,152]. All studies agreed that glucose (Gluc) establishes an isomerisation equilibrium with fructose (Fruc). It has been demonstrated that in hydrothermal conditions this equilibrium is more favourable towards the formation of fructose than glucose [64,71,159,160].

Glucose's dehydration produces 1,6-anhydro- β -D-glucose (AGluc) [71,159], which decomposes to formic and acetic acids [64,159]. The dehydration of fructose results in the production of 5-(hydroxymethyl)furfural (5-HMF) [71,103,144,152], which has been demonstrated to be influenced by water's density [73,103]. 5-HMF further reacts to produce 1,2,4-Benzenetriol (BTO) or levulinic and formic acids [104,144,152]. The degradation of this organic was also associated with the release of carbon dioxide, carbon monoxide, and hydrogen, as well as traces of hydrocarbon vapours [104]. Furthermore, Yin & Tan also attributed to 5-HMF the formation of solids in their experiments with cellulose [144], although this was not observed by Chuntanapum *et al.* [104] using a feed containing only this organic.

Both glucose and fructose react via retro-aldol condensation (RAC) to produce glyceraldehyde (Glyce), and a mixture of erythrose (Ery) and glycolaldehyde (Glyco) [144,159]. Martínez *et al.* review [73] concludes that glyceraldehyde is expected to result mainly fructose's reaction, while erythrose and glycolaldehyde are mainly a product from glucose. Furthermore, glyceraldehyde may isomerise into dihydroxyacetone (DHA), or dehydrate to pyruvaldehyde (Pyr) [64,103,144], with the latter considered preferential by Kabyemela *et al.* [159]. Pyruvaldehyde may be further dehydrated to produce lactic acid [103,144]. Like 1,6-anhydro- β -D-glucose, erythrose may also be degraded into smaller acids [64].

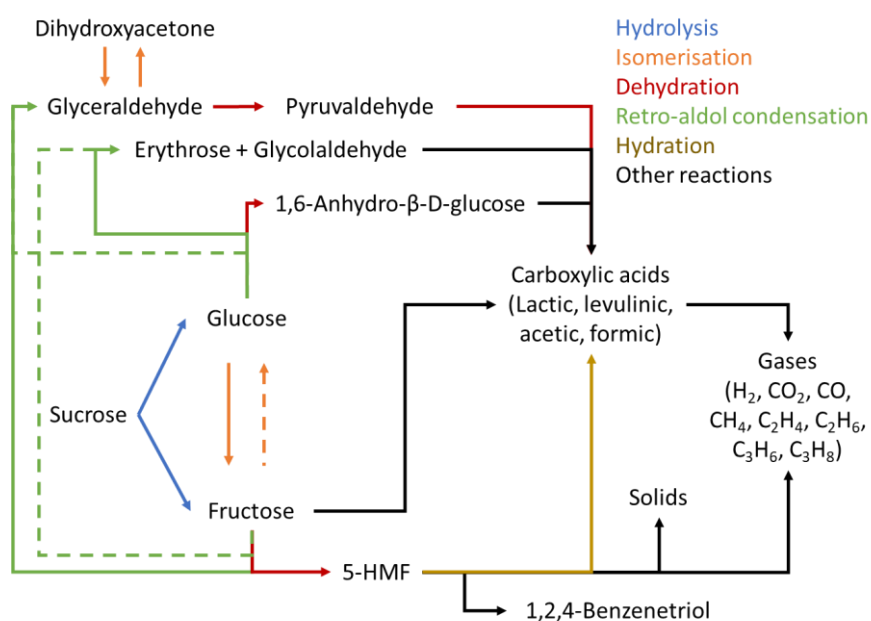


Figure 8.1: Expected reactional pathway for sucrose in hydrothermal medium. Dashed arrows represent non-preferential reactions.

Overall, the reviewed studies showed a strong interaction between glucose and fructose, each with their preferential pathways. Figure 8.1 summarises these reactions, with an additional step. Glucose and fructose are two monomers that naturally compose sucrose, being connected through an α -1 \rightarrow β -2 glucosidic bond [220]. They are also the direct products of the disaccharide hydrolysis [221,222]. Therefore, the pathway in Figure 8.1 was extended to include this reaction.

Figure 8.2 compares the chemical structures of cellulose and sucrose. Both have their monomers connected through glucosidic bonds, although they differ in the surrounding structure. Oomori *et al.* compared the hydrolysis of different disaccharides, demonstrating that the type of glucosidic bond affects the reaction rate [220]. From the 11 molecules in their study, sucrose was the one that required the shortest residence time to be fully converted.

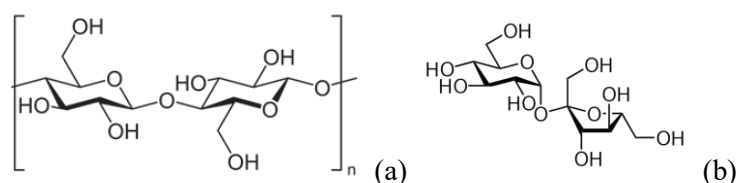


Figure 8.2: Chemical structures of cellulose (a) and sucrose (b).

8.1.2 Objectives

The aim of the present chapter is to demonstrate the capabilities of the installed hydrothermal liquefaction rig in processing a compound whose structure is representative of cellulose. Given fructose's relevance in glucose's reactional pathways, it was decided to evaluate the HTL rig's performance on degrading a dimer that contains both monomers, *i.e.*, sucrose.

The analysis of the rig's effluent was applied in the estimation of kinetic parameters. As shown in Figure 8.1, sucrose presents a diverse reactional pathway. Given the number of kinetic parameters and limited amount of experimental data, this is not a straightforward process. Therefore, it was also an objective of the current chapter to develop a systemic methodology capable of characterising the maximum number of relevant reactions, through the estimation of kinetic parameters, while avoiding overparameterization, and accounting for the effect of water's changing self-ionisation when pertinent.

8.2 Experimental setup

The hydrothermal liquefaction of sucrose was conducted in the continuous hydrothermal rig described in Section 3.3, following the procedure in Section 3.4. Unlike dibenzyl ether, which is nearly insoluble

in water, the solubility of sucrose is 179 g per 100 g of water [132], making it possible to test different organic feed concentrations. Those consisted of previously prepared aqueous solutions, with different mass fractions of sucrose: 10, 20, and 30 wt%.

The substances required for the performed experiments were included in Table 3.1 in Section 3.2. Besides DI water and sucrose, dichloromethane (DCM), sulfuric acid, and methanol (MeOH) were also required for solvent extraction, HPLC mobile phase, and GC sample preparation, respectively. Furthermore, standard solutions with different concentrations of sucrose, glucose (Gluc), fructose (Fruc), pyruvaldehyde (Pyr), 1,6-Anhydro- β -D-glucose (AGluc), and 5-(hydroxymethyl)furfural (5-HMF) were used in the calibration of the analytical equipment, which is shown in Appendix B.3 and Appendix B.4.

As in previous experiments, gas products were continuously analysed in the FTIR spectrometer described in Section 3.6.7, applying the gas sweeping method in Section 3.5.2. Measured species included water, CO, CO₂, methane, ethylene, ethane, propylene, propane, and formaldehyde.

At least two samples of the liquid effluent were collected per experiment. These were filtered and mixed with DCM following the procedures in Section 3.5.1 and Section 3.5.4. Before evaporating the solvent, a portion of the aqueous phase was taken and analysed via high-performance liquid chromatography with refractive index detection (HPLC-RID), as described in Section 3.6.1 and Section 3.6.3. The species measured through this method were: sucrose, glucose, fructose, pyruvaldehyde, and 1,6-anhydro- β -D-glucose.

Following solvent evaporation, the aqueous and organic-DCM phases were diluted in methanol and analysed via gas chromatography (GC) as presented in Section 3.6.4. Mass spectrometry (MS) was applied for component detection, while flame ionisation detection (FID) allowed the quantification of 5-(hydroxymethyl)-2-(dimethoxy methyl)furan (5-HDF) using 5-HMF's calibration.

8.2.1 Operating conditions

A total of 20 experiments were performed using an organic feed containing sucrose, under the operating conditions summarised in Table 8.2 and Table 8.3. These were divided in three groups according to the respective mass fraction of sucrose in the aqueous organic feed, *i.e.*, 10, 20, and 30 wt%.

All experiments were conducted at pressures close to 250 bar (246 – 254 bar), and fixed quench flowrate of 60 mL/min. The nominal volumetric flowrate ratio between SCW and organic feeds was kept at 3-to-1 in all experiments, thus sucrose's mass fraction at the reactor's inlet was the same in each group, *i.e.*, 2.4, 4.9, and 7.2 wt%. The organic nominal feed flowrate was changed between 6 and 10 mL/min,

leading to a mass flowrate at the inlet of the reactor inlet in the range 26 – 44 g/min¹⁰. The supercritical heater setpoint was also varied within each group, ranging from 406 to 460 °C. This resulted in temperatures between 292 and 367 °C at TT-1105. Under those conditions, the average residence time varied from 3 to 7 seconds.

Table 8.2: Flowrates and sucrose mass fractions for sucrose hydrothermal degradation experiments.

Exp	Nominal flowrate (mL/min)			Reactor flowrate (g/min)	Sucrose mass fraction (wt%)	
	SCW	Organic	Quench		Organic feed	Reactor inlet
1	24	8	60	34.7 ± 0.8	19.58 ± 0.01	4.9 ± 0.2
2	18	6	60	26.1 ± 0.6	19.58 ± 0.01	4.9 ± 0.2
3	30	10	60	43 ± 1	19.58 ± 0.01	4.9 ± 0.2
4	18	6	60	26.1 ± 0.6	19.803 ± 0.001	4.9 ± 0.2
5	24	8	60	34.7 ± 0.8	19.803 ± 0.001	4.9 ± 0.2
6	30	10	60	43 ± 1	19.803 ± 0.001	4.9 ± 0.2
7	21	7	60	30.4 ± 0.7	19.262 ± 0.002	4.8 ± 0.2
8	27	9	60	39.1 ± 0.9	19.262 ± 0.002	4.8 ± 0.2
9	21	7	60	30.4 ± 0.7	19.483 ± 0.002	4.9 ± 0.2
10	27	9	60	39.1 ± 0.9	19.483 ± 0.002	4.9 ± 0.2
11	21	7	60	30.1 ± 0.7	9.8279 ± 0.0007	2.38 ± 0.09
12	27	9	60	38.7 ± 0.9	9.8279 ± 0.0007	2.38 ± 0.09
13	18	6	60	25.8 ± 0.6	9.8279 ± 0.0007	2.38 ± 0.09
14	24	8	60	34.4 ± 0.8	9.8279 ± 0.0007	2.38 ± 0.09
15	30	10	60	43 ± 1	10.062 ± 0.004	2.44 ± 0.09
16	18	6	60	26.3 ± 0.6	29.6539 ± 0.0005	7.2 ± 0.3
17	24	8	60	35.1 ± 0.8	29.6539 ± 0.0005	7.2 ± 0.3
18	30	10	60	44 ± 1	29.6539 ± 0.0005	7.2 ± 0.3
19	21	7	60	30.7 ± 0.7	29.6539 ± 0.0005	7.2 ± 0.3
20	27	9	60	39.4 ± 0.9	29.6539 ± 0.0005	7.2 ± 0.3

Furthermore, the inlet and outlet temperatures of the reactor were estimated using the heat transfer coefficient estimated in Section 5.5 for a diluted organic feed, resulting in the predicted temperatures in Table 8.3. From these, the temperature variation across the reactor was expected to be between 11 and 27 °C, depending on the inlet flowrate.

8.2.2 Progress summary

The described experiments benefited from the experience acquired over the work presented in the previous chapter. The selected analytical methods were based on previous studies by Sirong He at Tianjin University [142,143] and during her visit to the group in 2020. Therefore, the 20 experiments

¹⁰ Organic feed flowrate considered the density of the solution, calculated using SAFT- γ Mie equation of state as described in Section 4.1.3. SCW flowrate accounted for HPLC pump flowrate correction in Section 5.2.

in Table 8.2 were conducted chronologically without significant modifications. Nonetheless, some aspects had to be reviewed throughout the study, particularly between experiments 10 and 11, as summarised in the following sections.

Table 8.3: Measured pressure and temperature, estimated temperature boundaries and average residence time for sucrose hydrothermal degradation experiments.

Exp	Pressure (bar)	Measured temperature (°C)			Predicted temperature (°C)				Average residence time (s)
		Setpoint	At TT-102	At TT-105	Inlet	Outlet	Difference	SCTT	
1	249	460	393	364	370	356	14	385	4
2	250	460	389	360	369	348	21	386	6
3	251	460	396	367	372	361	11	386	3
4	250	409	367	320	332	306	26	386	7
5	248	409	366	322	331	311	20	385	5
6	249	409	365	317	325	308	16	385	4
7	246	406	364	303	314	291	23	384	6
8	247	406	363	303	311	294	18	385	5
9	248	420	372	342	352	331	21	385	5
10	247	416	369	339	347	330	17	385	4
11	252	460	393	361	369	351	18	386	5
12	253	460	397	364	370	357	13	387	4
13	254	425	375	340	352	326	25	387	6
14	250	420	372	342	351	332	19	386	5
15	251	420	372	341	348	333	15	386	4
16	251	406	365	300	312	286	26	386	7
17	252	406	364	292	301	282	20	386	5
18	251	408	365	302	309	294	16	386	4
19	250	410	369	321	331	309	22	386	6
20	252	410	368	319	327	310	18	386	4

Seal replacement in P-3 (quench pump)

As mentioned, the experiments in Table 8.3 were performed in chronological order. As described in Section 8.3, before conducting experiment 11, it was found that the quench pump (P-3) was discharging a flowrate lower than specified, due to an internal leak. This was fixed before conducting the remaining experiments by replacing the pump's seals.

Solid filtration

Section 3.5.1 includes the description of two different filtration processes occurring during sucrose's hydrothermal processing and sample analysis. The first occurs during the rig's continuous operation, when the cooled product stream crosses the 100 μm mesh in one of the online filters (F-1A/B in Figure 3.1 of Section 3.3). The mass of solids retained was measured in selected experiments, after switching

the operating filter during steady state operation over a known period. The second filtration is the one mentioned previously in this chapter, after the liquid sample passes through the 11 μm filter paper during solvent extraction.

The average mass of solids accumulated per minute through the different filtration methods is presented in Table 8.4. The values in the second column are considerably smaller than the ones in the third. In fact, the mass of solids accumulated in the online filters is within the uncertainty of the mass retained during extraction. Based on those observations, the solids accumulated in F-1A/B during operation were neglected in all calculations.

Table 8.4: Average mass of solids accumulated per minute through the different filtration processes.

Experiment	Average mass of solids accumulated per minute (mg)	
	Retained in F-1A/B (> 100 μm)	Retained during extraction (> 11 μm)
1	3.5 ± 0.1	9 ± 9
4	1.7 ± 0.1	27 ± 1
7	0.7 ± 0.1	15 ± 2
9	0.7 ± 0.3	26 ± 5
13	0.8 ± 0.1	11 ± 3
16	0.2 ± 0.1	38 ± 3
19	0.1 ± 0.1	73 ± 5

Solvent evaporation

Solvent evaporation of water-soluble organics (WSO) was initially conducted under vacuum and elevated temperatures (125 $^{\circ}\text{C}$), using a rotary evaporator [142,143], which lead to the formation of a solid residue at the base of the flask. To evaluate the impact of this residue in the mass balance, tests were performed using WSO samples from experiments 7 to 10, comparing the mass remaining after using the rotary evaporator with letting the samples slowly evaporate at atmospheric conditions.

The obtained WSO masses are presented in Table 8.5, reflecting losses up to 0.52 g when using the rotary evaporator. Consequently, the solvent evaporation method in subsequent experiments was changed from vacuum at to atmospheric pressure and room temperature.

Table 8.5: Variation of WSO mass for equivalent samples evaporated using a rotary evaporator or atmospherically.

Sample	WSO mass (g)		
	Using rotary evaporator	Atmospheric	Variation
7.1	1.08 ± 0.01	1.235 ± 0.003	0.16 ± 0.01
8.1	1.76 ± 0.01	2.282 ± 0.004	0.52 ± 0.01
9.1	0.65 ± 0.01	0.987 ± 0.005	0.33 ± 0.01
10.1	1.21 ± 0.01	1.635 ± 0.004	0.43 ± 0.01

In order to retain the data previously obtained from workup at lower pressure and higher temperature (experiments 1 to 6), the uncertainty associated with the WSO mass was increased to the maximum difference in Table 8.5 increased in 25% (0.65 g).

Solvent for GC analysis

Regarding DCM-soluble organics (DSO), the solvent initially considered for diluting the GC samples was also DCM. However, evaporation of this highly volatile solvent between workup and analysis was of concern because it would impact the quantification of the components. For that reason, from experiment 11, the dilution of DSO for GC analysis applied the same solvent used in the analysis of WSO samples, *i.e.*, methanol. This resulted in the rejection of any GC analysis of experiments 1 to 10 in the results analysis.

8.3 Product analysis

During each experiment, once the gas product reached composition steady state, at least two samples were collected from the liquid outlet during approximately 90 seconds. These consisted of a liquid phase with a small amount of suspended solids, as exemplified in Figure 8.3 for increasing concentrations of sucrose in the feed.

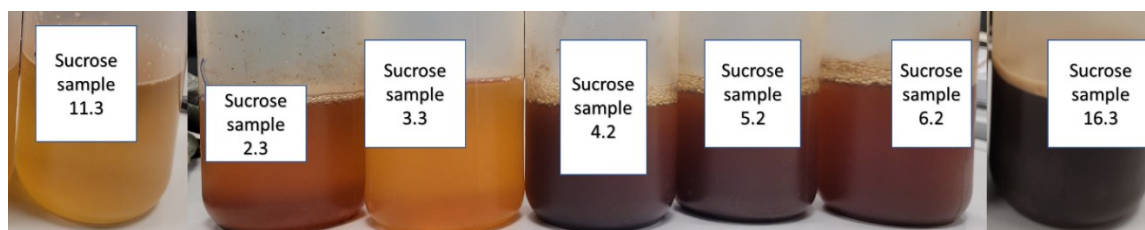


Figure 8.3: Examples of the effluent obtained at different concentrations and temperatures. Samples in order of increasing concentration and identified by the experiment numbers in Table 8.2.

As for the product analysis of dibenzyl ether, the production rate of each compound or group of compounds at the outlet was quantified as a yield (Y_i). However, given the inclusion of compound groups in this chapter, the yields were kept in a mass basis, *i.e.*, per unit mass of sucrose in the feed. The calculations to obtain these yields from experimental data are given in Appendix F, which also includes all sample specific data and associated uncertainties determined as described in Section 3.7.

To minimise the effect of random errors throughout sample processing and analysis, the values presented in this section for each experiment result from averaging the two samples with closest values. The only exceptions were experiments 4 to 6, which were based on the only sample evaporated under

room conditions, as all values apart from the WSO mass were similar. The obtained average values are also detailed in Appendix F.3.

The flowrate of each sample (in g/min) was determined by dividing their weight by the respective collection time. The flowrate difference between the sum of all feeds (total inlet) and the collected sample shown in Table 8.6 meant that the total mass balance was not closed. In Chapter 7 this was attributed to the formation of gaseous products in very small amounts, such as the ones identified in Section 8.3.2 for these experiments.

Table 8.6: HTL rig's flowrates: total inlet, suspension sample, and estimated gaseous product.

Exp.	Mass flowrate (g/min)			
	Inlet		Outlet	
	Sucrose	Total	Suspension	Gas (total – suspension)
1	8.0 ± 0.2	100 ± 2	97 ± 1	3 ± 2
2	6.0 ± 0.2	91 ± 2	89 ± 1	3 ± 2
3	10.0 ± 0.3	109 ± 2	105 ± 1	3 ± 3
4	6.0 ± 0.2	91 ± 2	88 ± 1	3 ± 2
5	8.0 ± 0.2	100 ± 2	97 ± 1	3 ± 2
6	10.0 ± 0.3	109 ± 2	104 ± 1	4 ± 3
7	7.0 ± 0.2	96 ± 2	90 ± 1	6 ± 2
8	9.0 ± 0.3	104 ± 2	98 ± 1	6 ± 2
9	7.0 ± 0.2	96 ± 2	88 ± 1	8 ± 2
10	9.0 ± 0.3	104 ± 2	96 ± 1	8 ± 2
11	7.3 ± 0.2	95 ± 2	94 ± 1	1 ± 2
12	9.4 ± 0.3	104 ± 2	102 ± 1	2 ± 2
13	6.3 ± 0.2	91 ± 2	90 ± 1	1 ± 2
14	8.4 ± 0.3	100 ± 2	98 ± 1	1 ± 2
15	10.4 ± 0.3	108 ± 2	106 ± 1	2 ± 3
16	6.7 ± 0.2	91 ± 2	91 ± 1	1 ± 2
17	9.0 ± 0.3	100 ± 2	98 ± 1	2 ± 2
18	11.2 ± 0.3	109 ± 2	107 ± 1	2 ± 3
19	7.8 ± 0.2	96 ± 2	95 ± 1	1 ± 2
20	10.1 ± 0.3	105 ± 2	103 ± 1	1 ± 3

However, the results in Table 8.6 show a significant difference between the total flowrate expected to enter the HTL rig based on pump specifications and the values measured at the outlet for the liquid product. This was particularly relevant in the first ten experiments, particularly from 7 to 10. Furthermore, those values were significantly close to the actual amount of sucrose entering the system (also shown in Table 8.6). Therefore, it was considered unlikely that the observed difference results in its totality from the gasification of sucrose. This abnormality suggested the malfunctioning in the quench pump mentioned in the previous section, which was confirmed by the negligible difference between inlet and outlet flowrates in the experiments that followed, *i.e.*, 11 to 20.

This fault in the quench pump resulted in total inlet flowrates lower than expected (*i.e.*, the ones in Table 8.6). Nonetheless, this error only affected the temperature and amount of water downstream of the quench, not influencing any further results. It was assumed that the inherent warmer temperatures downstream of the quench did not affect the HTL products significantly. Due to time limitations, it was not possible to repeat experiments 1 to 10, though it is recommended that comparison studies are conducted in the future.

8.3.1 Phase distribution

As described in Section 8.2, each liquid sample was simultaneously filtered and extracted with dichloromethane, from which were obtained solid, water-soluble, and DCM-soluble samples. The solvent was evaporated, resulting in extracts such as the ones in Figure 8.4. Their final weights were divided by the original sample collection time, giving the flowrates of solids, DCM-soluble organics (DSO), and water-soluble organics (WSO). The sum of WSO and DSO provides the flowrate of total soluble organics (TSO).



Figure 8.4: From left to right, examples of phase separation during solvent extraction, and evaporated samples of solids, WSO, and DSO.

The flowrate of TSO and solids was divided by the flowrate of sucrose in the organic feed, resulting in the mass yield distribution represented in Figure 8.5. Assuming that the total mass flowrate of organic matter in the system was not significantly affected by its reactions with water, the sum of the yields of TSO and solids should be close to 100%, *i.e.*, the total outlet flowrate of organic compounds is the same as the inlet flowrate of sucrose. As shown in Figure 8.5, this was not observed in any experiment. The difference between the two was assumed to be the flowrate of either gases produced in the hydrothermal reactor or evaporated alongside the solvent during sample work up. During the experimental analysis, those missing products were accounted for by an additional group of compounds designated volatiles.

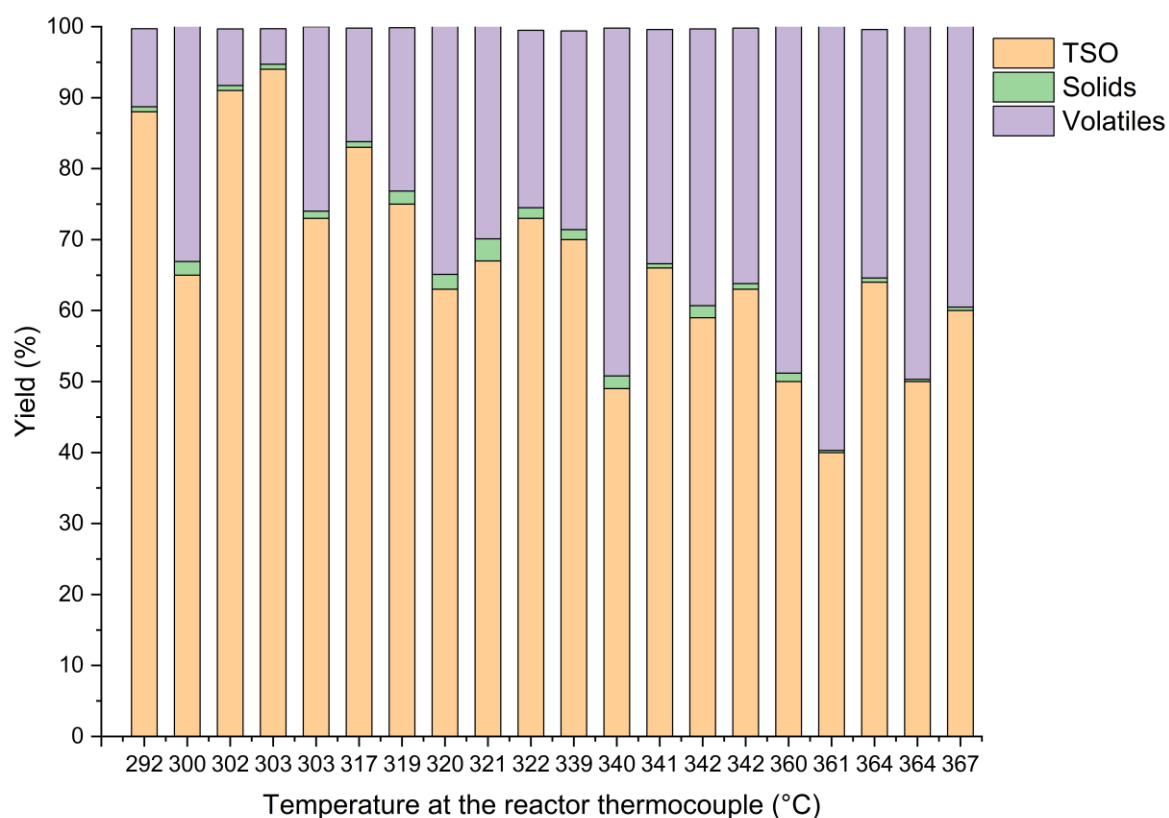


Figure 8.5: Distribution of products in total soluble organics (TSO), solids, and volatiles for increasing reactor temperature.

Generally, as temperature increases, the yield of soluble organics tends to decrease, going from a maximum of approximately 90% at 303 °C to a minimum of 40% at 361 °C. This trend was not followed by the yield of solids, reflecting that at higher temperatures, the degradation of soluble organics into volatile compounds is favoured. Nonetheless, this is not a monotonic trend, as exemplified by the sharp decreases at 300 and 361 °C. This was considered to result from the temperature not being the only variable changed between experiments. The plots in Figure 8.6 show the variation of these yields not only with temperature, but also with the average residence time (RT), and sucrose's mass fraction at the reactor's inlet, $w(\text{Suc})_0$.

Regarding TSO, their yield decreased with both temperature and residence time, showing this group contains feed, and intermediary organics that were consistently subject to degradation reactions. Conversely, the calculated yield of compounds assumed to be volatiles increased with temperature and residence time, varying between 8 and 60%, thus confirming that these are the major final products.

Solids were produced at a considerably smaller scale, with yields varying only between 0.5 and 3.1%. Their amount tended to increase with residence time, showing these were final products, not subject to further degradation. Nonetheless, the variation with temperature is not linear, showing a maximum at

intermediate temperatures. This suggested solids and volatiles formation are competitive reactions, with the latter overcoming the former after approximately 320 °C.

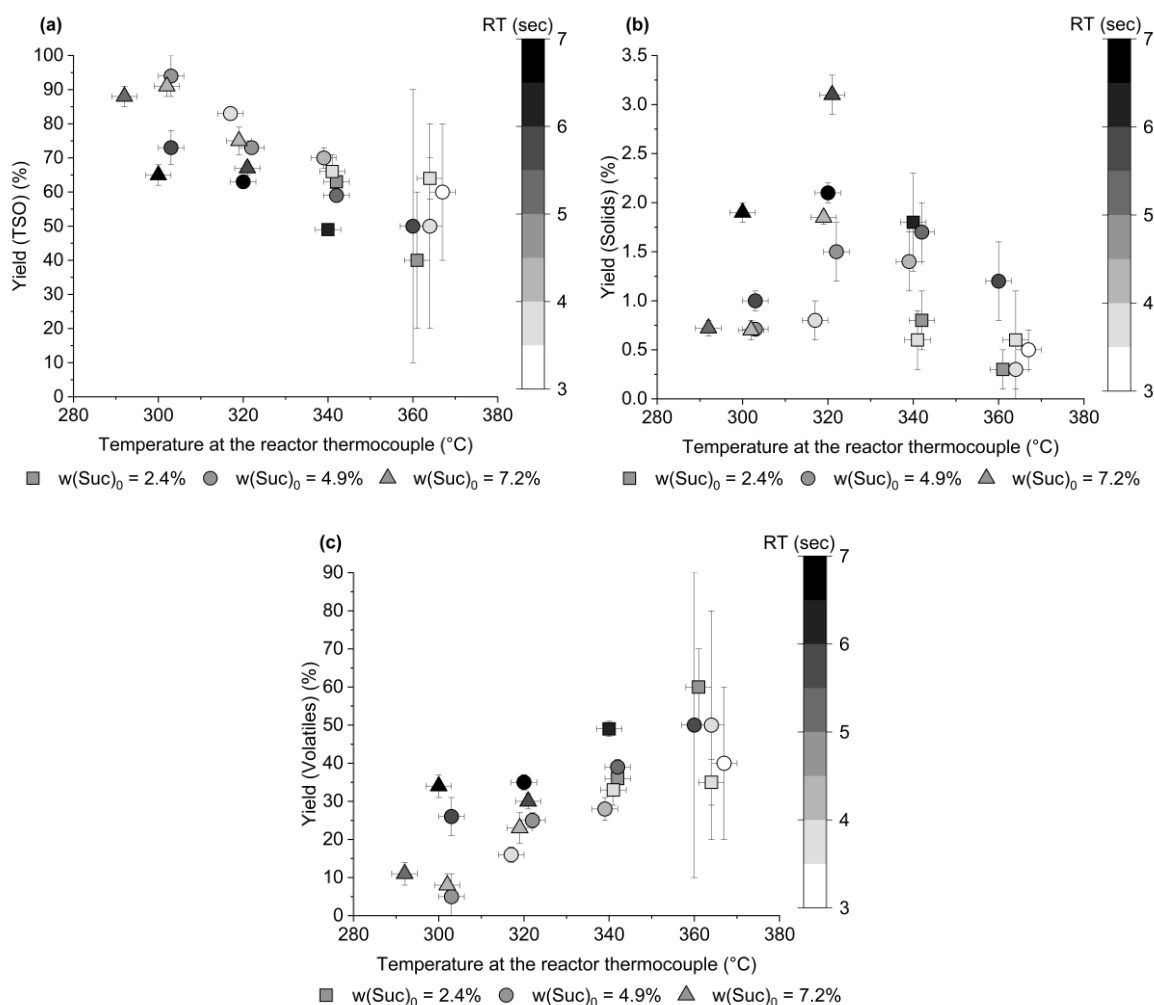


Figure 8.6: TSO (a), solids (b), and volatiles (c) yield variation with temperature, residence time (RT), and inlet composition. Larger error bars after 360 °C

Given the relatively small yields of solids, no additional qualitative analysis was pursued for these products. Nonetheless, their yield was included in the estimation of kinetic parameters in Section 8.5. On the other hand, the compositional analysis of liquid and gaseous products is further discussed in the following sections.

8.3.2 Gases

During all experiments, the composition of the gas effluent was monitored using an FTIR spectrometer. It included the tracking of the different species mentioned in Section 8.2, from which CO_2 , CO ,

methane, and ethylene were found in larger amounts (excluding water). Figure 8.7 exemplifies the compositions measured in the FTIR spectrometer during three consecutive experiments. Each plot contains two vertical dotted bars per experiment, representing the minute when the organic feed was initiated, and the minute when the first sample was collected. After this point the flow is disturbed and the composition decreases. The composition measurement is taken from the steady state section immediately before the sampling bar, *i.e.*, the second dotted line.

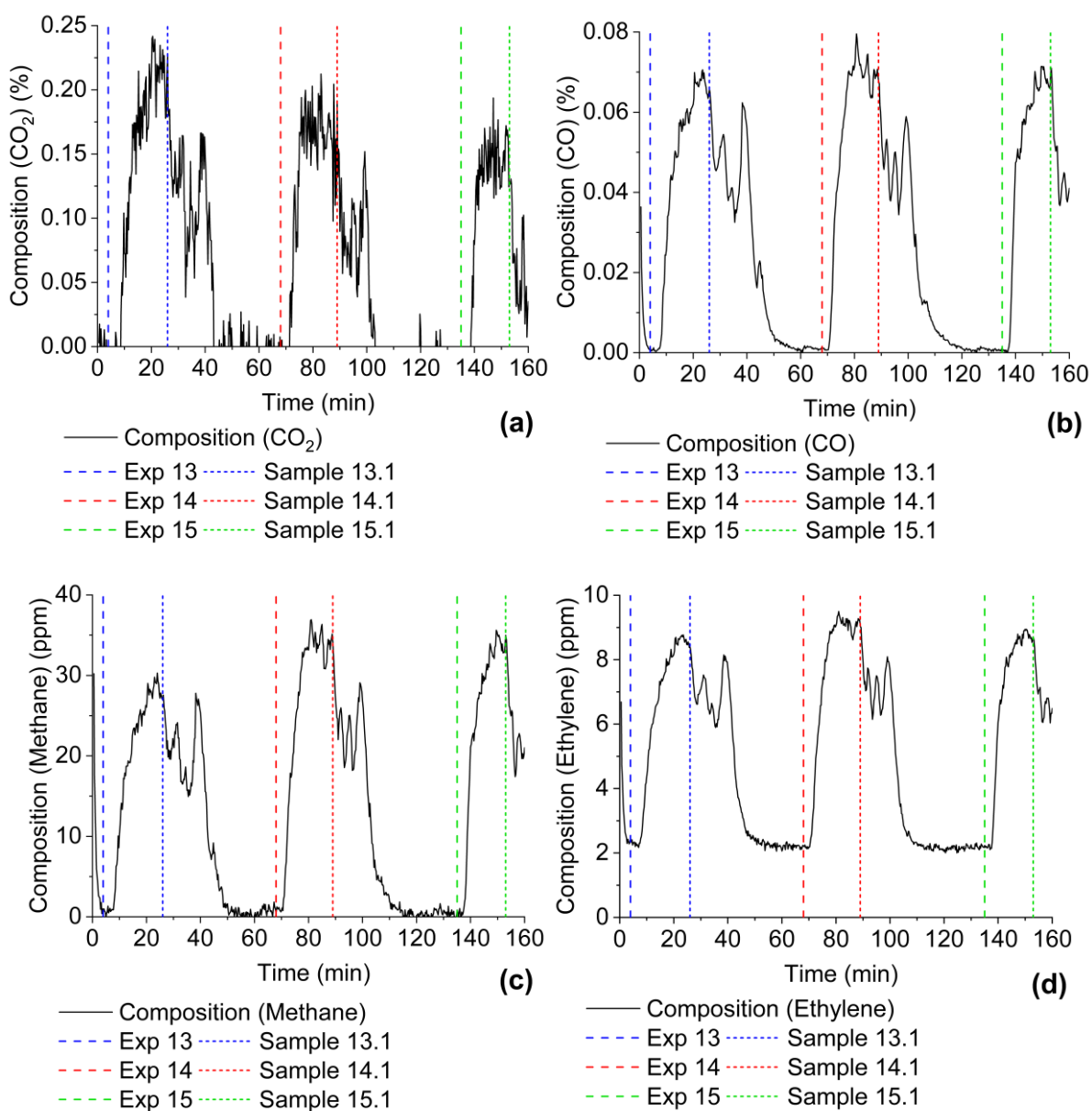


Figure 8.7: Compositions of CO₂ (a), CO (b), methane (c), and ethylene (d) measured in the FTIR analyser during experiments 13, 14, and 15. Each experiment is represented sequentially by two vertical bars. First vertical bar (long dashed) signals the minute when the organic feed was initiated. Second vertical bar (short dashed) signals the minute when the first liquid sample was collected. All compositions are in mass basis referred to the total flowrate of gas at the rig's outlet.

From the compositions above, the flowrate of each gas was determined using equation (3.3) in Section 3.6.7 (or equation (F.7) in Appendix F.1). Those flowrates were divided by the inlet flowrate of sucrose, producing the yields in Figure 8.8. The calculated yields demonstrated that CO₂ and CO were produced in substantially larger amounts when compared with methane and ethylene. This gas distribution is in line with the literature summarised in Table 8.1 [104,160]. Those sources consider a third major gas product, hydrogen, which is not detectable through FTIR spectrometry, thus was not quantified.

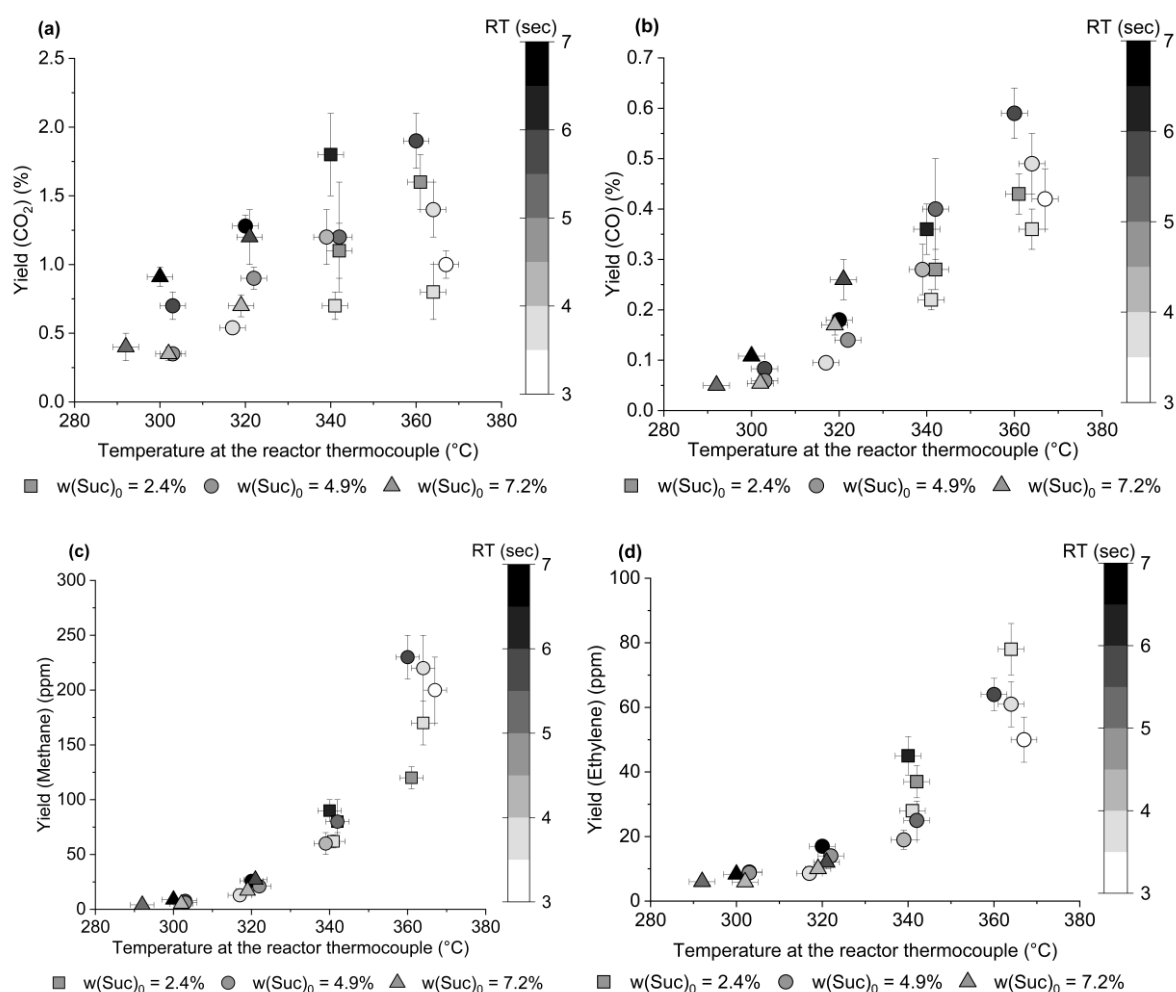


Figure 8.8: CO₂ (a), CO (b), methane (c), and ethylene (d) yield variation with temperature, residence time (RT), and inlet mass fraction ($w(\text{Suc})_0$). All yields were calculated in mass basis referred to the inlet mass of sucrose.

The yield of these gases presented a general increase with both temperature and residence time, a characteristic of end products. The effect of residence time was particularly marked for the yield of CO₂. Both CO₂ and CO presented an approximately linear increase with temperature, unlike methane and ethylene, which showed an exponential variation. Such behaviour suggested that the hydrocarbons were mainly produced through reactions occurring only at higher temperatures.

Figure 8.9 shows the relative amount of each measured gas within the amount attributed to volatiles, *i.e.*, compounds that were not in the liquid samples after solvent evaporation, nor in the produced solids. As presented, there was a large difference between measured gases and the total volatile fraction, with the first representing less than 6% of the last, as represented in Figure 8.9. The same chart reflects that methane and ethylene are found in significantly smaller amounts, and that the CO/CO₂ ratio increases with temperature, thus agreeing with Watanabe *et al.*'s observations [160].

This suggests that over 90% of the volatile fraction was composed by organics vaporised along the solvent during sample preparation. This was an undesirable outcome, thus requiring a re-evaluation of the solvent evaporation method in future work.

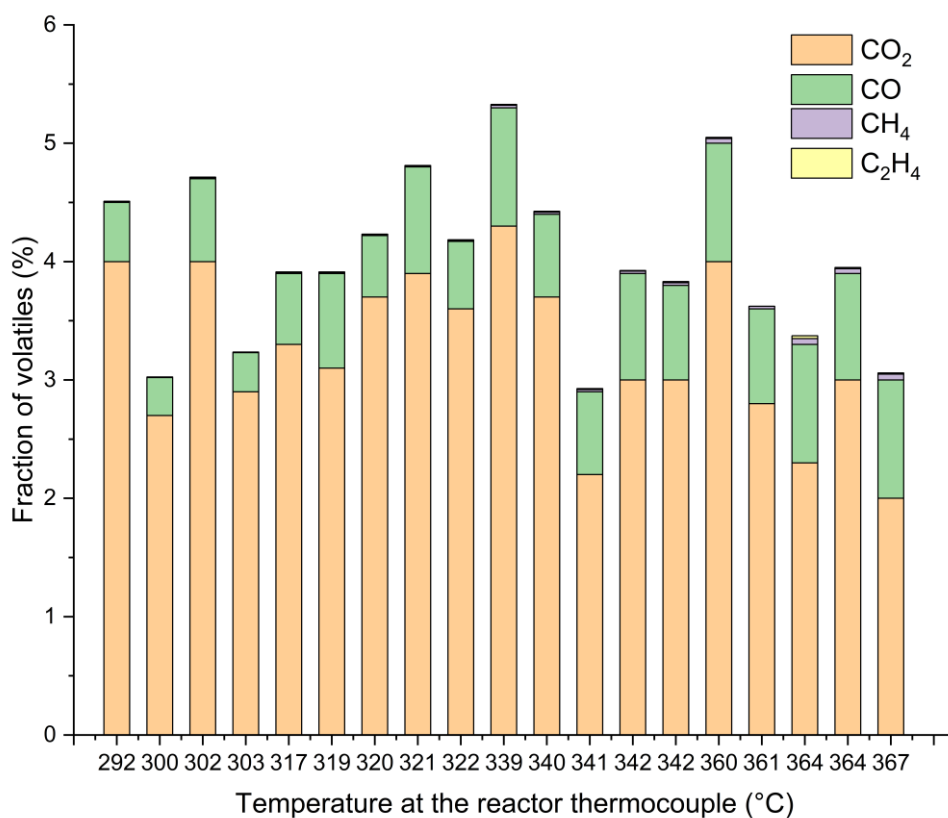


Figure 8.9: Gases relative distribution within volatiles for increasing reactor temperature.

8.3.3 Soluble organics

The TSO yields in Figure 8.6 resulted from summing the masses of DCM- and water-soluble organics obtained after solvent extraction and evaporation. The individual yields of those two fractions are plotted in Figure 8.10, showing the prevalence of WSO. These were responsible for TSO's overall trend, varying similarly with temperature and residence time. On the other hand, the DSO fraction hints at an initial increase with temperature and residence time.

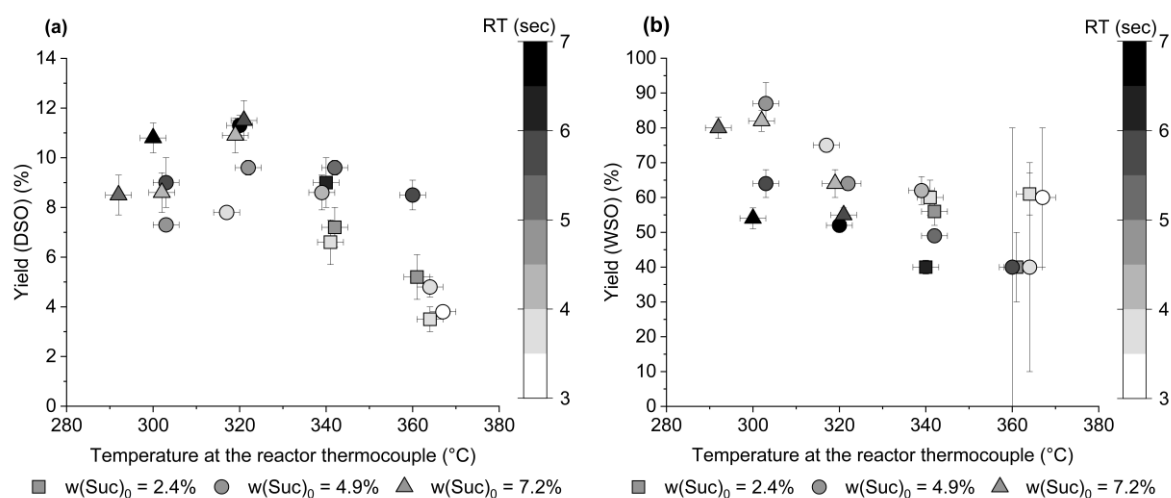


Figure 8.10: DSO (a) and WSO (b) yield variation with temperature, residence time (RT), and inlet mass fraction ($w(\text{Suc})_0$).

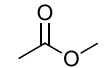
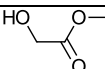
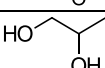
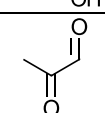
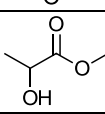
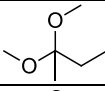
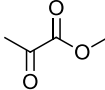
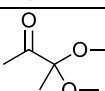
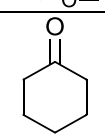
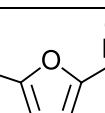
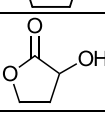
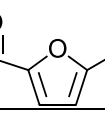
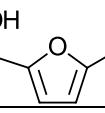
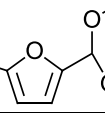
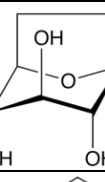
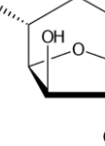
Qualitative analysis: GC-MS

As mentioned in Section 8.2.2, only WSO and DSO samples from experiments 11 to 20 were analysed through gas chromatography (GC) using methanol as a solvent. The associated mass spectrometry (MS) allowed the identification of the molecules in each sample, from which resulted the list in Table 8.7. Apart from the presented ones, larger chain hydrocarbons, such as oleic acid were identified at longer retention times with negligible peaks.

Comparing the different molecules found in DSO and WSO samples, the solvent extraction with DCM mainly removed 5-HMF and its derivatives, such as 5-HDF, from the aqueous phase, while acids and aldehydes remained in water. 5-HDF and 5-HMF were detected in both DSO and WSO samples, indicating an imperfect extraction process, which would have required an even larger volume of DCM to completely remove those species from the aqueous sample. Furthermore, quantitative analysis showed a non-negligible amount of the two in both phases, thus reducing the quantitative significance of the individual DSO and WSO yields plotted in Figure 8.10. Consequently, only the total amount of soluble organics was considered during the parameter estimation process in Section 8.5.

All chromatograms obtained during the GC-MS analysis of WSO and DSO samples from experiments 11 to 20 presented the largest peak at the same retention time, corresponding to 5-HDF. Furthermore, Table 8.7 shows that besides this molecule, other methyl esters like methyl glycolate, methyl lactate, and methyl pyruvate, were detected in WSO samples. These are the esterified forms of expected products glycolaldehyde, lactic acid, and pyruvaldehyde, respectively [223–225].

Table 8.7: Compounds identified through GC-MS.

Name	Molecular structure	Retention time (min)	Sample
Methyl acetate		7.1	WSO
Methyl Glycolate		7.5	WSO
Propylene Glycol		7.6	WSO
Pyruvaldehyde		7.9	WSO
Methyl lactate		8.3	WSO
2,2-Dimethoxybutane		8.5	DSO + WSO
Methyl pyruvate		9.1	WSO
3,3-Dimethoxy-2-butanone		10.2	DSO
Cyclohexanone		11.8	WSO
5-Methylfurfural		12.3	DSO
2-Hydroxy-γ-butyrolactone		12.8	WSO
2,5-Furandicarboxaldehyde		14.3	DSO
5-(Hydroxymethyl) furfural		16.4	DSO + WSO
5-(Hydroxymethyl)-2-(dimethoxy methyl)furan		17.2	DSO + WSO
1,6-Anhydro-β-D-glucose		19.6	WSO
1,6-Anhydro-β-D-glucofuranose		20.8	WSO

The presence of these compounds instead of the expected ones suggested that esterification may have occurred somewhere in the process. This transformation is characterised by the acid-catalysed reaction of a carboxylic acid, aldehyde, or ketone in the presence of an alcohol. If this alcohol is methanol, then a methyl ester is obtained. Furthermore, 5-HDF and similar methyl esters have been identified in the conversion of cellulose, glucose, and 5-HMF, when methanol was used in the solvent mixture [69,151,226].

On the other hand, the calibration of the flame ionisation detector with standard solutions of 5-HMF in methanol did not show any 5-HDF. This may have resulted from a shorter exposition period, since, unlike process samples, calibration standards were immediately analysed after preparation. It is also possible that 5-HMF esterification only occurred in the analysed samples due to the presence of additional species, such as acids, which catalysed the transformation.

March's *Advanced Organic Chemistry* book [217] refers that esterification of carboxylic acids may occur when an excessive amount of alcohol is added, or when water is removed from the mixture. This is the exact procedure applied during the preparation of samples for gas chromatography. Therefore, it is highly likely that the detected methyl esters were formed during this step. This was further confirmed by the rejected DSO chromatograms from experiments 1 to 10, which used DCM as a solvent instead of methanol. In those, 5-HDF was absent, and the largest peak corresponded to 5-HMF instead, thus confirming the reaction was caused by the new solvent.

Despite the detection of methyl esters instead of the original compounds, these still provided evidence of the last's presence before methanol dilution. Therefore, the planned qualitative analysis was still achieved. Regarding the quantitative analysis, unlike 5-HMF, 5-HDF is not commercially available, thus it was not possible to calibrate the FID using specific standard solutions. For that reason, it was assumed that, given their structural similarities, 5-HDF and 5-HMF produce equivalent signals in the FID chromatogram. Hence the calibration in Appendix B.4 was applied to quantify both species.

5-methyl furfural and 2,5-furandicarboxaldehyde were only identified among the DSO. The different forms of furfural compounds apart from 5-HDF and 5-HMF suggest the latter was substantially produced, and partially degraded.

The presence of a butyrolactone hints that levulinic acid was one of these degradation products [217]. The detection of pyruvaldehyde/methyl pyruvate and methyl lactate reflects that their respective pathway in Figure 8.1 was completely followed. On the other hand, the absence of glyceraldehyde derivatives suggests this species was quickly converted to pyruvaldehyde. The presence of methyl glycolate indicated that glycolaldehyde and erythrose were also produced from glucose and/or fructose but were either non-detectable through GC-MS or fully converted.

Overall, the detected compounds confirm all reaction pathways summarised in Figure 8.1. The only modification can be derived from the presence of not only 1,6-anhydro- β -D-glucose, but also 1,6-anhydro- β -D-glucofuranose, suggesting an additional reaction for glucose [71].

Quantitative analysis: GC-FID

From the compounds in Table 8.7, 5-HDF produced the largest peak in the GC-MS chromatograms. The chromatograms obtained through flame ionisation detection (FID) also presented the highest peak area at a similar retention time, thus indicating that both correspond to 5-HDF. Since this species is representative of fructose's dehydration into 5-HMF, its composition was quantified. Remaining intermediaries of interest, such as 1,6-anhydro- β -D-glucose, and pyruvaldehyde, which were detected only in the WSO sample, were quantified through HPLC-RID.

For each sample, the yields of 5-HDF and 5-HMF were calculated for both WSO and DSO. The resulting four values were summed up, returning the sample's yield of 5-HMF. Its variation with the temperature measured in the reactor, average residence time, and inlet composition is shown in Figure 8.11.

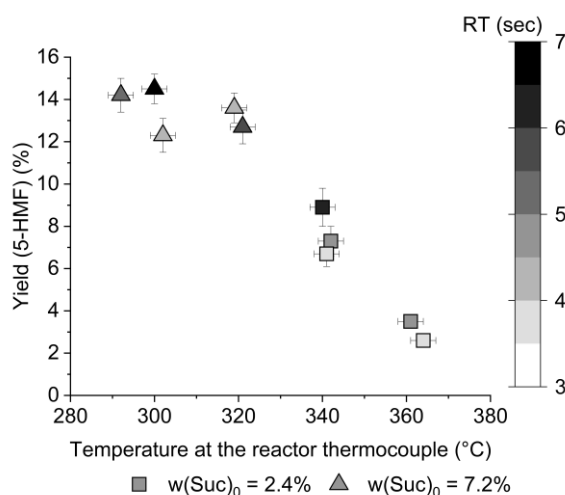


Figure 8.11: 5-HMF yield variation with temperature, residence time (RT), and inlet mass fraction ($w(\text{Suc})_0$). Includes only experiments 11 to 20.

The yield of 5-HMF is observed to decrease with temperature, whilst showing an overall tendency to increase with residence time. This effect can be attributed to increased rates of degradation or competitive reactions at higher temperatures, and to the decrease in water's self-ionisation product near its SCTT. The latter hypothesis indicates that 5-HMF's formation may be acid or base catalysed, further discussed in Section 8.5 via the comparison of estimated kinetic parameters.

Quantitative analysis: HPLC-RID

The compounds in water soluble samples before solvent evaporation were analysed by high-performance liquid chromatography with refractive index detection (HPLC-RID). While this analysis mainly focused on quantifying sucrose and the products of its hydrolysis, *i.e.*, glucose and fructose, it was also used to quantify other WSO resulting from further degradation of the two monomers. These were selected to represent each reactional pathway in Figure 8.1, based on their detectability by RID [159], as well as their commercial availability. Therefore, sucrose, glucose, fructose, 1,6-Anhydro- β -D-glucose, and pyruvaldehyde were quantified by HPLC-RID, using the calibration in Appendix B.3.

This analysis resulted in chromatograms as the ones in Figure 8.12, where the quantified components were identified. Sucrose's calibration in Appendix B.3 indicated an expected retention time of 11.3 minutes. However, none of the analysed samples displayed a significant peak at this time, reflecting total conversion of sucrose under the operating conditions tested in the present study. This is in line with several existing studies [220–222,227], referring to how easily sucrose's glucosidic bond is hydrolysed. Consequently, kinetic parameters could not be estimated for this reaction, owing to the full conversion. As a result, an equimolar mixture of glucose and fructose was considered as the feed to the reactor, henceforth referred to as “pseudo-feeds”.

Besides the quantified compounds, which were directly identified in Figure 8.12, peaks were consistently found at retention times of approximately 55 and 58 minutes. Despite being larger than the remaining peaks, this is not a direct indication of the associated relative amounts, as demonstrated by benzyl alcohol and benzaldehyde in Appendix B.2. Compared to the calibration peaks shown in Appendix B.3, no peaks were expected at retention times of approximately 55 and 58 minutes. Consequently, the compounds that generated those peaks remained unidentified. It is possible that those compounds were 5-HMF or related compounds since, according to Chuntanapum *et al.* [104], 5-HMF is also detectable through HPLC-RID at longer residence times.

The yields related to the remaining quantified compounds are plotted in Figure 8.13. Considering that sucrose is hydrolysed to glucose and fructose in equimolar proportions, their initial yield were 52-53 wt% with respect to the initial mass of sucrose (as defined in equation (8.1) in Section 8.4), with the additional 2 – 3% above 50% being due to the inclusion of a water molecule. From the two, fructose shows consistently lower yields, thus proving to be more reactive than glucose. An isomerisation equilibrium driven towards glucose, may also explain this observation. However, it is not supported by the literature [64,71,159].

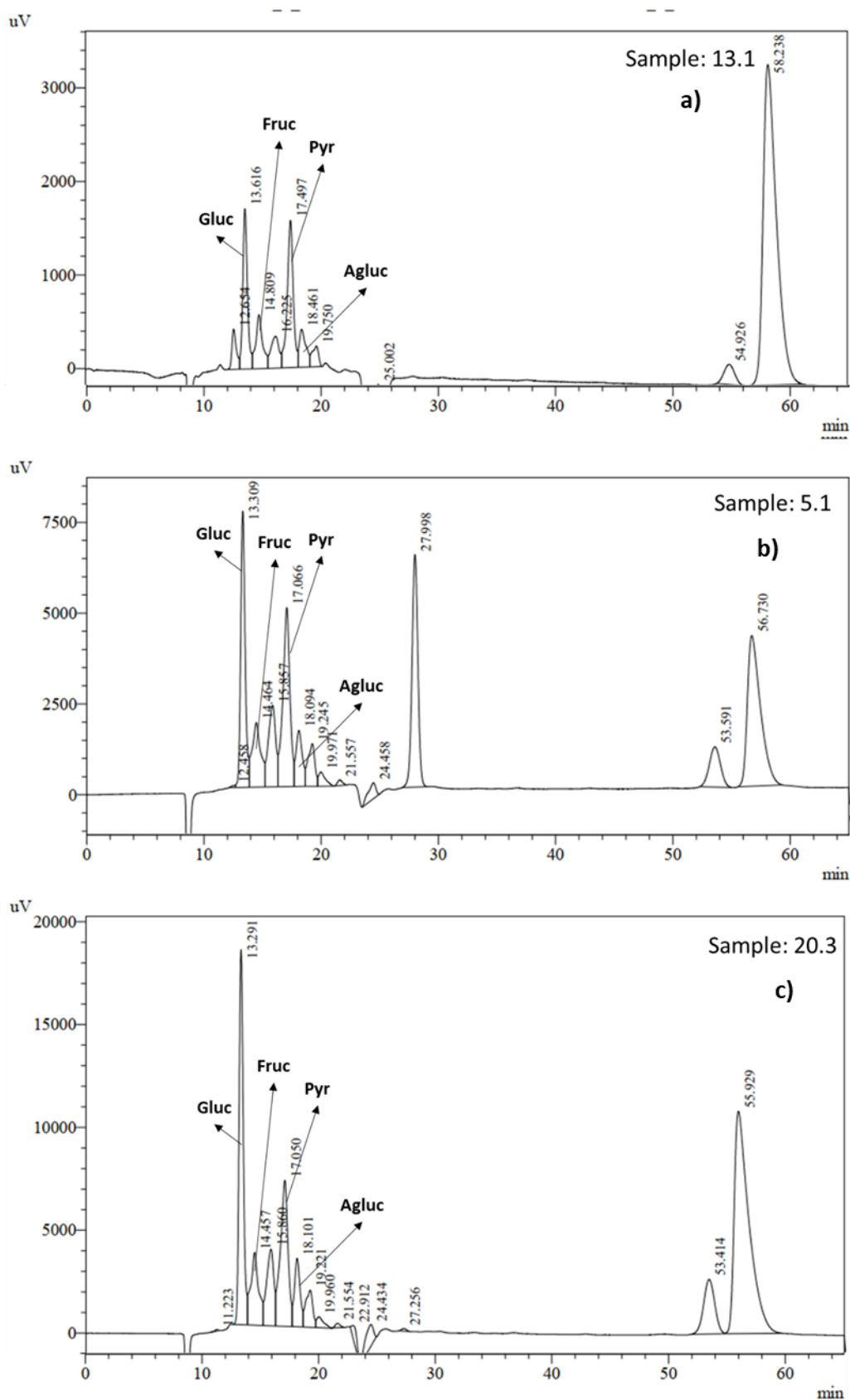


Figure 8.12: HPLC-RID chromatograms obtained for WSO samples representative of different feed concentrations. Sucrose mass fraction at the inlet of the reactor was 4.9, 2.38, and 7.3 % for samples 13.1 (a), 5.1 (b), and 20.3 (c), respectively.

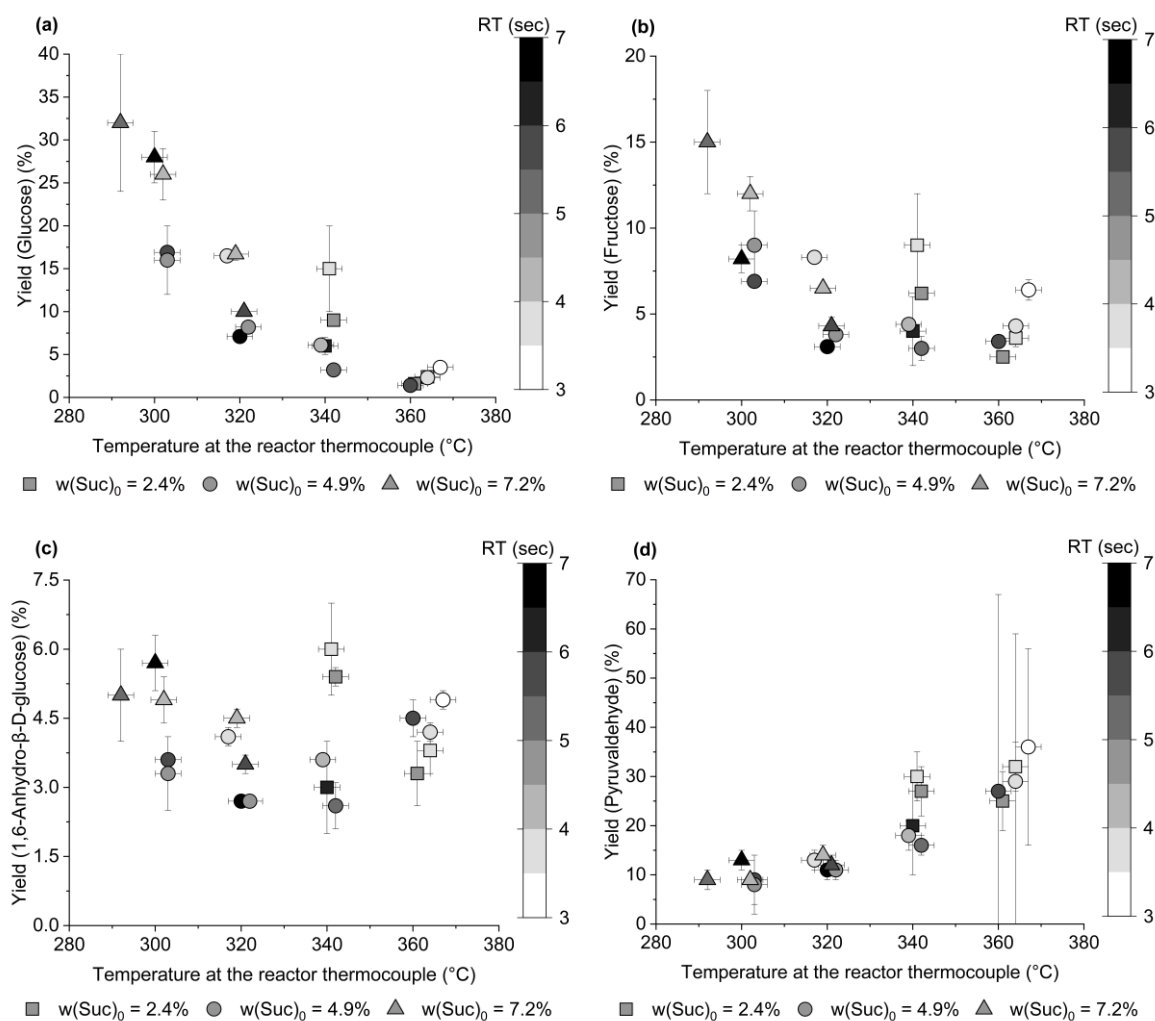


Figure 8.13: Glucose (a), fructose (b), 1,6-Anhydro- β -D-glucose (c), and pyruvaldehyde (d) yield variation with temperature, residence time (RT), and inlet mass fraction ($w(\text{Suc})_0$).

The yields of the two monosaccharides decreased with residence time and temperature. This reflected the compounds' behaviour as pseudo-feeds, *i.e.*, effectively forming the feeds to the reactor, since the slower they crossed the reactor the more they were consumed, while the hotter the feed is, the faster they degrade. The yield of monomers suggested a minimum near 350 °C, which could be caused by the residence time decrease after this point, or due to the decrease of water's self-ionisation product. The kinetic analysis in Section 8.5 investigates both possibilities.

The yield of 1,6-anhydro- β -D-glucose showed the smallest variation, which was a sign of similar formation and degradation rates. There was no clear trend regarding residence time, while a minimum is observed with temperature, around 340 °C. This could be an indication that the reduction in water's self-ionisation product promoted this species formation or hindered its degradation.

The formation of pyruvaldehyde prevailed over its degradation, with a consistent yield increase with temperature. The influence of residence time was masked by the uncertainty in the pyruvaldehyde yield, though it appeared its formation also benefited from longer residence times.

Total soluble organics distribution

Figure 8.14 shows how the relative distribution of products within the TSO fraction varied with temperature. At lower temperatures, the organics leaving the reactor in solution were mainly comprised of glucose, followed by similar amounts of fructose, 5-HMF, and unmeasured soluble organics (other SO), and smaller quantities of pyruvaldehyde and 1,6-anhydro- β -glucose. As temperature increased the soluble organics were enriched in pyruvaldehyde, while glucose significantly decreased. When measured, the fraction of 5-HMF also tended to decrease, while 1,6-anhydro- β -glucose marginally increased. The fraction of fructose remained similar, suggesting a compensation effect through the isomerisation of glucose.

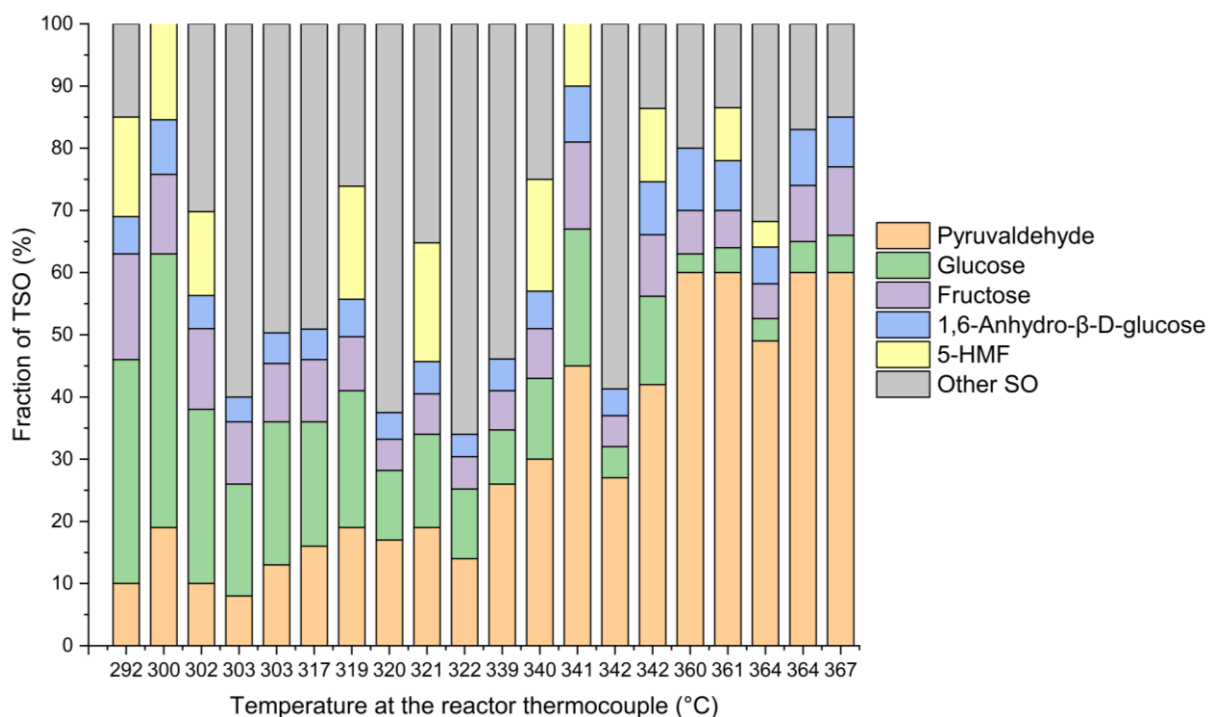


Figure 8.14: Soluble organic distribution for increasing reactor temperature. Absence of 5-HMF indicates it was not measured, thus being included as other WSO.

8.4 Mathematical model description

The 20 experiments were simulated using the reactor model previously applied to dibenzyl ether and described in Chapter 4. The same geometrical parameters were used ($ID = 3.86$ mm, $L_R = 35.4$ cm, and $l-L_{TC}/L_R = 0.47$), while operating conditions (pressure, flowrate and, temperature) were specified according to the values in Table 8.2 and Table 8.3.

On the other hand, since the fraction of organic matter was kept below 10 wt% of the reaction mixture in all experiments, the properties of pure water (*e.g.*, density and enthalpy) determined using IAPWS-95 [55] were assumed to sufficiently describe the mixture. Dispersion was neglected due to the low concentration of sucrose, and heat losses were accounted using the specific overall heat transfer coefficient estimated in Section 5.5 of $51 \text{ W}\cdot\text{m}^{-2}\cdot\text{K}^{-1}$.

8.4.1 Component list and reaction network

Figure 8.1 summarised the different reactions of sucrose, and subsequently glucose and fructose, that are expected to occur in a hydrothermal medium. Those comprise different compounds which were lumped in the component groups defined in Section 8.3.1, *i.e.*, soluble organics, solids, and volatiles. The molecules specifically analysed in Section 8.3.3 (sucrose, glucose, fructose, 5-HMF, 1,6-anhydro- β -D-glucose, and pyruvaldehyde) were extracted from those groups, resulting in the generic reaction network in Figure 8.15.

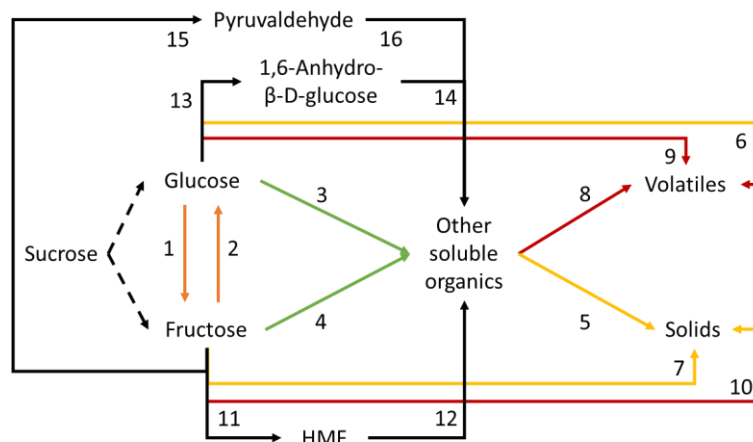


Figure 8.15: Modelled reaction pathway for glucose and fructose in hydrothermal medium.

Since sucrose was not detected in any of the analysed samples, its hydrolysis was omitted from the mathematical model, and the molecule was not included in the model's compound list, as it would unnecessarily increase its complexity. Consequently, the reactor's inlet composition was defined in

terms of glucose and fructose, considering an equimolar distribution of sucrose's mass fraction in Table 8.2, as described by equation (8.1).

$$w_{Gluc}^{in} = w_{Fruc}^{in} = \frac{w_{Suc}^{in} \times MW_{Gluc}}{MW_{Suc}} \quad (8.1)$$

The gaseous products (CO₂, CO, methane, and ethylene), discussed in Section 8.3.2, were also excluded from the reactor model, as they were not associated to specific reactions and represented less than 6% of the volatiles group.

Figure 8.15 shows the sixteen reactions, which were considered. In common with the studies presented in Table 8.1, all reactions were assumed to be of first order, and represented by one molecule of reactant producing the same number of product molecules. The influence of the water's self-ionisation product was included in the rate equation of each reaction as the approximated proton concentration described in Section 4.6. This was a crude approximation, as other species may significantly contribute to medium acidity apart from water. Nonetheless, given the high dilution of the reactional mixture, this approximation was kept. The inclusion or exclusion of this effect on each reaction was determined during the estimation of kinetic parameters in Section 8.5.

Overall, the sixteen reactions that describe the hydrothermal behaviour of sucrose revolved around three lumped component groups, and five known species. Together with the solvent, *i.e.*, water, they define the nine elements in the component list of the mathematical model. Since all reactions are of first order and defined as one-to-one, the molecular weight of each component becomes irrelevant. Therefore, the model was simplified by assuming all components have sucrose's molecular weight, automatically balancing all chemical reactions, and calculating a yield equivalent in either mass or molar basis.

8.5 Kinetic parameters estimation

The kinetic parameters relative to each reaction in Figure 8.15 were estimated by applying the procedure summarised in Section 4.1.3 to the gPROMS mathematical model described in the previous section. Each of the sixteen reactions comprises an activation energy (E_a) and kinetic constant at reference temperature (k_{ref}), thus a maximum of 32 parameters could be estimated.

The average yields presented throughout Section 8.3 and summarised in Appendix F.3 constitute the set of measured data used to fit the kinetic parameters. For experiments 11 to 20 in Table 8.2, those yields are relative to: TSO, solids, glucose, fructose, 5-HMF, 1,6-anhydro-β-D-glucose, and pyruvaldehyde¹¹. The first ten experiments considered the same yields except the ones relative to 5-HMF.

¹¹ TSO was modelled as the sum of all species apart from solids, volatiles, and water.

The volatile group was not included as measured data, since its yield resulted from closing the organic mass balance. This is already guaranteed by the mathematical formulation of the reactor model, thus making the inclusion of this fraction redundant. Therefore, a total of 130 data points was used for the estimation of the 32 kinetic parameters.

8.5.1 Systematic workflow

The parameter estimation process results in a set of optimal kinetic parameters and a minimised objective function (OF), which evaluates the error between measured and calculated values (see Section 4.1.3). Ignoring the effect of water's self-ionisation product, a direct estimation of the 32 kinetic parameters achieved an objective function of 738, with several reactions (4, 6, 7, 10, and 16) being assigned a rate of zero, while some of the estimated parameters have unreasonably high standard deviations ($E_{a,11} = 1 \pm 7$ kJ/mol; $E_{a,14} = 1 \pm 20$ kJ/mol). On the other hand, if all reactions account for the proton concentration, the objective function increased to 843, with some reactions also excluded (6 and 7) and unrealistically high activation energies (*e.g.*, $E_{a,4} = 500$ kJ/mol; $E_{a,16} = -500$ kJ/mol).

These preliminary results showed that not all reactions in Figure 8.15 were supported by experimental data. Keeping all the non-zero rate reactions resulted in parameters with unreasonably high uncertainty (overparameterization) and did not clarify for which reactions including the proton concentration was beneficial. Regarding the proton concentration, testing all possible combinations of including it or not would require 65 536 (2^{16}) different parameter estimations. Overall, this poses an unreliable and long estimation process. To improve it, the following objectives were defined:

- Minimise the objective function, thus reducing the difference between estimated and experimental data, by estimating the maximum number of kinetic parameters.
- Exclude from the model reactions that are not supported by experimental data.
- Detect when the estimation is overparameterized, and which parameters are responsible for that. Achieved by excluding parameters which standard deviation surpassed the estimated value.
- Apply the effect of varying water's self-ionisation product near the SCTT only when it improves the model fitting to experimental data.

Based on these goals, the workflow described by the flowchart in Figure 8.16 was developed. It starts by considering a simplified version of the kinetic model, which complexity is sequentially increased by introducing new reactions until the calculated objective function shows no improvement.

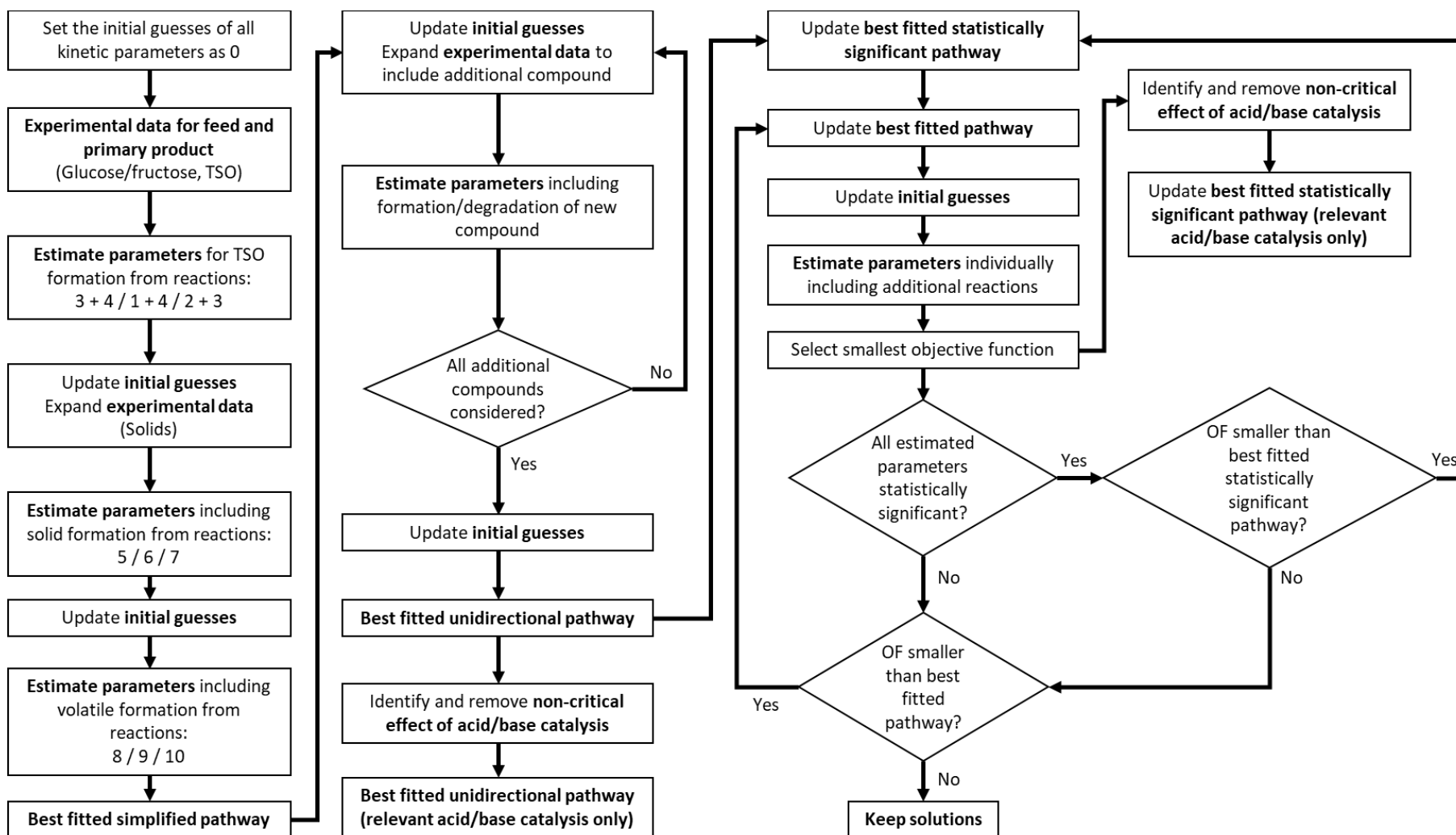


Figure 8.16: Workflow developed for the systematic estimation of kinetic parameters. Reaction number referred to the network in Figure 8.15.

Two main solutions were considered: best fitted statistically significant pathway, and best fitted pathway. The latter aimed to provide the lowest possible objective function given the model configuration and experimental data. The former requires that the estimated kinetic parameters have acceptable standard deviations, *i.e.*, significantly smaller than the estimated value [176]. This is ensured by applying the sub-workflow in Figure 8.17 during each individual estimation.

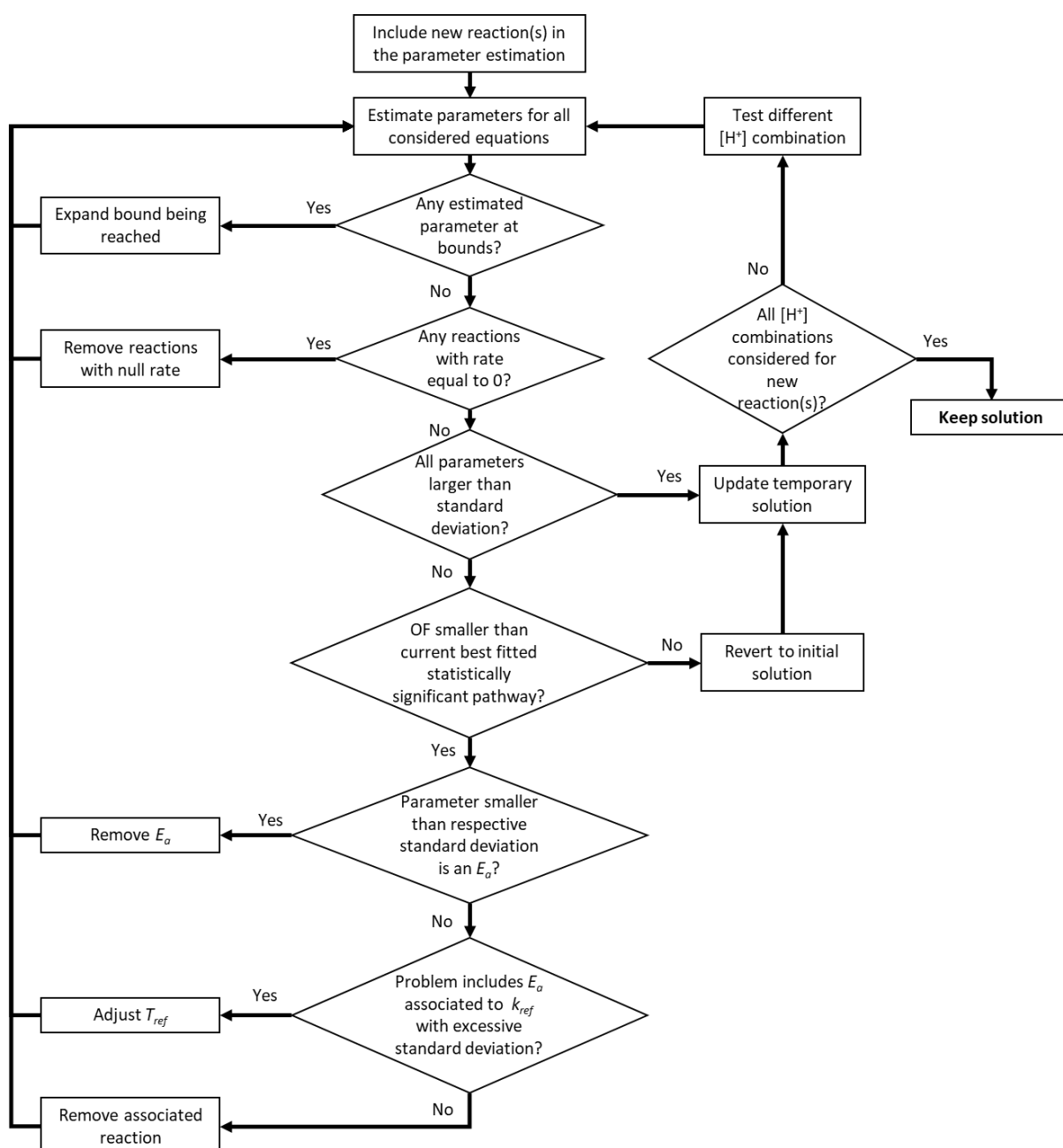


Figure 8.17: Sub-workflow applied in each individual parameter estimation.

This sub-workflow also shows that each time new reactions were introduced, the effect of including the estimated proton concentration, $[H^+]$, in their respective rate equations was tested. Furthermore, at the end of each estimation cycle, the proton effect on pre-existing rate equations was re-evaluated. While this helped to detect synergetic effects facilitated by the new reactions, it also reflected the actual relevance of considering water's self-ionisation product in each rate equation. This created a third solution, which only considered critical influence of the concentration of free protons, *i.e.*, $[H^+]$ was removed from rate equations when it was not required to describe a reaction's variation with temperature, showed by a negligible effect on the objective function.

The overall workflow also comprised an update of the parameters' initial guess between each estimation, using the results from the previous iteration. This ensured the next optimisation started from a previously accepted solution, thus reducing the required computational time, while improving the likelihood of convergence to an acceptable solution.

In the context of hydrothermal processing of sucrose, the developed workflow started by determining the best combination of reactions that produce soluble organics from the two pseudo-feeds (glucose and fructose). The solution with lowest objective function was completed by the reactions that best represented the formation of the other two compound groups, *i.e.*, solids and volatiles. The obtained combination of reactions defined the best simplified pathway, representing the most basic structure of the kinetic model giving an acceptable agreement with the experiments.

The model was further refined by estimating the parameters for formation and degradation of remaining known compounds. When these were exhausted, the best fitted unidirectional pathway was obtained, creating the estimation baseline. Afterwards, previously rejected reactions were individually re-introduced until no variation was observed in the model's fitting to experimental data.

8.5.2 Estimated parameters

The workflows in Figure 8.16 and Figure 8.17 allowed the estimation of kinetic parameters for the reactions involved in sucrose's hydrothermal degradation. The process required the 91 individual parameter estimations detailed in Appendix F.4, *i.e.*, significantly fewer than the 65 536 possible combinations mentioned in the previous section. The progress of the algorithm is summarised in Figure 8.18, which also includes the reaction pathways, and associated objective functions. Three alternative solutions were arrived at by individually including additional reactions or relaxing the effect of proton concentration: (1) best fitted statistically significant pathway (relevant acid-base catalysis only); (2) best fitted statistically significant pathway; and (3) best fitted pathway, were obtained. The estimated kinetic parameters are presented in Table 8.8.

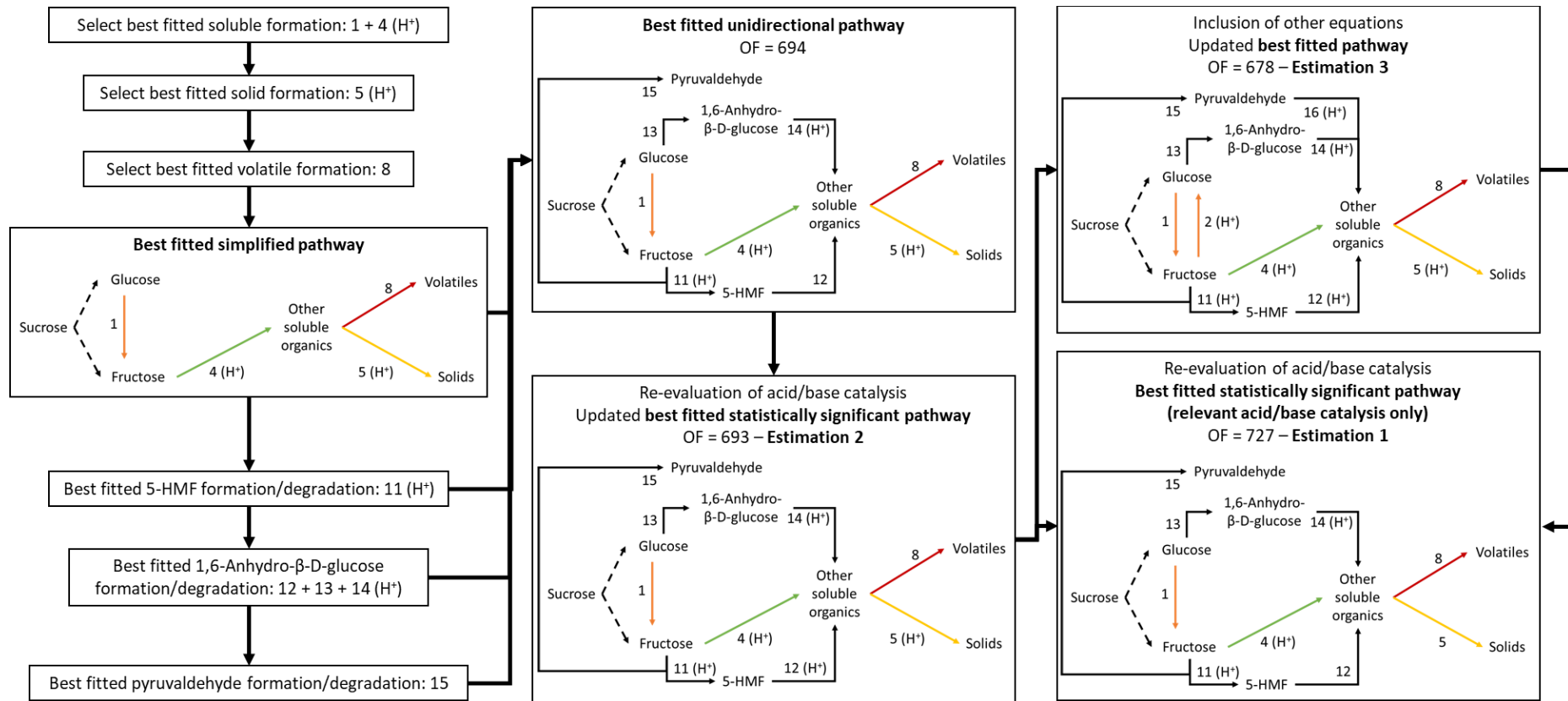


Figure 8.18: Steps followed during the estimation of kinetic parameters related to sucrose's hydrothermal degradation.

The resulting reaction network is similar for the three solutions, only differing in terms of which reactions are affected by the proton's concentration, or the presence of fructose isomerisation to glucose (reaction 2), and pyruvaldehyde's degradation (reaction 16).

Table 8.8: Activation energy (E_a) and kinetic constant (k_{ref}) at reference temperature (T_{ref}) estimated for the three considered solutions, and respective objective function (OF).

Estimation	1 (OF = 727)			2 (OF = 693)			3 (OF = 678)			T_{ref} (°C)
	[H ⁺] included	E_a (kJ/mol)	k_{ref} (s ⁻¹)	[H ⁺] included	E_a (kJ/mol)	k_{ref} (s ⁻¹)	[H ⁺] included	E_a (kJ/mol)	k_{ref} (s ⁻¹)	
1	-	73 ± 2	(325 ± 6) x10 ⁻³	-	73 ± 2	(324 ± 6) x10 ⁻³	-	40 ± 10	(5 ± 1) x10 ⁻¹	332.5
2	-	-	-	-	-	-	Yes	-30 ± 20	(2 ± 2) x10 ²	
3	-	-	-	-	-	-	-	-	-	
4	Yes	90 ± 3	(53 ± 2) x10	Yes	91 ± 3	(53 ± 1) x10	Yes	90 ± 8	(50 ± 3) x10	332.5
5	-	43 ± 6	(143 ± 8) x10 ⁻⁴	Yes	87 ± 6	(119 ± 6) x10 ⁻¹	Yes	78 ± 6	(120 ± 7) x10 ⁻¹	
6	-	-	-	-	-	-	-	-	-	
7	-	-	-	-	-	-	-	-	-	-
8	-	101 ± 9	(31 ± 2) x10 ⁻²	-	80 ± 8	(29 ± 1) x10 ⁻²	-	71 ± 9	(30 ± 1) x10 ⁻²	332.5
9	-	-	-	-	-	-	-	-	-	
10	-	-	-	-	-	-	-	-	-	
11	Yes	52 ± 9	(12 ± 1) x10	Yes	55 ± 9	(12 ± 1) x10	Yes	44 ± 10	(12 ± 1) x10	332.5
12	-	220 ± 60	(7 ± 1) x10 ⁻¹	Yes	320 ± 50	(18 ± 3) x10 ²	Yes	310 ± 60	(15 ± 3) x10 ²	
13	-	45 ± 7	(77 ± 5) x10 ⁻³	-	44 ± 7	(78 ± 5) x10 ⁻³	-	44 ± 7	(67 ± 4) x10 ⁻³	
14	Yes	45 ± 10	(22 ± 2) x10	Yes	44 ± 10	(22 ± 2) x10	Yes	30 ± 10	(17 ± 2) x10	332.5
15	-	71 ± 5	(185 ± 7) x10 ⁻³	-	68 ± 5	(180 ± 7) x10 ⁻³	-	60 ± 10	(24 ± 3) x10 ⁻²	
16	-	-	-	-	-	-	Yes	40 ± 60	(7 ± 3) x10	

The preference of reaction 1 over 2, showed that the isomerisation equilibrium was substantially driven towards fructose, with its reverse having a negligible effect. This agreed with earlier observations in literature [64,71,159]. It was also demonstrated that including $[H^+]$ in reaction 1, increase the objective function by only 4% (compared to estimation 3). Therefore, glucose's isomerisation to fructose is not expected to be affected by the self-ionisation product of water near the SCTT.

The preference of reaction 4 over 3 confirmed that fructose was more reactive than glucose. It was also observed that its degradation into other soluble organics occurred majorly through reactions affected by the concentration of H⁺ or OH⁻. Not including this effect on the generic degradation rate led to an objective increase of 12 % (compared to estimation 3).

The inclusion of reactions 5 and 8 instead of their alternatives (6, 7, 9, and 10) indicates that it was unlikely the monosaccharides are directly converted to either solid or volatile species. It was also observed that the conversion of soluble organics into volatiles was not improved by including the proton concentration. On the other hand, solid formation benefited slightly but not significantly by including the proton concentration in the rate equation, as it only reduced the objective function by 4% when omitted.

For the three solutions considered, fructose dehydration into 5-HMF (reaction 11) was confirmed to be favoured by a higher self-ionisation product of water. Even though, neglecting this effect reduced the estimation's objective function by only 2%, it also prevented a determination of a reasonable activation energy in an Arrhenius-type expression, thus highlighting the benefit of including $[H^+]$ in the rate equation. This observation agreed with existing literature, which points to the reaction's dependence with near-critical water's density and the medium's acidity [64,103,144]. The same could not be concluded about the degradation of 5-HMF, *i.e.*, reaction (12), in which the inclusion of $[H^+]$ had a very small effect on the objective function, and therefore was rejected by the workflow in estimation 1.

1,6-anhydro- β -D-glucose appeared to show the opposite behaviour to 5-HMF. Its formation (reaction 13) was not significantly affected by the variation in water's self-ionisation product, while degradation (reaction 14) required this term in the rate equation to accurately estimate an activation energy. Consequently, the rate of reaction 14 decreases at higher temperatures, as was evident in the experimental measurements presented in Section 8.3.3.

Pyruvaldehyde's degradation (reaction 16) was only considered in estimation 3, with parameters subject to high standard deviations. This confirms the importance of the formation of the compound (reaction 15) over degradation. As with 1,6-anhydro- β -D-glucose's formation, there was no benefit in including $[H^+]$ in the rate equation of reaction 15.

8.5.3 Fitting quality

The three solutions characterised by the kinetic parameters in Table 8.8 present successively smaller objective functions from 1 to 3, which means calculated yields become closer to the experimental values. This progression was analysed through the parity plots in Figure 8.22 and Figure 8.22 for each measured compound, where the diagonal passing through the origin represents the line where model and experiment are in complete agreement.

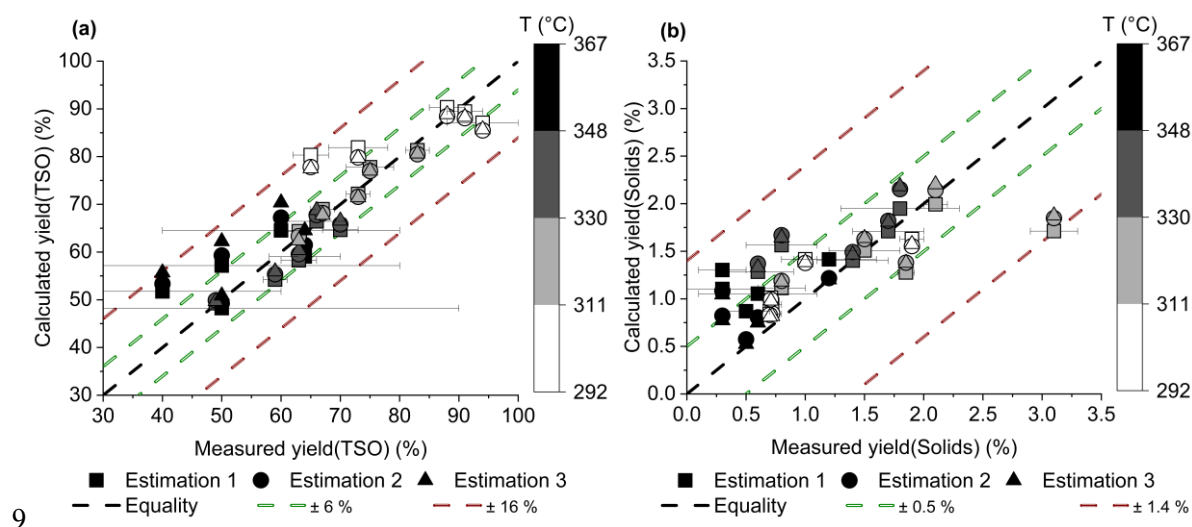


Figure 8.19: Parity plots for TSO (a) and solids (b) yields, considering the estimated kinetic parameters in Table 8.8. Diagonal passing through the origin represents equality between measured and predicted yields.

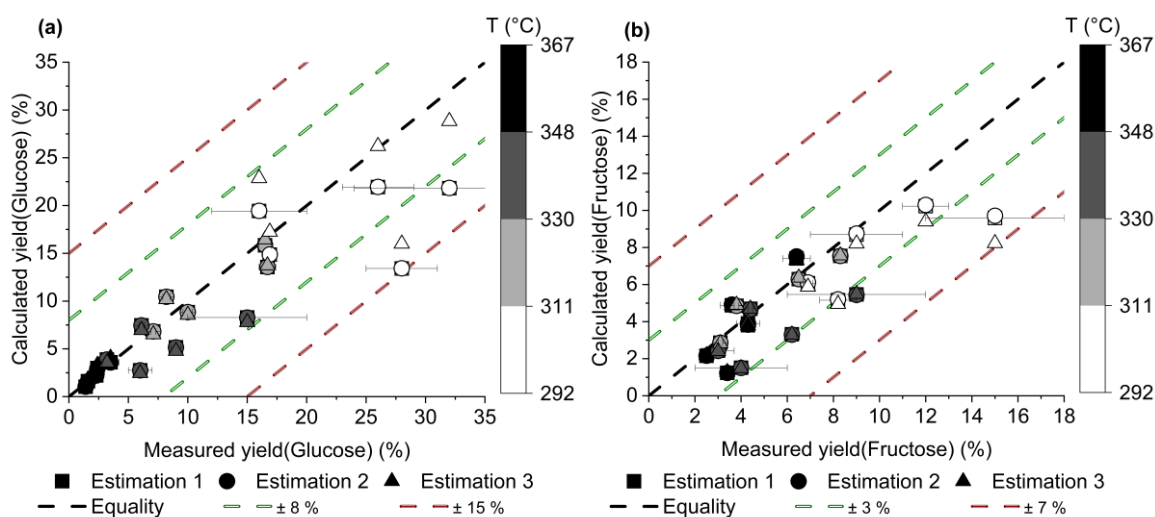


Figure 8.20: Parity plots for glucose (a) and fructose yields, considering the estimated kinetic parameters in Table 8.8. Diagonal passing through the origin represents equality between measured and predicted yields.

The three sets of estimated parameters produced similar results for almost all experiments. Regarding estimation 1, the higher objective function results from neglecting the effect of proton concentration in reaction 5, which generally worsens the fitting relative to the yield of solids.

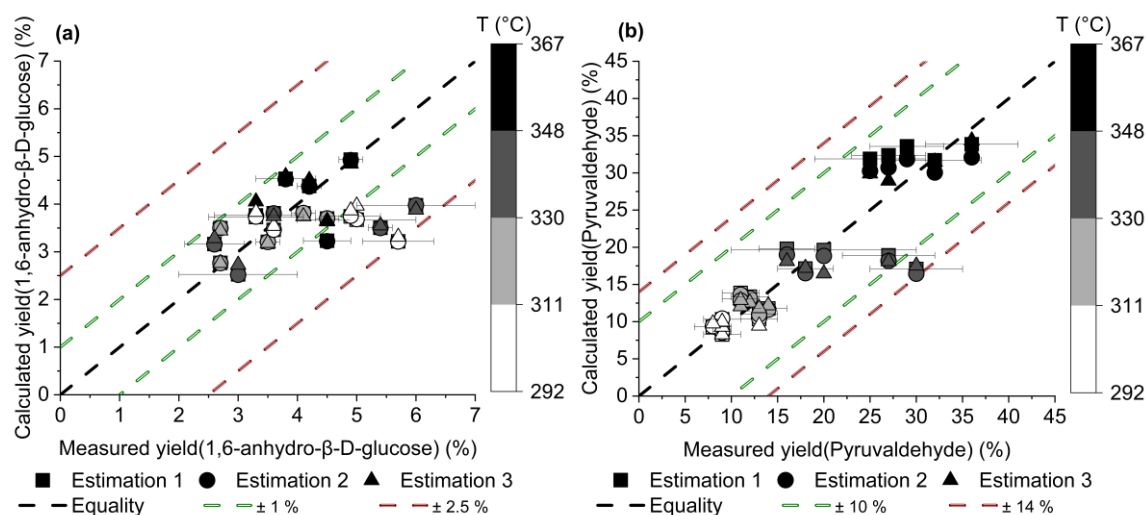


Figure 8.21: Parity plots for 1,6-anhydro- β -D-glucose (a) and pyruvaldehyde (b) yields, considering the estimated kinetic parameters in Table 8.8. Diagonal passing through the origin represents equality between measured and predicted yields.

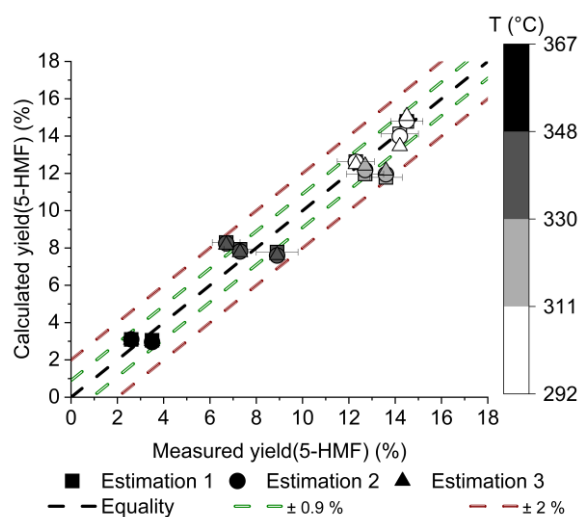


Figure 8.22: Parity plots for 5-HMF yields, considering the estimated kinetic parameters in Table 8.8. Diagonal passing through the origin represents equality between measured and predicted yields.

The most significant difference was observed for glucose's yield in estimation 3. For higher yields, which also corresponded to lower temperatures, the values calculated by this solution were significantly closer to the plot's diagonal, and consequently to the experimental data. This was justified by the introduction of reverse reaction 2, *i.e.*, isomerisation of fructose into glucose, with a negative activation energy, thus increasing the rate of reaction at lower temperatures. It should be considered that since the presented reactions do not necessarily represent elementary steps, a negative activation energy was not physically impossible, as it may indicate that another reaction begins to dominate the kinetics. On the other hand, estimation 3 presented a worse fitting at high fructose yields.

Estimation 3 differs from 1 and 2 by including in its pathway reactions 2 and 16, thus increasing the number of estimated parameters from 18 to 22. This resulted in the estimation of parameters with excessively high standard deviations. As in the previous chapter, the effect of this high uncertainty was analysed through a global system analysis, as described in Section 4.1.3.

The kinetic parameters were replaced by random values picked from a normal distribution centred around the estimated value and considering the estimation's standard deviation. The 20 experiments were simulated by combining 200 variations of each parameter, thus creating a scatter of predicted yields. The simulated standard deviation (SSD) of each yield was normalised by the initially predicted value and its variation plotted in Figure 8.23 to Figure 8.26 for the three estimations. In these plots, a higher SSD represents a greater range of predictions due to the uncertainty in the parameters.

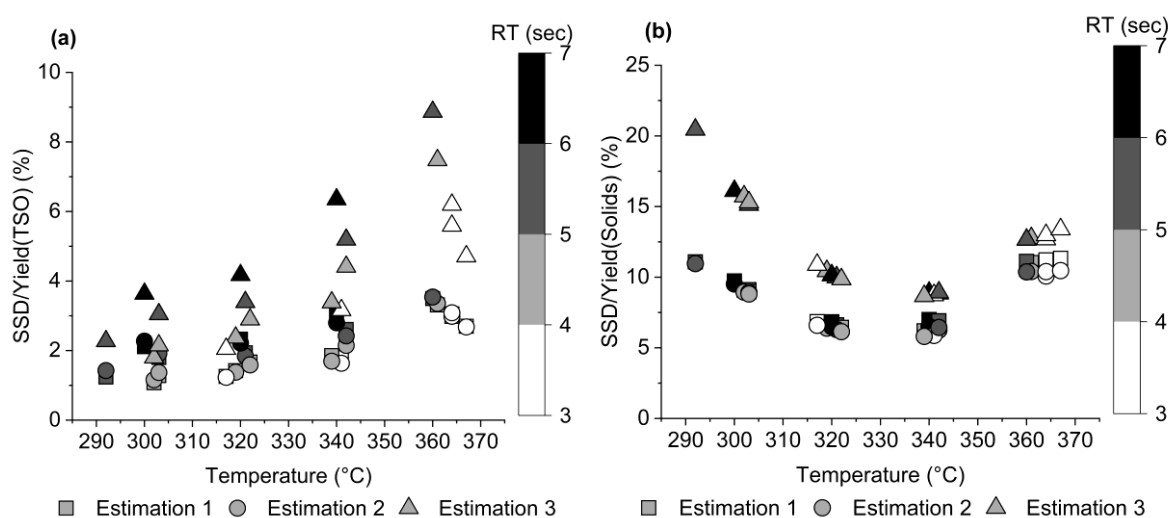


Figure 8.23: SSD ratio for TSO (a) and solids (b) yields, considering random variations of the estimated kinetic parameters in Table 8.8.

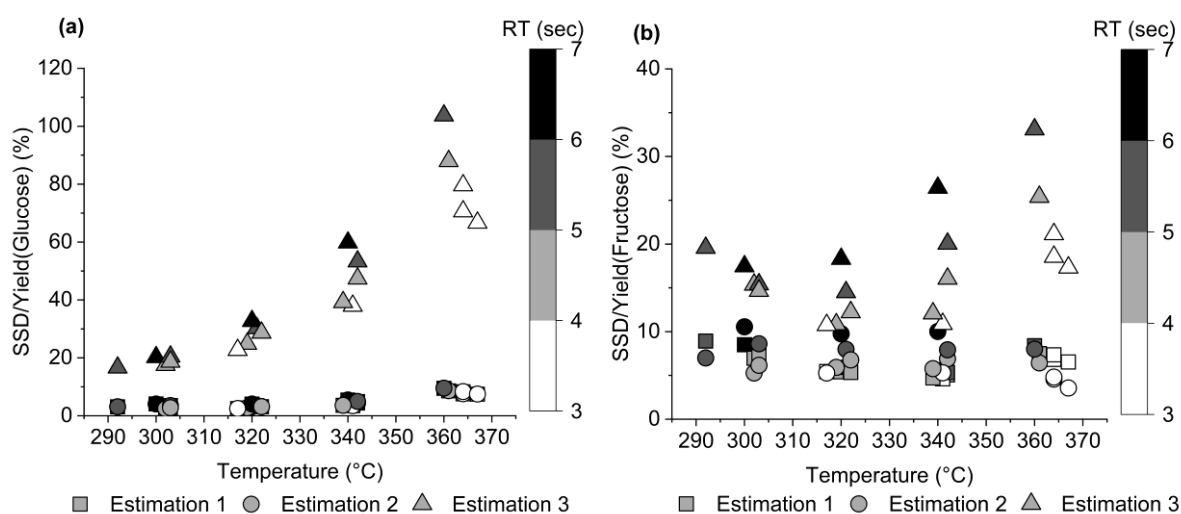


Figure 8.24: SSD ratio for glucose (a) and fructose (b) yields, considering random variations of the estimated kinetic parameters in Table 8.8.

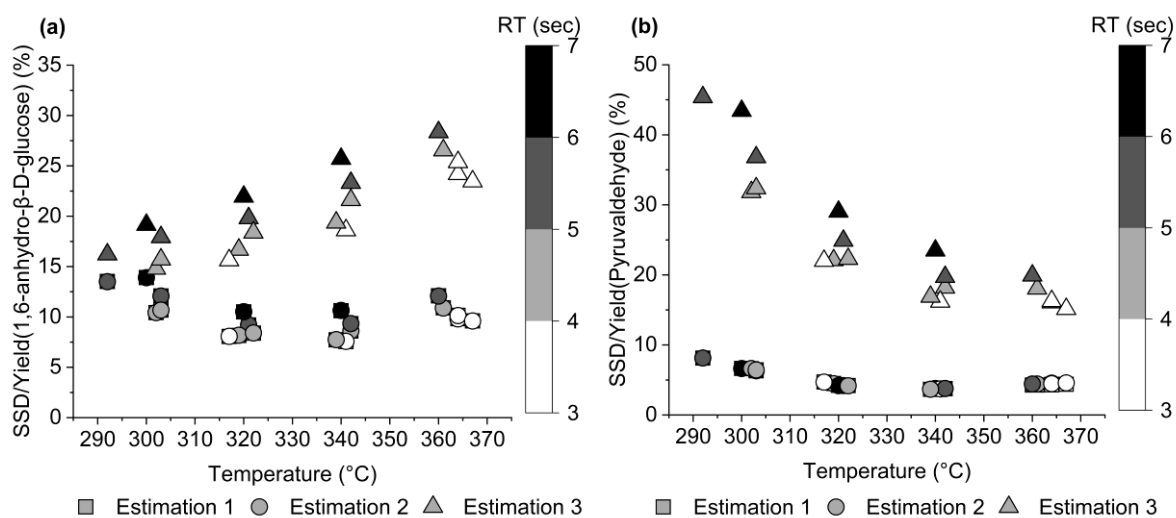


Figure 8.25: SSD ratio for 1,6-anhydro-β-D-glucose (a) and pyruvaldehyde (b) yields, considering random variations of the estimated kinetic parameters in Table 8.8.

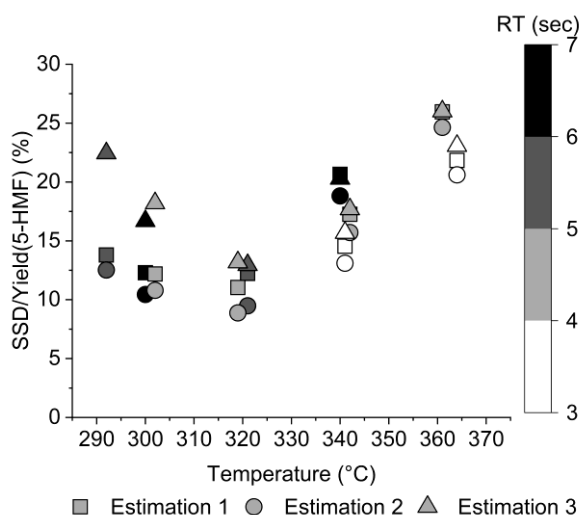


Figure 8.26: SSD ratio for 5-HMF yields, considering random variations of the estimated kinetic parameters in Table 8.8.

The plots presented in Figure 8.23 and Figure 8.26 reflect the high uncertainty in the kinetic parameters resulting from estimation 3. The respective SSD are significantly higher for all compounds when compared with the other two scenarios, in which the difference is negligible. Therefore, it was possible to conclude that, despite allowing the estimation of parameters related to fructose's isomerisation to glucose, and pyruvaldehyde's degradation, these overparameterized the process, resulting in an inaccurate model. Expanding the operation domain to conditions where those reactions become more relevant (lower T and higher *residence time*) will improve the estimation of the respective parameters.

Given the similarity between the predicted yields and simulated standard deviations, estimations 1 and 2 can be considered as equivalent when modelling the hydrothermal degradation of sucrose in the range of tested conditions. However, since the former is less reliant on the estimation of proton concentration, it is subject to fewer approximations, and is therefore considered the most adequate solution to represent sucrose's reactional behaviour under hydrothermal conditions.

8.5.4 Range of applicability

To evaluate if there were any particular conditions under which the kinetic models preferably fits or not the experimental data, the deviation between the calculated and estimated yields was divided by the respective uncertainty, plotted in Figure 8.27 to Figure 8.30. No clear trend is evident between the different plots, each showing isolated peaks at different positions regardless of temperature, residence time, or inlet composition.

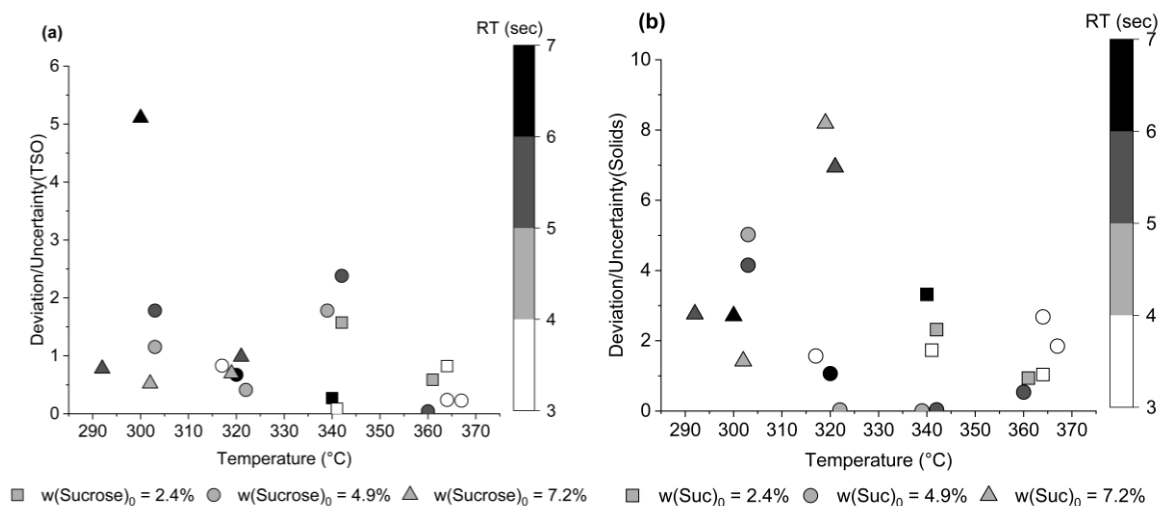


Figure 8.27: Ratio between deviation and uncertainty for TSO (a) and solids (b) yields, considering parameters from estimation 1.

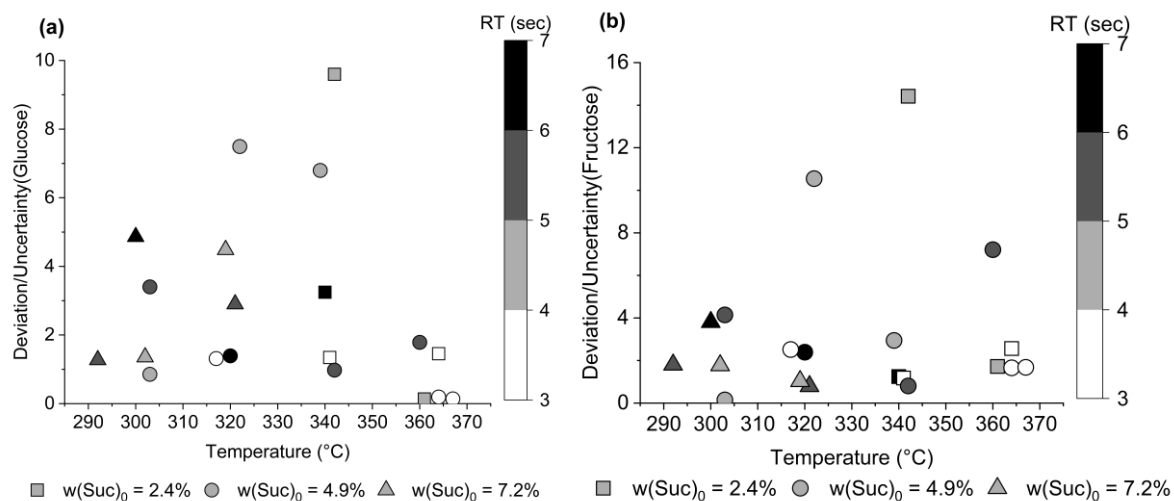


Figure 8.28: Ratio between deviation and uncertainty for glucose (a) and fructose (b) yields, considering parameters from estimation 1.

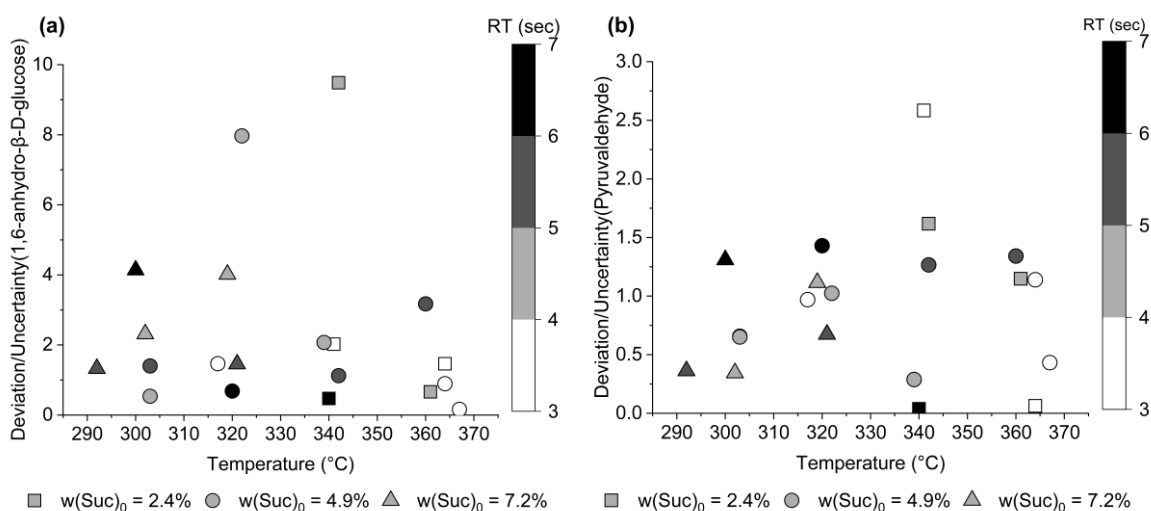


Figure 8.29: Ratio between deviation and uncertainty for 1,6-anhydro- β -D-glucose (a) and pyruvaldehyde (b) yields, considering parameters from estimation 1.

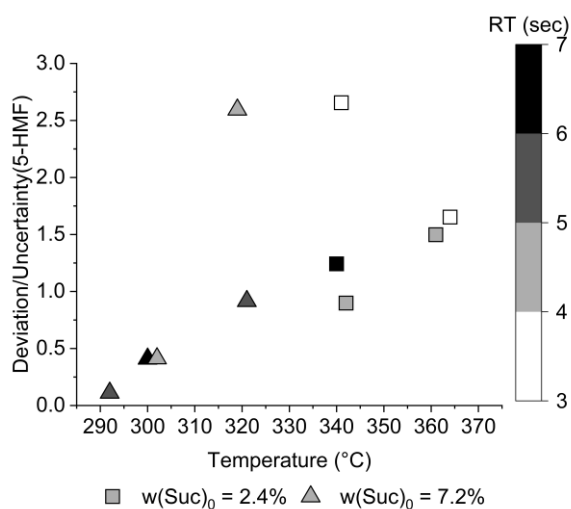


Figure 8.30: Ratio between deviation and uncertainty for 5-HMF, considering parameters from estimation 1.

8.5.5 Comparison with literature

The estimated kinetic parameters were compared with equivalent ones found in existing literature. This was possible for the reactions based on specific compounds, *i.e.*, reactions 1 and 11 to 15 in Figure 8.15, considering the kinetic parameters summarised in Table 8.9.

Table 8.9: Parameters used to calculate the kinetic constants in Figure 8.31, to compare the current study with literature values.

Reaction	Current study		Literature		
	E_a (kJ/mol)	k_{ref} (s ⁻¹)	E_a (kJ/mol)	$\ln(k_0$ (s ⁻¹))	Source
1	73 ± 2	(325 ± 6) × 10 ⁻³	112.69	21.81	[72,159]
11	52 ± 9	(12 ± 1) × 10	285	57.6	[72]
12	220 ± 60	(7 ± 1) × 10 ⁻¹	75.76	8.13	[104]
13	45 ± 7	(77 ± 5) × 10 ⁻³	65.93	9.11	[72,159]
14	45 ± 10	(22 ± 2) × 10	109.29	18.194	
15	71 ± 5	(185 ± 7) × 10 ⁻³	82.56	15.84	

Generally, the activation energies estimated in this study were somewhat smaller than the ones in literature, except for reaction 12, which presented a higher value. In fact, the reactions associated with 5-HMF formation and degradation (11 and 12) present the largest differences in kinetic parameters when compared to literature. It should be considered that the parameters retrieved from literature were obtained from experiments based on different feedstocks. Fructose dehydration was based on experiments using a cellulose feed [64], while degradation was studied with a pure 5-HMF feed [104]. Both result in different environments, which affect reaction rates differently, particularly if the reactions are acid catalysed.

Figure 8.31 plots the calculated kinetic constants in the temperature range of the experiments performed (280 – 370 °C). The values retrieved from literature result from only three distinct temperature points (300, 350 and 400 °C), while this work is based on 20 experiments over a similar operating range. Since in this study the rate equations relative to reactions 11 and 14 consider the influence of water's self-ionisation product, this was included in their kinetic constant. Therefore, for those reactions, the plotted values are the product $k_r/[H^+]$.

Despite the different activation energies, the kinetic constants estimated for reactions 1 and 13 to 15 are of the same magnitude as the ones calculated using literature data. This is particularly true for reaction 15, which results from combining the different reactions between fructose and pyruvaldehyde in Figure 8.1. For the reactions involving 5-HMF (*i.e.*, 11 and 12), the behaviour observed using the estimated parameters suggests a slow formation and fast degradation, which is the opposite of what was calculated from literature.

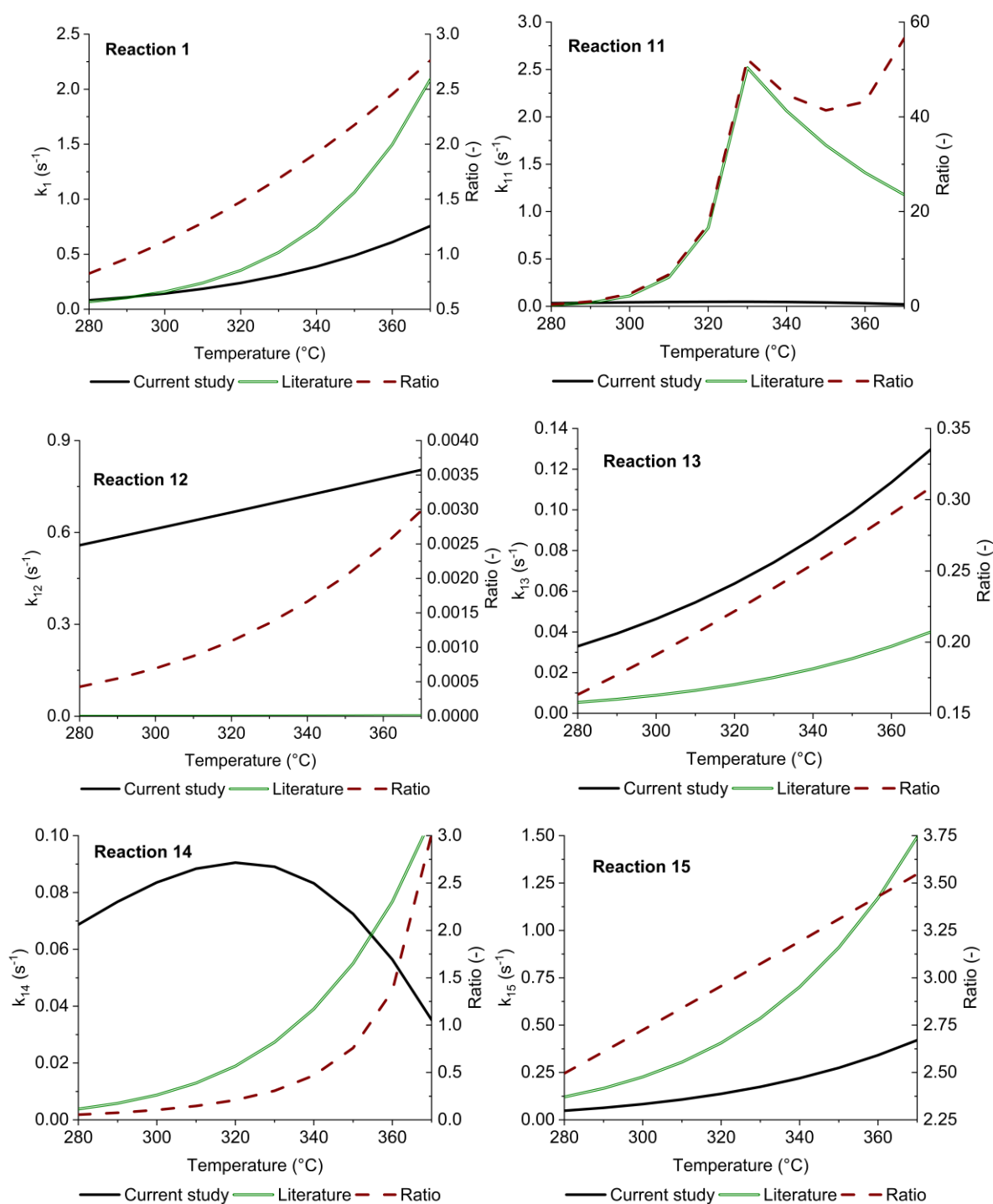


Figure 8.31: Comparison between kinetic constants calculated using estimated parameters and equivalent ones in literature, for reactions 1 and 11 to 15 in Figure 8.15 [64,104,159]. Ratio (on the left axis) defined as the literature values divided by the one estimated in this study.

Nonetheless, it must also be considered that the kinetic parameters estimated for reactions involving 5-HMF were based on yields calculated following a long evaporation process and using a calibration that assumed 5-HMF and 5-HDF resulted in similar responses of the GC-FID as described in Section 8.2.2.

In Section 8.3.3, it was commented that the extraction process conducted during sample preparation mainly resulted in the transfer of 5-HMF from the aqueous sample to the organic solvent. Furthermore, it was found that this process was incomplete, as 5-HDF was detected in a significant quantity in the WSO fraction. According to Chuntanapum *et al.* [104], 5-HMF is also detectable through HPLC-RID. Therefore, it is likely that one of the unidentified peaks at later retention times in Figure 8.12 corresponded to 5-HMF's fraction that remained in the WSO sample.

These observations show that there is an opportunity in hindsight to further refine the quantification of 5-HMF. Since this compound is water-soluble and detectable through HPLC-RID, there is no reason to apply the solvent extraction process. Apart from reducing solvent waste, excluding this step would allow 5-HMF's quantification before evaporation and without methanol dilution, thus preventing any vapour losses and its conversion into 5-HDF.

Repeating the experiments in this report with this simplified analytical method would provide more reliable 5-HMF yields. Ultimately, those yields can be used to confirm or correct the significant difference between the kinetic constants plotted in Figure 8.31 for 5-HMF formation and degradation (k_{11} and k_{12}).

8.6 Concluding remarks

This chapter described a study of sucrose's hydrothermal reactions based on experiments conducted in the hydrothermal rig. These were performed at different temperatures (292 – 367 °C at the reactor's centre), flowrates (organic feed: 6 – 10 mL/min, ratio between feeds: 3), and feed concentrations (10, 20, and 30 wt%), resulting in the production of a liquid effluent with suspended solids, as well as other gaseous compounds. The calculated mass yields of each fraction were used to characterise the reactions of sucrose reactions in hydrothermal medium. The following conclusions may be drawn:

Solid products represented up to 3.5% of the inlet sucrose mass, showing a maximum at approximately 320 °C. The fraction of solid particles with sizes above 100 µm was negligible compared to the one with sizes above 11 µm. Solid formation resulted from reactions among the non-quantified soluble organics, instead of directly from fructose or glucose.

The volatiles fraction was determined by closing the mass balance between sucrose at the inlet and organic compounds in the liquid and solid samples. This was assumed to include produced gases and compounds vapourised along with the solvent after extraction, which increased with temperature and residence time, from 5 to 60% of the inlet mass of sucrose.

Measured gases represent less than 6% of the total volatile fraction. Their main component is CO₂, followed by CO and traces of methane and ethylene. The ratio CO/CO₂ increased with temperature. Both observations agree with existing literature [160], considering that H₂ was not measured.

Based on the subsequent kinetic analysis, the volatile fraction is expected to mainly be produced from organic compounds in solution other than fructose or glucose.

The total fraction of soluble organics (TSO) varied from 90 to 40% of the initial mass of sucrose as temperature and residence time increased. From these organics, glucose, fructose, 1,6-anhydro-β-D-glucose, and pyruvaldehyde were quantified through HPLC-RID, while 5-HMF was measured through GC-FID.

Sucrose was not detected in any of the analysed samples. Therefore, no kinetics could be determined for this reaction, which was therefore assumed to be fast. Consequently, fructose and glucose were assumed to exist in equimolar amounts close to the inlet of the reactor.

At lower temperatures, glucose represented the largest fraction of soluble organics (~35 wt%). This consistently decreased in favour of pyruvaldehyde as temperature and residence time increased.

Fructose represented 5 to 15% of the TSO. Kinetic analysis suggested that the equilibrium between glucose and fructose favoured the latter. It was also concluded that this reaction rate was not affected by water's self-ionisation product.

The yield of 1,6-anhydro-β-D-glucose did not change significantly in the experiments. Kinetic parameters for both formation and degradation were estimated. Water's self-ionisation product was important in describing the degradation rate.

Pyruvaldehyde's yield increased significantly with temperature, with its fraction increasing from 10 to 60% of the TSO. Its apparent formation from fructose was successfully characterised. On the other hand, the kinetic shown that the degradation of this compound was not relevant in the tested conditions.

5-HMF's yield decreased with temperature. The kinetic parameters of both formation and degradation were estimated within a reasonable uncertainty. Water's self-ionisation product was required to fully characterise fructose's dehydration into 5-HMF.

From the kinetic analysis, it was also found that other soluble organics resulted preferentially from fructose instead of glucose. Overall, the rate of the reactions involved was expected to increase with water's self-ionisation product.

These non-identified soluble organics were expected to include compounds of smaller molecular weight such as glycolaldehyde and carboxylic acids lactic, levulinic, acetic, and formic acids. As presented in Figure 8.1, these result from the degradation of the measured compounds and were detected as methyl

esters in the GC-MS analysis (Table 8.7). Nonetheless, they were not quantified in the present study, thus reducing the applicability of the derived kinetic model, being a relevant area of improvement in future work.

The analysis of sucrose's reaction pathway started from approximated reactions based on compound groups. This network was expanded by including the formation and degradation of specific compounds, resulting in a total of 16 reactions. The estimation of the respective kinetic parameters aimed at selecting only relevant reactions, avoid overparameterization, and account for the effects of water self-ionisation product only when required to improve the predictive power of the model. This was achieved by developing the workflows in Figure 8.16 and Figure 8.17, requiring the sequential performance of 91 individual estimations to obtain kinetic parameters for 9 reactions, with meaningful standard deviations.

The last section of this chapter showed that, generally, the estimated kinetic parameters presented an acceptable agreement with equivalent ones in available literature, except for the reactions involving 5-HMF.

Future work

A simplification of the analytical method, by removing solvent extraction, and quantifying 5-HMF through HPLC-RID, was proposed to confirm the estimated parameters. Apart from this, the analysis of sucrose's reactions in hydrothermal medium can be further improved by the following:

- Expand the operating range to shorter residence times, thus capturing the kinetics of the hydrolysis of sucrose. This is achievable through the increase of feed flowrates or reduction of the reactor's length. In the current installation, the former is limited by the Isco pump's capacity, whilst the latter would limit temperature measurements.
- Use pH buffers to fix the medium's acidity, allowing a better understanding of acid or base catalytic effects. This would require compounds stable in hydrothermal conditions, and knowledge of their dissociative behaviour under those conditions.
- Expand the reactional network by including additional compounds such as dihydroxyacetone, glyceraldehyde, lactic acid, glycolaldehyde, erythrose, or levulinic acid.

Chapter 9

Conclusions

The overall goal of this work (see Chapter 1) was to close the gap between the kinetic models of simple model compounds and complex lignocellulosic biomass, aiming at developing flexible processes that can be optimised towards the production of biofuels, or any other relevant product. To achieve this goal, four objectives were identified: (1) hydrothermal experiments clearly defined operating conditions; (2) quantitative analysis of selected compounds; (3) mathematical modelling of appropriate complexity; and (4) accurate estimation of relevant kinetic parameters.

In this project, these four requirements were tested by experiments at subcritical conditions, where the organic feed contained dibenzyl ether (Chapter 7) or sucrose (Chapter 8). Those are molecules with bonds typically found in lignin and cellulose, respectively.

The first requirement was addressed by the hydrothermal liquefaction apparatus described in Chapter 3. The continuous process allowed the operating pressure to be controlled independently from the temperature. The confined jet mixer configuration that was used aimed at generating rapid mixing at the reactor's inlet. Cooling by quenching with water, followed by heat exchange with chilled water, was implemented to halt any reaction downstream of the reactor section. This configuration was expected to be scalable for industrial applications.

The performance of the continuous rig was evaluated in Chapter 5 and Chapter 6. The former highlighted flowrate deviations, and heat losses in the reactor, which were accounted for in later calculations. The latter analysed the mixing patterns around the confined jet mixer using CFD simulations at typical operating conditions. All simulations with water fed under supercritical conditions (gas-like properties) achieved 99.9% of average outlet composition 16 mm after the jet's outlet. This distance represented 7% of the reactor's length, and 18 times the jet's internal diameter. The latter was significantly higher than previous values reported in the literature [137,192], a difference that was attributed to different turbulence models. Conversion and yields obtained from models considering and omitting the confined jet mixer were similar in the cases which had a closed energy balance. Therefore, the objective of fast mixing was verified in the context of the present work, supporting the conclusion that modelling the confined jet mixer in detail was not required to analyse the experimental results. Instead, it could be assumed that mixing was very fast compared to the rate of reaction.

The second objective ensured the data obtained from each experiment is reliable. Chapter 3 also describes the separation and analytical methods applied to the HTL rig's effluents. The gaseous products were analysed both quantitatively and qualitatively by FTIR spectrometry. Solids, when they were found, were produced in small amounts compared to the products in the liquid phases, thus their composition was not further analysed. Aqueous and organic phases were separated in two different ways: with and without solvent extraction and filtration. The composition of selected compounds was analysed using HPLC with UV-vis or RID. GC-MS was also applied to identify species in more complex mixtures, with FID being used to quantify compounds expected to be absent from the HPLC chromatogram. This objective was achieved to a significant degree in Chapter 7 and Chapter 8. The solvent extraction process used in the latter proved to add little or no benefit to the analysis, as it resulted in the release of a significant amount of volatile compounds (up to 60 wt% of the inlet mass of sucrose). Furthermore, one of the key products, 5-HMF, which was found distributed in both aqueous and organic samples, was also detectable by direct injection of the aqueous products into a HPLC-RID, without needing prior solvent extraction.

The third objective was addressed by the mathematical model described in Chapter 4. This model represented the HTL reactor as a plug flow reactor with dispersion, using axial discretisation. It comprises sub-models that calculate reaction rates, heat losses through the tube wall, thermodynamic and transport properties, and dispersive flow. When appropriate, each of those sub-models was simplified by linear interpolation between selected points, thus minimising the number of thermodynamic calculations. The sub-model configuration allowed the same structure to be used in the simulations of Chapter 7 and Chapter 8. Models based on dibenzyl ether considered a simple two-reaction network with customised reaction rates and a thermodynamic model based on the equation of state SAFT- γ Mie, which accounted for the mixture's composition. Models based on sucrose (which dissociated completely and rapidly to glucose and fructose) applied a complex network of first order reactions, where one molecule of reactant produced an equal amount of a single product. These reactions were based on lumped groups of products (*i.e.*, soluble organic, solids, and volatiles), as well as specific components. Since the sucrose concentration was relatively low, properties of pure water were used, from the IAPWS-95 equation of state, and dispersion was neglected.

The fourth objective used the gPROMS[®] optimisation solver and parameter estimation. For the complex networks considered in Chapter 8, the workflows in Figure 8.16 and Figure 8.17 provided a stepwise approach to obtain parameters under different levels of accuracy and considering the effect of water's self-ionisation product in subcritical conditions when relevant. Analysing the standard deviation of the obtained kinetic parameters enabled the ones effectively contributing to improve the model's accuracy to be distinguished from the ones that overparameterized the estimation. Therefore, it was possible to obtain kinetic parameters that adequately fit the experimental data within an appropriate level of uncertainty.

9.1 Summary of estimated reaction pathways

9.1.1 Hydrolysis of dibenzyl ether

The hydrothermal cleavage of the ether bond in dibenzyl ether was studied based on 15 experiments conducted at temperatures from 287 to 369 °C, pressures in the range 245 – 254 bar, inlet organic mass fractions of 33 to 45%, and average residence times estimated between 5 and 7 seconds. The outlet products were distributed between three phases: gas, aqueous, and organic.

The composition of the gas included toluene, benzene, and carbon monoxide. Nonetheless, a negligible amount of this phase was produced compared to the total flowrate of products. The organic phase contained the unreacted dibenzyl ether, and produced toluene, benzyl alcohol, and benzaldehyde. The latter two components were also found in the aqueous phase. As reported in the literature [149], benzyl alcohol was the only compound produced in a significant quantity.

The process was modelled accounting for hydrolysis and degradation reactions. For the first, different rate equations were tested. These were based on S_N1 or S_N2 reaction mechanisms with different limiting steps and substitution nucleophiles (H₂O or OH⁻). Detailed hydrolysis rates including two observed kinetic constants provided a better fitting between experimental data and calculated values. However, the estimated parameters exhibited a large uncertainty, showing a wider range of data was required to estimate them accurately. Based on simplified reaction rates, DBE hydrolysis is expected to occur through an S_N2 mechanism with OH⁻ as the substitution nucleophile (scenario 5 in Table 7.7), with a rate dependent on the self-ionisation product of water, and with an activation energy estimated as 180 ± 2 kJ/mol.

9.1.2 Hydrothermal processing of sucrose

The degradation of sucrose in the hydrothermal medium was investigated in 20 experiments at temperatures from 282 to 372 °C, pressures in the range 246 – 254 bar, inlet organic mass fractions of 2.4 to 7.2%, and average residence times estimated between 3 and 7 seconds. The products were distributed between three phases: gas, liquid, and suspended solids. The system was modelled as a homogeneous liquid, with organic compounds divided in three groups: soluble organics, volatiles, and solids. Following the workflows in Figure 8.16 and Figure 8.17, 91 parameter estimations were conducted. This process selected 9 reactions from the 16 initially considered (Figure 8.15), which allowed the following conclusions.

Solid particles of sizes between 11 and 100 µm represented up to 3.5% of the mass of sucrose in the feed, with larger fragments being neglectable against this yield. This group was identified as most likely result from soluble organic products that were not measured ($E_a = 43 \pm 6$ kJ/mol), rather than directly

from glucose or fructose. The effect of $[H^+]$ or $[OH^-]$ resulting from water's self-ionisation, appeared to be negligible.

The volatiles group included all compounds in the gas phase, including gases produced in the reactor, and species assumed to have been released during the evaporation of the solvent used to extract the organics. The yield of this group increased with temperature, varying from 5 to 60%. The measured reaction gases represented less than 6% of this yield, and mainly included CO_2 and CO. Like solids, volatiles also resulted from non-measured soluble organics instead of glucose or fructose ($E_a = 101 \pm 9$ kJ/mol), with a negligible effect of $[OH^-]$ or $[H^+]$.

Conversely, the yield of organics in the liquid phase decreased with increasing temperature and residence time, going from 90 to 40%. This group was expanded by isolating specific compounds: glucose, fructose, 5-HMF, pyruvaldehyde, and 1,6-anhydro- β -D-glucose. Soluble organics other than these five compounds were mainly produced from fructose through reactions influenced by $[OH^-]$ or $[H^+]$, with an apparent activation energy of 90 ± 3 kJ/mol. Sucrose was not included in any simulation, as it was fully converted in all experiments. Consequently, it was not possible to derive any information regarding its hydrolysis into glucose and fructose, it being assumed that this reaction occurred significantly faster than any others.

As found in literature [71,72], the isomerisation between the two sucrose monomers was driven towards fructose. Over the operating conditions tested in this study, this reaction presented an activation energy estimated as 73 ± 2 kJ/mol and is not expected to be significantly affected by water's self-dissociation. 1,6-anhydro- β -D-glucose formation from glucose and degradation were defined by similar activation energies, which were estimated as 45 ± 7 and 45 ± 10 kJ/mol, respectively. The last was found to be significantly affected by $[OH^-]$ or $[H^+]$. Pyruvaldehyde's formation from fructose was defined by an activation energy of 71 ± 5 kJ/mol. Its degradation was negligible over the operating conditions. 5-HMF formation from fructose was also affected by $[OH^-]$ or $[H^+]$, with an activation energy of 52 ± 9 kJ/mol. Its degradation was not significantly affected by water's self-ionisation, showing an activation energy of 220 ± 60 kJ/mol. Kinetic parameters for these specific reactions were compared against existing values in literature [72,104,159]. In general, an acceptable agreement was found between kinetic constants calculated using parameters estimated in this study and equivalent ones found in literature, except in the reactions involving 5-HMF. This difference was attributed to shortcomings in the analytical method used to quantify this species.

The absence of sucrose in the analysed products, and consequently its exclusion from the derived kinetic models, presented a setback in the overall goal of closing the gap between the models of simple model compounds, *i.e.*, monomers, and complex lignocellulosic biomass, starting with dimers. Nonetheless, despite only including the reaction pathways associated with glucose and fructose, the derived models were based on experiments with a feed that directly represented the monomer proportion naturally

occurring from the degradation of sucrose. Consequently, the kinetics models derive in this study account for the competing reactions of the two monomers, as well as their isomerisation in a realistic environment, which is not observable in studies based on the individual degradation of the two monomers.

9.2 Future Work

The present research provides additional insights in the hydrothermal reaction mechanism of dibenzyl ether, and sucrose, particularly regarding the influence of H⁺ and, or OH⁻ due to water's varying self-ionisation product. Both are dimers representing typical chemical bonds found in lignocellulosic biomass. Therefore, their successful hydrolysis and simplified kinetic mechanism provide confidence in expanding the proposed methodology to more complex compounds. These case studies underpinned work done to meet the scientific objectives proposed in Chapter 1, which were all achieved. Nonetheless, there are improvements that need to be considered both under the current scope, and when expanding it towards woody biomass feedstocks. These were viable options that were not explored due to the time limitation of this project, instead being proposed as follow-up work in the following sections.

9.2.1 Improving current case studies

The amount of data used to estimate kinetic parameters in the different reaction mechanisms to fit within the limited time available. Additional data could have been obtained by expanding the range of operating conditions, independently manipulating the medium's pH by the addition of an acid or base and quantifying a more complete set of species in the product.

Operating at higher temperature or residence time would increase feedstock conversion, as well as increasing the extent of reactions, which were less significant under the conditions studied. For dibenzyl ether, higher temperature or residence time would increase benzyl alcohol's concentration, thus better distinguishing between the S_N1 and S_N2 reaction mechanisms described by two observed kinetic constants in Table 7.7. Furthermore, the formation of by-products is also expected to increase with temperature. This would allow a better characterisation of the pyrolysis reaction, which in the present study remained temperature independent.

On the other hand, since no solids were found during the hydrothermal conversion of DBE, repeating the experiments in Chapter 7 using a feed containing an ether with phenolic groups, *i.e.*, diphenyl ether or benzyl phenyl ether, could possibly capture the repolymerization reactions, which are typically during the hydrothermal liquefaction of lignin.

For sucrose, the above would allow a better characterisation of secondary reactions like pyruvaldehyde's degradation, or fructose isomerisation into glucose. However, it would also be useful to reduce conversion by operating at lower temperature and shorter residence times. This would prevent the dimer's full conversion, thus allowing its inclusion in the reaction network, and validating the assumption that it occurs very quickly compared to the other reactions.

For the experimental apparatus described in this thesis, operating at higher temperatures would require a higher-powered electrical heater, or a more efficient one, *i.e.*, with a smaller difference between the temperatures of the heating block and of the supercritical water at the inlet to the reactor. Furthermore, given the limited space available in the reservoir mounted on the organic feed pump, reducing residence times by increasing feed flowrates would minimise the time available for each experiment. Alternatively, the reactor's size could be reduced, but as shown in Section 3.3, this would require removing thermocouple TT-105, thus preventing online temperature measurements.

Manipulating the medium's pH by introducing an acid or base would allow the distinction between acid- and base-catalysed reaction. This distinction is not possible solely based on water's self-ionisation product, as the concentrations of both H^+ and OH^- is assumed to be the same. For sucrose, this would mean further understanding the mechanism of the reaction, where this effect was not required for good agreement between the model and experiments. For dibenzyl ether, it would allow a clearer distinction between substitution nucleophiles.

Nonetheless, independently manipulating the medium's pH would require adding to the mixture a wider range of compounds, with well-characterised behaviour at hydrothermal conditions. Furthermore, if the additional compound is inorganic, it is likely to become insoluble in water near the critical point. On the other hand, if an organic compound is selected, its hydrothermal degradation must also be considered in the overall process.

Finally, expanding the analytical method to quantify more components in the product would result in a larger reaction network. This is particularly true for sucrose's reactions, which could include species like dihydroxyacetone, glyceraldehyde, lactic acid, glycolaldehyde, erythrose, or levulinic acid. For the present study, this was not possible due to limited commercial availability of pure compounds to prepare standard solutions for calibration.

9.2.2 Further model validation

Two types of models were developed during this project: a two-dimensional axis symmetrical CFD model, with the mixing zone explicitly modelled, and a one-dimensional model assuming instantaneous mixing. The hydrodynamics surrounding the confined jet mixer were analysed using the first model, as detailed in Chapter 6. It was applied to define the distance required to reach 99.9% of full mixture, and

to evaluate the effect of feed mixing on process. The developed configuration was assumed to be valid based on literature applications of the selected models under different conditions, and similar models at subcritical conditions. Nonetheless, validating the developed model under the actual operating conditions, as performed in literature [130,135], would fully confirm the conclusions drawn from it.

The CFD model in this study assumed a fully vertical geometry to take advantage of the decreased computational effort by an axis-symmetrical configuration. Including the actual geometry of the reactor section is not expected to significantly affect the model outputs, although it may be confirmed using a full three-dimensional model. However, this will require a significant increase in complexity, requiring improved mathematical solver configurations and more powerful computing resources.

Both CFD and gPROMS models assume any reactions finish when the mixture is quenched, due to diluting and cooling effects. Nonetheless, as summarised in Table 5.5 in Section 5.3, the temperature downstream of this mixing point was predicted in some cases to be up to 160 °C. Those calculations were conducted solely from a safety perspective, not considering the possibility of reactions continuing after mixture. To evaluate if this effect is sufficient to stop any further reacting, the one-dimensional mathematical model can be expanded in the same flowsheet, by duplicating the existing unit, and specifying post-quench inlet conditions, known length, and a heat transfer coefficient based on the downstream cooler.

9.2.3 Expanding case studies

Following the methodology described in this thesis, the next step in the study of lignocellulosic biomass upgrading in hydrothermal medium is applying it to increasingly more complex compounds. Past the present demonstration on dimers, upgrading isolated biopolymers is the next logical step, followed by a mixture of those under known concentrations, and finally actual lignocellulosic residues.

Since lignocellulosic biopolymers are insoluble in water [47,74], an aqueous organic feed containing them can only be continuously supplied to the continuous hydrothermal reactor if it is chemically pre-treated or kept as a slurry with a homogeneous distribution. For cellulose, and Kraft or Organosolv technical lignin, this pre-treatment means solubilising the solid in an aqueous solution containing an acid, like H_2SO_4 , or a base, such as NaOH, amongst other additives [228–231]. However, besides requiring the addition of non-recoverable substances, thus increasing operating costs, these may precipitate in the reactor due to water's loss of solubilisation properties near the critical point.

Introducing the organic feed as a solid suspended in a liquid poses as a more viable option from a chemical point of view. However, as mentioned in Section 2.3, this may present technological limitations since it requires the reduction to a particle size that would not result in blockages throughout the system. Furthermore, to keep a consistent concentration throughout the experiment, continuous

stirring is required in both feed tanks. For a small laboratory set up the particle size may need to be < 30 μm to avoid blockages [89], whereas the particle size can be somewhat bigger as the process scales up, and the pipes and equipment become larger and less prone to blockage. This is important for commercial application, because grinding or chopping biomass is energy intensive, particularly for very small particle sizes [6,93–95].

Beside particle size, it should also be considered increasing the organic feed concentration, gradually moving from solid suspensions to actual slurries. This increase would not only affect the mixture's pumpability, but also as its reaction network, possibly resulting in a larger solid formation, given the smaller amount of available water to solubilise diluted organic compounds [3,54,90,96,97].

From a mathematical modelling perspective, the species added during pre-treatment may need to be included in the reactional scheme, and, if in relevant concentrations, in the thermodynamic model. On the other hand, feeding the biopolymers as solid particles may require a significantly more complex model that accounts for mass transfer between phases, as the one described in [77].

Finally, besides ensuring the system can process the reactional mixture, the analytical methods must be further refined to account for the chemically more complex feedstock, as well as the wider variety of products.

Appendices

Appendix A

Hydrothermal liquefaction apparatus

A.1 Operating procedure

This section details the steps followed during the operation of the hydrothermal liquefaction apparatus described in Section 3.3. The basis of this procedure is described in Section 3.4

A.1.1 Start-up

Inspection

1. BPV-1 is fully open.
2. V-1 is closed, and V-2/V-3 are open, connecting V-1 to the HPLC pumps.
3. Pneumatic valves XV-103-A/B are positioned to use the operating filter (F-1A/B) at the Isco pump controller:
 - a. Air supply is connected (>6 bar).
4. 4-way valve V-7 is connecting P-4 to waste and P-2 to the process.
5. 3-way outlet valve V-8 is open for liquid sampling.
6. The water level in T-1 is adequate:
 - a. If not, fill using P-5.
7. Trip temperature in H-1 controller (TS-104) is set to 0.
8. The collection/waste bottles (C-4/C-5/waste/liquid sample) are empty and connected:
 - a. Weight bottles for liquid sample collection.

Pressurising

9. Open V-1 (T-1 outlet).
10. HPLC pumps (P-1, P-2, and P-3) preparation:
 - a. Prime the HPLC pumps (P-1, P-2, and P-3) using a syringe at the dedicated outlet valve.
 - b. Input the selected flowrates and initiate the flow.
11. Open valve on C-1 (HP N₂ cylinder) and turn the regulator handle clockwise until the pressure gauge shows the required pressure.
12. Slowly close BPV-1 until a pressure of 20 bar is displayed.
 - a. Remove the plugs from the valves mounted on the filters (V-10/11).

- b. Open V-10/11 on the filters until no air bubbles are observed.
 - c. Switch filter.
 - d. Repeat until no bubbles are observed in either filter.
13. Fully pressurise the system:
- a. Increment pressure at 10 bar/s rate and in 40 bar steps, while observing if the pressure in the HPLC pumps display matches BPV-2's gauge.
14. Wait until stable pressure and flow are achieved (10 minutes).

Heating

15. Start the chiller C-3 for cooling water:
- a. Specify the desired temperature (11 °C) in the display.
16. Start the recording of the thermocouple (TT-101, TT-102 and TT-105) measurements.
17. Switch on supercritical heater H-1 controller:
- a. Set the trip temperature (TS-104) to a high enough value (510 °C).
 - b. Increase the temperature set point (TIC-103) in 5 minutes steps:
 - i. 100 °C / 200 °C / 300 °C / 350 °C / 400 °C / 420 °C / 435 °C / 450 °C.
 - b. Increase the temperature set point (TIC-103) in 5 minutes steps:
 - i. 460 °C / 470 °C / 480 °C / 490 °C / 500 °C
18. Wait until a steady-state temperature is observed in TT-101, TT-102 and TT-105.

Sweeping gas

19. Switch V-7 to accumulating mode.
20. Open valve on C-2 (LP N₂ cylinder):
- a. Adjust regulator until the pressure is the required for sweeping.
 - b. Use the valve downstream F-105 to regulate the nitrogen flowrate, based on the rotameter reading.
21. Accumulate enough water on collection bottle C-4 to prime additional transfer pump P-6:
- a. Prevent C-4 from running out of liquid or overflowing using P-6 when required.

FTIR spectrometer

22. Fill the equipment's liquid nitrogen tank:
- a. Keep the vent valve open until liquid comes out.
23. Switch the equipment on, including pre-heater temperature controller and respective trip:
- a. Set temperature controllers to the calibration temperature (191 °C).
24. Open additional needle valve downstream of C-2:
- a. Regulate until the flowrate of purge gas observed in the spectrometer mainboard is 2 L/min.

25. Select appropriate measured species list and recording interval.
26. Initiate recording.

Organic feed

27. Isco pump (P-4) preparation:
 - a. Fill T-2 with enough organic feed (turn on stirring if required).
 - b. Fill the pump reservoir from T-2 by automatically opening XV-101 using the pump's controller (flowrate up to 100 mL/min).
 - c. Input the selected flowrates and initiate the flow by automatically open XV-102 on the pump controller.
28. Pressurise waste line:
 - a. Wait until flow comes out of waste V-12.
 - b. Close V-12 and observe pressure increase at P-4's controller.
29. Switch V-7 to operating mode (P-4 to process and P-2 to waste).
 - a. Stop P-2's flow.

A.1.2 Steady state operation

30. Wait until temperature in TT-105 and gas composition in the FTIR have reached steady measurements over time (over 12 minutes).
 - a. Prevent C-4 from running out of liquid or overflowing using P-6 when required.
31. In the Isco pump controller, switch V-103A/B to the filter operating at steady state collection:
 - a. Simultaneously initiate the filter timer.
32. Switch V-8 to sampling mode and collect liquid:
 - a. Simultaneously initiate the sample timer.
 - b. Collect required amount of sample.
33. Switch V-8 to accumulation mode.
 - a. Simultaneously stop the sample timer.
34. Repeat previous two steps for the number of samples required.

A.1.3 Shut-down

35. Ensure the system shutdown is started before consuming all the liquid in P-4's cylinder.

Organic feed

36. In the Isco pump controller, switch V-103A/B to the filter not operating at steady state:
 - a. Simultaneously stop the filter timer.

37. Re-start P-2's flowrate.
38. Switch V-7 back to start-up mode (P-4 to waste).
39. Open V-12 to depressurise the feed waste line.

Sweeping nitrogen feed and FTIR spectrometer

40. Stop FTIR recordings:
 - a. Switch off the equipment, including pre-heater controller.
41. Close the valve on C-2.

Cooling

42. Set the supercritical heater trip temperature (TS-104) to 0.
43. Wait until temperature in TT-105 is below 60 °C.
 - a. Switch off C-3.
44. Wait until temperature in TT-101 is below 100 °C.
 - a. Initiate depressurisation.
45. Stop the recording of the thermocouple (TT-101, TT-102 and TT-105) measurements.

Depressurisation

46. Close C-1's regulator.
47. Gradually depressurise and repressurise the system using BPV-1, at 10 bar/s rate and in 40 bar steps:
 - a. Continue until the HP nitrogen pressure gauge on both side of BPV-1 reaches 0 bar.
48. Close the valve on C-1 and re-open the cylinder's regulator:
 - a. Repeat previous step.
49. Stop and turn off all pumps (P-1 / P-2 / P-3 / P-4) and controllers (H-1).
50. Close V-1.

A.2 Process and instrumentation diagram (P&ID)

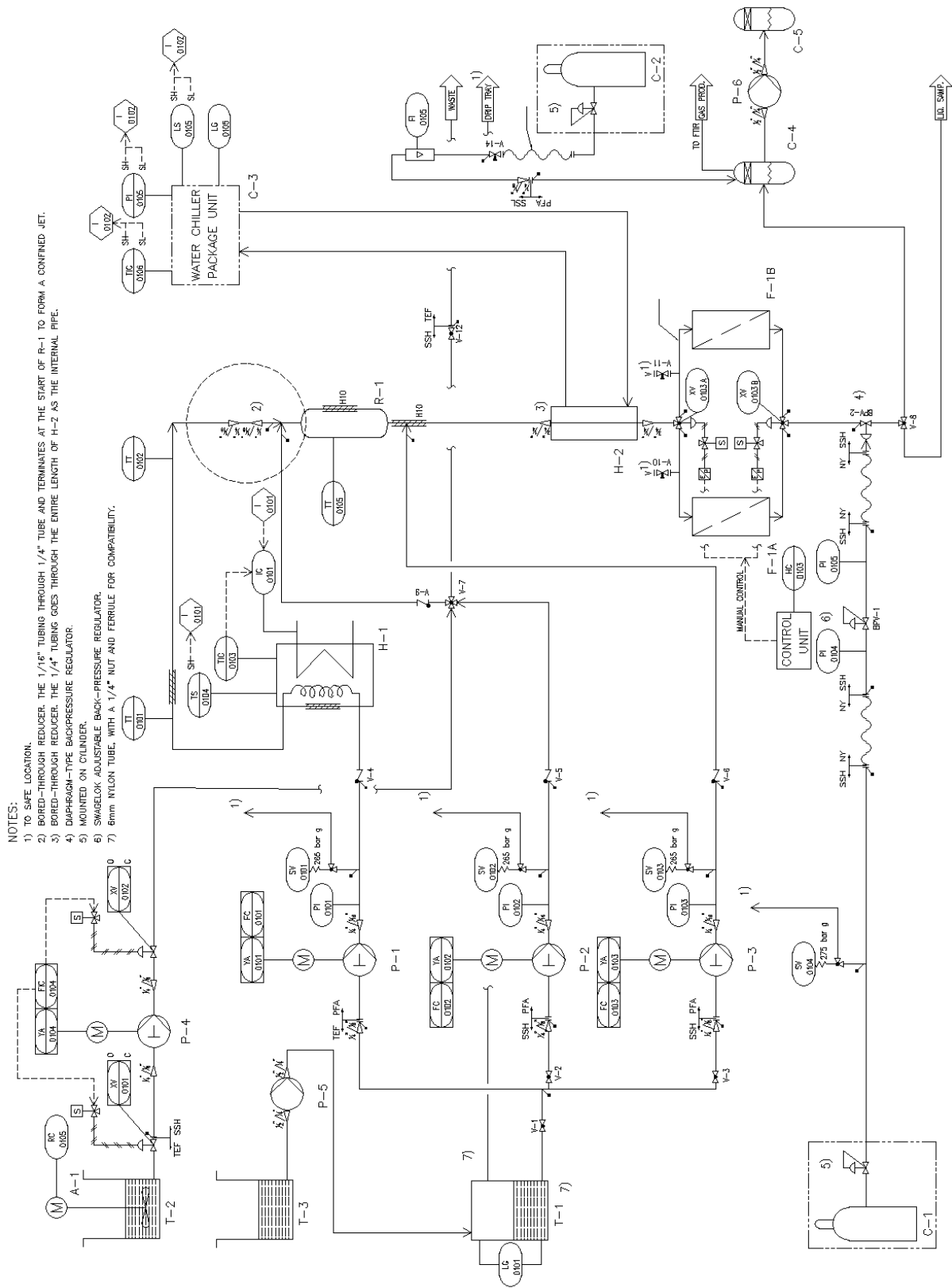


Figure A.1: Process and instrumentation diagram of the hydrothermal liquefaction rig described in Chapter 3.

Appendix B

Instrument calibration

B.1 Rotameter calibration

This calibration focused on quantifying the nitrogen flowrate used for gas sweep as described in Section 3.5.2. This flowrate varied with the pressure imposed in the regulator mounted on the low-pressure nitrogen cylinder C-2 (2 – 6 bar), and the position of rotameter FI-105 at its outlet (see Appendix A.2). It was quantified by measuring the time required by a soap bubble to cross a known volume while being pushed by water-saturated nitrogen.

The column volume was divided by the measured time, producing the volumetric flowrates in Figure B.1. A linear regression was applied to each pressure in Microsoft Excel, using the least-squares method, resulting in the parameters shown next to the plot.

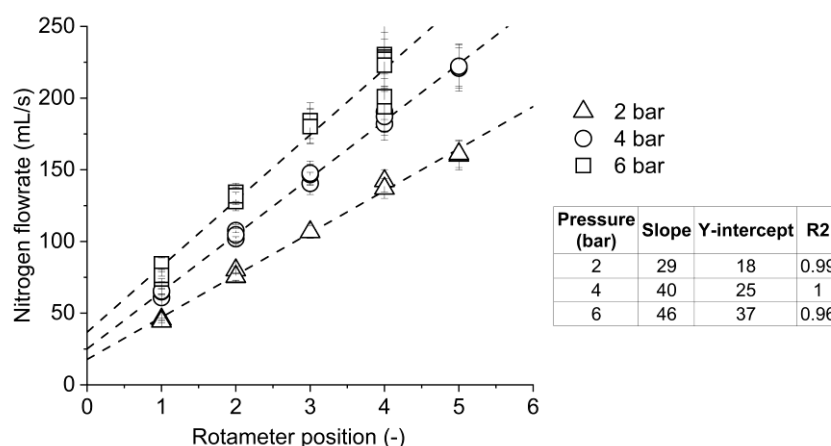


Figure B.1: Rotameter calibration plots for different feed pressures, and respective calibration parameters.

B.2 HPLC with UV-vis detection

This analytical method was used to characterise and quantify the liquid products from the hydrothermal processing of dibenzyl ether (DBE). It is described in Chapter 7, according to the methodology in Section 3.6.1 and Section 3.6.2. The compounds selected for this analysis were: dibenzyl ether, benzyl alcohol (BAL), benzaldehyde (BZA), and toluene (TOL).

B.2.1 Chromatographic method

For the analysis by HPLC with UV-vis detection, it was required to select: (1) absorption wavelength; (2) mobile phase composition; and (3) retention time. The first was selected based on the range of maximum UV absorption of each compound [154–157], which are shown in Table B.1. Since, 260 nm is part of the maximum absorption range of all analytes, it was the selected wavelength.

Table B.1: Maximum UV absorption wavelength [154–157], and elution time at different mobile phase concentrations for each analyte.

Substance	UV absorption range (nm)	Elution time (min) for a mobile phase containing acetonitrile at		
		54 wt%	42 wt%	34 wt%
Benzyl alcohol	243-268	4.0	4.7	5.5
Benzaldehyde	241-287	5.2	6.8	8.9
Toluene	207-276	9.5	15.8	27.4
Dibenzyl ether	252-265	14.2	30.5	> 60

The mobile phase composition defines each molecule's elution time, depending on the respective affinity to acetonitrile. As shown in Table B.1, three acetonitrile concentrations were tested (34, 42 and 54 wt%) by eluting a mixture containing the four analytes. For all, the elution time was significantly reduced by increasing the concentration of acetonitrile, thus reflecting the higher affinity of the analytes towards this molecule compared to water. Though allowing a faster analysis, the lowest concentration did not provide a good enough resolution between BAL and BZA. On the other hand, the lowest concentration extended the process unnecessarily. Consequently, the middle concentration (42 wt%) was used as the HPLC mobile phase, and, considering a 15-minute margin, the total elution time was fixed at 45 minutes.

B.2.2 Composition calibration

A quantitative calibration was conducted by eluting standard solutions of each analyte diluted in an aqueous solution of acetonitrile (85 wt%). As detailed in Section 3.6.2, it was considered that the area under each peak of the chromatogram was proportional to the concentration of the respective analyte [147]. Given the wide range of measured concentrations, two sets of calibrations were conducted for each analyte, thus minimising uncertainty. The measured signal area and concentrations are plotted in Figure B.2 to Figure B.5.

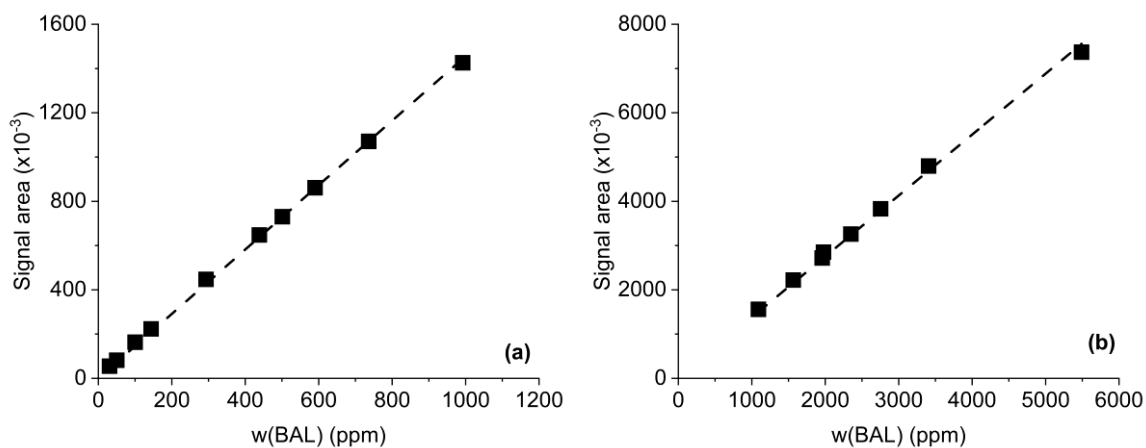


Figure B.2: HPLC with UV-vis detection: calibration plots for BAL at low (a) and high (b) composition ranges.

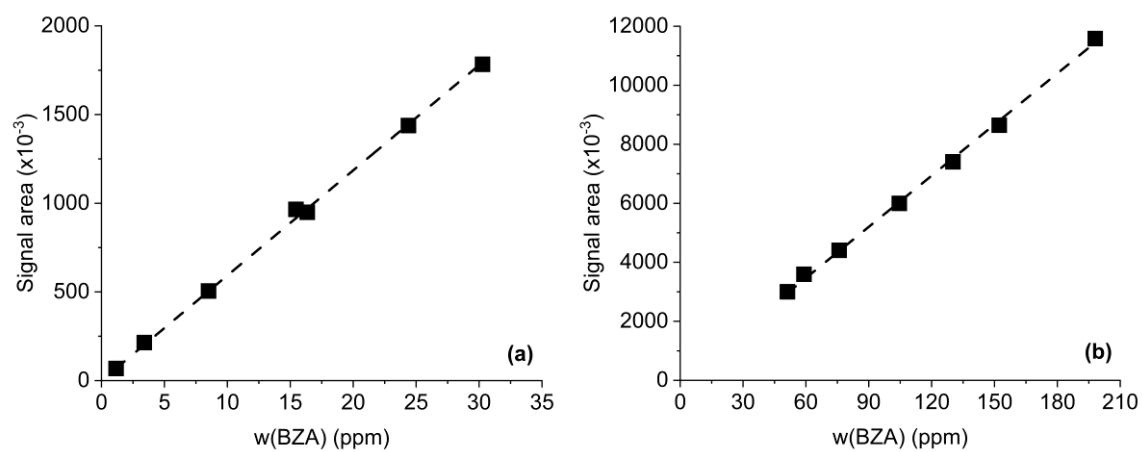


Figure B.3: HPLC with UV-vis detection: calibration plots for BZA at low (a) and high (b) composition ranges.

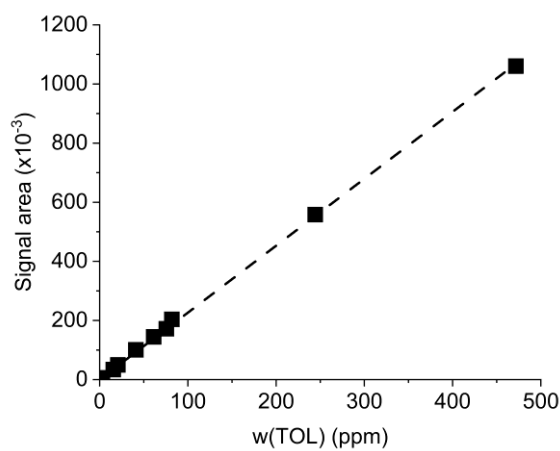


Figure B.4: HPLC with UV-vis detection: calibration plot for TOL.

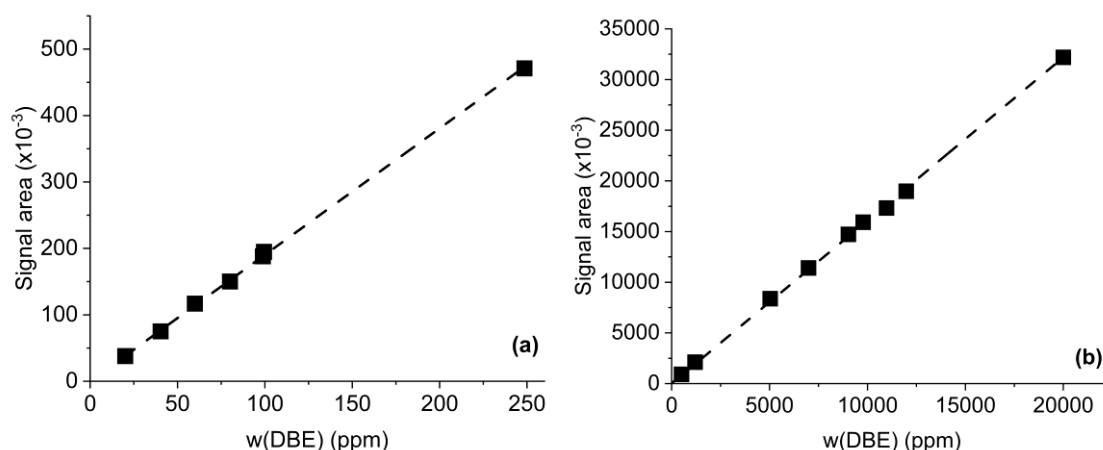


Figure B.5: HPLC with UV-vis detection: calibration plots for DBE at low (a) and high (b) composition ranges.

The respective linear regressions were conducted in Microsoft Excel, using the least-squares method, and forcing each line to cross the origin. The estimated slopes, *i.e.*, the proportionality constants between signal area and concentration are summarised in Table B.2.

Table B.2: HPLC with UV-vis calibration: calibration parameters.

Analyte	Low concentration standards			High concentration standards		
	Concentration range (ppm)	Slope	R ²	Concentration range (ppm)	Slope	R ²
Benzyl alcohol	30 – 992	1455 ± 8	1.00	1089 – 5489	1380 ± 10	1.00
Benzaldehyde	1 – 30	59300 ± 500	1.00	51 – 198	57800 ± 400	1.00
Toluene	1 – 472	2270 ± 10	1.00	–	–	–
Dibenzyl ether	20 – 249	1904 ± 9	1.00	1193 – 19999	1609 ± 8	1.00

B.3 HPLC with RID

This analytical method was used to characterise and quantify the water-soluble organics (WSO) obtained from the hydrothermal processing of sucrose. It is described in Chapter 8, according to the methodology in Section 3.6.1 and Section 3.6.3. The compounds selected for this analysis were sucrose, glucose, fructose, 1,6-anhydro- β -D-glucose, and pyruvaldehyde.

The concentration of the five analytes in the aqueous samples was within the detection limits of the equipment and provided adequate peak resolution. Therefore, no dilution was applied to the analysed samples. Despite the elution times presented in Table B.3, a total elution time of 60 minutes was required for each sample to ensure no organics were carried over between analysis.

A calibration was conducted by eluting standard solutions of each analyte diluted in water. As with UV-vis detection, it was considered that the area under each peak of the chromatogram was proportional to

the concentration of the respective analyte [147]. The measured signal area and concentrations are plotted in Figure B.6 to Figure B.8.

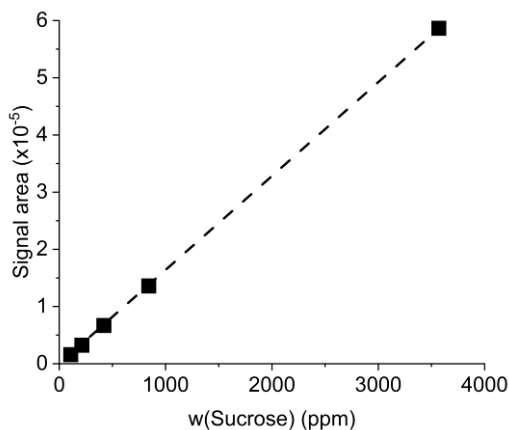


Figure B.6: HPLC with RID: calibration plot for sucrose.

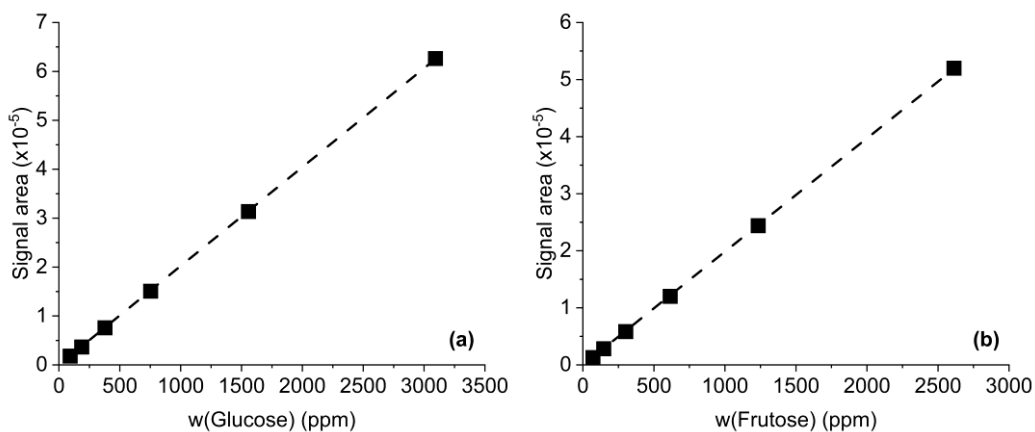


Figure B.7: HPLC with RID: calibration plot for glucose (a) and fructose (b).

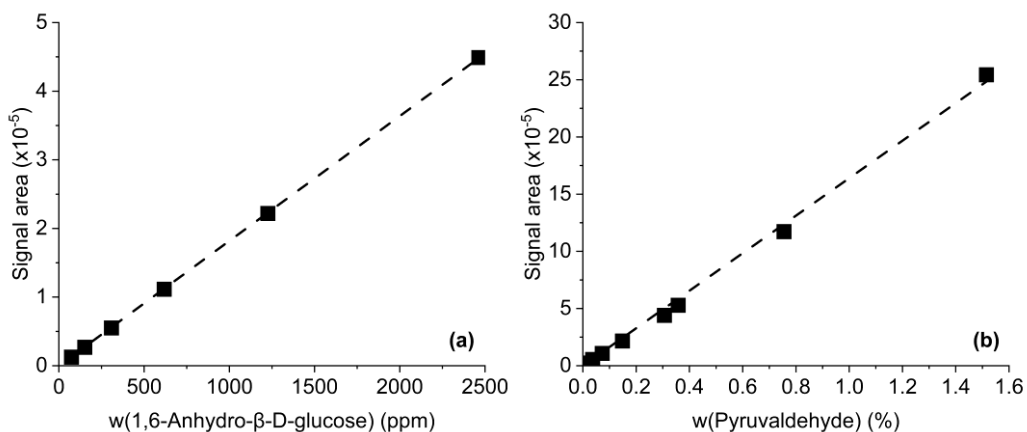


Figure B.8: HPLC with RID: calibration plot for 1,6-anhydro-β-D-glucose (a) and pyruvaldehyde (b).

The linear regressions for each analyte were conducted in Microsoft Excel, using the least-squares method, and forcing each line to cross the origin. The estimated slopes, *i.e.*, the proportionality constants between signal area and concentration are summarised in Table B.3.

Table B.3: HPLC with RID: calibration parameters.

Analyte	Elution time (min)	Concentration range (ppm)	Slope	R ²
Sucrose	11.3	107 – 3570	164.1 ± 0.5	1.00
Glucose	13.3	92 – 3093	202.2 ± 0.3	
Fructose	14.5	70 – 2612	198.6 ± 0.4	1.00
Pyruvaldehyde	16.9	89 – 15151	164 ± 2	0.99
1,6-Anhydro-β-D-glucose	18.1	69 – 2464	181.9 ± 0.3	1.00

B.4 GC with FID

This analytical method was used to quantify 5-hydroxymethylfurfural (5-HMF) in water- and DCM soluble organics (WSO and DSO) obtained from the hydrothermal processing of sucrose. It is described in Chapter 8, following the methodology in Section 3.6.4 and Section 3.6.6. The calibration of this method was conducted by eluting standard solutions of 5-HMF in Methanol. As with UV-vis detection and RID, it was considered that the area under each peak of the chromatogram was proportional to the concentration of the respective analyte [147]. The measured signal area and concentrations are plotted in Figure B.9.

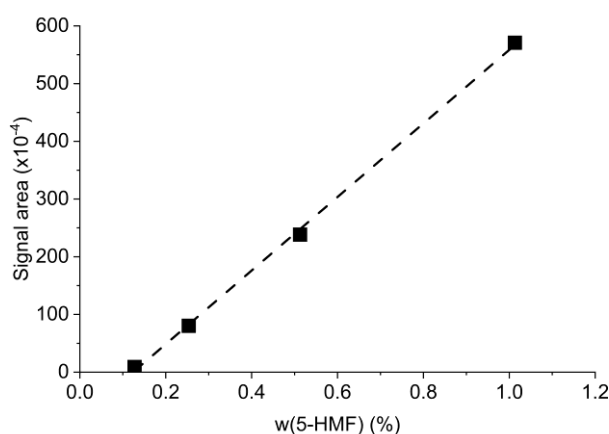


Figure B.9: GC with FID: calibration plot for 5-HMF.

The linear regression for 5-HMF was conducted in Microsoft Excel, using the least-squares method, without forcing it to cross the origin. The estimated slope and y-intercept are summarised in Table B.4.

Table B.4: GC with FID: calibration parameters.

Analyte	Elution time (min)	Concentration range (%)	Slope	Y-intercept	R ²
5-HMF	16.5	0.127 – 1.01	$(64 \pm 1) \times 10^5$	$(-79 \pm 8) \times 10^{-4}$	0.99

Appendix C

Detailed calculations and results: Preliminary analysis

C.1 Additional mass and energy balances

The following sections summarise the additional calculations required to estimate mixing compositions and temperatures at the inlet of the HTL reactor, as well as downstream of it, after dilution and cooling. These were applied in Chapter 5 to verify the equipment's capacity under different scenarios, and in Chapter 6 as inputs of simplified CFD model.

C.1.1 Feed mixing

Component i mass balance for calculating mass fractions at the reactor's inlet (w_i^R):

$$Q_{SCW} \times w_i^{SCW} + Q_{FO} \times w_i^{FO} = Q_R \times w_i^R \quad (C.1)$$

Energy balance to calculate the mixed stream specific enthalpy (h_R), from which the reactor's inlet temperature is estimated (T_R) based on thermodynamic model:

$$Q_{SCW} \times h_{water}(T_{SCW}, p, w_i^{SCW}) + Q_{FO} \times h_{FO}(T_{amb}, p, w_i^{FO}) = Q_R \times h_R(T_R, p, w_i^R) \quad (C.2)$$

C.1.2 Downstream cooling

Component i mass balance for calculating the quenched stream mass fractions (w_i^{out}):

$$Q_{quench} \times w_i^{quench} + Q_R \times w_i^R = Q_{out} \times w_i^{out} \quad (C.3)$$

Energy balance to calculate the quenched stream specific enthalpy (h_{hot}), from the cooler's inlet temperature is calculated (T_{hot}):

$$Q_{quench} \times h_{quench}(T_{amb}, p, w_i^{quench}) + Q_R \times h_R(T_R, p, w_i^R) = Q_{out} \times h_{hot}(T_{hot}, p, w_i^{out}) \quad (C.4)$$

Energy balance around double-pipe heat exchanger H-2, for the estimation of the cold stream's specific enthalpy and temperature (h_{cold} , T_{cold}), considering its heat duty (q_{H-2}):

$$Q_{out} \times h_{hot}(T_{hot}, p, w_i^{out}) - q_{H-2} = Q_{out} \times h_{cold}(T_{cold}, p, w_i^{out}) \quad (C.5)$$

H-2 heat duty calculated considering an approximated overall heat transfer coefficient (U_{H-2}), the inner tube's outer area (A_L^{H-2}), and logarithmic mean temperature difference (ΔT_{ln}), assuming a temperature increase (ΔT_{chill}) on the chilled water side (T_{chill}):

$$q_{H-2} = U_{H-2} \times A_L^{H-2} \times \Delta T_{ln} \quad (C.6)$$

$$\Delta T_{ln} = \frac{T_{hot} - T_{cold} - \Delta T_{chill}}{\ln\left(\frac{T_{hot} - (T_{chill} + \Delta T_{chill})}{T_{cold} - T_{chill}}\right)} \quad (C.7)$$

C.2 Detailed results

The following tables detail the temperatures measured during the preliminary tests described in Section 5.4. These also include equivalent temperatures calculated using the heat transfer coefficients estimated in Section 5.5. Table C.1 and Table C.2 are relative to preliminary experiments using DBE/water mixtures, while Table C.3 and Table C.4 contain data for water-only experiments.

Table C.1: Preliminary tests using DBE/water mixtures: operating conditions and measured temperatures.

Test	Q_y^{NOM} (mL/min)		Ratio	Q_m (g/min)	w_{DBE}^0 (%)	p (bar)	Measured temperature (°C)						
	SCW	FO		Total			Setpoint (TIC-103)	TT 101	TT 102	Δ	TT-105 (T_m)	TT-106 (T_{out})	Δ
1	16	8	2	26	33	244	460	382	381	2	358	346	12
2	15	10	1.5	27	39	243	460	382	380	2	344	330	14
3	15	12.5	1.2	30	45	244	460	382	380	2	332	318	14
4	18	15	1.2	36	45	251	460	384	383	0	335	322	13
5	19.5	13	1.5	35	39	250	460	384	384	0	350	337	12
6	26	13	2	42	33	249	460	385	386	-1	365	356	9

Table C.2: Preliminary tests using DBE/water mixtures: calculated temperatures using estimated heat transfer coefficients.

Test	Measured temperature (°C)		Temperature calculated using detailed model (°C)		Temperature calculated using simplified model (°C)			
	TT-105 (T_m)	TT-106 (T_{out})	TT-106 (T_{out}^*)	Δ	TT-105 (T_m^*)	Δ	TT-106 (T_{out}^*)	Δ
1	358	346	341	-5	356	-2	341	-5
2	344	330	325	-5	343	-1	325	-5
3	332	318	311	-6	330	-1	311	-6
4	335	322	317	-4	334	-1	317	-4
5	350	337	335	-3	349	-1	335	-3
6	365	356	355	-1	364	-1	355	-1

Table C.3: Preliminary tests using only water: operating conditions and measured temperatures.

Test	Q_v^{NOM} (mL/min)		Ratio	Q_{in} (g/min)	p (bar)	Measured temperature (°C)						
	SCW	FO		Total		Setpoint (TIC-103)	TT-101	TT-102	Δ	TT-105 (T_m)	TT-106 (T_{out})	Δ
1	21	7	3	31	248	460	386	386	0	361	349	12
2	21	10.5	2	34	248	460	386	386	0	345	333	12
3	21	12	1.75	36	249	460	387	386	0	326	315	11
4	15	5	3	22	247	460	385	383	2	358	345	13
5	15	7.5	2	25	247	460	385	383	2	338	325	14
6	15	10	1.5	27	247	460	385	383	2	318	305	13
7	15	15	1	33	247	460	385	383	2	283	272	10
8	18	6	3	26	237	375	318	310	7	226	214	12
9	18	6	3	26	251	400	341	335	6	249	236	12
10	18	6	3	26	250	420	363	366	-3	294	279	14
11	18	6	3	26	250	435	371	375	-4	339	324	15
12	18	6	3	26	250	450	378	379	-1	353	339	14
13	18	6	3	26	249	460	385	385	1	360	348	12
14	18	6	3	26	249	470	392	389	3	363	352	11
15	18	6	3	26	249	480	399	395	5	366	356	10
16	18	6	3	26	249	490	406	400	7	367	358	9
17	18	6	3	26	249	500	413	404	8	368	359	9
18	18	9	2	29	251	500	414	406	8	358	347	11
19	18	9	2	29	251	490	407	400	6	355	343	12
20	18	9	2	29	251	480	399	395	4	351	339	12
21	18	9	2	29	250	470	391	389	2	347	334	12
22	18	9	2	29	250	460	385	385	0	341	329	12
23	18	9	2	29	251	450	378	380	-2	333	320	12
24	18	9	2	29	251	435	371	375	-4	313	301	12
25	18	9	2	29	251	410	349	347	3	246	237	9
26	18	9	2	29	251	390	330	325	5	225	216	8
27	18	9	2	29	251	360	302	295	7	198	190	8
28	24	8	3	35	244	360	303	299	4	221	212	10
29	24	8	3	35	244	380	321	317	4	237	227	10
30	24	8	3	35	244	420	359	361	-2	289	278	12
31	24	8	3	35	244	440	371	375	-4	349	337	12
32	24	8	3	35	244	460	384	384	0	363	353	10
33	24	8	3	35	252	470	391	390	1	365	356	9
34	24	8	3	35	252	480	398	396	2	368	360	8
35	24	8	3	35	252	490	405	403	3	370	362	8
36	24	8	3	35	251	500	413	408	4	370	363	7
37	24	12	2	39	251	500	413	409	4	361	353	9
38	24	12	2	39	251	475	394	394	1	353	344	10
39	24	12	2	39	251	450	375	379	-4	334	324	10
40	24	12	2	39	250	425	358	359	-1	263	254	9
41	24	12	2	39	251	400	333	330	3	232	224	8

Table C.4: Preliminary tests using only water: calculated temperatures using estimated heat transfer coefficients.

Test	Measured temperature (°C)		Temperature calculated using detailed model (°C)		Temperature calculated using simplified model (°C)			
	TT-105 (T_m)	TT-106 (T_{out})	TT-106 (T_{out}^*)	Δ	TT-105 (T_m^*)	Δ	TT-106 (T_{out}^*)	Δ
1	361	349	351	2	360	-1	351	2
2	345	333	335	2	345	0	335	2
3	326	315	316	1	326	0	316	1
4	358	345	343	-2	356	-1	343	-2
5	338	325	324	-1	338	0	324	-1
6	318	305	304	-1	318	0	304	-1
7	283	272	271	-1	283	0	271	-1
8	226	214	214	0	226	0	214	0
9	249	236	236	0	249	0	236	0
10	294	279	280	0	294	0	280	0
11	339	324	325	1	338	0	325	1
12	353	339	340	1	352	-1	340	1
13	360	348	348	0	359	-1	348	0
14	363	352	352	0	362	-1	352	0
15	366	356	355	-1	365	-1	355	-1
16	367	358	357	-1	366	-1	357	-1
17	368	359	358	-2	367	-1	358	-2
18	358	347	347	0	357	-1	347	0
19	355	343	344	1	354	-1	344	1
20	351	339	340	1	351	-1	340	1
21	347	334	335	1	346	0	335	1
22	341	329	329	0	341	0	329	0
23	333	320	320	0	333	0	320	0
24	313	301	300	-1	312	0	300	-1
25	246	237	234	-3	246	0	234	-3
26	225	216	214	-2	225	0	214	-2
27	198	190	189	-1	198	0	189	-1
28	221	212	213	1	221	0	213	1
29	237	227	228	1	238	0	228	1
30	289	278	279	1	289	0	279	1
31	349	337	340	2	349	0	340	2
32	363	353	354	2	362	-1	354	2
33	365	356	357	1	365	-1	357	1
34	368	360	360	0	367	-1	360	0
35	370	362	362	0	369	-1	362	0
36	370	363	363	0	370	-1	363	0
37	361	353	354	1	361	0	354	1
38	353	344	345	1	353	0	345	1
39	334	324	325	1	334	0	325	1
40	263	254	254	0	263	0	254	0
41	232	224	224	0	232	0	224	0

Appendix D

Detailed calculations and results: CFD analysis

D.1 Discretisation mesh selection

The geometry in Figure 6.1 (a) was discretised using a rectangular grid. Across the vertical axis, a maximum length between nodes (MS) was defined based on the COMSOL's default values of 14.2 and 3.74 mm. The number of nodes across the radial direction was defined for each of the three sections (s) of length L_s , also considering the default distance of 3.74 mm, and multiplying it by an integer (I), as shown in equation (D.1).

$$N_s = \max\left(1, \text{round}\left(\frac{L_s}{0.00374}\right) \times I\right) \quad (\text{D.1})$$

Since large gradients are expected around the SCW jet, the obtained mesh was further refined in the fluid sections of jet and mixing, using a 4-level algorithm in COMSOL (ARL from 1 to 4).

The quality of the assembled mesh was evaluated by comparing the model's performance while increasing the three parameters above (I , MS , and ARL). This evaluation was applied to case S5 in Table 6.3, comparing: (1) the total organic mass fraction and velocity profiles; (2) variations on mass and energy balances; and (3) required simulation time, as well as average temperatures and yields.

D.1.1 Radial axis

The number of elements in the radial direction was increased by varying I in equation (D.1) from 1 to 150. The maximum element size in the vertical axis was kept as 14.2 mm, and automatic refinement was not applied. Obtained profiles are shown in Figure D.1. The obtained profiles show significant variations, particularly regarding the recirculation zone next to the jet's wall. In the first scenario, this swirl is absent, while the following scenarios show it moving up the cold feed.

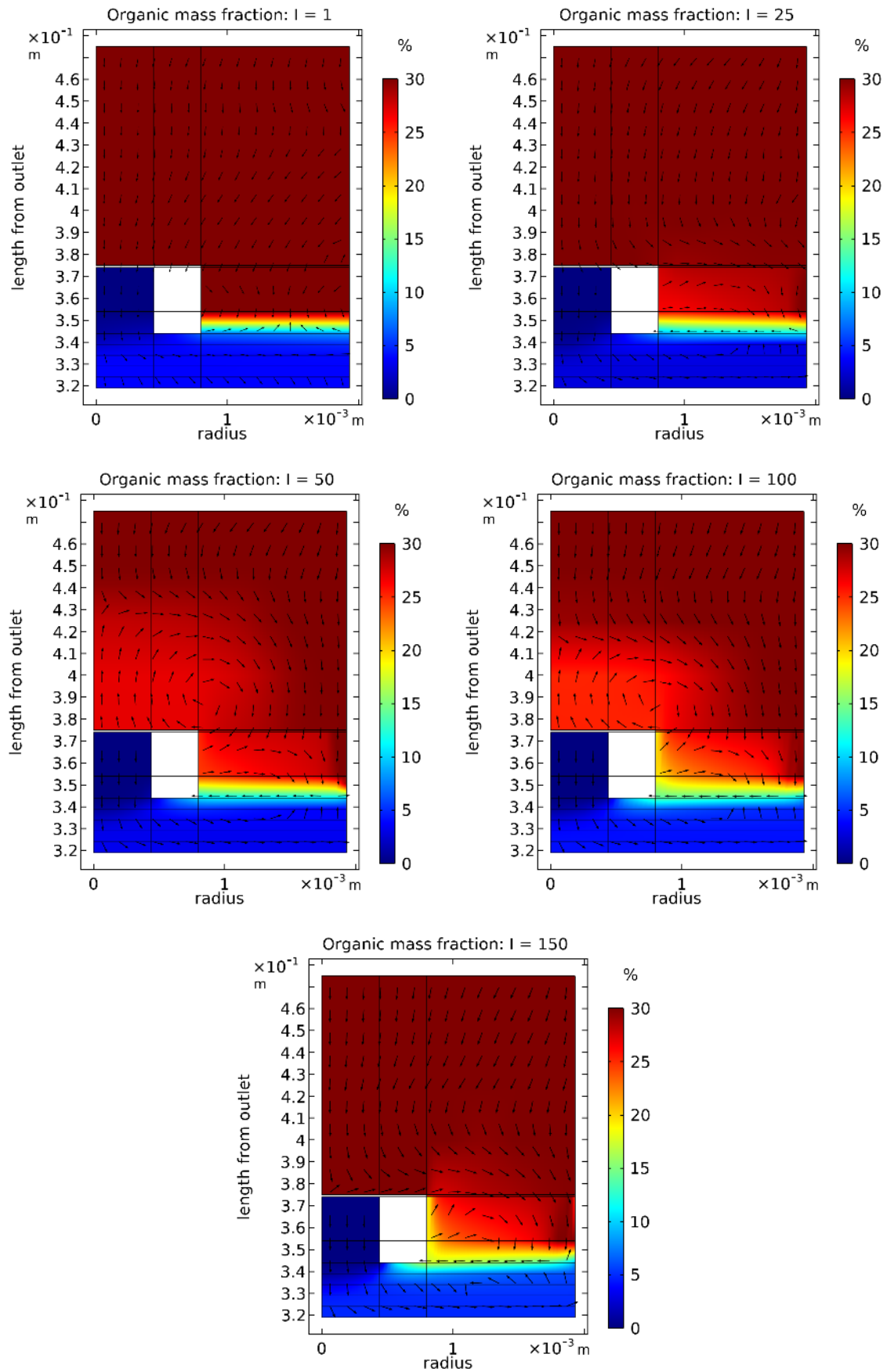


Figure D.1: Total organic mass fraction profiles for varying number of nodes in the radial axis ($I = 1, 25, 50, 100, \text{ and } 150$).

Table D.1 contains the variables used to further evaluate the profiles in Figure D.1. These include the conservation ratios defined in Section 6.3.2, by equations (6.11) to (6.20). Both total organic and energy balances show improvements, but only the last reaches acceptable values, *i.e.*, below 10%. Remaining estimated values show consistent values from $I = 100$. Hence this was considered the best option.

Table D.1: Conservation ratios, average temperatures, and yields for different number of nodes in the radial axis ($I = 1, 25, 50, 100, \text{ and } 150$).

I	Simulation time (sec)	Conservation ratio			Average T (°C)		Yield				
		R_{tot}	R_{org}	R_{heat}	TT-105	Outlet	Glucose	Fructose	TSO	Solids	Volatiles
1	606	0%	50%	-76%	379	374	1%	23%	43%	0%	33%
25	236	2%	64%	-10%	376	370	1%	13%	40%	0%	45%
50	563	2%	57%	-6%	376	370	2%	14%	41%	0%	43%
100	720	-1%	45%	-3%	372	366	2%	11%	40%	1%	46%
150	885	-2%	33%	-3%	372	365	2%	10%	41%	1%	46%

D.1.2 Vertical axis

The number of elements in vertical direction was increased by varying MS from 14.2 to 0.374 mm. I was kept as 1, and the automatic refinement was not applied. The estimated total organic mass fraction profiles and comparison variables are shown in Figure D.2 and Table D.2, respectively. The profiles in the former do not present any significant variation. The latter display a positive effect on the heat balance, but at the cost of the total organic mass balance. Nonetheless, the MS increase also increased the simulation time significantly, showing that, as an independent approach, increasing this parameter viable option.

Table D.2: Conservation ratios, average temperatures, and yields for different number of nodes in the vertical axis ($MS = 25.7, 3.74, \text{ and } 0.374 \text{ mm}$).

MS (mm)	Simulation time (sec)	Conservation ratio			Average T (°C)		Yield				
		R_{tot}	R_{org}	R_{heat}	TT-105	Outlet	Glucose	Fructose	TSO	Solids	Volatiles
25.7	606	0%	50%	-76%	379	374	1%	23%	43%	0%	33%
3.74	963	-1%	63%	1%	369	361	2%	6%	39%	1%	52%
0.374	1352	0%	99%	-1%	373	366	2%	10%	41%	0%	46%

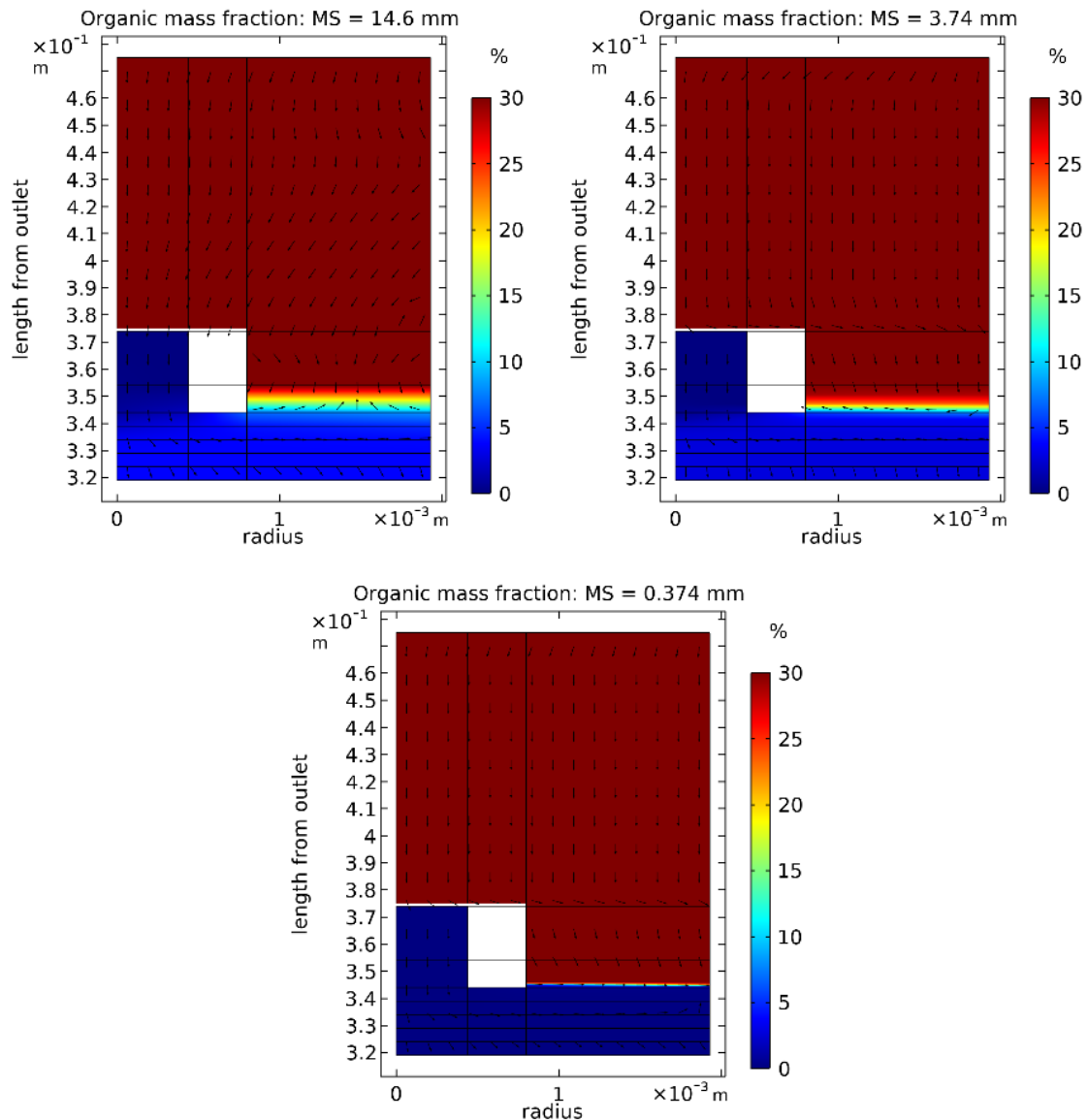


Figure D.2: Total organic mass fraction profiles for varying number of nodes in the vertical axis ($MS = 25.7, 3.74,$ and 0.374 mm).

D.1.3 Auto-refinement in jet and mixing sections

The number of nodes in the jet and mixing sections was refined using COMSOL's 4-level algorithm ($ARL = 1$ to 4). MS and I were kept as 14.2 mm and 1 respectively. Calculated profiles are shown in Figure D.3, showing variations in total organic mass fraction profiles, particularly when the refinement level was increased from 1 to 2, followed by a moderate variation from 2 to 3.

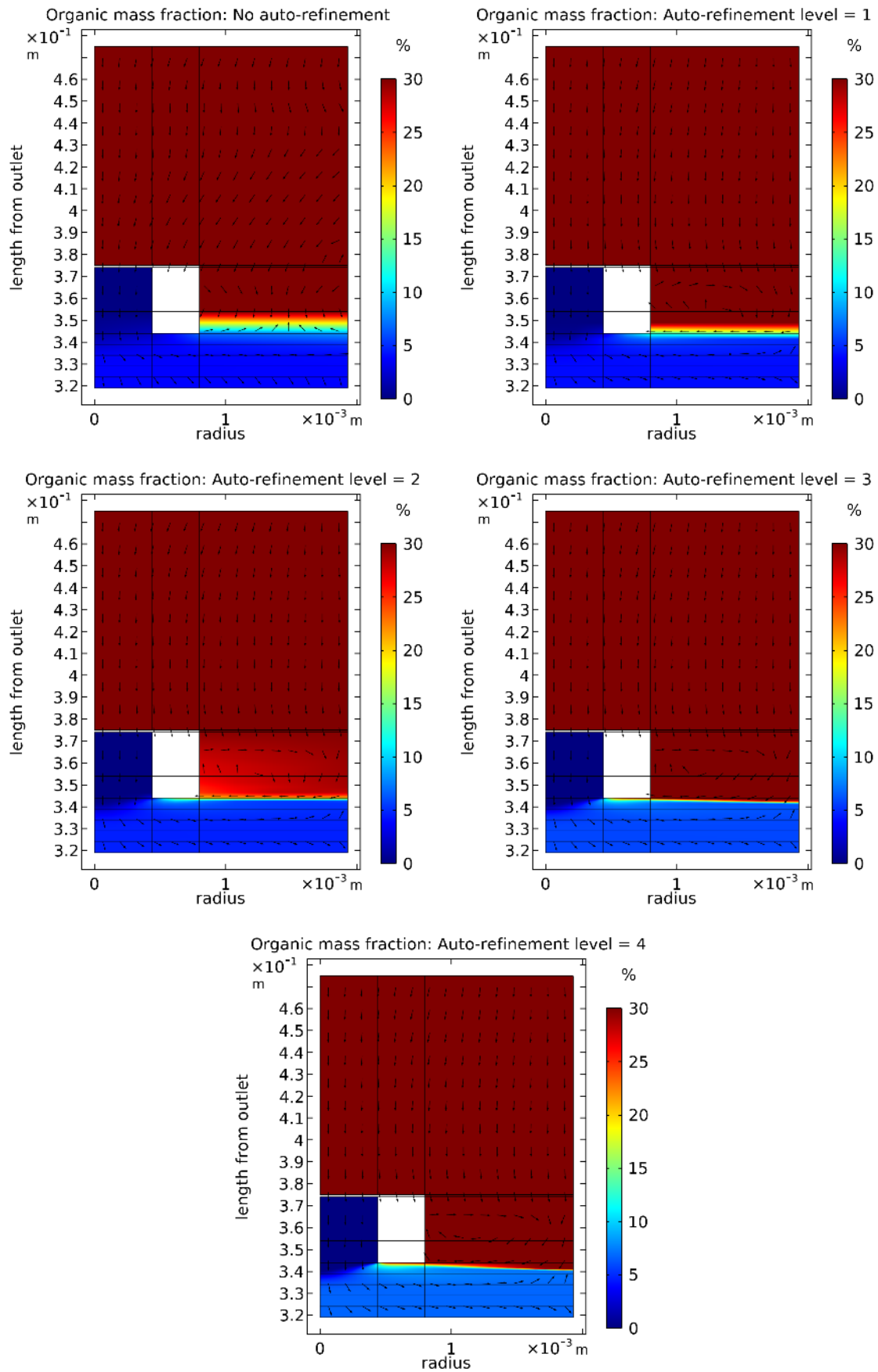


Figure D.3: Total organic mass fraction profiles for different auto-refinement levels in jet and mixing sections (No auto-refinement, and ARL from 1 to 4).

Table D.3 contains the estimate comparison variables. Significant yield and temperature variations occurred between auto-refinement levels 1 and 2. A positive effect on the energy balance was observed as the ARL increased, while the total organic mass balance steadily decreased. From these observations, an auto-refinement level 3 was considered the best option.

Table D.3: Conservation ratios, average temperatures, and yields for different auto-refinement levels in jet and mixing sections (No auto-refinement, and ARL from 1 to 4).

ARL	Simulation time (sec)	Conservation ratio			Average T (°C)		Yield				
		R_{tot}	R_{org}	R_{heat}	TT-105	Outlet	Glucose	Fructose	TSO	Solids	Volatiles
-	606	0%	50%	-76%	379	374	1%	23%	43%	0%	33%
1	1706	2%	47%	-4%	375	369	1%	12%	41%	0%	45%
2	925	-3%	36%	-2%	368	361	2%	6%	39%	1%	53%
3	984	0%	23%	1%	368	361	2%	5%	38%	1%	55%
4	1642	0%	10%	-1%	370	363	2%	7%	39%	1%	53%

D.1.4 Combined effect

The different variations tested in the previous sections were simultaneously evaluated, resulting in the organic mass fraction profiles in Figure D.4, and the comparison variables in Table D.4.

Table D.4: Conservation ratios, average temperatures, and yields for different mesh sizes, combining the effects of different I , MS , and ARL.

ARL	I	MS (mm)	Simulation time (sec)	Conservation ratio			Average T (°C)		Yield				
				R_{tot}	R_{org}	R_{heat}	TT-105	Outlet	Glucose	Fructose	TSO	Solids	Volatiles
3	1	25.7	984	0.2%	23%	1%	368	361	2%	5%	38%	1%	55%
3	25	25.7	2271	0.4%	15%	-11%	369	362	2%	7%	40%	1%	50%
3	50	25.7	4594	-1.8%	9%	-5%	370	363	2%	9%	41%	1%	48%
3	25	3.74	8446	-1%	7%	0%	371	363	2%	8%	41%	1%	49%
3	50	3.74	32367	-0.5%	4%	0%	371	364	2%	8%	41%	1%	48%

As in its independent variation, increasing the number of radial elements, *i.e.*, increasing I , affected the velocities profile, particularly from 1 to 25. Nonetheless, this effect was less evident, when the auto-refinement algorithm was applied. Increasing the number elements in the vertical axis had a minimal effect on the velocity or mass fraction profiles. However, it effectively reduced the undesired variations in the total organic and energy balances, bringing their variations to acceptable levels, *i.e.*, smaller than 10%. The final combination shows all variations below 5%. However, this came at the cost of increasing the simulation time nearly four times. Comparing the profile and comparison variables in the last two parameter combinations, this increase in simulation time was considered unnecessary. Therefore, the combination: $ARL = 3$, $I = 25$, and $MS = 3.74$ was considered to provide an adequate level of accuracy, requiring a reasonable simulation time.

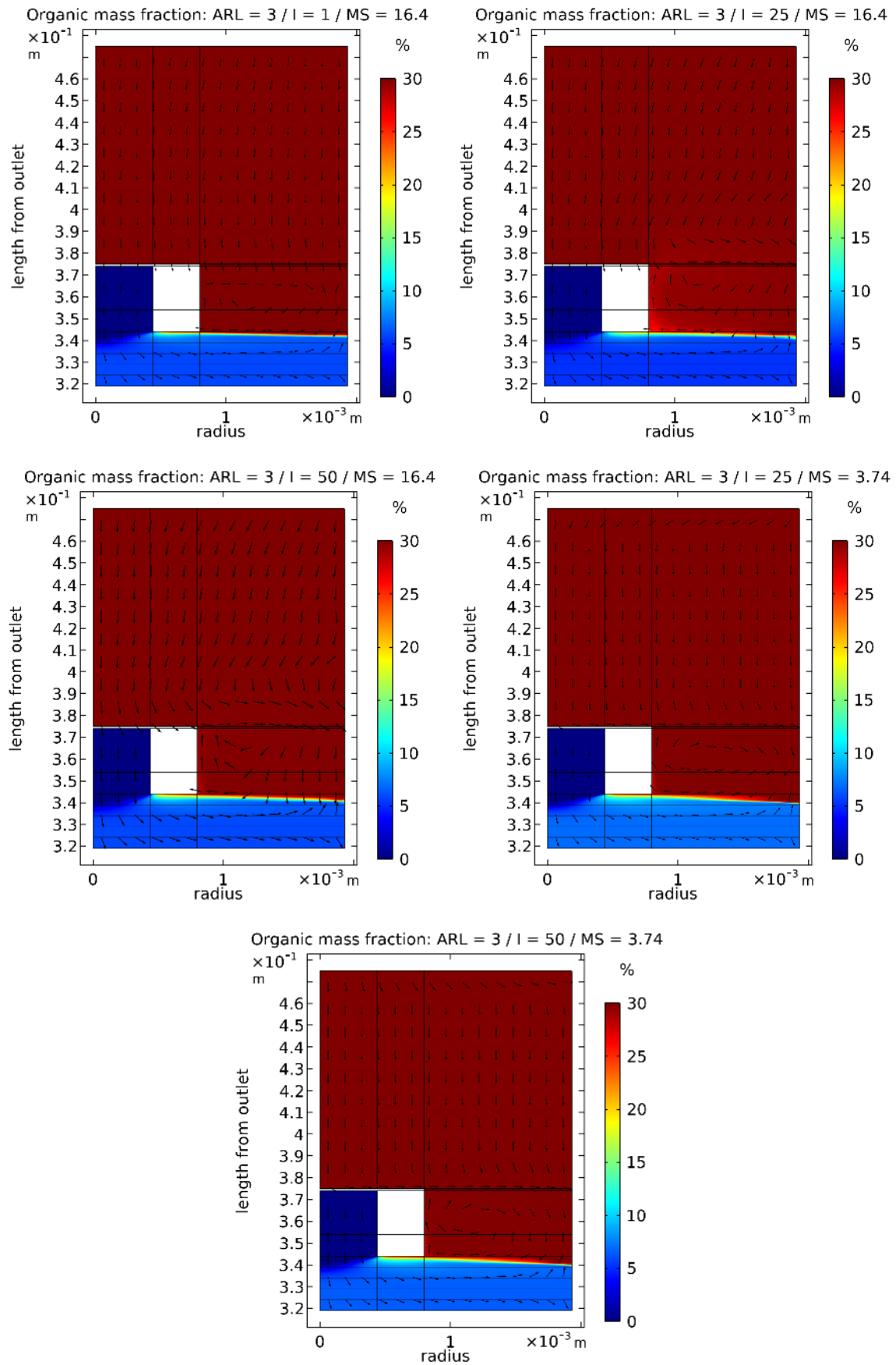


Figure D.4: Total organic mass fraction profiles for different mesh sizes, combining the effects of different I , MS , and ARL .

D.2 Complete geometry profiles

This section presents the temperature and total organic mass fraction profiles calculated for the complete geometry in Figure 6.1 (a) regarding the cases in Section 6.4. A closer look at the jet and mixing sections is shown in Figure 6.7 to Figure 6.10 of Section 6.4.2.

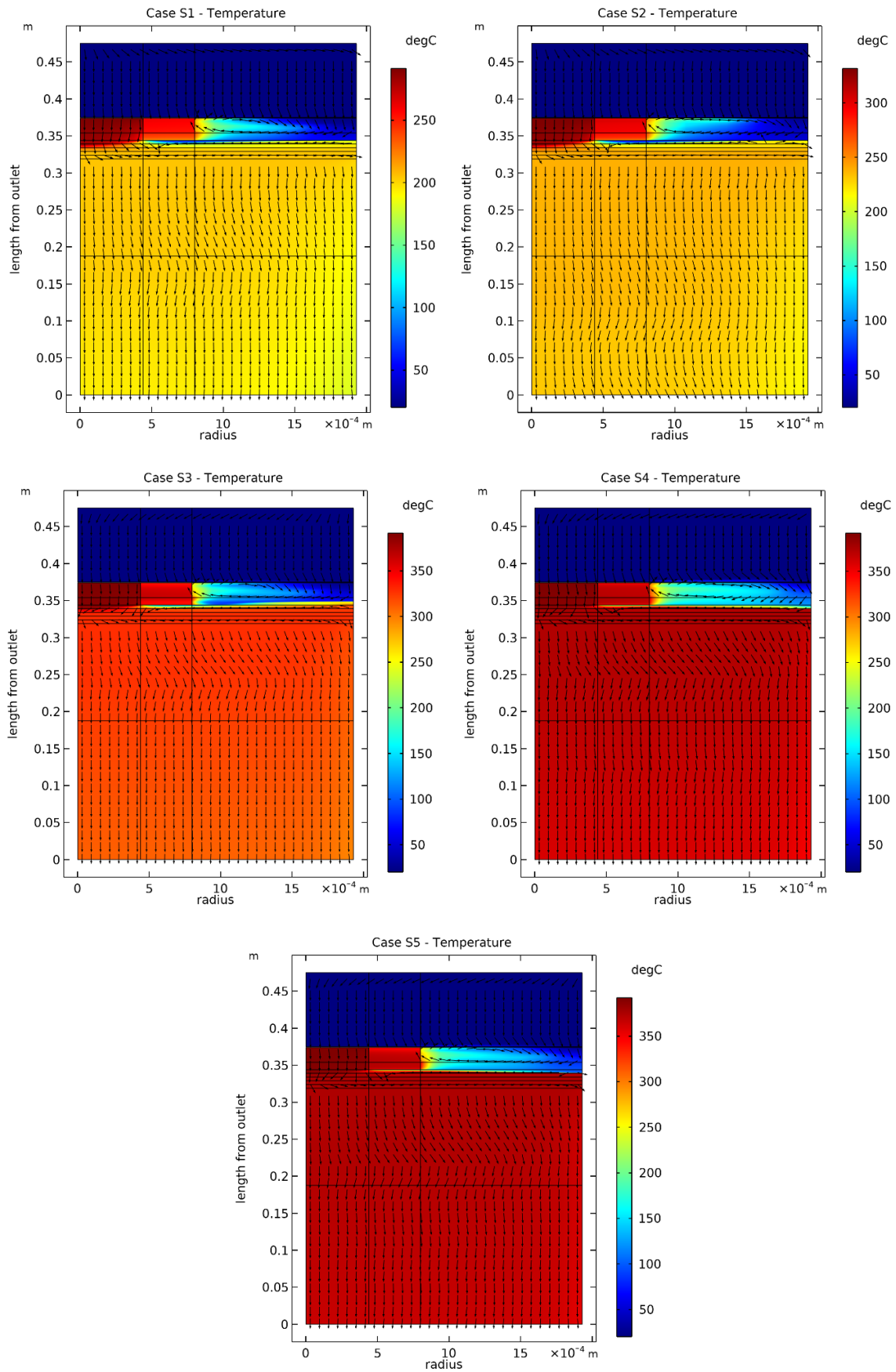


Figure D.5: Temperature profile in the complete reactor geometry for sucrose simulations (Scenarios S1 to S5). Velocity field indicated by non-scaled arrows.

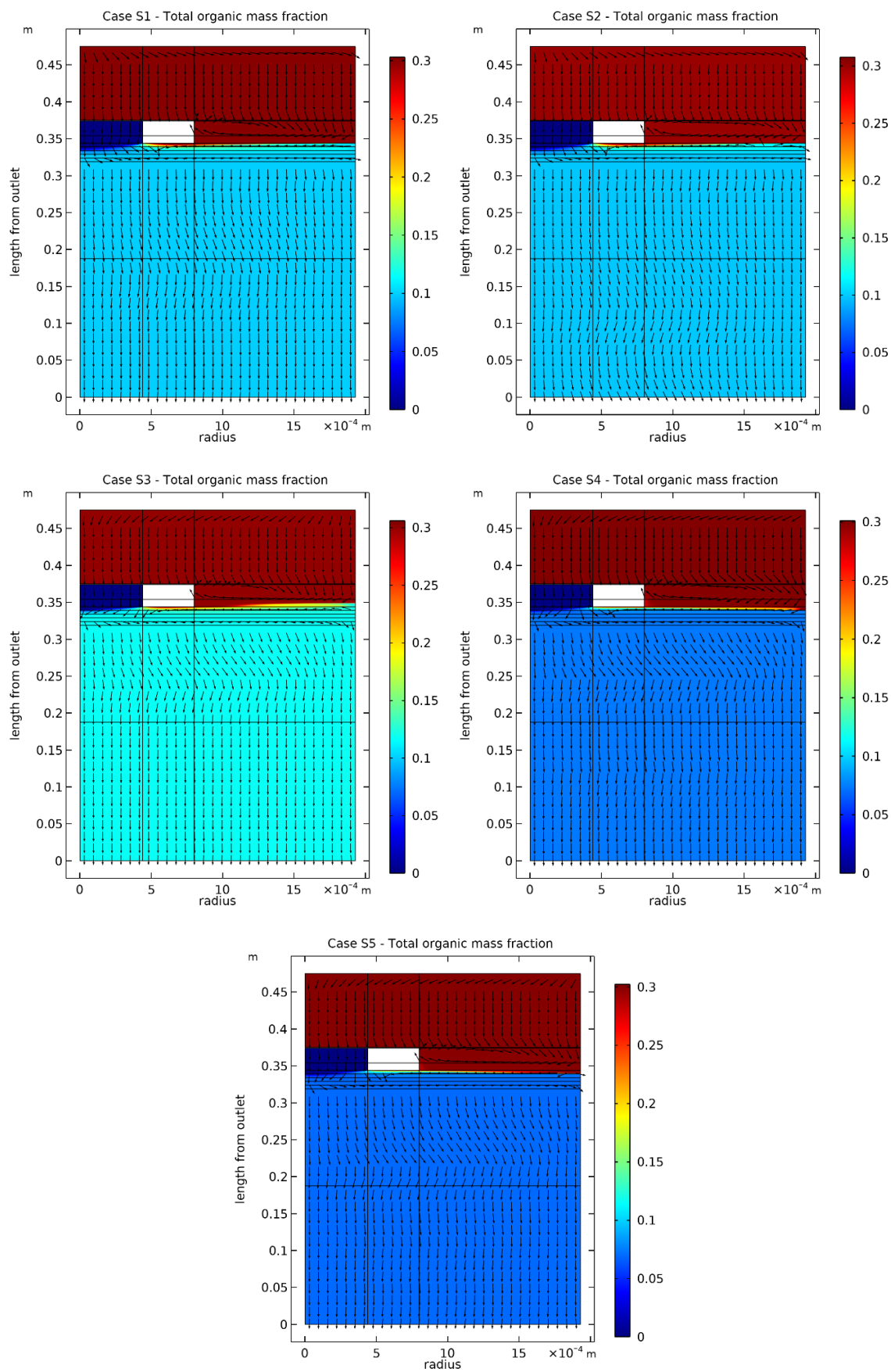


Figure D.6: Total organic mass fraction profile in the complete reactor geometry for sucrose simulations (Scenario S1 and S2). Velocity field indicated by non-scaled arrows.

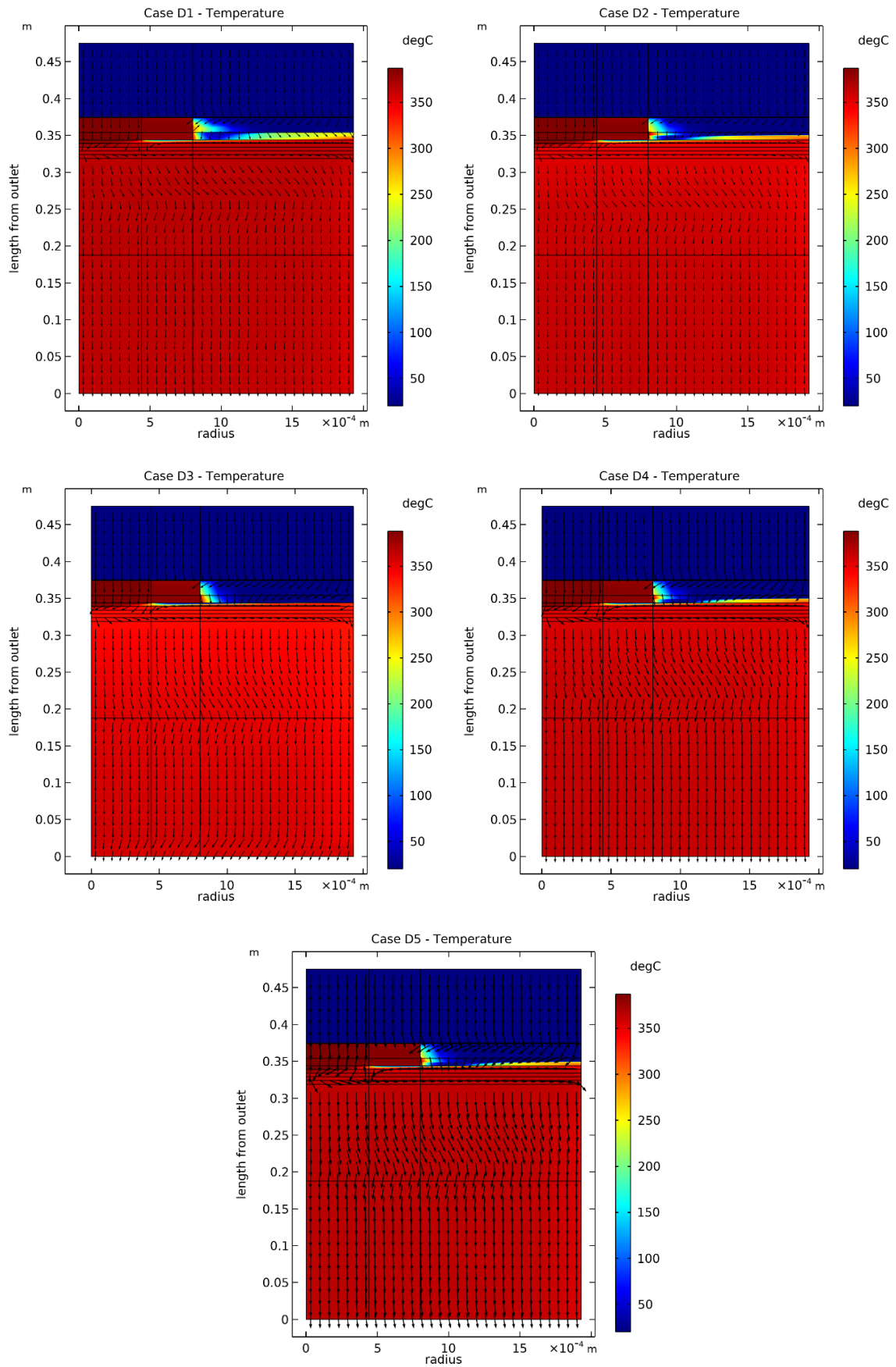


Figure D.7: Temperature profile in the complete reactor geometry for DBE simulations (Scenarios D1 to D5). Velocity field indicated by non-scaled arrows.

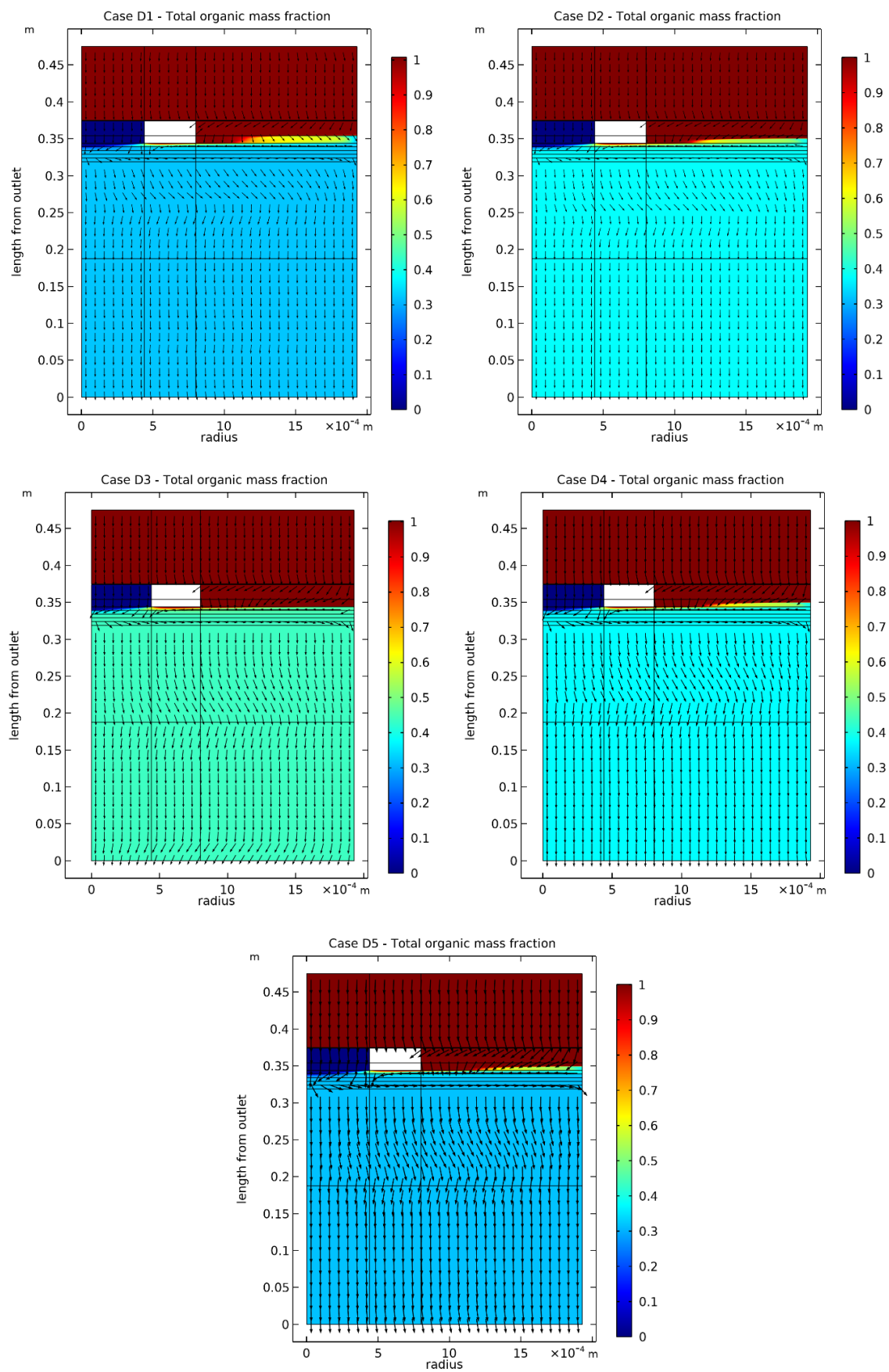


Figure D.8: Total organic mass fraction profile in the complete reactor geometry for DBE simulations (Scenarios D1 to D5). Velocity field indicated by non-scaled arrows.

Appendix E

Detailed calculations and results: Dibenzyl ether

The following section details the calculations required to calculate conversion and molar yields associated with the reactions of dibenzyl ether (DBE) in subcritical water, as described in Chapter 7. Section E.2 includes the results of these calculations for each experiment performed using DBE, while Section E.3 shows the averaged results, which are plotted in Section 7.3.

E.1 Calculation summary

Feed, total inlet and reactor mass flowrates (Q_f , Q_{in} and Q_R), and DBE mass fraction (w_{DBE}^{in}) calculated from: nominal volumetric flowrates (Qv_f^{Nom}); pump bias (β_f); and density at room temperature and operating pressure ($\rho_f^{T_{amb,p}}$).

$$Q_f = Qv_f^{NOM} \times (1 + \beta_f) \times \rho_f^{T_{amb,p}} \quad (E.1)$$

$$Q_{in} = \sum_f Q_f \quad (E.2)$$

$$Q_R = Q_{FO} + Q_{SCW} \quad (E.3)$$

$$w_{DBE}^{in} = \frac{Q_{FO}}{Q_R} \quad (E.4)$$

Liquid and gas mass flowrates at the reactor's outlet (Q_L and Q_G) calculated from: sample mass (m_s); collection time (t_c); and quench flowrate.

$$Q_L = \frac{m_s}{t_c} \quad (E.5)$$

$$Q_G = Q_{in} - Q_L \quad (E.6)$$

Mass phase fractions for each phase p in the liquid product (f_p) and in the reactor (f_p^R) calculated from each phase sample mass (m_p^s).

$$f_{aq} = \frac{m_{aq}^s}{\sum_p m_p^s} \quad (E.7)$$

$$f_{org} = 1 - f_{aq} \quad (E.8)$$

$$f_{aq}^R = \frac{m_{aq}^s - Q_{quench} \times t_c}{\sum_p m_p^s} \quad (E.9)$$

$$f_{org}^R = 1 - f_{aq}^R \quad (E.10)$$

Acetonitrile dilution factor (f_p^{ACN}) calculated from: the amount of phase sample collected for analysis before (m_p^{s2}) and after dilution in acetonitrile (m_p^{ACN}).

$$f_p^{ACN} = \frac{m_p^{s2}}{m_p^{ACN}} \quad (\text{E.11})$$

Component flowrate in each phase and overall (Q_i^p and Q_i^{out}) calculated from: each component analytical signal ($A_{i,p}$) and proportionality coefficient (mc_i).

$$w_{i,p}^{ACN} = \frac{A_{i,p}}{mc_i} \times 10^{-6} \quad (\text{E.12})$$

$$Q_{i,p} = \frac{w_{i,p}^{ACN}}{f_p^{ACN}} \times Q_L \times f_p \quad (\text{E.13})$$

$$Q_i^{out} = \sum_p Q_{i,p} \quad (\text{E.14})$$

Conversion (Cv) and molar yields (Y_i) calculated from: each components molecular weight (MW_i) and DBE's inlet flowrate.

$$Y_i = \frac{Q_i^{out}/MW_i}{Q_{in} \times w_{DBE}^{in}/MW_{DBE}} \quad (\text{E.15})$$

$$Cv = 1 - \frac{Q_{DBE}^{out}}{Q_{FO}} \quad (\text{E.16})$$

E.2 Detailed results

Table E.1: Detailed results for dibenzyl ether hydrothermal degradation.

Experiment	Sample	Sampling time (min)	t_c (sec)	m_s (g)			m_{s2} (g)		m_{ACN} (g)	
				Total	Aqueous	Organic	Aqueous	Organic	Aqueous	Organic
1	1	14	90 ± 1	135.88 ± 0.01	123.9 ± 0.1	11.4 ± 0.1	1.491 ± 0.001	0.105 ± 0.001	10.054 ± 0.001	10.301 ± 0.001
1	2	17	97 ± 1	147.27 ± 0.01	134.3 ± 0.1	12.2 ± 0.1	1.526 ± 0.001	0.104 ± 0.001	10.007 ± 0.001	10.935 ± 0.001
2	3	15	90 ± 1	136.26 ± 0.01	124.6 ± 0.1	11 ± 0.1	1.561 ± 0.001	0.101 ± 0.001	10.126 ± 0.001	10.2 ± 0.001
2	4	18	90 ± 1	136.32 ± 0.01	125.5 ± 0.1	10.3 ± 0.1	1.504 ± 0.001	0.109 ± 0.001	10.081 ± 0.001	11.042 ± 0.001
3	5	16	90 ± 1	135.86 ± 0.01	124.6 ± 0.1	10.7 ± 0.1	1.549 ± 0.001	0.12 ± 0.001	10.016 ± 0.001	13.101 ± 0.001
3	6	18	90 ± 1	137.17 ± 0.01	126 ± 0.1	10.9 ± 0.1	1.614 ± 0.001	0.102 ± 0.001	10.505 ± 0.001	10.664 ± 0.001
4	7	16	90 ± 1	135.53 ± 0.01	124.5 ± 0.1	10.3 ± 0.1	1.508 ± 0.001	0.105 ± 0.001	9.962 ± 0.001	10.478 ± 0.001
4	8	19	95 ± 1	145.41 ± 0.01	134.5 ± 0.1	10.4 ± 0.1	1.458 ± 0.001	0.122 ± 0.001	9.962 ± 0.001	13.472 ± 0.001
5	9	16	93 ± 1	141.09 ± 0.01	130 ± 0.1	10.6 ± 0.1	1.511 ± 0.001	0.121 ± 0.001	9.933 ± 0.001	8.785 ± 0.001
5	10	18	90 ± 1	135.46 ± 0.01	126.8 ± 0.1	8.3 ± 0.1	1.501 ± 0.001	0.114 ± 0.001	10.207 ± 0.001	10.779 ± 0.001
6	11	16	80 ± 1	119.63 ± 0.01	110.3 ± 0.1	8.6 ± 0.1	1.504 ± 0.001	0.113 ± 0.001	9.983 ± 0.001	11.75 ± 0.001
6	12	18	90 ± 1	136.28 ± 0.01	125.8 ± 0.1	10.2 ± 0.1	1.494 ± 0.001	0.111 ± 0.001	10.005 ± 0.001	11.566 ± 0.001
6	13	20	105 ± 1	154.2 ± 0.01	141.9 ± 0.1	12 ± 0.1	1.512 ± 0.001	0.119 ± 0.001	10.001 ± 0.001	11.856 ± 0.001
7	14	15	90 ± 1	137.06 ± 0.01	123.2 ± 0.1	13.3 ± 0.1	1.517 ± 0.001	0.103 ± 0.001	10.256 ± 0.001	10.313 ± 0.001
7	15	18	90 ± 1	137.58 ± 0.01	123.2 ± 0.1	13.9 ± 0.1	1.5 ± 0.001	0.103 ± 0.001	10.013 ± 0.001	10.254 ± 0.001
8	16	15	90 ± 1	137.92 ± 0.01	124.6 ± 0.1	12.8 ± 0.1	1.492 ± 0.001	0.116 ± 0.001	10.022 ± 0.001	11.242 ± 0.001
8	17	17	90 ± 1	137.38 ± 0.01	123 ± 0.1	13.7 ± 0.1	1.508 ± 0.001	0.124 ± 0.001	10.026 ± 0.001	12.723 ± 0.001
9	18	16	95 ± 1	144.72 ± 0.01	130.6 ± 0.1	13.7 ± 0.1	1.477 ± 0.001	0.135 ± 0.001	9.977 ± 0.001	13.079 ± 0.001
9	19	18	90 ± 1	136.51 ± 0.01	122.2 ± 0.1	13.7 ± 0.1	1.566 ± 0.001	0.129 ± 0.001	10.168 ± 0.001	12.021 ± 0.001
9	20	20	120 ± 1	182.11 ± 0.01	163.8 ± 0.1	17.7 ± 0.1	1.543 ± 0.001	0.11 ± 0.001	11 ± 0.001	11.241 ± 0.001
10	21	16	90 ± 1	138.98 ± 0.01	125 ± 0.1	13.4 ± 0.1	1.523 ± 0.001	0.103 ± 0.001	10.145 ± 0.001	10.038 ± 0.001
10	22	18	90 ± 1	138.24 ± 0.01	124.1 ± 0.1	13.7 ± 0.1	1.578 ± 0.001	0.105 ± 0.001	10.478 ± 0.001	10.118 ± 0.001
11	23	16	90 ± 1	142.97 ± 0.01	125.8 ± 0.1	16.8 ± 0.1	1.514 ± 0.001	0.103 ± 0.001	9.967 ± 0.001	10.18 ± 0.001
11	24	18	90 ± 1	142.54 ± 0.01	126.1 ± 0.1	15.9 ± 0.1	1.513 ± 0.001	0.102 ± 0.001	10.212 ± 0.001	9.98 ± 0.001
12	25	15	90 ± 1	141.74 ± 0.01	124 ± 0.1	17.2 ± 0.1	1.502 ± 0.001	0.115 ± 0.001	10.098 ± 0.001	11.016 ± 0.001
12	26	17	90 ± 1	142.02 ± 0.01	123 ± 0.1	18.5 ± 0.1	1.545 ± 0.001	0.102 ± 0.001	10.149 ± 0.001	10.027 ± 0.001
13	27	16	90 ± 1	142.08 ± 0.01	127.1 ± 0.1	14.3 ± 0.1	1.501 ± 0.001	0.112 ± 0.001	10.048 ± 0.001	11.077 ± 0.001
13	28	19	90 ± 1	142.49 ± 0.01	124.8 ± 0.1	16.7 ± 0.1	1.519 ± 0.001	0.102 ± 0.001	10.121 ± 0.001	10.14 ± 0.001
14	29	13	90 ± 1	142.46 ± 0.01	124.5 ± 0.1	17.2 ± 0.1	1.542 ± 0.001	0.106 ± 0.001	10.181 ± 0.001	10.379 ± 0.001
14	30	15	100 ± 1	157.2 ± 0.01	137.8 ± 0.1	18.6 ± 0.1	1.535 ± 0.001	0.131 ± 0.001	10.165 ± 0.001	13.478 ± 0.001
14	31	17	90 ± 1	141.98 ± 0.01	123.2 ± 0.1	17.8 ± 0.1	1.512 ± 0.001	0.108 ± 0.001	10.3 ± 0.001	10.007 ± 0.001
15	32	16	90 ± 1	141.69 ± 0.01	124.1 ± 0.1	17.2 ± 0.1	1.503 ± 0.001	0.106 ± 0.001	10.181 ± 0.001	10.126 ± 0.001
15	33	18	90 ± 1	141.85 ± 0.01	124.4 ± 0.1	17.3 ± 0.1	1.537 ± 0.001	0.098 ± 0.001	10.042 ± 0.001	10.255 ± 0.001

Continuation of Table C.5.												
Experiment	Sample	A_{aq}				A_{org}				Q_v^{NOM} (mL/min)		
		BAL	BZA	TOL	DBE	BAL	BZA	TOL	DBE	SCW	FO	Quench
1	1	2932372	204853	0	6939	1484223	1116681	29768	14720904	16 ± 0.5	8 ± 0.2	60 ± 2
1	2	2995872	186184	0	186184	1372364	1029024	28450	13575835	16 ± 0.5	8 ± 0.2	60 ± 2
2	3	4831022	200478	0	24073	3829258	1223434	36028	10212998	16 ± 0.5	8 ± 0.2	60 ± 2
2	4	4880142	223094	0	17029	4058747	1304494	38725	10630070	16 ± 0.5	8 ± 0.2	60 ± 2
3	5	5845643	287460	0	12113	4817441	1371142	56102	7925852	16 ± 0.5	8 ± 0.2	60 ± 2
3	6	5798019	281140	0	11482	5244329	1501439	42917	8476498	16 ± 0.5	8 ± 0.2	60 ± 2
4	7	5578330	1946134	0	46803	5253609	9364465	180280	9339461	16 ± 0.5	8 ± 0.2	60 ± 2
4	8	5390880	5390880	0	13897	4745839	8703382	139665	8403406	16 ± 0.5	8 ± 0.2	60 ± 2
5	9	5170711	1718855	1340	7919	6191400	6191400	218192	13507224	16 ± 0.5	8 ± 0.2	60 ± 2
5	10	5059924	1630020	1174	23816	4966339	9669760	164552	10344802	16 ± 0.5	8 ± 0.2	60 ± 2
6	11	4598754	1064764	0	0	3591632	6218869	134667	10669255	16 ± 0.5	8 ± 0.2	60 ± 2
6	12	4628491	1117780	0	0	3542137	6180634	130747	10410524	16 ± 0.5	8 ± 0.2	60 ± 2
6	13	4676791	1122097	0	0	3563959	6172711	130740	10384680	16 ± 0.5	8 ± 0.2	60 ± 2
7	14	4140058	179025	0	7224	3060531	1309135	36733	12362474	15 ± 0.5	10 ± 0.3	60 ± 2
7	15	4361946	206920	0	0	3092096	1336090	37372	12334227	15 ± 0.5	10 ± 0.3	60 ± 2
8	16	4721937	198127	0	4214	4928531	1676316	46848	11582960	15 ± 0.5	10 ± 0.3	60 ± 2
8	17	4985494	226867	0	7989	4391800	1501999	42519	10082429	15 ± 0.5	10 ± 0.3	60 ± 2
9	18	4763743	1206726	0	29367	4243835	7398779	159049	10036652	15 ± 0.5	10 ± 0.3	60 ± 2
9	19	5055509	1283381	0	10071	4540693	7919390	167362	10590636	15 ± 0.5	10 ± 0.3	60 ± 2
9	20	4496291	1130916	0	14911	4048731	7143629	134709	9410999	15 ± 0.5	10 ± 0.3	60 ± 2
10	21	3986151	285812	0	0	2886847	1926670	58295	13022413	15 ± 0.5	10 ± 0.3	60 ± 2
10	22	3968899	270520	0	7098	2906633	1945640	58330	13111412	15 ± 0.5	10 ± 0.3	60 ± 2
11	23	4765327	1710009	2812	40264	3735152	9090326	154157	9090326	16 ± 0.5	12.5 ± 0.4	60 ± 2
11	24	4689399	1713755	2016	2016	3828130	9312539	155342	11021652	16 ± 0.5	12.5 ± 0.4	60 ± 2
12	25	1956982	157409	0	11818	831593	1209371	32267	15643611	15 ± 0.5	12.5 ± 0.4	60 ± 2
12	26	2001893	191012	0	10510	817311	1205588	31317	15447464	15 ± 0.5	12.5 ± 0.4	60 ± 2
13	27	3943855	198960	0	0	2888940	1500531	40056	12771857	15 ± 0.5	12.5 ± 0.4	60 ± 2
13	28	4085865	208844	0	10627	2861763	1477142	40865	12471377	15 ± 0.5	12.5 ± 0.4	60 ± 2
14	29	4872054	915171	0	0	3904244	5327009	123635	11308016	15 ± 0.5	12.5 ± 0.4	60 ± 2
14	30	4815848	903329	0	15495	3638419	5022247	106812	10510910	15 ± 0.5	12.5 ± 0.4	60 ± 2
14	31	4686406	866289	0	0	3967513	5408576	114518	11459835	15 ± 0.5	12.5 ± 0.4	60 ± 2
15	32	4236138	263630	0	0	3343860	3343860	56345	12743712	15 ± 0.5	12.5 ± 0.4	60 ± 2
15	33	4391318	281935	0	0	3076249	1799304	51697	11723623	15 ± 0.5	12.5 ± 0.4	60 ± 2

Continuation of Table C.5.													
Experiment	Sample	Q^{in} (g/min)					w_{DBE}^0 (%)	Q^{out} (g/min)		f (%)		f_R (%)	
		SCW	FO	Quench	In	R		L	G	Aq	Org	Aq	Org
1	1	17.4 ± 0.5	8.5 ± 0.3	65 ± 2	91 ± 2	25.9 ± 0.6	31 ± 1	91 ± 1	0 ± 2	91.6 ± 0.1	8.4 ± 0.1	70.1 ± 0.2	29.9 ± 0.2
1	2	17.4 ± 0.5	8.5 ± 0.3	65 ± 2	91 ± 2	25.9 ± 0.6	31 ± 1	91.1 ± 0.9	0 ± 2	91.6 ± 0.1	8.4 ± 0.1	70.8 ± 0.2	29.2 ± 0.2
2	3	17.4 ± 0.5	8.5 ± 0.3	65 ± 2	91 ± 2	25.9 ± 0.6	31 ± 1	91 ± 1	0 ± 2	91.9 ± 0.1	8.1 ± 0.1	71.6 ± 0.2	28.4 ± 0.2
2	4	17.4 ± 0.5	8.5 ± 0.3	65 ± 2	91 ± 2	25.9 ± 0.6	31 ± 1	91 ± 1	0 ± 2	92.4 ± 0.1	7.6 ± 0.1	73.3 ± 0.2	26.7 ± 0.2
3	5	17.4 ± 0.5	8.5 ± 0.3	65 ± 2	91 ± 2	25.9 ± 0.6	31 ± 1	91 ± 1	0 ± 2	92.1 ± 0.1	7.9 ± 0.1	72 ± 0.2	28 ± 0.2
3	6	17.4 ± 0.5	8.5 ± 0.3	65 ± 2	91 ± 2	25.9 ± 0.6	31 ± 1	91 ± 1	0 ± 2	92 ± 0.1	8 ± 0.1	72.4 ± 0.2	27.6 ± 0.2
4	7	17.4 ± 0.5	8.5 ± 0.3	65 ± 2	91 ± 2	25.9 ± 0.6	31 ± 1	90 ± 1	1 ± 2	92.4 ± 0.1	7.6 ± 0.1	72.9 ± 0.2	27.1 ± 0.2
4	8	17.4 ± 0.5	8.5 ± 0.3	65 ± 2	91 ± 2	25.9 ± 0.6	31 ± 1	91.8 ± 1	-1 ± 2	92.8 ± 0.1	7.2 ± 0.1	75.4 ± 0.1	24.6 ± 0.1
5	9	17.4 ± 0.5	8.5 ± 0.3	65 ± 2	91 ± 2	25.9 ± 0.6	31 ± 1	91 ± 1	0 ± 2	92.4 ± 0.1	7.6 ± 0.1	73.5 ± 0.2	26.5 ± 0.2
5	10	17.4 ± 0.5	8.5 ± 0.3	65 ± 2	91 ± 2	25.9 ± 0.6	31 ± 1	90 ± 1	1 ± 2	93.9 ± 0.1	6.1 ± 0.1	78.1 ± 0.2	21.9 ± 0.2
6	11	17.4 ± 0.5	8.5 ± 0.3	65 ± 2	91 ± 2	25.9 ± 0.6	31 ± 1	90 ± 1	1 ± 2	92.7 ± 0.1	7.3 ± 0.1	73.7 ± 0.2	26.3 ± 0.2
6	12	17.4 ± 0.5	8.5 ± 0.3	65 ± 2	91 ± 2	25.9 ± 0.6	31 ± 1	91 ± 1	0 ± 2	92.5 ± 0.1	7.5 ± 0.1	73.6 ± 0.2	26.4 ± 0.2
6	13	17.4 ± 0.5	8.5 ± 0.3	65 ± 2	91 ± 2	25.9 ± 0.6	31 ± 1	88.1 ± 0.8	3 ± 2	92.2 ± 0.1	7.8 ± 0.1	70.1 ± 0.2	29.9 ± 0.2
7	14	16.3 ± 0.5	10.7 ± 0.3	65 ± 2	92 ± 2	27 ± 0.6	37 ± 1	91 ± 1	1 ± 2	90.2 ± 0.1	9.8 ± 0.1	66.2 ± 0.2	33.8 ± 0.2
7	15	16.3 ± 0.5	10.7 ± 0.3	65 ± 2	92 ± 2	27 ± 0.6	37 ± 1	92 ± 1	0 ± 2	89.8 ± 0.1	10.2 ± 0.1	65 ± 0.2	35 ± 0.2
8	16	16.3 ± 0.5	10.7 ± 0.3	65 ± 2	92 ± 2	27 ± 0.6	37 ± 1	92 ± 1	0 ± 2	90.7 ± 0.1	9.3 ± 0.1	68.1 ± 0.2	31.9 ± 0.2
8	17	16.3 ± 0.5	10.7 ± 0.3	65 ± 2	92 ± 2	27 ± 0.6	37 ± 1	92 ± 1	1 ± 2	90 ± 0.1	10 ± 0.1	65.4 ± 0.2	34.6 ± 0.2
9	18	16.3 ± 0.5	10.7 ± 0.3	65 ± 2	92 ± 2	27 ± 0.6	37 ± 1	91.4 ± 1	1 ± 2	90.5 ± 0.1	9.5 ± 0.1	67 ± 0.2	33 ± 0.2
9	19	16.3 ± 0.5	10.7 ± 0.3	65 ± 2	92 ± 2	27 ± 0.6	37 ± 1	91 ± 1	1 ± 2	89.9 ± 0.1	10.1 ± 0.1	64.6 ± 0.2	35.4 ± 0.2
9	20	16.3 ± 0.5	10.7 ± 0.3	65 ± 2	92 ± 2	27 ± 0.6	37 ± 1	91.1 ± 0.8	1 ± 2	90.24 ± 0.09	9.76 ± 0.09	65.8 ± 0.2	34.2 ± 0.2
10	21	16.3 ± 0.5	10.7 ± 0.3	65 ± 2	92 ± 2	27 ± 0.6	37 ± 1	93 ± 1	-1 ± 2	90.3 ± 0.1	9.7 ± 0.1	67.6 ± 0.2	32.4 ± 0.2
10	22	16.3 ± 0.5	10.7 ± 0.3	65 ± 2	92 ± 2	27 ± 0.6	37 ± 1	92 ± 1	0 ± 2	90.1 ± 0.1	9.9 ± 0.1	66.3 ± 0.2	33.7 ± 0.2
11	23	17.4 ± 0.5	13.4 ± 0.4	65 ± 2	96 ± 2	30.7 ± 0.7	41 ± 2	95 ± 1	1 ± 2	88.2 ± 0.1	11.8 ± 0.1	63 ± 0.2	37 ± 0.2
11	24	17.4 ± 0.5	13.4 ± 0.4	65 ± 2	96 ± 2	30.7 ± 0.7	41 ± 2	95 ± 1	1 ± 2	88.8 ± 0.1	11.2 ± 0.1	64.5 ± 0.2	35.5 ± 0.2
12	25	16.3 ± 0.5	13.4 ± 0.4	65 ± 2	95 ± 2	29.7 ± 0.6	42 ± 2	94 ± 1	0 ± 2	87.8 ± 0.1	12.2 ± 0.1	60.9 ± 0.2	39.1 ± 0.2
12	26	16.3 ± 0.5	13.4 ± 0.4	65 ± 2	95 ± 2	29.7 ± 0.6	42 ± 2	95 ± 1	0 ± 2	86.9 ± 0.1	13.1 ± 0.1	58.3 ± 0.2	41.7 ± 0.2
13	27	16.3 ± 0.5	13.4 ± 0.4	65 ± 2	95 ± 2	29.7 ± 0.6	42 ± 2	95 ± 1	0 ± 2	89.9 ± 0.1	10.1 ± 0.1	67.7 ± 0.2	32.3 ± 0.2
13	28	16.3 ± 0.5	13.4 ± 0.4	65 ± 2	95 ± 2	29.7 ± 0.6	42 ± 2	95 ± 1	0 ± 2	88.2 ± 0.1	11.8 ± 0.1	62.6 ± 0.2	37.4 ± 0.2
14	29	16.3 ± 0.5	13.4 ± 0.4	65 ± 2	95 ± 2	29.7 ± 0.6	42 ± 2	95 ± 1	0 ± 2	87.9 ± 0.1	12.1 ± 0.1	61.6 ± 0.2	38.4 ± 0.2
14	30	16.3 ± 0.5	13.4 ± 0.4	65 ± 2	95 ± 2	29.7 ± 0.6	42 ± 2	94.3 ± 0.9	0 ± 2	88.1 ± 0.1	11.9 ± 0.1	61.7 ± 0.2	38.3 ± 0.2
14	31	16.3 ± 0.5	13.4 ± 0.4	65 ± 2	95 ± 2	29.7 ± 0.6	42 ± 2	95 ± 1	0 ± 2	87.4 ± 0.1	12.6 ± 0.1	59.7 ± 0.2	40.3 ± 0.2
15	32	16.3 ± 0.5	13.4 ± 0.4	65 ± 2	95 ± 2	29.7 ± 0.6	42 ± 2	94 ± 1	0 ± 2	87.8 ± 0.1	12.2 ± 0.1	60.8 ± 0.2	39.2 ± 0.2
15	33	16.3 ± 0.5	13.4 ± 0.4	65 ± 2	95 ± 2	29.7 ± 0.6	42 ± 2	95 ± 1	0 ± 2	87.8 ± 0.1	12.2 ± 0.1	60.9 ± 0.2	39.1 ± 0.2

Continuation of Table C.5.											
Experiment	Sample	f_{ACN} (%)		w^{ACN}_{aq} (ppm)				w^{ACN}_{org} (ppm)			
		Aq	Org	BAL	BZA	Tol	DBE	BAL	BZA	TOL	DBE
1	1	14.83 ± 0.01	1.021 ± 0.01	2130 ± 80	3.5 ± 0.4	0 ± 3	4 ± 1	1020 ± 10	18.8 ± 0.4	13 ± 3	9100 ± 200
1	2	15.25 ± 0.01	0.95 ± 0.009	2180 ± 80	3.1 ± 0.4	0 ± 3	98 ± 2	940 ± 10	17.4 ± 0.4	13 ± 3	8400 ± 200
2	3	15.413 ± 0.01	0.99 ± 0.01	3510 ± 90	3.4 ± 0.4	0 ± 3	13 ± 1	2780 ± 80	20.6 ± 0.4	16 ± 3	6300 ± 200
2	4	14.92 ± 0.01	0.986 ± 0.009	3540 ± 90	3.8 ± 0.4	0 ± 3	9 ± 1	2950 ± 90	22 ± 0.4	17 ± 3	6600 ± 200
3	5	15.47 ± 0.01	0.918 ± 0.008	4250 ± 90	4.8 ± 0.4	0 ± 3	6 ± 1	3500 ± 90	23.1 ± 0.4	25 ± 3	4900 ± 200
3	6	15.368 ± 0.01	0.953 ± 0.009	4210 ± 90	4.7 ± 0.4	0 ± 3	6 ± 1	3810 ± 90	25.3 ± 0.4	19 ± 3	5300 ± 200
4	7	15.14 ± 0.01	1.001 ± 0.01	4050 ± 90	32.8 ± 0.5	0 ± 3	25 ± 1	3820 ± 90	162 ± 2	80 ± 3	5800 ± 200
4	8	14.64 ± 0.01	0.902 ± 0.007	3920 ± 90	93 ± 2	0 ± 3	7 ± 1	3450 ± 90	151 ± 2	62 ± 3	5200 ± 200
5	9	15.22 ± 0.01	1.38 ± 0.01	3760 ± 90	29 ± 0.5	1 ± 3	4 ± 1	4500 ± 90	107 ± 2	96 ± 3	8400 ± 200
5	10	14.704 ± 0.01	1.054 ± 0.009	3680 ± 90	27.5 ± 0.4	1 ± 3	13 ± 1	3610 ± 90	167 ± 2	73 ± 3	6400 ± 200
6	11	15.06 ± 0.01	0.965 ± 0.009	3340 ± 90	18 ± 0.4	0 ± 3	0 ± 1	2610 ± 80	108 ± 2	59 ± 3	6600 ± 200
6	12	14.93 ± 0.01	0.961 ± 0.009	3360 ± 90	18.9 ± 0.4	0 ± 3	0 ± 1	2570 ± 80	107 ± 2	58 ± 3	6500 ± 200
6	13	15.12 ± 0.01	1.004 ± 0.008	3400 ± 90	18.9 ± 0.4	0 ± 3	0 ± 1	2590 ± 80	107 ± 2	58 ± 3	6500 ± 200
7	14	14.789 ± 0.01	1.002 ± 0.01	3010 ± 90	3 ± 0.4	0 ± 3	4 ± 1	2220 ± 80	22.1 ± 0.4	16 ± 3	7700 ± 200
7	15	14.98 ± 0.01	1.003 ± 0.01	3170 ± 90	3.5 ± 0.4	0 ± 3	0 ± 1	2250 ± 80	22.5 ± 0.4	16 ± 3	7700 ± 200
8	16	14.89 ± 0.01	1.028 ± 0.009	3430 ± 90	3.3 ± 0.4	0 ± 3	2 ± 1	3580 ± 90	28.3 ± 0.4	21 ± 3	7200 ± 200
8	17	15.04 ± 0.01	0.975 ± 0.008	3620 ± 90	3.8 ± 0.4	0 ± 3	4 ± 1	3190 ± 90	25.3 ± 0.4	19 ± 3	6300 ± 200
9	18	14.8 ± 0.01	1.032 ± 0.008	3460 ± 90	20.4 ± 0.4	0 ± 3	15 ± 1	3080 ± 90	128 ± 2	70 ± 3	6200 ± 200
9	19	15.404 ± 0.01	1.074 ± 0.008	3670 ± 90	21.6 ± 0.4	0 ± 3	5 ± 1	3300 ± 90	137 ± 2	74 ± 3	6600 ± 200
9	20	14.031 ± 0.009	0.981 ± 0.009	3270 ± 90	19.1 ± 0.4	0 ± 3	8 ± 1	2940 ± 90	124 ± 2	59 ± 3	5800 ± 200
10	21	15.017 ± 0.01	1.03 ± 0.01	2900 ± 90	4.8 ± 0.4	0 ± 3	0 ± 1	1980 ± 10	32.5 ± 0.5	26 ± 3	8100 ± 200
10	22	15.063 ± 0.01	1.036 ± 0.01	2880 ± 90	4.6 ± 0.4	0 ± 3	4 ± 1	2000 ± 10	32.8 ± 0.5	26 ± 3	8100 ± 200
11	23	15.19 ± 0.01	1.009 ± 0.01	3460 ± 90	28.8 ± 0.5	1 ± 3	21 ± 1	2710 ± 80	157 ± 2	68 ± 3	5600 ± 200
11	24	14.811 ± 0.01	1.02 ± 0.01	3410 ± 90	28.9 ± 0.5	1 ± 3	1 ± 1	2780 ± 80	161 ± 2	69 ± 3	6800 ± 200
12	25	14.87 ± 0.01	1.039 ± 0.009	1340 ± 10	2.7 ± 0.4	0 ± 3	6 ± 1	571 ± 10	20.4 ± 0.4	14 ± 3	9700 ± 200
12	26	15.221 ± 0.01	1.02 ± 0.01	1380 ± 10	3.2 ± 0.4	0 ± 3	6 ± 1	562 ± 10	20.3 ± 0.4	14 ± 3	9600 ± 200
13	27	14.94 ± 0.01	1.012 ± 0.009	2860 ± 90	3.4 ± 0.4	0 ± 3	0 ± 1	1980 ± 10	25.3 ± 0.4	18 ± 3	7900 ± 200
13	28	15.007 ± 0.01	1.007 ± 0.01	2970 ± 90	3.5 ± 0.4	0 ± 3	6 ± 1	1970 ± 10	24.9 ± 0.4	18 ± 3	7700 ± 200
14	29	15.145 ± 0.01	1.019 ± 0.01	3540 ± 90	15.4 ± 0.4	0 ± 3	0 ± 1	2840 ± 80	92 ± 2	55 ± 3	7000 ± 200
14	30	15.102 ± 0.01	0.971 ± 0.007	3500 ± 90	15.2 ± 0.4	0 ± 3	8 ± 1	2640 ± 80	87 ± 2	47 ± 3	6500 ± 200
14	31	14.681 ± 0.01	1.082 ± 0.01	3400 ± 90	14.6 ± 0.4	0 ± 3	0 ± 1	2880 ± 90	94 ± 2	51 ± 3	7100 ± 200
15	32	14.759 ± 0.01	1.049 ± 0.01	3080 ± 90	4.4 ± 0.4	0 ± 3	0 ± 1	2430 ± 80	58 ± 2	25 ± 3	7900 ± 200
15	33	15.31 ± 0.01	0.955 ± 0.01	3190 ± 90	4.8 ± 0.4	0 ± 3	0 ± 1	2230 ± 80	30.4 ± 0.5	23 ± 3	7300 ± 200

Continuation of Table C.5.									
Experiment	Sample	Q_{aq} (g/min)				Q_{org} (g/min)			
		BAL	BZA	TOL	DBE	BAL	BZA	TOL	DBE
1	1	1.19 ± 0.05	0.0019 ± 0.0002	-	0.002 ± 0.0008	0.76 ± 0.02	0.0141 ± 0.0004	0.01 ± 0.003	6.8 ± 0.2
1	2	1.19 ± 0.05	0.0017 ± 0.0002	-	0.054 ± 0.001	0.76 ± 0.02	0.0139 ± 0.0004	0.01 ± 0.003	6.8 ± 0.2
2	3	1.9 ± 0.05	0.0018 ± 0.0002	-	0.0068 ± 0.0008	2.06 ± 0.08	0.0153 ± 0.0005	0.012 ± 0.003	4.7 ± 0.2
2	4	1.99 ± 0.05	0.0021 ± 0.0002	-	0.005 ± 0.0008	2.06 ± 0.07	0.0154 ± 0.0004	0.012 ± 0.002	4.6 ± 0.1
3	5	2.29 ± 0.05	0.0026 ± 0.0002	-	0.0034 ± 0.0008	2.73 ± 0.09	0.018 ± 0.0005	0.019 ± 0.003	3.8 ± 0.1
3	6	2.31 ± 0.06	0.0026 ± 0.0002	-	0.0033 ± 0.0008	2.91 ± 0.09	0.0194 ± 0.0005	0.014 ± 0.003	4 ± 0.1
4	7	2.23 ± 0.06	0.0181 ± 0.0003	-	0.0136 ± 0.0008	2.62 ± 0.08	0.111 ± 0.003	0.055 ± 0.003	4 ± 0.1
4	8	2.28 ± 0.06	0.054 ± 0.001	-	0.0043 ± 0.0009	2.52 ± 0.08	0.11 ± 0.003	0.045 ± 0.003	3.8 ± 0.1
5	9	2.08 ± 0.05	0.016 ± 0.0003	0 ± 0.002	0.0023 ± 0.0008	2.24 ± 0.06	0.053 ± 0.002	0.048 ± 0.002	4.2 ± 0.1
5	10	2.12 ± 0.06	0.0159 ± 0.0003	0 ± 0.002	0.0072 ± 0.0009	1.89 ± 0.07	0.088 ± 0.002	0.038 ± 0.002	3.4 ± 0.1
6	11	1.85 ± 0.05	0.0099 ± 0.0003	-	-	1.76 ± 0.07	0.073 ± 0.002	0.04 ± 0.003	4.5 ± 0.2
6	12	1.89 ± 0.05	0.0106 ± 0.0003	-	-	1.82 ± 0.07	0.076 ± 0.002	0.041 ± 0.003	4.6 ± 0.1
6	13	1.83 ± 0.05	0.0102 ± 0.0002	-	-	1.78 ± 0.07	0.073 ± 0.002	0.04 ± 0.002	4.4 ± 0.1
7	14	1.68 ± 0.05	0.0017 ± 0.0002	-	0.0021 ± 0.0008	1.98 ± 0.08	0.0197 ± 0.0005	0.014 ± 0.003	6.8 ± 0.2
7	15	1.74 ± 0.05	0.0019 ± 0.0002	-	-	2.09 ± 0.09	0.0209 ± 0.0006	0.015 ± 0.003	7.1 ± 0.2
8	16	1.92 ± 0.05	0.0019 ± 0.0002	-	0.0012 ± 0.0008	2.99 ± 0.09	0.0236 ± 0.0006	0.017 ± 0.003	6 ± 0.2
8	17	1.98 ± 0.05	0.0021 ± 0.0002	-	0.0023 ± 0.0008	3.01 ± 0.1	0.0239 ± 0.0006	0.018 ± 0.003	5.9 ± 0.2
9	18	1.93 ± 0.05	0.0114 ± 0.0003	-	0.0086 ± 0.0008	2.6 ± 0.09	0.108 ± 0.003	0.059 ± 0.003	5.3 ± 0.2
9	19	1.95 ± 0.05	0.0115 ± 0.0003	-	0.0028 ± 0.0008	2.82 ± 0.09	0.117 ± 0.003	0.063 ± 0.003	5.6 ± 0.2
9	20	1.91 ± 0.05	0.0112 ± 0.0003	-	0.0046 ± 0.0009	2.66 ± 0.09	0.112 ± 0.003	0.054 ± 0.003	5.3 ± 0.2
10	21	1.61 ± 0.05	0.0027 ± 0.0002	-	-	1.72 ± 0.04	0.0282 ± 0.0007	0.022 ± 0.003	7 ± 0.2
10	22	1.59 ± 0.05	0.0025 ± 0.0002	-	0.0021 ± 0.0008	1.76 ± 0.04	0.029 ± 0.0007	0.023 ± 0.003	7.2 ± 0.2
11	23	1.92 ± 0.05	0.016 ± 0.0003	0.001 ± 0.002	0.0117 ± 0.0008	3 ± 0.1	0.175 ± 0.004	0.076 ± 0.004	6.3 ± 0.2
11	24	1.94 ± 0.05	0.0165 ± 0.0003	0.001 ± 0.002	0.0006 ± 0.0008	2.9 ± 0.1	0.168 ± 0.004	0.072 ± 0.004	7.2 ± 0.2
12	25	0.75 ± 0.01	0.0015 ± 0.0002	-	0.0035 ± 0.0008	0.63 ± 0.02	0.0226 ± 0.0006	0.016 ± 0.004	10.8 ± 0.3
12	26	0.74 ± 0.01	0.0017 ± 0.0002	-	0.003 ± 0.0008	0.68 ± 0.02	0.0247 ± 0.0007	0.017 ± 0.004	11.6 ± 0.3
13	27	1.63 ± 0.05	0.0019 ± 0.0002	-	-	1.88 ± 0.04	0.024 ± 0.0006	0.017 ± 0.003	7.5 ± 0.2
13	28	1.66 ± 0.05	0.002 ± 0.0002	-	0.0031 ± 0.0008	2.2 ± 0.04	0.0278 ± 0.0007	0.02 ± 0.004	8.7 ± 0.2
14	29	1.95 ± 0.05	0.0085 ± 0.0002	-	-	3.2 ± 0.1	0.104 ± 0.003	0.062 ± 0.004	7.9 ± 0.2
14	30	1.92 ± 0.05	0.0084 ± 0.0002	-	0.0045 ± 0.0008	3.1 ± 0.1	0.1 ± 0.003	0.055 ± 0.004	7.5 ± 0.2
14	31	1.92 ± 0.05	0.0082 ± 0.0002	-	-	3.2 ± 0.1	0.104 ± 0.003	0.056 ± 0.004	7.9 ± 0.2
15	32	1.73 ± 0.05	0.0025 ± 0.0002	-	-	2.7 ± 0.1	0.063 ± 0.003	0.027 ± 0.004	8.7 ± 0.2
15	33	1.73 ± 0.05	0.0026 ± 0.0002	-	-	2.7 ± 0.1	0.0366 ± 0.0009	0.028 ± 0.004	8.8 ± 0.2

Continuation of Table C.5.											
Experiment	Sample	Q^{out} (g/min)				Yield (mol/mol _{DBE} %)					Conversion (%)
		BAL	BZA	TOL	DBE	BAL	BZA	TOL	DBE	Others	
1	1	1.95 ± 0.05	0.016 ± 0.0005	0.01 ± 0.003	6.9 ± 0.2	42 ± 2	0.35 ± 0.01	0.25 ± 0.07	80 ± 3	-3 ± 7	20 ± 3
1	2	1.95 ± 0.05	0.0156 ± 0.0005	0.01 ± 0.003	6.8 ± 0.2	42 ± 2	0.34 ± 0.01	0.25 ± 0.07	80 ± 3	-2 ± 7	20 ± 3
2	3	3.96 ± 0.09	0.0171 ± 0.0005	0.012 ± 0.003	4.7 ± 0.2	85 ± 3	0.37 ± 0.02	0.3 ± 0.07	55 ± 2	4 ± 6	45 ± 2
2	4	4.06 ± 0.09	0.0175 ± 0.0005	0.012 ± 0.002	4.6 ± 0.1	87 ± 3	0.38 ± 0.02	0.3 ± 0.06	54 ± 2	4 ± 6	46 ± 2
3	5	5 ± 0.1	0.0207 ± 0.0005	0.019 ± 0.003	3.8 ± 0.1	108 ± 4	0.45 ± 0.02	0.49 ± 0.07	45 ± 2	1 ± 6	55 ± 2
3	6	5.2 ± 0.1	0.022 ± 0.0006	0.014 ± 0.003	4 ± 0.1	112 ± 4	0.48 ± 0.02	0.36 ± 0.07	47 ± 2	-7 ± 6	53 ± 2
4	7	4.85 ± 0.1	0.129 ± 0.003	0.055 ± 0.003	4 ± 0.1	83 ± 3	2.26 ± 0.09	1.1 ± 0.06	47 ± 2	20 ± 5	53 ± 2
4	8	4.8 ± 0.1	0.164 ± 0.003	0.045 ± 0.003	3.8 ± 0.1	82 ± 3	2.9 ± 0.1	0.91 ± 0.06	45 ± 2	25 ± 5	55 ± 2
5	9	4.32 ± 0.08	0.069 ± 0.002	0.048 ± 0.003	4.2 ± 0.1	59 ± 2	0.97 ± 0.04	0.78 ± 0.05	49 ± 2	41 ± 5	51 ± 2
5	10	4.01 ± 0.09	0.104 ± 0.003	0.038 ± 0.003	3.4 ± 0.1	55 ± 2	1.45 ± 0.06	0.62 ± 0.05	40 ± 2	64 ± 4	60 ± 2
6	11	3.6 ± 0.09	0.082 ± 0.002	0.04 ± 0.003	4.5 ± 0.2	49 ± 2	1.15 ± 0.05	0.65 ± 0.05	52 ± 2	44 ± 5	48 ± 2
6	12	3.71 ± 0.09	0.086 ± 0.002	0.041 ± 0.003	4.6 ± 0.1	51 ± 2	1.21 ± 0.05	0.66 ± 0.05	54 ± 2	40 ± 5	46 ± 2
6	13	3.6 ± 0.08	0.083 ± 0.002	0.04 ± 0.002	4.4 ± 0.1	49 ± 2	1.17 ± 0.05	0.64 ± 0.04	52 ± 2	45 ± 5	48 ± 2
7	14	3.66 ± 0.1	0.0213 ± 0.0006	0.014 ± 0.003	6.8 ± 0.2	78 ± 3	0.47 ± 0.02	0.36 ± 0.08	64 ± 3	-7 ± 6	36 ± 3
7	15	3.8 ± 0.1	0.0229 ± 0.0006	0.015 ± 0.003	7.1 ± 0.2	82 ± 3	0.5 ± 0.02	0.39 ± 0.08	67 ± 3	-16 ± 6	33 ± 3
8	16	4.9 ± 0.1	0.0255 ± 0.0006	0.017 ± 0.003	6 ± 0.2	105 ± 4	0.56 ± 0.02	0.44 ± 0.07	56 ± 2	-19 ± 6	44 ± 2
8	17	5 ± 0.1	0.026 ± 0.0006	0.018 ± 0.003	5.9 ± 0.2	107 ± 4	0.57 ± 0.02	0.45 ± 0.08	55 ± 2	-19 ± 6	45 ± 2
9	18	4.5 ± 0.1	0.119 ± 0.003	0.059 ± 0.003	5.3 ± 0.2	62 ± 2	1.67 ± 0.06	0.95 ± 0.06	49 ± 2	37 ± 5	51 ± 2
9	19	4.8 ± 0.1	0.129 ± 0.003	0.063 ± 0.003	5.6 ± 0.2	66 ± 2	1.8 ± 0.07	1.02 ± 0.06	53 ± 2	26 ± 5	47 ± 2
9	20	4.6 ± 0.1	0.123 ± 0.003	0.054 ± 0.003	5.3 ± 0.2	63 ± 2	1.72 ± 0.06	0.87 ± 0.06	50 ± 2	35 ± 5	50 ± 2
10	21	3.34 ± 0.06	0.0309 ± 0.0007	0.022 ± 0.003	7 ± 0.2	72 ± 3	0.68 ± 0.03	0.56 ± 0.08	66 ± 3	-4 ± 6	34 ± 3
10	22	3.35 ± 0.06	0.0315 ± 0.0007	0.023 ± 0.003	7.2 ± 0.2	72 ± 3	0.69 ± 0.03	0.57 ± 0.08	67 ± 3	-8 ± 6	33 ± 3
11	23	4.9 ± 0.1	0.191 ± 0.004	0.076 ± 0.004	6.3 ± 0.2	85 ± 3	3.3 ± 0.1	1.5 ± 0.1	47 ± 2	16 ± 5	53 ± 2
11	24	4.8 ± 0.1	0.185 ± 0.004	0.072 ± 0.004	7.2 ± 0.2	83 ± 3	3.2 ± 0.1	1.45 ± 0.1	54 ± 2	5 ± 6	46 ± 2
12	25	1.38 ± 0.02	0.0241 ± 0.0006	0.016 ± 0.004	10.8 ± 0.3	29.7 ± 1	0.53 ± 0.02	0.4 ± 0.1	81 ± 3	8 ± 6	19 ± 3
12	26	1.43 ± 0.02	0.0264 ± 0.0007	0.017 ± 0.004	11.7 ± 0.3	24.5 ± 0.8	0.46 ± 0.02	0.34 ± 0.08	87 ± 3	0 ± 7	13 ± 3
13	27	3.52 ± 0.06	0.0259 ± 0.0006	0.017 ± 0.003	7.5 ± 0.2	60 ± 2	0.45 ± 0.02	0.34 ± 0.07	56 ± 2	26 ± 5	44 ± 2
13	28	3.85 ± 0.07	0.0298 ± 0.0007	0.02 ± 0.004	8.7 ± 0.2	66 ± 2	0.52 ± 0.02	0.41 ± 0.08	65 ± 3	3 ± 6	35 ± 3
14	29	5.2 ± 0.1	0.113 ± 0.003	0.062 ± 0.004	7.9 ± 0.2	71 ± 3	1.57 ± 0.06	0.99 ± 0.07	59 ± 2	8 ± 6	41 ± 2
14	30	5 ± 0.1	0.109 ± 0.003	0.055 ± 0.004	7.6 ± 0.2	68 ± 3	1.52 ± 0.06	0.88 ± 0.07	57 ± 2	16 ± 5	43 ± 2
14	31	5.1 ± 0.1	0.112 ± 0.003	0.056 ± 0.004	7.9 ± 0.2	70 ± 3	1.56 ± 0.06	0.9 ± 0.07	59 ± 2	9 ± 6	41 ± 2
15	32	4.4 ± 0.1	0.066 ± 0.003	0.027 ± 0.004	8.7 ± 0.2	75 ± 3	1.15 ± 0.06	0.55 ± 0.08	65 ± 3	-7 ± 6	35 ± 3
15	33	4.4 ± 0.1	0.0392 ± 0.0009	0.028 ± 0.004	8.8 ± 0.2	76 ± 3	0.69 ± 0.03	0.55 ± 0.09	66 ± 3	-9 ± 6	34 ± 3

E.3 Averaged results

Table E.2: Averaged results for dibenzyl ether hydrothermal degradation.

Experiment	Q_R (g/min)	f_{org} (%)	Yield (mol/mol _{DBE} %)			
			BAL	DBE	BZA	TOL
1	25.9 ± 0.6	29.5 ± 0.5	42 ± 2	80 ± 3	0.35 ± 0.01	0.25 ± 0.07
2	25.9 ± 0.6	28 ± 1	86 ± 3	55 ± 2	0.38 ± 0.02	0.3 ± 0.06
3	25.9 ± 0.6	27.8 ± 0.3	110 ± 4	46 ± 2	0.47 ± 0.02	0.43 ± 0.09
4	25.9 ± 0.6	26 ± 2	104 ± 4	46 ± 2	3.21 ± 0.54	1.25 ± 0.17
5	25.9 ± 0.6	24 ± 3	89 ± 5	44 ± 7	1.89 ± 0.53	1.09 ± 0.18
6	25.9 ± 0.6	28 ± 2	78 ± 3	53 ± 2	1.84 ± 0.07	1.01 ± 0.07
7	27 ± 0.6	34.4 ± 0.8	64 ± 3	65 ± 3	0.39 ± 0.02	0.3 ± 0.07
8	27 ± 0.6	33 ± 2	85 ± 3	56 ± 2	0.45 ± 0.02	0.35 ± 0.07
9	27 ± 0.6	34 ± 1	79 ± 3	51 ± 2	2.16 ± 0.09	1.18 ± 0.1
10	27 ± 0.6	33.1 ± 1	57 ± 2	67 ± 3	0.55 ± 0.02	0.45 ± 0.06
11	30.7 ± 0.7	36 ± 1	67 ± 3	50 ± 5	2.63 ± 0.1	1.2 ± 0.08
12	29.6 ± 0.6	40 ± 2	19 ± 1	84 ± 5	0.35 ± 0.02	0.26 ± 0.07
13	29.6 ± 0.6	35 ± 4	51 ± 3	61 ± 6	0.39 ± 0.04	0.3 ± 0.06
14	29.6 ± 0.6	39 ± 1	70 ± 3	58 ± 2	1.55 ± 0.06	0.92 ± 0.07
15	29.6 ± 0.6	39.1 ± 0.1	61 ± 2	65 ± 3	0.74 ± 0.26	0.44 ± 0.07

E.4 Rate equations for the hydrolysis of dibenzyl ether

This section details how the hydrolysis reaction rates presented in section 7.4.1 were obtained. Though generically described by equation (7.1), several authors have proposed that the hydrolysis of dibenzyl ether occurs through nucleophilic substitution, thus comprising more than one elementary step [149,211,213,215]. Earlier studies proposed a bimolecular mechanism (S_N2) [211,215], while recent ones proposed a unimolecular substitution (S_N1) step [149,213].

E.4.1 Mechanism: S_N1 / S_N2

Regardless of the substitution type, the reviewed studies consider that both pathways are preceded by an initial step, where dibenzyl ether is protonated (Figure E.1).

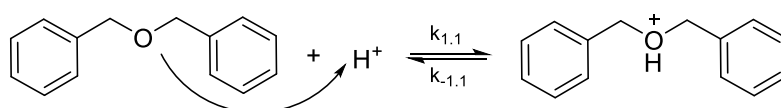


Figure E.1: Step 1.1 of the reaction mechanism for the hydrolysis of DBE (reaction 1) via S_N1 and S_N2 mechanisms.

Rate-limiting step: 1.1

If this is assumed to be the rate limiting step, the hydrolysis rate (r_1) is given by equation (7.3), which is commonly found in literature [149,213].

$$r_1 \approx r_{1.1} = k_{obs,1}[DBE][H^+] \quad (E.17)$$

E.4.2 Mechanism: S_N1

This mechanism considers a two-step reaction (1.2, and 1.3 respectively). These are represented in Figure E.2 and Figure E.3, and consists of the carbocation scission (1.2), followed by the addition of a water molecule (1.3) [217].

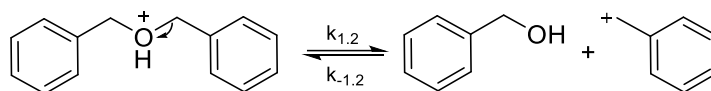


Figure E.2: Step 1.2 of the reaction mechanism for the hydrolysis of DBE (reaction 1) via S_N1 mechanism.

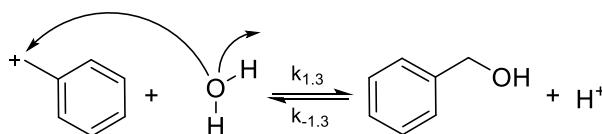


Figure E.3: Step 1.3 of the reaction mechanism for the hydrolysis of DBE (reaction 1) via S_N1 mechanism.

Reaction step 1.1 produces an intermediate, $DBEH^+$, which is consumed in step 1.2. Assuming there is no accumulation of this species, *i.e.*, it exists in steady state, formation ($r_{1.1}$ and $r_{-1.2}$) and degradation rates ($r_{1.2}$ and $r_{-1.1}$) are equal. Consequently, its concentration is given by the following:

$$\begin{aligned} r_{1.1} + r_{-1.2} &= r_{-1.1} + r_{1.2} \Leftrightarrow \\ \Leftrightarrow k_{1.1}[DBE][H^+] + k_{-1.2}[BAL][TOL^+] &= k_{-1.1}[DBEH^+] + k_{1.2}[DBEH^+] \Leftrightarrow \\ \Leftrightarrow [DBEH^+] &= \frac{k_{1.1}[DBE][H^+] + k_{-1.2}[BAL][TOL^+]}{k_{-1.1} + k_{1.2}} \end{aligned} \quad (E.18)$$

Reaction step 1.2 produces alongside BAL an intermediate, TOL^+ , which is consumed in step 1.3. Assuming there is no accumulation of this species, *i.e.*, it exists in steady state, formation ($r_{1.2}$ and $r_{-1.3}$) and degradation rates ($r_{1.3}$ and $r_{-1.2}$) are equal. Consequently, its concentration is given by the following:

$$\begin{aligned} r_{1.2} + r_{-1.3} &= r_{-1.2} + r_{1.3} \Leftrightarrow \\ \Leftrightarrow k_{1.2}[DBEH^+] + k_{-1.3}[BAL][H^+] &= k_{-1.2}[BAL][TOL^+] + k_{1.3}[TOL^+][H_2O] \Leftrightarrow \\ \Leftrightarrow \frac{k_{1.2}k_{1.1}[DBE][H^+] + k_{1.2}k_{-1.2}[BAL][TOL^+]}{k_{-1.1} + k_{1.2}} &+ k_{-1.3}[BAL][H^+] \\ &= k_{-1.2}[BAL][TOL^+] + k_{1.3}[TOL^+][H_2O] \Leftrightarrow \\ \Leftrightarrow k_{1.2}k_{1.1}[DBE][H^+] + (k_{-1.1} + k_{1.2})k_{-1.3}[BAL][H^+] & \\ &= k_{-1.1}k_{-1.2}[BAL][TOL^+] + (k_{-1.1} + k_{1.2})k_{1.3}[TOL^+][H_2O] \Leftrightarrow \\ \Leftrightarrow [TOL^+] &= \frac{k_{1.2}k_{1.1}[DBE][H^+] + (k_{-1.1} + k_{1.2})k_{-1.3}[BAL][H^+]}{k_{-1.1}k_{-1.2}[BAL] + (k_{-1.1} + k_{1.2})k_{1.3}[H_2O]} \end{aligned} \quad (E.19)$$

Rate-limiting step: 1.2

If step 1.2 is considered rate-limiting and irreversible ($k_{-1.2} \approx 0$), the hydrolysis reaction rate is given by:

$$r_1 \approx r_{1.2} = k_{1.2}[DBEH^+] = k_{1.2} \frac{k_{1.1}[DBE][H^+]}{k_{-1.1} + k_{1.2}} \quad (E.20)$$

This can be simplified into a single observed kinetic constant ($k_{obs,1}$):

$$r_1 \approx k_{obs,1}[DBE][H^+] \quad (E.21)$$

The obtained equation is equivalent to (E.17).

Rate-limiting step: 1.3

If step 1.3 is considered rate limiting and irreversible ($k_{-1.3} \approx 0$), the hydrolysis reaction rate is given by:

$$\begin{aligned}
 r_1 \approx r_{1.3} &= k_{1.3}[TOL^+][H_2O] = k_{1.3} \frac{k_{1.2}k_{1.1}[DBE][H^+]}{k_{-1.1}k_{-1.2}[BAL] + (k_{-1.1} + k_{1.2})k_{1.3}[H_2O]} [H_2O] \\
 &= \frac{k_{1.2}k_{1.1}}{k_{-1.1} + k_{1.2}} \frac{[DBE][H^+][H_2O]}{\frac{k_{-1.1}k_{-1.2}}{(k_{-1.1} + k_{1.2})k_{1.3}} [BAL] + [H_2O]} \quad (E.22)
 \end{aligned}$$

This can be simplified into two observed kinetic constants ($k_{obs,1.1}$ and $k_{obs,1.2}$):

$$r_1 \approx \frac{k_{obs,1.1}[DBE][H^+][H_2O]}{k_{obs,1.2}[BAL] + [H_2O]} \quad (E.23)$$

E.4.3 Mechanism: S_N2

This mechanism considers a single-step reaction (1.2), after the protonation of DBE. This is represented in Figure E.4, and consists of the carbocation cleavage [217].

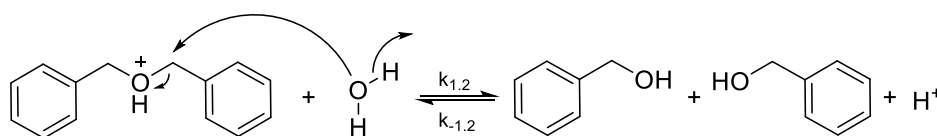


Figure E.4: Step 1.2 of the reaction mechanism for the hydrolysis of DBE (reaction 1) via S_N2 mechanism.

Reaction step 1.1 produces an intermediate, DBEH⁺, which is consumed in step 1.2. Assuming there is no accumulation of this species, *i.e.*, it exists in steady state, formation ($r_{1.1}$ and $r_{-1.2}$) and degradation rates ($r_{1.2}$ and $r_{-1.1}$) are equal. Consequently, its concentration is given by the following:

$$\begin{aligned}
 r_{1.1} + r_{-1.2} &= r_{-1.1} + r_{1.2} \Leftrightarrow \\
 \Leftrightarrow k_{1.1}[DBE][H^+] + k_{-1.2}[BAL]^2[H^+] &= k_{-1.1}[DBEH^+] + k_{1.2}[DBEH^+][H_2O] \Leftrightarrow \\
 \Leftrightarrow [DBEH^+] &= \frac{k_{1.1}[DBE][H^+] + k_{-1.2}[BAL]^2[H^+]}{k_{-1.1} + k_{1.2}[H_2O]} \quad (E.24)
 \end{aligned}$$

Rate-limiting step: 1.2

If step 1.2 is considered rate-limiting and irreversible ($k_{-1.2} \approx 0$), the hydrolysis reaction rate is given by:

$$\begin{aligned} r_1 \approx r_{1.2} &= k_{1.2}[DBEH^+][H_2O] = k_{1.2} \frac{k_{1.1}[DBE][H^+]}{k_{-1.1} + k_{1.2}[H_2O]} [H_2O] \\ &= \frac{\frac{k_{1.2}k_{1.1}}{k_{-1.1}} [DBE][H^+][H_2O]}{1 + \frac{k_{1.2}}{k_{-1.1}} [H_2O]} \end{aligned} \quad (E.25)$$

This can be simplified into two observed kinetic constants ($k_{obs,1.1}$ and $k_{obs,1.2}$):

$$r_1 \approx \frac{k_{obs,1.1}[DBE][H^+][H_2O]}{1 + k_{obs,1.2}[H_2O]} \quad (E.26)$$

Looking at equation (E.25), if the reverse of step 1.1 is considerably faster than step 1.2 ($k_{-1.1} \gg k_{1.2}$), the following approximation is valid:

$$1 + \frac{k_{1.2}}{k_{-1.1}} [H_2O] \approx 1 \quad (E.27)$$

This results in a new rate equation, which is based on a single observed kinetic constant ($k_{obs,1}$):

$$r_1 \approx k_{obs,1}[DBE][H^+][H_2O] \quad (E.28)$$

E.5 Proton concentration

The rate equations derived in this Appendix consider proton concentrations. If water is the only dissociated molecule in the reaction mixture, the proton concentration is equal to the concentration of OH⁻:

$$[H^+] = [OH^-] \quad (E.29)$$

Considering water self-ionisation, K_w , in mol²/kg², the proton concentration is given by:

$$K_w \rho_w^2 = [H^+][OH^-] = [H^+]^2 \quad (E.30)$$

The above equation was used throughout this study. On the other hand, if other species significantly contribute to the acidity of the mixture, *i.e.*, the concentration of protons, equations (E.29) becomes:

$$[H^+] = [OH^-] + \sum_{i \neq \text{water}} [X_i^-] \quad (E.31)$$

X_i is a species that dissociates in the reaction mixture, producing X_i^- and H^+ . The concentration of the dissociated species is calculated using by the associated equilibrium constant, K_{a_i} , which is defined as:

$$K_{a_i} = \frac{[X_i^-][H^+]}{[X_i]} \quad (E.32)$$

Therefore, the total proton concentration in the mixture is given by:

$$[H^+] = \frac{K_w \rho_w^2}{[H^+]} + \sum_{i \neq \text{water}} \frac{[X_i]}{[H^+]} \Leftrightarrow [H^+]^2 = K_w \rho_w^2 + \sum_{i \neq \text{water}} K_{a_i} [X_i] \quad (\text{E.33})$$

Appendix F

Detailed calculations and results: Sucrose

The following section details the calculations required to calculate the mass yields associated with the reactions of sucrose and its derivatives in subcritical water, as described in Chapter 8. Section C.4.2 includes the results of these calculations for each experiment performed using sucrose, while Section C.4.3 shows the averaged results, which are plotted in Section 8.3.

F.1 Calculation summary

Feed, total inlet and reactor mass flowrates calculated by equations (E.1) to (E.6) in Appendix E.1. Sucrose's mass fraction at the reactor's inlet (w_{Suc}^{in}) depends on the organic feed composition (w_{Suc}^{FO}), as do the equivalent inlet mass fractions of glucose and fructose (w_{Gluc}^{in} , w_{Fruc}^{in}).

$$w_{Suc}^{in} = \frac{w_{Suc}^{FO} \times Q_{FO}}{Q_R} \quad (F.1)$$

$$w_{Gluc}^{in} = w_{Fruc}^{in} = \frac{w_{Suc}^{in} \times MW_{Gluc}}{MW_{Suc}} \quad (F.2)$$

Dichloromethane-soluble organics (DSO) and solid mass flowrates at the reactor's outlet (Q_p) calculated from the mass of each phase's sample after solvent evaporation (m_p^s) and respective collection time (t_c).

$$Q_{p=\{DSO, solids\}} = \frac{m_p^s}{t_c} \quad (F.3)$$

Water soluble organics (WSO) flowrate also based on the equation above, but accounts for only a portion ($m_{WSO}^{o'}$) of the original sample (m_{WSO}^o) being evaporated.

$$Q_{WSO} = \frac{m_{WSO}^s}{t_c} \times \frac{m_{WSO}^o}{m_{WSO}^{o'}} \quad (F.4)$$

TSO mass flowrate at the reactor's outlet (Q_{TSO}) given by the sum of DSO and WSO flowrates.

$$Q_{TSO} = Q_{DSO} + Q_{WSO} \quad (F.5)$$

Volatiles mass flowrate at the reactor's outlet ($Q_{volatiles}$) given by the difference between inlet flowrate of sucrose and outlet flowrate of remaining phases.

$$Q_{volatiles} = w_{Suc}^{FO} \times Q_{FO} - \sum_{p \neq volatiles} Q_p \quad (F.6)$$

Measured gases outlet flowrate (Q_i^{out}) calculated from: respective molar fraction measured during steady state at the FTIR spectrometer (x_i^{GS}), the nitrogen molar flowrate (F_{N_2}), and molecular weight (MW_i).

$$Q_{i=\{CO_2, CO, CH_4, C_2H_4\}}^{out} = x_i^{GS} \times \frac{F_{N_2}}{1 - \sum_{i \neq N_2} x_i^{GS}} \times MW_i \quad (F.7)$$

5-HMF outlet flowrate (Q_{5-HMF}^{out}) calculated from: mass of DSO and WSO samples diluted in methanol (m_p^{MetOH}), 5-HMF and 5-HDF's analytical signals ($A_{5-HMF,p}$, $A_{5-HDF,p}$), and proportionality coefficient (mc_{5-HMF}).

$$w_{5-HMF,p}^{MetOH} = \frac{A_{5-HMF,p} + A_{5-HDF,p}}{mc_{5-HMF}} \times 10^{-4} \quad (F.8)$$

$$Q_{5-HMF}^{out} = \sum_{p=\{WSO, DSO\}} \left(w_{5-HMF,p}^{MetOH} \times \frac{m_p^{MetOH}}{t_c} \right) \quad (F.9)$$

Outlet flowrate of components measured through HPLC-RID (Q_i^{out}) calculated from the WSO sample original mass (m_p^0), the analytical signal of the component ($A_{i,p}$) and proportionality coefficient (mc_i).

$$w_{i,WSO}^{Water} = \frac{A_{i,WSO}}{mc_i} \times 10^{-5} \quad (F.10)$$

$$Q_{i=\{Suc, Gluc, Fruc, AGluc, Pyr\}}^{out} = w_{i,WSO}^{Water} \times \frac{m_{WSO}^0}{t_c} \quad (F.11)$$

Mass yields (Y_i) calculated from the flowrates of each component and sucrose at the reactor's inlet.

$$Y_i = \frac{Q_i^{out}}{w_{Suc}^{FO} \times Q_{FO}} \quad (F.12)$$

F.2 Detailed results

Table F.1: Detailed results for sucrose hydrothermal degradation – Inlet data.

Experiment	No. samples	Q_v^{NOM} (mL/min)			Q^{in} (g/min)					w^{FO}_{Suc} (%)	w^{in} (%)	
		SCW	FO	Quench	SCW	FO	Quench	In	R		Suc	Gluc/Fruc
1	3	24 ± 0.7	8 ± 0.2	60 ± 2	26.1 ± 0.8	8.7 ± 0.2	65 ± 2	100 ± 2	34.7 ± 0.8	19.58 ± 0.01	4.9 ± 0.2	2.57 ± 0.09
2	3	18 ± 0.5	6 ± 0.2	60 ± 2	19.6 ± 0.6	6.5 ± 0.2	65 ± 2	91 ± 2	26.1 ± 0.6	19.58 ± 0.01	4.9 ± 0.2	2.57 ± 0.09
3	3	30 ± 0.9	10 ± 0.3	60 ± 2	32.6 ± 1	10.8 ± 0.3	65 ± 2	109 ± 2	43 ± 1	19.58 ± 0.01	4.9 ± 0.2	2.57 ± 0.09
4	2	18 ± 0.5	6 ± 0.2	60 ± 2	19.6 ± 0.6	6.5 ± 0.2	65 ± 2	91 ± 2	26.1 ± 0.6	19.803 ± 0.001	4.9 ± 0.2	2.6 ± 0.1
5	2	24 ± 0.7	8 ± 0.2	60 ± 2	26.1 ± 0.8	8.7 ± 0.2	65 ± 2	100 ± 2	34.7 ± 0.8	19.803 ± 0.001	4.9 ± 0.2	2.6 ± 0.1
6	2	30 ± 0.9	10 ± 0.3	60 ± 2	32.6 ± 1	10.8 ± 0.3	65 ± 2	109 ± 2	43 ± 1	19.803 ± 0.001	4.9 ± 0.2	2.6 ± 0.1
7	3	21 ± 0.6	7 ± 0.2	60 ± 2	22.8 ± 0.7	7.6 ± 0.2	65 ± 2	96 ± 2	30.4 ± 0.7	19.262 ± 0.002	4.8 ± 0.2	2.53 ± 0.09
8	3	27 ± 0.8	9 ± 0.3	60 ± 2	29.4 ± 0.9	9.7 ± 0.3	65 ± 2	104 ± 2	39.1 ± 0.9	19.262 ± 0.002	4.8 ± 0.2	2.53 ± 0.09
9	3	21 ± 0.6	7 ± 0.2	60 ± 2	22.8 ± 0.7	7.6 ± 0.2	65 ± 2	96 ± 2	30.4 ± 0.7	19.483 ± 0.002	4.9 ± 0.2	2.55 ± 0.09
10	3	27 ± 0.8	9 ± 0.3	60 ± 2	29.4 ± 0.9	9.7 ± 0.3	65 ± 2	104 ± 2	39.1 ± 0.9	19.483 ± 0.002	4.9 ± 0.2	2.55 ± 0.09
11	3	21 ± 0.6	7 ± 0.2	60 ± 2	22.8 ± 0.7	7.3 ± 0.2	65 ± 2	95 ± 2	30.1 ± 0.7	9.8279 ± 0.0007	2.38 ± 0.09	1.25 ± 0.05
12	3	27 ± 0.8	9 ± 0.3	60 ± 2	29.4 ± 0.9	9.4 ± 0.3	65 ± 2	104 ± 2	38.7 ± 0.9	9.8279 ± 0.0007	2.38 ± 0.09	1.25 ± 0.05
13	3	18 ± 0.5	6 ± 0.2	60 ± 2	19.6 ± 0.6	6.3 ± 0.2	65 ± 2	91 ± 2	25.8 ± 0.6	9.8279 ± 0.0007	2.38 ± 0.09	1.25 ± 0.05
14	3	24 ± 0.7	8 ± 0.2	60 ± 2	26.1 ± 0.8	8.4 ± 0.3	65 ± 2	100 ± 2	34.4 ± 0.8	9.8279 ± 0.0007	2.38 ± 0.09	1.25 ± 0.05
15	3	30 ± 0.9	10 ± 0.3	60 ± 2	32.6 ± 1	10.4 ± 0.3	65 ± 2	108 ± 2	43 ± 1	10.062 ± 0.004	2.44 ± 0.09	1.28 ± 0.05
16	3	18 ± 0.5	6 ± 0.2	60 ± 2	19.6 ± 0.6	6.7 ± 0.2	65 ± 2	91 ± 2	26.3 ± 0.6	29.6539 ± 0.0005	7.2 ± 0.3	3.8 ± 0.1
17	3	24 ± 0.7	8 ± 0.2	60 ± 2	26.1 ± 0.8	9 ± 0.3	65 ± 2	100 ± 2	35.1 ± 0.8	29.6539 ± 0.0005	7.2 ± 0.3	3.8 ± 0.1
18	3	30 ± 0.9	10 ± 0.3	60 ± 2	32.6 ± 1	11.2 ± 0.3	65 ± 2	109 ± 2	44 ± 1	29.6539 ± 0.0005	7.2 ± 0.3	3.8 ± 0.1
19	3	21 ± 0.6	7 ± 0.2	60 ± 2	22.8 ± 0.7	7.8 ± 0.2	65 ± 2	96 ± 2	30.7 ± 0.7	29.6539 ± 0.0005	7.2 ± 0.3	3.8 ± 0.1
20	3	27 ± 0.8	9 ± 0.3	60 ± 2	29.4 ± 0.9	10.1 ± 0.3	65 ± 2	105 ± 2	39.4 ± 0.9	29.6539 ± 0.0005	7.2 ± 0.3	3.8 ± 0.1

Table F.2: Detailed results for sucrose hydrothermal degradation – FTIR data.

Experiment	x^{Gs} (%)			x^{Gs} (ppm)		F_{N_2} (mmol/min)	Q^{out} (mg/min)		Q^{out} (μ g/min)	
	H ₂ O	CO ₂	CO	CH ₄	C ₂ H ₄		CO ₂	CO	CH ₄	C ₂ H ₄
1	5 ± 0.6	0.45 ± 0.01	0.25 ± 0.01	196 ± 8	31.3 ± 1	111 ± 2	23 ± 3	8.3 ± 0.9	370 ± 40	100 ± 10
2	4.7 ± 0.4	0.46 ± 0.01	0.229 ± 0.005	156 ± 3	24.6 ± 0.3	111 ± 2	24 ± 2	7.5 ± 0.6	300 ± 20	81 ± 6
3	6.4 ± 0.9	0.39 ± 0.01	0.27 ± 0.01	218 ± 10	31.7 ± 0.9	111 ± 2	20 ± 3	9 ± 1	420 ± 60	110 ± 10
4	2.9 ± 0.1	0.191 ± 0.006	0.0426 ± 0.0009	10.6 ± 0.2	4 ± 0.05	189 ± 6	16.4 ± 1	2.3 ± 0.1	33 ± 2	22 ± 1
5	3.8 ± 0.3	0.178 ± 0.008	0.044 ± 0.001	11.4 ± 0.4	4.4 ± 0.1	189 ± 6	15 ± 1	2.4 ± 0.2	36 ± 3	25 ± 2
6	4.8 ± 0.2	0.133 ± 0.007	0.0365 ± 0.0007	8.6 ± 0.2	3.3 ± 0.2	189 ± 6	11.7 ± 0.9	2 ± 0.1	27 ± 2	18 ± 2
7	3.4 ± 0.3	0.13 ± 0.01	0.022 ± 0.0008	3.6 ± 0.2	2.3 ± 0.2	189 ± 6	11 ± 1	1.2 ± 0.1	11 ± 1	13 ± 1
8	4.6 ± 0.3	0.076 ± 0.009	0.02 ± 0.0009	3.6 ± 0.3	3 ± 0.2	189 ± 6	6.6 ± 0.9	1.1 ± 0.1	11 ± 1	17 ± 2
9	3.6 ± 0.4	0.4 ± 0.1	0.16 ± 0.05	60 ± 20	12 ± 2	111 ± 2	18 ± 6	5 ± 2	110 ± 40	38 ± 8
10	5.1 ± 0.7	0.44 ± 0.02	0.16 ± 0.02	59 ± 6	11.1 ± 0.6	111 ± 2	23 ± 3	5.2 ± 0.9	110 ± 20	37 ± 5
12	6.4 ± 0.6	0.14 ± 0.03	0.099 ± 0.008	83 ± 6	21.5 ± 1	111 ± 2	7 ± 2	3.3 ± 0.4	160 ± 20	72 ± 7
13	3.5 ± 0.5	0.22 ± 0.02	0.068 ± 0.002	28.4 ± 0.9	8.6 ± 0.1	111 ± 2	11 ± 2	2.2 ± 0.3	53 ± 7	28 ± 3
14	5.2 ± 0.7	0.17 ± 0.02	0.071 ± 0.004	34 ± 2	9.1 ± 0.2	111 ± 2	9 ± 1	2.3 ± 0.3	64 ± 9	30 ± 4
15	6.5 ± 0.5	0.14 ± 0.02	0.068 ± 0.002	34 ± 1	8.7 ± 0.1	111 ± 2	8 ± 1	2.3 ± 0.2	65 ± 6	29 ± 2
16	2.6 ± 0.1	0.36 ± 0.02	0.067 ± 0.003	9.6 ± 0.4	5.11 ± 0.1	111 ± 2	18 ± 1	2.2 ± 0.1	18 ± 1	16.5 ± 0.8
17	3.6 ± 0.9	0.2 ± 0.02	0.04 ± 0.001	5.8 ± 0.3	5.1 ± 0.1	111 ± 2	10 ± 3	1.3 ± 0.3	11 ± 2	17 ± 4
18	5.1 ± 0.7	0.22 ± 0.02	0.055 ± 0.001	8.9 ± 0.2	6 ± 0.2	111 ± 2	12 ± 2	1.8 ± 0.2	17 ± 2	20 ± 3
19	3.3 ± 0.6	0.54 ± 0.04	0.188 ± 0.008	33 ± 1	8.8 ± 0.2	111 ± 2	27 ± 4	6.1 ± 0.9	62 ± 9	28 ± 4
20	4.9 ± 0.5	0.4 ± 0.02	0.15 ± 0.01	27 ± 2	9.2 ± 0.4	111 ± 2	21 ± 2	5.1 ± 0.6	52 ± 6	30 ± 3

Table F.3: Detailed results for sucrose hydrothermal degradation – Experiments 1 to 10.

Experiment	Sample	Sampling time (min)	t_c (sec)	m_s (g)	m_s (mg)			m^0_{wso} (g)	m^0_{wso} (g)
				Total	DSO	WSO	Solids		
1	S1.1	13	80 ± 1	129.906 ± 0.001	137 ± 1	1000 ± 700	25 ± 1	127.845 ± 0.001	60.374 ± 0.001
1	S1.2	17	80 ± 1	129.395 ± 0.001	102 ± 1	900 ± 700	2 ± 1	119.123 ± 0.001	35.808 ± 0.001
1	S1.3	21	80 ± 1	129.98 ± 0.001	114 ± 1	900 ± 700	11 ± 1	117.042 ± 0.001	18.22 ± 0.001
2	S2.1	18	80 ± 1	118.405 ± 0.001	250 ± 1	700 ± 700	26 ± 1	113.969 ± 0.002	59.642 ± 0.002
2	S2.2	21	80 ± 1	117.996 ± 0.001	137 ± 1	600 ± 700	25 ± 6	114.431 ± 0.001	35.006 ± 0.001
2	S2.3	25	80 ± 1	118.164 ± 0.001	151 ± 1	700 ± 700	17 ± 1	111 ± 2	36.755 ± 0.001
3	S3.1	15	80 ± 1	140.569 ± 0.001	124 ± 1	1700 ± 700	25 ± 1	137.75 ± 0.001	45.063 ± 0.001
3	S3.2	17	80 ± 1	140.609 ± 0.001	106 ± 1	1500 ± 700	13 ± 6	139.27 ± 0.001	33.231 ± 0.001
3	S3.3	20	80 ± 1	140.574 ± 0.001	112 ± 1	1600 ± 700	13 ± 1	127.256 ± 0.001	31.568 ± 0.001
4	S4.1	24	80 ± 1	117.628 ± 0.001	194 ± 1	890 ± 4	36 ± 1	128.147 ± 0.001	43.093 ± 0.001
4	S4.2	26	80 ± 1	117.754 ± 0.001	227 ± 1	800 ± 700	37 ± 1	103.433 ± 0.001	16.004 ± 0.001
5	S5.1	21	82 ± 1	132.115 ± 0.001	224 ± 1	1495 ± 4	34 ± 6	194.585 ± 0.001	64.042 ± 0.001
5	S5.2	24	80 ± 1	128.089 ± 0.001	236 ± 1	1300 ± 700	33 ± 1	119.775 ± 0.001	18.203 ± 0.001
6	S6.1	19	80 ± 1	138.969 ± 0.001	222 ± 1	2142 ± 5	23 ± 6	235.756 ± 0.001	73.027 ± 0.001
6	S6.2	21	80 ± 1	139.407 ± 0.001	215 ± 1	2000 ± 700	26 ± 1	128.472 ± 0.001	21.199 ± 0.001
7	S7.1	17	82 ± 1	123.014 ± 0.001	157 ± 1	1235 ± 3	19 ± 1	96.6 ± 0.001	41.718 ± 0.001
7	S7.2	20	80 ± 1	119.547 ± 0.001	187 ± 1	1301 ± 3	22 ± 1	174.411 ± 0.001	72.642 ± 0.001
7	S7.3	23	80 ± 1	119.594 ± 0.001	222 ± 1	1200 ± 700	20 ± 1	111.707 ± 0.001	18.284 ± 0.001
8	S8.1	22	80 ± 1	131.393 ± 0.001	181 ± 1	2282 ± 4	17 ± 1	164.593 ± 0.001	58.343 ± 0.001
8	S8.2	24	81 ± 1	132.185 ± 0.001	186 ± 1	2080 ± 5	19 ± 1	198.61 ± 0.001	53.699 ± 0.001
8	S8.3	26	80 ± 1	131.313 ± 0.001	208 ± 1	1800 ± 700	17 ± 1	139.701 ± 0.001	16.022 ± 0.001
9	S9.1	28	81 ± 1	117.893 ± 0.001	188 ± 1	987 ± 5	30 ± 1	202.282 ± 0.001	61.912 ± 0.001
9	S9.2	30	80 ± 1	117.61 ± 0.001	192 ± 1	963 ± 4	39 ± 1	182.695 ± 0.001	58.962 ± 0.001
9	S9.3	32	81 ± 1	117.691 ± 0.001	226 ± 1	600 ± 700	36 ± 1	133.063 ± 0.001	20.884 ± 0.001
10	S10.1	20	81 ± 1	128.958 ± 0.001	208 ± 1	1635 ± 4	31 ± 1	198.794 ± 0.001	70.563 ± 0.001
10	S10.2	22	81 ± 1	129.361 ± 0.001	232 ± 1	1506 ± 6	40 ± 1	250.443 ± 0.001	57.537 ± 0.001
10	S10.3	24	81 ± 1	129.71 ± 0.001	259 ± 1	1300 ± 700	30 ± 1	138.599 ± 0.001	19.856 ± 0.001

Continuation of Table C.9.												
Experiment	Sample	Q^{out} (g/min)	Q^{out} (mg/min)					Yield (g/g _{Suc} %)				
		Outlet	DSO	WSO	TSO	Solids	Volatiles	DSO	WSO	TSO	Solids	Volatiles
1	S1.1	97 ± 1	103 ± 2	800 ± 500	900 ± 500	19 ± 1	800 ± 700	6.1 ± 0.2	40 ± 30	50 ± 30	1.09 ± 0.07	50 ± 30
1	S1.2	97 ± 1	77 ± 1	700 ± 500	800 ± 500	1 ± 1	900 ± 700	4.5 ± 0.2	40 ± 30	50 ± 30	0.07 ± 0.06	50 ± 30
1	S1.3	97 ± 1	86 ± 2	700 ± 500	800 ± 500	8 ± 1	900 ± 700	5.1 ± 0.2	40 ± 30	50 ± 30	0.47 ± 0.06	50 ± 30
2	S2.1	89 ± 1	188 ± 3	500 ± 500	700 ± 500	20 ± 1	600 ± 700	14.8 ± 0.5	40 ± 40	50 ± 40	1.55 ± 0.1	50 ± 40
2	S2.2	88 ± 1	103 ± 2	500 ± 500	600 ± 500	19 ± 5	700 ± 700	8.1 ± 0.3	40 ± 40	40 ± 40	1.5 ± 0.4	50 ± 40
2	S2.3	89 ± 1	113 ± 2	500 ± 500	600 ± 500	13 ± 1	600 ± 700	8.9 ± 0.3	40 ± 40	50 ± 40	1.01 ± 0.09	50 ± 40
3	S3.1	105 ± 1	93 ± 2	1300 ± 500	1400 ± 500	19 ± 1	700 ± 700	4.4 ± 0.1	60 ± 20	60 ± 20	0.87 ± 0.06	30 ± 20
3	S3.2	105 ± 1	79 ± 1	1200 ± 500	1200 ± 500	10 ± 5	900 ± 700	3.7 ± 0.1	50 ± 20	60 ± 20	0.5 ± 0.2	40 ± 20
3	S3.3	105 ± 1	84 ± 1	1200 ± 500	1300 ± 500	10 ± 1	800 ± 700	4 ± 0.1	60 ± 20	60 ± 20	0.45 ± 0.05	40 ± 20
4	S4.1	88 ± 1	146 ± 2	668 ± 9	813 ± 9	27 ± 1	450 ± 40	11.3 ± 0.4	52 ± 2	63 ± 2	2.1 ± 0.1	35 ± 2
4	S4.2	88 ± 1	170 ± 2	600 ± 500	800 ± 500	27 ± 1	500 ± 700	13.2 ± 0.4	50 ± 40	60 ± 40	2.1 ± 0.1	40 ± 40
5	S5.1	97 ± 1	164 ± 2	1090 ± 10	1260 ± 10	25 ± 5	430 ± 50	9.6 ± 0.3	64 ± 2	73 ± 2	1.5 ± 0.3	25 ± 2
5	S5.2	96 ± 1	177 ± 2	1000 ± 500	1200 ± 500	25 ± 1	500 ± 700	10.3 ± 0.3	60 ± 30	70 ± 30	1.46 ± 0.08	30 ± 30
6	S6.1	104 ± 1	166 ± 2	1610 ± 20	1770 ± 20	17 ± 5	350 ± 70	7.8 ± 0.2	75 ± 2	83 ± 2	0.8 ± 0.2	16 ± 2
6	S6.2	105 ± 1	161 ± 2	1500 ± 500	1700 ± 500	19 ± 1	400 ± 700	7.5 ± 0.2	70 ± 20	80 ± 20	0.9 ± 0.06	20 ± 20
7	S7.1	90 ± 1	115 ± 2	900 ± 10	1020 ± 10	14 ± 1	430 ± 40	7.9 ± 0.3	62 ± 2	70 ± 2	0.95 ± 0.08	29 ± 2
7	S7.2	90 ± 1	140 ± 2	980 ± 10	1120 ± 10	16 ± 1	330 ± 40	9.6 ± 0.3	67 ± 2	76 ± 2	1.12 ± 0.08	22 ± 2
7	S7.3	90 ± 1	167 ± 2	900 ± 500	1100 ± 500	15 ± 1	400 ± 700	11.4 ± 0.4	60 ± 30	70 ± 30	1.01 ± 0.08	20 ± 30
8	S8.1	99 ± 1	136 ± 2	1710 ± 20	1850 ± 20	13 ± 1	20 ± 60	7.2 ± 0.2	91 ± 3	98 ± 3	0.69 ± 0.06	1 ± 3
8	S8.2	98 ± 1	138 ± 2	1540 ± 20	1680 ± 20	14 ± 1	180 ± 60	7.4 ± 0.2	82 ± 3	90 ± 3	0.73 ± 0.06	10 ± 3
8	S8.3	98 ± 1	156 ± 2	1300 ± 500	1500 ± 500	13 ± 1	400 ± 700	8.3 ± 0.3	70 ± 30	80 ± 30	0.69 ± 0.06	20 ± 30
9	S9.1	88 ± 1	140 ± 2	736 ± 10	876 ± 10	22 ± 1	580 ± 40	9.5 ± 0.3	50 ± 2	59 ± 2	1.51 ± 0.09	39 ± 2
9	S9.2	88 ± 1	143 ± 2	718 ± 10	862 ± 10	29 ± 1	580 ± 40	9.7 ± 0.3	49 ± 2	58 ± 2	1.98 ± 0.09	40 ± 2
9	S9.3	88 ± 1	168 ± 2	500 ± 500	600 ± 500	27 ± 1	800 ± 700	11.4 ± 0.4	30 ± 30	40 ± 30	1.81 ± 0.09	50 ± 30
10	S10.1	96 ± 1	155 ± 2	1220 ± 20	1370 ± 20	23 ± 1	500 ± 60	8.2 ± 0.3	64 ± 2	72 ± 2	1.2 ± 0.07	26 ± 2
10	S10.2	96 ± 1	173 ± 2	1120 ± 10	1290 ± 10	30 ± 1	570 ± 60	9.1 ± 0.3	59 ± 2	68 ± 2	1.57 ± 0.07	30 ± 2
10	S10.3	96 ± 1	192 ± 3	900 ± 500	1100 ± 500	22 ± 1	700 ± 700	10.1 ± 0.3	50 ± 30	60 ± 30	1.17 ± 0.07	40 ± 30

Continuation of Table C.9.													
Experiment	Sample	<i>A_{ws}</i> (HPLC-RID)				<i>w_{ws}</i> ^{Water} (ppm)				<i>Q</i> ^{out} (mg/min)			
		Gluc	Fruc	AGluc	Pyr	Gluc	Fruc	AGluc	Pyr	Gluc	Fruc	AGluc	Pyr
1	S1.1	106123	161828	139621	819219	525 ± 5	815 ± 8	770 ± 20	5000 ± 600	50.3 ± 0.8	78 ± 1	74 ± 2	480 ± 60
1	S1.2	76376	151741	138401	855061	378 ± 5	764 ± 8	760 ± 20	5200 ± 700	33.8 ± 0.6	68 ± 1	68 ± 2	470 ± 60
1	S1.3	101958	173374	151340	942901	504 ± 5	873 ± 9	830 ± 20	5800 ± 700	44.3 ± 0.7	77 ± 1	73 ± 2	510 ± 60
2	S2.1	58083	112000	128082	655456	287 ± 5	564 ± 7	700 ± 20	4000 ± 500	24.6 ± 0.5	48.2 ± 0.8	60 ± 1	340 ± 40
2	S2.2	36288	94543	114864	635918	179 ± 5	476 ± 7	630 ± 10	3900 ± 500	15.4 ± 0.5	40.8 ± 0.8	54 ± 1	330 ± 40
2	S2.3	46999	109443	132271	692694	232 ± 5	551 ± 7	730 ± 20	4200 ± 500	19.3 ± 0.6	46 ± 1	60 ± 2	350 ± 40
3	S3.1	170733	271292	183635	1168175	844 ± 9	1370 ± 10	1010 ± 20	7100 ± 900	87 ± 1	141 ± 2	104 ± 3	740 ± 90
3	S3.2	120708	240741	174458	1138084	597 ± 6	1210 ± 10	960 ± 20	6900 ± 900	62 ± 1	127 ± 2	100 ± 2	730 ± 90
3	S3.3	178276	301714	204974	1352176	882 ± 9	1520 ± 20	1130 ± 20	8000 ± 1000	84 ± 1	145 ± 2	108 ± 3	790 ± 100
4	S4.1	192112	83679	65531	232414	950 ± 10	421 ± 7	360 ± 8	1400 ± 300	91 ± 1	40.5 ± 0.8	34.6 ± 0.9	140 ± 30
4	S4.2	302932	134747	103630	365785	1500 ± 20	678 ± 7	570 ± 10	2200 ± 300	116 ± 2	52.6 ± 0.8	44 ± 1	170 ± 20
5	S5.1	200426	91916	58271	207672	990 ± 10	463 ± 7	320 ± 7	1300 ± 300	141 ± 2	66 ± 1	46 ± 1	180 ± 40
5	S5.2	415081	195011	123027	444734	2050 ± 20	982 ± 10	680 ± 10	2700 ± 300	184 ± 3	88 ± 1	61 ± 2	240 ± 30
6	S6.1	404697	198726	90146	262605	2000 ± 20	1000 ± 10	500 ± 10	1600 ± 300	354 ± 6	177 ± 3	88 ± 2	280 ± 50
6	S6.2	695957	348136	157804	455824	3440 ± 30	1750 ± 20	870 ± 20	2800 ± 300	332 ± 5	169 ± 3	84 ± 2	270 ± 30
7	S7.1	689355	276864	133279	306336	3410 ± 30	1390 ± 10	730 ± 20	1900 ± 300	241 ± 4	99 ± 2	52 ± 1	130 ± 20
7	S7.2	389196	155977	73479	174243	1930 ± 20	785 ± 8	404 ± 9	1100 ± 300	252 ± 4	103 ± 2	53 ± 1	140 ± 40
7	S7.3	623512	255925	120824	287047	3080 ± 30	1290 ± 10	660 ± 10	1800 ± 300	258 ± 4	108 ± 2	56 ± 1	150 ± 20
8	S8.1	412318	220046	73911	158016	2040 ± 20	1110 ± 10	406 ± 9	1000 ± 300	252 ± 4	137 ± 2	50 ± 1	120 ± 30
8	S8.2	500871	267430	89111	192451	2480 ± 30	1350 ± 10	490 ± 10	1200 ± 300	364 ± 6	198 ± 3	72 ± 2	170 ± 40
8	S8.3	858187	465814	156084	334302	4240 ± 40	2350 ± 20	860 ± 20	2000 ± 300	445 ± 7	246 ± 4	90 ± 2	210 ± 30
9	S9.1	72829	68135	51418	282595	360 ± 5	343 ± 7	283 ± 6	1700 ± 300	54 ± 1	52 ± 1	43 ± 1	260 ± 40
9	S9.2	59044	54235	44005	247359	292 ± 5	273 ± 7	242 ± 5	1500 ± 300	39.8 ± 0.9	37 ± 1	33 ± 0.8	210 ± 40
9	S9.3	97623	103069	80659	455058	483 ± 5	519 ± 7	443 ± 9	2800 ± 300	47.9 ± 0.8	51.5 ± 0.9	44 ± 1	280 ± 30
10	S10.1	158436	114896	83482	379145	784 ± 8	578 ± 7	459 ± 10	2300 ± 300	116 ± 2	86 ± 1	68 ± 2	340 ± 40
10	S10.2	126465	87971	66080	306339	626 ± 6	443 ± 7	363 ± 8	1900 ± 300	117 ± 2	83 ± 2	68 ± 2	350 ± 50
10	S10.3	235456	181009	137909	596337	1160 ± 10	911 ± 9	760 ± 20	3600 ± 500	120 ± 2	94 ± 1	78 ± 2	370 ± 50

Continuation of Table C.9.									
Experiment	Sample	Yield (g/g _{Suc} %)						Yield (g/g _{Suc} ppm)	
		Gluc	Fruc	AGluc	Pyr	CO ₂	CO	CH ₄	C ₂ H ₄
1	S1.1	2.97 ± 0.1	4.6 ± 0.1	4.3 ± 0.2	28 ± 4	1.4 ± 0.2	0.49 ± 0.06	220 ± 30	61 ± 7
1	S1.2	1.99 ± 0.07	4 ± 0.1	4 ± 0.2	28 ± 4	1.4 ± 0.2	0.49 ± 0.06	220 ± 30	61 ± 7
1	S1.3	2.61 ± 0.08	4.5 ± 0.1	4.3 ± 0.2	30 ± 4	1.4 ± 0.2	0.49 ± 0.06	220 ± 30	61 ± 7
2	S2.1	1.93 ± 0.07	3.8 ± 0.1	4.7 ± 0.2	27 ± 3	1.9 ± 0.2	0.59 ± 0.05	230 ± 20	64 ± 5
2	S2.2	1.21 ± 0.05	3.2 ± 0.1	4.3 ± 0.2	26 ± 3	1.9 ± 0.2	0.59 ± 0.05	230 ± 20	64 ± 5
2	S2.3	1.52 ± 0.07	3.6 ± 0.1	4.8 ± 0.2	28 ± 4	1.9 ± 0.2	0.59 ± 0.05	230 ± 20	64 ± 5
3	S3.1	4.1 ± 0.1	6.7 ± 0.2	4.9 ± 0.2	35 ± 4	1 ± 0.1	0.42 ± 0.06	200 ± 30	50 ± 7
3	S3.2	2.94 ± 0.1	6 ± 0.2	4.7 ± 0.2	34 ± 4	1 ± 0.1	0.42 ± 0.06	200 ± 30	50 ± 7
3	S3.3	4 ± 0.1	6.8 ± 0.2	5.1 ± 0.2	37 ± 5	1 ± 0.1	0.42 ± 0.06	200 ± 30	50 ± 7
4	S4.1	7.1 ± 0.2	3.1 ± 0.1	2.7 ± 0.1	11 ± 2	1.28 ± 0.08	0.18 ± 0.01	26 ± 2	17 ± 1
4	S4.2	9 ± 0.3	4.1 ± 0.1	3.4 ± 0.1	13 ± 2	1.28 ± 0.08	0.18 ± 0.01	26 ± 2	17 ± 1
5	S5.1	8.2 ± 0.3	3.8 ± 0.1	2.66 ± 0.1	11 ± 2	0.9 ± 0.08	0.14 ± 0.01	21 ± 2	14 ± 1
5	S5.2	10.8 ± 0.3	5.1 ± 0.2	3.5 ± 0.1	14 ± 2	0.9 ± 0.08	0.14 ± 0.01	21 ± 2	14 ± 1
6	S6.1	16.5 ± 0.5	8.3 ± 0.3	4.1 ± 0.2	13 ± 2	0.54 ± 0.04	0.095 ± 0.006	12.8 ± 0.8	8.6 ± 0.8
6	S6.2	15.5 ± 0.5	7.9 ± 0.3	3.9 ± 0.1	13 ± 2	0.54 ± 0.04	0.095 ± 0.006	12.8 ± 0.8	8.6 ± 0.8
7	S7.1	16.5 ± 0.5	6.8 ± 0.2	3.6 ± 0.1	9 ± 1	0.75 ± 0.1	0.083 ± 0.008	7.7 ± 0.9	9 ± 1
7	S7.2	17.3 ± 0.6	7 ± 0.2	3.6 ± 0.1	10 ± 2	0.75 ± 0.1	0.083 ± 0.008	7.7 ± 0.9	9 ± 1
7	S7.3	17.7 ± 0.6	7.4 ± 0.2	3.8 ± 0.1	10 ± 2	0.75 ± 0.1	0.083 ± 0.008	7.7 ± 0.9	9 ± 1
8	S8.1	13.4 ± 0.4	7.3 ± 0.2	2.7 ± 0.1	6 ± 2	0.35 ± 0.05	0.059 ± 0.006	6.1 ± 0.7	8.8 ± 0.9
8	S8.2	19.4 ± 0.6	10.6 ± 0.3	3.8 ± 0.1	9 ± 2	0.35 ± 0.05	0.059 ± 0.006	6.1 ± 0.7	8.8 ± 0.9
8	S8.3	23.7 ± 0.8	13.1 ± 0.4	4.8 ± 0.2	11 ± 2	0.35 ± 0.05	0.059 ± 0.006	6.1 ± 0.7	8.8 ± 0.9
9	S9.1	3.7 ± 0.1	3.5 ± 0.1	2.9 ± 0.1	18 ± 3	1.2 ± 0.4	0.4 ± 0.1	80 ± 20	25 ± 6
9	S9.2	2.7 ± 0.1	2.52 ± 0.1	2.24 ± 0.08	14 ± 3	1.2 ± 0.4	0.4 ± 0.1	80 ± 20	25 ± 6
9	S9.3	3.2 ± 0.1	3.5 ± 0.1	3 ± 0.1	19 ± 2	1.2 ± 0.4	0.4 ± 0.1	80 ± 20	25 ± 6
10	S10.1	6.1 ± 0.2	4.5 ± 0.1	3.6 ± 0.1	18 ± 2	1.2 ± 0.2	0.28 ± 0.05	59 ± 10	19 ± 3
10	S10.2	6.1 ± 0.2	4.4 ± 0.1	3.6 ± 0.1	18 ± 3	1.2 ± 0.2	0.28 ± 0.05	59 ± 10	19 ± 3
10	S10.3	6.3 ± 0.2	4.9 ± 0.2	4.1 ± 0.2	20 ± 3	1.2 ± 0.2	0.28 ± 0.05	59 ± 10	19 ± 3

Table F.4: Detailed results for sucrose hydrothermal degradation – Experiments 11 to 20.

Experiment	Sample	Sampling time (min)	t_c (sec)	m_s (g)	m_s (mg)			m^0_{wso} (g)	m^o_{wso} (g)	m_{MeOH} (g)	
				Total	DSO	WSO	Solids			DSO	WSO
11	S11.1	19	92 ± 1	144.759 ± 0.001	51 ± 1	518 ± 3	14 ± 1	228.684 ± 0.001	94.981 ± 0.001	11.12 ± 0.01	29.77 ± 0.01
11	S11.2	23	90 ± 1	141.57 ± 0.001	63 ± 1	507 ± 3	2 ± 1	236.478 ± 0.001	104.083 ± 0.001	22.24 ± 0.01	34.17 ± 0.01
11	S11.3	27	92 ± 1	144.21 ± 0.001	49 ± 1	299 ± 3	5 ± 1	124.995 ± 0.001	67.48 ± 0.001	14.87 ± 0.01	25.38 ± 0.01
12	S12.1	20	90 ± 1	153.585 ± 0.001	44 ± 1	905 ± 3	14 ± 1	222.222 ± 0.002	92.424 ± 0.002	12.67 ± 0.01	41.14 ± 0.01
12	S12.2	22	94 ± 1	159.355 ± 0.001	56 ± 1	819 ± 3	4 ± 6	238.596 ± 0.001	105.399 ± 0.001	21.85 ± 0.01	58.22 ± 0.01
12	S12.3	25	90 ± 1	154.292 ± 0.001	45 ± 1	731 ± 9	5 ± 1	223 ± 2	89.563 ± 0.001	17.82 ± 0.01	35.02 ± 0.01
13	S13.1	22	91 ± 1	135.285 ± 0.001	73 ± 1	390 ± 3	20 ± 1	212.501 ± 0.001	92.528 ± 0.001	17.54 ± 0.01	29.34 ± 0.01
13	S13.2	27	90 ± 1	135.024 ± 0.001	83 ± 1	348 ± 3	8 ± 1	214.311 ± 0.001	98.086 ± 0.001	38.5 ± 0.01	27.71 ± 0.01
13	S13.3	30	90 ± 1	135.343 ± 0.001	88 ± 1	355 ± 4	13 ± 1	202.243 ± 0.001	64.249 ± 0.001	41.99 ± 0.01	19.47 ± 0.01
14	S14.1	21	90 ± 1	147.622 ± 0.001	82 ± 1	724 ± 4	7 ± 1	220.027 ± 0.001	73.434 ± 0.001	21.93 ± 0.01	39.37 ± 0.01
14	S14.2	24	90 ± 1	147.208 ± 0.001	95 ± 1	507 ± 4	7 ± 1	216.902 ± 0.001	79.378 ± 0.001	27.82 ± 0.01	34.46 ± 0.01
14	S14.3	27	90 ± 1	147.63 ± 0.001	96 ± 1	657 ± 5	12 ± 1	212.429 ± 0.001	63.848 ± 0.001	38.55 ± 0.01	28.32 ± 0.01
15	S15.1	18	76 ± 1	133.872 ± 0.001	79 ± 1	845 ± 3	5 ± 1	231.65 ± 0.001	94.97 ± 0.001	11.63 ± 0.01	49.98 ± 0.01
15	S15.2	20	79 ± 1	140.22 ± 0.001	92 ± 1	795 ± 5	6 ± 6	203.625 ± 0.001	62.18 ± 0.001	32.99 ± 0.01	39.47 ± 0.01
15	S15.3	23	75 ± 1	133.221 ± 0.001	95 ± 1	732 ± 4	10 ± 1	219.812 ± 0.001	81.121 ± 0.001	30.4 ± 0.01	35.91 ± 0.01
16	S16.1	21	90 ± 1	136.229 ± 0.001	321 ± 1	1677 ± 4	55 ± 1	240.793 ± 0.001	96.14 ± 0.001	58.88 ± 0.01	79.59 ± 0.01
16	S16.2	26	90 ± 1	136.107 ± 0.001	326 ± 1	2039 ± 4	20 ± 1	169.514 ± 0.001	68.225 ± 0.001	52.55 ± 0.01	103.52 ± 0.01
16	S16.3	31	90 ± 1	135.899 ± 0.001	326 ± 1	1539 ± 3	60 ± 1	248.28 ± 0.001	110.704 ± 0.001	42.94 ± 0.01	75.13 ± 0.01
17	S17.1	20	90 ± 1	147.583 ± 0.001	334 ± 1	3161 ± 3	26 ± 1	219.591 ± 0.002	107.766 ± 0.002	43.2 ± 0.01	161.37 ± 0.01
17	S17.2	23	90 ± 1	147.134 ± 0.001	315 ± 1	3407 ± 3	57 ± 6	180.976 ± 0.001	86.283 ± 0.001	45.32 ± 0.01	168.29 ± 0.01
17	S17.3	26	90 ± 1	147.463 ± 0.001	341 ± 1	3225 ± 3	31 ± 1	214.977 ± 0.001	92.971 ± 0.001	41.43 ± 0.01	140.94 ± 0.01
18	S18.1	19	80 ± 1	142.665 ± 0.001	384 ± 1	3665 ± 3	30 ± 1	218.075 ± 0.001	105.189 ± 0.001	54.81 ± 0.01	189.93 ± 0.01
18	S18.2	21	80 ± 1	142.219 ± 0.001	407 ± 1	3566 ± 3	29 ± 6	214.518 ± 0.001	92.045 ± 0.001	77.91 ± 0.01	172.74 ± 0.01
18	S18.3	23	80 ± 1	142.01 ± 0.001	355 ± 1	3738 ± 4	35 ± 1	231.176 ± 0.001	86.074 ± 0.001	47.8 ± 0.01	149.63 ± 0.01
19	S19.1	22	90 ± 1	142.141 ± 0.001	388 ± 1	1918 ± 3	115 ± 1	239.143 ± 0.001	97.959 ± 0.001	48.79 ± 0.01	93.14 ± 0.01
19	S19.2	26	90 ± 1	143.026 ± 0.001	418 ± 1	1924 ± 2	105 ± 1	233.484 ± 0.001	139.13 ± 0.001	65.74 ± 0.01	127.47 ± 0.01
19	S19.3	28	91 ± 1	142.653 ± 0.001	405 ± 1	1768 ± 3	116 ± 1	259.489 ± 0.001	134.549 ± 0.001	46.47 ± 0.01	104.86 ± 0.01
20	S20.1	23	80 ± 1	137.916 ± 0.001	435 ± 1	2447 ± 3	72 ± 1	199.455 ± 0.001	85.285 ± 0.001	55.12 ± 0.01	115.07 ± 0.01
20	S20.2	25	82 ± 1	140.948 ± 0.001	449 ± 1	2759 ± 3	78 ± 1	212.291 ± 0.001	112.106 ± 0.001	68.21 ± 0.01	149.68 ± 0.01
20	S20.3	27	79 ± 1	136.05 ± 0.001	422 ± 1	2747 ± 3	73 ± 1	233.875 ± 0.001	95.512 ± 0.001	52 ± 0.01	118.46 ± 0.01

Continuation of Table C.10.												
Experiment	Sample	Q^{out} (g/min)	Q^{out} (mg/min)					Yield (g/gSuc%)				
		Outlet	DSO	WSO	TSO	Solids	Volatiles	DSO	WSO	TSO	Solids	Volatiles
11	S11.1	94 ± 1	33.3 ± 1	338 ± 4	371 ± 4	8.9 ± 0.9	340 ± 20	4.6 ± 0.2	47 ± 2	52 ± 2	1.2 ± 0.1	47 ± 2
11	S11.2	22.8 ± 0.7	42 ± 1	338 ± 4	380 ± 4	1.1 ± 0.9	340 ± 20	5.8 ± 0.2	47 ± 2	53 ± 2	0.2 ± 0.1	47 ± 2
11	S11.3	22.8 ± 0.7	32.3 ± 1	195 ± 3	227 ± 3	2.9 ± 0.9	490 ± 20	4.5 ± 0.2	27.2 ± 0.9	31.7 ± 0.9	0.4 ± 0.1	68 ± 1
12	S12.1	29.4 ± 0.9	29.4 ± 1	604 ± 7	633 ± 7	9.5 ± 0.9	280 ± 30	3.2 ± 0.1	65 ± 2	69 ± 2	1 ± 0.1	30 ± 3
12	S12.2	29.4 ± 0.9	35.5 ± 1	522 ± 6	558 ± 6	2 ± 4	360 ± 30	3.8 ± 0.2	57 ± 2	60 ± 2	0.3 ± 0.4	39 ± 3
12	S12.3	29.4 ± 0.9	29.8 ± 1	487 ± 8	517 ± 8	3 ± 0.9	400 ± 30	3.2 ± 0.1	53 ± 2	56 ± 2	0.3 ± 0.1	44 ± 3
13	S13.1	19.6 ± 0.6	48 ± 1	257 ± 4	306 ± 4	12.9 ± 0.9	300 ± 20	7.9 ± 0.3	42 ± 1	50 ± 1	2.1 ± 0.2	48 ± 2
13	S13.2	19.6 ± 0.6	55 ± 1	232 ± 3	287 ± 3	5.3 ± 0.9	320 ± 20	8.9 ± 0.3	38 ± 1	47 ± 1	0.9 ± 0.2	52 ± 2
13	S13.3	19.6 ± 0.6	59 ± 1	237 ± 4	296 ± 4	8.7 ± 0.9	310 ± 20	9.6 ± 0.3	38 ± 1	48 ± 1	1.4 ± 0.2	51 ± 2
14	S14.1	26.1 ± 0.8	55 ± 1	483 ± 6	537 ± 6	4.9 ± 0.9	280 ± 30	6.7 ± 0.2	59 ± 2	65 ± 2	0.6 ± 0.1	34 ± 3
14	S14.2	26.1 ± 0.8	63 ± 1	338 ± 5	401 ± 5	4.5 ± 0.9	420 ± 30	7.7 ± 0.3	41 ± 1	49 ± 1	0.5 ± 0.1	51 ± 2
14	S14.3	26.1 ± 0.8	64 ± 1	438 ± 6	502 ± 6	8 ± 0.9	310 ± 30	7.8 ± 0.3	53 ± 2	61 ± 2	1 ± 0.1	38 ± 3
15	S15.1	32.6 ± 1	63 ± 1	667 ± 9	730 ± 9	4 ± 1	320 ± 30	6 ± 0.2	64 ± 2	69 ± 2	0.4 ± 0.1	30 ± 3
15	S15.2	32.6 ± 1	70 ± 1	604 ± 8	674 ± 9	4 ± 5	370 ± 30	6.7 ± 0.2	57 ± 2	64 ± 2	0.4 ± 0.5	35 ± 3
15	S15.3	32.6 ± 1	76 ± 2	586 ± 8	662 ± 9	8 ± 1	380 ± 30	7.2 ± 0.3	56 ± 2	63 ± 2	0.7 ± 0.1	36 ± 3
16	S16.1	19.6 ± 0.6	214 ± 3	1120 ± 10	1330 ± 10	36 ± 1	630 ± 60	10.7 ± 0.3	56 ± 2	67 ± 2	1.82 ± 0.08	31 ± 3
16	S16.2	19.6 ± 0.6	217 ± 3	1360 ± 20	1580 ± 20	13.1 ± 1	410 ± 60	10.9 ± 0.4	68 ± 2	79 ± 2	0.66 ± 0.05	20 ± 3
16	S16.3	19.6 ± 0.6	217 ± 3	1030 ± 10	1240 ± 10	40 ± 1	710 ± 60	10.9 ± 0.4	51 ± 2	62 ± 2	2.02 ± 0.08	36 ± 2
17	S17.1	26.1 ± 0.8	223 ± 3	2110 ± 20	2330 ± 20	17.5 ± 1	310 ± 90	8.4 ± 0.3	79 ± 3	88 ± 3	0.66 ± 0.04	12 ± 4
17	S17.2	26.1 ± 0.8	210 ± 3	2270 ± 30	2480 ± 30	38 ± 4	140 ± 90	7.9 ± 0.3	85 ± 3	93 ± 3	1.4 ± 0.2	5 ± 4
17	S17.3	26.1 ± 0.8	227 ± 3	2150 ± 20	2380 ± 20	20.7 ± 1	260 ± 90	8.5 ± 0.3	81 ± 3	89 ± 3	0.78 ± 0.04	10 ± 4
18	S18.1	32.6 ± 1	288 ± 4	2750 ± 30	3040 ± 30	23 ± 1	300 ± 100	8.7 ± 0.3	83 ± 3	91 ± 3	0.68 ± 0.04	8 ± 4
18	S18.2	32.6 ± 1	305 ± 4	2670 ± 30	2980 ± 30	22 ± 5	300 ± 100	9.2 ± 0.3	80 ± 3	90 ± 3	0.7 ± 0.1	10 ± 4
18	S18.3	32.6 ± 1	266 ± 3	2800 ± 40	3070 ± 40	26 ± 1	200 ± 100	8 ± 0.3	84 ± 3	92 ± 3	0.79 ± 0.04	7 ± 4
19	S19.1	22.8 ± 0.7	258 ± 3	1280 ± 10	1540 ± 10	76 ± 1	710 ± 70	11.1 ± 0.4	55 ± 2	66 ± 2	3.3 ± 0.1	31 ± 3
19	S19.2	22.8 ± 0.7	279 ± 3	1280 ± 10	1560 ± 10	70 ± 1	700 ± 70	12 ± 0.4	55 ± 2	67 ± 2	3 ± 0.1	30 ± 3
19	S19.3	22.8 ± 0.7	267 ± 3	1170 ± 10	1430 ± 10	77 ± 1	820 ± 70	11.5 ± 0.4	50 ± 2	62 ± 2	3.3 ± 0.1	35 ± 2
20	S20.1	29.4 ± 0.9	326 ± 4	1840 ± 20	2160 ± 20	54 ± 1	780 ± 100	10.9 ± 0.4	61 ± 2	72 ± 2	1.8 ± 0.07	26 ± 3
20	S20.2	29.4 ± 0.9	328 ± 4	2020 ± 20	2350 ± 30	57 ± 1	590 ± 100	11 ± 0.4	67 ± 2	78 ± 2	1.9 ± 0.07	20 ± 3
20	S20.3	29.4 ± 0.9	320 ± 4	2090 ± 30	2410 ± 30	56 ± 1	530 ± 100	10.7 ± 0.4	70 ± 2	80 ± 2	1.86 ± 0.07	18 ± 3

Continuation of Table C.10.													
Experiment	Sample	<i>A</i> _{WSO} (HPLC-RID)				<i>w</i> _{WSO} ^{Water} (ppm)				<i>Q</i> ^{out} (mg/min)			
		Gluc	Fruc	AGluc	Pyr	Gluc	Fruc	AGluc	Pyr	Gluc	Fruc	AGluc	Pyr
11	S11.1	108215	69506	67987	277347	535 ± 5	350 ± 7	374 ± 8	1700 ± 300	80 ± 1	52 ± 1	56 ± 1	250 ± 40
11	S11.2	14366	24013	31345	219917	71 ± 5	121 ± 7	172 ± 5	1300 ± 300	11.2 ± 0.8	19 ± 1	27.2 ± 0.9	210 ± 40
11	S11.3	28570	40310	44052	309468	141 ± 5	203 ± 7	242 ± 5	1900 ± 300	11.5 ± 0.4	16.5 ± 0.6	19.7 ± 0.5	150 ± 20
12	S12.1	33391	49499	47282	351190	165 ± 5	249 ± 7	260 ± 6	2100 ± 300	24.5 ± 0.8	37 ± 1	38.5 ± 0.9	320 ± 40
12	S12.2	25286	39780	37507	286624	125 ± 5	200 ± 7	206 ± 5	1700 ± 300	19 ± 0.8	30 ± 1	31.4 ± 0.9	270 ± 40
12	S12.3	46990	59019	63981	389873	232 ± 5	297 ± 7	352 ± 8	2400 ± 300	34.5 ± 1	44 ± 1	52 ± 1	350 ± 40
13	S13.1	47403	23670	16013	56717	234 ± 5	119 ± 7	88 ± 5	300 ± 300	32.9 ± 0.8	16.7 ± 1	12.3 ± 0.7	50 ± 40
13	S13.2	21677	21553	20404	138303	107 ± 5	109 ± 7	112 ± 5	800 ± 300	15.3 ± 0.8	15.5 ± 1	16 ± 0.8	120 ± 40
13	S13.3	64701	44227	32180	175821	320 ± 5	223 ± 7	177 ± 5	1100 ± 300	43.1 ± 0.9	30 ± 1	23.9 ± 0.8	140 ± 40
14	S14.1	104869	71151	56353	250156	519 ± 5	358 ± 7	310 ± 7	1500 ± 300	76 ± 1	53 ± 1	45 ± 1	220 ± 40
14	S14.2	53838	51616	36148	265466	266 ± 5	260 ± 7	199 ± 5	1600 ± 300	38.5 ± 0.9	38 ± 1	28.7 ± 0.8	230 ± 40
14	S14.3	101975	69927	55632	249934	504 ± 5	352 ± 7	306 ± 7	1500 ± 300	71 ± 1	50 ± 1	43 ± 1	220 ± 40
15	S15.1	218401	126837	76068	311872	1080 ± 10	639 ± 7	418 ± 9	1900 ± 300	198 ± 3	117 ± 2	76 ± 2	350 ± 50
15	S15.2	99272	75779	53086	271386	491 ± 5	381 ± 7	292 ± 6	1700 ± 300	76 ± 1	59 ± 1	45 ± 1	260 ± 40
15	S15.3	135661	88902	56991	256515	671 ± 7	448 ± 7	313 ± 7	1600 ± 300	118 ± 2	79 ± 2	55 ± 1	280 ± 50
16	S16.1	759129	216723	138136	276670	3750 ± 40	1090 ± 10	760 ± 20	1700 ± 300	603 ± 9	175 ± 3	122 ± 3	270 ± 40
16	S16.2	527062	147256	93650	189268	2610 ± 30	741 ± 7	510 ± 10	1200 ± 300	295 ± 4	84 ± 1	58 ± 1	130 ± 30
16	S16.3	636743	184376	114804	229295	3150 ± 30	928 ± 9	630 ± 10	1400 ± 300	521 ± 8	154 ± 2	104 ± 3	230 ± 40
17	S17.1	1372478	625553	214837	325911	6790 ± 70	3150 ± 30	1180 ± 30	2000 ± 300	990 ± 10	461 ± 7	173 ± 4	290 ± 40
17	S17.2	1087375	495123	161958	241091	5380 ± 50	2490 ± 30	890 ± 20	1500 ± 300	649 ± 10	301 ± 5	107 ± 3	180 ± 30
17	S17.3	1002809	463664	151684	226789	4960 ± 50	2330 ± 20	830 ± 20	1400 ± 300	710 ± 10	335 ± 5	120 ± 3	200 ± 40
18	S18.1	1093590	502425	184728	321739	5410 ± 50	2530 ± 30	1020 ± 20	2000 ± 300	880 ± 10	414 ± 7	166 ± 4	320 ± 40
18	S18.2	1148109	537350	195158	337072	5680 ± 60	2710 ± 30	1070 ± 20	2100 ± 300	910 ± 10	435 ± 7	173 ± 4	330 ± 40
18	S18.3	917533	425566	157311	271787	4540 ± 50	2140 ± 20	860 ± 20	1700 ± 300	790 ± 10	371 ± 6	150 ± 4	290 ± 50
19	S19.1	285140	115068	87902	278682	1410 ± 10	579 ± 7	480 ± 10	1700 ± 300	225 ± 3	92 ± 1	77 ± 2	270 ± 40
19	S19.2	310692	139861	97834	324243	1540 ± 20	704 ± 7	540 ± 10	2000 ± 300	239 ± 4	110 ± 2	84 ± 2	310 ± 40
19	S19.3	427363	190135	132217	413683	2110 ± 20	957 ± 10	730 ± 20	2500 ± 300	362 ± 5	164 ± 2	124 ± 3	430 ± 50
20	S20.1	694771	264303	169646	495998	3440 ± 30	1330 ± 10	930 ± 20	3000 ± 400	514 ± 8	199 ± 3	140 ± 3	450 ± 60
20	S20.2	631105	245194	152301	432113	3120 ± 30	1230 ± 10	840 ± 20	2600 ± 300	485 ± 8	192 ± 3	130 ± 3	410 ± 50
20	S20.3	456833	169714	112877	326539	2260 ± 20	854 ± 9	620 ± 10	2000 ± 300	401 ± 7	152 ± 2	110 ± 3	350 ± 50

Continuation of Table C.10.							
Experiment	Sample	<i>A_{DSO}</i> (GC-FID)		<i>A_{WSO}</i> (GC-FID)	<i>w</i> _{5-HMF^{MetOH}} (ppm)		<i>Q</i> ^{out} (mg/min)
		5-HDF	5-HMF	5-HDF	DSO	WSO	5-HMF
11	S11.1	881654	9635	49300	0.26 ± 0.02	-	19 ± 1
11	S11.2	588431	-	53702	0.22 ± 0.02	-	30 ± 2
11	S11.3	588924	1523	73670	0.22 ± 0.02	-	21 ± 2
12	S12.1	631863	-	36381	0.22 ± 0.02	-	19 ± 1
12	S12.2	518975	1124	42854	0.21 ± 0.02	-	29 ± 2
12	S12.3	442207	-	60484	0.19 ± 0.02	-	23 ± 2
13	S13.1	1337712	-	77103	0.33 ± 0.02	-	39 ± 2
13	S13.2	638186	1038	144752	0.22 ± 0.02	0.15 ± 0.02	85 ± 5
13	S13.3	424426	1134	100116	0.19 ± 0.02	0.14 ± 0.02	72 ± 5
14	S14.1	880669	-	58424	0.26 ± 0.02	-	38 ± 2
14	S14.2	980078	1402	972198	0.28 ± 0.02	0.28 ± 0.02	115 ± 5
14	S14.3	602301	-	93828	0.22 ± 0.02	0.14 ± 0.02	82 ± 5
15	S15.1	2188113	4705	61868	0.47 ± 0.02	-	43 ± 2
15	S15.2	896274	1155	186864	0.26 ± 0.02	0.15 ± 0.02	112 ± 7
15	S15.3	724493	-	94415	0.24 ± 0.02	0.14 ± 0.02	98 ± 6
16	S16.1	2615486	-	234172	0.53 ± 0.02	0.16 ± 0.02	290 ± 10
16	S16.2	2149806	5944	340220	0.46 ± 0.02	0.18 ± 0.02	280 ± 10
16	S16.3	3485827	10180	368761	0.67 ± 0.02	0.18 ± 0.02	282 ± 10
17	S17.1	2442972	700436	244757	0.74 ± 0.02	0.16 ± 0.02	390 ± 20
17	S17.2	2688272	22715	180006	0.55 ± 0.02	0.15 ± 0.02	340 ± 20
17	S17.3	3880339	53022	316684	0.73 ± 0.02	0.17 ± 0.02	370 ± 20
18	S18.1	3035177	26862	72371	0.6 ± 0.02	-	247 ± 7
18	S18.2	1487096	-	133225	0.36 ± 0.02	0.14 ± 0.02	400 ± 20
18	S18.3	2723501	207594	157741	0.71 ± 0.02	0.15 ± 0.02	420 ± 20
19	S19.1	2815871	2029	357979	0.57 ± 0.02	0.18 ± 0.02	300 ± 10
19	S19.2	441760	191449	298842	0.35 ± 0.02	0.17 ± 0.02	300 ± 20
19	S19.3	3042555	1368	294897	0.6 ± 0.02	0.17 ± 0.02	300 ± 10
20	S20.1	2463039	165140	283652	0.66 ± 0.02	0.17 ± 0.02	420 ± 20
20	S20.2	1984015	1642	264465	0.44 ± 0.02	0.17 ± 0.02	400 ± 20
20	S20.3	447921	590248	345516	0.41 ± 0.02	0.18 ± 0.02	320 ± 20

Continuation of Table C.10.										
Experiment	Sample	Yield (g/g _{Suc} %)							Yield (g/g _{Suc} ppm)	
		Gluc	Fruc	AGluc	Pyr	5-HMF	CO ₂	CO	CH ₄	C ₂ H ₄
12	S12.1	2.6 ± 0.1	4 ± 0.2	4.2 ± 0.2	34 ± 4	2 ± 0.2	0.8 ± 0.2	0.36 ± 0.04	170 ± 20	78 ± 8
12	S12.2	2.1 ± 0.1	3.3 ± 0.2	3.4 ± 0.1	29 ± 5	3.1 ± 0.3	0.8 ± 0.2	0.36 ± 0.04	170 ± 20	78 ± 8
12	S12.3	3.7 ± 0.2	4.8 ± 0.2	5.7 ± 0.2	38 ± 5	2.5 ± 0.2	0.8 ± 0.2	0.36 ± 0.04	170 ± 20	78 ± 8
13	S13.1	5.3 ± 0.2	2.7 ± 0.2	2 ± 0.1	8 ± 6	6.3 ± 0.4	1.8 ± 0.3	0.36 ± 0.05	90 ± 10	45 ± 6
13	S13.2	2.5 ± 0.1	2.5 ± 0.2	2.6 ± 0.1	20 ± 6	13.8 ± 0.9	1.8 ± 0.3	0.36 ± 0.05	90 ± 10	45 ± 6
13	S13.3	7 ± 0.3	4.9 ± 0.2	3.9 ± 0.2	23 ± 6	11.6 ± 0.9	1.8 ± 0.3	0.36 ± 0.05	90 ± 10	45 ± 6
14	S14.1	9.3 ± 0.3	6.4 ± 0.2	5.5 ± 0.2	27 ± 5	4.7 ± 0.3	1.1 ± 0.2	0.28 ± 0.04	80 ± 10	37 ± 5
14	S14.2	4.7 ± 0.2	4.6 ± 0.2	3.5 ± 0.1	29 ± 5	14 ± 0.7	1.1 ± 0.2	0.28 ± 0.04	80 ± 10	37 ± 5
14	S14.3	8.7 ± 0.3	6.1 ± 0.2	5.3 ± 0.2	26 ± 5	10 ± 0.7	1.1 ± 0.2	0.28 ± 0.04	80 ± 10	37 ± 5
15	S15.1	18.8 ± 0.6	11.1 ± 0.4	7.3 ± 0.3	33 ± 5	4.1 ± 0.2	0.7 ± 0.1	0.22 ± 0.02	62 ± 6	28 ± 2
15	S15.2	7.2 ± 0.2	5.6 ± 0.2	4.3 ± 0.2	24 ± 4	10.7 ± 0.7	0.7 ± 0.1	0.22 ± 0.02	62 ± 6	28 ± 2
15	S15.3	11.2 ± 0.4	7.5 ± 0.3	5.2 ± 0.2	26 ± 5	9.3 ± 0.6	0.7 ± 0.1	0.22 ± 0.02	62 ± 6	28 ± 2
16	S16.1	30 ± 1	8.8 ± 0.3	6.1 ± 0.2	14 ± 2	14.8 ± 0.7	0.91 ± 0.07	0.108 ± 0.008	8.8 ± 0.6	8.3 ± 0.5
16	S16.2	14.8 ± 0.5	4.2 ± 0.1	2.9 ± 0.1	7 ± 2	14.2 ± 0.7	0.91 ± 0.07	0.108 ± 0.008	8.8 ± 0.6	8.3 ± 0.5
16	S16.3	26.1 ± 0.9	7.7 ± 0.3	5.2 ± 0.2	12 ± 2	14.2 ± 0.6	0.91 ± 0.07	0.108 ± 0.008	8.8 ± 0.6	8.3 ± 0.5
17	S17.1	37 ± 1	17.3 ± 0.6	6.5 ± 0.3	11 ± 2	14.6 ± 0.8	0.39 ± 0.1	0.05 ± 0.01	4.1 ± 0.9	6 ± 1
17	S17.2	24.4 ± 0.8	11.3 ± 0.4	4 ± 0.2	7 ± 1	12.6 ± 0.8	0.39 ± 0.1	0.05 ± 0.01	4.1 ± 0.9	6 ± 1
17	S17.3	26.7 ± 0.9	12.6 ± 0.4	4.5 ± 0.2	7 ± 1	13.7 ± 0.7	0.39 ± 0.1	0.05 ± 0.01	4.1 ± 0.9	6 ± 1
18	S18.1	26.6 ± 0.9	12.4 ± 0.4	5 ± 0.2	10 ± 1	7.4 ± 0.3	0.35 ± 0.05	0.054 ± 0.007	5 ± 0.7	5.9 ± 0.8
18	S18.2	27.5 ± 0.9	13.1 ± 0.4	5.2 ± 0.2	10 ± 1	11.9 ± 0.8	0.35 ± 0.05	0.054 ± 0.007	5 ± 0.7	5.9 ± 0.8
18	S18.3	23.7 ± 0.8	11.2 ± 0.4	4.5 ± 0.2	9 ± 1	12.6 ± 0.7	0.35 ± 0.05	0.054 ± 0.007	5 ± 0.7	5.9 ± 0.8
19	S19.1	9.7 ± 0.3	4 ± 0.1	3.3 ± 0.1	12 ± 2	12.7 ± 0.6	1.2 ± 0.2	0.26 ± 0.04	27 ± 4	12 ± 2
19	S19.2	10.3 ± 0.3	4.7 ± 0.2	3.6 ± 0.1	13 ± 2	12.8 ± 0.8	1.2 ± 0.2	0.26 ± 0.04	27 ± 4	12 ± 2
19	S19.3	15.5 ± 0.5	7 ± 0.2	5.3 ± 0.2	19 ± 2	13 ± 0.6	1.2 ± 0.2	0.26 ± 0.04	27 ± 4	12 ± 2
20	S20.1	17.2 ± 0.6	6.7 ± 0.2	4.7 ± 0.2	15 ± 2	14 ± 0.7	0.7 ± 0.08	0.17 ± 0.02	17 ± 2	10 ± 1
20	S20.2	16.2 ± 0.5	6.4 ± 0.2	4.3 ± 0.2	14 ± 2	13.3 ± 0.7	0.7 ± 0.08	0.17 ± 0.02	17 ± 2	10 ± 1
20	S20.3	13.4 ± 0.5	5.1 ± 0.2	3.7 ± 0.1	12 ± 2	10.8 ± 0.6	0.7 ± 0.08	0.17 ± 0.02	17 ± 2	10 ± 1

F.3 Averaged results

Table F.5: Averaged yields for sucrose hydrothermal processing.

Experiment	Yield (g/g _{suc} %)												Yield (g/g _{suc} ppm)	
	DSO	WSO	TSO	Solids	Volatiles	Gluc	Fruc	AGluc	Pyr	5-HMF	CO ₂	CO	CH ₄	C ₂ H ₄
1	4.8 ± 0.4	40 ± 30	50 ± 30	0.3 ± 0.3	50 ± 30	2.3 ± 0.4	4.3 ± 0.3	4.2 ± 0.2	29 ± 4	4.8 ± 0.4	1.4 ± 0.2	0.49 ± 0.06	220 ± 30	61 ± 7
2	8.5 ± 0.6	40 ± 40	50 ± 40	1.2 ± 0.4	50 ± 40	1.4 ± 0.2	3.4 ± 0.3	4.5 ± 0.4	27 ± 4	8.5 ± 0.6	1.9 ± 0.2	0.59 ± 0.05	230 ± 20	64 ± 5
3	3.8 ± 0.1	60 ± 20	60 ± 20	0.5 ± 0.2	40 ± 20	3.5 ± 0.7	6.4 ± 0.6	4.9 ± 0.2	36 ± 5	3.8 ± 0.1	1 ± 0.1	0.42 ± 0.06	200 ± 30	50 ± 7
4	11.3 ± 0.4	52 ± 2	63 ± 2	2.1 ± 0.1	35 ± 2	7.1 ± 0.2	3.1 ± 0.1	2.7 ± 0.1	11 ± 2	11.3 ± 0.4	1.28 ± 0.08	0.18 ± 0.01	26 ± 2	17 ± 1
5	9.6 ± 0.3	64 ± 2	73 ± 2	1.5 ± 0.3	25 ± 2	8.2 ± 0.3	3.8 ± 0.1	2.7 ± 0.1	11 ± 2	9.6 ± 0.3	0.9 ± 0.08	0.14 ± 0.01	21 ± 2	14 ± 1
6	7.8 ± 0.2	75 ± 2	83 ± 2	0.8 ± 0.2	16 ± 2	16.5 ± 0.5	8.3 ± 0.3	4.1 ± 0.2	13 ± 2	7.8 ± 0.2	0.54 ± 0.04	0.095 ± 0.006	12.8 ± 0.8	8.6 ± 0.8
7	9 ± 1	64 ± 4	73 ± 5	1 ± 0.1	26 ± 5	16.9 ± 0.6	6.9 ± 0.2	3.6 ± 0.1	9 ± 2	9 ± 1	0.7 ± 0.1	0.083 ± 0.008	7.7 ± 0.9	9 ± 1
8	7.3 ± 0.2	87 ± 6	94 ± 6	0.71 ± 0.06	5 ± 6	16 ± 4	9 ± 2	3.3 ± 0.8	8 ± 2	7.3 ± 0.2	0.35 ± 0.05	0.059 ± 0.006	6.1 ± 0.7	8.8 ± 0.9
9	9.6 ± 0.3	49 ± 2	59 ± 2	1.7 ± 0.3	39 ± 2	3.2 ± 0.7	3 ± 0.7	2.6 ± 0.5	16 ± 3	9.6 ± 0.3	1.2 ± 0.4	0.4 ± 0.1	80 ± 20	25 ± 6
10	8.6 ± 0.7	62 ± 4	70 ± 3	1.4 ± 0.3	28 ± 3	6.1 ± 0.2	4.4 ± 0.1	3.6 ± 0.1	18 ± 3	8.6 ± 0.7	1.2 ± 0.2	0.28 ± 0.05	60 ± 10	19 ± 3
11	5.2 ± 0.9	40 ± 10	40 ± 20	0.3 ± 0.2	60 ± 10	1.6 ± 0.1	2.5 ± 0.2	3.3 ± 0.7	25 ± 6	3.5 ± 0.3	-	-	-	-
12	3.5 ± 0.5	61 ± 6	64 ± 6	0.6 ± 0.5	35 ± 6	2.4 ± 0.4	3.6 ± 0.5	3.8 ± 0.5	32 ± 5	2.6 ± 0.3	0.8 ± 0.2	0.36 ± 0.04	170 ± 20	78 ± 8
13	9 ± 1	40 ± 2	49 ± 1	1.8 ± 0.5	49 ± 2	6 ± 1	4 ± 2	3 ± 1	20 ± 10	8.9 ± 0.9	1.8 ± 0.3	0.36 ± 0.05	90 ± 10	45 ± 6
14	7.2 ± 0.8	56 ± 4	63 ± 3	0.8 ± 0.3	36 ± 3	9 ± 0.4	6.2 ± 0.2	5.4 ± 0.2	27 ± 5	7.3 ± 0.7	1.1 ± 0.2	0.28 ± 0.04	80 ± 10	37 ± 5
15	6.6 ± 0.9	60 ± 5	66 ± 5	0.6 ± 0.3	33 ± 4	15 ± 5	9 ± 3	6 ± 1	30 ± 5	6.7 ± 0.6	0.7 ± 0.1	0.22 ± 0.02	62 ± 6	28 ± 2
16	10.8 ± 0.6	54 ± 3	65 ± 3	1.9 ± 0.1	34 ± 3	28 ± 3	8.2 ± 0.8	5.7 ± 0.6	13 ± 2	14.5 ± 0.7	46 ± 0.07	0.108 ± 0.008	8.8 ± 0.6	8.3 ± 0.5
17	8.5 ± 0.8	80 ± 3	88 ± 3	0.72 ± 0.08	11 ± 4	32 ± 8	15 ± 3	5 ± 1	9 ± 2	14.2 ± 0.8	0.4 ± 0.1	0.05 ± 0.01	4.1 ± 0.9	6 ± 1
18	8.6 ± 0.8	82 ± 3	91 ± 3	0.7 ± 0.1	8 ± 4	26 ± 3	12 ± 1	4.9 ± 0.5	9 ± 1	12.3 ± 0.8	0.35 ± 0.05	0.054 ± 0.007	5 ± 0.7	5.9 ± 0.8
19	11.5 ± 0.8	55 ± 2	67 ± 2	3.1 ± 0.2	30 ± 3	10 ± 0.4	4.3 ± 0.5	3.5 ± 0.2	12 ± 2	12.7 ± 0.8	1.2 ± 0.2	0.26 ± 0.04	27 ± 4	12 ± 2
20	10.9 ± 0.7	64 ± 4	75 ± 4	1.85 ± 0.07	23 ± 4	16.7 ± 0.7	6.5 ± 0.2	4.5 ± 0.2	14 ± 2	13.6 ± 0.7	0.7 ± 0.08	0.17 ± 0.02	17 ± 2	10 ± 1

Table F.6: Averaged fractional values for sucrose hydrothermal processing.

Experiment	Fraction of TSO (g/g _{TSO} %)					Fraction of Volatiles (g/g _{Volatiles} %)		Fraction of Volatiles (g/ g _{Volatiles} ppm)	
	Gluc	Fruc	AGluc	Pyr	5-HMF	CO ₂	CO	CH ₄	C ₂ H ₄
1	5 ± 3	9 ± 6	9 ± 6	60 ± 40	-	3 ± 2	0.9 ± 0.7	400 ± 300	110 ± 90
2	3 ± 2	7 ± 6	10 ± 8	60 ± 50	-	4 ± 4	1 ± 1	400 ± 500	100 ± 100
3	6 ± 3	11 ± 4	8 ± 3	60 ± 30	-	2 ± 2	1 ± 0.9	500 ± 400	100 ± 100
4	11.2 ± 0.5	5 ± 0.2	4.3 ± 0.2	17 ± 3	-	3.7 ± 0.4	0.52 ± 0.05	74 ± 8	49 ± 5
5	11.2 ± 0.5	5.2 ± 0.2	3.6 ± 0.2	14 ± 3	-	3.6 ± 0.5	0.57 ± 0.08	80 ± 10	57 ± 8
6	20 ± 0.9	10 ± 0.4	4.9 ± 0.2	16 ± 3	-	3.3 ± 0.7	0.6 ± 0.1	80 ± 20	50 ± 10
7	23 ± 1	9.4 ± 0.4	4.9 ± 0.2	13 ± 3	-	2.9 ± 0.6	0.33 ± 0.06	30 ± 6	34 ± 7
8	18 ± 6	10 ± 3	4 ± 1	8 ± 3	-	0 ± 200	0 ± 30	0 ± 3000	1000 ± 4000
9	5 ± 1	5 ± 1	4.3 ± 0.7	27 ± 5	-	3 ± 1	0.9 ± 0.3	190 ± 60	60 ± 20
10	8.7 ± 0.4	6.3 ± 0.3	5.1 ± 0.2	26 ± 4	-	4.3 ± 0.8	1 ± 0.2	210 ± 40	70 ± 10
11	4 ± 1	6 ± 2	8 ± 1	60 ± 10	8.5 ± 0.4	2.8 ± 0.4	0.8 ± 0.1	220 ± 30	#NUM!
12	3.6 ± 0.3	5.6 ± 0.4	5.9 ± 0.4	49 ± 8	4.1 ± 0.2	2.3 ± 0.6	1 ± 0.2	500 ± 90	230 ± 40
13	13 ± 3	8 ± 3	6 ± 3	30 ± 20	18 ± 1	3.7 ± 0.6	0.7 ± 0.1	170 ± 30	90 ± 10
14	14.2 ± 0.8	9.9 ± 0.6	8.5 ± 0.5	42 ± 8	11.8 ± 0.7	3 ± 0.6	0.8 ± 0.1	220 ± 40	100 ± 20
15	22 ± 7	14 ± 3	9 ± 2	45 ± 8	10.3 ± 0.8	2.2 ± 0.4	0.7 ± 0.1	190 ± 30	80 ± 10
16	44 ± 3	12.8 ± 0.7	8.8 ± 0.5	19 ± 4	22 ± 1	2.7 ± 0.3	0.32 ± 0.04	26 ± 3	25 ± 3
17	36 ± 9	17 ± 4	6 ± 2	10 ± 3	16 ± 0.7	4 ± 2	0.5 ± 0.2	40 ± 20	60 ± 30
18	28 ± 4	13 ± 2	5.3 ± 0.6	10 ± 2	13.5 ± 0.7	4 ± 3	0.7 ± 0.4	60 ± 40	70 ± 40
19	15 ± 0.9	6.5 ± 0.7	5.2 ± 0.3	19 ± 3	19.1 ± 0.9	3.9 ± 0.7	0.9 ± 0.2	90 ± 20	40 ± 7
20	22 ± 2	8.7 ± 0.7	6 ± 0.6	19 ± 3	18.2 ± 0.9	3.1 ± 0.7	0.8 ± 0.2	80 ± 20	50 ± 10

F.4 Progression of the parameter estimation workflow

This section summarises the individual parameter estimation processes performed while progressing along the workflow in Figure 8.18 of Section 8.5.2. Table F.7 contains: (1) the reactions included in each parameter estimation; (2) which reactions include $[H^+]$ in the rate equation; (3) the estimation objective function; (4) an evaluation of the quality of the estimated parameters compared to the associated standard deviation; and (5) a decision regarding the progression along the workflow. As referred in Section 4.13, the objective function (OF) represented how close predicted values are to the experimental inputs. Therefore, the parameter estimation process calculated the kinetic parameters that minimise the objective function. Evaluation (4) determined if any parameter or reaction should be removed from the reaction network at that point due to overparameterization, *i.e.*, the estimated parameters being smaller than the associated standard deviation. The decision (5) resulted from an effective reduction in (3), and favourable evaluation in (4).

Table F.7: Reactions included, objective function, and progression comments for each parameter estimation.

Parameter estimation	Reaction (X: included; H+: included and accounts for $[H^+]$; - : excluded)																OF	Standard deviations smaller than estimated values?	Progress decision
	1	2	3	4	5	6	7	8	9	10	11	12	13	14	15	16			
1.1.1	-	-	X	X	-	-	-	-	-	-	-	-	-	-	-	-	2733	Yes	Estimation 1.1.3 progresses.
1.1.2	-	-	H+	X	-	-	-	-	-	-	-	-	-	-	-	-	2771	Yes	
1.1.3	-	-	X	H+	-	-	-	-	-	-	-	-	-	-	-	-	2712	Yes	
1.1.4	-	-	H+	H+	-	-	-	-	-	-	-	-	-	-	-	-	2749	Yes	
1.2.1	X	-	-	X	-	-	-	-	-	-	-	-	-	-	-	-	2755	Yes	Estimation 1.2.3 replaces previous.
1.2.2	H+	-	-	X	-	-	-	-	-	-	-	-	-	-	-	-	2787	Yes	
1.2.3	X	-	-	H+	-	-	-	-	-	-	-	-	-	-	-	-	2671	Yes	
1.2.4	H+	-	-	H+	-	-	-	-	-	-	-	-	-	-	-	-	2736	Yes	
1.3.1	-	X	X	-	-	-	-	-	-	-	-	-	-	-	-	-	2732	Yes	Estimation 1.2.3 replaces remains.
1.3.2	-	H+	X	-	-	-	-	-	-	-	-	-	-	-	-	-	2739	Yes	
1.3.3	-	X	H+	-	-	-	-	-	-	-	-	-	-	-	-	-	2788	Yes	
1.3.4	-	H+	H+	-	-	-	-	-	-	-	-	-	-	-	-	-	2839	Yes	
2.1	X	-	-	H+	X	-	-	-	-	-	-	-	-	-	-	-	2594	Yes	Estimation 2.2 progresses.
2.2	X	-	-	H+	H+	-	-	-	-	-	-	-	-	-	-	-	2528	Yes	
2.3	X	-	-	H+	-	X	-	-	-	-	-	-	-	-	-	-	2680	Yes	
2.4	X	-	-	H+	-	H+	-	-	-	-	-	-	-	-	-	-	2585	Yes	
2.5	X	-	-	H+	-	-	X	-	-	-	-	-	-	-	-	-	2826	Yes	
2.6	X	-	-	H+	-	-	H+	-	-	-	-	-	-	-	-	-	2695	Yes	

Continuation of Table F.1.																			
Parameter estimation	Reaction (X: included; H+: included and accounts for $[H^+]$; - : excluded)																OF	Standard deviations smaller than estimated values?	Progress decision
	1	2	3	4	5	6	7	8	9	10	11	12	13	14	15	16			
3.1	X	-	-	H+	H+	-	-	X	-	-	-	-	-	-	-	-	533	Yes	Estimation 3.1: Best fitted unidirectional simplified pathway.
3.2	X	-	-	H+	H+	-	-	H+	-	-	-	-	-	-	-	-	545	Yes	
3.3	X	-	-	H+	H+	-	-	-	X	-	-	-	-	-	-	-	634	<i>Ea</i> removed	
3.4	X	-	-	H+	H+	-	-	-	H+	-	-	-	-	-	-	-	656	<i>Ea</i> removed	
3.5	X	-	-	H+	H+	-	-	-	-	X	-	-	-	-	-	-	598	Yes	
3.6	X	-	-	H+	H+	-	-	-	-	H+	-	-	-	-	-	-	580	Yes	
4.1	X	-	-	H+	H+	-	-	X	-	-	X	X	-	-	-	-	654	Reaction removed	Estimation 4.2 progresses.
4.2	X	-	-	H+	H+	-	-	X	-	-	H+	X	-	-	-	-	582	Reaction removed	
4.3	X	-	-	H+	H+	-	-	X	-	-	X	H+	-	-	-	-	654	Reaction removed	
4.4	X	-	-	H+	H+	-	-	X	-	-	H+	H+	-	-	-	-	582	Reaction removed	
5.1	X	-	-	H+	H+	-	-	X	-	-	H+	X	X	X	-	-	686	<i>Ea</i> removed	Estimation 5.3 progresses.
5.2	X	-	-	H+	H+	-	-	X	-	-	H+	X	H+	X	-	-	837	<i>Ea</i> removed	
5.3	X	-	-	H+	H+	-	-	X	-	-	H+	X	X	H+	-	-	655	Yes	
5.4	X	-	-	H+	H+	-	-	X	-	-	H+	X	H+	H+	-	-	724	Yes	
6.1	X	-	-	H+	H+	-	-	X	-	-	H+	X	X	H+	X	X	694	Reaction removed	Estimation 6.1: Best fitted unidirectional pathway.
6.2	X	-	-	H+	H+	-	-	X	-	-	H+	X	X	H+	H+	X	698	Unfinished	
6.3	X	-	-	H+	H+	-	-	X	-	-	H+	X	X	H+	X	H+	694	Reaction removed	
6.4	X	-	-	H+	H+	-	-	X	-	-	H+	X	X	H+	H+	H+	695	<i>Ea</i> removed	

Continuation of Table F.1.																			
Parameter estimation	Reaction (X: included; H+: included and accounts for $[H^+]$; - : excluded)																OF	Standard deviations smaller than estimated values?	Progress decision
	1	2	3	4	5	6	7	8	9	10	11	12	13	14	15	16			
7.1	H+	-	-	H+	H+	-	-	X	-	-	H+	X	X	H+	X	X	727	Unfinished	Estimation 7.6: Best fitted statistically significant pathway.
7.2	X	-	-	X	H+	-	-	X	-	-	H+	X	X	H+	X	X	767	Unfinished	
7.3	X	-	-	H+	X	-	-	X	-	-	H+	X	X	H+	X	X	726	Unfinished	
7.4	X	-	-	H+	H+	-	-	H+	-	-	H+	X	X	H+	X	X	709	Unfinished	
7.5	X	-	-	H+	H+	-	-	X	-	-	X	X	X	H+	X	X	709	Unfinished	
7.6	X	-	-	H+	H+	-	-	X	-	-	H+	H+	X	H+	X	X	693	Reaction removed	
7.7	X	-	-	H+	H+	-	-	X	-	-	H+	X	H+	H+	X	X	715	Unfinished	
7.8	X	-	-	H+	H+	-	-	X	-	-	H+	X	X	X	X	X	722	Unfinished	
7.9	X	-	-	H+	H+	-	-	X	-	-	H+	X	H+	H+	H+	X	698	Unfinished	
7.10	X	-	-	H+	H+	-	-	X	-	-	H+	X	X	H+	X	H+	694	Yes	
8.1	X	X	-	H+	H+	-	-	X	-	-	H+	H+	X	H+	X	X	684	No	Estimation 8.2: Best fitted pathway.
8.2	X	H+	-	H+	H+	-	-	X	-	-	H+	H+	X	H+	X	X	679	No	
8.3	X	-	X	H+	H+	-	-	X	-	-	H+	H+	X	H+	X	X	692	Ineffective	
8.4	X	-	H+	H+	H+	-	-	X	-	-	H+	H+	X	H+	X	X	692	Ineffective	
8.5	X	-	-	H+	H+	X	-	X	-	-	H+	H+	X	H+	X	X	692	Ineffective	
8.6	X	-	-	H+	H+	H+	-	X	-	-	H+	H+	X	H+	X	X	692	Ineffective	
8.7	X	-	-	H+	H+	-	X	X	-	-	H+	H+	X	H+	X	X	692	Ineffective	
8.8	X	-	-	H+	H+	-	H+	X	-	-	H+	H+	X	H+	X	X	692	Ineffective	
8.9	X	-	-	H+	H+	-	-	X	X	-	H+	H+	X	H+	X	X	692	Ineffective	
8.10	X	-	-	H+	H+	-	-	X	H+	-	H+	H+	X	H+	X	X	692	Ineffective	
8.11	X	-	-	H+	H+	-	-	X	-	X	H+	H+	X	H+	X	X	692	Ineffective	
8.12	X	-	-	H+	H+	-	-	X	-	H+	H+	H+	X	H+	X	X	692	Ineffective	

Continuation of Table F.1.																			
Parameter estimation	Reaction (X: included; H+: included and accounts for $[H^+]$; - : excluded)																OF	Standard deviations smaller than estimated values?	Progress decision
	1	2	3	4	5	6	7	8	9	10	11	12	13	14	15	16			
9.1	H+	H+	-	H+	H+	-	-	X	-	-	H+	H+	X	H+	X	X	708	Unfinished	Estimation 9.11: Best fitted pathway (update).
9.2	X	X	-	H+	H+	-	-	X	-	-	H+	H+	X	H+	X	X	684	No	
9.3	X	H+	-	X	H+	-	-	X	-	-	H+	H+	X	H+	X	X	730	Unfinished	
9.4	X	H+	-	H+	X	-	-	X	-	-	H+	H+	X	H+	X	X	709	Unfinished	
9.5	X	H+	-	H+	H+	-	-	H+	-	-	H+	H+	X	H+	X	X	694	Unfinished	
9.6	X	H+	-	H+	H+	-	-	X	-	-	X	H+	X	H+	X	X	690	Unfinished	
9.7	X	H+	-	H+	H+	-	-	X	-	-	H+	X	X	H+	X	X	679	Unfinished	
9.8	X	H+	-	H+	H+	-	-	X	-	-	H+	H+	H+	H+	X	X	708	Unfinished	
9.9	X	H+	-	H+	H+	-	-	X	-	-	H+	H+	X	X	X	X	689	Unfinished	
9.10	X	H+	-	H+	H+	-	-	X	-	-	H+	H+	X	H+	H+	X	684	Unfinished	
9.11	X	H+	-	H+	H+	-	-	X	-	-	H+	H+	X	H+	X	H+	678	No	
10.1	X	H+	X	H+	H+	-	-	X	-	-	H+	H+	X	H+	X	H+	678	Ineffective	No update.
10.2	X	H+	H+	H+	H+	-	-	X	-	-	H+	H+	X	H+	X	H+	678	Ineffective	
10.3	X	H+	-	H+	H+	X	-	X	-	-	H+	H+	X	H+	X	H+	678	Ineffective	
10.4	X	H+	-	H+	H+	H+	-	X	-	-	H+	H+	X	H+	X	H+	678	Ineffective	
10.5	X	H+	-	H+	H+	-	X	X	-	-	H+	H+	X	H+	X	H+	678	Ineffective	
10.6	X	H+	-	H+	H+	-	H+	X	-	-	H+	H+	X	H+	X	H+	678	Ineffective	
10.7	X	H+	-	H+	H+	-	-	X	X	-	H+	H+	X	H+	X	H+	678	Ineffective	
10.8	X	H+	-	H+	H+	-	-	X	H+	-	H+	H+	X	H+	X	H+	678	Ineffective	
10.9	X	H+	-	H+	H+	-	-	X	-	X	H+	H+	X	H+	X	H+	678	Ineffective	
10.10	X	H+	-	H+	H+	-	-	X	-	H+	H+	H+	X	H+	X	H+	678	Ineffective	

Continuation of Table F.1.																			
Parameter estimation	Reaction (X: included; H+: included and accounts for $[H^+]$; - : excluded)																OF	Standard deviations smaller than estimated values?	Progress decision
	1	2	3	4	5	6	7	8	9	10	11	12	13	14	15	16			
11.1	H+	H+	-	H+	H+	-	-	X	-	-	H+	H+	X	H+	X	H+	708	Ineffective	It is a proton inclusion.
11.2	X	X	-	H+	H+	-	-	X	-	-	H+	H+	X	H+	X	H+	683	Unfinished	Reaction 2 is not part of the final solution.
11.3	X	H+	-	X	H+	-	-	X	-	-	H+	H+	X	H+	X	H+	759	Unfinished	No update.
11.4	X	H+	-	H+	X	-	-	X	-	-	H+	H+	X	H+	X	H+	707	Unfinished	Not significant.
11.5	X	H+	-	H+	H+	-	-	H+	-	-	H+	H+	X	H+	X	H+	693	Unfinished	It is a proton inclusion.
11.6	X	H+	-	H+	H+	-	-	X	-	-	X	H+	X	H+	X	H+	689	Unfinished	Reaction 11 loses E_a .
11.7	X	H+	-	H+	H+	-	-	X	-	-	H+	X	X	H+	X	H+	694	Reaction removed	Not significant.
11.8	X	H+	-	H+	H+	-	-	X	-	-	H+	H+	H+	H+	X	H+	708	Unfinished	It is a proton inclusion.
11.9	X	H+	-	H+	H+	-	-	X	-	-	H+	H+	X	X	X	H+	688	Unfinished	Reaction 14 loses E_a .
11.10	X	H+	-	H+	H+	-	-	X	-	-	H+	H+	X	H+	H+	H+	695	Reaction removed	It is a proton inclusion.
11.11	X	H+	-	H+	H+	-	-	X	-	-	H+	H+	X	H+	X	X	679	No	Reaction 16 is not part of the final solution.
11.12	X	-	-	H+	X	-	-	X	-	-	H+	X	X	H+	X	-	727	Reaction removed	Estimation 11.12: Best fitted statistically significant pathway (relevant acid-catalysis only)

Bibliography

- [1] World Bank Group. The World Bank. Data (Basel) 2022. <https://www.worldbank.org/en/home> (accessed August 2, 2022).
- [2] Tekin K, Karagöz S, Bektaş S. A review of hydrothermal biomass processing. *Renewable and Sustainable Energy Reviews* 2014;40:673–87. <https://doi.org/10.1016/j.rser.2014.07.216>.
- [3] Baloch HA, Nizamuddin S, Siddiqui MTH, Riaz S, Jatoi AS, Dumbre DK, et al. Recent advances in production and upgrading of bio-oil from biomass: A critical overview. *J Environ Chem Eng* 2018;6:5101–18. <https://doi.org/10.1016/j.jece.2018.07.050>.
- [4] Castello D, Pedersen T, Rosendahl L. Continuous Hydrothermal Liquefaction of Biomass: A Critical Review. *Energies (Basel)* 2018;11:3165. <https://doi.org/10.3390/en11113165>.
- [5] Yang C, Wang S, Yang J, Xu D, Li Y, Li J, et al. Hydrothermal liquefaction and gasification of biomass and model compounds: A review. *Green Chemistry* 2020;22:8210–32. <https://doi.org/10.1039/d0gc02802a>.
- [6] Mishra RK, kumar V, Kumar P, Mohanty K. Hydrothermal liquefaction of biomass for bio-crude production: A review on feedstocks, chemical compositions, operating parameters, reaction kinetics, techno-economic study, and life cycle assessment. *Fuel* 2022;316. <https://doi.org/10.1016/j.fuel.2022.123377>.
- [7] Jansen RA. *Second Generation Biofuels and Biomass: Essential Guide for Investors, Scientists and Decision Makers*. Weinheim: Wiley-VCH Verlag & Co. KGaA; 2012.
- [8] UNFCCC. *Convention on Climate Change: Climate Agreement of Paris*. 2015.
- [9] UK Government. *United Kingdom of Great Britain and Northern Ireland's Nationally Determined Contribution*. London: 2020.
- [10] UK Government. *Climate Change Act 2008*. 2022.
- [11] Department for Business Energy & Industrial Strategy. *2020 UK Greenhouse Gas Emissions, Final Figures*. London: 2022.
- [12] Department for Transportation. *Renewable Transport Fuel Obligation Guidance Part One Process Guidance*. 2021.
- [13] Department for Transportation. *Renewable Transport Fuel Obligation Guidance Part Two Carbon and Sustainability*. 2021.

- [14] Department for Transportation. Renewable Fuel Statistics 2020 Final Report. 2021.
- [15] Naik SN, Goud V V., Rout PK, Dalai AK. Production of first and second generation biofuels: A comprehensive review. *Renewable and Sustainable Energy Reviews* 2010;14:578–97. <https://doi.org/10.1016/j.rser.2009.10.003>.
- [16] Searchinger T, Heimlich R, Houghton RA, Dong F, Elobeid A, Fabiosa J, et al. Use of U.S. Croplands for Biofuels Increases Greenhouse Gases Through Emissions from Land-Use Change. *Science* (1979) 2008;319:1238–40. <https://doi.org/10.1126/science.1151861>.
- [17] Maia RGT, Bozelli H. The importance of GHG emissions from land use change for biofuels in Brazil: An assessment for current and 2030 scenarios. *Resour Conserv Recycl* 2022;179. <https://doi.org/10.1016/j.resconrec.2021.106131>.
- [18] Austin KG, Jones JPH, Clark CM. A review of domestic land use change attributable to U.S. biofuel policy. *Renewable and Sustainable Energy Reviews* 2022;159. <https://doi.org/10.1016/j.rser.2022.112181>.
- [19] Anastasakis K, Biller P, Madsen RB, Glasius M, Johannsen I. Continuous Hydrothermal Liquefaction of Biomass in a Novel Pilot Plant with Heat Recovery and Hydraulic Oscillation. *Energies* (Basel) 2018;11:1–23. <https://doi.org/10.3390/en11102695>.
- [20] Cao L, Yu IKM, Liu Y, Ruan X, Tsang DCW, Hunt AJ, et al. Lignin valorization for the production of renewable chemicals: State-of-the-art review and future prospects. *Bioresour Technol* 2018;269:465–75. <https://doi.org/10.1016/j.biortech.2018.08.065>.
- [21] Elliott DC, Biller P, Ross AB, Schmidt AJ, Jones SB. Hydrothermal liquefaction of biomass: Developments from batch to continuous process. *Bioresour Technol* 2015;178:147–56. <https://doi.org/10.1016/j.biortech.2014.09.132>.
- [22] Hoffmann J, Jensen CU, Rosendahl LA. Co-processing potential of HTL bio-crude at petroleum refineries - Part 1: Fractional distillation and characterization. *Fuel* 2016;165:526–35. <https://doi.org/10.1016/j.fuel.2015.10.094>.
- [23] Nguyen TDH, Maschietti M, Belkheiri T, Åmand LE, Theliander H, Vamling L, et al. Catalytic depolymerisation and conversion of Kraft lignin into liquid products using near-critical water. *Journal of Supercritical Fluids* 2014;86:67–75. <https://doi.org/10.1016/j.supflu.2013.11.022>.
- [24] Peterson AA, Vogel F, Lachance RP, Fröling M, Antal MJ, Tester JW. Thermochemical biofuel production in hydrothermal media: A review of sub- and supercritical water technologies. *Energy Environ Sci* 2008;1:32–65. <https://doi.org/10.1039/b810100k>.

- [25] Sauvanaud L, Mathieu Y, Corma A, Humphreys L, Rowlands W, Maschmeyer T. Co-processing of lignocellulosic biocrude with petroleum gas oils. *Appl Catal A Gen* 2018;551:139–45. <https://doi.org/10.1016/j.apcata.2017.09.029>.
- [26] Matsumura Y, Minowa T, Potic B, Kersten SRA, Prins W, van Swaaij WPM, et al. Biomass gasification in near- and super-critical water: Status and prospects. *Biomass Bioenergy* 2005;29:269–92. <https://doi.org/10.1016/j.biombioe.2005.04.006>.
- [27] Mark Crocker, P. E. Savage, R. B. Levine, C. M. Huelsman. *Thermochemical Conversion of Biomass to Liquid Fuels and Chemicals*. Cambridge: Royal Society of Chemistry; 2010. <https://doi.org/10.1039/9781849732260>.
- [28] Heidari M, Dutta A, Acharya B, Mahmud S. A review of the current knowledge and challenges of hydrothermal carbonization for biomass conversion. *Journal of the Energy Institute* 2018. <https://doi.org/10.1016/j.joei.2018.12.003>.
- [29] Qadi N, Takeno K, Mosqueda A, Kobayashi M, Motoyama Y, Yoshikawa K. Effect of Hydrothermal Carbonization Conditions on the Physicochemical Properties and Gasification Reactivity of Energy Grass. *Energy & Fuels* 2019;acs.energyfuels.9b00994. <https://doi.org/10.1021/acs.energyfuels.9b00994>.
- [30] Bridgwater A V. Review of fast pyrolysis of biomass and product upgrading. *Biomass Bioenergy* 2012;38:68–94. <https://doi.org/10.1016/j.biombioe.2011.01.048>.
- [31] Speight JG. *The Biofuels Handbook*. Cambridge: The Royal Society of Chemistry; 2010. <https://doi.org/10.1039/9781849731027-FP005>.
- [32] Venkatakrishnan VK, Degenstein JC, Smeltz AD, Delgass WN, Agrawal R, Ribeiro FH. High-pressure fast-pyrolysis, fast-hydroxylation and catalytic hydrodeoxygenation of cellulose: Production of liquid fuel from biomass. *Green Chemistry* 2014;16:792–802. <https://doi.org/10.1039/c3gc41558a>.
- [33] Zhu Z, Rosendahl L, Toor SS, Yu D, Chen G. Hydrothermal liquefaction of barley straw to biocrude oil: Effects of reaction temperature and aqueous phase recirculation. *Appl Energy* 2015;137:183–92. <https://doi.org/10.1016/j.apenergy.2014.10.005>.
- [34] Dahlquist E. *Biomass as energy source: resources, systems and applications*. vol. 51. London: CRC Press/Balkema; 2013. <https://doi.org/10.5860/choice.51-2104>.
- [35] Gillet S, Petitjean L, Aguedo M, Lam CH, Blecker C, Anastas PT. Impact of lignin structure on oil production via hydroprocessing with a copper-doped porous metal oxide catalyst. *Bioresour Technol* 2017;233:216–26. <https://doi.org/10.1016/j.biortech.2017.02.090>.

- [36] Pandey MP, Kim CS. Lignin Depolymerization and Conversion: A Review of Thermochemical Methods. *Chem Eng Technol* 2011;34:29–41. <https://doi.org/10.1002/ceat.201000270>.
- [37] Mohd Azhar SH, Abdulla R, Jambo SA, Marbawi H, Gansau JA, Mohd Faik AA, et al. Yeasts in sustainable bioethanol production: A review. *Biochem Biophys Rep* 2017;10:52–61. <https://doi.org/10.1016/j.bbrep.2017.03.003>.
- [38] Robak K, Balcerek M. Review of second generation bioethanol production from residual biomass. *Food Technol Biotechnol* 2018;56:174–87. <https://doi.org/10.17113/ftb.56.02.18.5428>.
- [39] Rabii A, Aldin S, Dahman Y, Elbeshbishy E. A Review on Anaerobic Co-Digestion with a Focus on the Microbial Populations and the Effect of Multi-Stage Digester Configuration. *Energies (Basel)* 2019;12:1106. <https://doi.org/10.3390/en12061106>.
- [40] Bhuiya MMK, Rasul MG, Khan MMK, Ashwath N, Azad AK, Hazrat MA. Second generation biodiesel: Potential alternative to-edible oil-derived biodiesel. *Energy Procedia* 2014;61:1969–72. <https://doi.org/10.1016/j.egypro.2014.12.054>.
- [41] Vasić K, Knez Ž, Leitgeb M. Bioethanol production by enzymatic hydrolysis from different lignocellulosic sources. *Molecules* 2021;26. <https://doi.org/10.3390/molecules26030753>.
- [42] Pereira SA, Araújo VQ, Reboucas M V., Vieira FS V., De Almeida MVA, Chinalia FA, et al. Toxicity of biodiesel, diesel and biodiesel/diesel blends: Comparative sub-lethal effects of water-soluble fractions to microalgae species. *Bull Environ Contam Toxicol* 2012;88:234–8. <https://doi.org/10.1007/s00128-011-0430-9>.
- [43] Yang Z, Kumar A, Huhnke RL. Review of recent developments to improve storage and transportation stability of bio-oil. *Renewable and Sustainable Energy Reviews* 2015;50:859–70. <https://doi.org/10.1016/j.rser.2015.05.025>.
- [44] Pandey MP, Kim CS. Lignin Depolymerization and Conversion: A Review of Thermochemical Methods. *Chem Eng Technol* 2011;34:29–41. <https://doi.org/10.1002/ceat.201000270>.
- [45] Peterson AA, Vogel F, Lachance RP, Fröling M, Antal MJ Jr, Tester JW. Thermochemical biofuel production in hydrothermal media: A review of sub- and supercritical water technologies. *Energy Environ Sci* 2008;1:32–65. <https://doi.org/10.1039/b810100k>.
- [46] Elliott DC, Liquids C, Oxygen-containing R, Engineering F. United States Patent (19) Baker et al. 54) METHOD OF UPGRADING OILS “Chemistry of Hydrocracking,” Langlois et al “Catalytic Hydrogenation and Hydrocracking of Fluoranthene: Reaction Pathways and Kinetics,” Lapinas et al “Hydrocracking of a Coal Extract w 1993.

- [47] Cocero MJ, Cabeza Á, Abad N, Adamovic T, Vaquerizo L, Martínez CM, et al. Understanding biomass fractionation in subcritical & supercritical water. *Journal of Supercritical Fluids* 2018;133:550–65. <https://doi.org/10.1016/j.supflu.2017.08.012>.
- [48] Gollakota ARK, Kishore N, Gu S. A review on hydrothermal liquefaction of biomass. *Renewable and Sustainable Energy Reviews* 2018;81:1378–92. <https://doi.org/10.1016/j.rser.2017.05.178>.
- [49] Huang H-J, Yuan X-Z. Recent progress in the direct liquefaction of typical biomass. *Prog Energy Combust Sci* 2015;49:59–80. <https://doi.org/10.1016/j.pecs.2015.01.003>.
- [50] Nazari L, Yuan Z, Souzanchi S, Ray MB, Xu C. Hydrothermal liquefaction of woody biomass in hot-compressed water: Catalyst screening and comprehensive characterization of bio-crude oils. *Fuel* 2015;162:74–83. <https://doi.org/10.1016/j.fuel.2015.08.055>.
- [51] Bolan N, Hoang SA, Beiyuan J, Gupta S, Hou D, Karakoti A, et al. Multifunctional applications of biochar beyond carbon storage. *International Materials Reviews* 2022;67:150–200. <https://doi.org/10.1080/09506608.2021.1922047>.
- [52] Furimsky E. Catalytic hydrodeoxygenation. *Appl Catal A Gen* 2000;199:147–90. [https://doi.org/10.1016/S0926-860X\(99\)00555-4](https://doi.org/10.1016/S0926-860X(99)00555-4).
- [53] Yang T, Shi L, Li R, Li B, Kai X. Hydrodeoxygenation of crude bio-oil in situ in the bio-oil aqueous phase with addition of zero-valent aluminum. *Fuel Processing Technology* 2019;184:65–72. <https://doi.org/10.1016/j.fuproc.2018.10.025>.
- [54] Malins K. Production of bio-oil via hydrothermal liquefaction of birch sawdust. *Energy Convers Manag* 2017;144:243–51. <https://doi.org/10.1016/j.enconman.2017.04.053>.
- [55] Wagner W, Pruß A. The IAPWS formulation 1995 for the thermodynamic properties of ordinary water substance for general and scientific use. *J Phys Chem Ref Data* 2002;31:387–535. <https://doi.org/10.1063/1.1461829>.
- [56] Marshall WL, Franck EU. Ion product of water substance, 0-1000 °C, 1-10,000 bars New International Formulation and its background. *J Phys Chem Ref Data* 1983;10:295–304. <https://doi.org/10.1063/1.555643>.
- [57] Uematsu M, Frank EU. Static Dielectric Constant of Water and Steam. *J Phys Chem Ref Data* 1980;9:1291–306. <https://doi.org/10.1063/1.555632>.
- [58] Savage PE. Organic Chemical Reactions in Supercritical Water. *Chem Rev* 1999;99:603–21. <https://doi.org/10.1021/cr9700989>.

- [59] Belkheiri T, Andersson SI, Mattsson C, Olausson L, Theliander H, Vamling L. Hydrothermal Liquefaction of Kraft Lignin in Subcritical Water: Influence of Phenol as Capping Agent. *Energy and Fuels* 2018;32:5923–32. <https://doi.org/10.1021/acs.energyfuels.8b00068>.
- [60] Demirkaya E, Dal O, Yüksel A. Liquefaction of waste hazelnut shell by using sub- and supercritical solvents as a reaction medium. *Journal of Supercritical Fluids* 2019;150:11–20. <https://doi.org/10.1016/j.supflu.2019.03.019>.
- [61] Chen C, Zhu J, Jia S, Mi S, Tong Z, Li Z, et al. Effect of ethanol on Mulberry bark hydrothermal liquefaction and bio-oil chemical compositions. *Energy* 2018;162:460–75. <https://doi.org/10.1016/j.energy.2018.08.026>.
- [62] Sasaki M, Adschiri T, Arai K. Kinetics of Cellulose Conversion at 25 MPa in Sub- and Supercritical Water. *AIChE Journal* 2004;50:192–202. <https://doi.org/10.1002/aic.10018>.
- [63] Fuwape JA. Gross heat of combustion of Gmelina (*Gmelina arborea* (Roxb)) chemical components. *Biomass* 1989;19:281–7. [https://doi.org/10.1016/0144-4565\(89\)90072-3](https://doi.org/10.1016/0144-4565(89)90072-3).
- [64] Cantero DA, Bermejo MD, Cocero MJ. Kinetic analysis of cellulose depolymerization reactions in near critical water. *Journal of Supercritical Fluids* 2013;75:48–57. <https://doi.org/10.1016/j.supflu.2012.12.013>.
- [65] Akhtar J, Amin NAS. A review on process conditions for optimum bio-oil yield in hydrothermal liquefaction of biomass. *Renewable and Sustainable Energy Reviews* 2011;15:1615–24. <https://doi.org/10.1016/j.rser.2010.11.054>.
- [66] Van Putten RJ, Van Der Waal JC, De Jong E, Rasrendra CB, Heeres HJ, De Vries JG. Hydroxymethylfurfural, a versatile platform chemical made from renewable resources. *Chem Rev* 2013;113:1499–597. <https://doi.org/10.1021/cr300182k>.
- [67] Cantero DA, Álvarez A, Bermejo MD, Cocero MJ. Transformation of glucose into added value compounds in a hydrothermal reaction media. *Journal of Supercritical Fluids* 2015;98:204–10. <https://doi.org/10.1016/j.supflu.2014.12.015>.
- [68] Girisuta B, Janssen LPBM, Heeres HJ. A kinetic study on the decomposition of 5-hydroxymethylfurfural into levulinic acid. *Green Chemistry* 2006;8:701–9. <https://doi.org/10.1039/b518176c>.
- [69] Feng J, Zhang L, Jiang J, Hse C, Shupe TF, Pan H. Directional synergistic conversion of lignocellulosic biomass with matching-solvents for added-value chemicals. *Green Chemistry* 2019;21:4951–7. <https://doi.org/10.1039/c9gc02365h>.

- [70] Xu J, Huang W, Bai R, Queneau Y, Jérôme F, Gu Y. Utilization of bio-based glycolaldehyde aqueous solution in organic synthesis: Application to the synthesis of 2,3-dihydrofurans. *Green Chemistry* 2019;21:2061–9. <https://doi.org/10.1039/c8gc04000a>.
- [71] Sasaki M, Takahashi K, Haneda Y, Satoh H, Sasaki A, Narumi A, et al. Thermochemical transformation of glucose to 1,6-anhydroglucose in high-temperature steam. *Carbohydr Res* 2008;343:848–54. <https://doi.org/10.1016/j.carres.2008.02.005>.
- [72] Cantero DA, Dolores Bermejo M, José Cocero M. High glucose selectivity in pressurized water hydrolysis of cellulose using ultra-fast reactors. *Bioresour Technol* 2013;135:697–703. <https://doi.org/10.1016/j.biortech.2012.09.035>.
- [73] Martínez CM, Cantero DA, Bermejo MD, Cocero MJ. Hydrolysis of cellulose in supercritical water: reagent concentration as a selectivity factor. *Cellulose* 2015;22:2231–43. <https://doi.org/10.1007/s10570-015-0674-3>.
- [74] Rinaldi R, Jastrzebski R, Clough MT, Ralph J, Kennema M, Bruijninx PCA, et al. Paving the Way for Lignin Valorisation: Recent Advances in Bioengineering, Biorefining and Catalysis. *Angewandte Chemie - International Edition* 2016;55:8164–215. <https://doi.org/10.1002/anie.201510351>.
- [75] Garrote G, Domínguez H, Parajó JC. Hydrothermal processing of lignocellulosic materials. *Holz Als Roh- Und Werkstoff* 1999;57:191–202. <https://doi.org/10.1007/s001070050039>.
- [76] Paksung N, Matsumura Y. Decomposition of Xylose in Sub- and Supercritical Water. *Ind Eng Chem Res* 2015;54:7604–13. <https://doi.org/10.1021/acs.iecr.5b01623>.
- [77] Mittal A, Chatterjee SG, Scott GM, Amidon TE. Modeling xylan solubilization during autohydrolysis of sugar maple and aspen wood chips: Reaction kinetics and mass transfer. *Chem Eng Sci* 2009;64:3031–41. <https://doi.org/10.1016/j.ces.2009.03.011>.
- [78] Hosseini SA, Lambert R, Kucherenko S, Shah N. Multiscale modeling of hydrothermal pretreatment: From hemicellulose hydrolysis to biomass size optimization. *Energy and Fuels* 2010;24:4673–80. <https://doi.org/10.1021/ef9012246>.
- [79] Hosseini SA, Shah N. Multiscale modelling of biomass pretreatment for biofuels production. *Chemical Engineering Research and Design* 2009;87:1251–60. <https://doi.org/10.1016/j.cherd.2009.04.018>.
- [80] Forchheim D, Hornung U, Kruse A, Sutter T. Kinetic Modelling of Hydrothermal Lignin Depolymerisation. *Waste Biomass Valorization* 2014;5:985–94. <https://doi.org/10.1007/s12649-014-9307-6>.

- [81] Bentivenga G, Bonini C, D'auria M, De Bona A. Degradation of steam-exploded lignin from beech by using Fenton's reagent. vol. 24. 2003.
- [82] Mahmood N, Yuan Z, Schmidt J, Xu C. Depolymerization of lignins and their applications for the preparation of polyols and rigid polyurethane foams: A review. *Renewable and Sustainable Energy Reviews* 2016;60:317–29. <https://doi.org/10.1016/j.rser.2016.01.037>.
- [83] Zhang B, Huang HJ, Ramaswamy S. Reaction kinetics of the hydrothermal treatment of lignin. *Appl Biochem Biotechnol* 2008;147:119–31. <https://doi.org/10.1007/s12010-007-8070-6>.
- [84] Yong TL-K, Matsumura Y. Reaction Kinetics of the Lignin Conversion in Supercritical Water. *Ind Eng Chem Res* 2012;51:11975–88. <https://doi.org/10.1021/ie300921d>.
- [85] Yong TLK, Matsumura Y. Kinetic analysis of lignin hydrothermal conversion in sub- and supercritical water. *Ind Eng Chem Res* 2013;52:5626–39. <https://doi.org/10.1021/ie400600x>.
- [86] Berl E. Production of Oil from Plant Material. *Science* (1979) 1944;99:309–12.
- [87] Elliott DC. Historical developments in hydroprocessing bio-oils. *Energy and Fuels* 2007;21:1792–815. <https://doi.org/10.1021/ef070044u>.
- [88] Kozliak EI, Kubátová A, Artemyeva AA, Nagel E, Zhang C, Rajappagowda RB, et al. Thermal Liquefaction of Lignin to Aromatics: Efficiency, Selectivity, and Product Analysis. *ACS Sustain Chem Eng* 2016;4:5106–22. <https://doi.org/10.1021/acssuschemeng.6b01046>.
- [89] Berglin EJ, Enderlin CW, Schmidt AJ. Review and Assessment of Commercial Vendors / Options for Feeding and Pumping Biomass Slurries for Hydrothermal Liquefaction. 2012.
- [90] Agbor VB, Cicek N, Sparling R, Berlin A, Levin DB. Biomass pretreatment: Fundamentals toward application. *Biotechnol Adv* 2011;29:675–85. <https://doi.org/10.1016/j.biotechadv.2011.05.005>.
- [91] Zhu JY. Physical pretreatment - Woody biomass size reduction - For forest biorefinery. *ACS Symposium Series* 2011;1067:89–107. <https://doi.org/10.1021/bk-2011-1067.ch004>.
- [92] Cantero D, Jara R, Navarrete A, Pelaz L, Queiroz J, Rodríguez-Rojo S, et al. Pretreatment Processes of Biomass for Biorefineries: Current Status and Prospects. *Annu Rev Chem Biomol Eng* 2019;10:289–310. <https://doi.org/10.1146/annurev-chembioeng-060718-030354>.
- [93] Liu Y, Wang J, Wolcott MP. Assessing the specific energy consumption and physical properties of comminuted Douglas-fir chips for bioconversion. *Ind Crops Prod* 2016;94:394–400. <https://doi.org/10.1016/j.indcrop.2016.08.054>.

- [94] Temmerman M, Jensen PD, Hébert J. Von Rittinger theory adapted to wood chip and pellet milling, in a laboratory scale hammermill. *Biomass Bioenergy* 2013;56:70–81. <https://doi.org/10.1016/j.biombioe.2013.04.020>.
- [95] Manouchehrinejad M, van Giesen I, Mani S. Grindability of torrefied wood chips and wood pellets. *Fuel Processing Technology* 2018;182:45–55. <https://doi.org/10.1016/j.fuproc.2018.10.015>.
- [96] Cheng S, DCruz I, Wang M, Leitch M, Xu C. Highly efficient liquefaction of woody biomass in hot-compressed alcohol-water co-solvents. *Energy and Fuels* 2010;24:4659–67. <https://doi.org/10.1021/ef901218w>.
- [97] Huang H, Yuan X, Zeng G, Wang J, Li H, Zhou C, et al. Thermochemical liquefaction characteristics of microalgae in sub- and supercritical ethanol. *Fuel Processing Technology* 2011;92:147–53. <https://doi.org/10.1016/j.fuproc.2010.09.018>.
- [98] Dărăban IM, Rosendahl LA, Pedersen TH, Iversen SB. Pretreatment methods to obtain pumpable high solid loading wood-water slurries for continuous hydrothermal liquefaction systems. *Biomass Bioenergy* 2015;81:437–43. <https://doi.org/10.1016/j.biombioe.2015.07.004>.
- [99] Sintamarean IM, Grigoras IF, Jensen CU, Toor SS, Pedersen TH, Rosendahl LA. Two-stage alkaline hydrothermal liquefaction of wood to biocrude in a continuous bench-scale system. *Biomass Convers Biorefin* 2017;7:425–35. <https://doi.org/10.1007/s13399-017-0247-9>.
- [100] Kim JY, Lee HW, Lee SM, Jae J, Park YK. Overview of the recent advances in lignocellulose liquefaction for producing biofuels, bio-based materials and chemicals. *Bioresour Technol* 2019;279:373–84. <https://doi.org/10.1016/j.biortech.2019.01.055>.
- [101] Brand S, Hardi F, Kim J, Suh DJ. Effect of heating rate on biomass liquefaction: Differences between subcritical water and supercritical ethanol. *Energy* 2014;68:420–7. <https://doi.org/10.1016/j.energy.2014.02.086>.
- [102] Tran KQ. Fast hydrothermal liquefaction for production of chemicals and biofuels from wet biomass – The need to develop a plug-flow reactor. *Bioresour Technol* 2016;213:327–32. <https://doi.org/10.1016/j.biortech.2016.04.002>.
- [103] Aida TM, Sato Y, Watanabe M, Tajima K, Nonaka T, Hattori H, et al. Dehydration of d-glucose in high temperature water at pressures up to 80 MPa. *Journal of Supercritical Fluids* 2007;40:381–8. <https://doi.org/10.1016/j.supflu.2006.07.027>.
- [104] Chuntanapum A, Yong TLK, Miyake S, Matsumura Y. Behavior of 5-HMF in subcritical and supercritical water. *Ind Eng Chem Res* 2008;47:2956–62. <https://doi.org/10.1021/ie0715658>.

- [105] Feng S, Wei R, Leitch M, Xu CC. Comparative study on lignocellulose liquefaction in water, ethanol, and water/ethanol mixture: Roles of ethanol and water. *Energy* 2018;155:234–41. <https://doi.org/10.1016/j.energy.2018.05.023>.
- [106] Mazaheri H, Lee KT, Bhatia S, Mohamed AR. Sub/supercritical liquefaction of oil palm fruit press fiber for the production of bio-oil: Effect of solvents. *Bioresour Technol* 2010;101:7641–7. <https://doi.org/10.1016/j.biortech.2010.04.072>.
- [107] Yaws, L C. *Yaws' handbook of thermodynamic and physical properties of chemical compounds*. vol. 3. Knovel; 2003.
- [108] Belkheiri T, Vamling L, Dieu T, Nguyen H, Maschietti M, Olausson L, et al. Kraft Lignin Depolymerization in Near-Critical Water: Effect of Changing Co-Solvent. *CELLULOSE CHEMISTRY AND TECHNOLOGY Cellulose Chem Technol* 2014;48:813–8.
- [109] Xu D, Lin G, Guo S, Wang S, Guo Y, Jing Z. Catalytic hydrothermal liquefaction of algae and upgrading of biocrude: A critical review. *Renewable and Sustainable Energy Reviews* 2018;97:103–18. <https://doi.org/10.1016/j.rser.2018.08.042>.
- [110] Zhong C, Wei X. A comparative experimental study on the liquefaction of wood. *Energy* 2004;29:1731–41. <https://doi.org/10.1016/j.energy.2004.03.096>.
- [111] Zhu Z, Toor SS, Rosendahl L, Yu D, Chen G. Influence of alkali catalyst on product yield and properties via hydrothermal liquefaction of barley straw. *Energy* 2015;80:284–92. <https://doi.org/10.1016/j.energy.2014.11.071>.
- [112] Belkheiri T, Mattsson C, Andersson SI, Olausson L, Åmand LE, Theliander H, et al. Effect of pH on Kraft Lignin Depolymerisation in Subcritical Water. *Energy and Fuels* 2016;30:4916–24. <https://doi.org/10.1021/acs.energyfuels.6b00462>.
- [113] Ma Q, Chen D, Wei L, Shen Q, Ji Z, Chen Y, et al. Bio-oil production from hydrogenation liquefaction of rice straw over metal (Ni, Co, Cu)-modified CeO₂ catalysts. *Energy Sources, Part A: Recovery, Utilization and Environmental Effects* 2018;40:200–6. <https://doi.org/10.1080/15567036.2017.1409295>.
- [114] Toor SS, Rosendahl L, Nielsen MP, Glasius M, Rudolf A, Iversen SB. Continuous production of bio-oil by catalytic liquefaction from wet distiller's grain with solubles (WDGS) from bio-ethanol production. *Biomass Bioenergy* 2012;36:327–32. <https://doi.org/10.1016/j.biombioe.2011.10.044>.

- [115] Hammerschmidt A, Boukis N, Hauer E, Galla U, Dinjus E, Hitzmann B, et al. Catalytic conversion of waste biomass by hydrothermal treatment. *Fuel* 2011;90:555–62. <https://doi.org/10.1016/j.fuel.2010.10.007>.
- [116] Watanabe M, Inomata H, Osada M, Sato T, Adschiri T, Arai K. Catalytic effects of NaOH and ZrO₂ for partial oxidative gasification of n-hexadecane and lignin in supercritical water. *Fuel* 2003;82:545–52. [https://doi.org/10.1016/S0016-2361\(02\)00320-4](https://doi.org/10.1016/S0016-2361(02)00320-4).
- [117] Duan P, Savage PE. Hydrothermal liquefaction of a microalga with heterogeneous catalysts. *Ind Eng Chem Res* 2011;50:52–61. <https://doi.org/10.1021/ie100758s>.
- [118] Li W, Dou X, Zhu C, Wang J, Chang H min, Jameel H, et al. Production of liquefied fuel from depolymerization of kraft lignin over a novel modified nickel/H-beta catalyst. *Bioresour Technol* 2018;269:346–54. <https://doi.org/10.1016/j.biortech.2018.08.125>.
- [119] Knorr D, Lukas J, Schoen P. Production of Advanced Biofuels via Liquefaction - Hydrothermal Liquefaction Reactor Design: April 5, 2013 2013. <https://doi.org/10.2172/1111191>.
- [120] Hognon C, Delrue F, Texier J, Grateau M, Thiery S, Miller H, et al. Comparison of pyrolysis and hydrothermal liquefaction of *Chlamydomonas reinhardtii*. Growth studies on the recovered hydrothermal aqueous phase. *Biomass Bioenergy* 2015;73:23–31. <https://doi.org/10.1016/j.biombioe.2014.11.025>.
- [121] Yang J, He Q (Sophia), Corcadden K, Niu H. The impact of downstream processing methods on the yield and physiochemical properties of hydrothermal liquefaction bio-oil. *Fuel Processing Technology* 2018;178:353–61. <https://doi.org/10.1016/j.fuproc.2018.07.006>.
- [122] Biller P, Sharma BK, Kunwar B, Ross AB. Hydroprocessing of bio-crude from continuous hydrothermal liquefaction of microalgae. *Fuel* 2015;159:197–205. <https://doi.org/10.1016/j.fuel.2015.06.077>.
- [123] Pedersen TH, Jensen CU, Sandström L, Rosendahl LA. Full characterization of compounds obtained from fractional distillation and upgrading of a HTL biocrude. *Appl Energy* 2017;202:408–19. <https://doi.org/10.1016/j.apenergy.2017.05.167>.
- [124] Shah PS. Continuous Hydrothermal Synthesis of Magnetic Nanoparticles and Optimisation of their Separation and Purification - PhD thesis. Imperial College London, 2020.
- [125] Figueroa C, Schaleger LL, Davis HG. LBL continuous bench-scale liquefaction unit, operation and results. 6th Annual Conference on Energy from Biomass Wastes VI, Lake Buena Vista, FL, January 25-29, 1982, University of California; 1981.

- [126] Mørup AJ, Becker J, Christensen PS, Houlberg K, Lappa E, Klemmer M, et al. Construction and Commissioning of a Continuous Reactor for Hydrothermal Liquefaction. *Ind Eng Chem Res* 2015;54:5935–47. <https://doi.org/10.1021/acs.iecr.5b00683>.
- [127] Boldrin P, Hebb AK, Chaudhry AA, Otley L, Thiebaut B, Bishop P, et al. Direct synthesis of nanosized NiCo₂O₄ spinel and related compounds via continuous hydrothermal synthesis methods. *Ind Eng Chem Res* 2007;46:4830–8. <https://doi.org/10.1021/ie061396b>.
- [128] Darr JA, Tighe CJ, Gruar RI. Co-current mixer, apparatus, reactor and method for precipitating nanoparticles. US 9192901 B2, 2015.
- [129] Darr JA, Tighe CJ, Gruar RI. Co-current mixer, apparatus, reactor and method for precipitating nanoparticles. EP 2576036 B1, 2016.
- [130] Darr JA, Tighe CJ, Gruar RI. Co-current mixer, apparatus, reactor and method for precipitating nanoparticles. WO 2011/148121 A1, 2011.
- [131] Hendry D, Wickramathilaka M, Wilkinson N, Miller A, Venkitasamy C, Jacoby W. Continuous, fluid-powered, slurry feeding into high-pressure, high-temperature environments. Columbia: 2013.
- [132] Perry RH, Green DW. *Perry's Chemical Engineers' Handbook*. 8th ed. New York: McGraw-Hill; 2008.
- [133] O'Neil MJ, Royal Society of Chemistry (Great Britain). *The Merck index : an encyclopedia of chemicals, drugs, and biologicals*. 15th ed. Cambridge, UK : Royal Society of Chemistry; 2013.
- [134] Swagelok®. Swagelok Products 2022. <https://products.swagelok.com/> (accessed June 7, 2022).
- [135] Gruar RI, Tighe CJ, Darr JA. Scaling-up a confined jet reactor for the continuous hydrothermal manufacture of nanomaterials. *Ind Eng Chem Res* 2013;52:5270–81. <https://doi.org/10.1021/ie302567d>.
- [136] Zhdanov V, Chorny A. Development of macro- and micromixing in confined flows of reactive fluids. *Int J Heat Mass Transf* 2011;54:3245–55. <https://doi.org/10.1016/j.ijheatmasstransfer.2011.04.006>.
- [137] Ma CY, Wang XZ, Tighe CJ, Darr JA. Modelling and simulation of counter-current and confined jet reactors for continuous hydrothermal flow synthesis of nano-materials. *IFAC Proceedings Volumes (IFAC-PapersOnline)* 2012;8:874–9. <https://doi.org/10.3182/20120710-4-SG-2026.00073>.

- [138] Denis CJ, Tighe CJ, Gruar RI, Makwana NM, Darr JA. Nucleation and Growth of Cobalt Oxide Nanoparticles in a Continuous Hydrothermal Reactor under Laminar and Turbulent Flow. *Cryst Growth Des* 2015;15:4256–65. <https://doi.org/10.1021/acs.cgd.5b00551>.
- [139] Ma CY, Chen M, Wang XZ. Modelling and simulation of counter-current and confined jet reactors for hydrothermal synthesis of nano-materials. *Chem Eng Sci* 2014;109:26–37. <https://doi.org/10.1016/j.ces.2014.01.006>.
- [140] Middelkoop V, Tighe CJ, Kellici S, Gruar RI, Perkins JM, Jacques SDM, et al. Imaging the continuous hydrothermal flow synthesis of nanoparticulate CeO₂ at different supercritical water temperatures using in situ angle-dispersive diffraction. *Journal of Supercritical Fluids* 2014;87:118–28. <https://doi.org/10.1016/j.supflu.2013.12.022>.
- [141] ThermoFisher Scientific. ThermoFlex™ Recirculating chillers - ThermoFisher Scientific 2022. <https://www.thermofisher.com/order/catalog/product/TF900> (accessed June 9, 2022).
- [142] He S, Zhao M, Wang J, Cheng Z, Yan B, Chen G. Hydrothermal liquefaction of low-lipid algae *Nannochloropsis* sp. and *Sargassum* sp.: Effect of feedstock composition and temperature. *Science of the Total Environment* 2020;712:135677. <https://doi.org/10.1016/j.scitotenv.2019.135677>.
- [143] He S, Wang J, Cheng Z, Dong H, Yan B, Chen G. Synergetic effect and primary reaction network of corn cob and cattle manure in single and mixed hydrothermal liquefaction. *J Anal Appl Pyrolysis* 2021;155:105076. <https://doi.org/10.1016/j.jaap.2021.105076>.
- [144] Yin S, Tan Z. Hydrothermal liquefaction of cellulose to bio-oil under acidic, neutral and alkaline conditions. *Appl Energy* 2012;92:234–9. <https://doi.org/10.1016/j.apenergy.2011.10.041>.
- [145] Jindal MK, Jha MK. Hydrothermal liquefaction of wood: A critical review. *Reviews in Chemical Engineering* 2016;32:459–88. <https://doi.org/10.1515/revce-2015-0055>.
- [146] Shimadzu UK. Prominence Modular HPLC | Shimadzu Europa 2022. <https://www.shimadzu.co.uk/prominence-modular-hplc> (accessed June 15, 2022).
- [147] Skoog DA, Holler FJ, Crouch SR. *Principles of Instrumental Analysis*. vol. 18. 6th ed. David Harris; 2006. <https://doi.org/10.2307/1505543>.
- [148] Williams DH, Fleming I. *Spectroscopic Methods in Organic Chemistry*. 5th ed. Berkshire: McGraw-Hill Publishing Company; 1995.
- [149] González G, Montané D. Kinetics of dibenzylether hydrothermolysis in supercritical water. *AIChE Journal* 2005;51:971–81. <https://doi.org/10.1002/aic.10362>.

- [150] Rasrendra CB, Makertihartha IGBN, Adisasmito S, Heeres HJ. Green chemicals from D-glucose: Systematic studies on catalytic effects of inorganic salts on the chemo-selectivity and yield in aqueous solutions. *Top Catal* 2010;53:1241–7. <https://doi.org/10.1007/s11244-010-9570-0>.
- [151] Qiu G, Wang X, Huang C, Li Y, Chen B. Facile, one-pot, two-step, strategy for the production of potential bio-diesel candidates from fructose. *Catalysts* 2017;7:1–14. <https://doi.org/10.3390/catal7080237>.
- [152] Kammoun M, Istasse T, Ayeb H, Rassaa N, Bettaieb T, Richel A. Hydrothermal dehydration of monosaccharides promoted by seawater: Fundamentals on the catalytic role of inorganic salts. *Front Chem* 2019;7. <https://doi.org/10.3389/fchem.2019.00132>.
- [153] Dong MW. *HPLC and UHPLC for Practicing Scientists*. 2nd ed. John Wiley & Sons; 2019.
- [154] National Center for Biotechnology Information. PubChem Annotation Record for BENZALDEHYDE, Source: Hazardous Substances Data Bank (HSDB) 2022. <https://pubchem.ncbi.nlm.nih.gov/source/hsdb/388> (accessed May 17, 2022).
- [155] National Center for Biotechnology Information. PubChem Annotation Record for TOLUENE, Source: Hazardous Substances Data Bank (HSDB) 2022. <https://pubchem.ncbi.nlm.nih.gov/source/hsdb/131> (accessed May 17, 2022).
- [156] National Center for Biotechnology Information. PubChem Annotation Record for DIBENZYL ETHER, Source: Hazardous Substances Data Bank (HSDB) 2022. <https://pubchem.ncbi.nlm.nih.gov/source/hsdb/6030> (accessed May 17, 2022).
- [157] National Center for Biotechnology Information. PubChem Annotation Record for BENZYL ALCOHOL, Source: Hazardous Substances Data Bank (HSDB) 2022. <https://pubchem.ncbi.nlm.nih.gov/source/hsdb/46> (accessed May 17, 2022).
- [158] Subba RD, Venkateswara RK, Ravi PA, Chiranjivi C. Extraction of Acetonitrile from Aqueous Mixtures. 2. Ternary Liquid Equilibria. *J Chem Eng Data* 1979;24:241–4. <https://doi.org/10.1021/je60082a014>.
- [159] Kabyemela BM, Adschiri T, Malaluan RM, Arai K. Glucose and fructose decomposition in subcritical and supercritical water: Detailed reaction pathway, mechanisms, and kinetics. *Ind Eng Chem Res* 1999;38:2888–95. <https://doi.org/10.1021/ie9806390>.
- [160] Watanabe M, Aizawa Y, Iida T, Levy C, Aida TM, Inomata H. Glucose reactions within the heating period and the effect of heating rate on the reactions in hot compressed water. *Carbohydr Res* 2005;340:1931–9. <https://doi.org/10.1016/j.carres.2005.05.019>.

- [161] Shimadzu UK. Nexis GC-2030 | Shimadzu Europa 2022. <https://www.shimadzu.co.uk/gc-2030> (accessed June 16, 2022).
- [162] Grob RL, Barry EF. *Modern Practice of Gas Chromatography*. Hoboken, NJ, USA: John Wiley & Sons, Inc.; 2004. <https://doi.org/10.1002/0471651141>.
- [163] National Institute of Standards and Technology. Electron Ionization Library Component of the NIST/EPA/NIH Mass Spectral Library and NIST GC Retention Index Database 2017;59. <https://www.nist.gov/programs-projects/electron-ionization-library-component-nistepanih-mass-spectral-library-and-nist-gc> (accessed June 17, 2022).
- [164] MKS Instruments I. MULTIGAS-2030-CEM-CERT 2022. <https://www.mks.com/p/MULTIGAS-2030-CEM-CERT> (accessed June 15, 2022).
- [165] Ku HH. Notes on the use of propagation of error formulas. *Journal of Research of the National Bureau of Standards, Section C: Engineering and Instrumentation* 1966;70C:263. <https://doi.org/10.6028/jres.070C.025>.
- [166] Siemens Process Systems Engineering. gPROMS Process Home 2022. <https://www.psenterprise.com/products/gproms/process/> (accessed May 20, 2022).
- [167] Oh M, Pantelides CC. A modelling and simulation language for combined lumped and distributed parameter systems. *Comput Chem Eng* 1996;20:611–33. [https://doi.org/10.1016/0098-1354\(95\)00196-4](https://doi.org/10.1016/0098-1354(95)00196-4).
- [168] Lafitte T, Apostolakou A, Avendaño C, Galindo A, Adjiman CS, Müller EA, et al. Accurate statistical associating fluid theory for chain molecules formed from Mie segments. *Journal of Chemical Physics* 2013;139. <https://doi.org/10.1063/1.4819786>.
- [169] Papaioannou V, Lafitte T, Avendaño C, Adjiman CS, Jackson G, Müller EA, et al. Group contribution methodology based on the statistical associating fluid theory for heteronuclear molecules formed from Mie segments. *Journal of Chemical Physics* 2014;140. <https://doi.org/10.1063/1.4851455>.
- [170] Horng TC, Ajlan M, Lee LL, Starling KE, Ajlan M. Generalized Multiparameter Correlation for Nonpolar and Polar Fluid Transport Properties. *Ind Eng Chem Res* 1988;27:671–9. <https://doi.org/10.1021/ie00076a024>.
- [171] Hayduk W, Minhas BS. Correlations for prediction of molecular diffusivities in liquids. *Can J Chem Eng* 1982;60:295–9. <https://doi.org/10.1002/cjce.5450600213>.
- [172] Astrom KJ. Maximum Likelihood and Prediction Error Methods. *IFAC Proceedings Volumes* 1979;12:551–74. [https://doi.org/10.1016/s1474-6670\(17\)53976-2](https://doi.org/10.1016/s1474-6670(17)53976-2).

- [173] Devore JL. Probability and Statistics for Engineering and the Sciences. vol. 47. 8th ed. 2010. <https://doi.org/10.2307/2532427>.
- [174] Loosdrecht MCM van, Nielsen PH, Lopez-Vazquez CM, Brdjanovic D. Experimental Methods in Wastewater Treatment. IWA Publishing; 2016.
- [175] Nocedal J, Wright SJ. Numerical Optimization. 2nd ed. Springer Science+Business Media; 2006.
- [176] Dekking FM, Kraaikamp C, Lopuhaa HP, Meester LE. A Modern Introduction to Probability and Statistics. Delft: Springer-Verlag London Limited; 2005.
- [177] Shonkwiler RW, Mendivil F. Explorations in Monte Carlo Methods. Springer Science+Business Media, LLC; 2009.
- [178] Cockrell C, Brazhkin V V., Trachenko K. Transition in the supercritical state of matter: Review of experimental evidence. Phys Rep 2021;941:1–27. <https://doi.org/10.1016/j.physrep.2021.10.002>.
- [179] Cussler EL. Diffusion: Mass Transfer in Fluid Systems. Cambridge University Press; 2009.
- [180] Ravi R, Vinu R, Gummadi SN. Coulson and Richardson's Chemical Engineering, Volume 3A - Chemical and Biochemical Reactors and Reaction Engineering. 4th ed. Elsevier; 2017. <https://doi.org/10.1016/C2014-0-01372-X>.
- [181] Levenspiel O. Chemical Reaction Engineering. 3rd ed. John Wiley & Sons, Inc.; 1999.
- [182] Danckwerts PV. Continuous flow systems. Chem Eng Sci 1953;2:1–13. [https://doi.org/10.1016/0009-2509\(53\)80001-1](https://doi.org/10.1016/0009-2509(53)80001-1).
- [183] Oh M. Modelling and simulation of combined lumped and distributed processes. Imperial College of Science, Technology and Medicine, 1995.
- [184] Schwaab M, Pinto JC. Optimum reference temperature for reparameterization of the Arrhenius equation. Part 1: Problems involving one kinetic constant. Chem Eng Sci 2007;62:2750–64. <https://doi.org/10.1016/j.ces.2007.02.020>.
- [185] Coulson JM, Richardson JF, Backhurst JR, Harker JH. Coulson and Richardson's Chemical Engineering Volume 1 - Fluid Flow, Heat Transfer and Mass Transfer. 6th ed. Elsevier; 1999.
- [186] Silverstein TP, Heller ST. PKa Values in the Undergraduate Curriculum: What Is the Real pKa of Water? J Chem Educ 2017;94:690–5. <https://doi.org/10.1021/acs.jchemed.6b00623>.
- [187] Teledyne SSI. Documents, Manuals, and Downloads - Teledyne SSI 2022. <https://www.teledynessi.com/manuals> (accessed June 9, 2022).

- [188] Teledyne Isco. Pumps product manuals - Teledyne Isco 2022. <https://www.teledyneisco.com/en-us/pumps/manuals> (accessed June 9, 2022).
- [189] Thermostatic Mixing Valve Manufacturers Association. Recommended Code of Practice for Safe Water Temperatures. London: 2000.
- [190] Sinnott RK, Coulson JM, Richardson JF. Chemical Engineering Volume 6 - Design. vol. 6. 4th ed. Elsevier; 2005.
- [191] TC limited. Type K Thermocouple - TC ltd 2022. <https://www.tc.co.uk/thermocouples/type-k-thermocouple.html> (accessed June 10, 2022).
- [192] Tighe CJ, Gruar RI, Ma CY, Mahmud T, Wang XZ, Darr JA. Investigation of counter-current mixing in a continuous hydrothermal flow reactor. *Journal of Supercritical Fluids* 2012;62:165–72. <https://doi.org/10.1016/j.supflu.2011.11.027>.
- [193] Chung TJ. Computational Fluid Dynamics. Cambridge University Press; 2010. <https://doi.org/10.1017/CBO9780511780066>.
- [194] Magoules F. Computational Fluid Dynamics. Chapman and Hall/CRC; 2011. <https://doi.org/10.1201/b11033>.
- [195] Li QY, Wang XZ. Population balance and cfd simulation of particle aggregation and growth in a continuous confined jet mixer for hydrothermal synthesis of nanocrystals. *Crystals (Basel)* 2021;11:1–15. <https://doi.org/10.3390/cryst11020144>.
- [196] Lira-Teco JE, Rivera F, Farías-Moguel O, Torres-González J, Reyes Y, Antaño-López R, et al. Comparison of experimental and CFD mass transfer coefficient of three commercial turbulence promoters. *Fuel* 2016;167:337–46. <https://doi.org/10.1016/j.fuel.2015.11.053>.
- [197] Marum VJ de O, Reis LB, Maffei FS, Ranjbarzadeh S, Korkischko I, Gioria R dos S, et al. Performance analysis of a water ejector using Computational Fluid Dynamics (CFD) simulations and mathematical modeling. *Energy* 2021;220:119779. <https://doi.org/10.1016/j.energy.2021.119779>.
- [198] Ghasemzadeh K, Ghahremani M, Yousefi Amiri T, Basile A, Iulianelli A. Hydrogen production by silica membrane reactor during dehydrogenation of methylcyclohexane: CFD analysis. *Int J Hydrogen Energy* 2021;46:19768–77. <https://doi.org/10.1016/j.ijhydene.2020.05.046>.
- [199] Faizal A, Deshpande A. Modeling and CFD simulation of heat transfer process coupled with Unmixed Combustion for the application of generating superheated steam. *Appl Therm Eng* 2022;209:118286. <https://doi.org/10.1016/j.applthermaleng.2022.118286>.

- [200] Gyurik L, Ulbert Z, Molnár B, Varga T, Chován T, Egedy A. CFD Based Nozzle Design for a Multijet Mixer. *Chemical Engineering and Processing - Process Intensification* 2020;157. <https://doi.org/10.1016/j.cep.2020.108121>.
- [201] Reis LB, Gioria R dos S. Optimization of liquid jet ejector geometry and its impact on flow fields. *Appl Therm Eng* 2021;194:117132. <https://doi.org/10.1016/j.applthermaleng.2021.117132>.
- [202] Sangare D, Bostyn S, Moscossa-Santillan M, Gökalp I. Hydrodynamics, heat transfer and kinetics reaction of CFD modeling of a batch stirred reactor under hydrothermal carbonization conditions. *Energy* 2021;219. <https://doi.org/10.1016/j.energy.2020.119635>.
- [203] Aliaga DM, Feick R, Brooks WK, Mery M, Gers R, Levi JF, et al. Modified solar chimney configuration with a heat exchanger: Experiment and CFD simulation. *Thermal Science and Engineering Progress* 2021;22:100850. <https://doi.org/10.1016/j.tsep.2021.100850>.
- [204] Khaled C, Driss N, Nouredine SC. CFD Simulation of Turbulent Flow and Heat Transfer over Rough Surfaces. *Energy Procedia* 2015;74:909–18. <https://doi.org/10.1016/j.egypro.2015.07.826>.
- [205] Wilcox DC. Formulation of the $k-\omega$ turbulence model revisited. *AIAA Journal* 2008;46:2823–38. <https://doi.org/10.2514/1.36541>.
- [206] Kays WM. Turbulent Prandtl Number - Where are we? 1994.
- [207] Hill Bembenic MA, Burgess Clifford CE. Subcritical water reactions of lignin-related model compounds with nitrogen, hydrogen, carbon monoxide, and carbon dioxide gases. *Energy and Fuels* 2013;27:6681–94. <https://doi.org/10.1021/ef401113a>.
- [208] Fisher Scientific. Lab Equipment and Lab Supplies 2023. <https://www.fishersci.co.uk/gb/en/home.html> (accessed May 1, 2023).
- [209] Townsend H. Dibenzyl ether as a probe into the supercritical fluid solvent extraction volatiles from coal with water 1985;64:635–8.
- [210] Townsend SH, Abraham MA, Huppert GL, Klein MT, Paspek SC. Solvent Effects during Reactions in Supercritical Water 1988:143–9. <https://doi.org/10.1021/ie00073a026>.
- [211] Torry LA, Kaminsky R, Klein MT, Klotz MR. The effect of salts on hydrolysis in supercritical and near-critical water: Reactivity and availability. *J Supercrit Fluids* 1992;5:163–8. [https://doi.org/10.1016/0896-8446\(92\)90003-3](https://doi.org/10.1016/0896-8446(92)90003-3).
- [212] Funazukuri T, Serikawa RM, Yamaura K. Rate of dibenzyl ether decomposition in supercritical water. *Fuel* 1997;76:865–70. [https://doi.org/10.1016/S0016-2361\(97\)00055-0](https://doi.org/10.1016/S0016-2361(97)00055-0).

- [213] Comisar CM, Hunter SE, Walton A, Savage PE. Effect of pH on ether, ester, and carbonate hydrolysis in high-temperature water. *Ind Eng Chem Res* 2008;47:577–84. <https://doi.org/10.1021/ie0702882>.
- [214] Eagleson M. *Concise Encyclopedia Chemistry*. De Gruyter; 1994. <https://doi.org/10.1515/9783110854039>.
- [215] Klein MT, Torry LA, Wu BC, Townsend SH, Paspek SC. Hydrolysis in supercritical water: Solvent effects as a probe of the reaction mechanism. *J Supercrit Fluids* 1990;3:222–7. [https://doi.org/10.1016/0896-8446\(90\)90026-I](https://doi.org/10.1016/0896-8446(90)90026-I).
- [216] Penninger JML, Kersten RJA, Baur HCL. Reactions of diphenylether in supercritical water - Mechanism and kinetics. *Journal of Supercritical Fluids* 1999;16:119–32. [https://doi.org/10.1016/S0896-8446\(99\)00024-8](https://doi.org/10.1016/S0896-8446(99)00024-8).
- [217] Smith MB, March J. *March's Advanced Organic Chemistry: Reactions, Mechanisms, and Structure*. 7th ed. 2013.
- [218] Murzin DYu. *Engineering Catalysis*. De Gruyter; 2020. <https://doi.org/10.1515/9783110614435>.
- [219] Solomons TWG, Fryhle CB, Snyder SA. *Organic chemistry*. 11th ed. John Wiley & Sons, Inc.; 2014.
- [220] Oomori T, Khajavi SH, Kimura Y, Adachi S, Matsuno R. Hydrolysis of disaccharides containing glucose residue in subcritical water. *Biochem Eng J* 2004;18:143–7. <https://doi.org/10.1016/j.bej.2003.08.002>.
- [221] Haghghat Khajavi S, Kimura Y, Oomori T, Matsuno R, Adachi S. Kinetics on sucrose decomposition in subcritical water. *LWT - Food Science and Technology* 2005;38:297–302. <https://doi.org/10.1016/j.lwt.2004.06.005>.
- [222] Steinbach D, Kruse A, Sauer J, Vetter P. Sucrose is a promising feedstock for the synthesis of the platform chemical hydroxymethylfurfural. *Energies (Basel)* 2018;11. <https://doi.org/10.3390/en11030645>.
- [223] Feng L, Li G, Yan Y, Hou W, Zhang Y, Tang Y. Direct conversion of C6 sugars to methyl glycerate and glycolate in methanol. *RSC Adv* 2018;8:30163–70. <https://doi.org/10.1039/c8ra05612a>.
- [224] Wan Y, Zheng C, Lei X, Zhuang M, Lin J, Hu W, et al. Oxidative esterification of acetol with methanol to methyl pyruvate over hydroxyapatite supported gold catalyst: Essential roles of

- acid-base properties. *Chinese Journal of Catalysis* 2019;40:1810–9. [https://doi.org/10.1016/S1872-2067\(19\)63368-1](https://doi.org/10.1016/S1872-2067(19)63368-1).
- [225] Troupe RA, Kobe KA. Kinetics of Methanol–Lactic Acid Reaction - Reactions with 85% Acid. *Ind Eng Chem* 1950;42:801–10. <https://doi.org/10.1021/ie50485a020>.
- [226] Hu X, Lievens C, Larcher A, Li CZ. Reaction pathways of glucose during esterification: Effects of reaction parameters on the formation of humin type polymers. *Bioresour Technol* 2011;102:10104–13. <https://doi.org/10.1016/j.biortech.2011.08.040>.
- [227] Bower S, Wickramasinghe R, Nagle NJ, Schell DJ. Modeling sucrose hydrolysis in dilute sulfuric acid solutions at pretreatment conditions for lignocellulosic biomass. *Bioresour Technol* 2008;99:7354–62. <https://doi.org/10.1016/j.biortech.2007.05.045>.
- [228] Melro E, Alves L, Antunes FE, Medronho B. A brief overview on lignin dissolution. *J Mol Liq* 2018;265:578–84. <https://doi.org/10.1016/j.molliq.2018.06.021>.
- [229] Melro E, Filipe A, Sousa D, Valente AJM, Romano A, Antunes FE, et al. Dissolution of kraft lignin in alkaline solutions. *Int J Biol Macromol* 2020;148:688–95. <https://doi.org/10.1016/j.ijbiomac.2020.01.153>.
- [230] Alves L, Medronho B, Antunes FE, Topgaard D, Lindman B. Dissolution state of cellulose in aqueous systems. 1. Alkaline solvents. *Cellulose* 2016;23:247–58. <https://doi.org/10.1007/s10570-015-0809-6>.
- [231] Alves L, Medronho B, Antunes FE, Topgaard D, Lindman B. Dissolution state of cellulose in aqueous systems. 2. Acidic solvents. *Carbohydr Polym* 2016;151:707–15. <https://doi.org/10.1016/j.carbpol.2016.06.015>.
- [232] Bureau International des Poids et Mesures - 9th edition. *The International System of Units*. 2019.